ERL-0193-SD

LEVEL

AR-002-576

DEPARTMENT OF DEFENCE

DEFENCE SCIENCE AND TECHNOLOGY ORGANISATION

ELECTRONICS RESEARCH LABORATORY

DEFENCE RESEARCH CENTRE SALISBURY
SOUTH AUSTRALIA

SPECIAL DOCUMENT

ERL-0193-SD

PROCEEDINGS OF THE FOURTH LASER HYDROGRAPHY SYMPOSIUM

30 SEPTEMBER - 3 OCTOBER 1980

DEFENCE RESEARCH CENTRE SALISBURY, SOUTH AUSTRALIA

AND

ROYAL AUSTRALIAN NAVY HYDROGRAPHIC OFFICE
NORTH SYDNEY, NEW SOUTH WALES

Edited by

M.F. PENNY and D.M. PHILLIPS

Approved for Public Release

COPY No. 05

81 10 26 087

DEPARTMENT OF DEFENCE

AR-002-576

DEFENCE SCIENCE AND TECHNOLOGY ORGANISATION

ELECTRONICS RESEARCH LABORATORY

SPECIAL DOCUMENT

ERL-0193-SD

PROCEEDINGS OF THE FOURTH LASER HYDROGRAPHY SYMPOSIUM

30 SEPTEMBER - 3 OCTOBER 1980

AT

DEFENCE RESEARCH CENTRE SALISBURY, SOUTH AUSTRALIA

AND

ROYAL AUSTRALIAN NAVY HYDROGRAPHIC OFFICE,

NORTH SYDNEY, NEW SOUTH WALES

F. Penny and D.M. Phillips

Editors

SUMMARY

At this Symposium, research on laser hydrography and related
development programs currently in progress in the United
States of America, Canada, and Australia, were reported. The
depth sounding systems described include the US Airborne
Oceanographic Lidar and Hydrographic Airborne Laser Sounder,
the Canadian Profiling Lidar Bathymeter, and the Australian
Laser Airborne Depth Sounder. Other papers presented
research on blue-green lasers, theoretical modelling, position
fixing, and data processing.

DOCUMENT CONTROL DATA SHEET

Security classification of this page | UNCLASSIFIED

1	DOCUMENT NUMBERS	2	SECURITY CLASSIFICATION

AR Number:	AR-002-576

Report Number:	ERL-0193-SD

Other Numbers:	

a. Complete Document:	Unclassified

b. Title in Isolation:	Unclassified

c. Summary in Isolation:	Unclassified

3 TITLE

PROCEEDINGS OF THE FOURTH LASER HYDROGRAPHY SYMPOSIUM

4 PERSONAL AUTHOR(S):

M.F. Penny and D.M. Phillips

5 DOCUMENT DATE:

April 1981

6	6.1	TOTAL NUMBER OF PAGES	550

	6.2	NUMBER OF REFERENCES:	

7 7.1 CORPORATE AUTHOR(S):

Electronics Research Laboratory

7.2 DOCUMENT SERIES AND NUMBER

Electronics Research Laboratory
0193-TR

8 REFERENCE NUMBERS

a. Task:	NAVY 77/020

b. Sponsoring Agency:	

9 COST CODE:

313413

10 IMPRINT (Publishing organisation)

Defence Research Centre Salisbury

11 COMPUTER PROGRAM(S)
(Title(s) and language(s))

12 RELEASE LIMITATIONS (of the document):

Approved for Public Release

12.0	OVERSEAS	NO	P.R.	1	A		B		C		D		E	

Security classification of this page: | UNCLASSIFIED

---

13 | ANNOUNCEMENT LIMITATIONS (of the information on these pages):

No limitation

---

14 | DESCRIPTORS: | | **15** | COSATI CODES:

a. EJC Thesaurus Terms

Lasers	Optical radar
Hydrography	Data processing
Meetings	Position finding
Depth sounding	
Airborne equipment	

2005
0810

b. Non-Thesaurus Terms

WRELADS
Airborne oceanographic lidar
Hydrographic airborne laser sounder
Profiling lidar bathymeter
Laser airborne depth sounder

---

16 | LIBRARY LOCATION CODES (for libraries listed in the distribution):

---

17 | SUMMARY OR ABSTRACT:
(if this is security classified, the announcement of this report will be similarly classified)

At this Symposium, research on laser hydrography and related development programs currently in progress in the United States of America, Canada, and Australia, were reported. The depth sounding systems described include the US Airborne Oceanographic Lidar and Hydrographic Airborne Laser Sounder, the Canadian Profiling Lidar Bathymeter, and the Australian Laser Airborne Depth Sounder. Other papers presented research on blue-green lasers, theoretical modelling, position fixing, and data processing.

Accession

NTIS GRA&I
DTIC T'B
Unannounced
Justification

By
Distribution/

Availability Codes
Avail and/or
Dist   Special

A

TABLE OF CONTENTS

ERL-0193-SD

LIST OF DELEGATES

NAME	ORGANISATION	PAPER
UNITED STATES OF AMERICA		
Mr M.T. Cooper	Naval Coastal Systems Center	16
Mr D.B. Enabnit	NOAA/National Ocean Survey	6, 7, 25
Mr G. Ferguson	Naval Air Development Center	13
Mr G.C. Guenther	NOAA/National Ocean Survey	8, 19, 22
Mr M. Houck	Naval Ocean Research & Development Activity	4, 26
Dr M.J. Miller	AVCO Everett Research Laboratories	12, 20, 30
CDR V.K. Nield	Defense Mapping Agency	2
Mr R.N. Swift	EG&G Washington Analytical Services	9, 27
Dr R.W. Thomas	EG&G Inc. Bedford, Massachusetts	19, 22
Dr M.B. White	Office of Naval Research	14
CANADA		
Mr A.J. Dow	Canadian Hydrographic Service	3, 24
Dr R. O'Neil	Canada Centre for Remote Sensing	3, 5
UNITED KINGDOM		
CMDR D.C. Webb	Hydrographic Department	
Mr P. Reich	BDRSS	
FRANCE		
Mr P. Souquiere	Hydrographic & Oceanographic Service	

NAME	ORGANISATION	PAPER
AUSTRALIA - EASTERN STATES		
Mr K. Burrows	Hydrographic Service, RAN	23
CAPT M. Calder	Hydrographic Service/RAN	1
Mr J.H. Cohen	DSTO Canberra	
COL P.R. Eddy	Army Survey Canberra	
Mr J. Garlick	DSTO Canberra	
CMDR P.R. Hart	Navy Office Canberra	
Mr B.A. Murphy	Division of National Mapping	
Mr J.E. Patterson	DIMP Canberra	
Mr D. Pender	DSTO Canberra	
LCDR M.W. Varley	Staff Office, Hydrography	
SOUTH AUSTRALIA		
Mr R.H. Abbot	Electronics Research Laboratory	10
Mr V.J. Bosher	Electronics Research Laboratory	
Mr L.J. Dunne	Electronics Research Laboratory	
Mr D.W. Faulkner	Electronics Research Laboratory	15
Mr K. Fueloep	Electronics Research Laboratory	
LEUT M.F. Gale	Hydrographic Service/RAN	15
Mr B.W. Koerber	Electronics Research Laboratory	
Mr M.F. Penny	Electronics Research Laboratory	1
Dr D.M. Phillips	Electronics Research Laboratory	17, 21
Mr J.R. Pyle	Electronics Research Laboratory	
Mr D. Rees	Electronics Research Laboratory	
Dr J. Richards	Electronics Research Laboratory	
Mr M.L. Scholz	Electronics Research Laboratory	
Mr V.W. Thomas	Electronics Research Laboratory	
Mr G.J. Watts	Electronics Research Laboratory	18
Mr P.J. Wilsen	Electronics Research Laboratory	
Mr B. Woodcock	Electronics Research Laboratory	
Mr L. Spaans	Advanced Engineering Laboratory	
GPCAPT R. Green	RAAF: Aircraft Research and Development Unit	
Dr G. Morgan	RAAF: Aircraft Research and Development Unit	
Mr B.A. See	Quentron Optics Pty Ltd (formerly ERL)	11

ORGANISATIONS REPRESENTED

UNITED STATES OF AMERICA

Avco Everett Research Laboratory Inc.
2385 Revere Beach Parkway
Everett
Massachusetts   01249

Defence Mapping Agency
Building 56
US Naval Observatory
Washington   DC   20305

EG&G
6801 Kenilworth Avenue
Riverdale   MD   20840

Naval Air Development Center
Warminster
Pennsylvannia   18974

Naval Coastal Systems Center
Panama City
Florida

Naval Ocean Research & Development Activity
Navy Department
NSTL Station
Bay Street   Louis
Mississippi   39529

NOAA/National Ocean Survey
Engineering Development Laboratory
6001 Executive Blvd
Rockville   MD   20852

Office of Naval Research
Eastern/Central Regional Office
666 Summer Street
Boston
Massachusetts   02210

Washington Analytical Services Center Inc.
Box 476
Pomoke City
Maryland   21851

CANADA

  Canada Centre for Remote Sensing
  Department of Energy Mines & Resources
  2464 Sheffiled Road
  Ottawa,   Ontario   KIA OY7

  Canadian Hydrographic Service
  Data Acquisition Division
  Canada Centre for Remote Sensing
  Ottawa,   Ontario   KIA OY7

UNITED KINGDOM

  Hydrographic Department
  Ministry of Defence
  Taunton   Somerset   England

FRANCE

  Mission Oceanographique du Pacifique
  BP 38 Noumea
  New Caledonia

AUSTRALIA

  British Defence Research & Supply Staff
  3rd Floor
  Block 1 Anzac Park West Building
  Constitution Avenue
  Canberra   ACT   2600

  Army Survey
  Department of Defence
  Russell Offices
  Canberra   ACT   2600

  Aircraft Research & Development Unit
  Building 44
  Contractors Area
  DRCS   Salisbury   5108

  Defence Industry & Material Policy Division
  Industry Development Branch
  Russell Offices
  Canberra   ACT   2600

  Electronics Research Laboratory
  Defence Research Centre Salisbury
  Box 2151 GPO
  Adelaide   SA   5001

Defence Science & Technology Organisation
22 Andrews Street
Watson   ACT   2602

Division of National Mapping
7 Morrissett Street
Queanbeyan   NSW   2620

Hydrographic Service
RAN, PO Box 1332
North Sydney   NSW   2060

Quentron Optics Pty Ltd
75a Angas Street
Adelaide   SA   5000

Royal Australian Navy
Russell Offices
Canberra   ACT   2600

PAPER 1

AUSTRALIAN OVERVIEW

Captain M. Calder A.M. Hydrographer RAN

Mike Penny WRELADS Programme Manager

Defence Science and Technology Organisation
Electronics Research Laboratory
Salisbury   South Australia

In 1972 in response to a request from the Royal Australian Navy,
what is now the Electronics Research Laboratory began investigations into
techniques that might be employed to increase the speed, and reduce the
cost, of conducting hydrographic surveys of Australia's Continental Shelf.
Resulting from these investigations it was apparent that only airborne
laser techniques gave promise of any substantial manpower and cost
economy   while at the same time providing positive validation of data
obtained. In 1974 background work commenced at ERL in this new area of
technology and this has led to the experimental system WRELADS II, the
equipment you will see demonstrated this afternoon.

The Australian requirement for shallow water mapping is very real.
The Australian Continental Shelf covers an area of 660,000 square nautical
miles, half of which is less than 50 metres deep and just over a quarter
is less than 30 metres deep. It is in these shallow areas, which demand
close examination by surface vessels, that the gain of productivity by
operation of LADS, the manufactured version of WRELADS II, will be greatest.

It is not only the rate of coverage that will benefit the hydrographer,
since, due to the detail provided by LADS, the overall survey should be
superior to that estimated from running profiles established by echo
sounder.

The ship and the echo sounder, however, are far from being redundant.
Acoustic methods and airborne laser techniques fit different sections of
the overall hydrographic requirement and will undoubtedly compliment each
other. In my opinion, the airborne depth sounder will provide hydrographers
of the world with the most productive sounding system ever devised for
coastal waters. There are problems however, for example the handling and
storage of the data which you will hear more about on Friday at the
Hydrographic Office Sydney. Another area of possible concern relates to
the need for high precision survey over a particular hazard identified by
the airborne operation. This we envisage will be achieved by conventional
means in calm conditions.

In summary I suggest that history will show that laser airborne depth
sounding will have as profound an effect on hydrography as acoustic
sounding had in the days of the lead line. I would remind you that transi-
tion occurred only 50 years ago. I shall now ask Mike Penny to continue.

At the last Laser Hydrography Symposium held in Washington in October
1977 I reported on the exploratory WRELADS I Programme. Since that time
we have addressed the requirements of the RAN and developed the experimental
system WRELADS II, which has been installed in a C47 aircraft operated by
the RAAF Aircraft Research and Development Unit (ARDU). The equipment is
currently undergoing evaluation trials.

Figure 1 shows the system concept and highlights the need for two basic
subsystems, the laser depth sounding section, the position fixing and
navigation elements. Figure 2 shows the scanning principle. The IR out-
put of the frequency doubled Nd:YAG laser is projected vertically downward

to establish, by the integration of consecutive aircraft to sea measurements, a sea level datum. The 532 nm green component of the laser, used for subsurface interrogation, is scanned back and forth by a reflecting mirror which is oscillated about two axes to yield a rectangular pattern of depth soundings on the sea surface. Since the basic timing datum for depth measurements is originated in the IR channel an additional airpath traversed by the green beam i.e. H sec $(\phi - 1)$ must be calculated. H corresponds to aircraft height above the sea and ϕ the beam inclination. With this configuration the effect of waves on sounding accuracy is minimal since the error introduced arises from the assumption that the laser light is passing through water in lieu of air (or vice versa) for half the wave crest to trough vertical distance. Taking into account the respective light velocities in the two mediums the maximum error is approximately one seventh the crest to trough height.

Figure 3 shows the pattern of soundings generated in one second, by the scanning system described. Also shown for comparitive purposes is the output of a surface vessel, in shallow water, using an echo sounder. In addition to the obvious increase in speed of survey the diagram does illustrate an essential difference between the two techniques. Whereas airborne laser hydrography provides an area coverage, launch hydrography provides line profiles as a basis for chart production. Furthermore, side looking sonars and drag wire techniques, although capable of detecting obstacles between the line profiles, are unable to detect small perturbations in depth between the lines. A fundamental difference between the two techniques is therefore apparent: the traditional line sampling echo sounder approach, with little information about sea depth between the lines and the detailed grid of information provided by the laser technique. This suggests that in order to achieve a basic depth prediction of an area of sea bottom, the accuracy requirements for the airborne system, relative to the echo sounder, may be relaxed. This basic philosophy has influenced the RAN requirement which is illustrated in figure 4 i.e., one metre for single sounding accuracy and 0.5 metre for the special case described. Horizontal position, of each sounding referred to shore based datums is 25 metres.

Figure 5 shows part of the installation which comprises the Transmitting, Receiving and Scanner (TRS) assembly, Services Rack and Depth Sounding Rack. Figures 6 and 7 show the WRELADS under-floor bay and the Navigation Rack respectively. Two 42 pps identical lasers are mounted as the TRS assembly and operate alternately to provide a combined rate of 84 pps. Each laser develops 5 millijoule 5 nanosecond duration pulses at 532 nm. The lasers have been operating successfully for about a year but are shortly to be replaced by a single unit operating at 168 pps. One of the two laser options currently being evaluated for this task is a "Birefringence Coupled Laser" which is shown in figure 8.

A block diagram illustrating the depth sounding section of the equipment is shown in figure 9. The dual laser package contains a Coupling Unit which combines the outputs of the two lasers and then separates the beam into the green and IR components. This package will be simplified when the single laser is introduced.

The photomultiplier detector used in the green receiver (an EMI 9813-GB) is operated in a high gain, pulsed condition. Over the time period when subsurface signals are expected, the gain is automatically controlled for optimum signal detection. A method of changing the voltage of individual dynode has been developed in order to modify the gain of the tube. This technique, to compress dynamic range, permits gain to be changed in a controlled fashion as dictated by backscatter and reflected sunlight, throughout the 500 nanosecond time gate of the system, with no significant change in rise time or tube transit time. To allow for high current gain operation, the tube is pulsed on for the required period by a control grid.

The green subsurface signals are digitized at 2 nanosecond intervals
(equivalent to 0.2 metres depth) and stored in a Biomation type 6500 digitiser.
Data is read from this unit, processed to obtain depth and recorded for
subsequent re-analysis on the ground.

WRELADS uses the Cubic Western Data System ARGO DM54 for position fixing.
This equipment is now in standard use by the hydrographic ships of the RAN
but, in conjunction with the company, was modified for high speed airborne
WRELADS application. ARGO DM54 operates in the HF band using a shore based
chain of transmitting stations. For WRELADS, the system operates in a
dedicated hyperbolic format with position fixes established at a rate of three
per second. Using a nose to fin antenna, insensitivity to aircraft manoeuvres
have been demonstrated and a range in daylight of 250 nautical miles from an
inline transmitting chain.

Using a small on-board computer, a PDP11-03, lane count information is
converted from hyperbolic to Australian Map Grid Co-ordinates to simplify
computation and to aid mission planning and monitoring. The computer also
drives a pilots display for track keeping in straight and level survey runs
and for the display of course corrections in the end of run, 180° turns.
Again all data is recorded for analysis on the ground. The various elements
of the navigation/position fixing systems are shown in figure 10.

One major and obvious application region for WRELADS is the 2000 km long
Great Barrier Reef covering, with the coastal channel, approximately
100,000 square kilometers. In a four week period in July - August this
year the system was based at Townsville. Figure 11 shows the result of an
exploratory mission from Townsville northward along the reef, in a zig-zag
fashion, to the Torres Strait. The figure shows the extinction depths
recorded on that flight and Figure 12 shows estimated fluctuations in beam
attenuation coefficient (c) based on backscatter observations measured on
the same flight. This latter data have most significant implications since
if (c) can be estimated reliably then extinction depths can be predicted.
Thus, with a knowledge of extinction depth d_e, it is valid to predict that
should a bottom exist at a depth of d_e or less, then the bottom signal should
be detectable. However, if no bottom is detected then it can be assumed
that the water is deeper than d_e. With appropriate safety margins this
approach will make possible the class of sounding "No bottom at ..." This
information is understood to be of considerable use to hydrographic
authorities.

Figure 13 illustrates this type of sounding. The two uppermost sets of
soundings correspond to consecutive across track subsurface signals. The
lower set corresponds to the "No bottom at ..." class of sounding. The
method of determining (c) is based on backscatter measurements of the sub-
surface signal and will be discussed in later papers. The actual range of
(c) measured in this sortie covered two orders of magnitude i.e. .05 m^{-1} at
Ribbon Reef and 5.0 m^{-1} in the Torres Strait. It is of some interest to
note that the same region of the Torres Strait was line profiled in June 1977
with WRELADS I. In that instance excellent bottom signals were recorded.
The difference between the two results can be attributed to 35 - 40 knot
winds and the resulting high seas, existing at the time of the recent trial.
Such conditions would be expected to produce vertical mixing and hence,
because of the shallow bottom, an increase in water turbidity.

A microsurvey of a selected reef has been completed and photographs of
a model, constructed using WRELADS data, are shown in figures 14 and 15.
The latter shows the coral heads found in the reef lagoon. This survey
which took approximately one minute of flying time covered 1 square kilometer
further details will be presented later in the symposium.

In reference to aircraft track keeping it has now been demonstrated that tracks can be held to 10 m RMS error in the C47. This has been achieved with an appropriate display and pilot control and is within the operational requirement. The pilots task is demanding and preliminary planning for system operation is based on automatic pilot control for the straight survey runs, with pilot control in turns assisted by an optimised computer controlled display.
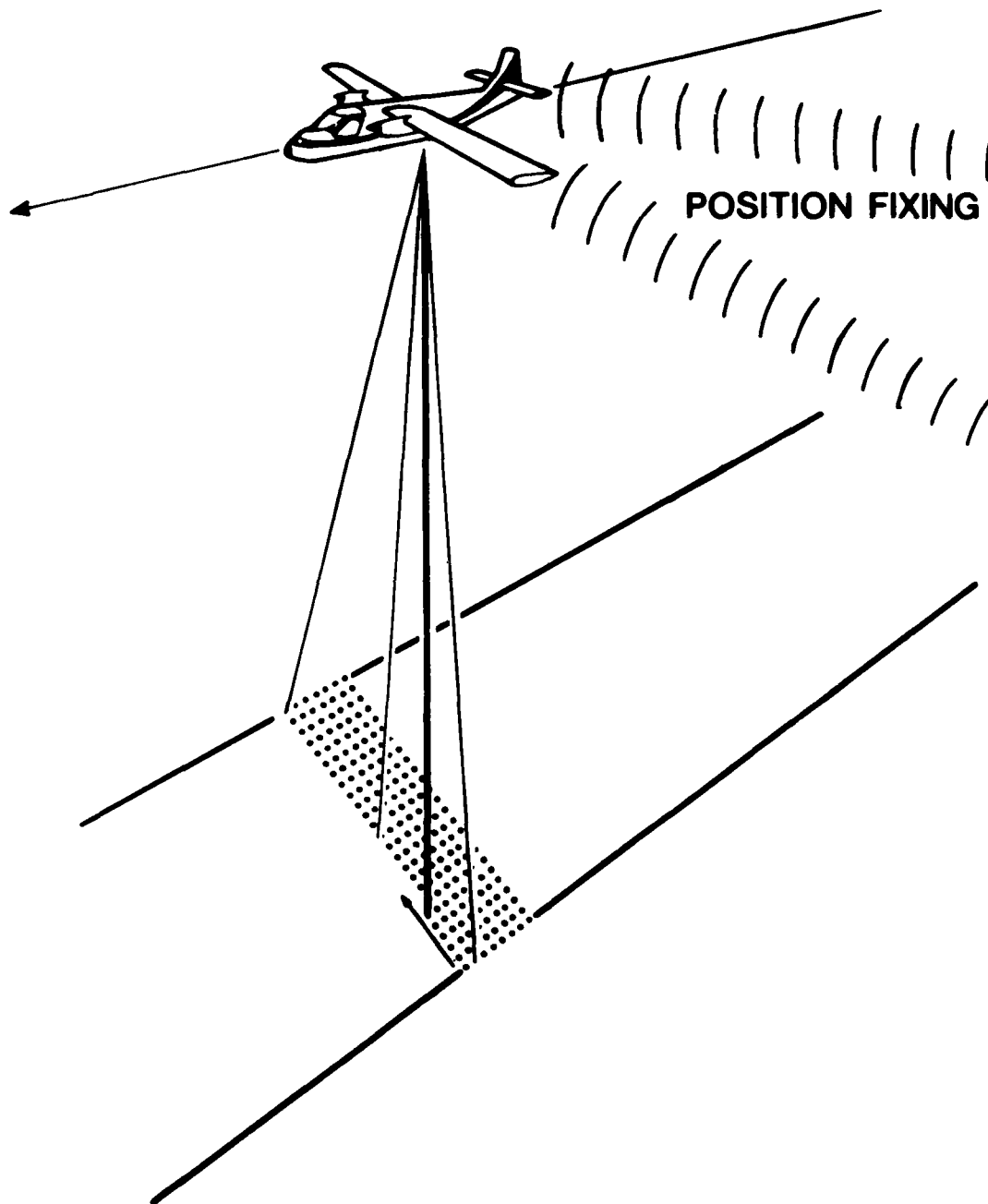
Let us now examine how the whole system is planned to operate. Figure 16 shows the various phases commencing with the airborne operation, working from land bases, on the left. The next phase, the Evaluation Process, although not changing the data, will be designed to confirm that the recorded information is sound in all respects.

The next transition involves the transfer of data from the field to the Hydrographic Office Sydney. Here the data will be processed to yield refined estimates of depth, and position (xyz) and a classification (C) appropriate to each sounding. Tidal corrections will also be made at this stage. Finally, the xyz and C data will be filed in a Hydrographic Data Bank at an estimated rate of 7.10^6 soundings per week. The data will subsequently be retrieved from the Data Bank for comparison with other data sources and will finally drive plotters to produce hydrographic charts.

Whilst the main thrust of the WRELADS Programme has been directed at developing the airborne system, background studies have been continued in a number of areas. These include studies using the WRELADS Test Tank, a 14 m vertical water column, and an installation at Port Stanvac to measure the slope frequency spectrum of the open sea together with other marine and meteorological parameters.

Boat work has continued for ground position fixing exercises and turbidity studies using transmissometer measurements of beam attenuation coefficient. The Department of Transport vessel Candela has been used for this work and also the RAAF SAR boat for the Townsville based trials.

Figure 17 shows a block diagram which reflects planning at the present time. The R&D elements of the programme will continue to 1983 and provides feedback into the production cycle. It is anticipated that contracts will be let to industry for the two production systems for operation use by Navy.

POSITION FIXING

WRELADS Ⅱ

Figure 1

GREEN BEAM
±15° TRANSVERSE SCAN

ϕ_B

IR BEAM
(HELD VERTICAL)

H
500 m

SKEW CORRECTION
H (sec ϕ_B -1)

(MAX. AMPLITUDE 17.6 m)

MAX. UNDERWATER
SKEW CORRECTION
0.6 m (D=30 m)

D

MAX. DISPLACEMENT
6 m
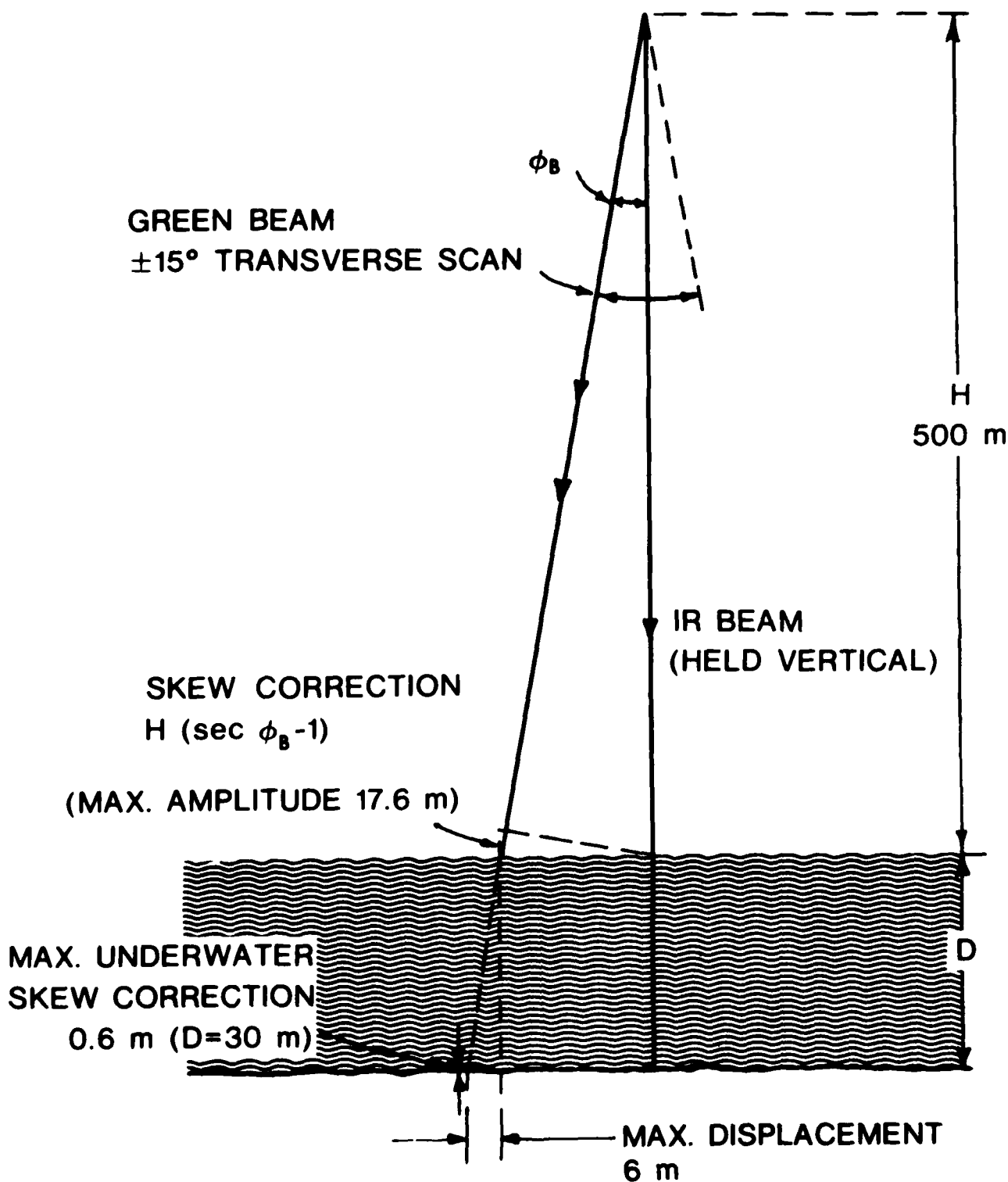
SCANNING GEOMETRY

Figure 2

SURFACE VESSEL
DEPTH SOUNDINGS RECORDED IN ONE SECOND

1 SECOND
(5 METRES)

BOAT TRACK

AIRCRAFT
DEPTH SOUNDINGS RECORDED IN ONE SECOND

268 m

AIRCRAFT TRACK

1 SECOND
70 METRES

Figure 3

CONSECUTIVE LASER PULSES

SEA SURFACE

NOMINAL SPACING
BETWEEN SOUNDINGS
10 METRES

POSITIONAL ACCURACY (XY)
25 METRES (WITH REFERENCE
TO SHORE DATUMS)

DEPTH
d

BOTTOM

$d(max) = (.019 + .048c)^{-1}$ metres.

where c = beam extinction coefficient m^{-1}

i.e. when $c = 0.3 \ m^{-1}$

$d = 30m$

DEPTH SOUNDING ACCURACY

INDIVIDUAL SOUNDINGS 1.0 METRE (10x10 m RESOLUTION)

FLAT BOTTOM CASE 0.5 METRE (30x30 m RESOLUTION)

Figure 4   FUNCTIONAL REQUIREMENT WRELADS II
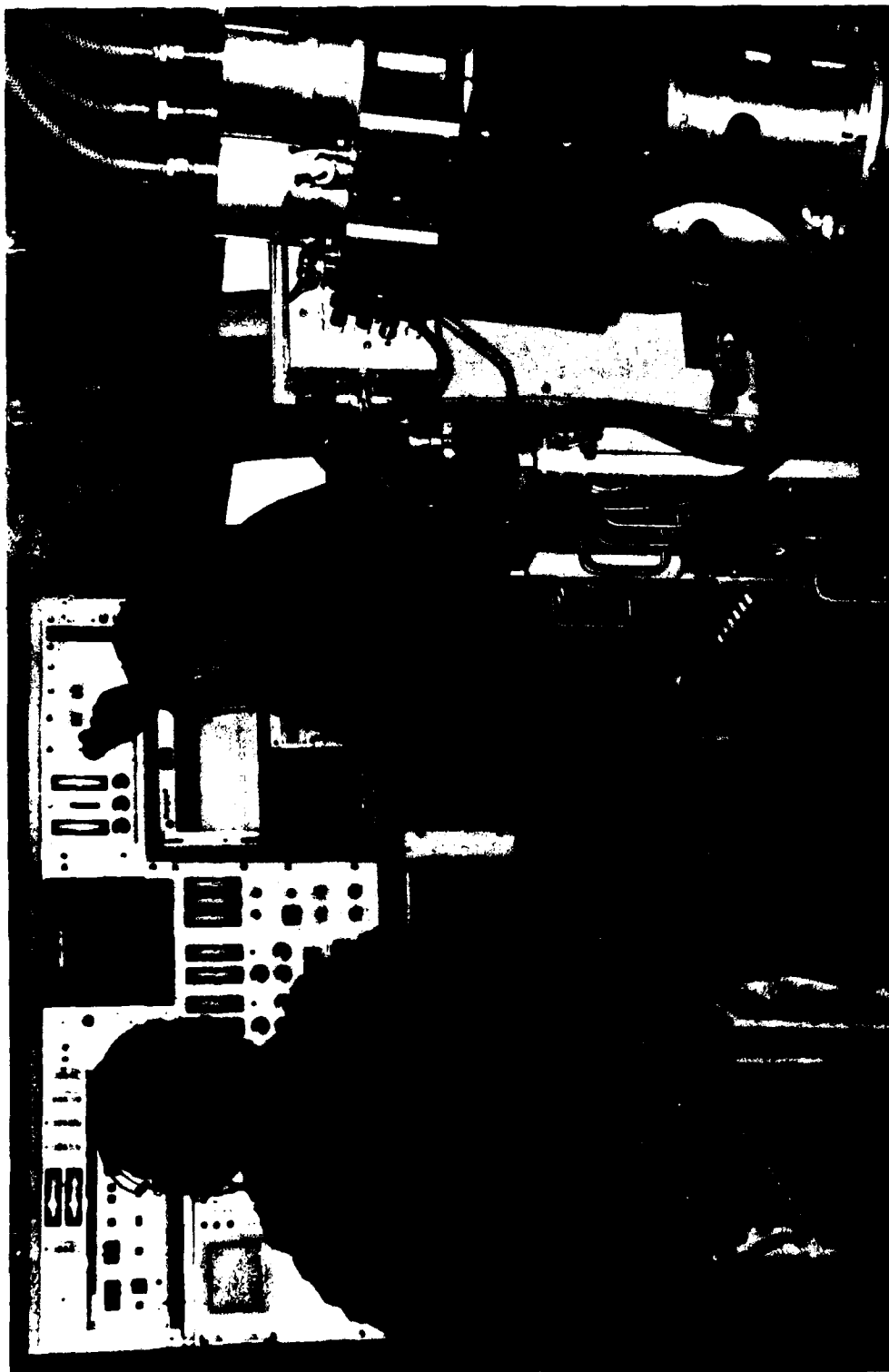
Figure 5   Part of the WRELADS II installation showing the TRS Assembly.
Services Rack and Depth Sounder Rack
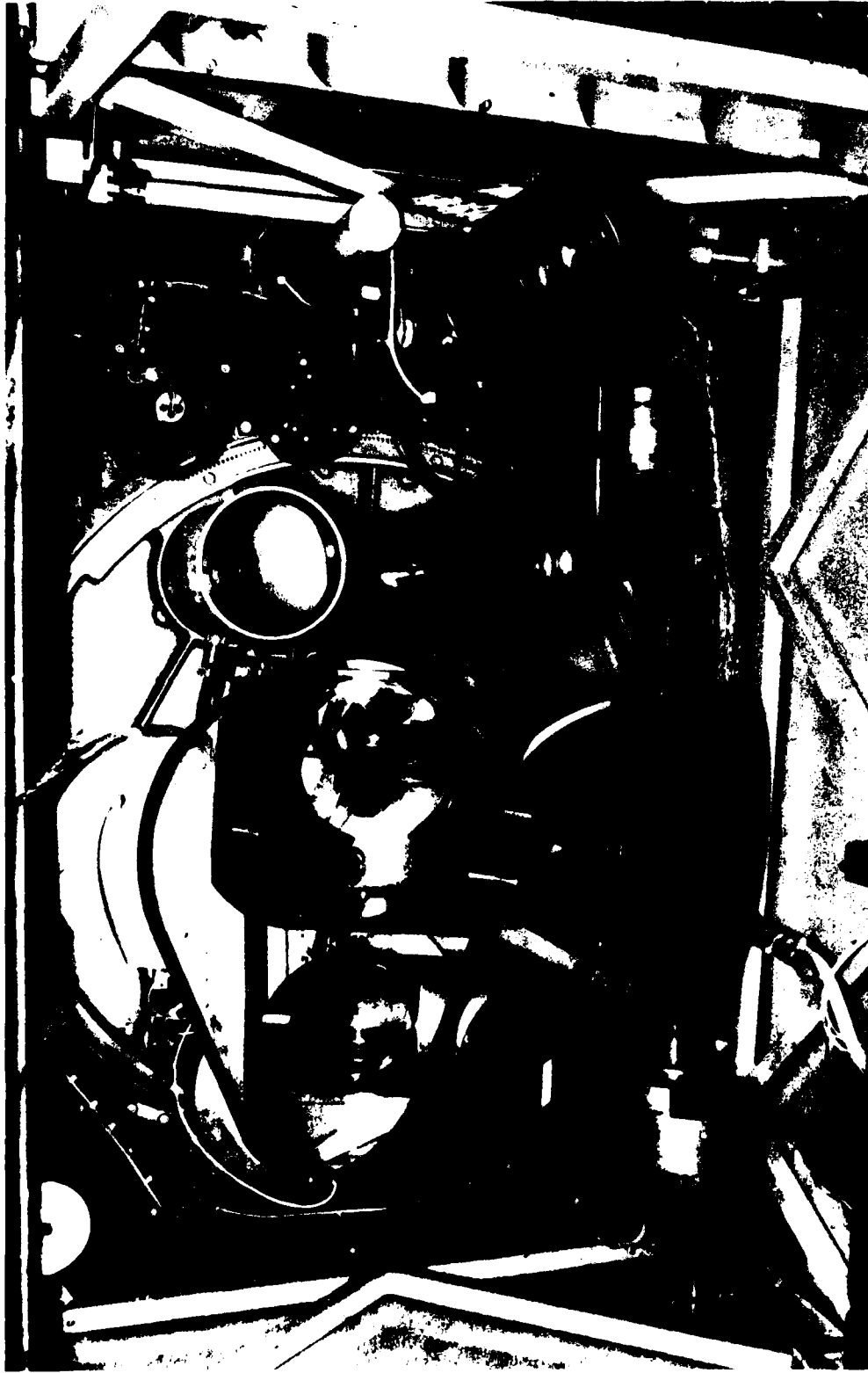
Figure 6 WRELADS under-floor bay showing Transmitting and Receiving Telescopes, Scanning Mirror, Camera and Elements associated with the Roll Stabilisation System

Figure 7   WRELADS Ⅱ Navigation Rack
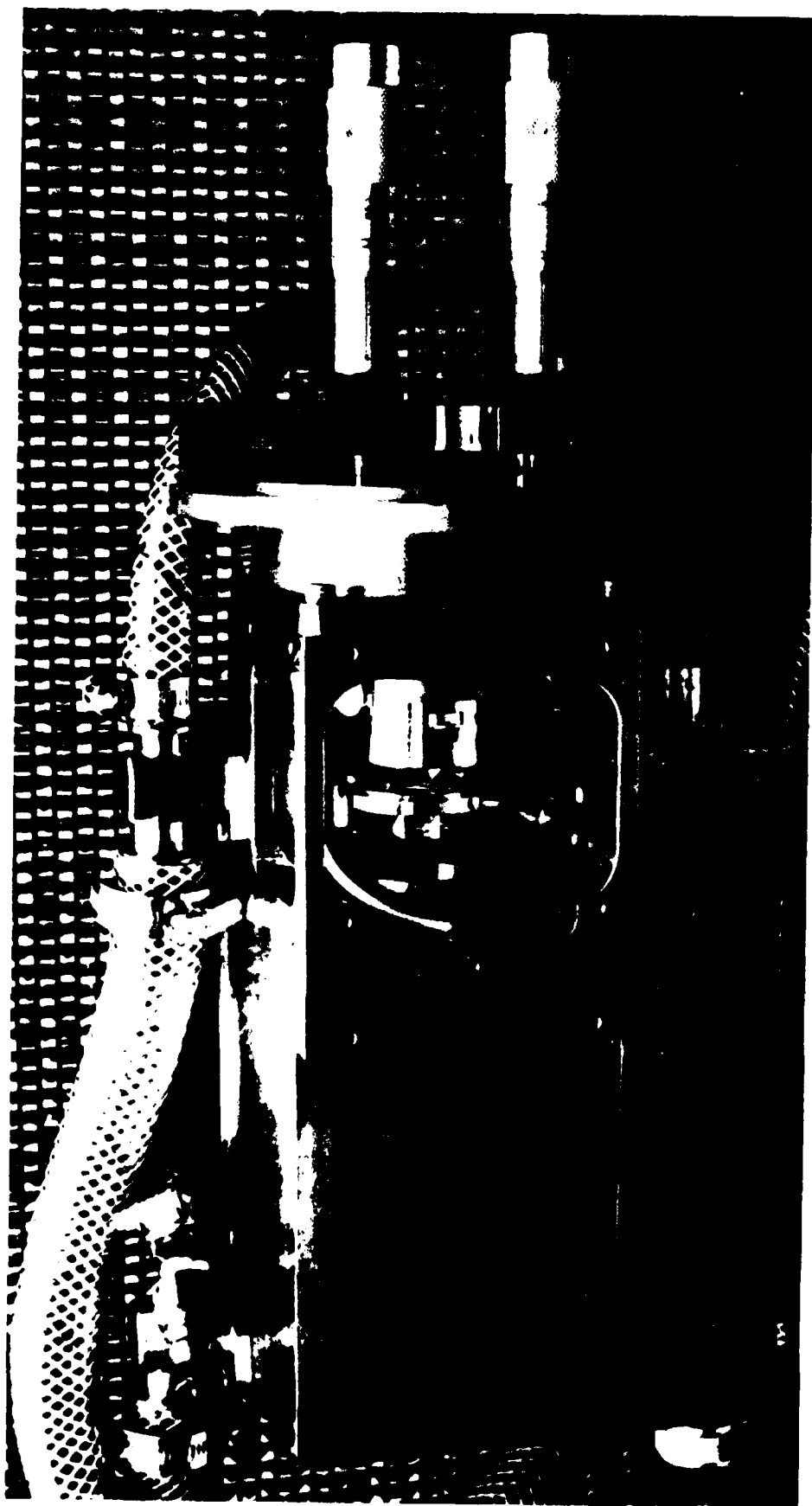
Figure 8   Birefringence Coupled Laser

ERL-0193-SD
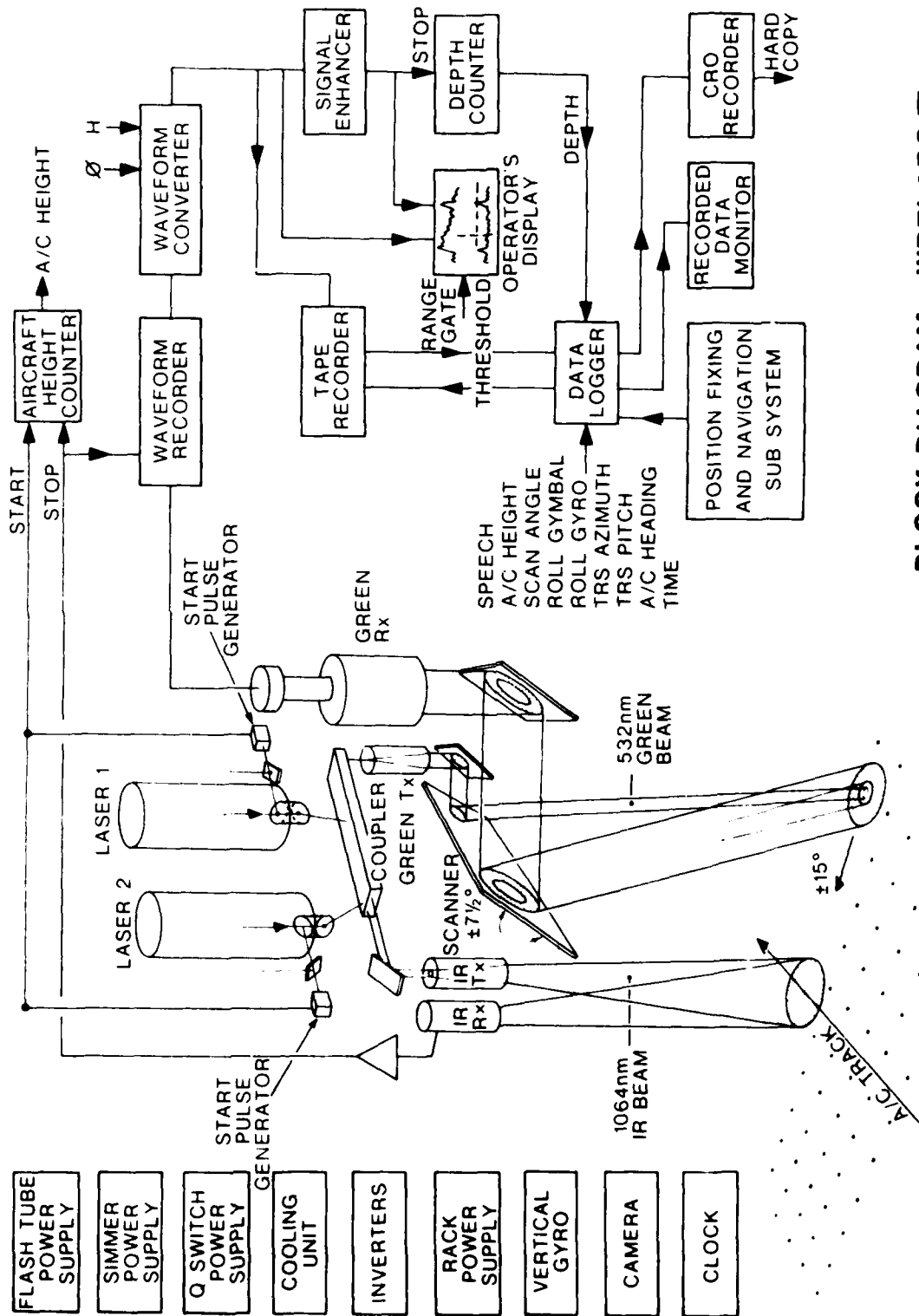
BLOCK DIAGRAM - WRELADS II

Figure 9

Figure 10

THURSDAY ISLAND

TRIAL No. 250T. 10.8
25k WIND SE.
CLEAR SUNNY
MODERATE SEAS

TRIAL No.249T.
35k. WINDS SE.
PATCHY CLOUD
HAZY SUN
ROUGH SEAS

BLACKWOOD
CHANNEL

YULE REEF

WEIPA

LONG SANDY REEF

BLIGHT REEF

EVE REEF
MORRIS ISLAND

TYDEMAN REEF

JEWEL REEF

COOKS PASSAGE

DEPTHS SHOWN ARE
EXTINCTION DEPTHS
(de)metres

RIBBON REEF

FORRESTER REEF

COOKTOWN

ARCHER PT

PICKERSGILL REEF

MORNING REEF

OPAL REEF

HOPE REEF

100   200   300

SCOTT REEF

KILOMETRES

KARUMBA

GIBSON REEF

POTTER REEF

PITH
REEF

KELSO
REEF

TOWNSVILLE

Figure 11

Figure 12

BOTTOM DETECTION

NO BOTTOM AT ....

CLASSIFICATION OF SOUNDINGS

Figure 13

BRITOMART REEF
TOWNSVILLE QUEENSLAND

250m

Figure 14

Figure 15

FIELD OPERATIONS   HYDROGRAPHIC OFFICE SYDNEY
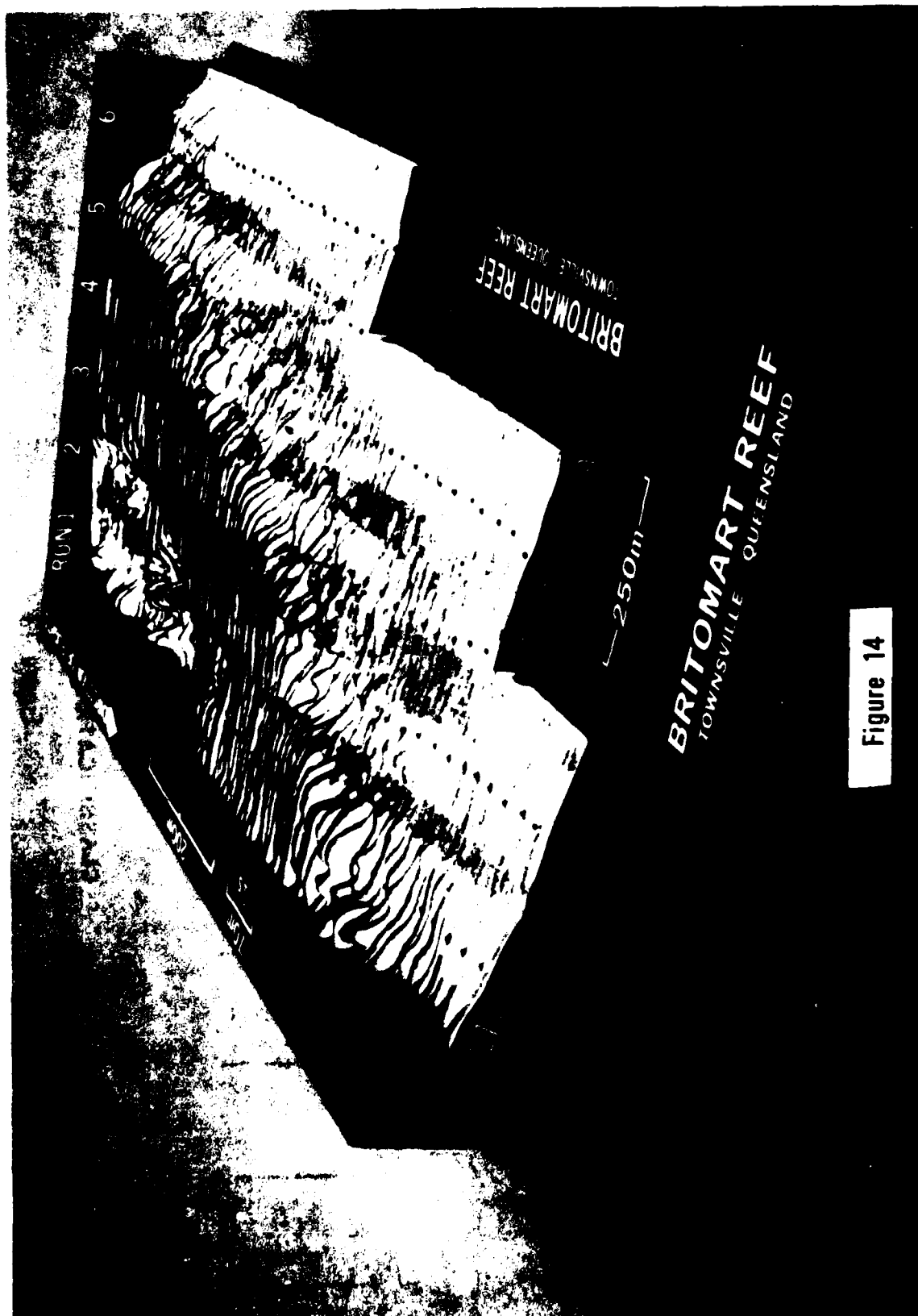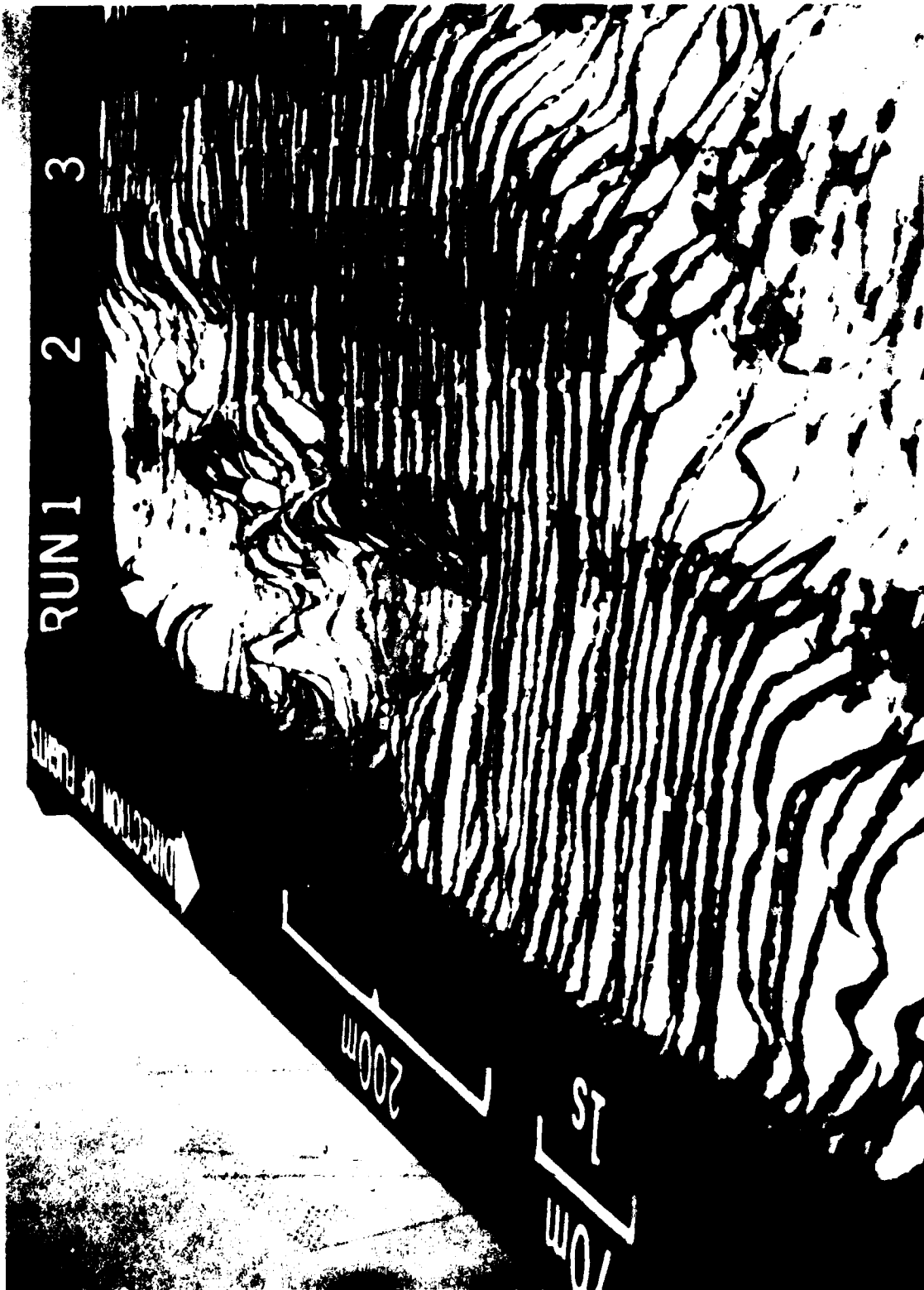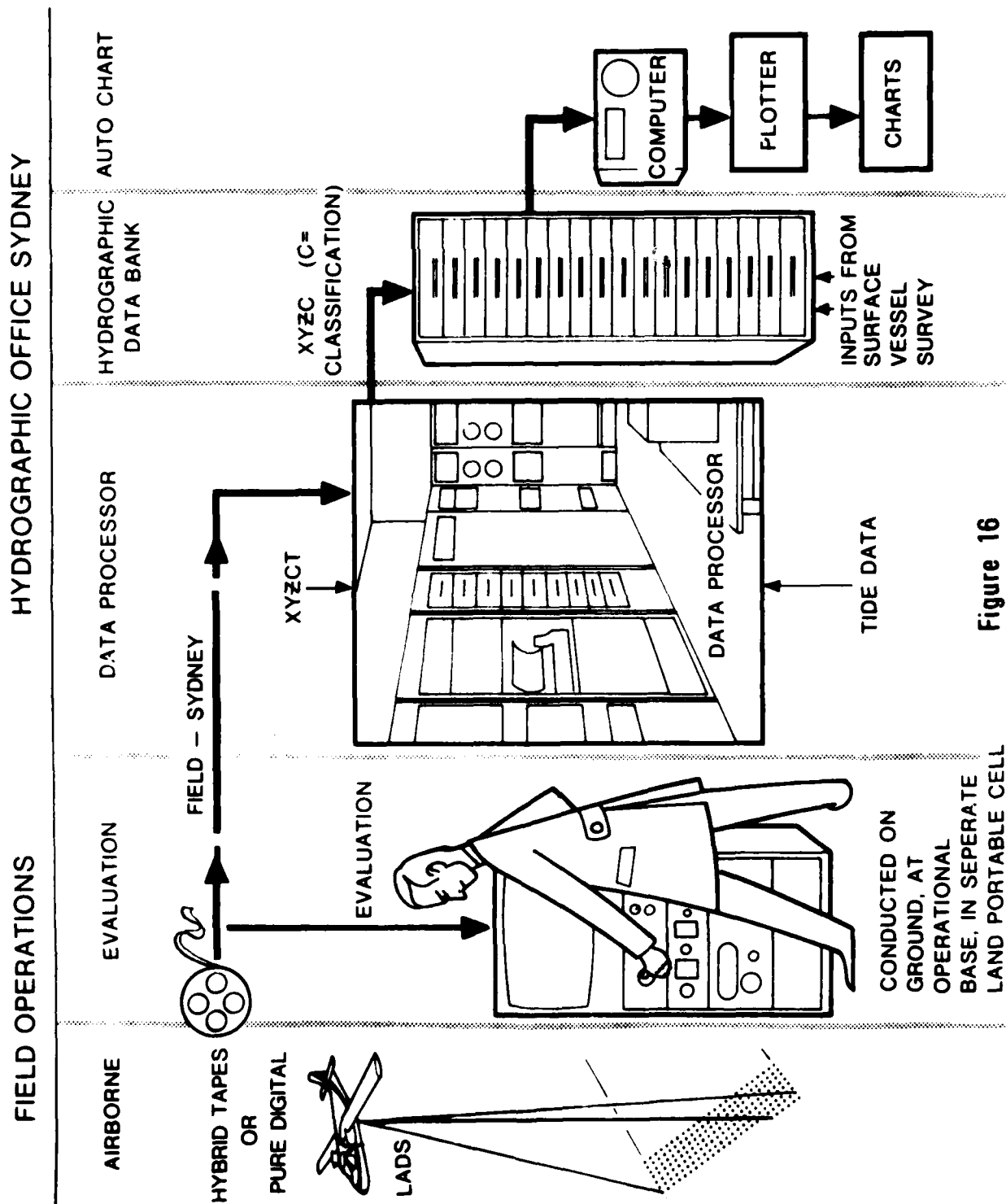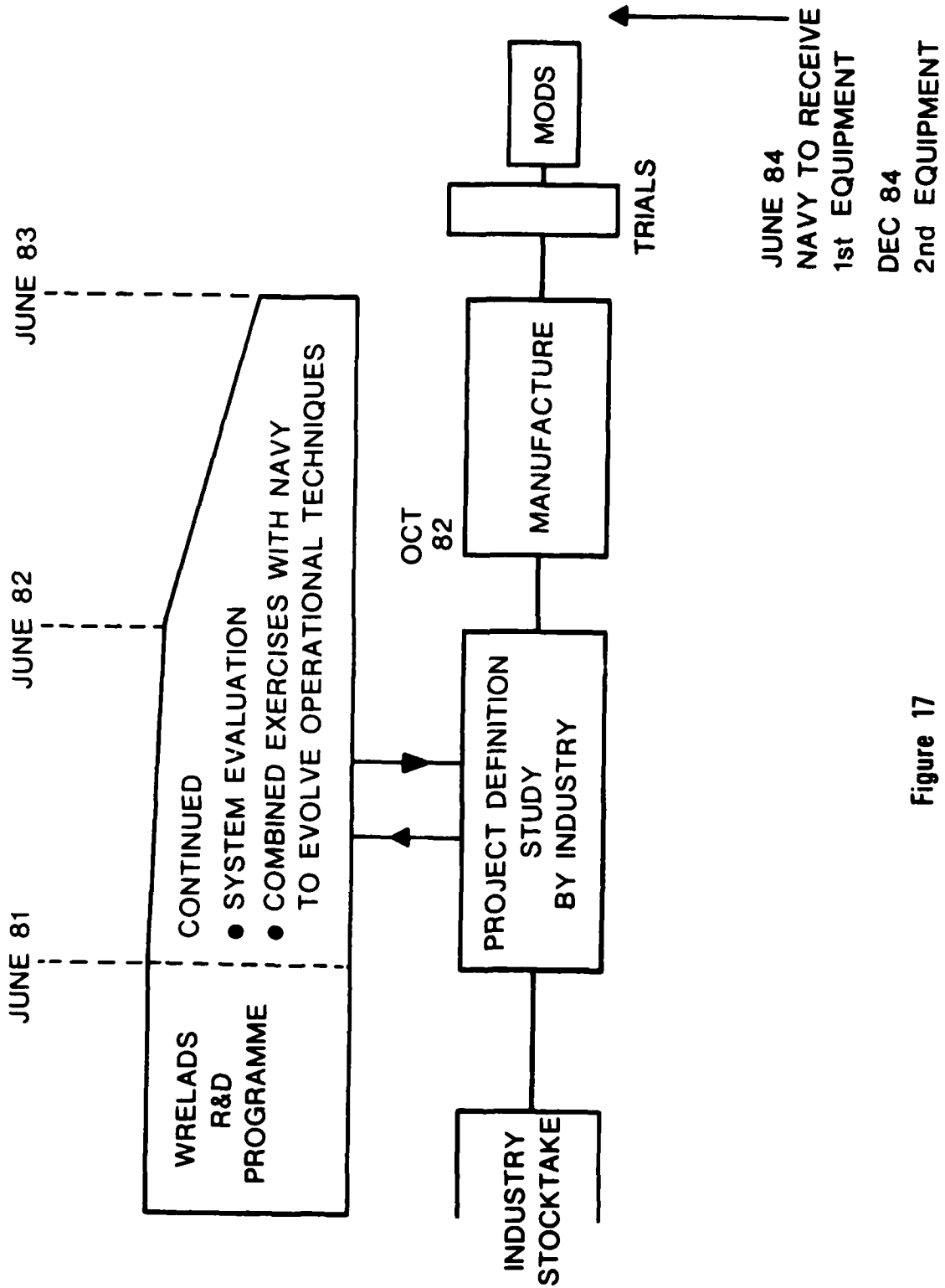
Figure 16

Figure 17

AIRBORNE LASER HYDROGRAPHY IN THE UNITED STATES

Commander Van K. Nield, USN
Headquarters, Defense Mapping Agency
U.S. Naval Observatory
Washington, D. C.   20305
USA

AIRBORNE LASER HYDROGRAPHY IN THE UNITED STATES

Commander Van K. Nield, USN
Headquarters, Defense Mapping Agency
U.S. Naval Observatory
Washington, D. C. 20305
U.S.A.

ABSTRACT

Conventional waterborne hydrographic survey methods have become exceedingly
expensive while the need for improvement of charts is increasing rapidly.

The U.S. Government is developing a suite of techniques to conduct far
more rapid, efficient surveys; airborne laser bathymeters are foremost
among these. The first operational system, the Hydrographic Airborne
Laser Sounder (HALS) is now being procured by the Department of Defense,
and should be in use by late 1982. It will have a depth capability of
28 meters under typical conditons and will be flown in a helicopter from
the Navy coastal survey ships. Development of a hybrid system, which uses
a pulsed laser to calibrate an airborne multispectral scanner with respect
to depth, has begun for surveying extensive clear, tropical shoal areas.
Advanced very high pulse rate active laser systems are also under study.

INTRODUCTION

In the U.S., the Defense Mapping Agency (DMA) is responsible for providing
navigational information on foreign and international waters to all United
States shipping, both civil and military. Our National Ocean Survey (NOS)
has similar responsibility for U.S. coastal waters -- which is now taken
to be on the order of 200 miles offshore -- and includes the U.S. islands in
the Atlantic and Pacific. Even if all of our charts were completely adequate,
and if we continue our data exchange agreements with other countries -- which
we have every expectation of doing -- just our necessary maintenance surveys
would be an enormous task. As it is, a majority of the DMA charts are less
than fully adequate, and NOS also has a substantial survey backlog, especially
in Alaska and the Pacific islands. The situation is magnified by a rapidly
increasing need for completed, accurate chart coverage. Fuel costs demand
the most efficient ship routing, which can now be assisted by satellite
navigation systems and weather forecasting. Ships' drafts have greatly increased.
In a few years, the NAVSTAR Global Positioning System (GPS) will allow ships to
navigate so accurately that many existing charts will be far more inadequate
than they are now; landfalls and other piloting operations will be confusing
to the point of genuine hazard. In addition to all those factors, the
complexities of international commerce and politics can require change in
ship movements, that are often difficult to predict, through poorly charted
areas. All of these things make a drastic improvement in hydrography a real
necessity.

NOS, actually, has managed to sustain its part of the effort reasonably
well. They have a sizeable fleet of ships and launches, their own uniformed

officer corps (who become part of the Navy in wartime) and a large complement
of civilian surveyors and engineers. They are altogether a highly specialized
professional organization and accomplish a lot with the resources available
to them. In recent years, they, like everyone else, have been handicapped
by inflated expenses and they have sought a means of increasing survey
efficiency, i.e., a way to collect more data faster and cheaper. To this end,
they have begun a modest photogrammetry program, which has been successful
but obviously only a partial answer. It is limited to shallow, clear water
and data reduction is still very laborious. They are also outfitting two
of their ships with new multibeam sonar equipment which shows considerable
promise. Over the last several years, a number of people at NOS have seen
that airborne laser bathymetry could be used for quickly and cheaply surveying
close inshore areas, which are always disproportionately expensive and time-
consuming--and frequently dangerous-- to survey with launches. They have
studied that technology carefully and presented a detailed analysis to their
management.

Within our Department of Defense, hydrography did not fare quite so well
for a while. Having to compete with extremely high weapon system and personnel
costs, and not being nearly as visible, military hydrography shrank severely
over a period of several years. At this point, our coastal survey operation
is down to one 400-foot ship, USNS CHAUVENET, and her four 36-foot launches.
(CHAUVENET is currently in Indonesia surveying the Makassar Straits area.)
Inasmuch as DMA's fundamental survey backlog amounts to about 200 ship years
of work at the present rate, the situation has become quite serious and, if
some action were not taken, would be likely to remain so, with all the attendant
implications.

Fortunately, the problem has been recognized and is being dealt with. To start, there have been reorganizations within both DMA and the Navy to bring the correct expertise to bear. Plans exist to recommission CHAUVENET's sister ship, HARKNESS, and to let some commercial survey contracts.

At the same time, and of greatest significance, we have established a research and development program to produce a suite of tools which will collect and process data orders of magnitude more efficiently. The program includes various satellite sensors, notably the Landsat multispectral scanners; airborne systems; and improved acoustic sensors, which we will always need to survey those waters too deep and/or opaque for use of electro-optical methods. Automated digital data reduction, storage and retrieval and chart production techniques are under development to use the immensely increased volume of data which will result.

It is the airborne laser system that we are counting on for a near term increase in survey rate, however. Landsat is beginning to be very helpful in detecting and correctly locating features, within its 80 meter resolution capability, but it will be a number of years before we can use it to calculate depths with much accuracy. The sonar developments will probably not be completed for another five years, and our other airborne technique, the hybrid active/passive multispectral scanner-laser system could also take nearly that long, depending on budget decisions.

BACKGROUND

Laser bathymetry has been under consideration in the U.S. for about
fifteen years, beginning with the early basic studies supported by our Office
of Naval Research (ONR) at Syracuse University. During the late sixties and
early seventies, our Naval Oceanographic Office (NAVOCEANO) conducted
extensive engineering feasibility experiments. These tests were highly
encouraging, but some of the key technologies -- notably automatic data
processing -- were not mature enough to allow development of a cost
effective operational system. Later, in the mid-seventies, some former
Oceanographic Office people, then at the Naval Ocean Research and Development
Activity (NORDA), tried an approach which would combine photogrammetric
and laser bathymetry techniques but this, too, proved uneconomical. Meanwhile,
about 1973, our National Aeronautical and Space Administration (NASA), under
its charter to transfer space related technology to other applications,
began development of their Airborne Oceanographic Lidar (AOL), a laser device
intended for both bathymetry and fluorosensing. Some NOS engineers, also
aware of the Navy work, arranged a joint study with NASA of the bathymetry
application. A year or so later, DMA and the Navy joined the effort. Flight
tests were held in late 1977 on some offshore Atlantic shoals and in the
Chesapeake Bay. The results, while not absolutely conclusive regarding
accuracy, provided a strong indication of what could be produced which would
rapidly, accurately and safely survey shallow water at a fraction of the cost
of launch operations.

HALS DEVELOPMENT PROGRAM

In view of the compelling need to improve our coastal hydrography effort,
DMA decided to proceed. NORDA, under DMA oversight and funding sponsorship,
was designated to manage the project, including writing the specifications
and contracting the actual design, fabrication and initial testing. NOS
was to assist with the studies and analyses of which they are uniquely capable,
at the same time considering how the DMA system could be adapted for their
own operational requirments. In order to minimize costs, as well as to
improve our survey rate as soon as possible, it was decided to push the
state of technology the relatively small amount necessary to achieve an
operationally capable prototype rather than simply an advanced development
model beyond which an operational system would have to be produced. The
confidence to attempt this was derived from past Navy experiments and NASA
and NOS' work with the AOL, as well as the considerable knowledge gained
by the Naval Air Development Center (NADC) in their studies of the use of
airborne lasers for locating submarines. A great deal of care and time
was taken in developing the specifications for the system, which was to
be called the Hydrographic Airborne Laser Sounder (HALS). Much specific
effort was given to forecasting operational requirements; maximum communi-
cation for this purpose was established with NAVOCEANO, whose task it is
to conduct hydrographic surveys for DMA. ONR, NADC and NASA were
also closely involved. It took well over a year to evolve the specification,
but it is expected that the investment will prove to be more than sound.

There were several basic constraints within which HALS had to be designed.
The data have to meet International Hydrographic Bureau (IHB) accuracy

standards and be compatible with production processing; the system must have sufficient depth capability to justify development; operational costs must be kept within budget; and the operation must be eye safe to observers. The most important areas of technology advance needed to achieve these goals were developing a laser of requisite pulse length, repetition rate and power, and accounting for errors related to the geometry of the laser energy propagation in the water and through the surface.

Initially, HALS will be employed in the helicopter carried by the CHAUVENET class ships for support of their radio navigation aid sites ashore. This has disadvantages related to the size, vibration and low speed of these aircraft, but is necessary because of the normal remoteness of our survey areas from airfields from which fixed wing planes could operate. An advantage will be close coordination of the airborne operations with those of the boats and ships. Besides, the HALS will have to use the same shore based navigation net as the ships until GPS becomes available in the late eighties. While it is recognized that this interim scenario will not allow use of HALS to its full potential, analysis shows that addition of the airborne system to the surface surveys will permit, under typical turbidity and depth conditions, collection of about 30% more data at approximately the same cost as the present operation. With the shiptime as expensive as it is, this will be well worthwhile.

A contract for the design, fabrication and testing of HALS was let in late 1979 to AVCO Everett Research Laboratories, Inc., of Everett, Massachussetts; the design phase was completed in mid-1980 and fabrication

commenced. Laboratory testing of the completed system and subsequent
delivery to NORDA for technical evaluation is expected in early 1982.
NAVOCEANO will receive HALS for operational evaluation and shakedown
employment by, hopefully, October of 1982.

NOS PROGRAM

NOS meanwhile has concentrated on the above mentioned analyses, related
largely to signal processing, light propagation modelling and horizontal
positioning, in support both of HALS and a possible system of their own. An
NOS system would be similar to HALS, taking advantage of the basic design,
but with more rigorous horizontal accuracy requirements -- for their more
frequent large scale surveys -- and employed in a fixed wing aircraft.
Whether NOS' budget will permit them to build a system soon seems, unfortunately,
somewhat in doubt. It may be, however, that HALS could be used to satisfy
some NOS survey requirements as well as for DMA.

NASA

NASA has kept the AOL flying for various experimental purposes since
1977. Its primary use has been for surface wave spectra and shoreline
mapping and the fluorosensing application. Experiments are planned for
nearshore/beach profiling and the locations of schooling fish, as well
as inland terrain mapping.

ACTIVE/PASSIVE TECHNIQUE

Another laser bathymetry technique which we have considered for some time is a hybrid system in which sunlight reflected from the ocean bottom is received by a multispectral scanner and periodically calibrated with respect to depth by a pulsed laser. This approach has been studied for amphibious warfare reconnaissance by the Naval Coastal Systems Center (NCSC). It is less accurate, is limited to the depth capability of the passive scanner, and requires specific ambient lighting conditions. It would come close to meeting IHB standards under many circumstances, however, and provide -- depending on field of view and altitude -- near photographic resolution. Installed in a fast, long range fixed wing aircraft, it should be extremely valuable for surveying the vast, complex clear water tropical areas. Precise positioning will have to await GPS or improvements in inertial navigation systems -- or some combination thereof -- although it should also be possible sometimes to digitally register the airborne MSS data to Landsat imagery.

We were about to -- reluctantly -- decline this option as being of reconnaissance value only, since it would generally not achieve IHB accuracy. However, DMA decided to seriously consider publishing certain charts in a format which would permit use of high reconnaissance quality surveys, in areas where that would be an improvement over present data; ranges of depth in specific areas would be portrayed vice discrete individual soundings. With this decision, the hybrid, or Active/Passive,

technique was included in the R&D program. We have begun a preliminary
design phase to optimize an exisiting experimental system for bathymetry,
which is paced with a parallel computer emulation effort to determine how
the enormous data throughput can best be handled. Results of the data
processing study are expected in early 1982; the remaining development
will hopefully proceed rapidly from there, assuming the new chart
presentation meets with expected approval by navigators.

ADDITIONAL DEVELOPMENTS

With the change in charting philosophy under discussion, it is also
seen of course that the pre-GPS HALS could be put to considerably more use
in a fixed wing aircraft for collection of good reconnaissance quality data,
although its highest priority employment would still be in areas where compliance
with IHB accuracy standards is needed. Such areas would include those of possible
naval operations, harbors, approaches, etc. Looking to a next generation active
laser system, we are watching the development of high pulse rate laser
technology, including metal vapor lasers which should pulse at a rate of
the order of 6000 Hz. Such a transmitter, flown in a high speed aircraft,
with necessary attendant advances in data processing and navigation, would
be able to survey at a rate difficult at present to imagine. In our long range
R&D program, we envision commencing serious development of an operational
high pulse rate active laser system about 1986.

Another important consideration related to airborne bathymetry is the
recording of the tidal cycle during the survey in order to relate the

bathymetry to the local tidal datum. The concept currently envisioned is
an expendable, air deployable telemetering hydrostatic pressure tide gauge.
The various pieces of technology appear to be available to do this, but
the synthesis would of course be non-trivial and cost will be a major
factor. We have just begun to study this problem, but hope to evolve
a design within a year or two.

CONCLUSION

    As is evident from the investment we are making, we in the United
States are relying heavily on airborne electro-optical technology to make
a profound improvement in our hydrographic survey operations.

PAPER 3

Canadian Program Overview

R.A. O'Neil
Canada Centre for Remote Sensing

A.J. Dow
Canadian Hydrographic Service
c/o Data Acquisition Division
Canada Centre for Remote Sensing
2464 Sheffield Road
Ottawa, K1A 0Y7 Canada

Telephone: 613 998-9060
Telex: 053-3777

Summary:

In Canada two complementary techniques have been developed for airborne hydrographic charting in shallow coastal waters. The first technique combines high precision aircraft position and attitude data with stereo photography of the area to be surveyed. An analytical photogrammetric plotter is used for the stereo-restitution and to apply the refraction corrections as the bottom contours are followed. A profiling lidar bathymeter is bore sighted with the metric camera and measures water depth along the centre line of each stereo pair. Water depths obtained with the lidar are merged with the photogrammetric depths to improve the quality of the photogrammetric data and allow the precision of the aircraft attitude data to be relaxed. Total coverage is obtained in the near shore areas with the lidar providing profiles into deeper water.

The planning and reconnaissance stages of an aerial hydrographic mission will be aided by a conventional photo interpretation using existing data, water colour and the local geomorphology to locate the approximate position of the depth contours and to indicate areas deserving special attention. This may, in the future, be supplemented by making use of a model dependent interpretation of multispectral passive electro-optical imagery. The model, which is still under development, is an extension of the algorithms being used to extract, water quality parameters from satellite and airborne MSS data.

Three surveys have been carried out to date in Canada using the aerial hydrography system. A pilot study in the St. Lawrence River and a lidar field trial in the Magdalen Islands were flown in the summer of 1979. In the summer of 1980, 60 km section of Bruce Peninsula (Lake Huron) was flown.

Detailed plans are now being laid to carry out a production survey in the Victoria Strait of Arctic Canada.

THE HYDROGRAPHIC AIRBORNE LASER SOUNDER (HALS)

DEVELOPMENT PROGRAM

M. W. Houck
D. C. Bright
H. J. By

U.S. Naval Ocean Research and Development Activity

Bay St. Louis, Mississippi

Presented at the

LASER HYDROGRAPHY SYMPOSIUM

Salisbury, South Australia

1 October 1980

THE HYDROGRAPHIC AIRBORNE LASER SOUNDER (HALS)

DEVELOPMENT PROGRAM

M. W. Houck
D. C. Bright
H. J. Byrnes

U.S. Naval Ocean Research and Development Activity

Bay St. Louis, Mississippi

ABSTRACT

There has been a long standing requirement for more rapid and cost effective methods to perform hydrographic surveying in shallow, near shore waters. In response to this requirement, the Naval Ocean Research and Development Activity (NORDA) is developing the Hydrographic Airborne Laser Sounder (HALS) under the sponsorship of the Defense Mapping Agency (DMA). The system design, fabrication, and assembly are being performed under contract with an industrial firm from specifications developed by NORDA. The system will consist of a scanning laser sounder and altimeter, orientation equipment, data processor and recorder, and electronic positioning equipment. It will be installed and used in the helicopter carried by the Naval Oceanographic Office's hydrographic survey ship. The HALS will collect and record data from which water depths and their geographic positions can be resolved to within IHB accuracy standards. Using a Nd:YAG scanning laser operating at 532 nm, the HALS will measure depths to at least 3.2 optical diffuse attenuation lengths. At an altitude of 150 meters and a speed of 70 knots, the area coverage will be 8,000 square meters per second with an average density of one sounding every 20 square meters. Delivery of the HALS is expected in 1982 for evaluation by NORDA. The system is expected to be operationally deployed by the Naval Oceanographic Office in late 1982 or early 1983.

INTRODUCTION

The U.S. Navy has been involved with the development of a practical airborne laser bathymetry system for the last 14 years. The U.S. Naval Oceanographic Office (NAVOCEANO) successfully demonstrated the feasibility of laser bathymetry from an airborne platform in late 1969 when the Pulsed Light Airborne Depth Sounding (PLADS) System, delivered by the Raytheon Company, was tested in

the Chesapeake Bay area from an SH-3 helicopter. Although the
PLADS depth penetration capability was specified as three beam
attenuation lengths, depth penetration capability in excess of
five beam attenuation lengths was demonstrated for daytime op-
eration [1]. The PLADS accuracy objective was .46 m at altitu-
des varying from 61 to 305 m, water clarity conditions varying
from $\alpha=0.1$ to 1.0 m^{-1}, and bottom reflectivity varying from zero
to 30 percent [1]. The PLADS frequency doubled Nd:YAG laser
operated at a pulse repetition rate variable from 1 to 30 pps,
with a peak power of 2.8 MW and a pulsewidth of 5 nsec [1].
The PLADS optical receiver had a 5-inch aperature, folded
collection optics, variable field of view to 75 mrad, inter-
ference filter with a bandwidth of 30 Å centered at 530 nm,
and a dynode gated photomultiplier tube detector [1]. The
PLADS was plagued by reliability problems which precluded ex-
tended testing beyond concept feasibility demonstration.

During the period of December 1973 through March 1975,
NAVOCEANO was involved in a joint program with NASA Wallops
Flight Center to further develop and evaluate the laser bathym-
etry concept. The ultimate goal of this program was to construct
a more reliable and complete operational system [2]. During
this program the existing NASA fluorosensing unit was modified
for laser bathymetry, and an aerial camera was installed. During
this same time period, NAVOCEANO was proposing to combine aerial
photography with the airborne laser system. The proposed
system concept was called the Coastal Aerial Photo-Laser Survey
(CAPS) System [3]. This system was installed on the NAS-427
aircraft (military version of the DC-4) and was tested during
47 flights in the Key West, Florida area [2]. The results of
those tests reconfirmed the feasibility of airborne bathymetry
for shallow coastal waters. However, it was concluded that
because of the heavy dependence on labor-intensive processes
associated with photogrammetry, and the less than optimal use
of both laser and camera subsystems when flown jointly, the CAPS
development should be terminated. A decision was made to
concentrate development efforts toward a scanning laser system
capable of cost effective shallow water hydrographic surveying.

The Hydrographic Airborne Laser Sounder (HALS) development
was initiated in 1976 by the U.S. Naval Ocean R&D Activity (NORDA)
under the sponsorship of the U.S. Defense Mapping Agency (DMA).
This program proposed the development of a scanning laser system
utilizing available components integrated into a reliable field-
worthy, production system.

Because of the similarity between the capabilities of the
proposed HALS and the NASA Airborne Oceanographic Lidar (AOL)
System [4], NORDA entered into a joint test program for the AOL
with NASA and the U.S. National Ocean Survey (NOS). Results of
those tests [5] demonstrated the feasibility of the scanning

laser concept, and also demonstrated the capability to trarmit,
receive, and record laser pulses at a high repetition rate (400 Hz)
with sufficient precision to accurately determine water depths
from an airborne platform. The AOL airborne tests proved beyond
reasonable doubt that the HALS would provide a cost effective
alternative to the sound boat methods for shallow water hydro-
graphic surveys.

The U.S. Naval Air Development Center (NADC) has also been
actively involved in development of laser systems capable of
penetrating the ocean waters. Although not specifically designed
to accurately measure the water depth, the ORIC/ORAD development
[12] has provided valuable spinoff contributions to the HALS
development. The NADC demonstrated the scanning laser concept
in 1971 and 1972 [12] and developed performance equations from
empirical data which were used as a guide in developing the
specifications for the HALS. The NADC system was used during
tests at Key West, Florida in May 1979 to experimentally
investigate the system attenuation coefficient for HALS [13].
NADC's Ferguson and Rankin have pioneered much of the develop-
ment effort for the high pulse repetition rate, narrow pulse
width Nd:YAG laser.

HALS DEVELOPMENT SCHEDULE

The HALS Purchase Description [8], containing all system
specifications and requirements, was prepared by NORDA during
1978 and a request for proposals was issued in April 1979. As
a result of the proposal evaluations during June and July 1979,
AVCO Everett Research Laboratory (AERL) was selected as the
prime HALS contractor. Under the terms of the contract, effec-
tive September 1979, AERL will design, fabricate, and test the
HALS with final acceptance and delivery to NORDA scheduled for
February 1982.

Following the field acceptance tests, NORDA will conduct
an intensive six-month technical evaluation of the HALS at se-
lected sites in the United States. At the conclusion of the
HALS technical evaluation NAVOCEANO will accept the system and
conduct their own operational evaluation with technical assist-
ance from NORDA. Actual operational deployment is scheduled for
1983.

At the present time, the HALS development is in the final
design phase. NORDA has conducted periodic design reviews at
the contractor's facility during the design phase of the con-
tract. AERL has initiated procurement action for HALS hardware
equipment to be purchased from commercial sources or developed
under subcontracts.

HALS SYSTEM REQUIREMENTS

The HALS performance requirements are summarized in Table 1.

TABLE 1

HALS PERFORMANCE REQUIREMENTS [3]

Altitude	100 to 800 m; 150 m nominal.
Forward Velocity	37 m/s nominal.
Vertical Depth	0.5 to 50 m (0.5 to 20 m required at maximum scan angle for $K = 0.16$ m^{-1}).
Slant Range Measuring Accuracy	
Altitude	$\pm$ 0.1 m or 0.05% of range (larger).
Water Depth	$\pm$ 0.28 m for depths from 0.5 to 20 m; $\pm$ 1.0 for depths > 20 m.
Area Coverage	One sounding per 20 m^2 (average) at an altitude of 150 m, velocity of 37 m/s and maximum scan angle. Also, one sounding in every circle of 9 m diameter.
Scan Angle	Variable, 0 to 624 mrad.
Sea State	Operation to Beaufort 3 wind conditions.
Solar Angle	Operation at zenith angles > 46° required.
Horizontal Position Accuracy	1.65 sigma value of 1.5 mm times the scale of survey.

The HALS electrical and physical characteristics are summarized in Table 2.

TABLE 2

HALS ELECTRICAL AND PHYSICAL CHARACTERISTICS [8]

Electrical Power	Not to exceed 5000 watts from 115 V AC, 3 Phase, 400 Hz source.
Size	Not to exceed 2 m^3.
Weight	Not to exceed 400 kg.
Construction and Installation	Modular construction. Six hours installation time (two men).
Operation	One operator.

The HALS environmental requirements are summarized in Table 3.

TABLE 3

HALS ENVIRONMENTAL REQUIREMENTS [8]

Temperature	-2° to 54° C.
Humidity	Operate at relative humidities of 5 to 95%.
Shock	Procedure I, Method 516, MIL-STD-810C, 15 g, 11 msec, half sine, shock mounted.
Vibration	Procedure I, Method 514, MIL-STD-810C, 0.2 inches DA, 5 to 14 Hz; 2 g, 14 to 500 Hz.
Salt Spray	System shall not be damaged by salt spray or fog.
Fungus	Fungus inert materials per MIL-STD-454E, requirement 4, nonmercurial substances.

The HALS reliability and maintainability requirements are summarized in Table 4.

TABLE 4

HALS RELIABILITY, MAINTAINABILITY, AND SAFETY REQUIREMENTS [8]

Reliability	100 hours MTBF
Maintainability	4 hours MTTR
Workmanship	Per MIL-STD-454E
Operational Life	8 years
Safety	Eye safe at 150 m, electrical interlocks.

HALS SYSTEM DESIGN

The HALS can be separated into four major subassemblies, as illustrated in the simplified system block diagram of Figure 1. These subassemblies are: (1) Transceiver, consisting of the laser transmitter, optical receiver, and scanner assembly;
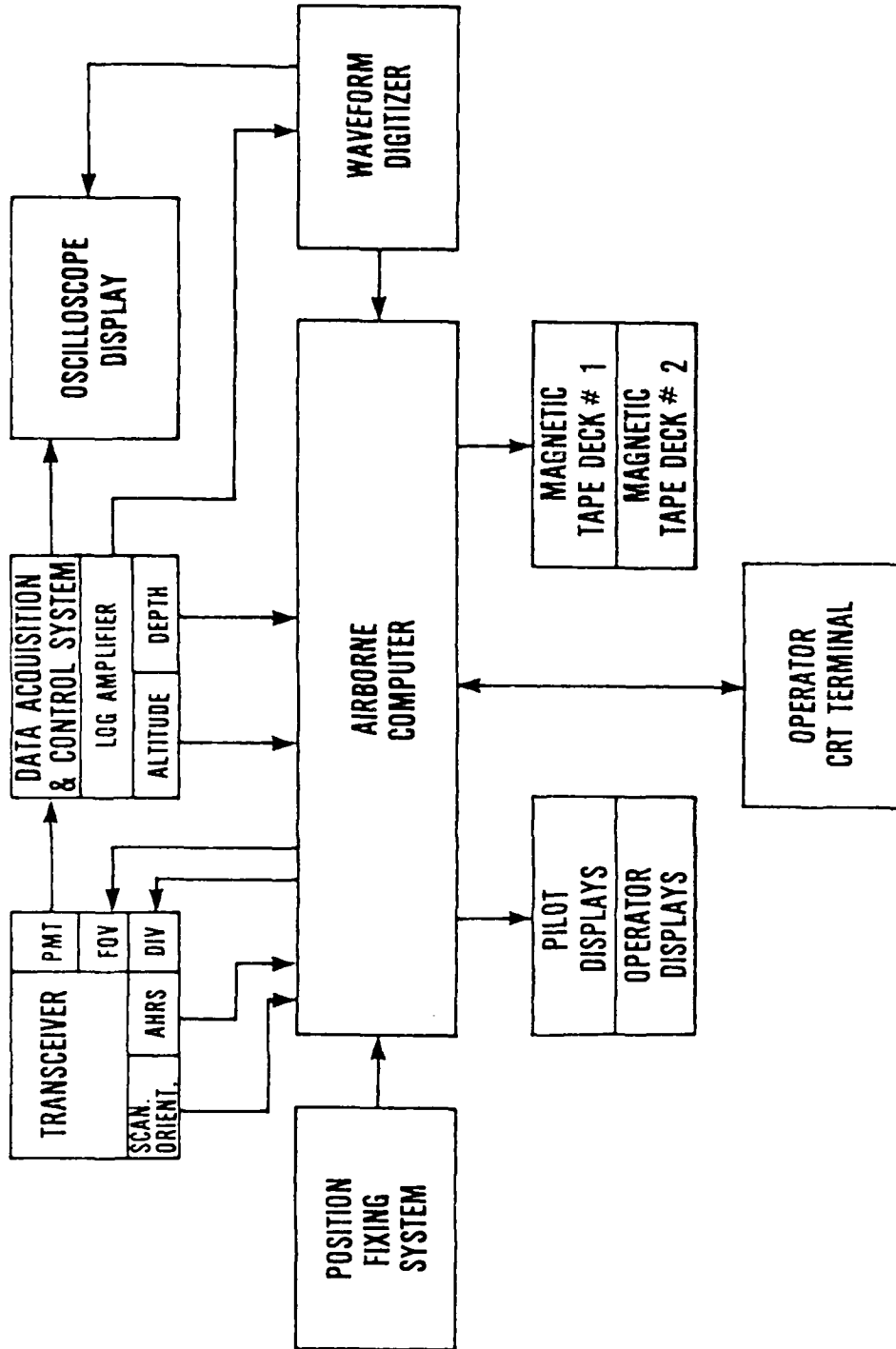
Figure 1

HALS System Block Diagram

(2) Data Acquisition and Sequence Control Electronics System;
(3) Horizontal Position Control System; and (4) Digital Processor,
Display and Recording System.

Transceiver

The HALS Transceiver assembly is illustrated in Figure 2.
All components of the transceiver are rigidly mounted to the
mounting plate, which is in turn attached to the aircraft
structure utilizing four vibration isolators. The scanner
assembly is designed to project out the door on the left
side of the aircraft for the planned HH-2D helicopter in-
stallation. The contractor's transceiver design requirements
to satisfy the HALS specifications are included in Table 5.

The HALS scanner design is the same as that which was
successfully utilized by AERL in the NASA Airborne Oceanographic
Lidar (AOL) System [4, 10]. The scanner, illustrated in Figure 2,
consists of a mirror rotating on an axis at 45° to the optical
system axis, with the mirror tilted on the axis. The resulting
scan pattern can be varied by changing the angle of tilt relative
to the axis [10]. Proper interlace on the target surface is a
function of aircraft speed and the scanner rotation speed,
which is variable to 4 Hz. Those parameters are determined
during pre-mission planning. AERL has described the interlace
procedure in detail [4].

The HALS laser is a single cavity, frequency doubled,
flashlamp pumped, pulse transmission mode (PTM) Neodymium YAG
design which has been developed by AERL. The PTM resonator
is illustrated in Figure 3. AERL has stated [8] that much
of their earlier high pulse repetition PTM Nd:YAG laser
development efforts were based on the work of Ferguson and
Rankin [11]. The laser features a straight resonator path
which simplifies the task of packaging for the HALS airborne
application [10]. The mechanical design of the laser head
features adjustable, rigid, and compact mirror mounts with
small moment arms [9, 10]. The baseplate area and optics are
designed inside a sealed enclosure with a nitrogen purge
fitting to provide a dust free environment [10]. Cooling for
the HALS laser will by provided by a 50/50 mixture of water
and ethylene glycol with heat exchanging to the aircraft cabin
air [9, 10].

The receiver optics system, illustrated in Figure 4, uses
an aspheric lens refractor configuration. The detector is the
ITT F4084 six-stage photomultiplier tube. The receiver optics
design provides an unobscured aperature; is insensitive to
misalignment compared to reflectors; and it allows a space
envelope which can decrease in width as the focal plane is
approached [10].
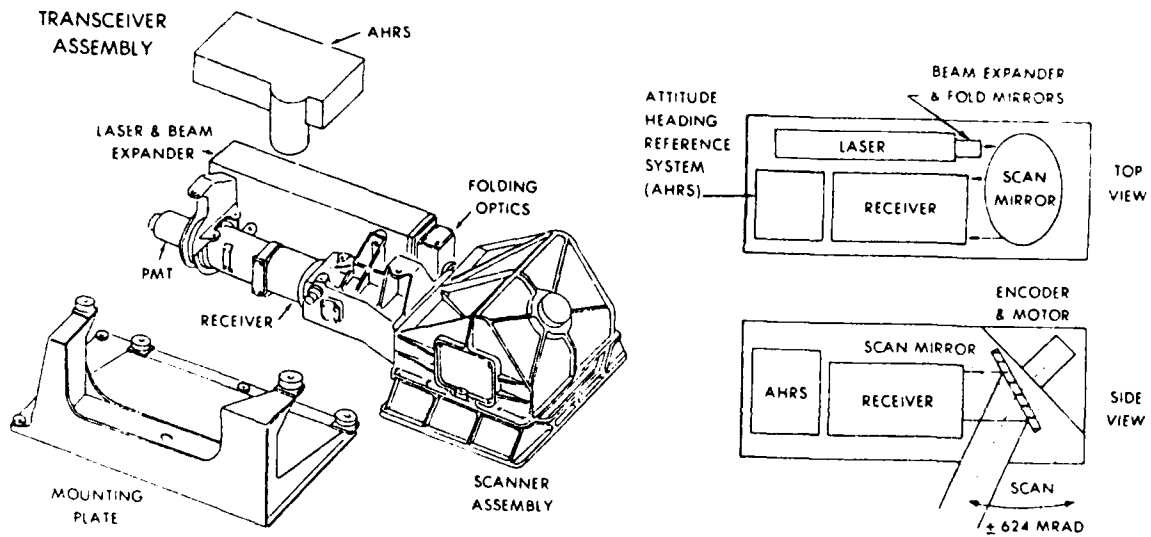
Figure 2

HALS Transceiver

TABLE 5

HALS TRANSCEIVER DESIGN REQUIREMENTS [7, 8]

Laser

Wavelength	510 to 560 nm
Pulse Energy	$\geq$ 2 mJ (at 532 nm)
Pulse Width	$\leq$ 7 nsec (FWHM)
Pulse Peak Power	$\geq$ 4 X 10^5 W
Pulse Background Power	< 1 W for t > 40 nsec from Peak
PRF	400 Hz
Beam Quality	3 mrad
Efficiency (Laser Head)	> 0.08%
Lamp Life	10^7 shots to 10% degradation.

Expander

Divergence	1-50 mrad (variable)

Receiver

Field of View	80 mrad (variable)
Aperature Area	388 cm^2
Bandwidth	0.5 - 3 nm (narrow as possible)
Detector	ITT F4084 Photomultiplier Tube

Scanner

Scan Pattern	Elliptical
Scan Rate	0 - 4 Hz (variable)
Scan Half Angle	0, 5, 10, 15, 18.5 Degrees
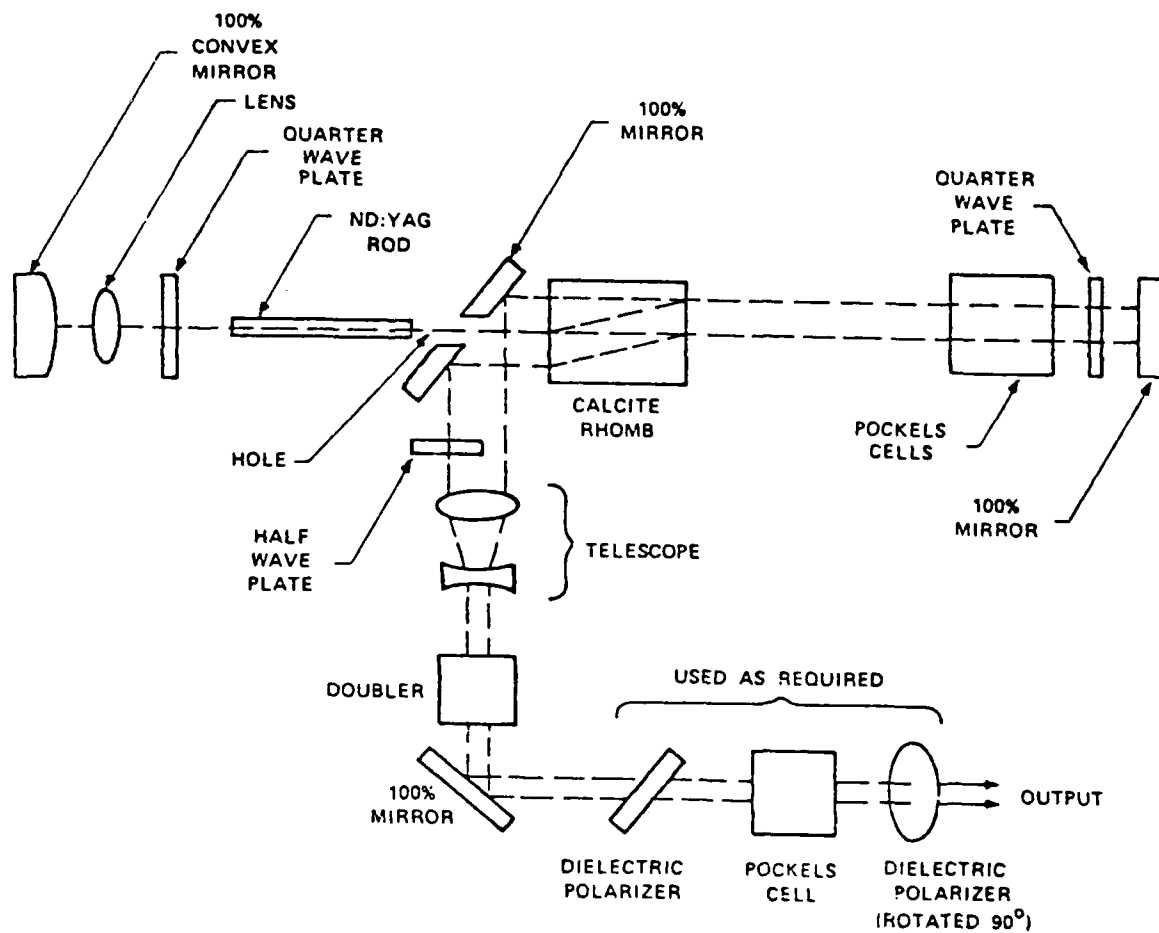
Figure 3

Proposed HALS PTM Resonator
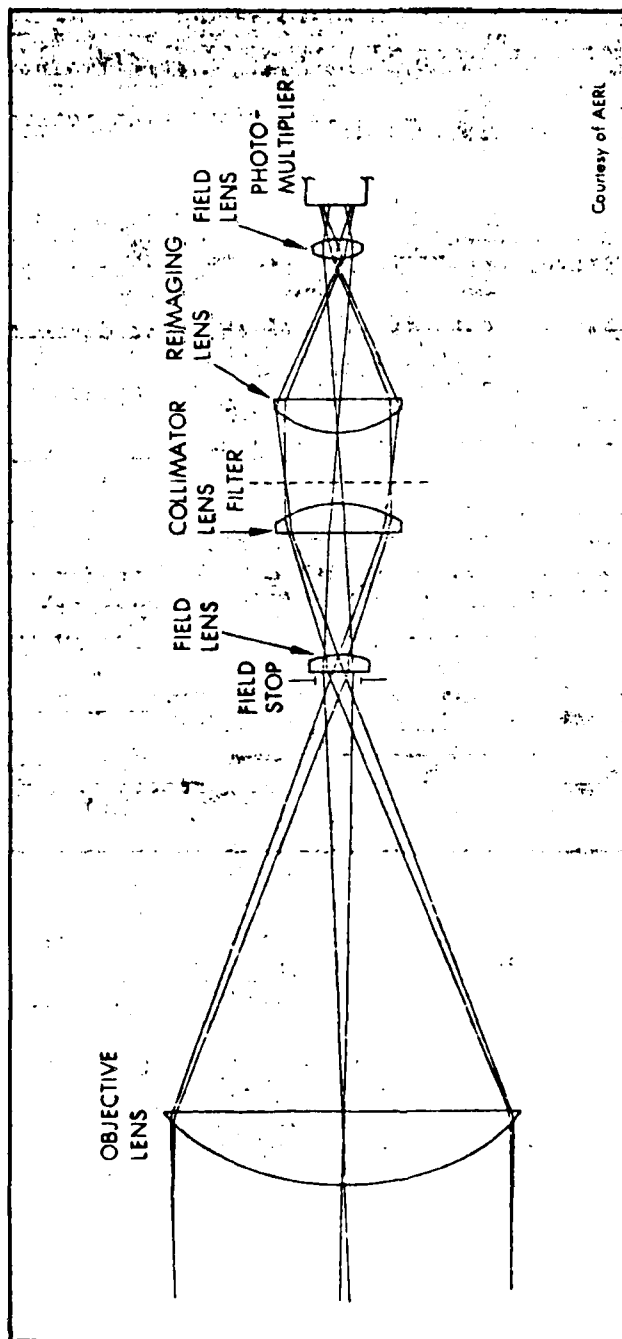
Figure 4

HALS Receiver Optics Assembly

Data Acquisition and Sequence Control Electronics

The HALS top level electronics system is illustrated in block diagram form in Figure 5. The HALS electronics system can be separated into the following subsystems: (1) Laser electronics; (2) Data acquisition electronics; and (3) Servo and control electronics.

Laser Electronics System

The laser electronics system is illustrated in Figure 6. The laser electronics has the capability to either generate the pulse repetition rate or process and limit an externally generated trigger. The flashlamp and Pockels cell driver circuits are of a differential design for fast turn on and turn off. The laser electronics design utilizes high noise immunity 15-volt I/C logic, and has separate grounds for analog, digital, and high current interfaces [9]. The laser power measurement is made by detecting a small fraction of the out-going pulse with a fast photodiode and converting the inte-grated charge into a digital word in a charge digitizer [10].

Analog Signal Detection and Processing Electronics System

The analog signal detection and processing electronics system is illustrated in Figure 7. A single detector is used for all range measurements. The detector is the ITT F4084 6-stage, grid controlled, gateable photomultiplier tube (PMT), with a dynamic range of four decades for single mode operation (on-off) and an extinction ratio of three decades [9, 10]. The logarithmic amplifier is AERL's own design and will cover five decades of dynamic range with a bandwidth in excess of 100 MHz.

The altitude measurement is determined from the time interval measurement between the outgoing pulse, as detected from scattered light from the scan mirror, and the surface return. The trigger pulses for the Hewlett Packard Model 5370A Time Interval Meter are provided from an EG&G Model 934 Constant Fraction Discriminator. The PMT is gated off until shortly before the expected arrival of the surface return. The system also has an optional mode to gate the PMT on after the detection of the surface return at small incidence angles near nadir. [9]

The slant depth measurement is also a time interval meas-urement, with trigger pulses generated by a second EG&G Model 934 Constant Fraction Discriminator. One of the bipolar outputs of the log amplifier is delayed approximately one pulse interval, and summed with the other output to form a normalized incremental first derivative. The resulting differential signal emphasizes features with temporal characteristics of approximately the
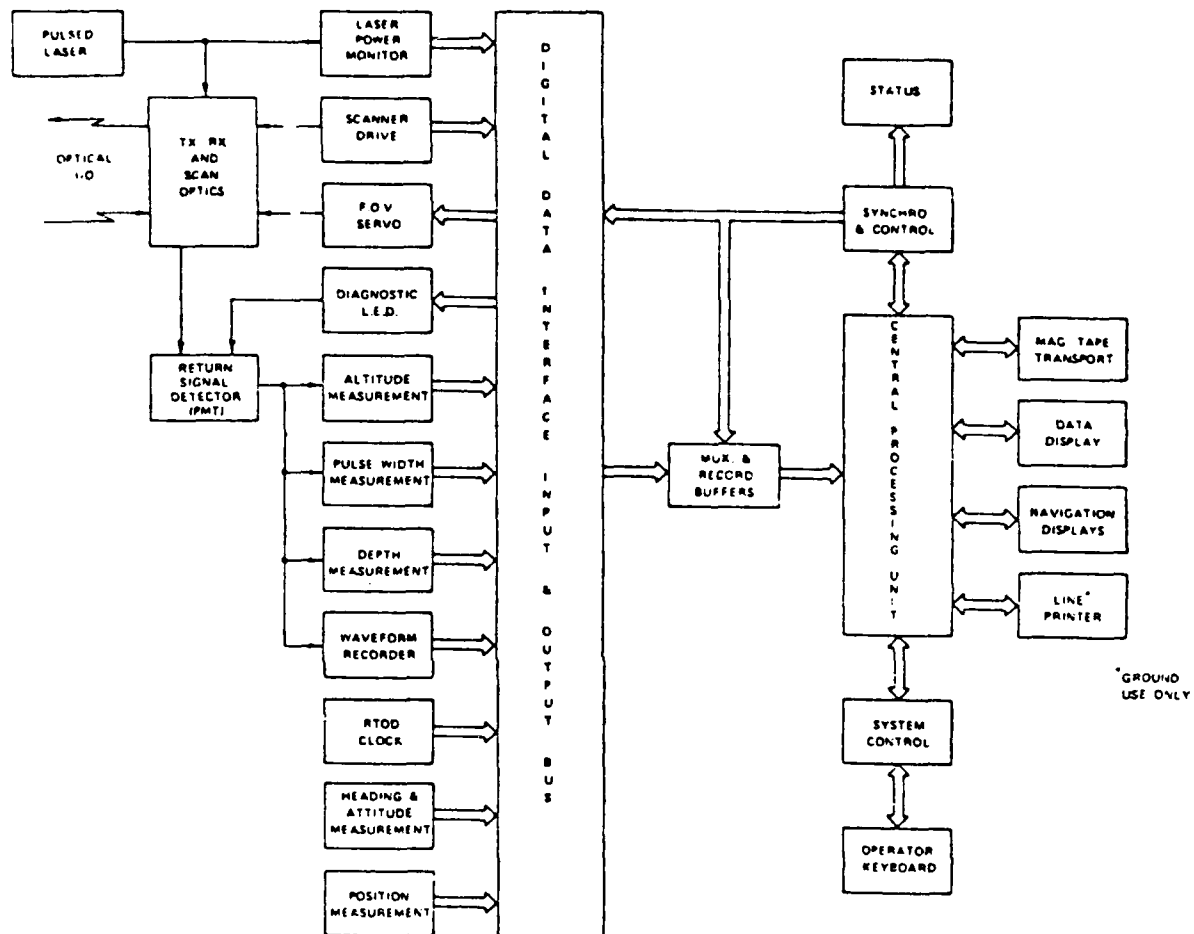
Courtesy of AERL

Figure 5

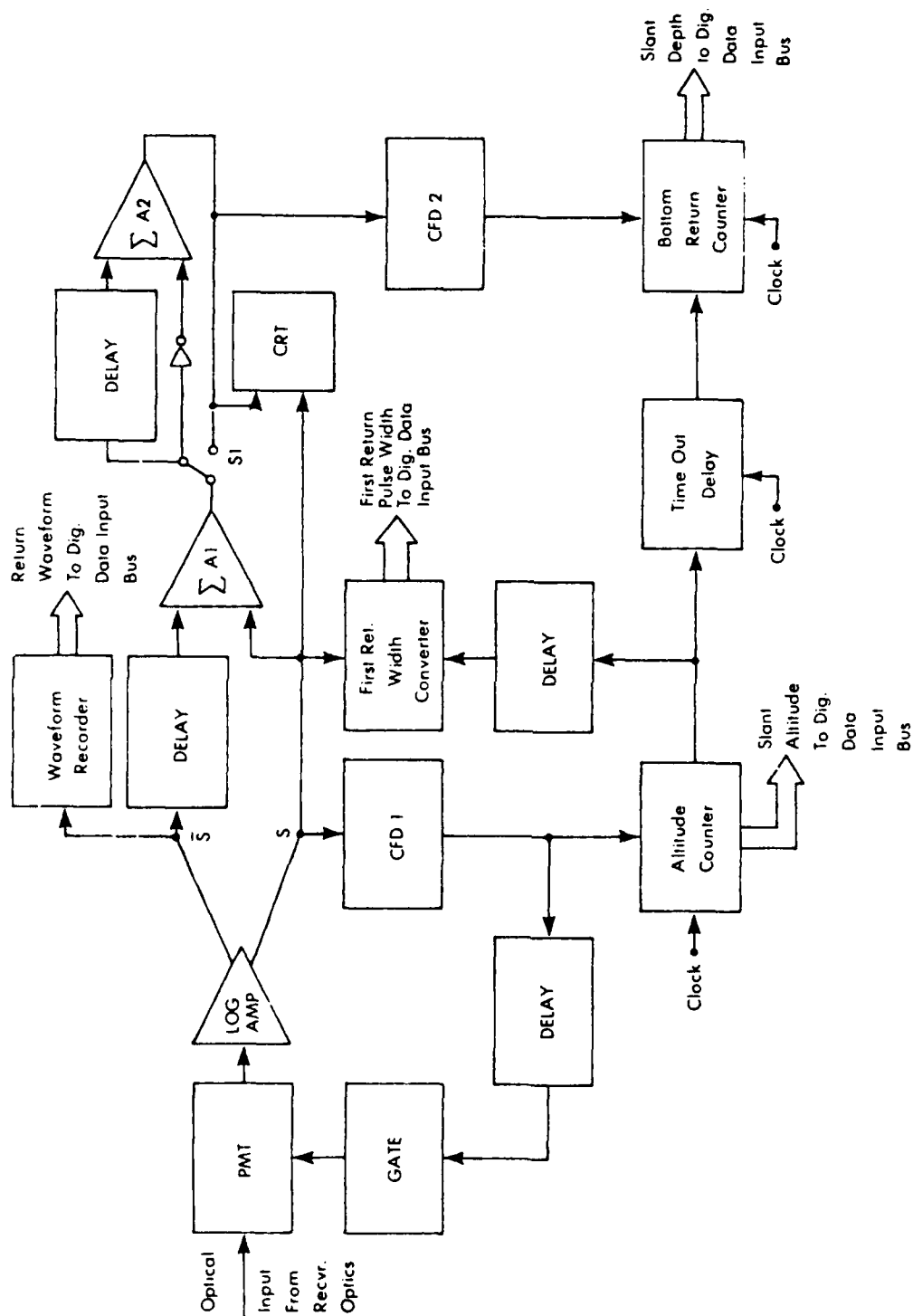HALS Top Level Electronics System Block Diagram

Courtesy of AERL

Figure 6

HALS Laser Electronics System

Figure 7

HALS Analog Signal Detection and Processing Electronics

pulse duration. The second selectable derivative processor is included for extended operation during nighttime and/or in turbid water conditions to ensure proper zero crossing detection within the constant fraction discriminator. The bottom return counter begins to count down from a preset maximum depth value when the surface return has been detected. Subsequent detection of any subsurface return pulse resets the counter to the maximum time-out value. Counting ceases upon command from a fixed, time-out delay, with the residual count being a measure of the time interval between detection of the surface and bottom pulses. [10]

Because of the inability to clearly resolve the surface and bottom returns for shallow waters (less than approximately two meters), a pulsewidth measurement of the first event (surface return) is made for each sounding [10]. Depth, as related to the width of this first event, is recorded as an 8-bit digital word from a threshold referenced tapped delay line.

The Tektronix Model 7912AD Digitizer will provide a means to digitize the entire sequence of signal events periodically (less than 10 Hz) for analysis during data post-processing. The accurately digitized waveform data will play a very significant role during post-processing since it provides estimates of relative signal and background amplitudes, pulse shapes, etc., which are necessary to correct for the processor bias inherent in the HALS hardware design. The digitized data will also be utilized in making water parameter estimates which are essential for propagation bias corrections which are independent of the HALS hardware design.

Servo and Control Electronics System

The servo and control electronics system is illustrated in Figure 8. The scanning mirror is driven at a constant speed by a direct-coupled brushless torquer. The drive signal to the power amplifier originates in a servo signal generator with the speed of rotation being manually set to the desired scan rate determined during premission planning. The angular orientation of the scanner is measured by an 8-bit incremental optical encoder which is directly coupled to the scanner drive shaft. The contents of the counter is dumped to the computer data buffer each time the laser is triggered. The receiver field of view and the laser beam divergence are motorized adjustments driven from the computer control with a manual override feature. [9, 10]

Horizontal Position Control System

The aircraft position fixing system specified for the HALS is the Cubic Western ARGO Model DM-54 medium range system. The
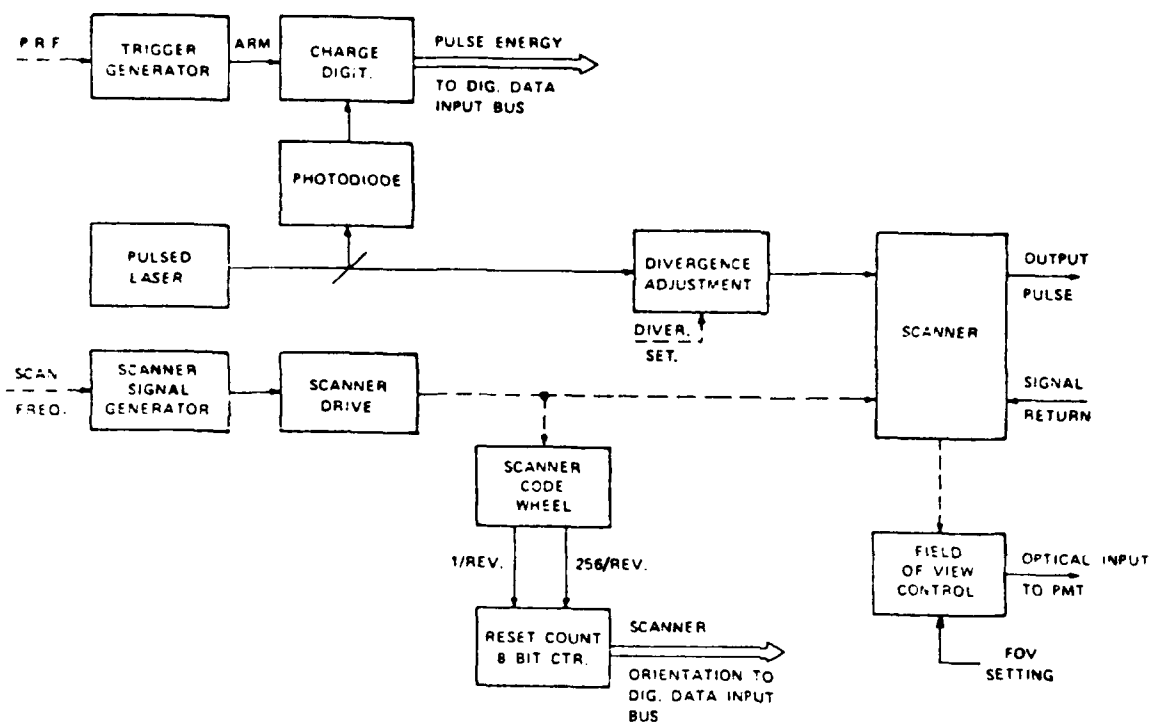
Courtesy of AERL

Figure 8

HALS Servo and Control Electronics

position fixing system must provide sufficient information to
the pilot and operator to ensure that the survey area to be
covered can be easily located and mapped. The digital output
from the system is recorded at a maximum update rate of four
times per second [9]. In addition, the HALS will be compatible
with, and interface provided for, the Del Norte Flying Flagman,
or equivalent, short range positioning system [8]. The short
range system will be used for all surveys made at scales of
1/25,000 or larger. In order to determine the horizontal
placement of each sounding, the aircraft pitch, roll, heading,
and scanner orientation are recorded at the instant the sounding
is made. The Lear Siegler, Inc. Model 6000A1 Attitude and Heading
Reference System (AHRS) has been selected for the HALS program.
This unit has demonstrated accurate performance with excellent
reliability as production equipment in several military aircraft
applications. Expected error for pitch and roll is 8.0 mrad
and 25.0 mrad heading error which includes alignment uncertainty.
Expected uncertainty for scanner orientation is 12.0 mrad. When
the scan is completely over water the pitch and roll can be
computed from the laser data to an accuracy of 3.5 mrad under
normal survey conditions by the optimal filter technique
developed by Byrnes and Fagin [13]. Altitude can also be
computed to an accuracy of 0.2 m by the same technique.

Digital Processor, Display and Recording System

The HALS digital processor is the Rolm Corp. Model 1664,
which is a militarized computer built around the Data General
architecture with 64K words of memory [9, 10]. As data is
acquired, it is transferred to CPU memory via direct memory
access from a pair of record buffers in a flip-flop manner,
and subsequently to magnetic tape after formatting in the
CPU [10]. In addition, the computer is required to calculate,
in real time, the signal-to-noise ratio from the waveform
digitizer data, periodically process slant altitude and slant
depth information to provide the operator with a valid data
estimate, process laser output power data and control the beam
divergence as a function of laser power and altitude, and
process and compute aircraft position from the position fixing
system for display to the operator and pilot [9, 10]. A disk
system and line printer will be provided for system software
development and a quick-look dump of the acquired data on the
ground [9, 10]. The computer will provide the interactive
communication, via the keyboard, between the operator and the
system for premission initialization and during the mission.

The HALS displays will include a navigational display for
the aircraft pilot. This display is planned as a cross hair
device with a logarithmic sensitivity to direct the pilot to,
and maintain a preprogrammed survey track. The operator will
also have position, status, and operational displays available

upon command to the computer. An oscilloscope display will be available to permit the operator to examine the analog signal at selected test points of the analog processing system.

The information pertinent to a particular survey will be recorded on industry compatible ½-inch, nine track, 800 BPI magnetic tape, time correlated to one millisecond [8, 9, 10]. This format is compatible with the computers on board the NAVOCEANO survey ships, as well as most main frame computing facilities throughout the world. It is planned to utilize two Miltope Corp. Model CR600 Recorders [9, 10]. This recorder is unique in that it is a cartridge/reel device, compatible with industry standard tape transports. The cartridge feature allows the operator to change tapes in 10 seconds or less. Since the transports will operate automatically in flip-flop fashion as one tape is filled, the survey continues uninterrupted. Both transports will have a read after write capability to check parity and indicate recording errors. It is proposed that the raw sounder data, scanner position, and laser output power will be recorded at a maximum rate of 400 Hz [10]. General housekeeping, heading and attitude information will be collected at a 20 Hz rate, and position fixing information will be recorded at a 4 Hz rate, or the maximum update rate from the positioning system [9, 10]. In addition, the waveform digitizer data will be recorded at a rate still to be determined (minimum of 2 Hz). The current estimate of recording time for each tape cartridge/reel of 600 feet is approximately 25 minutes.

Data Processing

NORDA has the responsibility to develop the HALS post-processing software, while AERL has the responsibility for the on board realtime mission data processing. Actual depth soundings and horizontal placement of the soundings will be accomplished during the post-mission data processing. A two-dimensional optimal filter is proposed which will deal with both depth and horizontal position errors simultaneously. The optimal process will convert data into equally spaced grid representation of depths, utilizing data redundancy on a statistical basis.

The survey ship's computer processing will evaluate agreement between soundings from the HALS principal survey lines and the HALS cross-check lines [12]. The processing will also evaluate the agreement where the HALS soundings and the acoustical soundings from deeper water surveys overlap [12]. Final editing will be performed and "smooth sheets" will be produced on the ship's plotters [12].

REFERENCES

[1]   Raytheon Company, "Pulsed Light Airborne Depth Sounding
      (PLADS) System," Final Report, 30 April 1970, pp. 1-2.

[2]   Hongsuk H. Kim, Peter O. Cervenka, and Charles B. Lankford,
      "Development of an Airborne Laser Bathymeter," NASA Technical
      Note TN D-8079, October 1975.

[3]   Duane C. Bright, "Coastal Aerial Photo-Laser Survey (CAPS),"
      Proceedings of the American Congress on Surveying and Mapping,
      35th Annual Meeting, March 1975.

[4]   AVCO Everett Research Laboratory, Inc., "Airborne Oceano-
      graphic Lidar System," Final Report (NASA CR-141407), October
      1975.

[5]   Gary C. Guenther, Lowell R. Goodman, Frank Hoge, Robert N.
      Swift, Robert W. L. Thomas, Duane C. Bright, "AOL Bathy-
      metric Field Test Program," Airborne Laser Hydrography
      Symposium III, October 1977.

[6]   "Air/Underwater Laser Radar Test Results, Analysis, and
      Performance Predictions," (U) ORIC(ORAD) Program (U) Naval
      Air Test Center, Warminster, PA 18974, January 1976 Report
      No. NADC-76005-20 (CONFIDENTIAL)

[7]   H. Krumboltz, "Experimental Investigation of System
      Attenuation Coeffecient for HALS," Naval Air Development
      Center, Warminster, PA 18974, August 1979, Report No.
      NADC 80035-30.

[8]   Naval Ocean Research and Development Activity, "Hydrographic
      Airborne Laser Sounder (HALS) System, Purchase Description,"
      NSTL Station, MS, 30 March 1979.

[9]   AVCO Everett Research Laboratory, Inc., "HALS Preliminary
      Design Review and HALS System Design Review," November 1979
      and January 1980.

[10] AVCO Everett Research Laboratory, Inc., "Proposal for
      Hydrographic Airborne Laser Sounder," AERLP 269, June 1979.

[11] M. B. Rankin and G. D. Ferguson, SPIE Proceedings 160,
      67 (1978).

[12] Larry B. Bourquin and Maxim F. van Norden, "The
      Hydrographic Airborne Laser Sounder: A Planning and
      Operational Scenario (II)," U.S. Naval Oceanographic
      Office, July 1980.

[13] H. J. Byrnes and Samuel L. Fagin, "Optimal Filtering and
      Analysis of Scanning Laser Data," NORDA Technical Note 24,
      June 1978.

PAPER 5

FIELD TRIALS OF A LIDAR BATHYMETER IN

THE MAGDALEN ISLANDS

by

R.A. O'Neil

Data Acquisition Division
Canada Centre for Remote Sensing
2464 Sheffield Road
Ottawa, K1A 0Y7, Canada

Telephone: 613-998-9060
Telex: 053-3777

presented at:

Laser Hydrography Symposium

September 30, 1980

Defence Research Centre Salisbury
Adelaide, South Australia

Abstract

Field trials of the CCRS MkII lidar bathymeter were
conducted in the Magdalen Islands in the Gulf of St. Lawrence.
The northern islands of the group surround a shallow tidal
lagoon whose bottom is covered with vegetation. The beam
attenuation coefficient, α, was measured to be 1.7 m^{-1}. On the
Gulf side of the islands, where the bottom is clean sand, the
observed effective lidar attenuation coefficient was found to be
in reasonable agreement with the measured beam attenuation
coefficient $\alpha = 0.7 \ m^{-1}$.

A total of 305 line km were flown in August 1979. Water
depths up to 18 metres were routinely sounded yielding a system
performance of $\alpha D_{max} = 14$ (where D_{max} is the maximum depth
sounded for a given α).

1. Introduction

The basic operating principle of a lidar bathymeter is
illustrated in Fig. 1. The laser transmits a pulse of green
light from the aircraft to the water where a portion of the
incident energy is reflected from the surface and some fraction
of the remainder is reflected from the bottom. The time delay,
t, between the arrival of the surface and bottom returns at the
receiver is related to water depth, D, through the relation
$D = ct/2$, where c is the speed of light in water.

The efficacy of the above technique depends in large part
on the available laser power and the ability of the optical
receiver and data recording system to cope with signals whose
relative amplitudes may vary rapidly over a wide dynamic range
along a flight line. Bottom signal strengths, in particular,
can vary greatly depending on such factors as water depth, water
clarity, and bottom reflectance.

The CCRS MkII lidar bathymeter was designed to map water
depths in shallow coastal areas. The ultimate user of the
technology, the Canadian Hydrographic Service, was particularly
interested in regions with water depths shallower than 10
metres. Although little was known of the optical character-
istics of Canadian coastal waters at the time the system was
specified, a useful lidar system was expected to chart out to 10
metre contour when the water attenuation coefficient was less
than 1 m^{-1} (at the laser wavelength). So that the lidar could
be flown simultaneously with the photo hydrography package (Reid
et ai, 1980), it had to operate in daylight from altitudes up to
1524 m (5000 ft).

2.   System Design

Fig. 2 is a block diagram of the MkII lidar bathymeter
showing its main functional components. The transmitter is an
International Laser Systems NT-462 frequency-doubled Nd:YAG
laser which delivers up to 10 MW peak pulse power at 532 nm and
15 MW pulse power at 1064 nm simultaneously. The output pulse
width at 532 nm is 5 ns. The laser pulse repetition frequency
is 10 Hz.

A schematic of the 532 nm (green) receiver is shown in
Fig. 3. The receiver consists of a 20 cm aperture, f/1
refracting telescope, a 3 nm bandwidth filter, variable field
stops, and an ITT F4084 grid-gated photomultiplier tube (PMT)
with a 2 ns risetime. Fig. 4 relates the gate pulse amplitude
to the amplitude of the PMT output current pulse. A logarithmic
amplifier, designed in-house at CCRS, is used to compress the
dynamic range of the PMT output signal. The characteristic of
this amplifier is shown in Fig. 5. The 1064 nm (infrared)
receiver incorporates a 5 cm aperture, f/2 refracting telescope,
an 8.3 nm bandwidth filter, and a General Electric LE-103B
Laser-Eye photodiode detector with 8 ns risetime. The two
receivers were designed and integrated with the transmitter by
Optech Inc.

The lidar altimeter measures the slant range from the
transmitter to the water surface. The trigger pulse for this
circuit is obtained from the IR receiver. The measured lidar

slant range is used to drive the lidar forewarning system which
in turn permits the bathymeter operator to select the time at
which the green-receiver PMT is gated on thereby compensating
for electronic propagation delays in the system. The receiver
gate timing is illustrated in Fig. 5. By appropriate selection
of the magnitude and risetime of the gating pulse, the operator
can set the PMT gain to a relatively low value at the water
surface where the reflected laser signal is strong, and then
increase the PMT gain as the return signal becomes weaker on the
way to the bottom. This gain variability feature, when used in
combination with logarithmic compression of the PMT output
signal, enables the green receiver to accommodate a 90 dB range
in input power.

The bathymeter data acquisition system consists of a
Tektronix R7912 transient digitizer, a Kennedy 9800 computer
compatible tape (CCT) transport, and a transient digitizer
interface (TDI). The digitizer has an input bandwidth of 500
MHz, and samples the incoming waveforms in 0.4 ns steps when a
20 ns/div timebase is used. The amplitude of the waveform is
digitized to 9 bits resolution. The digitizer also incorporates
a 4096 x 10 bit memory option. The TDI was designed by the
Genesys Group and incorporates an LSI-11/2 microprocessor, 8K x
16 bits of PROM memory and 32K x 16 bits of RAM memory. The TDI
extracts data from the digitizer, fires the laser, and annotates
each lidar return with the time. The interface outputs data to
the CCT in the standard Johnson Space Centre (JSC) non-imagery
format.

At the time of this experiment a general purpose Airborne
Data Acquisition System (ADAS) was used to record the laser
power and slant range by means of the General Digital Interface
(GDI). ADAS also records the camera firing times, the aircraft
position and sensor attitude data. The time recorded by both
the TDI and ADAS allows the two data sets to be related.

The lidar bathymeter sensor head is shown in the photograph
in Fig. 6. The IR receiver is in the foreground, with the laser
transmitter to its left and the green receiver to its right.
The logarithmic amplifier is located adjacent to the green
receiver. The entire transceiver assembly weighs about 45 kg
(100 lb). The transceiver and the Wild Heerbrugg RC-10 metric
camera are mounted together on a bridge structure which holds
the two units in rigid alignment in adjacent bays in the DC-3
aircraft. A Litton LTN-51 Inertial Navigation Unit (INU) is
bolted to the top of the RC-10 camera in order to provide
precise measurement of the attitude of both the film plane and
the lidar transceiver.

3.   Surface Measurements

The bathymeter was deployed to the Magdalen Islands in the
Gulf of St. Lawrence, to sound the depths of the coastal waters
and sheltered lagoons in the Ile de l'Est region. This site is
excellent for testing a lidar bathymeter since it provides a
wide range of water turbidities, bottom characteristics and sea
states.

Fig. 8 shows a topographic map of the area of the Magdalens surveyed with the lidar bathymeter. Water depths reach only about 8 m in the lagoon while exceeding 20 m in the water off the north coast.

The beam attenuation coefficient, α, was measured along several lines in the Cap du Dauphin area on the day of the airborne missions. A Martek transmissometer with 10 nm band-width filter centred at 532 nm was used. A mean value of 0.7 m^{-1} was recorded in the clear waters off the Island's northern coast, whereas a mean α of 1.7 m^{-1} was measured in the relatively turbid lagoon. The point to point variation was quite small and no appreciable variation occured with depth.

As the lidar bathymeter operates in a background limited mode, the upwelling sea surface radiance was measured. To do this, the green receiver PMT was gated on while the receiver was viewing only the solar radiation reflected from the water. The resultant signal was then converted to a radiance value using the known sensitivity, collecting area, and field of view of the receiver. The radiance value so calculated was 7×10^{-5} W/(m^2·Sr·A). This was measured with the aircraft flying at 1524 m near local noon August 2, 1979 over deep water off the south coast of the islands. This radiance value is within an order of magnitude of typical values found in the literature, (Austin, 1970).

4.   Airborne Measurements

One of a total of thirty flight lines flown with the bathymeter is shown superposed on a topographic map of the Magdalen Islands in Fig. 8. A total of 305 line km were flown in two sorties on August 2, 1979. The first sortie took place between 1210 and 1700 GMT and the second sortie was flown between 1820 and 2114 GMT on August 2, 1979. The flight altitude for all the lines was 1524 m. Local weather was sunny with a few scattered clouds at 5500 m (18,000 ft.) and surface winds were moderate. (Some areas in the lagoon were dead calm.) Approximately 40,000 individual lidar returns were recorded during the mission.

The laser was operated at 7 MW pulse power and its repetition rate was set to 9.3 Hz so that the data rate would not exceed the capability of the TDI. The aircraft ground speed was approximately 75.7 m s^{-1} (149 knots) for all flight lines. This resulted in an along-track depth sampling interval of approximately 8.1 m.

Since the Magdalen project was not a production hydrography mission, only one RC-10 camera was employed to provide photo fixes to aid in correcting the raw depth measurements.

The lidar echo returns were displayed individually on a graphics terminal to identify the surface and bottom returns from which the water depth was calculated. The initial analysis of raw bathymeter data produced a file of uncorrected or raw depths. An example of this type of output is shown in Fig. 9.

This is a plot of raw depths observed along flight line 7 as shown in Fig. 8. The horizontal scale of this plot is the distance along the line measured from an arbitrary starting point. The flight line began on the south shore of the islands, proceeded northwest across the lagoon, and then into the north-coast waters. The plot illustrates the bathymeter's capability for high resolution mapping of bottom contours. Several pronounced sand dunes are visible in the lidar data and have been confirmed by the RC-10 photographs from this flight line. The water penetration capability of the sensor is also quite evident in Fig. 9, since depths approaching 18 m are recorded. (Depths slightly greater than 20 m were successfully sounded on other flight lines.) The minimum depth recorded on flight line 7 was 0.8 m. The uncertainty in the raw depth values is approximately 0.2 m. These results were obtained without sophisticated processing of the lidar returns or any assumptions concerning the scattering properties of the water. The primary problem in extracting the bottom in many areas was the large amount of volumetric backscattering in the water column which broadened the bottom pulse as well as producing a high 'clutter' level in the region of the bottom peak. When such a situation arises, as it often does in the relatively turbid lake waters, no advantage is gained in increasing laser power or range gating the receiver since the effective 'noise' level increases along with the desired signal.

Using the INU data in combination with the RC-10
photographs and lidar slant range information, it is possible to
correct the raw depths for the laser beam incidence angle and
the aircraft attitude and position, (Reid et al, 1980). No
tidal or sea-state corrections have yet applied to these data.

5.   Discussion

In most places the sea floor, on the Gulf side of the
Magdalen Islands, is a clear sandy bottom. In the lagoons the
water is shallower, more turbid and the bottom is covered with
vegetation. It should be possible to determine the effective
attenuation coefficient for the lidar beam by a measurement of
the power observed in the bottom return if the only variable
parameter is the water depth. In the course of a single flight
line the laser power and slant range were essentially constant
and it was possible to select intervals along the flight line
with similar bottom characteristics by means of the aerial
photography. Fig. 10 is a 3-dimensional plot of the amplitude
of the bottom echo (actually this is proportional to the
logarithm of the bottom echo peak power because the system
incorporates a logarithmic amplifier in the receiver); the time
or distance along the flight line; and the water depth. Flight
line 10, shown in this figure, began in the lagoon, passed over
the sand dunes and into the clear water on the Gulf side of the
island. The green "cloud" of points is the data in 3-space: the
projections of this data are shown in blue on the time-depth

plane and in red on the depth-amplitude plane. The projection
on the time depth plane is the water depth profile. Two
features are of note on the depth-amplitude projection. The
first is a very dense cluster of points in the low amplitude
shallow depth regime arising from soundings made in the lagoon.
The second feature is a line of points lying above the cluster
and extending from about 1 meter to 14 meters in depth. The
slope of a line in such a plot is related, through the log-
arithmic conversion coefficient (Fig. 5) of the amplifier, to
the effective attenuation coefficient of the lidar beam as it
makes the sounding. The general slope of the cluster is not a
great deal different from that of the line even though the beam
attenuation coefficient in the lagoon and in the Gulf differ by
a factor of 2.4. We have been unable yet to arrive at a
satisfactory explanation of this although it is believed to be
related to the field of view of the receiver and the beam
spreading out in the water.

A similar plot for flight line 18 is shown in Fig. 11 which
passed over only the Gulf. The amplitude-depth plane has been
replotted in Fig. 12 in a rectangular coordinate system. A
straight line fitted through the points yields an effective
attenuation coefficient of 0.84 m^{-1}. Using the transmissometer,
beam attenuation coefficients along this flight line were found
to vary between 0.58 and 0.92 m^{-1}. (In the very shallow water
next to the beach, the value of α increased to 2.5 m^{-1}). Using

Shannon's (1976) emperical relationship, the corresponding mean

diffuse attenuation coefficient $k = 0.19 \text{ m}^{-1}$. Thus there is a

reasonable agreement between the effective attenuation

coefficient and the beam attenuation coefficient for the

particular circumstances of this measurement.

6. Conclusions

An examination of all the Magdalen Island data files

processed to date reveals the bathymeter's depth sounding

capability to be 0.6 to 20 m in the clear water off the islands'

north coast where the mean attenuation of the water was 0.7 m^{-1}.

Depths to 8 m were sounded in the shallow, turbid lagoon water

where the mean α was 1.7 m^{-1}. The overall performance of the

system at this site was quite impressive in view of the fact

that the mission was flown in broad daylight at an altitude of

1524 m. A very useful parameter for describing the performance

of the sensor is the product of the mean attenuation coefficient

and the maximum recorded depth. This product, αD_{max}, was

approximately 14 based on the Magdalen Island results*.

---

* In other trials of the MkII lidar bathymeter, the following

performance has been obtained:

Prince Edward County - June 1979 $\alpha D_{max} = 13$

Gananoque - July 1979 $\alpha D_{max} = 12$

Bruce Peninsula - July 1980 $\alpha D_{max} = 18$

The CCRS MkII lidar bathymeter has proven to be a reliable, accurate, and efficient means for remote sounding of water depths in coastal regions. Further development of the sensor along with refinements to the data acquisition and processing will be undertaken so that the existing profiling lidar system may be used in a production environment until a scanning lidar bathymeter has been built. Bathymeter test flights will be made at other locations and attempts will be made to better quantify the effects of sensor operating parameters, water turbidity, sea state, and bottom characteristics on the overall performance of the bathymeter.

References

R.W. Austin; in Optical Aspects of Oceanography, edited by N.G.
   Jerlov and E.S. Nielsen Academic Press, New York, 1974, pp.
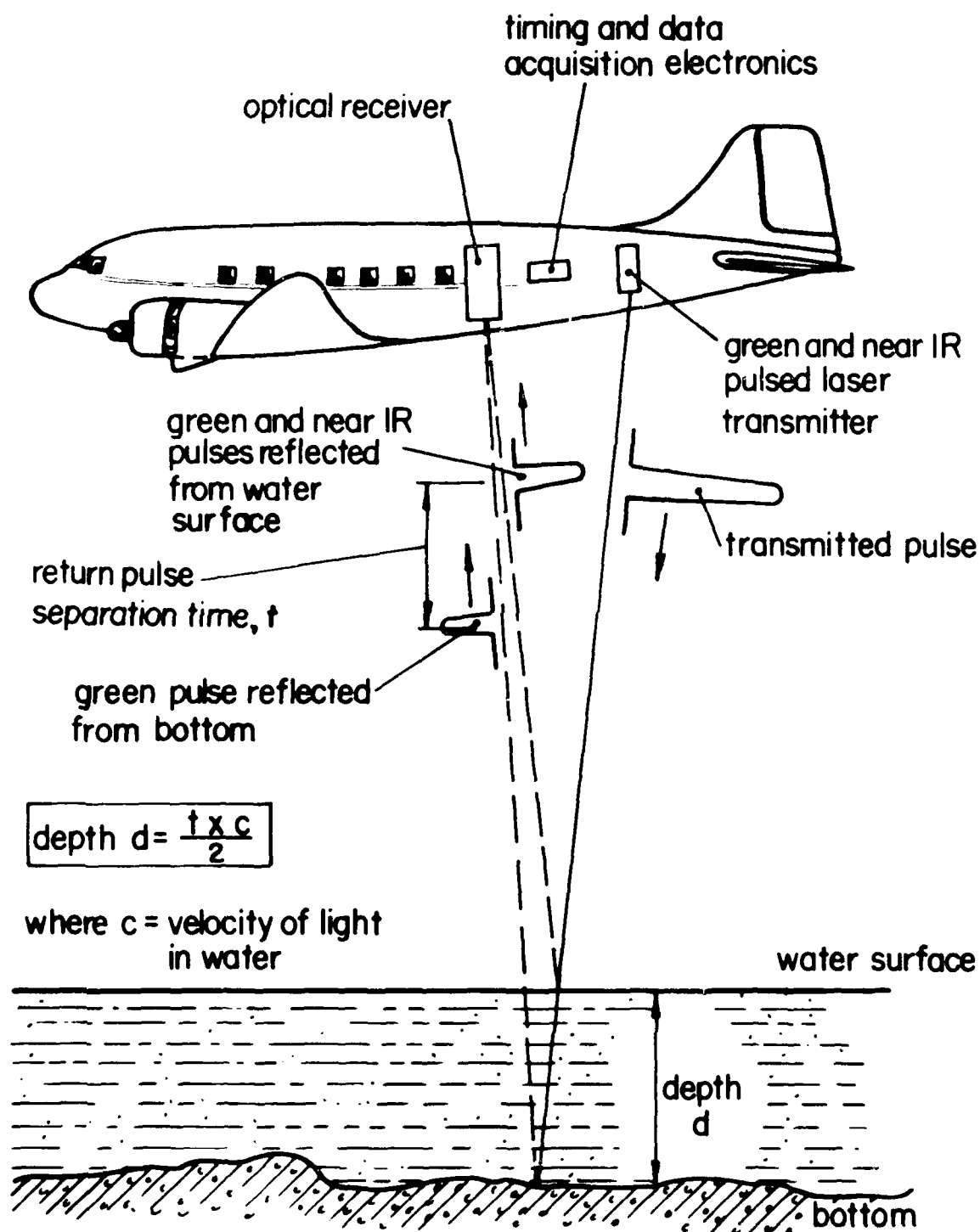   317-344.

D.B. Reid, S.E. Masry, A.J. Dow and J.R. Gibson; System Concept
   and Results of the Canadian Aerial Hydrography Project,
   presented at the Laser Hydrography Symposium, Defence
   Research Centre Salisbury, Adelaide, South Australia,
   September 30, 1980.

J.G. Shannon; Correlation of Beam and Diffuse Attenuation
   Coefficients Measured in Selected Ocean Waters.   SPIE 64
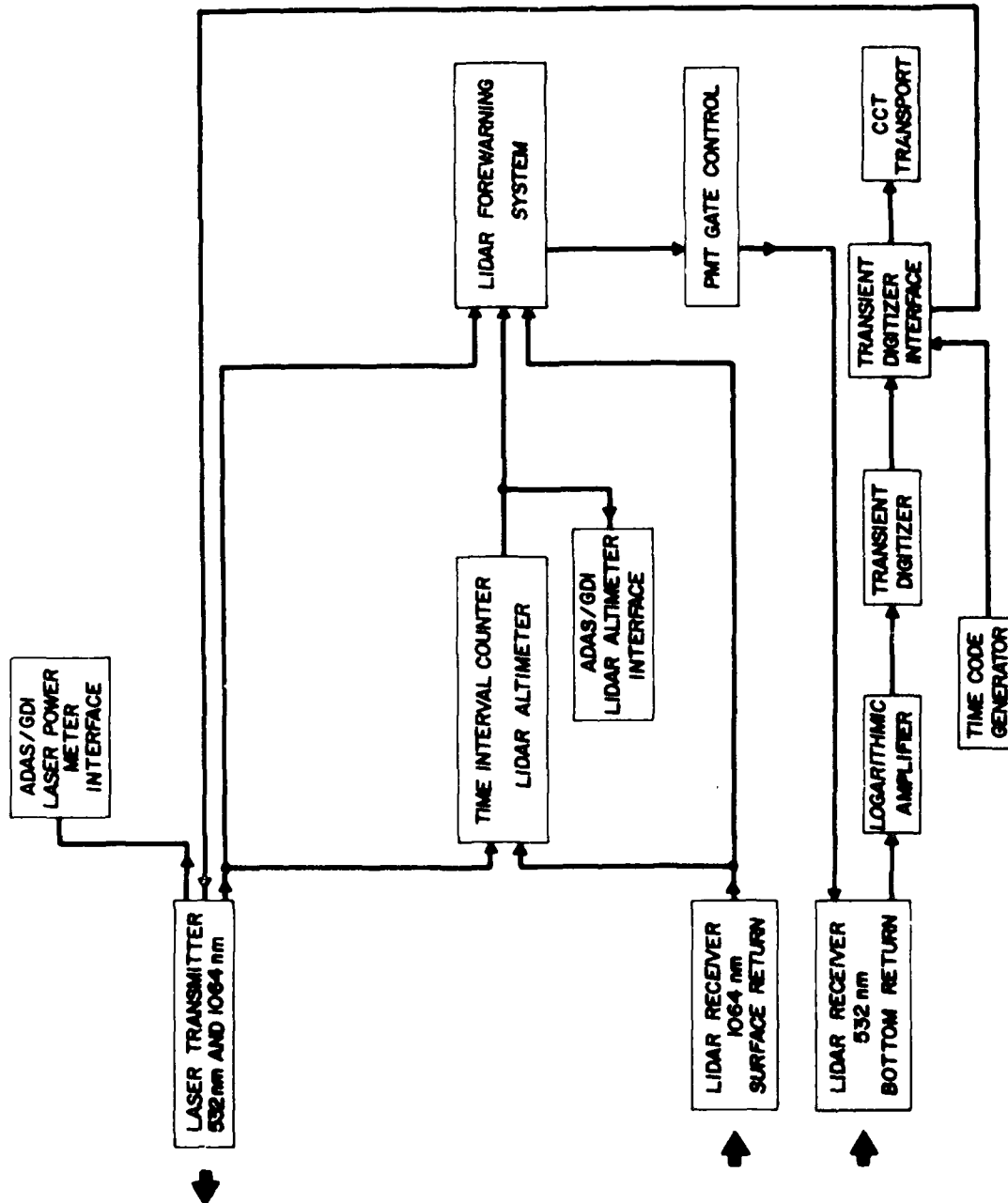   (1975) pp. 3-11.

FIGURE CAPTIONS

Fig. 1   Principle of operation of a lidar bathymeter. The
          water depth can be calculated from a measurement of
          the difference in arrival time between the surface
          and bottom reflections of the green laser pulse.

Fig. 2   Block diagram of the CCRS MkII lidar bathymeter.
          The principal components are the lidar transceiver,
          the gating electronics, and the signal capture and
          recording systems.

Fig. 3   Block diagram of the green receiver in the CCRS
          MkII lidar bathymeter.

Fig. 4   The output current of the ITT F4084 grid gated
          photomultiplier tube as a function of the gating
          pulse amplitude. The grid potential is normally 3
          volts more negative than the photo cathode in which
          case the tube is off. The gating pulse is applied
          to the grid makes it more positive than the photo
          cathode and turns the tube on. In practice, a
          gating pulse of the opposite polarity is applied to
          the photocathode to achieve the same effect.

Fig. 5   The characteristic of the logarithmic amplifier
          used in the lidar bathymeter.

          $V_{out}[mV] = 32.7 \log I_{in}[mA]$

Fig. 6   A timing diagram for the lidar bathymeter showing
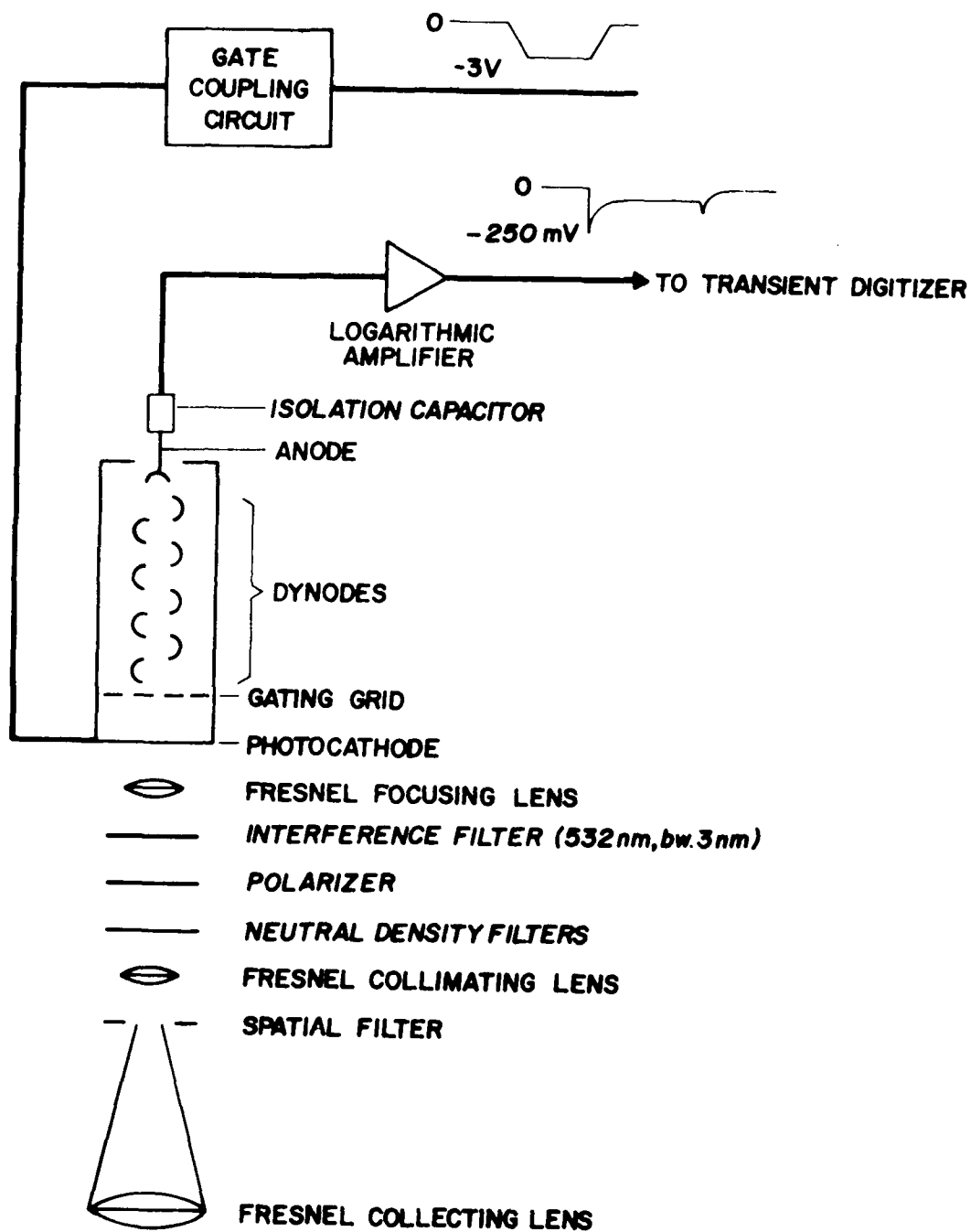   the manner in which the green receiver is gated.

Fig. 7   The transceiver of the CCRS MkII lidar bathymeter.

The laser transmitter is to the left. The IR

receiver is in the lower centre and the green

receiver is on the right.

Fig. 8   Topographic map of the Magdalen Islands with flight

line 7 marked. The line was flown SE-NW.

Fig. 9   Water depth profile along flight line 7. The line

begins on the edge of the lagoon, passes over the

sand dunes (1.3 minutes into the line) and proceeds

into the Gulf of St. Lawrence. Two underwater sand

dunes are clearly visible on the shore of the Gulf.

Fig. 10   A 3-dimensional plot showing the amplitude of the

bottom echo as a function of time (distance) along

flight line and water depth for flight line 10.

The data points are plotted in the green, the

projection onto the amplitude-depth plane is in red

and the projection onto the time-depth plane is

plotted in blue.

Fig. 11   A 3-dimensional plot showing the amplitude of

bottom echo as a function of time (distance) along

flight line, and water depth for flight line 18.

Fig. 12   The amplitude of the bottom echo as a function of

water depth for flight line 18. The slope of the

fitted straight line corresponds to an effective

lidar attenuation coefficient of 0.84 m^{-1}.

timing and data acquisition electronics

optical receiver

green and near IR pulsed laser transmitter

green and near IR pulses reflected from water surface

transmitted pulse

return pulse separation time, t

green pulse reflected from bottom

$$depth\ d = \frac{t \times c}{2}$$

where c = velocity of light in water

water surface

depth d

bottom

LIDAR BATHYMETER : PRINCIPLE OF OPERATION

LIDAR BATHYMETER SYSTEM

GATE
COUPLING
CIRCUIT

0
-3V

0
-250 mV

TO TRANSIENT DIGITIZER

LOGARITHMIC
AMPLIFIER

ISOLATION CAPACITOR

ANODE

DYNODES

GATING GRID

PHOTOCATHODE

FRESNEL FOCUSING LENS

INTERFERENCE FILTER (532nm, bw.3nm)

POLARIZER

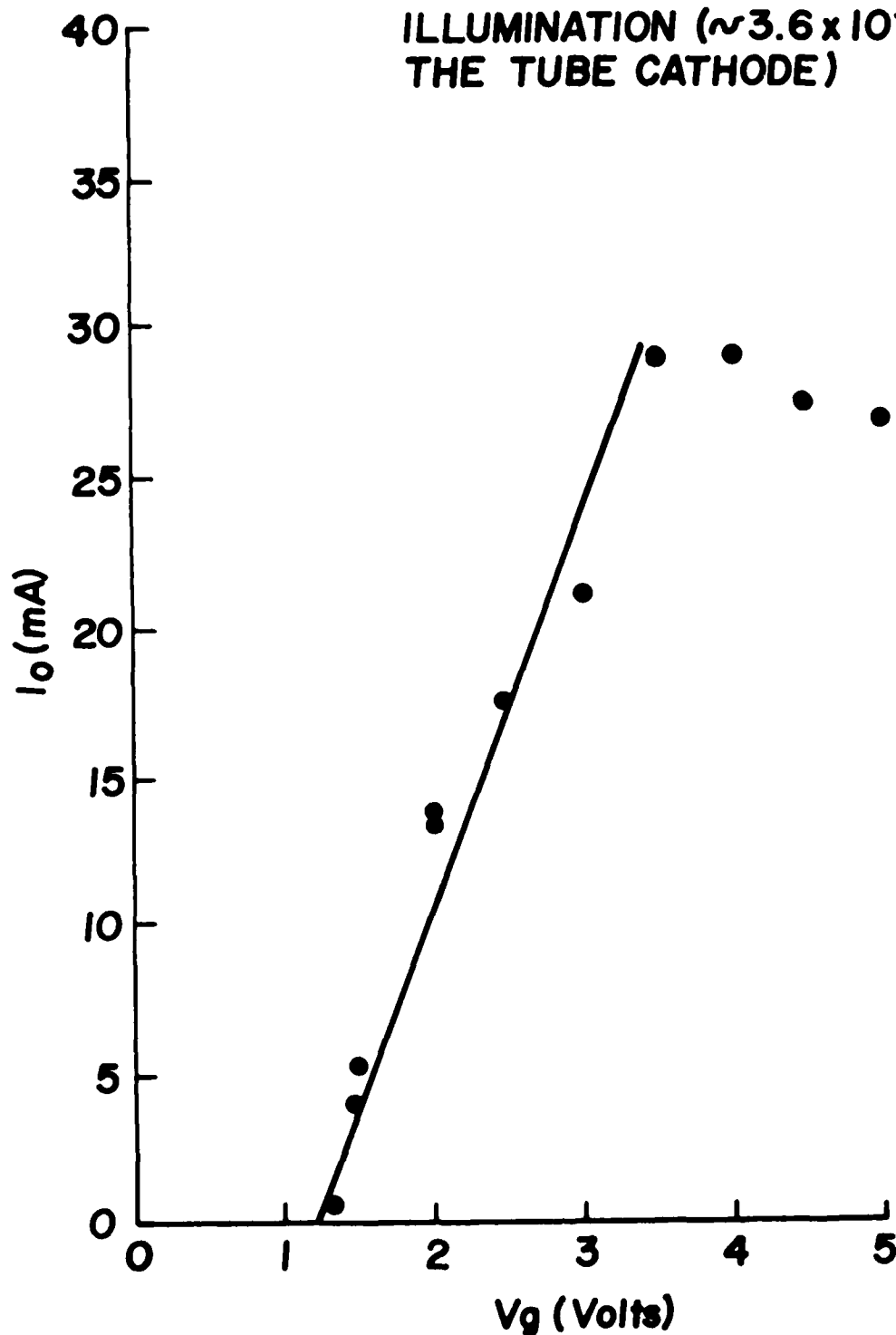NEUTRAL DENSITY FILTERS

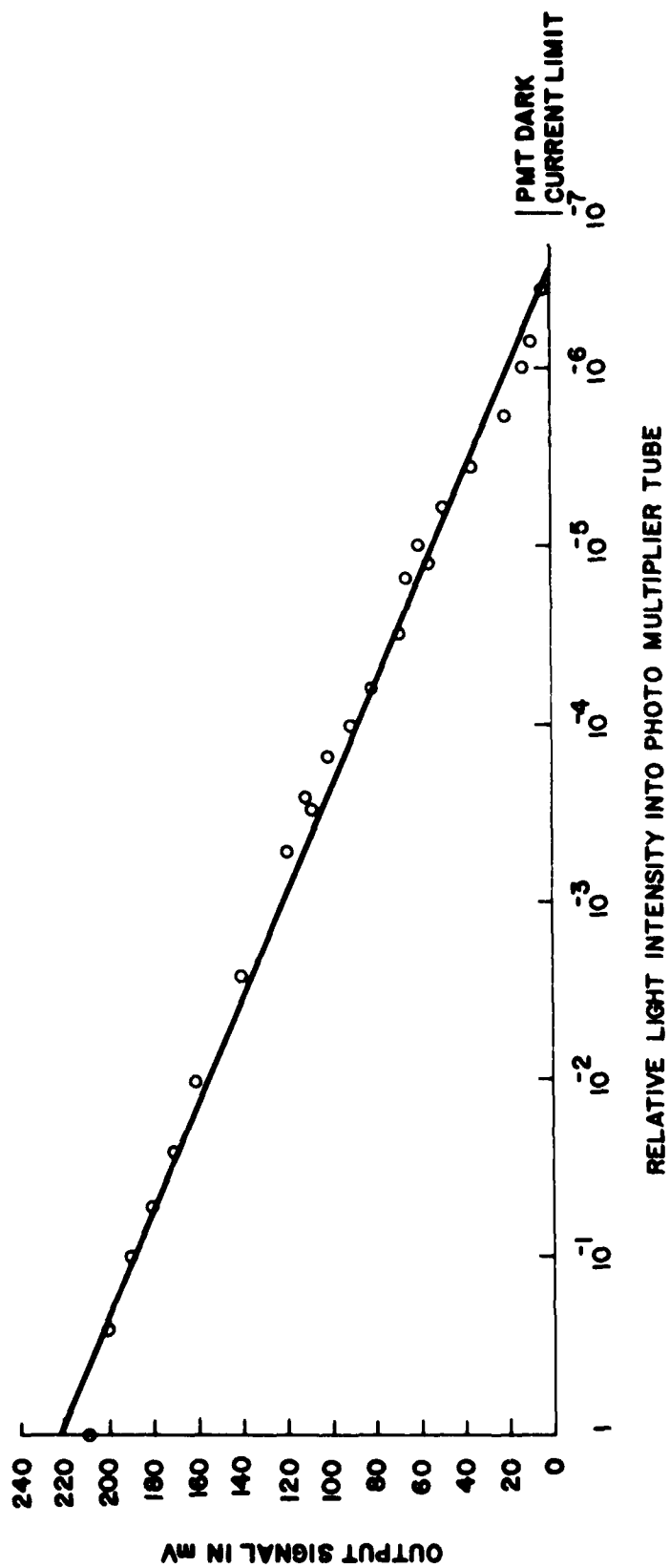FRESNEL COLLIMATING LENS

SPATIAL FILTER
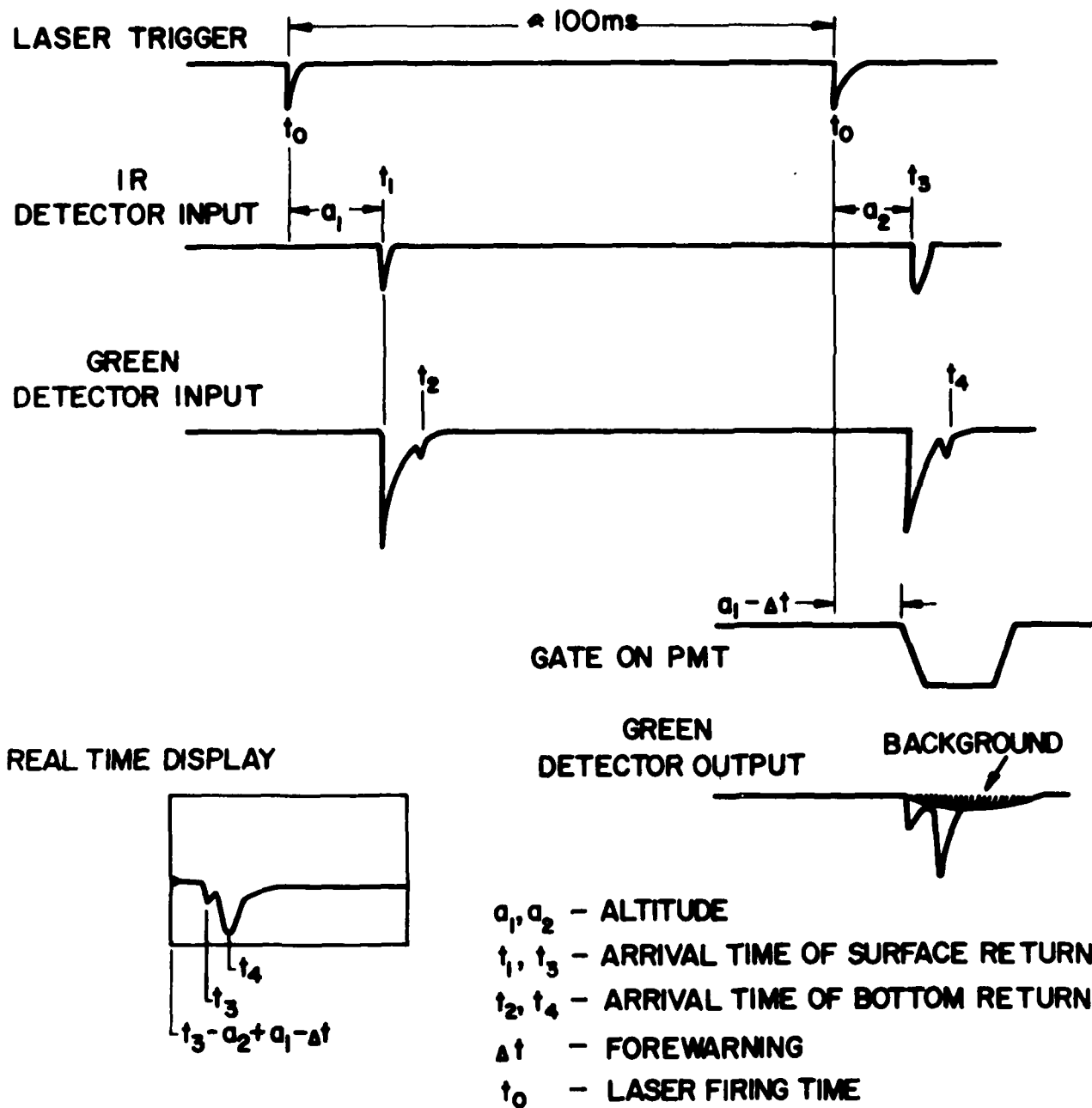
FRESNEL COLLECTING LENS

LIDAR BATHYMETER RECEIVER

PMT OUTPUT CURRENT Vs GRID CONTROL PULSE AMPLITUDE (Vg) FOR A CONSTANT LOW LEVEL ILLUMINATION ($\sim 3.6 \times 10^{-7}$ W AT THE TUBE CATHODE)
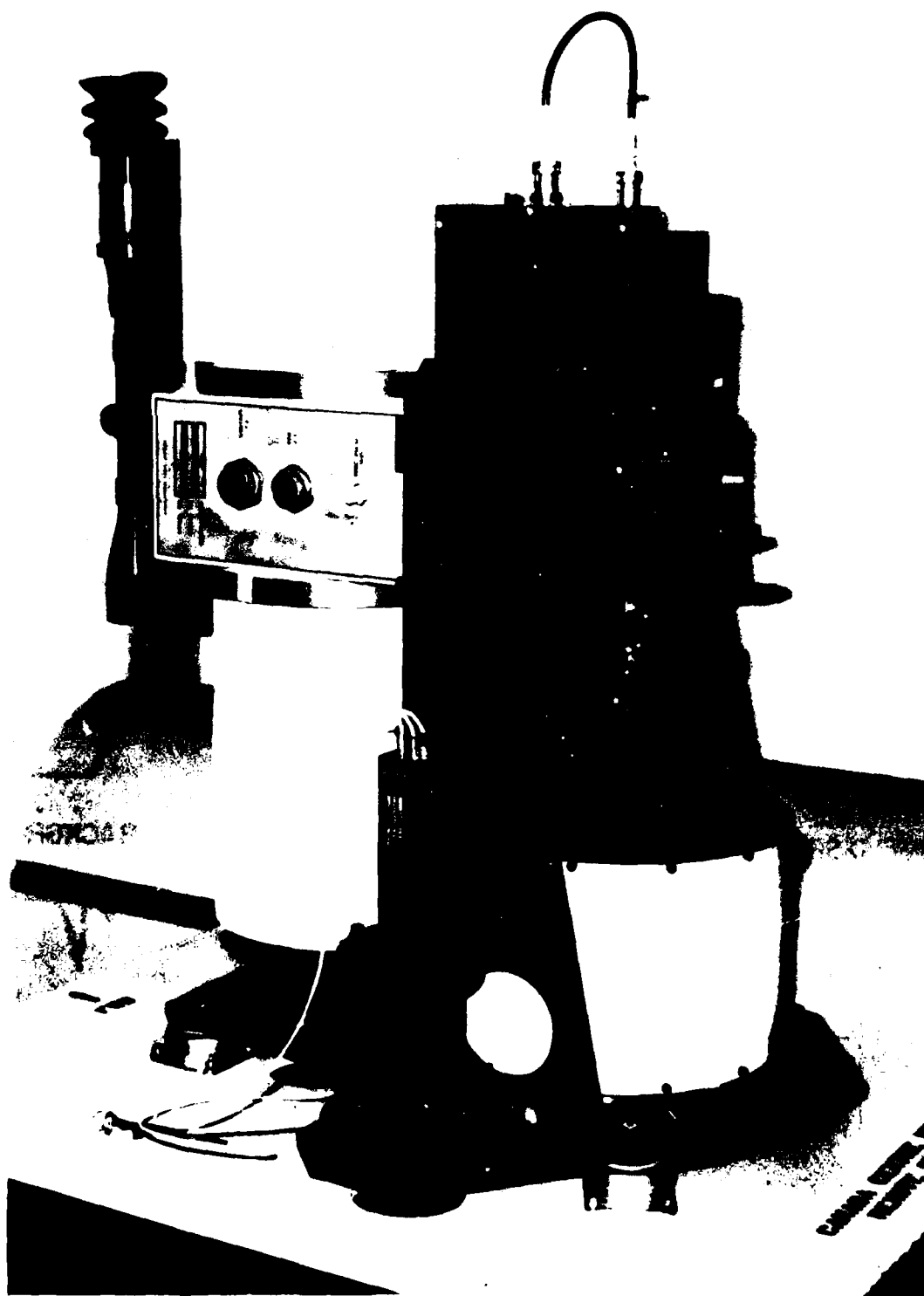
TRANSIMPEDANCE LOGARITHMIC AMPLIFIER CHARACTERISTIC AS
MEASURED WITH A PHOTOMULTIPLIER SIGNAL SOURCE AND
CALIBRATED NEUTRAL DENSITY FILTERS

LIDAR BATHYMETER TIMING

LASER TRIGGER

← 100ms →

t_0

t_0

IR DETECTOR INPUT

a_1

t_1

a_2

t_3

GREEN DETECTOR INPUT

t_2

t_4

$a_1 - \Delta t$

GATE ON PMT

REAL TIME DISPLAY

GREEN DETECTOR OUTPUT

BACKGROUND

t_4

t_3

$t_3 - a_2 + a_1 - \Delta t$

a_1, a_2 — ALTITUDE

t_1, t_3 — ARRIVAL TIME OF SURFACE RETURN

t_2, t_4 — ARRIVAL TIME OF BOTTOM RETURN

Δt — FOREWARNING

t_0 — LASER FIRING TIME
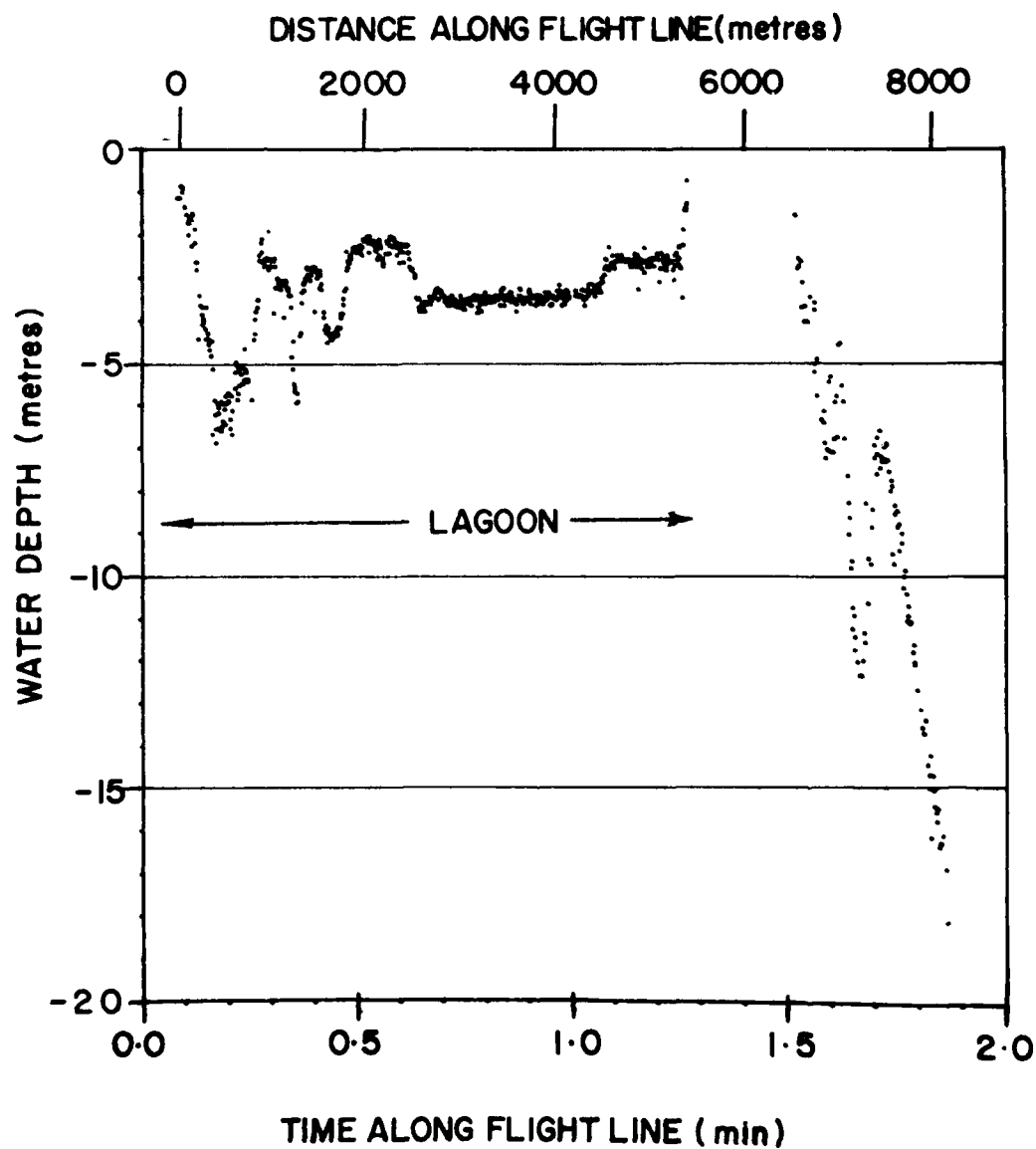
CANADA

GULF OF ST LAWRENCE

ILES DE LA

MADELEINE

Lidar Bathymeter
Magdalen Islands
C-GRSA
Flight line 7
August 2, 1979

ILE DE L'EST

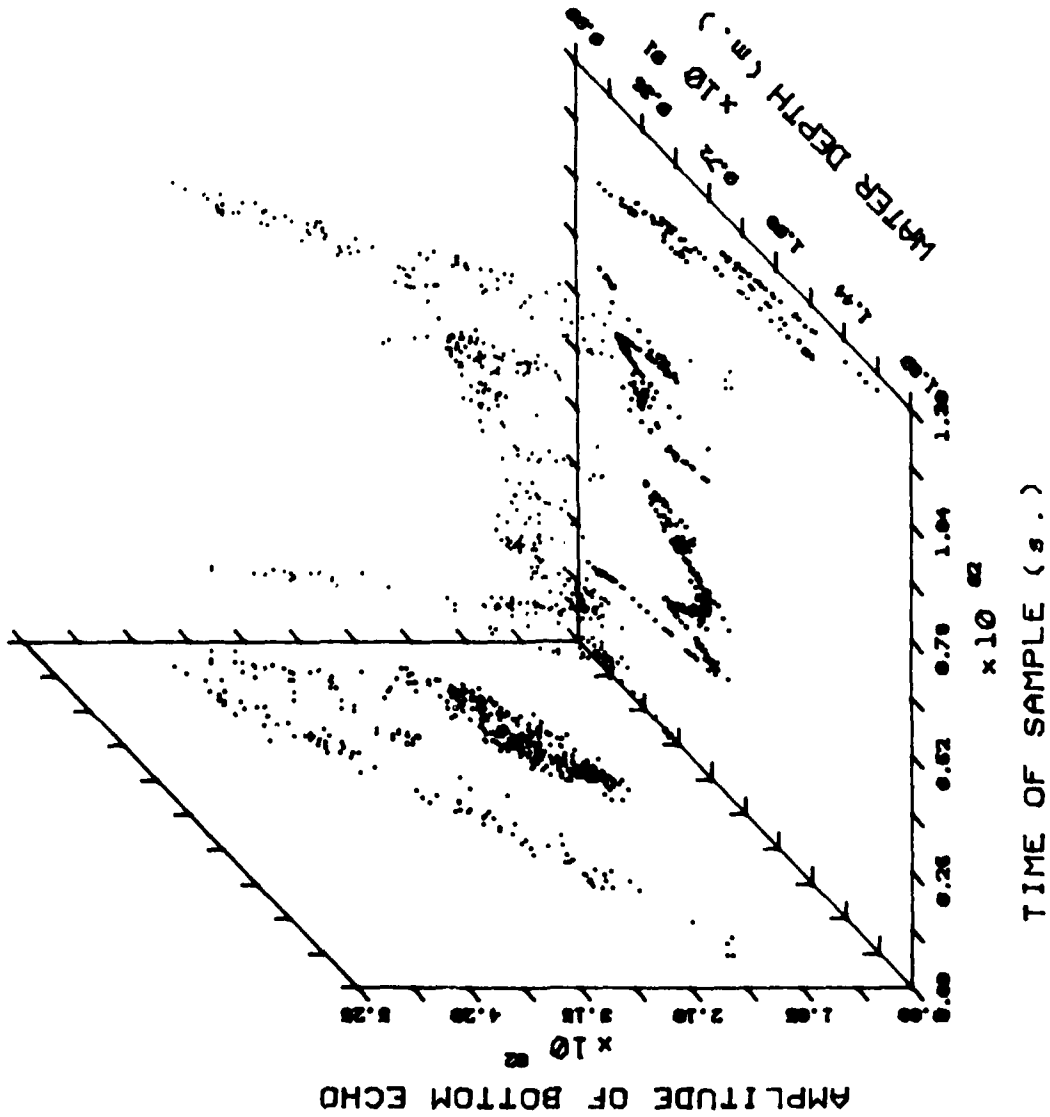# LIDAR BATHYMETER :
MAGDALEN ISLANDS

C-GRSA
AUGUST 2.1979
FLIGHT LINE 7
12 : 56 : 42 GMT

DISTANCE ALONG FLIGHT LINE (metres)

TIME ALONG FLIGHT LINE (min)

LIDAR BATHYMETER

PROJECT ID: MAGDALEN
FLIGHT LINE: 10
FLIGHT DATE: 2- 8-79
START TIME: 18:32:62.472
FILE: LH00 10202021.6LR

WATER DEPTH (m.)

×10

TIME OF SAMPLE (s.)

×10

AMPLITUDE OF BOTTOM ECHO

LIDAR BATHYMETER

PROJECT ID: MAGDALEN
FLIGHT LINE: 18
FLIGHT DATE: 2- 8-79
START TIME: 14:47:50.954
FILE: LH04 :002209.SLR

WATER DEPTH (m.)

TIME OF SAMPLE (s.)

AMPLITUDE OF BOTTOM ECHO
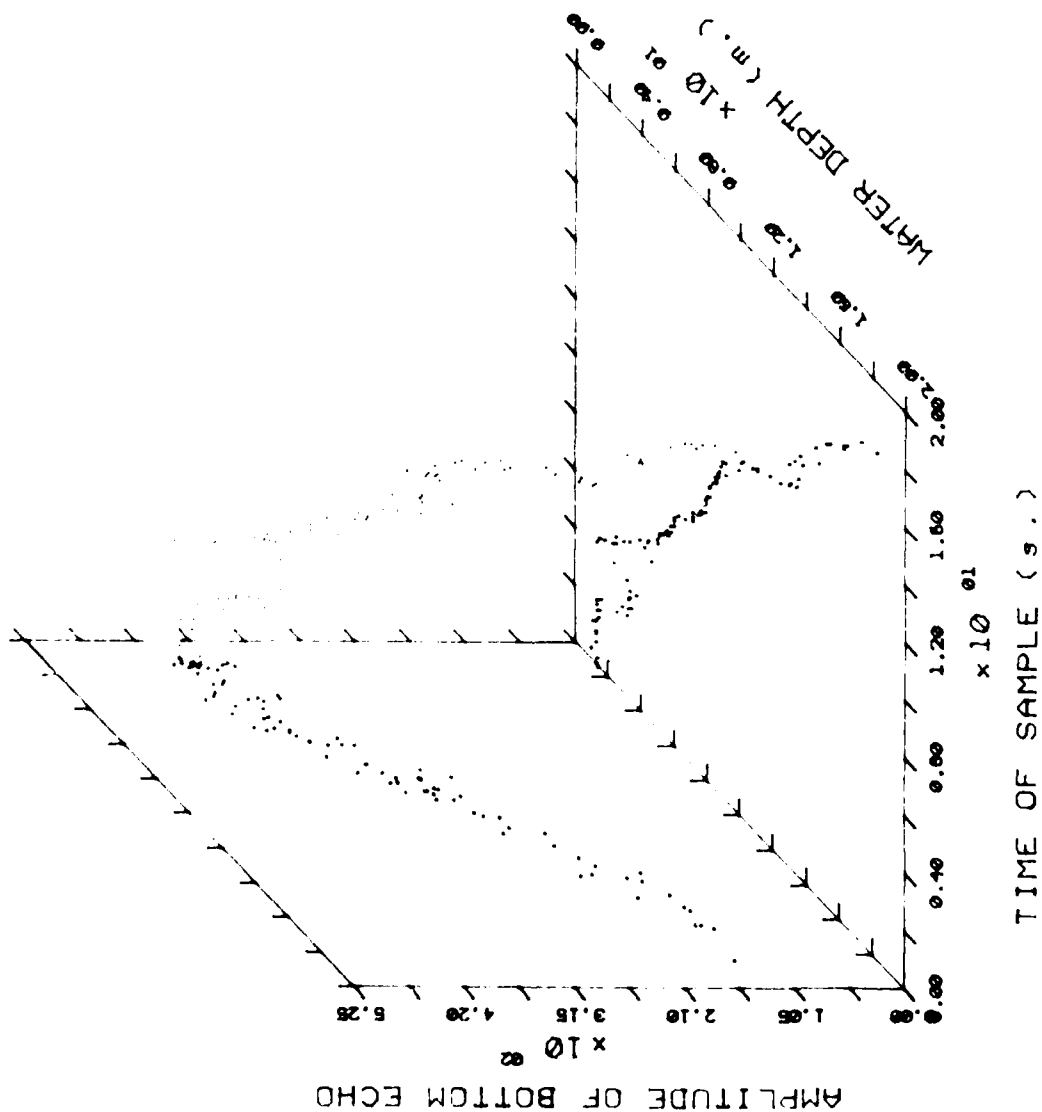
EFFECTIVE ATTENUATION COEFFICIENT

SENSOR : LIDAR BATHYMETER
PROJECT : MAGDALEN ISLANDS
FLIGHT LINE : 18
AIRCRAFT : C - GRSA
START TIME : 14:47:50.954 (2/8/79)
FILE : LH04:002209.SRL

AMPLITUDE OF BOTTOM ECHO $\times 10^2$

WATER DEPTH (m.) $\times 10^1$
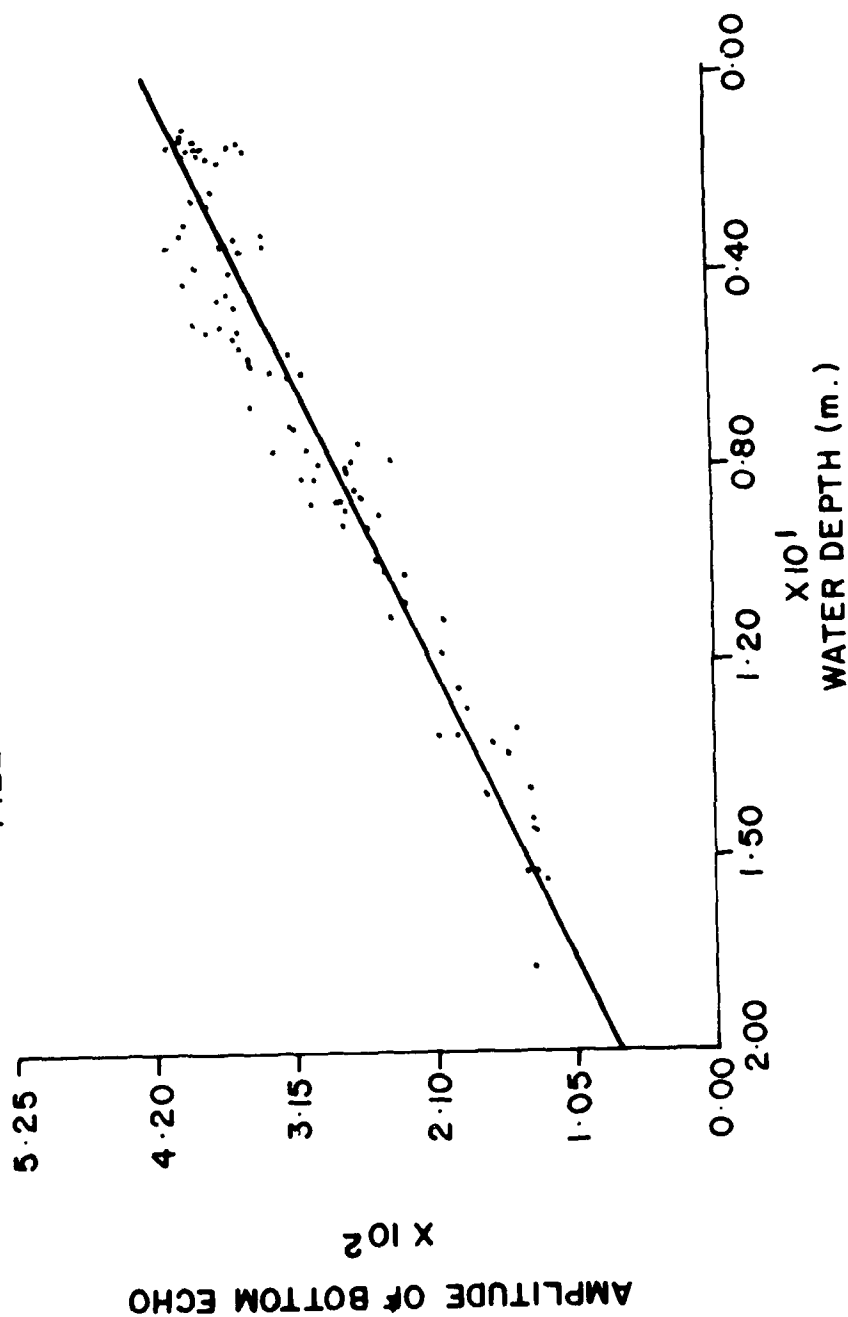
PAPER 6

An Evaluation Of Airborne Laser Hydrography

David B. Enabnit
Engineering Development Office
National Ocean & Atmospheric Administration
United States

1.0 INTRODUCTION

The United States National Ocean Survey's (NOS) involvement in laser hydrography began in 1970. At that time it was recognized that an airborne laser system had the potential of performing accurate hydrography at low cost, and that it could be an appropriate technology for meeting the NOS survey requirements of the 1980's and 1990's.

The NOS effort to date has accomplished two important things. First, through experiment and analysis, the technique has been developed to a point where an airborne laser hydrography system suitable for NOS application is a realizable option. Second, sufficient information has been developed to make an informed decision on whether to implement the laser technology. This paper will summarize the principal results achieved in accomplishing these two objectives

2.0 THE AIRBORNE LASER HYDROGRAPHY CONCEPT

The airborne laser hydrography technique uses an aircraft-mounted, pulsed laser system to collect a swath of discrete soundings along each flight line. It measures water depth exactly like a sonar, but using light instead of sound. The NOS operational system will take 600 soundings per second over a 220-meter wide swath with an average distribution of 1 per 25 m^2. The system will operate from a light, twin-engine aircraft flying at 300 meters altitude and at a speed of 75 m/sec. The laser will have a green wavelength for maximum water penetration and will be totally eye safe for bystanders in the survey area.

3.0 BENEFITS OF AIRBORNE LASER HYDROGRAPHY

The National Ocean Survey expects to realize four benefits with airborne laser hydrography: a reduced cost per unit of area surveyed; a reduced amount of manpower used per unit of area surveyed; an increase in the spatial density of soundings; and an increase in the amount of area surveyed annually. These interrelated benefits have been quantified to allow laser hydrography to be compared with other surveying techniques.

3.1 Cost Effectiveness

The financial benefits of laser hydrography were estimated using an economic analysis. First, a proposed system useage plan was established. The cost of surveying that proposed amount of area with the existing, launch-based sonar systems was then determined. Finally, the cost of surveying the proposed area with a mixed fleet (laser plus a reduced launch fleet) was computed. The difference between the two costs is the financial benefit of using laser hydrography.

The proposed useage plan for the NOS airborne laser hydrography system is as follows: launch hydrography will be decreased 50 percent (from 1600 square nautical miles (NM^2) annually to 800 NM^2); laser hydrography will be increased from 0 to 2000 NM^2 annually; total shallow water hydrography will thus increase 75 percent (from 1600 NM^2 to 2800 NM^2 annually).

The cost of surveying with launches was determined in a special study of historical costs performed for the laser hydrography project, and from other similar studies (table 1). The resulting estimate is that launch-based sonar systems survey for $2,730 per square nautical mile (NM^2).

SOURCE OF ESTIMATE	$/nm^2	nm^2
Special Study	$2341/nm^2	1607 nm^2
Cdr. Collins' study	$1641/nm^2	1322 nm^2
Capt. Mobley's study	$4801/nm^2	977 nm^2
"Groundtruth" survey	$2714/nm^2	122 nm^2
GKY estimate	$3059/nm^2	122 nm^2
Weighted[1] average cost of launch hydrography	$2730/nm^2	

[1] Each $/nm^2 is weighted the number of nm^2 surveyed at that cost.

Table 1.   Launch Hydrography Costs

The cost of surveying by laser is a combination of amoritized acquisition costs (table 2) and operating costs (table 3). Acquisition costs for sonar and launches were treated as sunk costs.

	82	83	84	85	Total
Laser subsystem	460	615	0	0	1075
Positioning	310	219	0	0	529
Data Processing	367	298	0	0	665
Aircraft	0	0	463	0	463
Transition	0	0	0	425	425
System operating costs (test, train, etc.)	0	0	664	689	1353
Other (scientific analysis, studies, test, consumables)	63	68	73	86	290
Data verification	75	75	75	75	300
	1275	1275	1275	1275	5100

Table 2.   Estimated Laser Hydrography Acquisition Costs

Laser Crew (3)	$221.75 K
Air Crew (2)	147.5 K
Data Verification Personnel (2)	147.5 K
Scientific Support Personnel (1)	73.75 K
Travel	85.5 K
Laser Maintenance	51.3 K
Aircraft Operation and Maintenance	123.2 K
Total	$850 K

Table 3.   Estimated Laser Hydrography Operation Costs

Table 4 shows the economic analysis of airborne laser hydrography. Costs are charged in the year they are incurred. The present method costs are for an all-launch fleet.   The proposed method is the combined laser/launch fleet. Table 5 summarize the results of this economic analysis. The computed savings of $25 million and the benefit/cost ratio of 7 is felt to be sufficiently large, in spite of the uncertainties inherent in estimates of this type, that NOS can be confident of significant savings through the use of airborne laser hydrography.

Project Year	Present Method	Proposed Method	Differential	Discounted Differential	Surveying Produced
1 (FY 1982)	$6966 K (Launch Hydro)	$6966 K + $1275 K (Launch Hydro. + Laser Devel.)	-$1275 K	-$1159 K	1600 nm^2
2 (FY 1983)	$6966 K	$6966 K + $1275 K	-$1275 K	-$1053 K	1600 nm^2
3 (FY 1984)	$6966 K	$6966 K + $1275 K	-$1275 K	-$ 958 K	1600 nm^2
4 (FY 1985)	$6966 K	$6966 K + $1275 K	-$1275 K	-$ 871 K	1600 nm^2
5 (FY 1986)	$12191 K (2800 nm^2 of Launch Hydro)	$3483 K + $ 850 K (800 nm^2 Launch Hydro + 2000 nm^2 Laser Hydro)	$7858 K	$4880 K	2800 nm^2
6 (FY 1987)	$12191 K	$3483 K + $ 850 K	$7858 K	$4432 K	2800 nm^2
7 (FY 1988)	$12191 K	$3483 K + $ 850K	$7858 K	$4031 K	2800 nm^2
8 (FY 1999)	$12191 K	$3483 K + $ 850 K	$7858 K	$3670 K	2800 nm^2
9 (FY 1990)	$12191 K	$3483 K + $ 850 K	$7858 K	$3332 K	2800 nm^2
10 (FY 1991)	$12191 K	$3483 K + $ 850 K	$7858 K	$3033 K	2800 nm^2
11 (FY 1992)	$12191 K	$3483 K + $ 850 K	$7858 K	$2750 K	2800 nm^2
12 (FY 1993)	$12191 K	$3483 K + $ 850 + $107 K (Aircraft Residual Value)	$7965 K	$2541 K	2800 nm^2
			Present value net benefit computed for FY 1982	$24628 K	

Table 4.   Economic Analysis of Laser Hydrography

Present Value Cost in FY 1982   • $4007 K

Present Value Benefit in FY 1982   • $28,635 K

Present Value Net Benefit in FY 1982   • $24,628 K ≃ $25 M

Benefit/Cost Ratio   • 7.15

Increase Amount of Surveying   • 1200nm^2 = 75% annually

                                       • 9600 nm^2 total

Table 5. Summary of Economic Analysis

3.2 Manpower Effectiveness

The manpower savings of laser hydrography can be quantified using a methodology similar to that used for cost savings. Manpower savings are computed distinct from their direct cost savings because manpower is regulated independently of cost through "positions". Depending on the constraints in any year, the manpower savings may be more important than the cost savings.

The manpower required for launch-based sonar hydrography was estimated from historical data. Figure 1 shows the productivity of NOS survey manpower. A weighted average of 57 NM^2 per manyear was computed from the vessel productivity data to use as a comparison figure.

(NM)^2/MANYEAR

300

250   NSL #1 (140)
             MT. MITCHELL LAUNCHES (66)
ALL LAUNCH WEIGHTED AVERAGE (57)
             NSL #4 (29)
             NFP #3 (22)
150   PEIRCE LAUNCHES (14)
             NFP #2 (9.3)
100   RAMIER LAUNCHES (9)
             DAVIDSON LAUNCHES (9)
50   WHITING LAUNCHES (4.4)
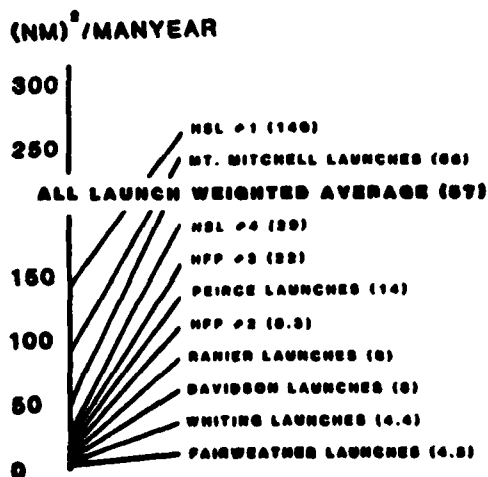   FAIRWEATHER LAUNCHES (4.2)
0

Figure 1. Productivity of Manpower for Launch Hydrography

The manpower required for laser hydrography includes development manpower and operating manpower. From the NOS laser hydrography development plan, five manyears per year are required during each of the four years of system development and test. From the NOS plans for system operation eight manyears per year are required for each of the eight years of operation. These eight manyears of operating manpower include a five-man survey party, two data verifiers, and one manyear per year of scientific support.

Table 6 shows a manpower analysis which uses the above data and follows a procedure similar to that in section 3.1 on cost effectiveness. The analysis shows that an estimated 196 manyears would be saved over the lifetime of the system. As with cost, this is felt to be sufficiently large that significant manpower savings should result in spite of any inaccuracies in the estimate.

Project Year	Present Method	Proposed Method	Differential	Amount of Surveying
1 (FY 1982)	28 MY	33 MY	-5 MY	1600 nm^2
2 (FY 1983)	28 MY	33 MY	-5 MY	1600 nm^2
3 (FY 1984)	28 MY	33 MY	-5 MY	1600 nm^2
4 (FY 1985)	28 MY	33 MY	-5 MY	1600 nm^2
5 (FY 1986)	49 MY	22 MY	27 MY	2800 nm^2
6 (FY 1987)	49 MY	22 MY	27 MY	2800 nm^2
7 (FY 1988)	49 MY	22 MY	27 MY	2800 nm^2
8 (FY 1989)	49 MY	22 MY	27 MY	2800 nm^2
9 (FY 1990)	49 MY	22 MY	27 MY	2800 nm^2
10 (FY 1991)	49 MY	22 MY	27 MY	2800 nm^2
11 (FY 1992)	49 MY	22 MY	27 MY	2800 nm^2
12 (FY 1993)	49 MY	22 MY	27 MY	2800 nm^2
			196 manyears	

Table 6. Manpower Savings Analysis

3.3 Other Benefits

The third benefit that NOS expects to realize with airborne laser hydrography is an increase in the spatial density of soundings. Clearly, the density of soundings is not independent of the cost and manpower savings. Two unsuccessful attempts were made to determine the optimum density of soundings. To circumvent the inability to find an optimum density, a moderate increase in sounding density was chosen (to 1 per 25 m^2) and defined to be the design goal. The value is roughly related to the uncertainty in positioning the soundings (4.6 m RMS) on the grounds that if one cannot distinguish the location of two soundings, their depths are not extremely useful. The cost and manpower savings were quantfied using this density of 1 per 25 m^2. Table 7 shows the planned laser sounding density and those for various scales of sonar hydrographic surveys.

Technique	Scale	Line Spacing (meters)	Density (meter^2/sounding)[1]
Laser	1:1,000	Overlapping swaths	25 m^2/sounding
Sonar	1:2,500	25 m	312 m^2/sounding
Sonar	1:5,000	50 m	1,250 m^2/sounding
Sonar	1:10,000	100 m	5,000 m^2/sounding
Sonar	1:20,000	200 m	20,000 m^2/sounding
Sonar	1:40,000	400 m	80,000 m^2/sounding

(1) Plotted sonar soundings are 5 mm apart at the scale of the survey

Table 7. Spatial Density of Soundings

The fourth benefit that NOS expects to realize with airborne laser hydrography is an increase in the amount of area surveyed annually. Like sounding density, the amount of area surveyed affects the system's economics. Also like sounding density, there is no obvious figure of merit which would allow selection of the optimum increase in annual surveying. Therefore, a modest increase of 75 percent in the amount of shallow water surveyed annually was defined as the design goal, and system economics determined for that value. Both the added surveying and the increase sounding density are then treated as intangible benefits.

4.0 PERFORMANCE

Performance means the ability to accurately measure the depth by laser and then to accurately position those soundings. The required accuracy standards are a depth accuracy standard of 0.3 m RMS in water 0-20 m deep and positioning accuracy to 1.5 mm at the scale of the survey. Depth accuracy is relaxed to 1 m RMS in water deeper than 20m.

4.1 Bathymetric Accuracy

Bathymetric accuracy has been investigated through a combined experimental and theoretical program. Field experiments were performed in 1977 using a NASA prototype laser system as a research tool. Those experiments were to measure the effects on performace of environmental and system parameters, to provide data for verification of performance models, and to make an accuracy intercomparison with sonar. The objective of the theoretical program was to model system behavior, to extrapolate from the performance of the NASA prototype laser to the performance of the NOS operational laser, and to explain experimental results.

Three terms are used when discussing the bathymetric performance of a laser: precision, bias, and profile correlation. Precision is the random error in depth around the average depth and is a measure of system and environmental noise. Results on the theoretical and experimental estimates of system precision are presented in a separate paper.

Bias is the constant offset between the measured depth and the true depth. Since true depth is not known, an intercomparison was made between laser and sonar measured depths in an attempt to infer laser bias. In 1977, NOS and NASA, with support from the Defense Mapping Agency and U.S. Navy, gathered 1 ½ million laser soundings over a test range that had been surveyed by NOS with launch-based sonars. Table 8 displays the results of eight flight lines of laser data that were compared with the sonar data.

PASS ID	BIAS (INCHES)	BIAS (CENTIMETERS)	BIAS DIRECTION	DEPTH RANGE(FT)	DEPTH RANGE(M)	$\propto$ (M^{-1})
1-7-3 (J)	7.3 IN	18.5 CM	LASER DEEP	5-7.5 FT	1.5-2.3 M	3.15 M^{-1}
2-1-13	12 IN	30 CM	-----	5.5-7 FT	1.7-2.1 M	2.7-4.7 M^{-1}
2-2-4	1 IN	2.5 CM	LASER SHALLOW	5-6.5 FT	1.5-2.0 M	2.9-3.6 M^{-1}
2-2-9 (S)	2.5 IN	6.4 CM	LASER DEEP	5.5-7.25 FT	1.7-2.2 M	2.9-3.6 M^{-1}
2-2-15	12 IN	30 CM	LASER SHALLOW	5.5-8.5 FT	1.7-2.6 M	2.9-3.6 M^{-1}
2-2-23	12 IN	30 CM	-----	5.5-9(?)FT	1.7-2.7 M	2.9-3.6 M^{-1}
2-2-24	15 IN	38 CM	LASER DEEP	5.5-9 FT	1.7-2.7 M	2.9-3.6 M^{-1}
3-2-1XR	4 IN	10 CM	LASER SHALLOW	4.75-9.75FT	1.4-3 M	2.8 M^{-1}

AVERAGE BIAS = 8.2 IN ± 5.2 IN
                    21 CM ± 13 CM

Table 8. Laser/Sonar Intercomparison

In such an intercomparison, one does not expect to see perfect agreement between systems because error can be introduced by both of them. An error budget can, however, be used to deconvolve these errors. Table 9 is a simple error budget for the laser/sonar intercomparison. The observed laser/sonar

difference in Table 9 is the average of the eight comparisons in Table 8. The
sonar, tide, and mispositioning errors were determined separately. If the
errors are independent then the observed difference must be the root-sum-
square of the four error componenets. Clearly then, the inferred laser bias
can be determined, and its value is 6.4 inches ±4 inches.

ERROR SOURCE	ERROR
SONAR	3" ± 2"
POSITIONING	4" ± 2"
TIDES	1" ± 0"
LASER	TO BE INFERRED
OBSERVED LASER/SONAR DIFFERENCE	8.2" ± 5"

Table 9.   Laser/Sonar Intercomparison Error Budget

The third facet of performance is profile correlation. This is a measure
of whether the laser and sonar are consistently seeing the same bottom, i.e.,
do the peaks and deeps line up. Profile correlation is measured by removing
the constant laser/sonar difference on an ad hoc basis and compiling
statistics on the residual differences (figure 2). Based on the experiment
error budget, the residual difference should have a standard deviation of less
than 10 cm. The experimentally observed standard deviation is indeed on the
order of 10 cm and thus it is felt that the laser and sonar were consistently
seeing the same bottom during the experiment.
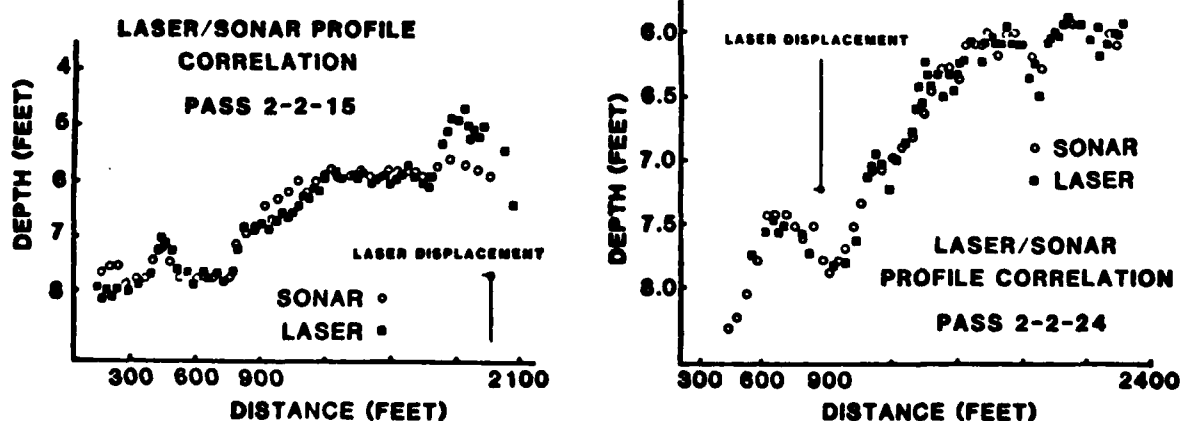
Figure 2.   Laser/Sonar Profile Correlations

4.2 Positioning Accuracy

The accuracy requirement for laser hydrography is to be able to position the soundings to within 4.6 m RMS. This would be sufficiently accurate for a 1:5,000 scale survey - the largest scale done with any regularity by NOS. This 4.6 m was apportioned among the different sources of error in order to find the most important individual component (table 10). The result was that positioning the aircraft would be the largest single error and that of the 4.6 m, 3.9 m RMS could be allocated to it.

PARAMETER	ACCURACY
HORIZONTAL POSITION (X, Y)	3.9 M RMS
VERTICAL (Z)	1 M RMS
OFF-NADIR ERROR (PITCH AND ROLL)	0.25°
HEADING ERROR (LASER POINTING PLUS AIRCRAFT HEADING)	0.5°

Table 10. Positioning Error Budget

Since NOS was not actively developing horizontal positioning systems for laser hydrography, a search of the technical literature was performed to see what accuracies could be achieved. The following data was found:

   a. Two documented tests of the Cubic Corporation's Autotape DM43 showed encouraging results. In one test, a ship-mounted system was compared against theodolite-determined positions. Agreement to within 4.6 m RMS was found. In a second test, the Autotape was used to determine offshore oil platform positions. The results agreed with satellite-determined positions of the same platforms to within 0.4 m RMS.
   b. At Holloman AFB, N.M., a Cubic Corporation CR-100 microwave system was being used for aircraft positioning. Personnel using the system claim to be satisfied that it is accurate to better than 3 m RMS. No published test results were available.
   c. The satellite-based Global Positioning System (GPS) has been tested in the differential mode by the GPS Program Office aboard a helicopter. Differential GPS was shown to determine aircraft position to better than 4 m RMS of accuracy.

The performance cited above indicate that the required positioning accuracy will probably be within the state-of-the-art at the time it is needed, but that it will be difficult to achieve.

5.0 APPLICABILITY

The subject of applicability deals with how widely useable a laser system is. What one needs to know is: the types of areas which could be surveyed, how much surveyable area there is, and whether those areas are of importance to NOS.

Since the laser is an optical technique, its ability to survey an area is determined primarily by water clarity, depth, and the laser system parameters. Water depth is known from NOS charts. Laser system design goal parameters have been selected. Thus, for locations where water clarity data is available, an estimate of the amount of area surveyable by laser can be made.

A search was made of oceanographic data archives for water clarity data. In a few cases there were sufficient, discrete measurements of water optical properties on file to estimate surveyability. Additionally, NOS had a series of aerial photographs that had been examined to determine the applicability of photobathymetry. An extrapolation was made from the photobathymetrically surveyable area to the laser surveyable area using the relative penetrating ability of the two techniques.

The resulting water clarity data, depth, and laser system parameters were combined to estimate surveyability at ten locations. Unfortunately, these are not estimates in which one can have a lot of confidence. Table 11 presents these results.

LOCATION	ESTIMATED % SURVEYABLE*	APPROXIMATE SURVEYABLE AREA	SOURCE OF WATER CLARITY DATA	TYPICAL MAX DEPTH	CONFIDENCE IN ESTIMATE
Chesapeake Bay (North Half)	65%	1,460 km²	Discrete Measurements	9-10 m	Low
Chesapeake Bay (South Half)	80%	2,050 km²	Discrete Measurements	9-11 m	Medium
James River (Lower End)	65%	44 km²	Discrete Measurements	3-4 m	Low
Tampa Bay	100%	926 km²	Aerial Photography	10-11 m	Medium
Nantucket Sound	90%	1,625 km²	Aerial Photography	18 m	Medium
Gulf of Mexico (one section north of Tampa Bay)	N/A	6,500 km²	Aerial Photography	21-30 m	Low
Lake Erie	65%	16,730 km²	Discrete Measurements	18 m	Low
Lake Ontario	39%	6,830 km²	Discrete Measurements	8-11 m	Low
Lake Huron	56%	32,700 km²	Discrete Measurements	35 m	Low
Raritan Bay & Lower Bay N.Y.	70%	57 km²	Discrete Measurements and Aerial Photography	7 m	Low

* for laser extinction coefficient of αD = 80

Table 11. Estimated Area Surveyable by Laser

6.0 LASER OPERATIONS

Laser hydrography operations were evaluated to determine if the system could be used as conceptualized and to determine if the benefits would remain after operating problems were considered. It is important to establish that the benefits would not be seriously degraded through operational compromises.

Laser operations were investigated using an operational scenario and the experience gathered during the 1977 field experiments. Since most of the results relate specifically to the way NOS conducts surveys, a detailed presentation of the operating scenario is omitted. Four conclusions, however, are worth mentioning:

a. The use of positioning system with shore-based transponders was identified as a potential, benefit-degrading operating constraint. Both the limited range of microwave systems and the required establishment and maintenance of the transponders could impact the cost and manpower effectiveness.

b. The requirement for tide measurement was extensive enough so that a Tide Measurement Subsystem was added to the NOS Airborne Laser Hydrography System. The long flight lines can cross many tide zones in complicated areas like Chesapeake Bay. This requires the simultaneous operation of many, widespread tide guages.

c. A library of water clarity data is needed to identify the optimum season to survey an area. Only satellite-based multispectral scanners (MSS) have been identified as a possible source for this data. The ability of the MSS to accurately measure the correct optical property, however, has not yet been proven.

d. The actual, day-to-day use and management of the system was felt to be well within the capabilities of NOS.

7.0 IMPACTS

Any new process or technology can impact an organization. Because the impacts could affect the desirability of airborne laser hydrography, an attempt was made to identify them. The principal, identified impacts are listed below. Those relating only to NOS are omitted.

a. Increased amount of area surveyed annually - Impact will be in the area of chart production as they try to produce products for the increased area.

b. Increased amount of data - Both the increased number of soundings per unit area and the increased area surveyed will impact the hydrographic data processing system.

c. Financial - Paying for the laser hydrography system will preclude exploiting other opportunities.

d. Acceptance of system accuracy - The new technique of measuring depth has not been tested in a court of law as acoustically measured depths have.

e. Changing responsibilities and retraining - Personnel will need to be trained to run laser surveys, maintain the equipment, and evaluate laser hydrography data. Other trained personnel may be reassigned if some launch hydrography systems are supplanted by laser hydrography.

8.0 SUMMARY

Five subjects have been addressed in evaluating airborne laser hydrography: benefits, performance, applicability, operations, and impacts. Together they show airborne laser hydrography to be a technology which is ready to exploit and which offers significant potential benefits. The management of NOS has reveiwed the information prepared for this evaluation and decided to proceed with the implementation of a system as soon as funds are available.

PAPER 7

The U.S. National Ocean Survey's
Airborne Laser Hydrography
Development Project

David B. Enabnit
Engineering Development Office
National Oceanic & Atmospheric Adminisration
United States

1.0 INTRODUCTION

The United States National Ocean Survey (NOS) is part of the National Oceanic and Atmospheric Administration, U.S. Department of Commerce. NOS provides a spectrum of marine and aeronautical charts and of geodetic and oceanographic data.

NOS has been involved in airborne laser hydrography for 10 years. The goal of NOS in developing the technique is to reduce the cost and manpower required for performing hydrographic surveys. The resulting survey data is intended for use in producing nautical charts of which NOS distributes 2 million annually.

The desire for improved cost and manpower effectiveness is a different goal from other airborne laser hydrography development projects. The U.S. Defense Mapping Agency (DMA) and U.S. Navy, for example, are principally interested in increasing the amount of area surveyed annually in their foreign areas of responsibility. In contrast, NOS operates a high quality survey fleet of approximately six ships and 20 launches and has responsibility for charting the comparatively well-surveyed U.S. coastal zone. Additional surveying capacity is, therefore, not a priority item. In fact, it is not desired if that added surveying capacity clogs the subsequent data verification, chart compilation, and data storage system.

The different desired benefit, different geographic area of responsibility, and the intense competition from an established, skilled, survey fleet has resulted in an NOS airborne laser hydrography project with a unique emphasis and which has produced highly original work. This paper will outline the NOS project and its goals. Areas of anticipated technical difficulty and areas of difference between the NOS and other laser hydrography projects will be highlighted. Present project status will be discussed. Work planned for 1981 will be described. Results from completed work will be reported in separate papers.

2.0 THE NOS PROJECT

The NOS airborne laser hydrography project has four phases: a Research and Evaluation Phase, a Development Phase, a Transition Phase, and an Operational Phase. The Research and Evaluation Phase was begun in 1970 and is today essentially complete. That phase established and quantified the benefits of laser hydrography - principally that it could survey for one-sixth cost and with one-fifth the manpower of conventional launch-based sonar hydrography systems. The Research and Evaluation Phase also demonstrated through experiment that accurate soundings (.3m RMS) could be gathered using an airborne laser. Other investigations concluded that a significant amount

of U.S. coastal water could be surveyed by laser; that the system could be managed; that the benefits would not be degraded through operational compromises; and that the impacts on the rest of NOS were acceptable. The detailed results of this phase are documented elsewhere (ref. 1, 2) and will be summarized in a separate paper.

During 1981, the NOS project will be in an interim status between the Research and Evaluation Phase and the Development Phase. Undocumented research and evaluation results will be published. A few new, small investigations will be performed. Meanwhile, NOS will be trying to identify funds to proceed with the Development, Transition, and Operating Phases.

3.0   THE DEVELOPMENT PHASE

The objective of the proposed Development Phase will be to develop, fabricate, and test an airborne laser hydrography system suitable for operational use by NOS. Only one system is planned. It will serve both as a prototype and, when certified, as NOS's sole operational system.

3.1   System Concept

Figure 1 is a block diagram of the system concept. A complete system is being proposed. When manned by five people, it will gather, process, and verify all the data needed to produce a complete hydrographic survey. The planned, official record of the survey will be a digital data set that has been certified as accurate at a level comparable to present acoustic hydrographic surveys. No work is planned by the Laser Hydrography Project on that data verification, chart compilation, and data storage which normally occurs after acceptance of the field data set. The emphasis instead will be on smoothly interfacing with the existing verification, compilation, and data storage system.

Figure 1.   NOS Airborne Laser Hydrography System
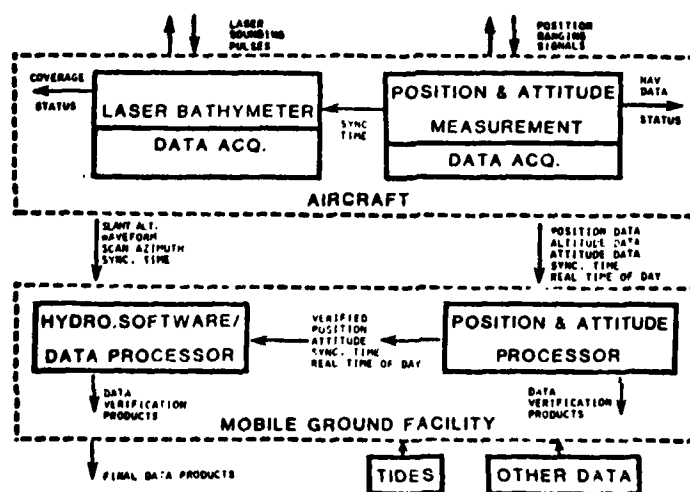
The proposed system will be composed of six subsystems: the Laser Bathymeter, the Position and Attitude Measuring Subsystem (PAMS), the Hydrographic Software/Data Processing Subsystem (HS/DP), the aircraft, a Mobile Ground Facility (MGF), and a Tides Measurement Subsystem (TMS).

The airborne suite of equipment will include the Laser Bathymeter with its data acquisition system, and part of the Position and Attitude Measurement Subsystem with an independent data acquisition system. The airborne suite will be designed to function without an operator. Unattended operation is desired for several reasons. First, the pilot and copilot will be fully occupied flying the airplane. Second, the cost of an operator, his display equipment and software, and the larger aircraft needed to carry them will reduce the system cost and manpower effectiveness. Next, the added complexity of a real-time, interactive system will increase the developmental difficulty and reduce system reliability. Finally, it is not clear that an operator can make meaningful evaluations and decisions in real-time and then take an appropriate and timely action. The airborne suite is thus visualized simply as a data acquisition instrument. Only that processing, displaying, and human intervention will be performed which is necessary for successful system operation. That processing, displaying, and intervention is expected to be: a binary indication of successful system functioning; a binary decision on successful soundings presented as a "coverage" display; aircraft navigation data; diagnostics for air-recoverable failures; and the ability to read and alter mission parameters such as flight line spacing.

The ground-based suite of equipment is planned as a trailered, data processing center which will accept the recorded raw survey data from the airborne suite and produce the survey results. This Mobile Ground Facility will contain two separate processing systems - one from the PAMS for computing aircraft position and attitude, and the HS/DP subsystem which computes depth, merges depth and position, and then allows manual verification and certification of the survey results. The PAMS and HS/DP processors (and the PAMS and Laser Bathymeter data acquisition units) are distinct to allow the PAMS to operate in a stand-alone mode. This stand-alone capability is desired to allow the PAMS to be used in other NOAA applications, to give it sufficient portability to allow easy adoption by the DMA/Navy laser hydrography system, and to allow easier, parallel, subsystems development by different contractors through minimum commonality and interfaces.

Table 1 lists the desired performance parameters of the NOS laser hydrography system. NOS is very serious about meeting the depth accuracy requirements. Competition from the launches makes it a necessity. The positioning accuracy requirements are also extremely tight - more so than for any other airborne laser system. The positioning requirement is derived from the scales of the surveys to be performed. Since 70% of NOS surveys are at scales of 1:20,000 or larger, and 40% are performed at 1:10,000 or larger, the NOS airborne laser system must determine position accurately enough to perform these large scale surveys in order to be useful.

BATHYMETRIC ACCURACY (WITH POST PROCESSING)	0.5m RMS IN WATER 0-20m DEEP 1.0m RMS IN WATER 20-60m DEEP
BATHYMETRIC ACCURACY (REAL TIME)	BINARY - SUCCESSFUL SOUNDING OR NOT
POSITIONING ACCURACY OF SOUNDING (ABSOLUTE, WITH POST PROCESSING)	4.6m RMS FOR AREAS 0-15km FROM LAND 9.2m RMS FOR AREAS 15-30km FROM LAND 15.4m RMS FOR AREAS 30-60km FROM LAND
POSITIONING ACCURACY OF AIRCRAFT (ABSOLUTE, REAL TIME)	460m RMS
POSITIONING ACCURACY OF AIRCRAFT (RELATIVE, REAL TIME)	10m RMS
ALTITUDE ACCURACY (ABSOLUTE, REAL TIME)	15m RMS
DENSITY OF SOUNDINGS	1 PER 25m² AVERAGE
MINIMUM MEASURABLE DEPTH	0 METERS
EXTINCTION COEFFICIENT	= D - 20
WEIGHT	400 kg
POWER	5 kw
SIZE	TO BE DETERMINED
OPERATIONAL AVAILABILITY	0.9
ENDURANCE	4 HOURS
LIFETIME	8 YEARS
MAINTENANCE	2 LEVELS

Table 1. Desired Performance Parameters

Table 2 lists the range of environmental parameters within which NOS expects to perform laser hydrography. Water clarities are significantly worse than found by other laser systems under development.

PARAMETER	RANGE
RANGE OF WATER CLARITIES	$\alpha = .4m^{-1}$ TO $1.5m^{-1}$
WAVES	0 - 1.5m
WIND (SEA SURFACE)	0 - 5m/s
WIND (AIRCRAFT ALTITUDE)	0 - 15m/s
BOTTOM REFLECTIVITIES	4 - 15%
WEATHER	NO PRECIPITATION OR FOG
TIDES	ARBITRARY

Table 2. Environmental Parameters

3.2 Laser Bathymeter Subsystem

A block diagram of the proposed Laser Bathymeter Subsystem is shown in figure 2. A transceiver similar to that of the DMA/Navy laser system is expected to be adequate. NOS, however, desires an all digital system with depths being computed during post-flight processing in the Mobile Ground Facility. The digital approach is preferred for several reasons. First, apparent depths will need to be corrected using properties of the return

waveform. This waveform must, therefore, be preserved and be in a form suitable for digital processing. Second, experience in laser hydrography is very limited. It is felt to be unrealistic to design a system with a hardwired depth computer and expect it to be accurate over the range of unexperienced environmental and operating parameters. Third, the optimum depth computing algorithm has not been selected so flexibility is preserved by using the digital approach. It might even be necessary to resort to an environmental subtraction as was performed with the NASA Airborne Oceanographic Lidar. Finally, digital processing of the return waveform offers the easiest way to compute measures of data quality based on signal characteristics. Table 3 shows the present design goals for the Laser Bathymeter.
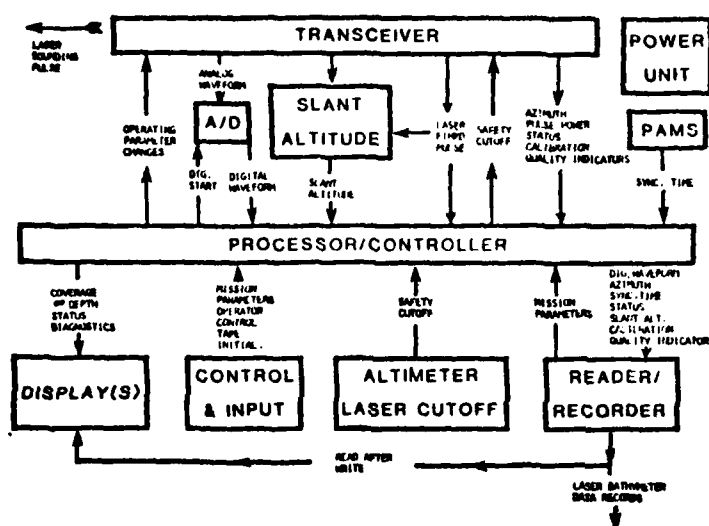
Figure 2.   Laser Bathymeter Subsystem

WAVELENGTH	540 NANOMETERS
LASER BANDWIDTH	0.1 NANOMETERS
LASER PULSE RATE	600 PER SECOND
LASER PULSE WIDTH	5 NANOSECONDS
PROBABILITY OF BOTTOM DETECTION	99%
PROBABILITY OF FALSE ALARMS	10^{-6}
SCAN ANGLE	VARIABLE TO ± 20° FROM NADIR
SCAN RATE	5 PER SECOND
BEAM DIVERGENCE	5 MILLIRADIANS
RECEIVER FIELD OF VIEW	90 MILLIRADIANS
RECEIVER TEMPORAL RESOLUTION	1 NANOSECOND
RECEIVER DYNAMIC RANGE	10^{7}
SCAN PATTERN	ARC THROUGH NADIR
WAVEFORM AMPLITUDE RESOLUTION	10 BITS
LASER PULSE PEAK POWER	900 KILOWATTS
POWER	3.5 KILOWATTS
WEIGHT	450 KILOGRAMS
SIZE	TO BE DETERMINED
PLATFORM	LIGHT, TWIN ENGINE AIRCRAFT
MISSION ENDURANCE	4 HOURS
ALLOWABLE POST-PROCESSING TIME	2.2 HOURS PER HOUR OF DATA

Table 3.   Laser Bathymeter Design Goals

Three areas of technical risk have been identified in the proposed Laser
Bathymeter. One of these is the analog-to-digital (A/D) converter. The
design goals call for sampling each waveform at a rate of one gigahertz with
10 bits of resolution per sample. Each waveform will be sampled at 200 points
and new waveforms occur at 600/second. The second area of technical risk is
the data recorder which is expected to hold 10 gigabits of data from a four
hour mission on one or two magnetic tapes. The third area of technical risk
is a lightweight, aircraft-safe, 3-5 KW power unit.

Work on the laser bathymeter in 1981 will be confined to two items:
completion of the scientific analysis of laser pulse propagation in water; and
specification of those laser bathymeter design and operating parameters which
can be determined from the scientific analysis.

3.3 Position and Attitude Measurement Subsystem

The second subsystem to be discussed is the Position and Attitude
Measuring Subsystem (PAMS)(figure 3). This subsystem will measure the 3
degrees of positioning freedom and the 3 degrees of attitude freedom which,
when combined with the laser pointing direction in post-flight processing,
will give the location of the laser sounding. The PAMS will also provide
aircraft navigation data to the pilot, a synchronization time to the laser
bathymeter, and real-time-of-day for applying tide correctors.
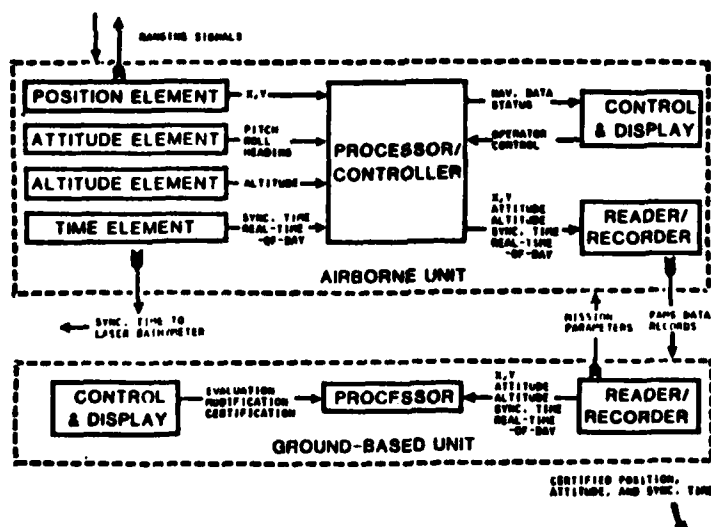
Figure 3. Position and Attitude Measurement Subsystem

Table 4 shows the performance requirements of the PAMS. Real time
positioning information is required for navigation, but not to the same
accuracy as required for positioning the soundings. Real-time relative
accuracy is high to allow the minimum overlap between swaths of laser
soundings while still being assured of complete coverage. Real-time absolute
accuracy is needed to accomodate the difference in datums between charts and
surveys to insure that surveys cover the desired area. Real-time vertical

accuracy is needed to keep the swath the right width for complete coverage and to keep an adequate density of soundings. Table 5 is an error budget for measuring each of the 6 degrees of aircraft freedom. This error budget is felt to be consistent with the state of the art at the time NOS will need hardware.

	OVER LAND	DURING TURNS	DISTANCE TO NEAREST LAND			
			0-8.5"	8-16"M	16-32MM	32MM
AIRCRAFT REL. HORIZONTAL (X,Y) REAL TIME	25M	25M	10M	10M	10M	10M
AIRCRAFT ABS. HORIZONTAL (X,Y) REAL TIME	460M	460M	460M	460M	460M	460M
AIRCRAFT ABS. VERTICAL (Z) REAL TIME	NO REQ.	NO REQ.	15M	15M	15M	15M
LASER ABS. HORIZONTAL POST-PROCESSING	NO REQ.	NO REQ.	4.5M	9.1M	18.2M	36.5M

Table 4.   Positioning Requirements

PARAMETER	ACCURACY
HORIZONTAL POSITION (X, Y)	3.9 M RMS
VERTICAL (Z)	1 M RMS
OFF-NADIR ERROR (PITCH AND ROLL)	0.25°
HEADING ERROR (LASER POINTING PLUS AIRCRAFT HEADING)	0.5°
AZIMUTH	0.3°

Table 5.   Positioning Error Budget

The area of greatest technical risk in the PAMS is felt to be determining the aircraft's horizontal position. At this time, the NAVSTAR Global Positioning System (GPS) used in the differential mode is the most promising solution. Tests performed by the NAVSTAR project office and data processed by Texas Instruments Corp. achieved errors of 4 meters or less using the differential mode and the high precision P-code. The accuracy is consistent with the error budget shown in table 5.

Work on the PAMS during 1981 will be to finish a procurement specification of the subsystem and to circulate it to potential contractors for comment.

3.4 Hydrographic Software/Data Processing Subsystem

The third subsystem of the Airborne Laser Hydrography System is the ground-based, Hydrographic Software/Data Processing Subsystem (figure 4). This subsystem will compute water depth, apply necessary correctors, and merge the depth and position data. NOS has a legal requirement to perform a meaningful level of manual inspection, or "verification," of the data. This subsystem will provide the tools for that manual evaluation of completeness and accuracy. Finally, the HS/DP subsystem will help prepare the output products of the survey. By putting this subsystem on the ground, NOS is trying to minimize the amount of hardware in the airborne suite and its sophistication. Such a plan removes many constraints on size, weight, power, and computer speed.
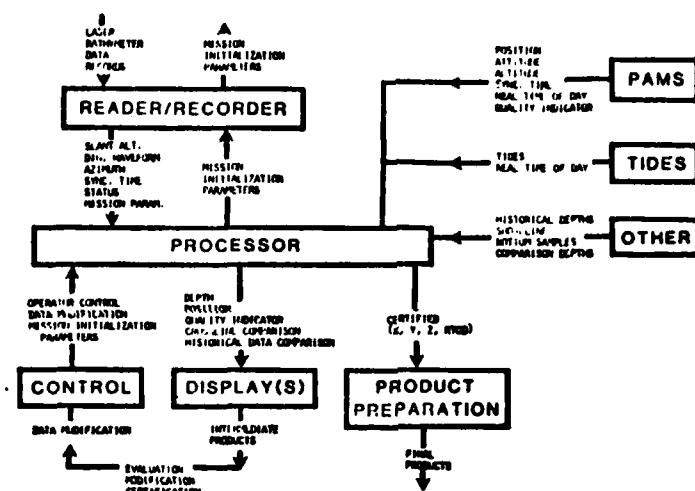
Figure 4.   Hydrographic Software/Data Processing Subsystem

Table 6 shows the three configuration items of the hydrographic software and their principal functions.   One area of anticipated difficulty in the HS/DP subsystem is establishing an adequate definition of "verification." For sonar surveying, verification means manually scanning fathograms to insure that representative soundings were digitized; manually contouring data to see that contours closed and did not cross; looking for non-physical features in the data; and comparing crosslines and historical data with main scheme survey lines.   These verification procedures resulted from experience, personal opinion, and 173 years of tradition. The large amount of laser data will make these procedures impractical yet the intent must still be satisfied.

STEP	FUNCTIONS	OUTPUT
PRELIMINARY PROCESSING	● UNPACK	● ALL (x, y, D, T, e,)
	● COMPUTE DEPTH	● ANOMALIES
	● MERGE xyz	● REFLY DECISION
	● COMPUTE e,	
INTERMEDIATE PROCESSING	● SORT	● ALL ACCEPTABLE (xyzTe,)
	● EDIT	
	● INTERMEDIATE PRODUCTS	● ANOMALIES
	● HYDROGRAPHIC EVALUATION	
	● PRIOR SURVEY COMPARISON	
FINAL PROCESSING	● REDUCE NUMBER OF SOUNDINGS	● SELECTED (xyzT)
	● CERTIFICATION	● ALL ACCEPTABLE (xyzT)
	● PREPARE OUTPUTS	
	● PREPARE REPORTS	

Table 6. Data Processing Configuration Items

A second area of difficulty in the HS/DP will be in selecting that small subset of all the soundings that best represent the bathymetry. This sounding selection is necessary to avoid innundating the chart compilers and their data processing systems with data. Sounding selection as done by cartographers, like data verification, has years of tradition which will affect the acceptability of proposed sounding selection procedures.

In 1981, a requirements baseline will be established for the HS/DP subsystem, a functional design will be created, and functions allocated to hardware, software, and firmware. Finally a development plan, including schedule and estimated cost, will be produced.

3.5 Other Subsystems

The remaining three subsystems are the aircraft, the Mobile Ground Facility, and the Tide Measuring Subsystem. The airborne suite is being sized to operate in a light, twin-engine, low performance aircraft. The Cessna Titan represents the largest such aircraft considered suitable. Most technical problems with the aircraft, such as disposal of waste heat, are expected to be small compared with the difficulty of procuring a plane within the Federal Government. It is impossible to specify in advance the type of aircraft that will actually be purchased. This, in turn, makes specification of the airborne suite size, weight, and fit impossible. No work on the aircraft is planned for 1981.

The ground based equipment is expected to operate from a 20-foot, trailered, Mobile Ground Facility (MGF). The MGF should contain the HS/DP hardware, the PAMS ground based suite, a power supply, plus equipment and space for maintenance, calibration, mission planning, data evaluation, and the storage of spare parts. No work is planned on the MGF during 1981.

Little effort has been devoted to the Tides Measurement Subsystem. A tides telemetering system has recently been developed by NOS for the Bathymetric Swath Survey System. It is anticipated that the laser system will use a similar solution. No work is planned on the TMS in 1981.

This completes the brief discussion of the proposed NOS airborne laser hydrography system. The design, fabrication, and test would be done on contract with private industry. During the Development Phase, NOS personnel will be establishing detailed requirements, writing specifications, monitoring the contract work, and planning the subsequent phases. The Development Phase is planned to last four years and cost $4.3 M.

4.0 TRANSITION PHASE

Following acceptance of the hardware and system integration, NOS is planning a Transition Phase. This one year phase will be used to accomplish the following:

a. Training in system operation and maintenance.
b. Developmental testing to test system readiness for transition to the user, to evaluate technical aspects of support equipment, to assure continued performance in the aircraft environment, and to determine required modifications based on technical performance.
c. Operational testing to evaluate the worth of the system to the user, to test effectiveness in the operating environment, to test operational suitability in a realistic environment, to generate reliability, availability, and maintainability statistics, and to determine required modifications based on human engineering factors.
d. Techniques development to test the adequacy of the employment and supportability concepts, and to proceduralize the details of performing a mission.
e. System modification and finalization based on the results of the developmental and operational testing.
f. System certification and user acceptance.

System certification is presently not practiced by NOS hydrographers. New systems are operated until obvious shortcomings are removed and the organization becomes accustomed to the new hardware. In an attempt to improve this situation, the airborne laser hydrography will be submitted to controlled, quantitative, certification procedures of three types. First, the Position and Attitude Measurement Subsystem will be certified as measuring accurately the aircraft's 6 degrees of freedom. This will be done in an aircraft, using a simultaneous photogrametric measurement of the six parameters as ground truth. The photogrammetric technique is claimed to be able to measure aircraft position with mean errors of less than one meter and attitude within .02° when flying at 4000 m. Accuracies improve at lower altitudes.

The second certification procedure will be of the Laser Bathymeter in a static environment. The subsystem will be mounted either on an appropriate fixed platform or on a helicopter and used to measure depth over a small, instrumented area. A range of environmental conditions will be experienced at each of several sites.

The final certification will be an operational certification during which the entire system will be certified with its operators. Ground truth is expected to be launch-sonar measured depths where an intercomparison among launches is performed first. This intercomparison among launches will establish the distribution of "true" values. The result of the laser/sonar intercomparison would thus be a measure of whether the laser is "as good as" the standard accepted technique in a hypothesis testing sense.

5.0 OPERATIONAL PHASE

The final phase of the proposed NOS Airborne Hydrography Project is the Operational Phase. This Phase will last 8 years and cost $850 K per year. The principal areas of intended system utilization will be the U.S. Great Lakes, east coast, and Gulf of Mexico. Table 7 lists characteristics of planned system usage. Table 8 lists planned survey mission characteristics. Data gathered during a survey will be submitted to the NOS Atlantic Marine Center (AMC).

AREA SURVEYED ANNUALLY	6800 KM^2
FLIGHT HOURS PER YEAR	600 HOURS
SURVEY HOURS PER YEAR	300 HOURS
SURVEY LINE LENGTH DESIRED	70 KM
SURVEY RATE	22 KM^2/HOUR
NUMBER OF SURVEY SITES PER YEAR	4 - 10
TYPES OF SURVEYS PERFORMED	BASIC RECONNAISSANCE
SOUNDINGS PER YEAR	650 MILLION
MONEY SAVED (1982 VALUE)	U.S. $25 MILLION
MANPOWER SAVED	196 MANYEARS
SURVEY SITE	GULF OF MEXICO
	EAST COAST
	U.S. GREAT LAKES

Table 7. System Usage

ALTITUDE	150 M - 600 M 300 M NOMINAL
SPEED	75 M/S
SWATH WIDTH	220 M
SWATH OVERLAP	10%
SURVEY SITE AREA	150 KM^2 TO 3500 KM^2
AVERAGE SOUNDING SPACING	1 PER 25 M^2
SURVEY SCALE	1:1,000
MISSION DURATION	4 HOURS
SURVEY PATTERN	SLIDING RACETRACK PREFERRED
TURN RATE	3° PER SEC.
DISTANCE TO AIRPORT	30 KM AVERAGE
SURVEY PARTY	5 PERSONS - 2 PERSON AIR PARTY, 3 PERSON GROUND PARTY
SEASON OF OPERATION	DURING MINIMUMS IN PLANKTON AND FIELD VEGETATION
OTHER	DAY AND NIGHT OPERATIONS ANTICIPATED
OPERATOR ACTIVITIES	SYSTEM OPERATES UNATTENDED
ADDITIONAL DATA GATHERED	COMPARISON DEPTHS BOTTOM SAMPLES TIDE WATER CLARITY ? FIELD EDIT DATA COAST PILOT DATA

Table 8. Mission Characterizations

6.0 1981 Project Plans

As was mentioned at the beginning of this paper, the Development, Transition, and Operating phases are not yet funded. Since the appearance of the required funds is uncertain, 1981 will be used to conclude ongoing work and prepare for an indefinite suspension of activity. The following items of work will be performed in 1981:

a. Using the scientific results achieved over the past several years, an algorithm will be written for computing the correct water depth.
b. Scientific results will be completed and documented.
c. The Position and Attitude Measuring Subsystem purchase description will be completed.
d. A Hydrographic Software/Data Processing Subsystem functional design and development plan will be created.
e. A limited capability laser hydrography system will be flown to establish greater confidence in the amount of area surveyable by laser.

References

1. "Airborne Laser Hydrography, A Briefing Prepared for the Director of the National Ocean Survey", prepared by the Office of Marine Technology, National Ocean Survey, 11 May 1979.

2. Enabnit, D.B., "Airborne Laser Hydrogaphy, FY 1982 Issue Paper", 1 May 1980.

PAPER 8

ACCURACY AND PENETRATION MEASUREMENTS
FROM HYDROGRAPHIC TRIALS OF THE AOL SYSTEM

Gary C. Guenther
NOAA/NOS
EDL/C61
Rockville, MD   20852

A series of controlled experiments were flown over
two test areas in the Atlantic Ocean and Chesapeake Bay to
investigate the effects of environmental parameters and system
variables on AOL performance in the hydrographic mode. Results
for penetration and depth measurement accuracy are reported
and compared with existing models. Depth measurement biases
are reported and discussed. The effects of off-nadir angle
and receiver field-of-view are also reported.

Accuracy and Penetration Measurements from
Hydrographic Trails of the AOL System

Mr Gary Guenther, NOAA/NOS

(Transcript edited by Ralph Abbot)

 I brought with me a significantly larger amount of material than I
can hope to be able to cover, and I shall try to survey what is
available, almost library card fashion. I shall present a catch-up
on old data from the AOL flights in 1977. We've only just finished
crunching the data which has been sitting around whilst doing a lot
of theoretical work at the same time.

I want to cover the following topics :-

>   Precision of Depth Measurements : Predictions and Data
>
>   Field of View Restriction in AOL
>
>   Profile Correlation/Depth Measurement Bias
>
>   Pulse Stretching via Propagation
>
>   Wave Correction
>
>   Volume Return
>
>   Volume/Interface Return "Flip-Flop"
>
>   Resolution of AOL Biases
>
>   Off-Nadir Angle : Bottom Return
>
>   Off-Nadir Angle & Wind Speed : Surface Return "Loss" Curves
>
>   Limiting Volume Return Strength
>
>   Volume/Interface Return Ratio

Some AOL data is presented in Figure 1 which shows Standard Deviation
of Location Estimate as a function of Peak Bottom Signal (received
power). A Monte Carlo simulation has been used to predict precision
against signal strength, as shown by the solid line. It shows
excellent agreement with the data : high signal strength gives precision
down to about 5 cm RMS whereas for weak signals the precision zooms
to much larger figures.

It is very difficult to calculate the Field of View (FOV) required for
a system. Figure 2 shows AOL data from a constant flat bottom, 6m
deep. At altitude 137m, which is quite low, received power increased
with FOV to the maximum 20mR. At 440m it can be seen that there is
saturation at 20mR FOV. At that altitude 20mR is not sufficient to
encompass the return signal even from a very shallow 6m bottom, much
less from a deeper bottom in which there will be more spreading and
require a greater FOV. As a result of this work the FOV for HALS
shall be increased to at least 60mR.

In figures 3 to 7, are shown comparisons between AOL data and sonar
surveys. Figures 3, 5 and 7 show excellent agreement. Figure 4 shows
laser depths consistently a foot and a quarter deep. Analysing these
biases has taken considerable effort.

Figure 8 shows results of two passes, an hour and a half apart, one
with calm wind giving results a foot shallower than the sonar data, and
the later one after the wind had picked up showing a foot deeper. The
significance of these results will be seen later.

Figure 9 shows a result of the simulation work which helps explain the
deeper biases (of which there were more than shallow). The top curve is
a plot of the leading edge of the bottom return (impulse response). The
depth is 3m (as presented in the previous few results) $D = 12$, single
scatter albedo Wo = 0.9, the NOS "dirty" phase function and 15% off-
nadir. With 2nS rise time a peak detector gives a deep bias of 3nS, or
a foot. On the bottom diagram is plotted the depth bias against
optical depth for varying proportional thresholds and single scatter
albedos. For example, with 50% proportional threshold and Wo = 0.9,
curve 4 shows that for $D = 10$, a 6cm error results at 3m depth. Since
the error scales linearly with depth, a 60cm error results at 18m depth.
These errors are propagation (or scattering) delays in water.

Figure 10 is a compilation of depth measurement bias against surface
return power for all of the AOL biases on the various passes. Surface
return power is the only parameter which showed any correlation at all,
and such a correlation was very difficult to understand. It can be
seen that all the shallow biases are for extremely weak surface signal
strength : all the others are deep biases, about a foot deep, due to
propagation delay.

Figure 11 presents Standard Deviation of Measured Depth plotted as a
function of Standard Deviation of Measured Aircraft Altitude. It
implies wave noise, since the imprecision in height correlates with the
imprecision in depth.

One simple way of taking out wave noise is presented in Figure 12. The
aircraft altitude changes slowly with time, as does the bottom contour;
however, the waves vary rapidly. Thus the distance from the aircraft
to the bottom should be constant, irrespective of the waves. Wave
correction is demonstrated in Figure 13. The waves are evident in the
raw depth (top, the tics on the Y axis are one metre tics) with
J = 29cm. The variations in the aircraft to surface data show
J = 39cm, and the sum of the two has a standard deviation of 12cm.
The correlation coefficient is -0.94 (showing that when one measurement
is long, the other is short). The potential for wave correction is
obviously there.

Another way of showing the correlation in Figure 13 is shown in
Figure 14, which plots altitude measured above sea surface against
measured water depth. The slope is -0.93 with r^2 = 0.58; obviously
the two are strongly correlated.

Figure 15 is a plot of precision against Bottom Return Power. The
big block of scattered data in the centre results from wave noise,
and of wave correction as just discussed is applied then Figure 16
results, which demonstrates its success. To achieve a good match
between the data and the Monte Carlo simulation, wave correction is
necessary.

Another example is shown in Figure 17. The lower graph is for
uncorrected data, and it can be seen by the upper graph in which the
data is corrected that the scatter in points between 20 and 30 units
of bottom return power has been reduced. It can be seen that in the
raw data the standard deviation for high power returns is down around
5cm, whereas in the corrected data it's about 8cm. This resulted
from the course bins in the altitude machine, which has since been
modified to make them finer.

A summary of wave corrected data is shown in Figure 18, which plots
standard deviations of the wave corrected data as a function of that
for the raw data. Anything above the 45° line indicates degraded
performance, anything below is an improvement. It can be seen that
the fine precision depths were degraded because of the imprecision
in the altitude measurement - in a properly designed system there
would be an improvement. In the mid band the data shows improvement
due to wave correction, whilst the data with large deviation due to
low signal strength shows no benefit.

A most unusual result is depicted in Figure 19, a plot of measured
altitude as a function of measured depth. It shows excellent
correlation (r^2 = 0.96), however the slope is -1.38, which means the
size of waves as measured by the altimeter was bigger than the size
of the waves measured in the depth. Figure 20 helped to explain this.
Surface return power is plotted as a function of measured water depth.
In the deeper water there is considerable variance, typical of surface
return from waves, however in the water 6 to 8 feet deep the signal
return is constant. This is because it's a volume backscatter
return, not a specular surface return.

Figure 21 shows a calculation of the depth error expected due to a
volume return instead of a surface interface return; using a 6.5nS
triangular pulse. The results depend on water clarity since the location
of the volume peak is a function of that. For K = 0.3 and a pulse
location threshold of 50%, a 30cm error results from volume return
rather than interface. With a peak detector, f = 1.0 the error is 45cm.
It is easy to see that when using a peak detector in cleaner ocean
waters (where the peak of the volume backscatter occurs deeper than in
dirtier water) an error of a foot or two can occur.

We have now explained all the AOL biases, as shown again in Figure 22. The deeper biases have been explained by propagation delays. However for weak signal strengths some of the returns are interface and some are volume which give depths which are shallow by about two feet. It can be seen that the biases oscillate back and forth depending on the nature of the return.

Finally, off-nadir angle. The mathematics is shown in Figure 23, and the results plotted in Figure 24. Bottom return power is plotted as a function of air off-nadir angle. The dotted curves are for constant altitude, and as an example, for 450m it can be seen how the bottom return power drops with increasing off-nadir angles, and also with increasing altitude. The solid lines show bottom return against off-nadir angle for constant swath width. As an example, for a constant swath of 150m, the peak bottom return occurs with an angle of around 27° (and the altitude which those figures demand).

The effect of air off-nadir angle on surface interface return power is shown in Figure 25, which shows very sharp falls for low wind speed and less sensitivity to angle for stronger winds.

Figure 26 is a plot of the log of the surface return power against log of the air off-nadir angle (flipped backwards). It shows the same kind of thing; another way of achieving the same information as for the bottom return power. The maximum power is delivered to the place where the slope of the curve is minus 2, i.e., somewhere from 6° to 10° off-nadir angle. It's not really important as nobody wants to optimize surface return power!

Figure 27 presents the air off-nadir angle of maximum power for
differing wind speeds. It can be seen that depending on wind speed,
0 to 20 knots, the peak surface return signal will occur at an
angle between 6 and 11 degrees. Figures 31 to 33 relate to the
backscatter coefficient which is important and in which a great deal
of interest has been expressed. The data comes from Petzold, 1972,
a book which is full of phase functions and associated water clarity
that were measured near San Diego and the Bahamas, with both extremely
clear and extremely dirty water. In calculating the magnitude of
volume return, the term β/K appears (fig. 31), where β is the backscatter
coefficient into unit solid angle measured at $180°$ backscatter, and K
is the diffuse attenuation coefficient. Petzold reported values of
data, but never put them together. I divided β by K and looked for
correlation with other likely parameters. Figure 32 shows β/K
against K, and the scatter plot indicates no correlation. Similarly
β/K against , the beam attenuation coefficient shows no correlation.
However when plotted against W_o (fig. 33), where W_o is the single
scatter albedo (ratio of scattering to total attenuation, S/α), a
strong correlation is indicated.

This may be what was happening with WRELADS data when backscatter
as a function of beam attenuation rose up until fairly dirty water
and then turned over in even dirtier water. W_o rises with increasing
until the water is so dirty that absorption takes over from scattering
and then you start to return to lower values of W_o and hence lower
values of backscatter.

I do not have time to present all my data, but I will leave it here
for publication.
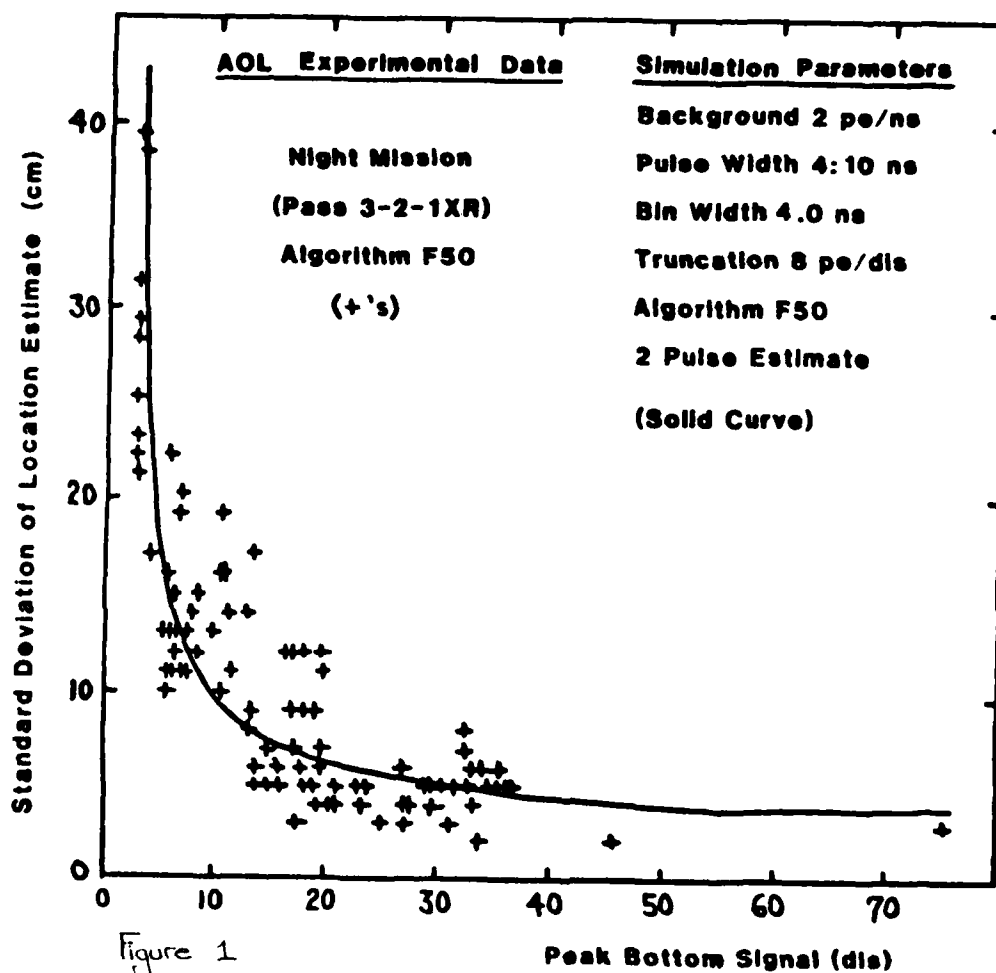
Figure 1

BOTTOM RETURN POWER AT D = 6m VS RECEIVER FOV

AOL FLIGHT TEST DATA
Ph 1 - M2   SEPTEMBER 1977
$\alpha = 0.8 \pm 0.2 \; m^{-1}$
ATLANTIC OCEAN
(WQS)
TX DIV. 5 mr
WIND 2-4 kt

A/C ALTITUDE ON CURVES

Figure 2

Figure 3

Figure 4

OOO LASER HYDRO

DEPTH (FT.)

TIME (SEC.)
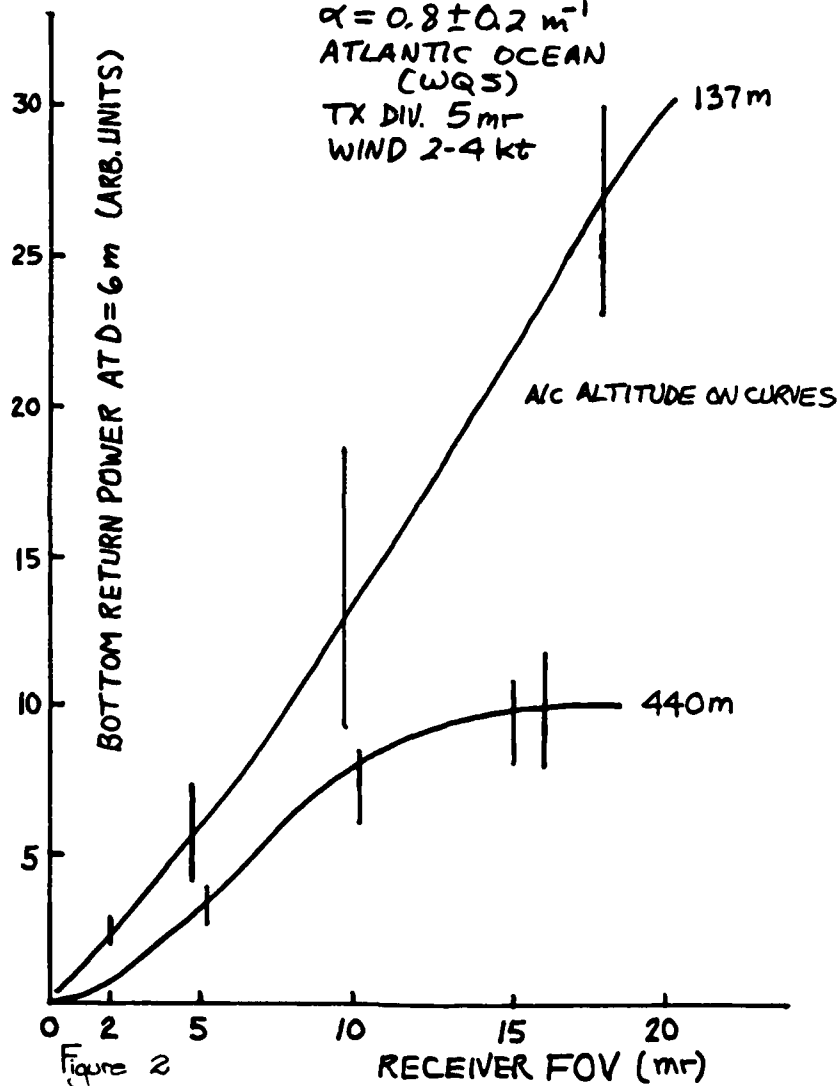
Figure 5

FIGURE 2. COMPARISON OF LASER AND ACOUSTIC DEPTH
ESTIMATES INDICATING 1 FOOT BIAS

PASS 2-2-24 (10/25/77)
TANGIER SOUND

END OF LAUNCH
HYDRO

o o o LASER HYDRO
● ● ● AMC HYDRO
(1 SEC. = 250')

DEPTH (FT.)

5.5
6.0
7.0
8.0
9.0

40   50

LASER TIME (SECONDS)

Figure 6

FIGURE 1. DATUM FREE PROFILE CORRELATION OF LASER AND ACOUSTIC DEPTH ESTIMATES

PASS 2-2-24 (10/25/77)
TANGIER SOUND

Figure 7

MLW
DEPTH (FT)

AOL FLIGHT TEST DATA
OCTOBER 1977
TIDE CORRECTED
JANE'S ISLAND SIDE
$\alpha \sim 2.8 \pm 0.4 \, m^{-1}$
1½ hours apart

5° OFF- NADIR
WIND CALM
"2-2-15"

SONAR

"2-2-24"
WIND 5 kt
NADIR

DISTANCE ALONG FLIGHT PATH

|←150m→|
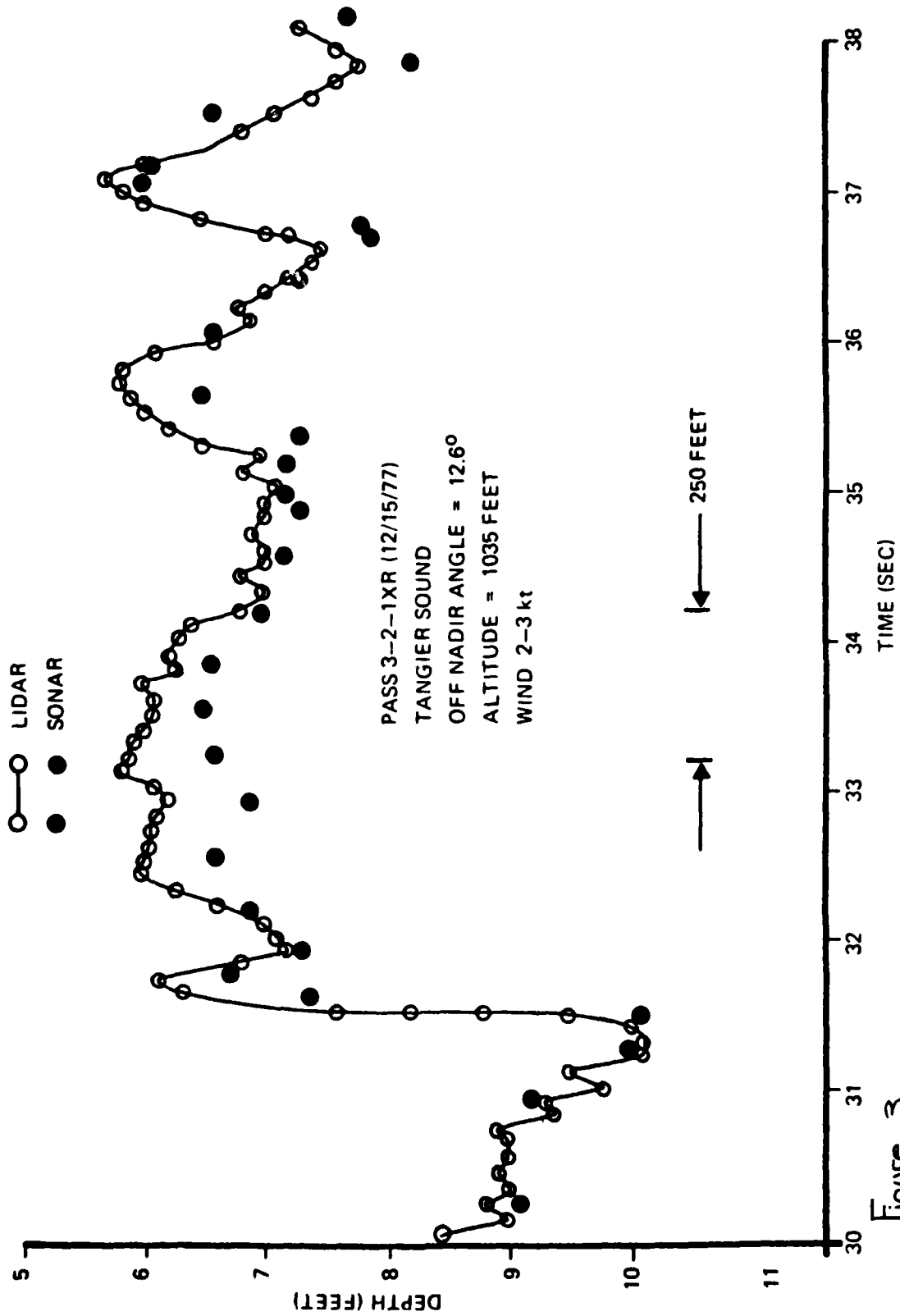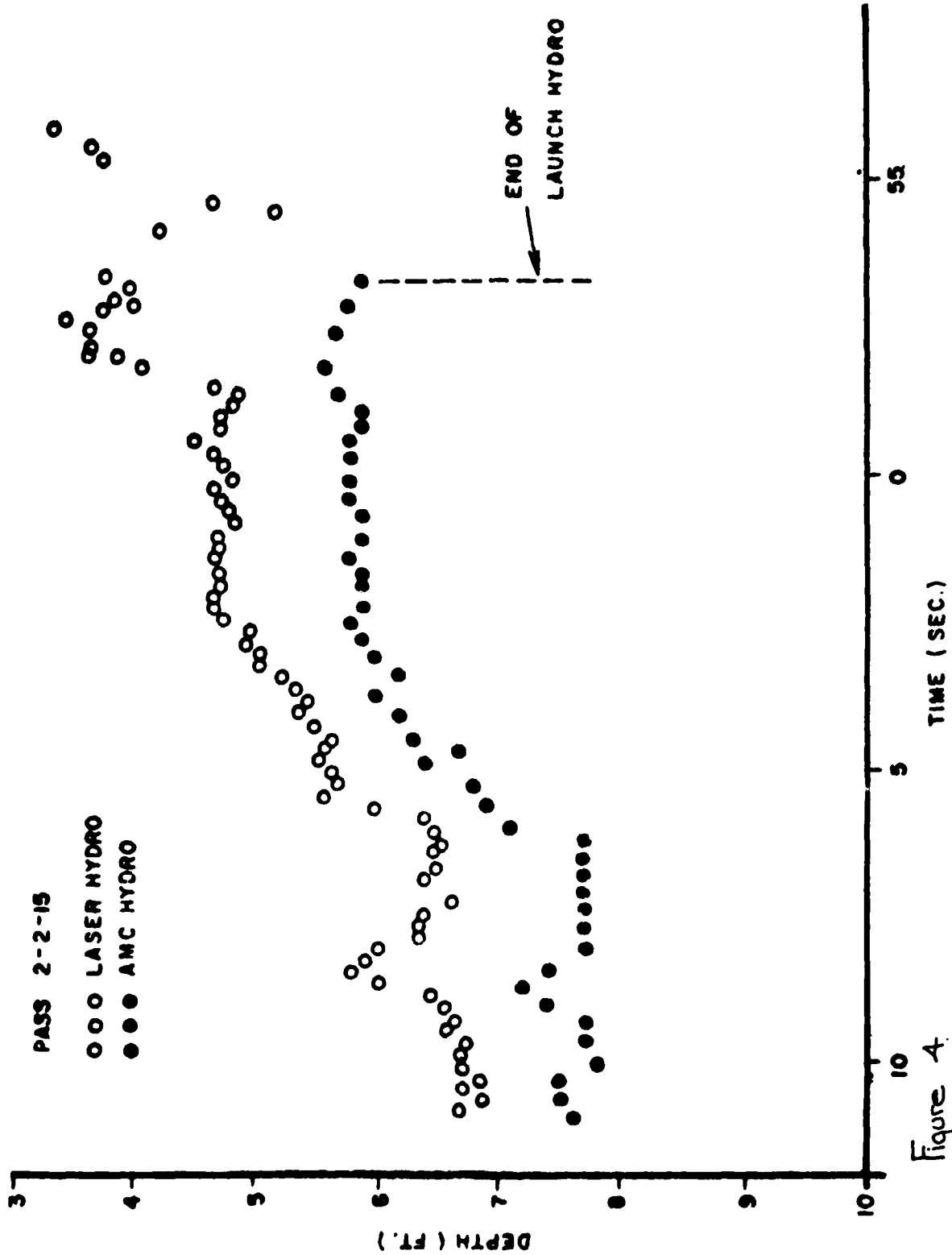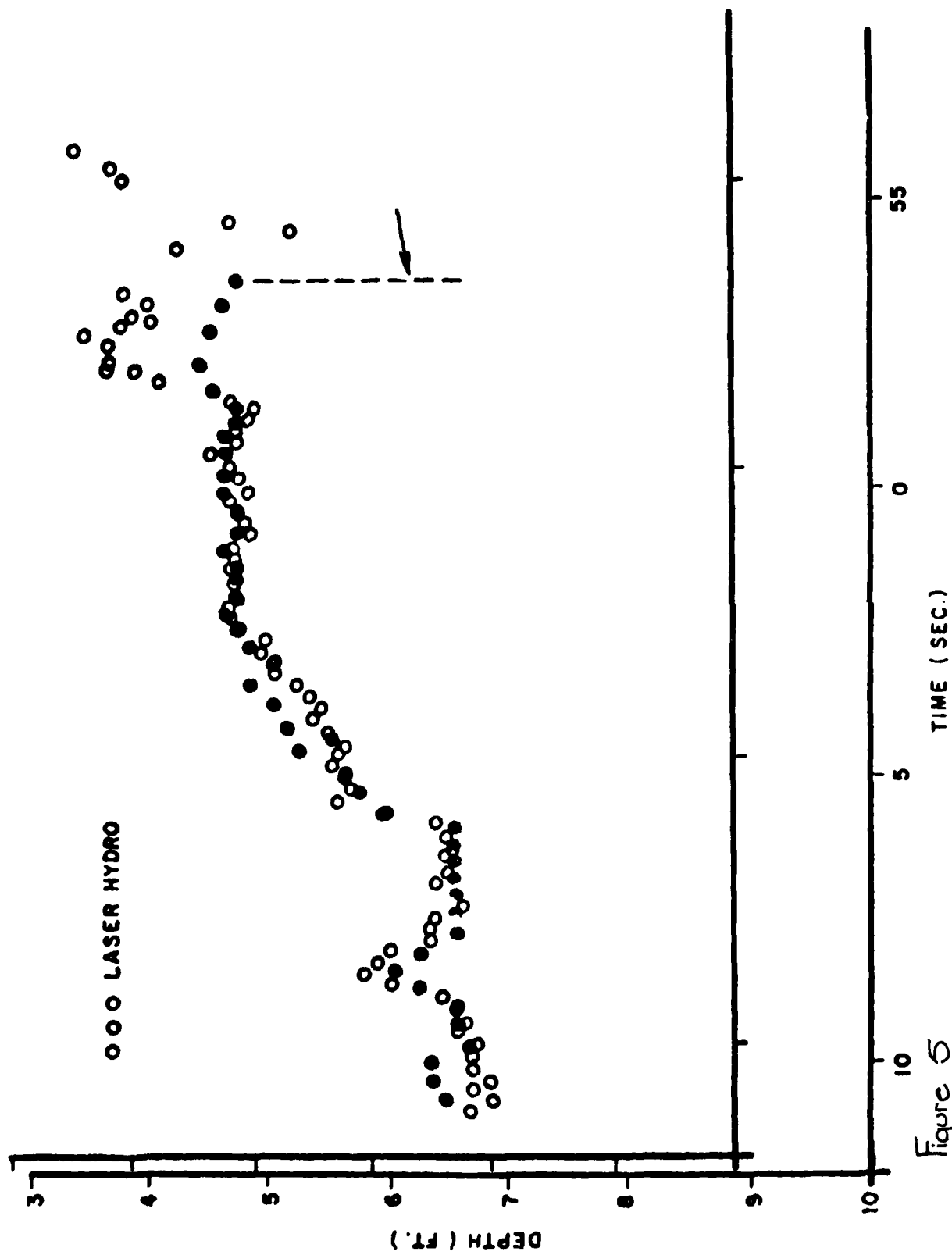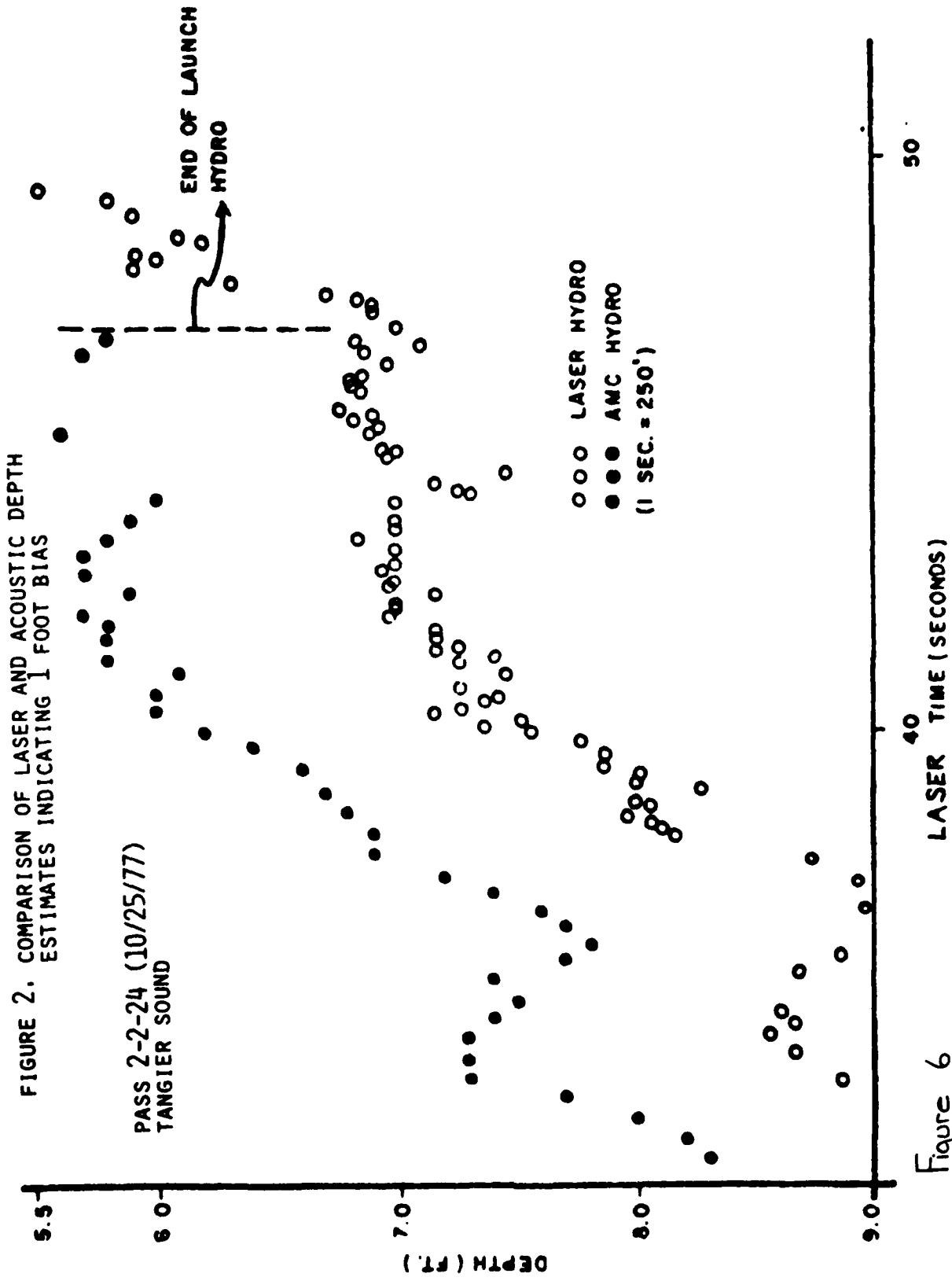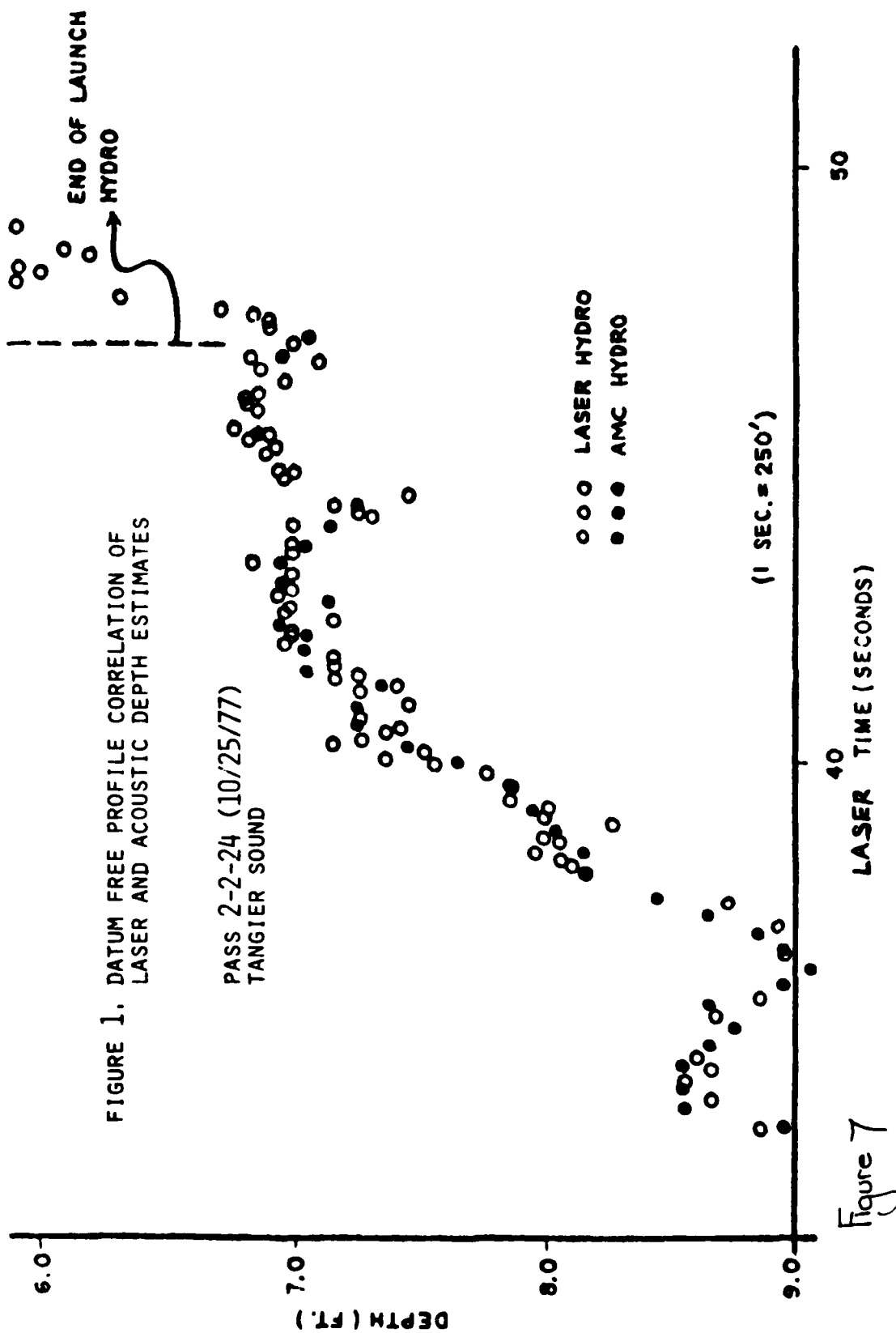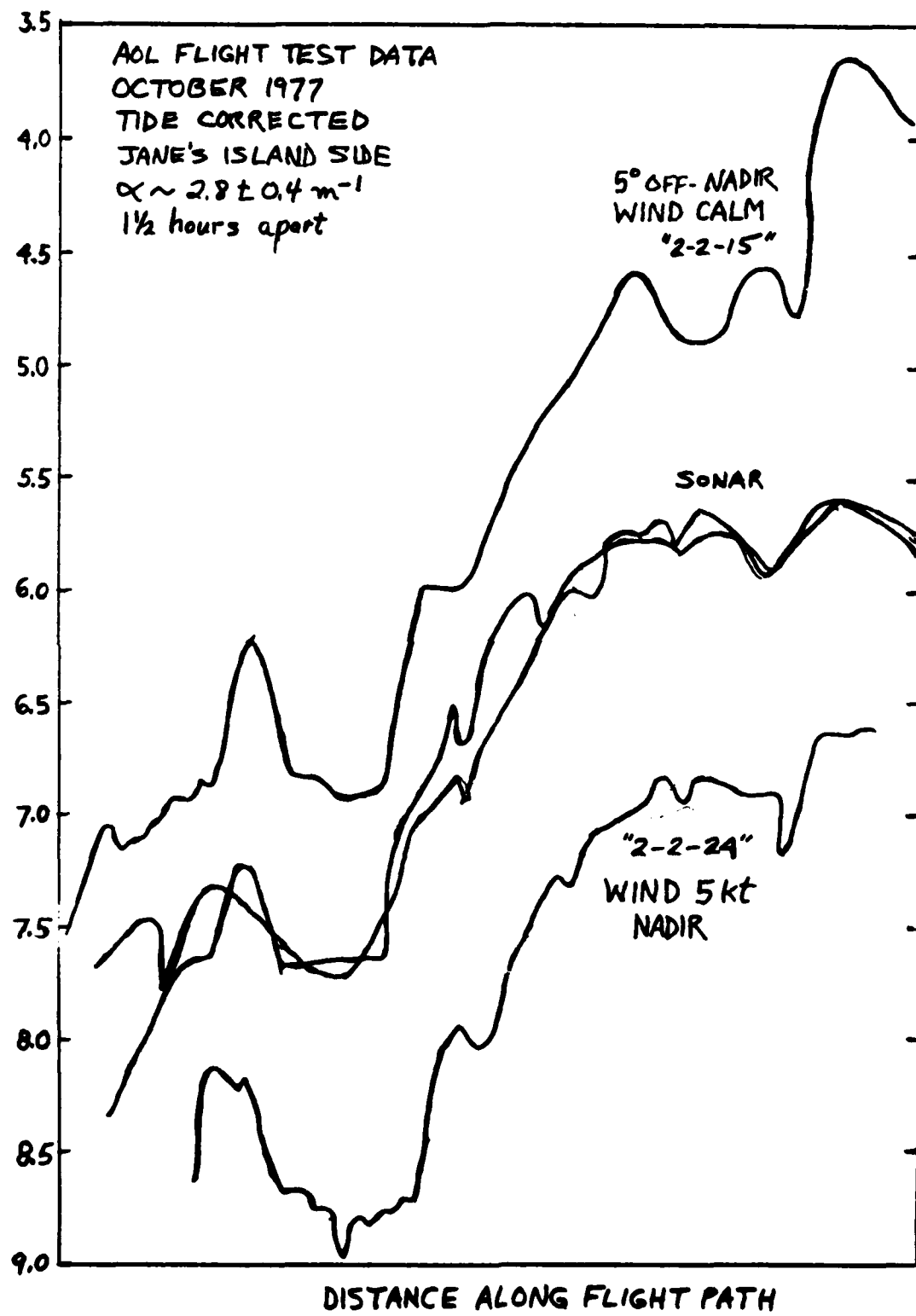
Figure 8

AOL TEST EXAMPLE

Impulse Response

"NOS" ; 15°

$\alpha D = 12$; $\omega_o = 0.9$

D = 3m

REF

P

TIME (NS)

1: 20% , 0.8
2: 20% , 0.9
3: 50% , 0.8
4: 50% , 0.9
5: 80% , 0.8
6: 80% , 0.9

"NOS" ; 15°

D = 3m

Depth Measurement Bias (cm)

Optical Depth
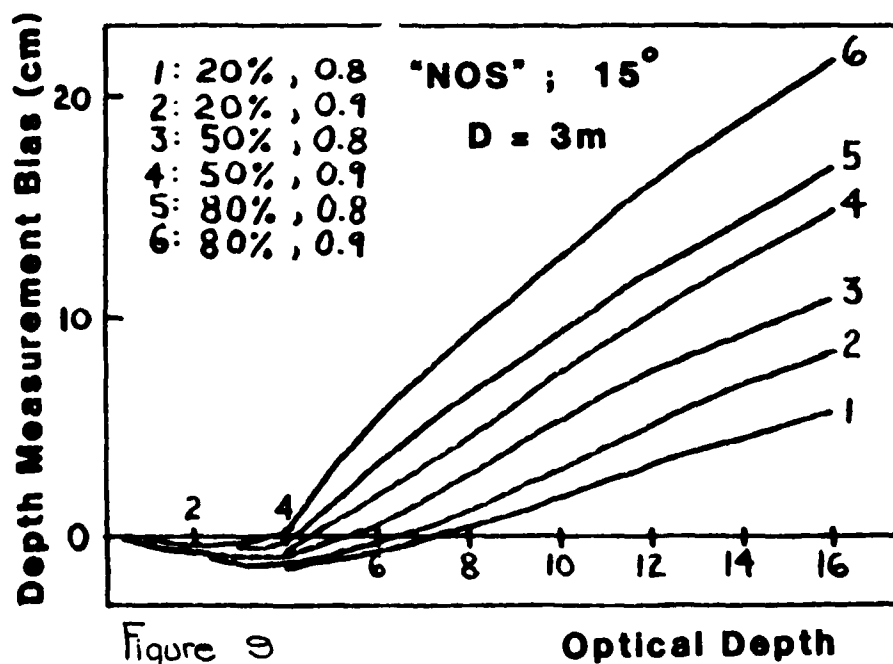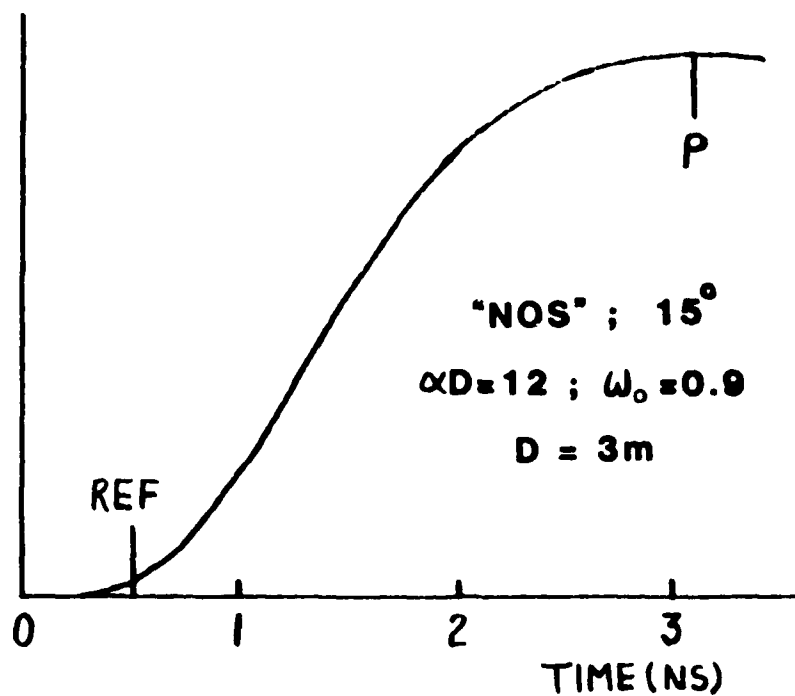
Figure 9

DEPTH MEASUREMENT BIAS VS "SURFACE" RETURN POWER
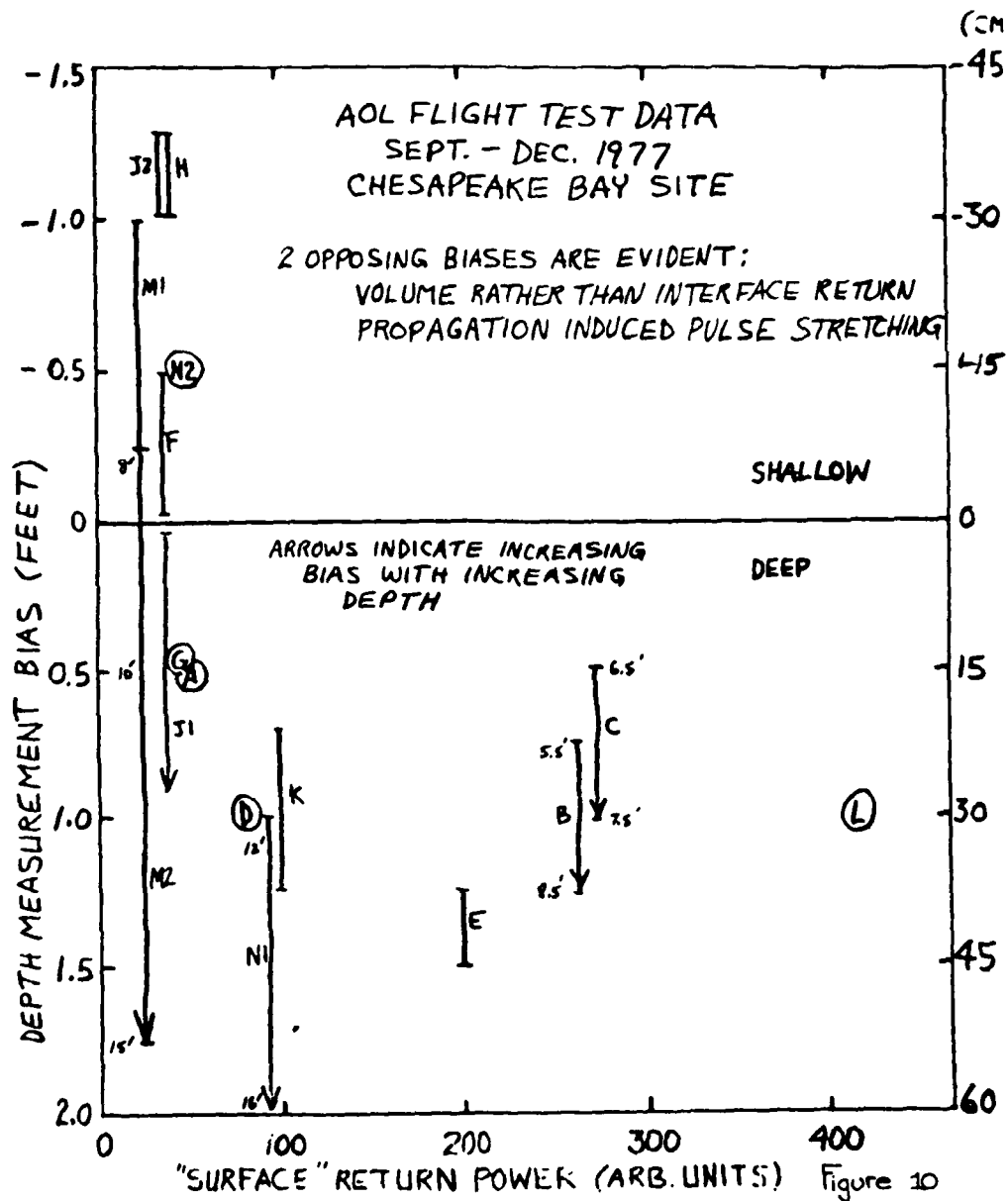
Figure 10

STANDARD DEVIATION OF MEASURED DEPTH VS. STANDARD DEVIATION OF MEASURED AIRCRAFT ALTITUDE

AOL FLIGHT TEST DATA
PASS 3-2-1XR (4A4)
DECEMBER 1977

STANDARD DEVIATION OF MEASURED DEPTH (m)

STANDARD DEVIATION OF MEASURED AIRCRAFT ALTITUDE (m)
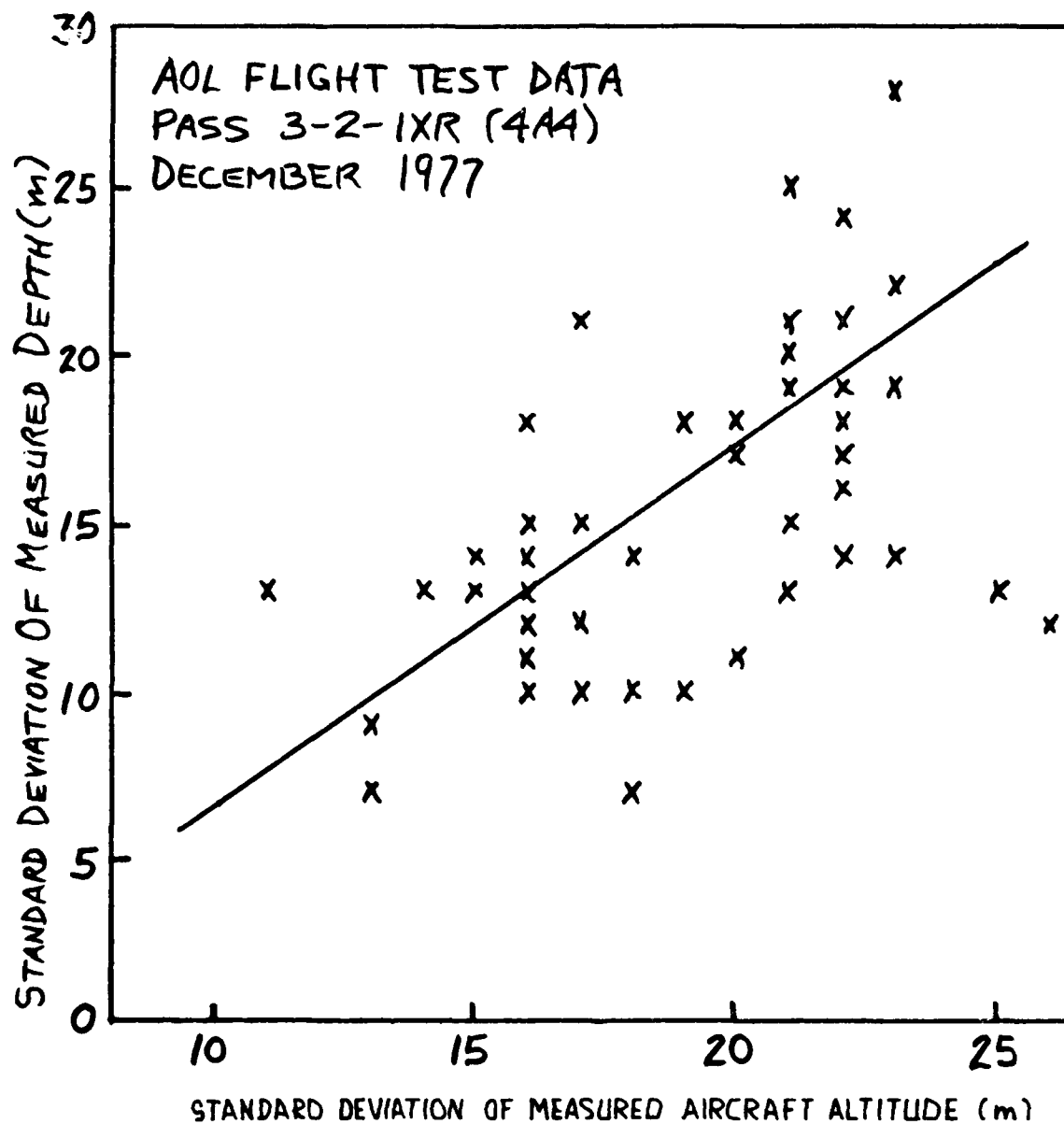
Figure 11

Note: This demonstrates that much of the depth measurement
noise is due to surface waves.
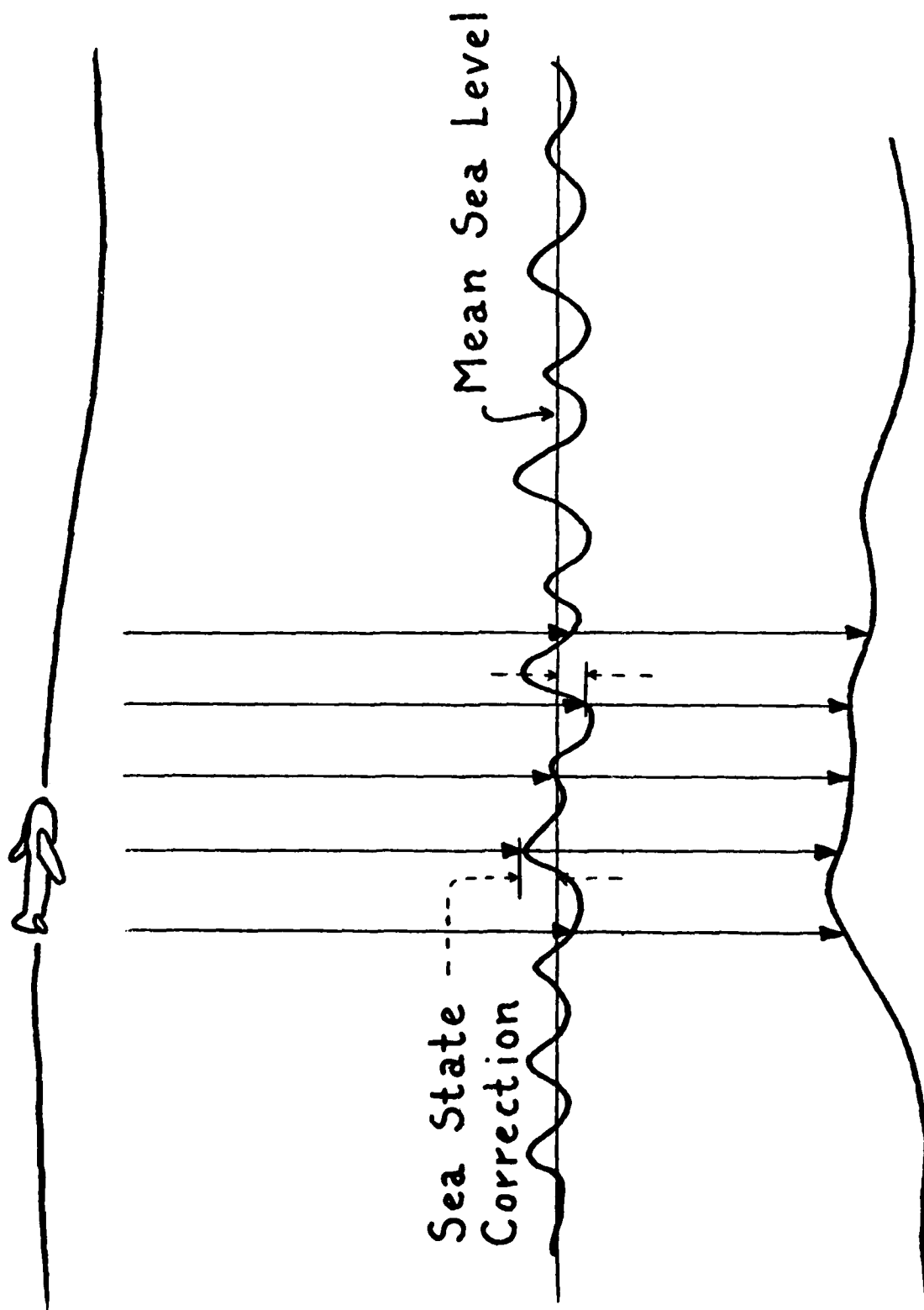
Figure 12

WAVE CORRECTION GEOMETRY

WAVE CORRECTION DEMONSTRATION

RAW DEPTH

$\sigma = 29$ cm

ALTITUDE

$\sigma = 39$ cm

ALTITUDE + RAW DEPTH

$\sigma = 12$ cm

$\rho = -0.94$

AOL FLIGHT TEST DATA
Pass 2-2-9 (3Q)
OCTOBER 1977

VERTICAL DISTANCE (1m TICS)

ARBITRARY TIME (MS)
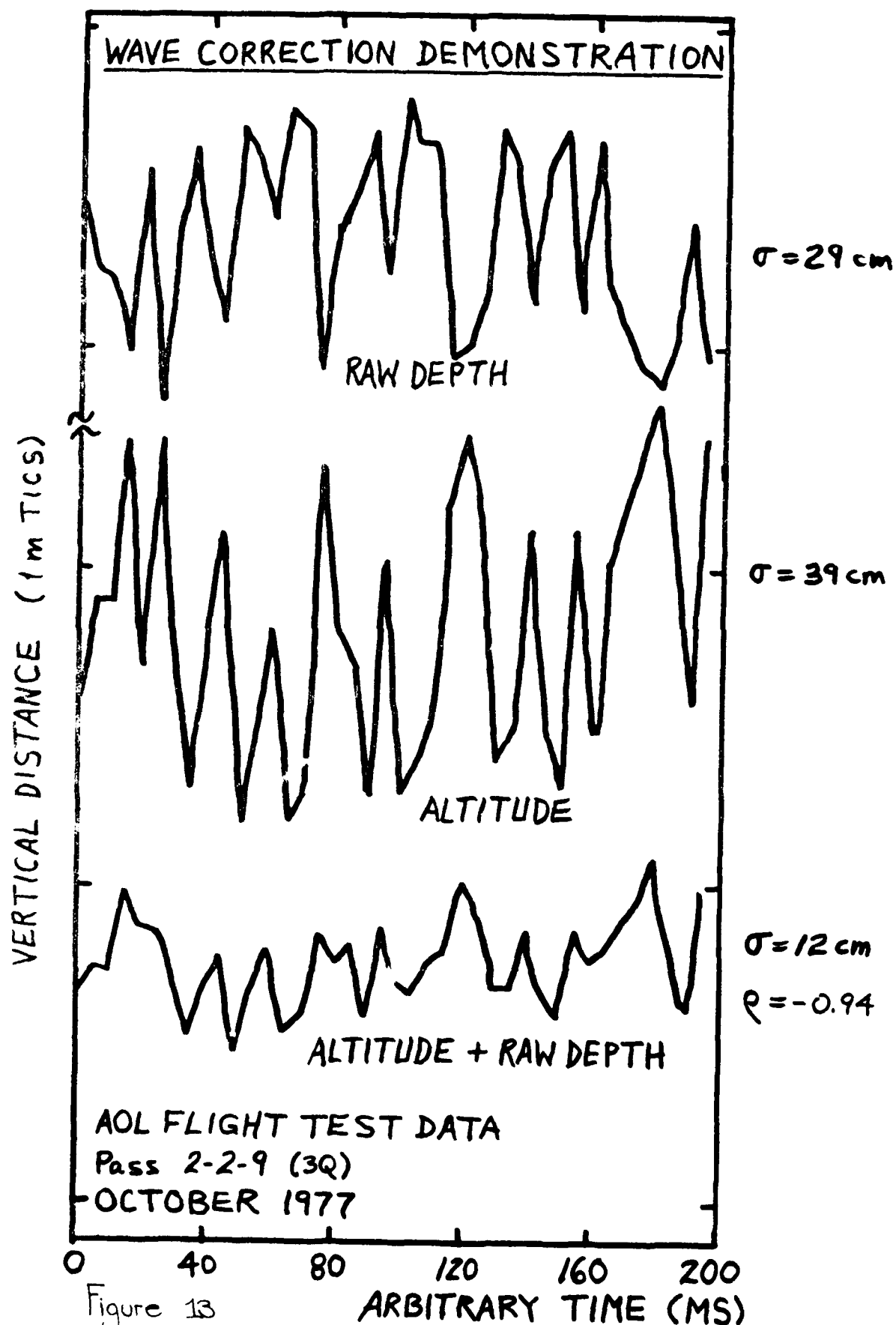
Figure 13

WAVE CORRELATION IN ALTITUDE AND DEPTH

MEASUREMENT

AOL FLIGHT TEST DATA
PASS 2-2-9 (3Q)
OCTOBER 1977

SLOPE = -0.93
r^2 = 0.58

Capillaries Fully Excited

MEASURED ALTITUDE ABOVE SEA SURFACE (m)

MEASURED WATER DEPTH (m)
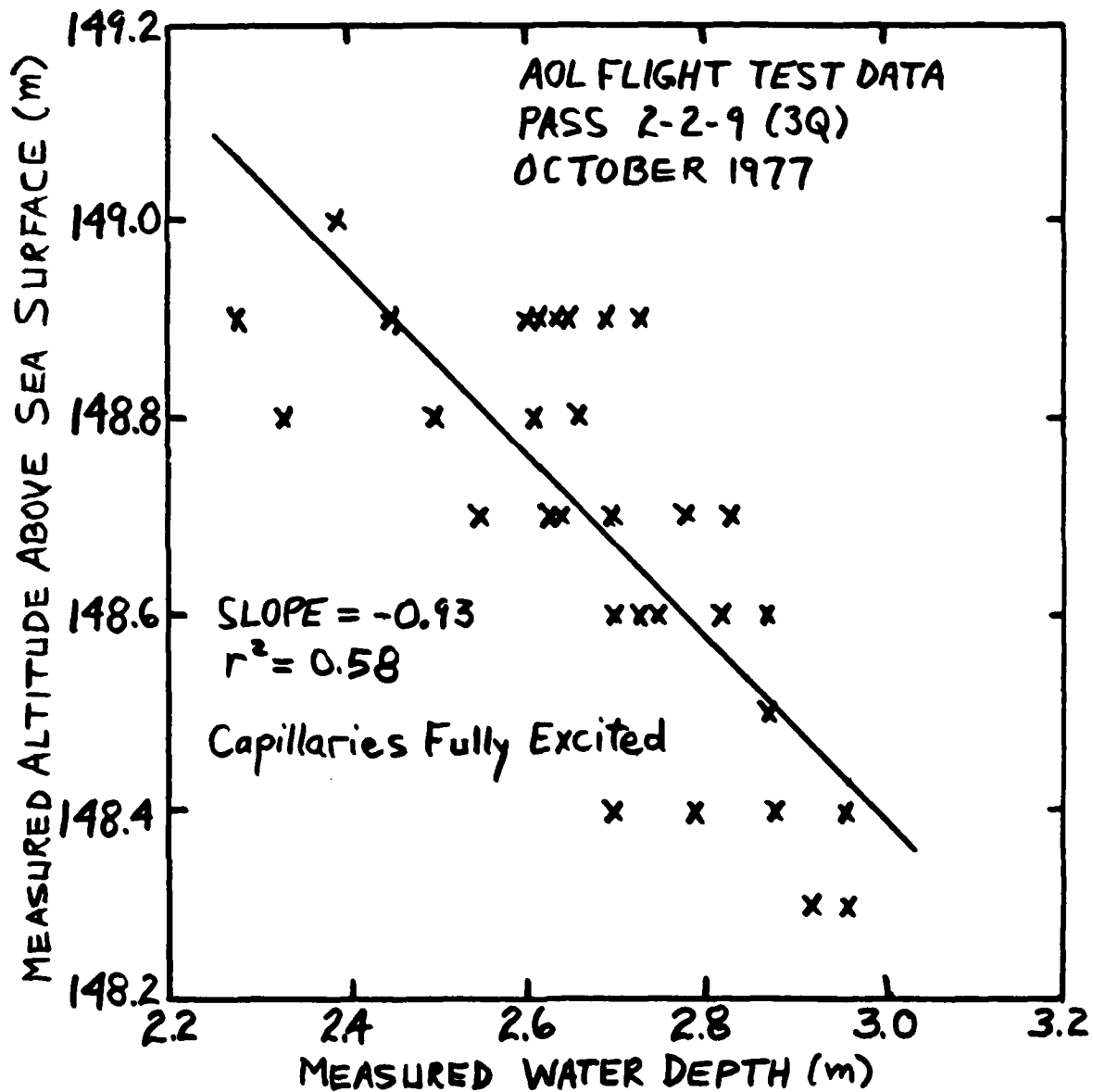
Figure 14

STANDARD DEVIATION OF RAW DEPTH MEASUREMENT (CONTAMINATED WITH WAVE NOISE) VS. BOTTOM RETURN POWER
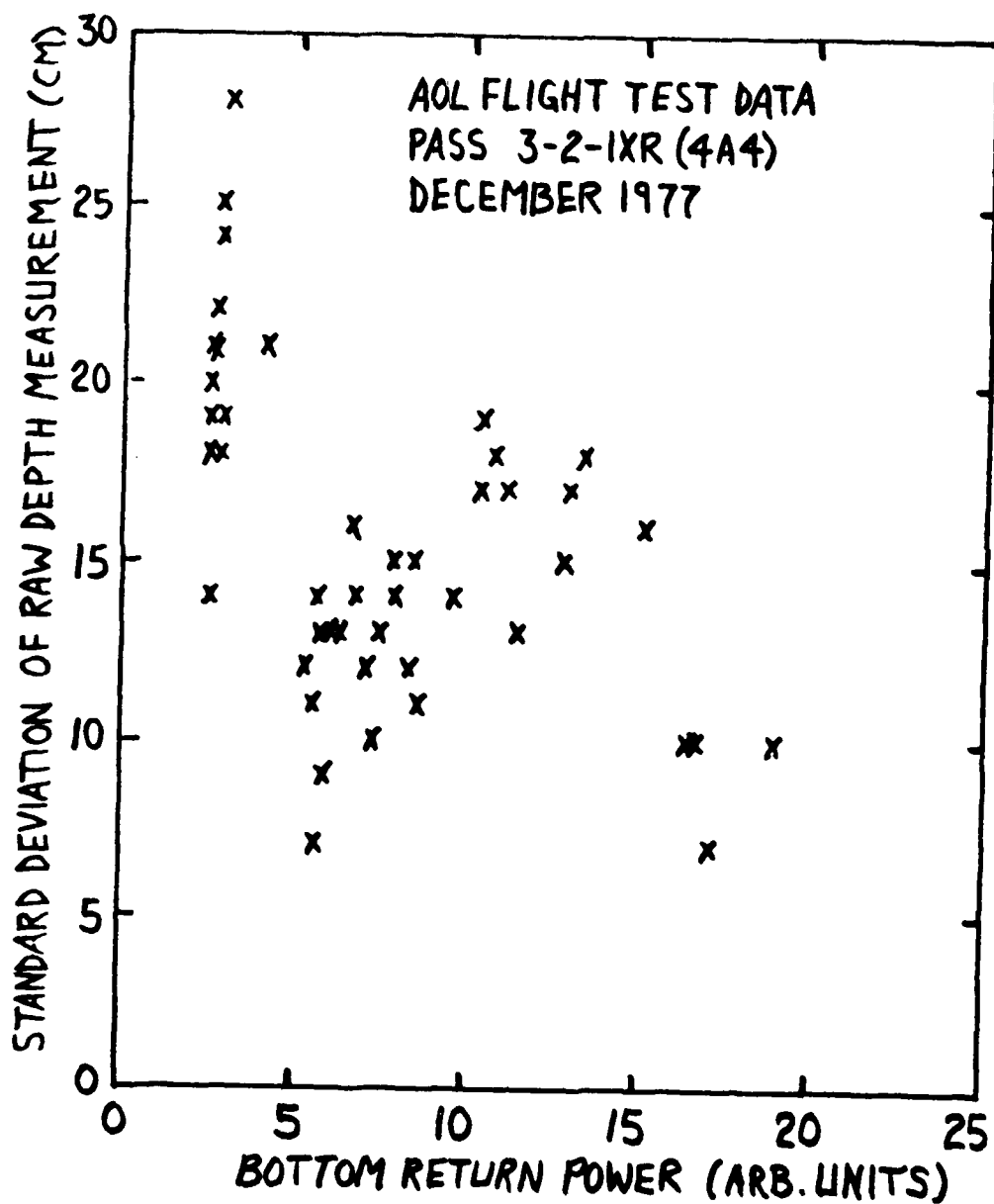
Figure 15

STANDARD DEVIATION OF WAVE CORRECTED DEPTH VS. BOTTOM RETURN POWER
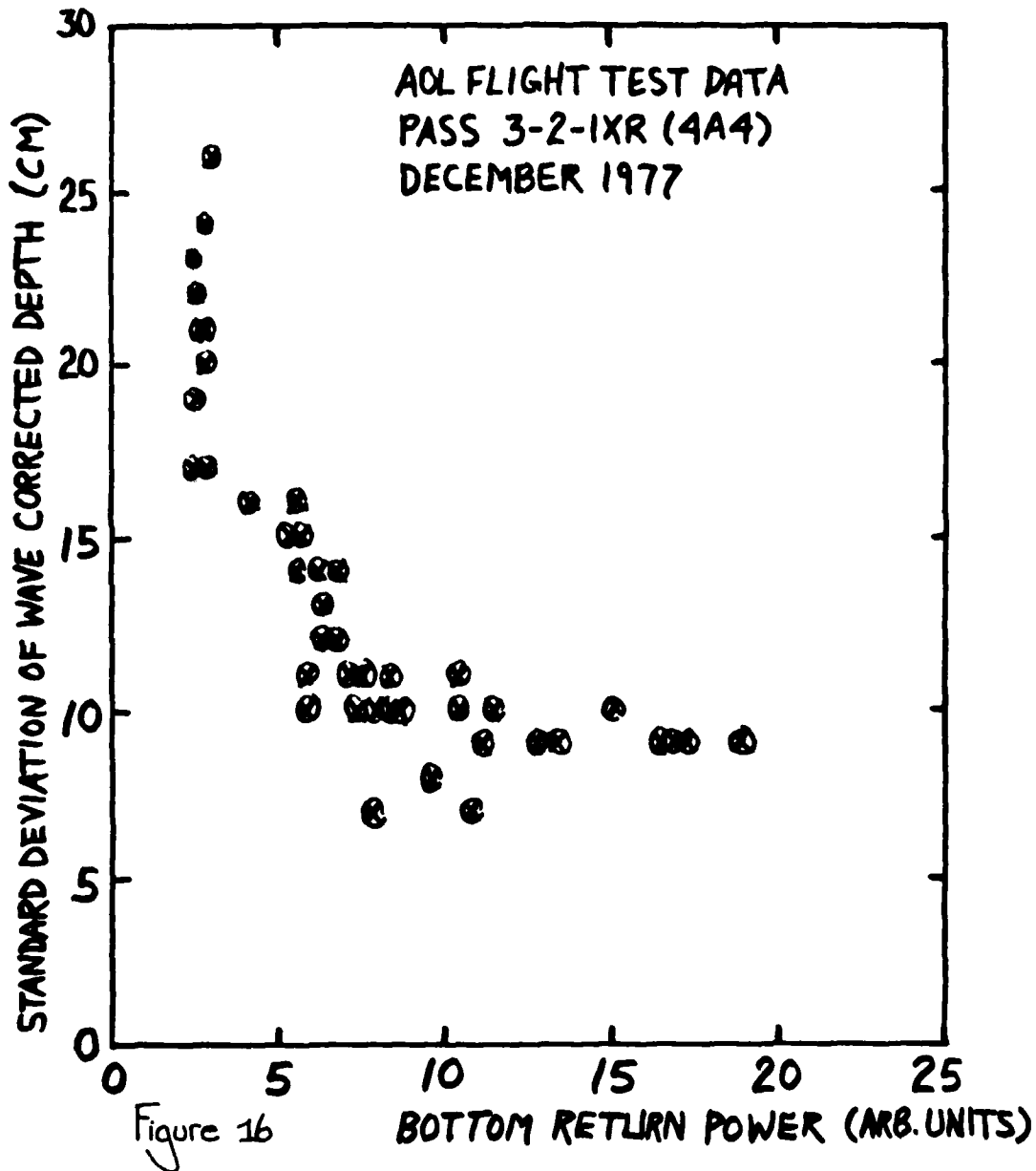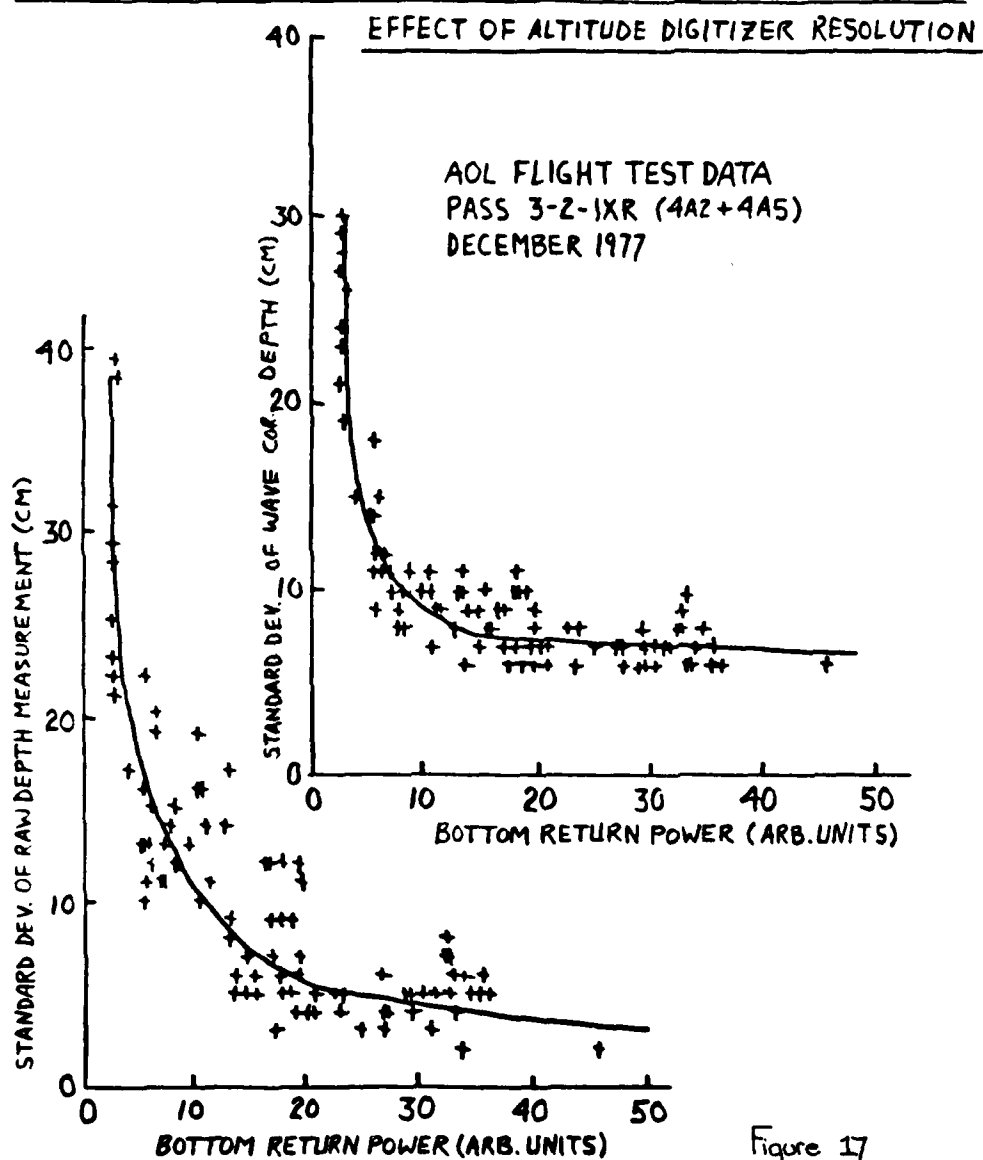
Figure 16

Figure 17

RESULTS OF WAVE CORRECTION PROCEDURE
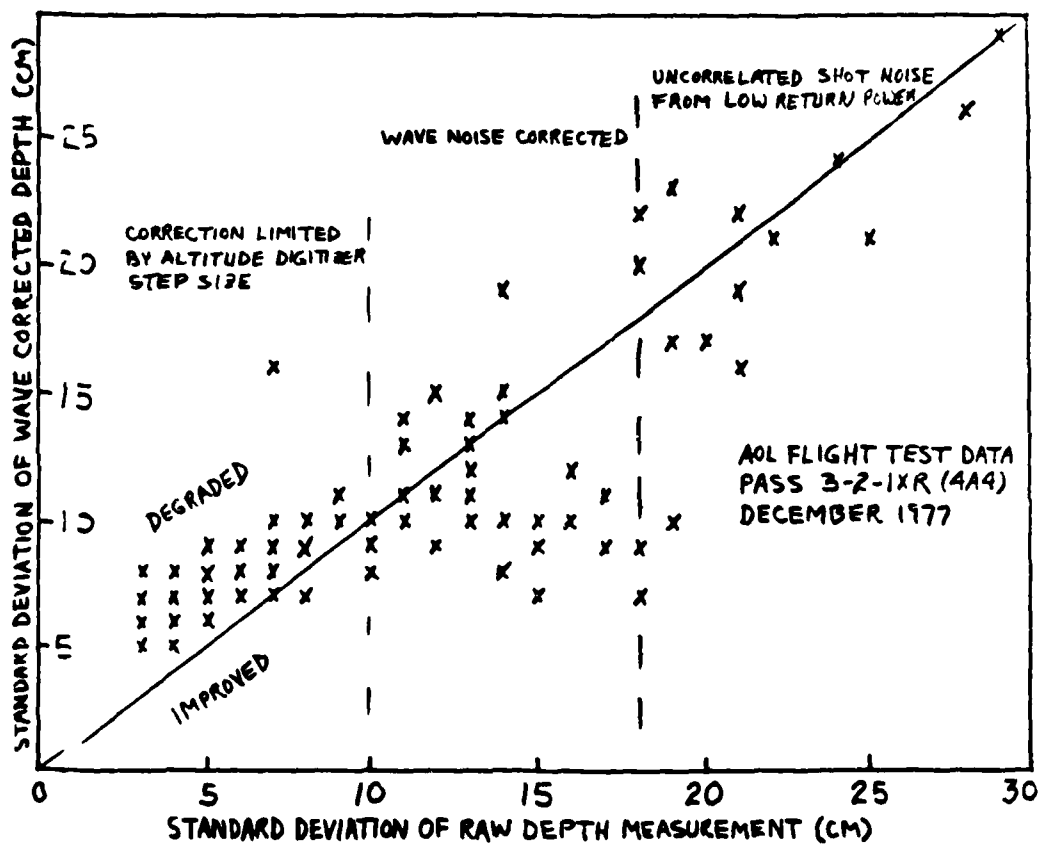
Figure 18

WAVE CORRELATION IN ALTITUDE AND DEPTH MEASUREMENT
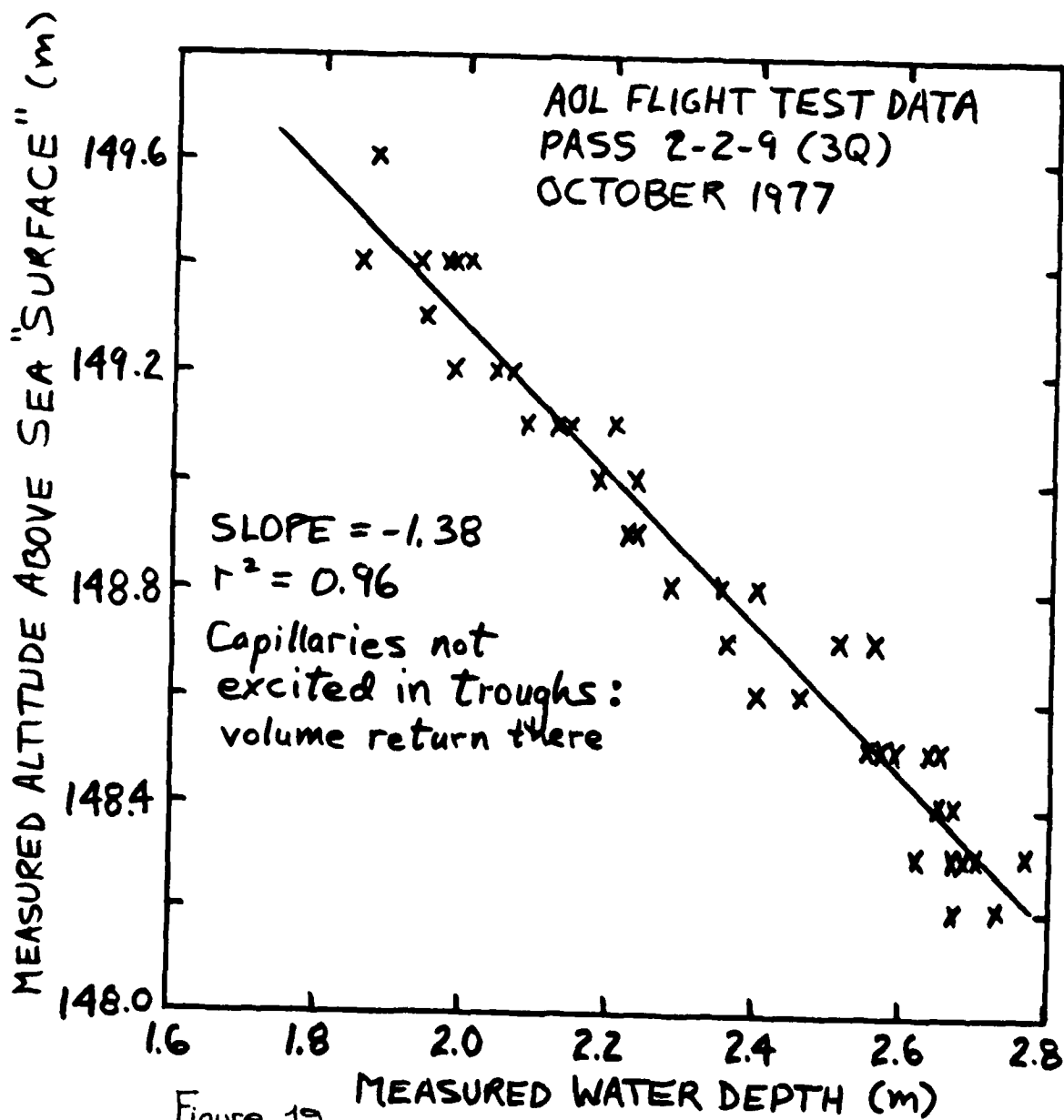
Figure 19

"SURFACE" RETURN POWER vs. MEASURED WATER DEPTH
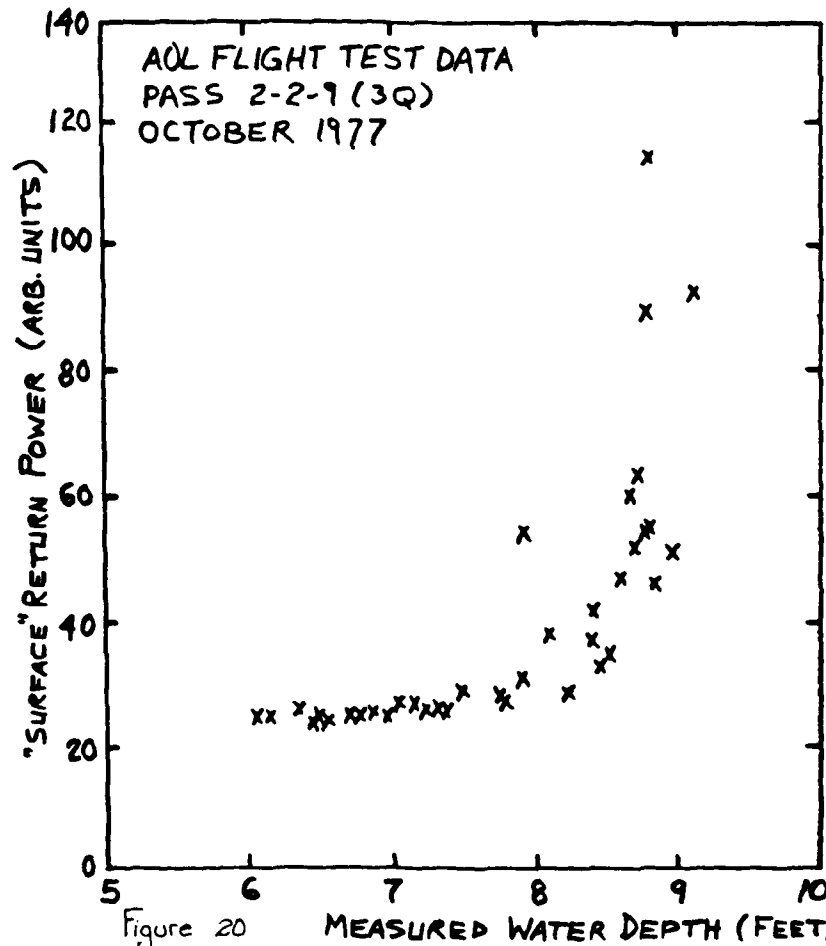
Figure 20

Note: This data demonstrates *low variance* of return power from volume scattering in shallow, "glassy" water and *large variance* of interface return from deeper water where capillaries are excited.

DEPTH MEASUREMENT BIAS DUE TO SURFACE UNCERTAINTY
(USE OF VOLUME RATHER THAN INTERFACE RETURN)
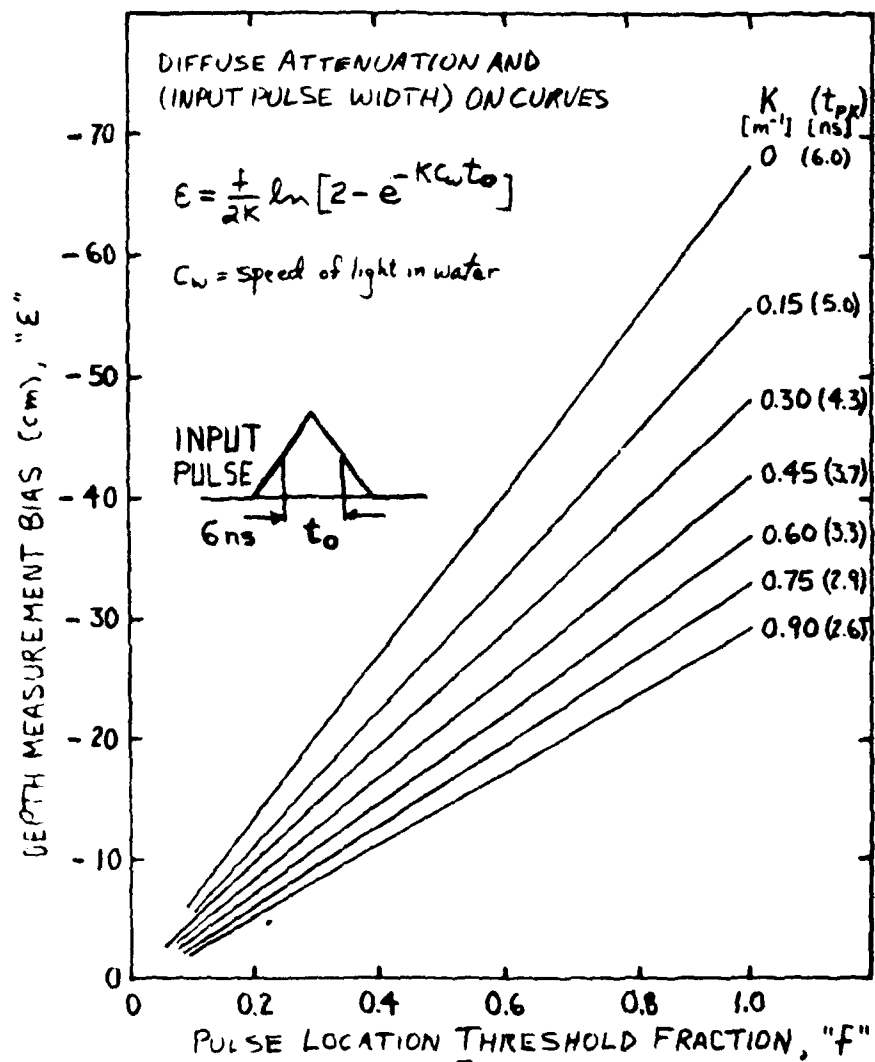
Figure 21

DEPTH MEASUREMENT BIAS VS "SURFACE" RETURN POWER

AOL FLIGHT TEST DATA
SEPT. - DEC. 1977
CHESAPEAKE BAY SITE

2 OPPOSING BIASES ARE EVIDENT:
VOLUME RATHER THAN INTERFACE RETURN
PROPAGATION INDUCED PULSE STRETCHING

SHALLOW

DEEP

ARROWS INDICATE INCREASING
BIAS WITH INCREASING
DEPTH

"SURFACE" RETURN POWER (ARB. UNITS) Figure 22
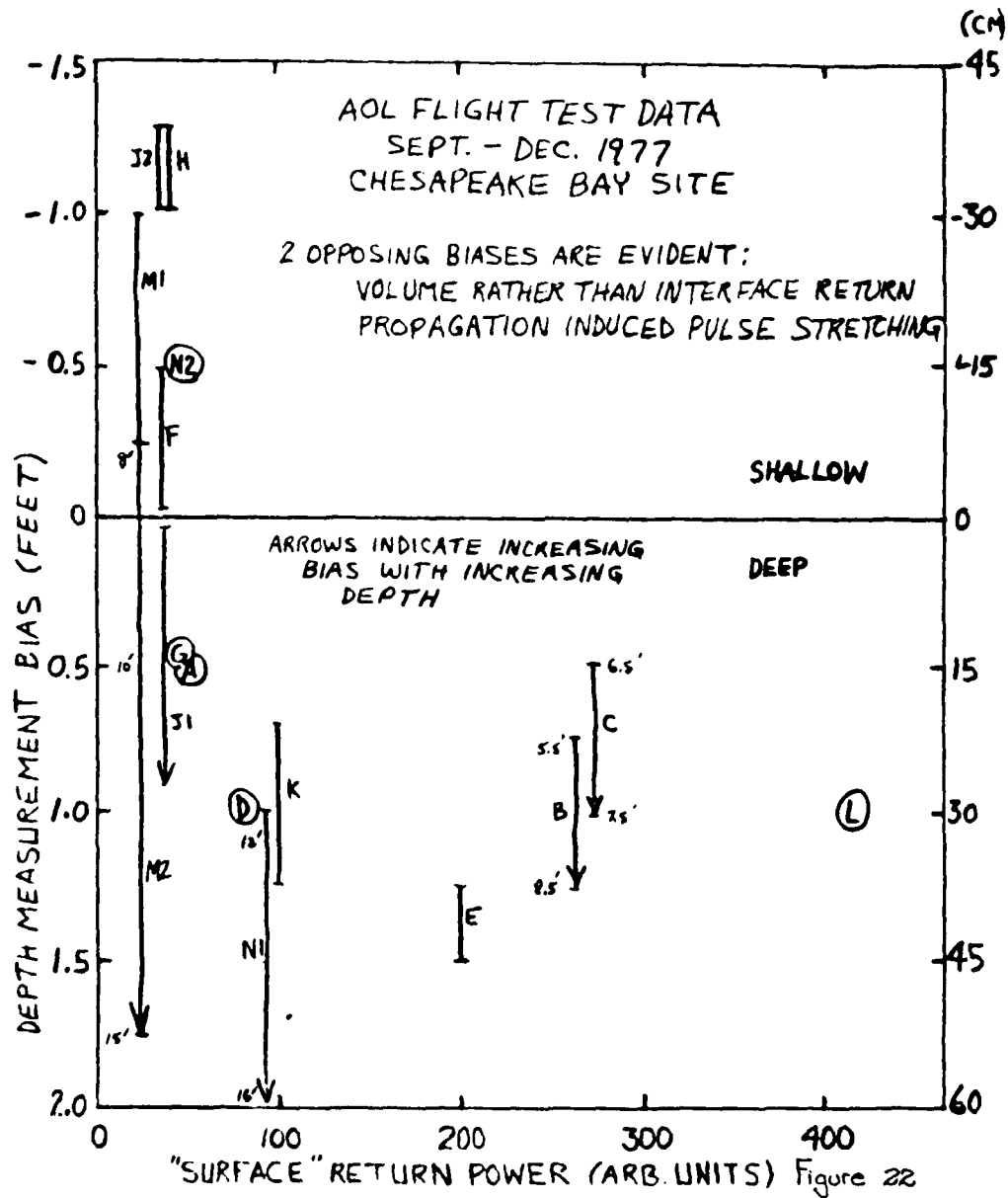
DERIVATION OF CONSTANT ALTITUDE AND CONSTANT SWATH WIDTH CURVES FOR BOTTOM RETURN POWER VS. AIR OFF-NADIR ANGLE

$$P_B = \frac{A\,f(\theta)\,\cos^2\theta}{H^2} \qquad (\text{CONST. ALT.})$$

where:

$\theta(°)$	0	10	20	30	40
$f(\theta)$	0.85	0.75	0.46	0.26	0.12

DETERMINED BY MONTE CARLO SIM.
$(\alpha D = 10 \,; \; \omega_0 = 0.8)$

$$L = 2H \tan\theta \;\Rightarrow\; P_B = \frac{4A\,f(\theta)\,\sin^2\theta}{L^2}$$

(CONST. SWATH WIDTH)

$A = $ CONSTANT
$\theta = $ AIR OFF-NADIR ANGLE
$H = $ ALTITUDE
$P_B = $ BOTTOM RETURN POWER
$L = $ SWATH WIDTH

Figure 23

BOTTOM RETURN POWER VS. AIR OFF-NADIR ANGLE

CONSTANT ALTITUDE AND SWATH WIDTH CURVES
BASIC ANGLE DEPENDANCE FROM MONTE CARLO SIM.
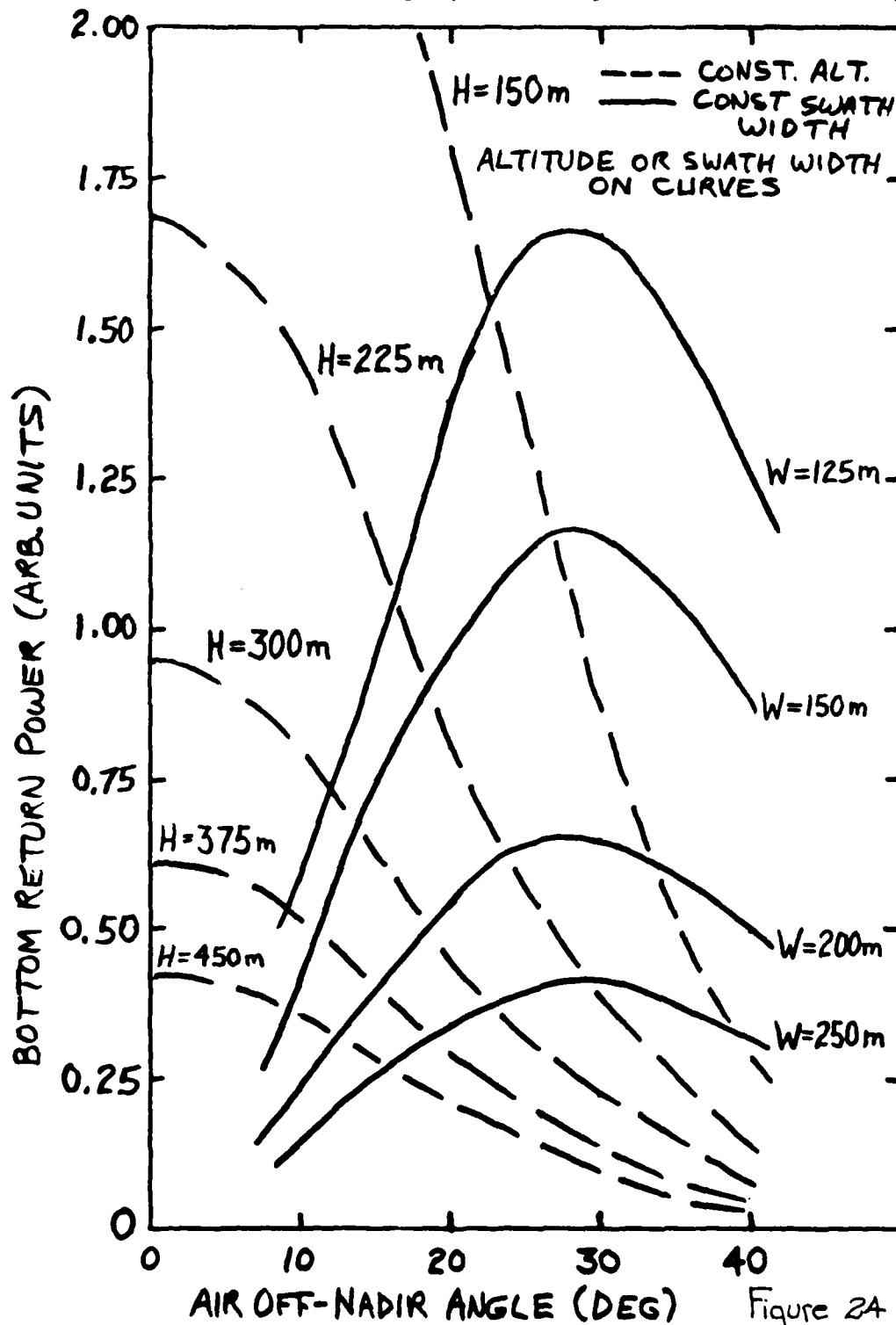
Figure 24

SURFACE INTERFACE RETURN POWER vs. AIR OFF-NADIR ANGLE AT VARIOUS WIND SPEEDS
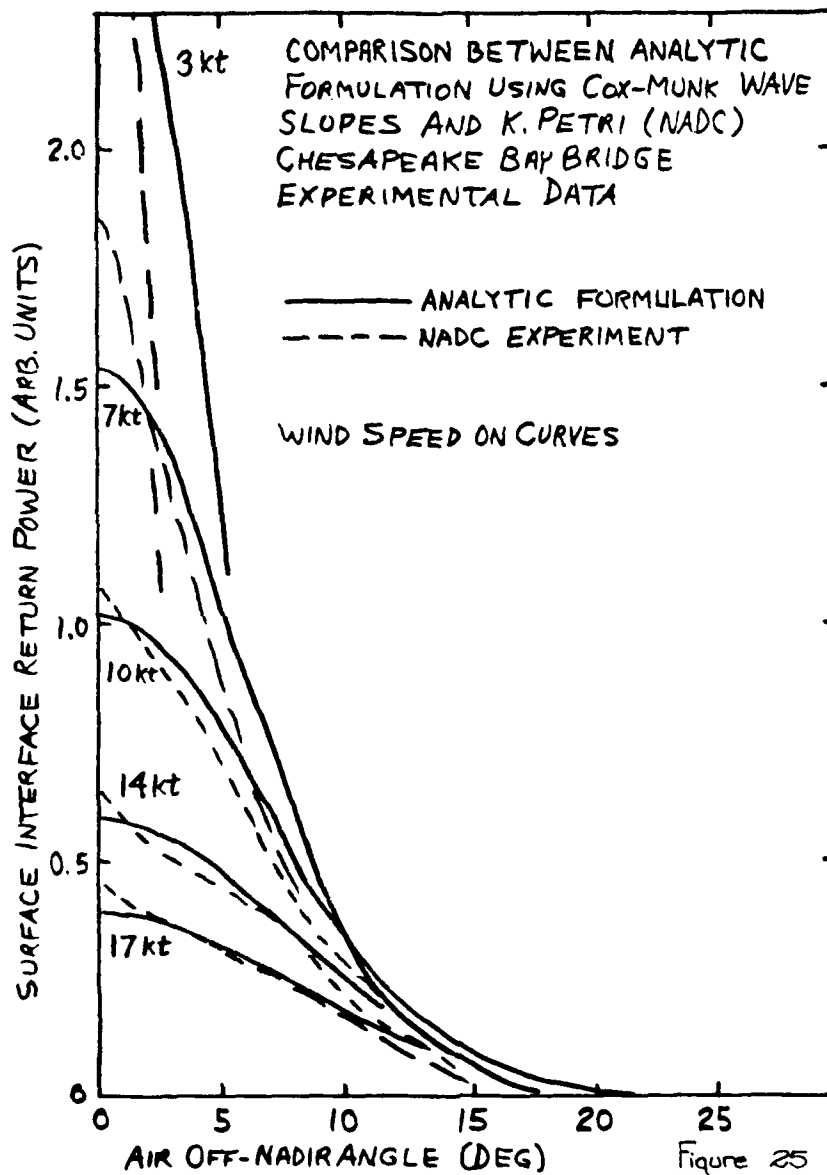
Figure 25

LOG SURFACE INTERFACE RETURN POWER VS. LOG AIR OFF-NADIR ANGLE AT VARIOUS WIND SPEEDS

LOG AIR OFF-NADIR ANGLE (DEG) Figure 26.
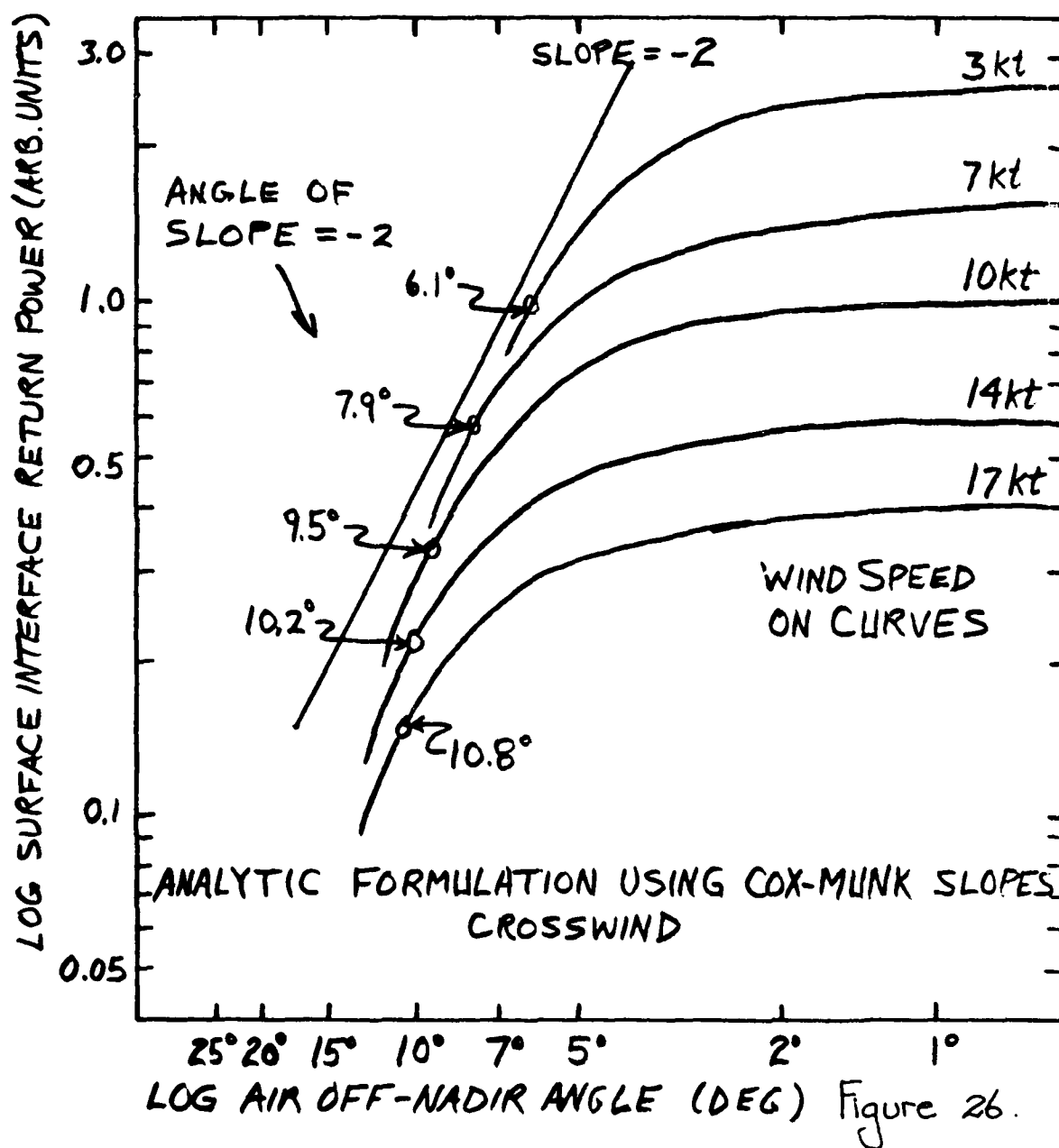
AIR OFF-NADIR ANGLE OF MAXIMUM SURFACE INTERFACE RETURN
POWER FOR CONSTANT SWATH WIDTHS VS. WIND SPEED.

COX-MUNK WAVE SLOPES CROSSWIND
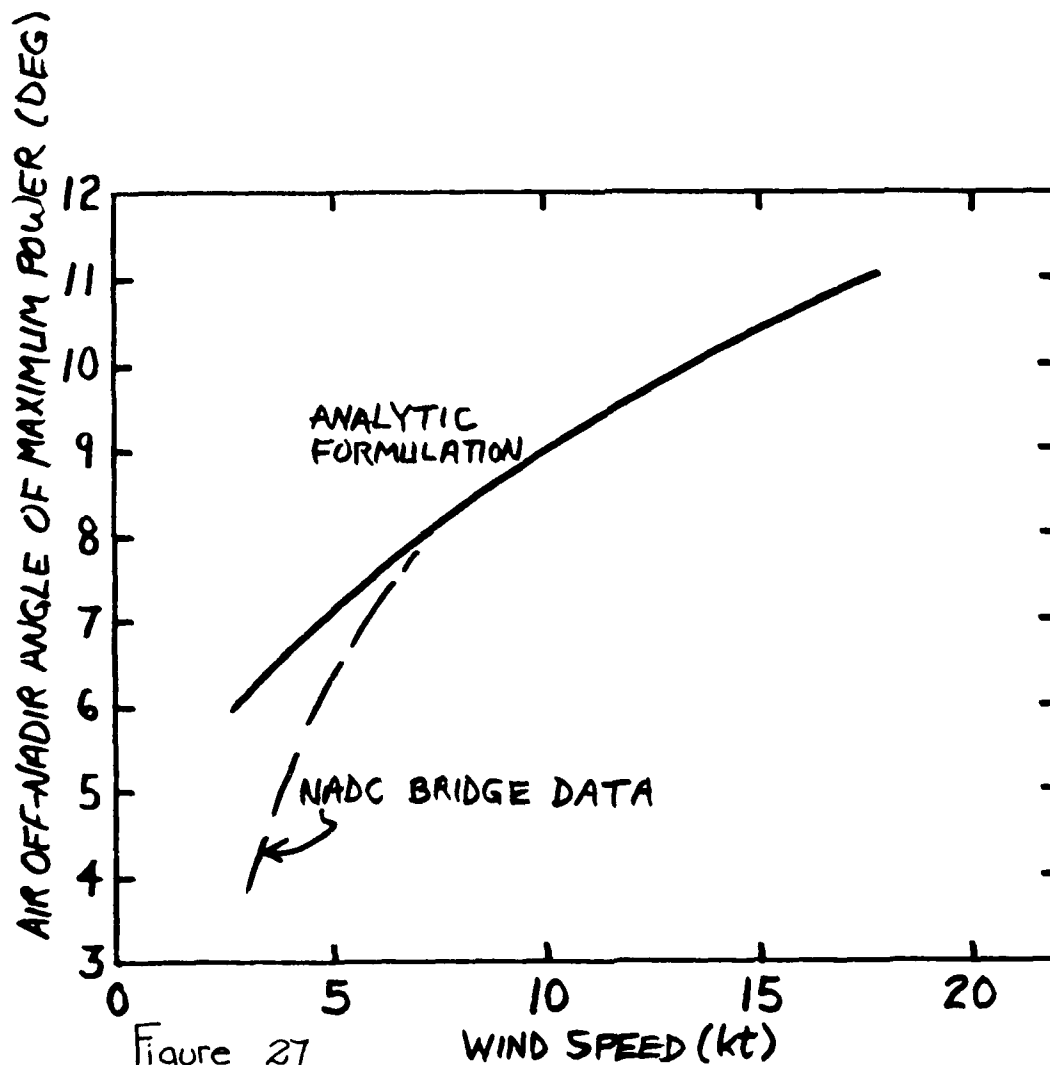
Figure 27

<u>DERRIVATION OF CONSTANT ALTITUDE AND CONSTANT SWATH WIDTH CURVES FOR SURFACE INTERFACE RETURN POWER VS. AIR OFF-NADIR ANGLE</u>

$$P_S = \frac{A\, N(\theta, W)\, \cos^2\theta\; \rho_s^*(w)}{\pi H^2} \quad \text{(CONST. ALT.)}$$

where :

$$N(\theta, W) = e^{-\frac{1}{2}\frac{\theta^2}{\sigma_i^2}} \qquad i = \{u, c\}$$

$$\sigma_c^2 = 0.003 + 0.00096\, W(kt)$$

$$\sigma_u^2 = 0.00158\, W(kt)$$

$$L = 2H\tan\theta \;\Rightarrow\; P_S = \frac{4A\, N(\theta, W)\, \sin^2\theta\; \rho_s^*(w)}{\pi L^2}$$

(CONST. SWATH WIDTH)

A = CONSTANT
θ = AIR OFF-NADIR ANGLE
W = WIND SPEED
H = ALTITUDE
P_S = SURFACE INTERFACE RETURN POWER
L = SWATH WIDTH
$\rho_s^*(w)$ = LAMBERTIAN REFLECTIVITY

$$P_S = B\, \rho_s^*(w)\, \cos^2\theta\, N(\theta, W) \equiv B\alpha_s$$

B = CONSTANT
α_s = SURFACE "LOSS FACTOR" = $\rho_s^*(w)\, \cos^2\theta\, N(\theta, W)$

Figure 28

SURFACE INTERFACE RETURN POWER vs. AIR OFF-NADIR ANGLE
CONSTANT ALTITUDE AND CONSTANT SWATH WIDTH CURVES

Figure 29

SURFACE INTERFACE RETURN LOSS FACTOR CONSTRAINT
EQUATIONS IN AIR OFF-NADIR ANGLE AND WIND SPEED
CROSSWIND CASE

Figure 30.

Within the figure: LOSS FACTOR ON CURVES; curve labels 10^{-7}, 10^{-6}, 10^{-5}, 10^{-4}, 10^{-3}, 10^{-2}, 10^{-1}; y-axis AIR OFF-NADIR ANGLE (DEG); x-axis WIND SPEED (kt).
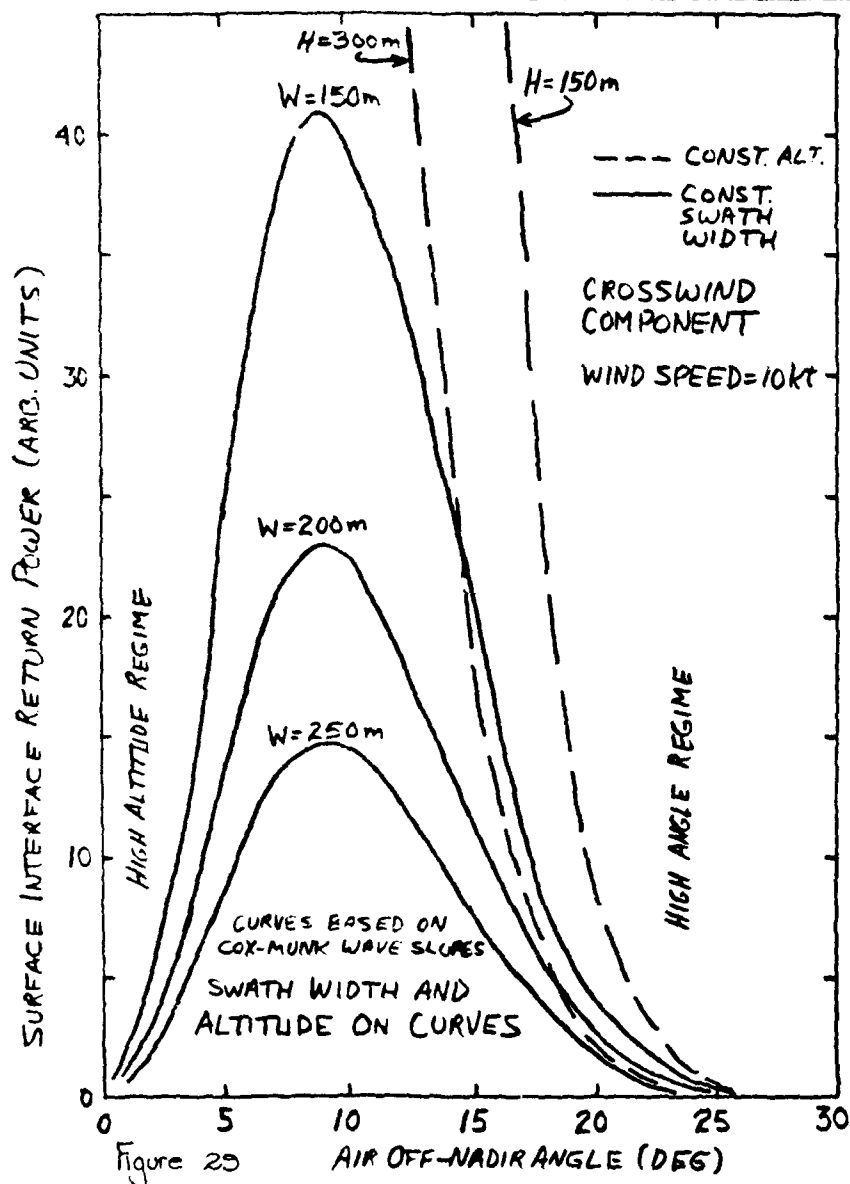
$$\text{LOSS FACTOR} \equiv \varrho_s^2(w)\cos^2\theta\, N(\theta,w)$$
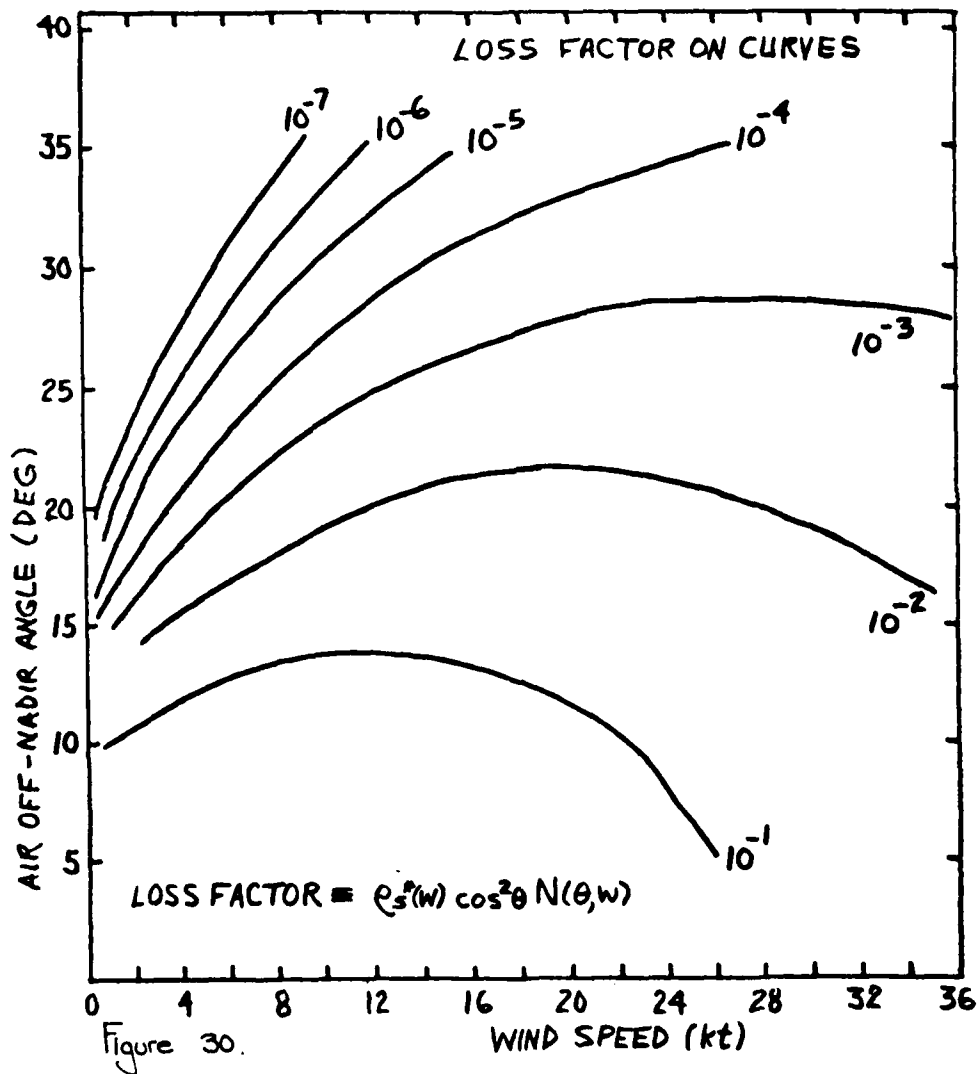
Volume Return to Surface Return Power Ratio

$$P_S = A\, \rho_s(w)\, \cos^2\theta\; N(\theta,w) / \pi$$

$$P_V = A\, \rho_v(K)\, \cos^2\theta / n^2$$

$$\boxed{\frac{P_V}{P_S} = \frac{\pi}{n^2}\; \frac{\rho_v(K)}{\rho_s(w)\, N(\theta,w)}}$$

$$\rho_v(K) = \frac{\beta_\pi(K)}{2K}\left[1 - \frac{1}{K c_w t_p}\ln\left(2 - e^{-K c_w t_p}\right)\right]$$

Ref: M.Miller (AVCO); R.Thomas (EG+G)

$$\rho_s(w) = 4.033\; e^{-0.1374\, W(kt)}$$

Ref: G. Guenther (NOAA) - NADC Data

$$N_i(\theta,w) = \exp\left[-\tfrac{1}{2}\,\theta^2 / \sigma_i^2(w)\right]\;;\quad i = \{u,c\}$$

$$\sigma_u^2 = 0.00158\; W(kt)$$

$$\sigma_c^2 = 0.003 + 0.00096\, W(kt)$$

Ref: Cox - Munk

PV=Volume Return Peak Power ; PS=Surface Return Peak Power

A =System Constant ; W=Wind Speed(kt)

θ =Air Off-Nadir Angle(rad) ; K=Diffuse Attenuation Coefficient

c_w=Speed of Light in Water ; n=Index of Refraction of Water (4/3)

$\rho_s(w)/\pi$=Effective Surface Reflectivity per Unit Solid Angle

N(θ,W)=Normalized Cox-Munk Wave Slope Distribution

ρ_v(K)=Effective Backscatter Reflectivity per Unit Solid Angle

β_π(K)=Backscatter Coefficient per Unit Solid Angle at 180 Degrees

(see Petzold, SIO Ref 72-78 (1972)

t_p=Half Width of Incident (Triangular) Laser Pulse

Figure 31

BACKSCATTER TO DIFFUSE ATTENUATION RATIO VS. "K" AND "α"
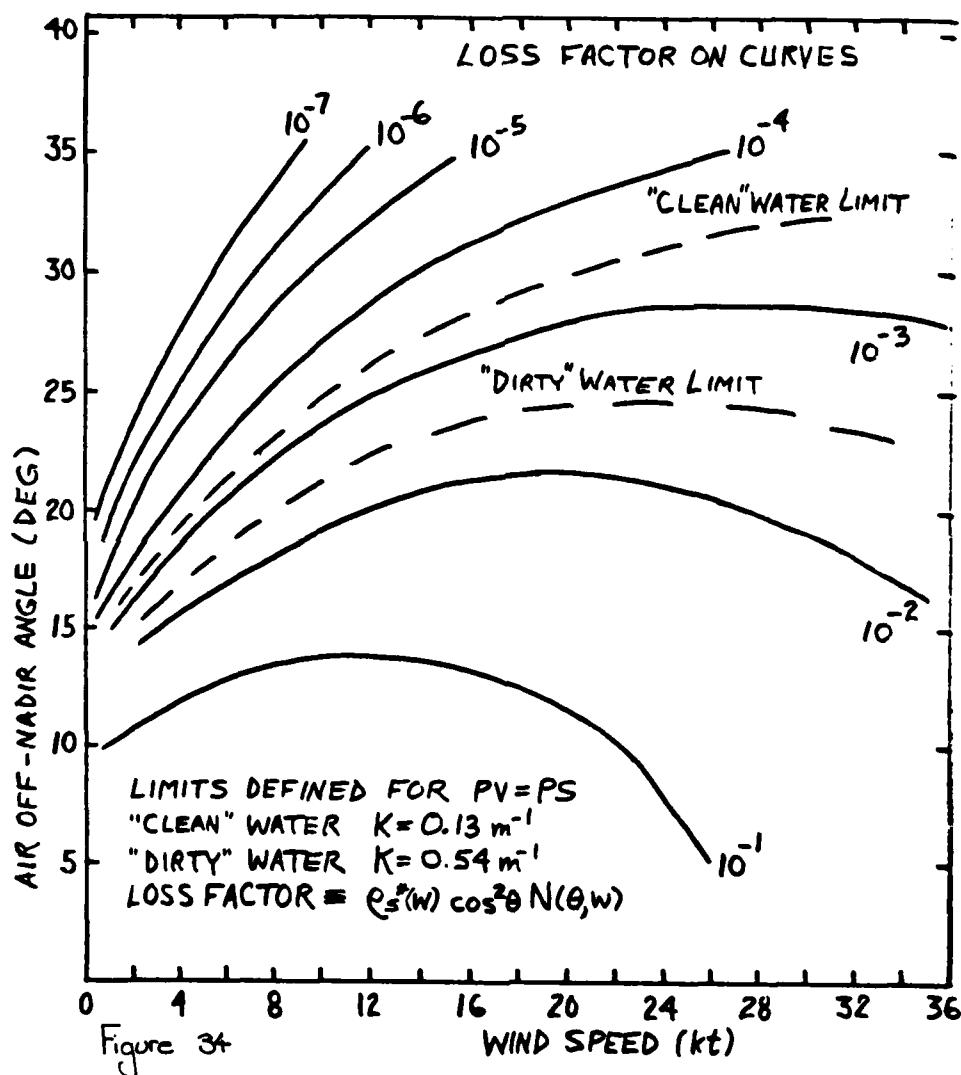
RAW DATA: REF. PETZOLD SIO REF 72-78 (1972)

Figure 32
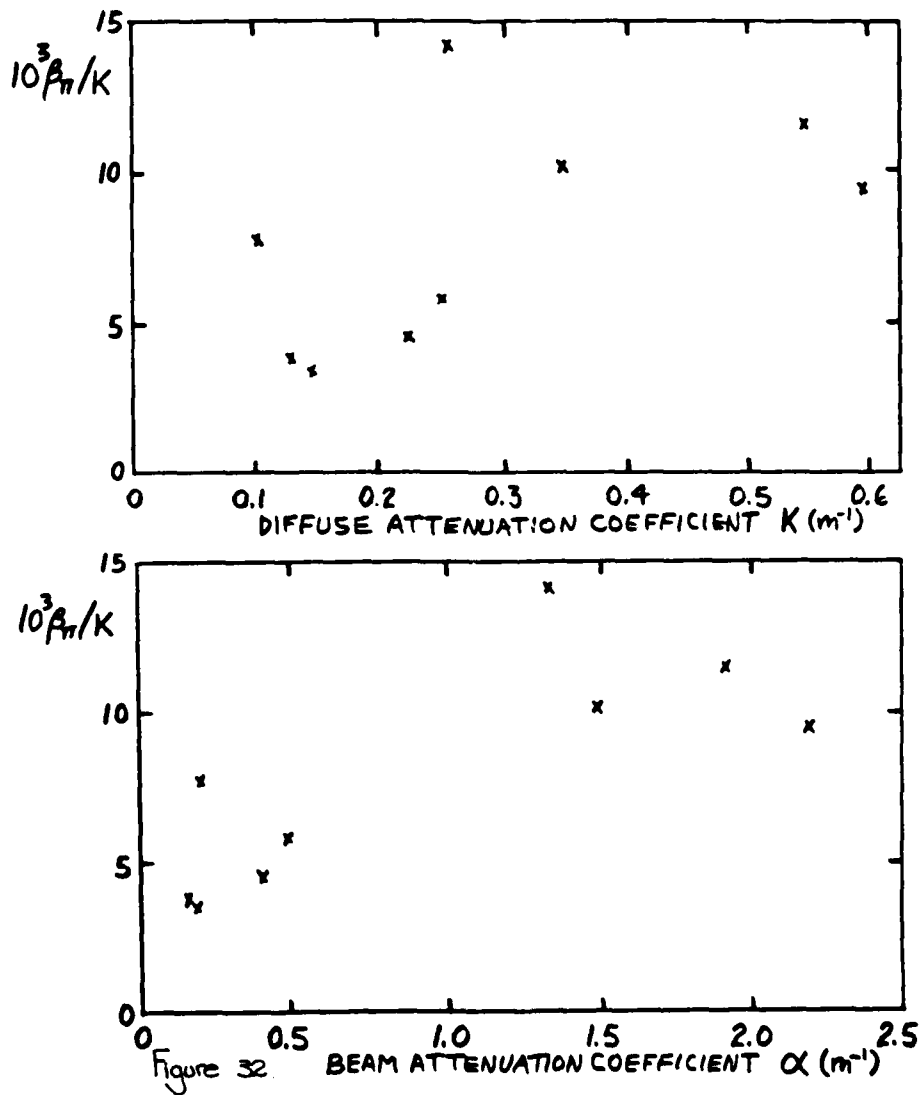
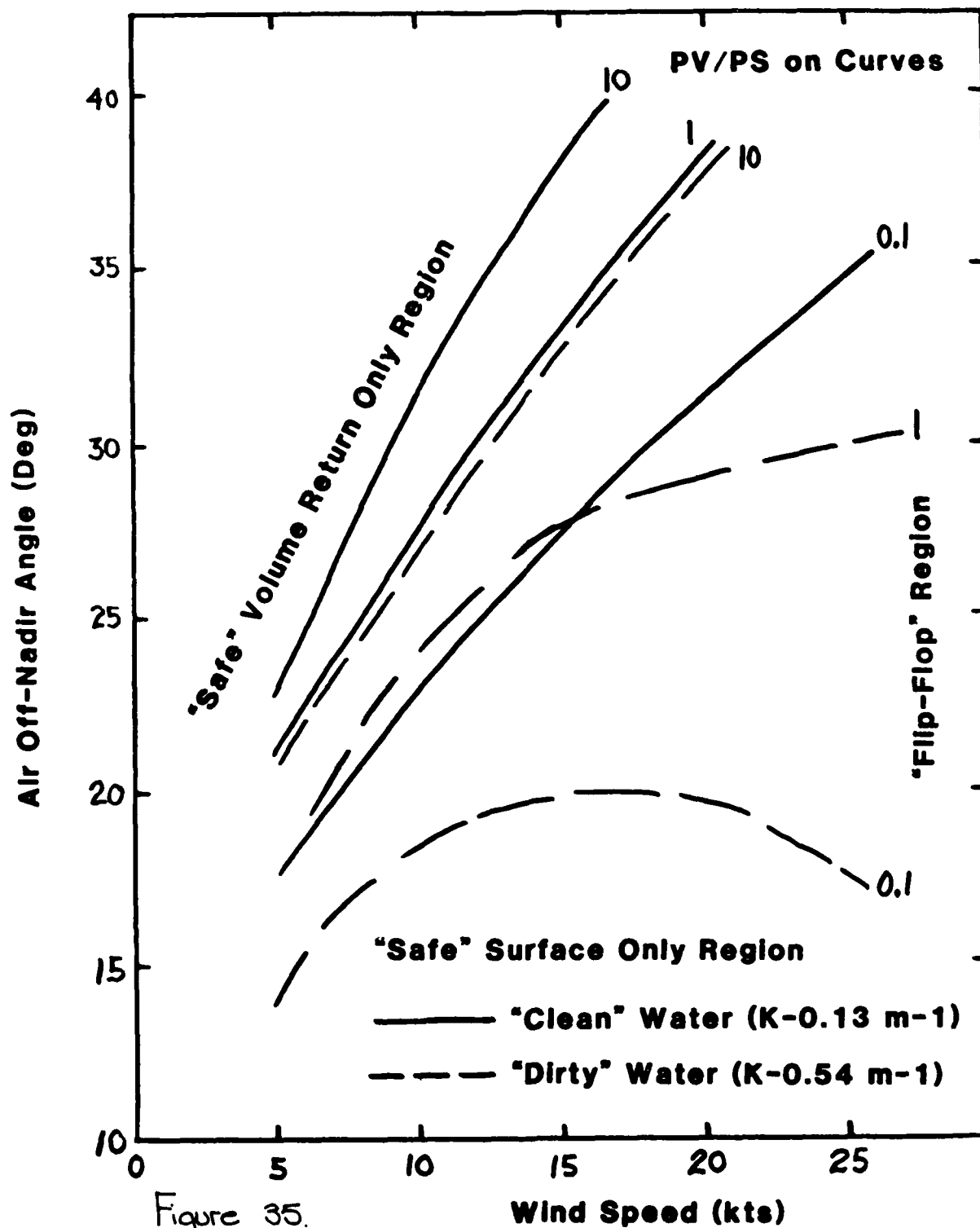## Backscatter to Diffuse Attenuation Ratio vs. Single Scatter Albedo

Figure 33.
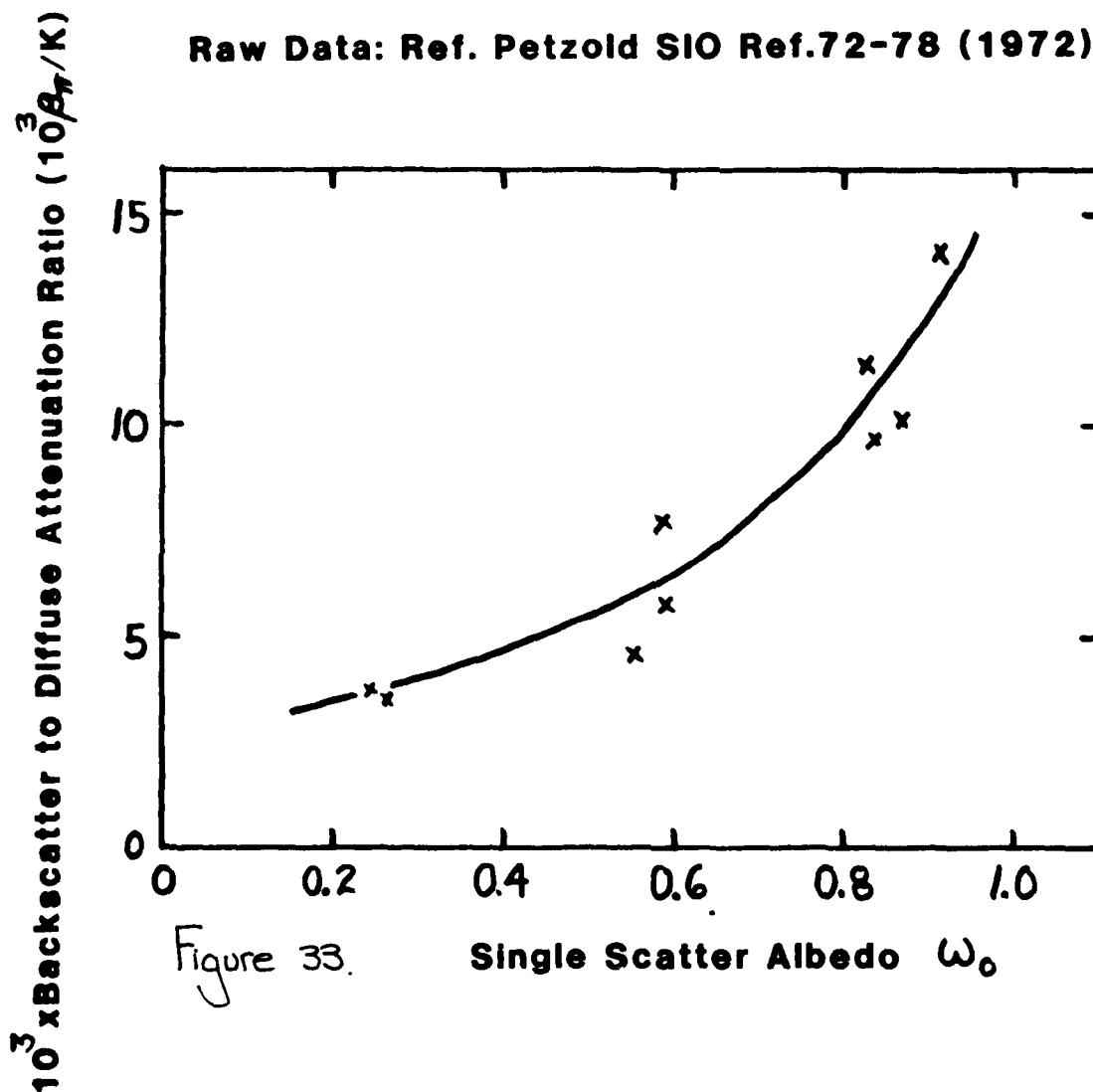
Note: Peak Volume Return Power, PV $\propto \beta_{\pi}/K$; Hence PV=PV(w$_o$)

SURFACE INTERFACE RETURN LOSS FACTOR CONSTRAINT
EQUATIONS IN AIR OFF-NADIR ANGLE AND WIND SPEED
CROSSWIND CASE

Figure 34

Volume to Surface Return Ratio Constraint Equations
Wind and Off-Nadir Angle Effects
Up/Down Wind Case

Figure 35.

Volume to Surface Return Ratio Constraint Equations
Wind and Off-Nadir Angle Effects
Crosswind Case
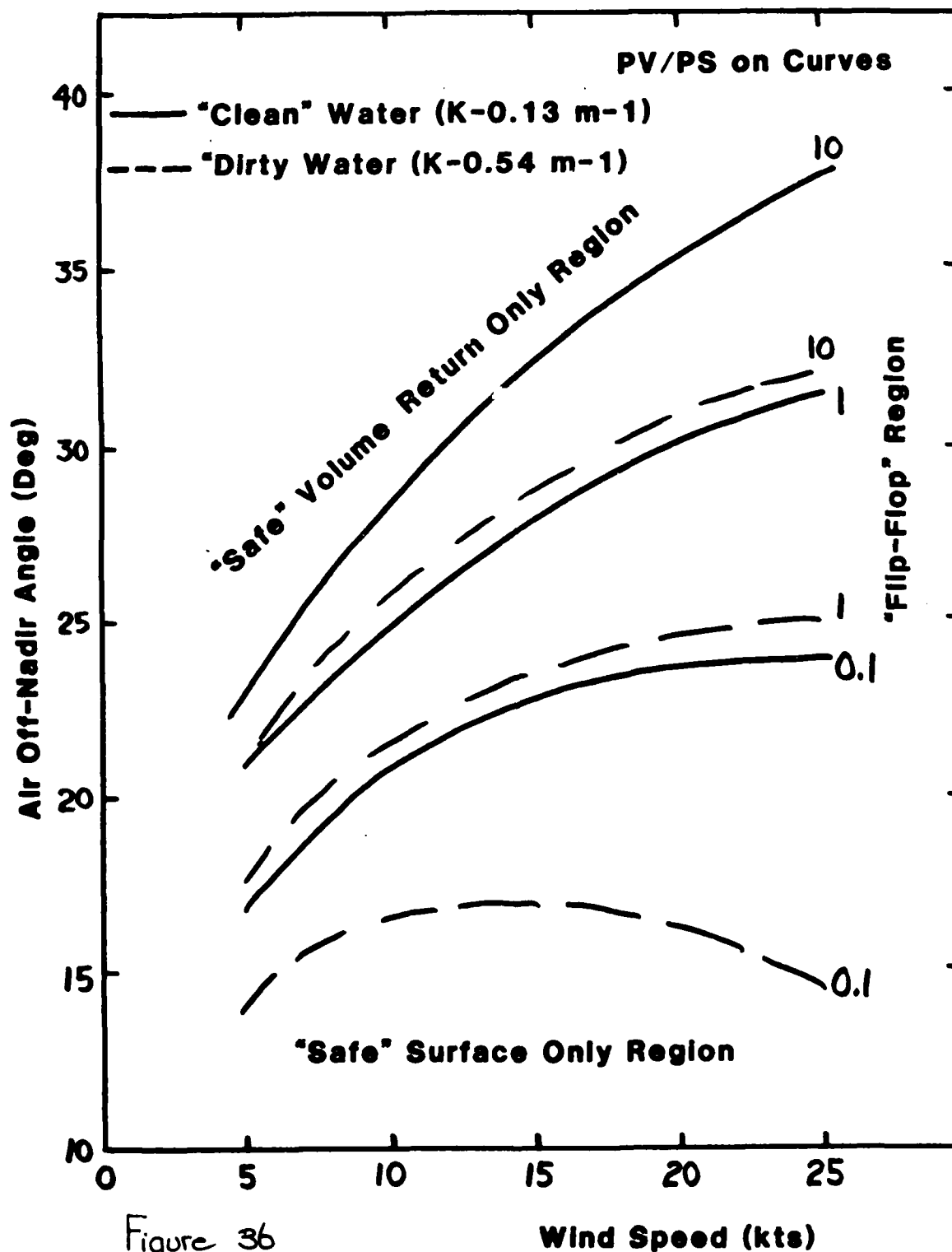
Figure 36

Wind Speed (kts)

Volume to Surface Return Ratio Constraint Equations
Wind and Off-Nadir Angle Effects
General Case   (Scanning)
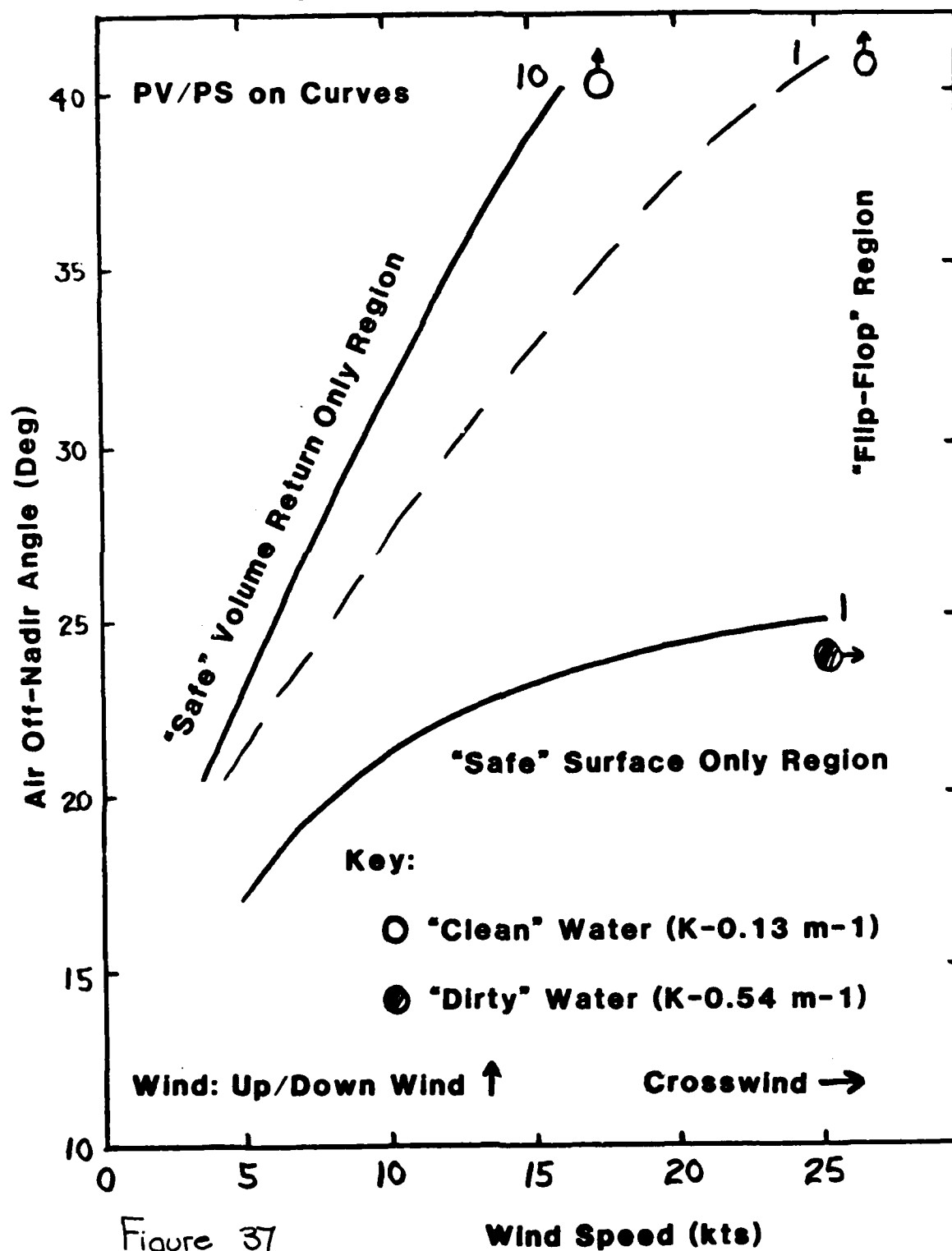
Figure 37

APPLICATION OF THE AIRBORNE OCEANOGRAPHIC LIDAR

TO SHORELINE MAPPING

R. N. Swift
EG&G Washington Analytical Services Center, Inc.
Pocomoke City, MD 21851

W. B. Krabill and F. E. Hoge '
NASA Wallops Flight Center
Wallops Island, VA 23337

ABSTRACT

The mapping of shallow water submarine features and nearby positive shore-line relief are important potential airborne laser bathymetric applications that must be addressed. The area surrounding the land/water interface is among the most dynamic morphological features with which man must deal. Much of the world's coastal regions are under constant flux with continuous exchange of material between adjacent positive and submerged features. Predominating currents and contributions of sediments through tributaries and inlets yield areas of net shoaling and erosion. Typically such areas require frequent hydro-graphic and shoreline surveys in connection with maintaining navigable water-ways, ascertaining legal boundaries, recreational utilization, and erosion control programs. These areas however are among the most expensive and logis-tically difficult to survey using presently available techniques. Bathymetric measurements are performed with low speed launches and shallow water craft often necessitating the use of hand-held lead-lines and mechanical positioning. Data obtained from such surveys is difficult to assimilate with modern hydrographic processing thereby resulting in both increased acquisition and utilization costs. The shoreline is generally measured either by survey crews or using photogrammetry. Survey parties are expensive and provide low density data. Photogrammetry is constrained by rather narrow weather and ambient light toler-ances and in many areas these surveys must be performed during a very narrow window centered around mean low water. The potential of performing both shore-line mapping and shallow water bathymetry with an airborne laser system is particularly attractive from both cost and logistical standpoints provided inherent difficulties with this technique can be overcome.

The major problem with performing shallow water laser bathymetric surveying is associated with measuring points falling within $\pm$ 2 m of the waterline. Due to the large dynamic range differences between surface and bottom signal returns and the close temporal proximity of the two returns, recognition of the bottom return and measurement of the separation between the returns appears to be a major obstacle. The problem is made even more difficult because of increased waves, white water foam, and turbidity within this very dynamic zone. Work performed with the NASA WFC Airborne Oceanographic Lidar (AOL) at test sites in the vicinity of Wallops Flight Center suggests that these problems may be surmountable.

Deep water subtraction techniques developed during the 1977 joint NASA/ NOAA/NORDA Airborne Laser Bathymetry Experiments have been applied to resolving shallow water laser returns. This technique previously reported in the 1977 Laser Hydrography Conference (NOAA Headquarters, Rockville, Maryland) involves the development of a surface return amplitude look-up table over optically thick portions of the survey site and applying corrections to individual pulses taken in shoaler water by selection of arrays from the look-up table keyed to surface return amplitude. This technique yields a residual waveform which appears "clean" in that the surface return portion of the waveform is reduced and flattened and the effects of laser induced shot noise as well as electronic ringing from the high gain PMT are removed for the most part. Residual waveforms from pulses taken over water of < 1 m yield reasonably definable bottom return peaks. Residual waveforms obtained over positive (land) targets yield negative channels 10-15 ns after the surface return location thereby enhancing recognition of pulses falling on the shore.

Recent improvements in preflight calibration techniques show notable improvement in correcting gain and bias problems between sampling channels. Profile and scanning passes presented support the conclusion that shoreline mapping and shallow water bathymetry may be achievable with present hardware and technology.

1.0 INTRODUCTION

During the period from April to December 1977 NASA/Wallops Flight Center
(WFC) participated with NOAA/NOS and NORDA in an interagency airborne laser
hydrography program. The program was designed to demonstrate the feasibility of
performing laser bathymetry from an airborne platform under a variety of environ-
mental conditions. Results of various aspects of these experiments have been
reported by all participating agencies and additional analysis on the large
volume of data gathered during the joint program is still ongoing. This paper
deals in particular with the application of a "deep water subtraction" technique
to the recognition of pulses striking land or water targets, and to the extrac-
tion of depth from return pulses acquired over shallow water < 2 m deep. This
technique has been presented previously as a feasible mechanism for removing
system and environmental noise from recorded waveforms.[1,2,3] Forthcoming
programs to be performed jointly with NOAA/NOS and the U.S. Army Corps of
Engineers (CE) require the capability of conducting laser hydrography over water
bodies shoaler than 2 m. The WFC Airborne Oceanographic Lidar (AOL) group has
therefore re-examined data from the 1977 hydrography program to determine the
utility of extending the "deep water subtraction" technique for target recogni-
tion and shallow water bathymetry. Unfortunately the objectives of that program
did not address beach mapping and resolving water depths of less than 2 m,
therefore available data for this current WFC interest was obtained incidently
and is fairly meager. Nonetheless we feel that the results of our recent
analytic effort presented herein are sufficient to suggest that refinement of
the "deep water subtraction" technique will permit extension of present AOL
hydrographic capabilities to include shoreline mapping and shallow water bathymetry.

The ability to monitor coastal zone underwater topography, shoreline
change, and related environmental factors with conventional techniques is very

costly and time consuming. A need exists to provide this data for large reaches
of the coastline in a cost effective manner. Coastal mapping presents one of
the most obvious applications for the AOL system due in part to the frequency
that these surveys must be performed. The interface between land and water is
one of the most dynamic zones with which man must deal. Agencies charged with
mapping, understanding, or controlling shorelines are faced with the chronic
problem of changing morphology. The majority of the coastline is bounded by a
cushion of weathered rock fragments of varied size and composition that extends
both above and below the mean low water line. Alteration in the distribution of
these materials along shorelines is brought about by the agents of tide, current,
and wind. Along sandy fringes changes are discernible daily and are especially
dramatic following the passage of significant weather events. Generally these
shifts in the distribution of sand are short term. Material is stripped from
the beach and is deposited on nearshore bars during turbulent storms; then
during quiescent periods the normal action of waves gradually transports the
sand from the bars back to the beach. Most coastal regions have a predominant
direction from which wind and waves approach. This condition results in a
longshore transport of beach sediment typically with a net loss along large
stretches of coastline and net deposition near inlets or other breaks in the
trend of the coastline.

This long term erosion and deposition of beach material is a problem of
significant consequence to various federal and state agencies as well as to
property owners and recreationalists in the private sector. In general, erosion
takes place where deposition would be desirable and vice versa. The erosion of
beaches results in financial loss to investors and property owners while the
deposition threatens navigational waterways which must be maintained by expensive
dredging. In recent years, with increasing utilization of limited coastal
resources for recreational, commercial, and environmental interests there has

been a growing demand to come to grips with this problem and invoke measures to

eliminate or significantly retard the longshore transport of the beach materials.

Various means have been contrived and applied. Man-made structures such as

groins, jetties, breakwaters, bulkheads, and submerged reefs have been constructed

and methods of replenishment through dredge and fill techniques and inlet by-

passing have been tried all with varying degrees of success.

Adequate mapping of coastal areas both in detail and frequency is vital for

the following reasons:

1. The shoreline is in a continuous flux within these zones so that legal
    boundaries must be constantly readjusted.

2. An adequate understanding of both short and long term patterns of
    beach transport must be understood before implementing corrective
    procedures and more importantly perhaps, to evaluate the effectiveness
    of those procedures once implemented in order to avoid duplication of
    errors on other, similar projects.

3. These maps are essential for gauging the impact on the environment of
    any corrective measure.

4. Reconnaissance surveying is required on a regular basis in areas of
    chronic filling in order to determine the necessity and extent of
    maintenance dredging necessary.

5. Permit applications for marine dredging and construction from state
    and private sectors require surveys to ascertain compliance.

Hydrographic surveys presently are almost entirely performed using com-

puterized sonar recording systems supplemented by frequent lead line depth

measurements. These hydrographic surveys are costly and must necessarily be run

in profiles usually normal to the trend of a coastline. A smaller number of

closing profiles are run parallel to the coastline. Areas between profiles are

thus unsampled.

Two basic techniques for surveying beaches are presently applied, both with limitations. Detailed and synoptic surveying can be performed using photogrammetry to reduce overlapping aerial photographs to useful contour maps or digitized information. Photogrammetry, however, is too expensive to be performed on a regular basis, cannot be extended to produce contours of submerged features in many areas, and must be performed at a time near low water for optimal results. The second method is to survey cross-sections normal to the coastline extending from the landward base of the dunes (if present) to 1-2 m below the mean low water datum. This technique is rather inexpensive and the site can be frequently reoccupied; however, detailed information between survey points is necessarily sacrificed.

Figures 1 and 2 are examples of rather gross alteration in coastal morphology and relief in the vicinity of WFC that are typical along many coastlines worldwide. Figure 1 indicates net bathymetric changes across the mouth of the Delaware Bay between 1842 and 1968 while Figure 2 indicates the historic alteration of the coastlines of Assateague and Chincoteague Islands, Virginia.

The recognition of laser pulses striking positive targets from those striking adjacent shallow water targets is vital to the application of airborne laser systems to meeting these problems. This is especially true for a conically scanning laser system where a Kalman or other single sided filter cannot track trends set by previous pulses due to the large spatial separation between pulses or for any scanning system where large variations in relief prohibit the use of a software bottom tracker. Alternatively trends measured using pulses clearly acquired from positive targets can be extended to meet trends from pulses clearly gathered from water targets with resolvable depths. In practice, however, such a technique would be extremely limited since the dynamic region surrounding the land/water interface is extremely varied in both trend and relief.
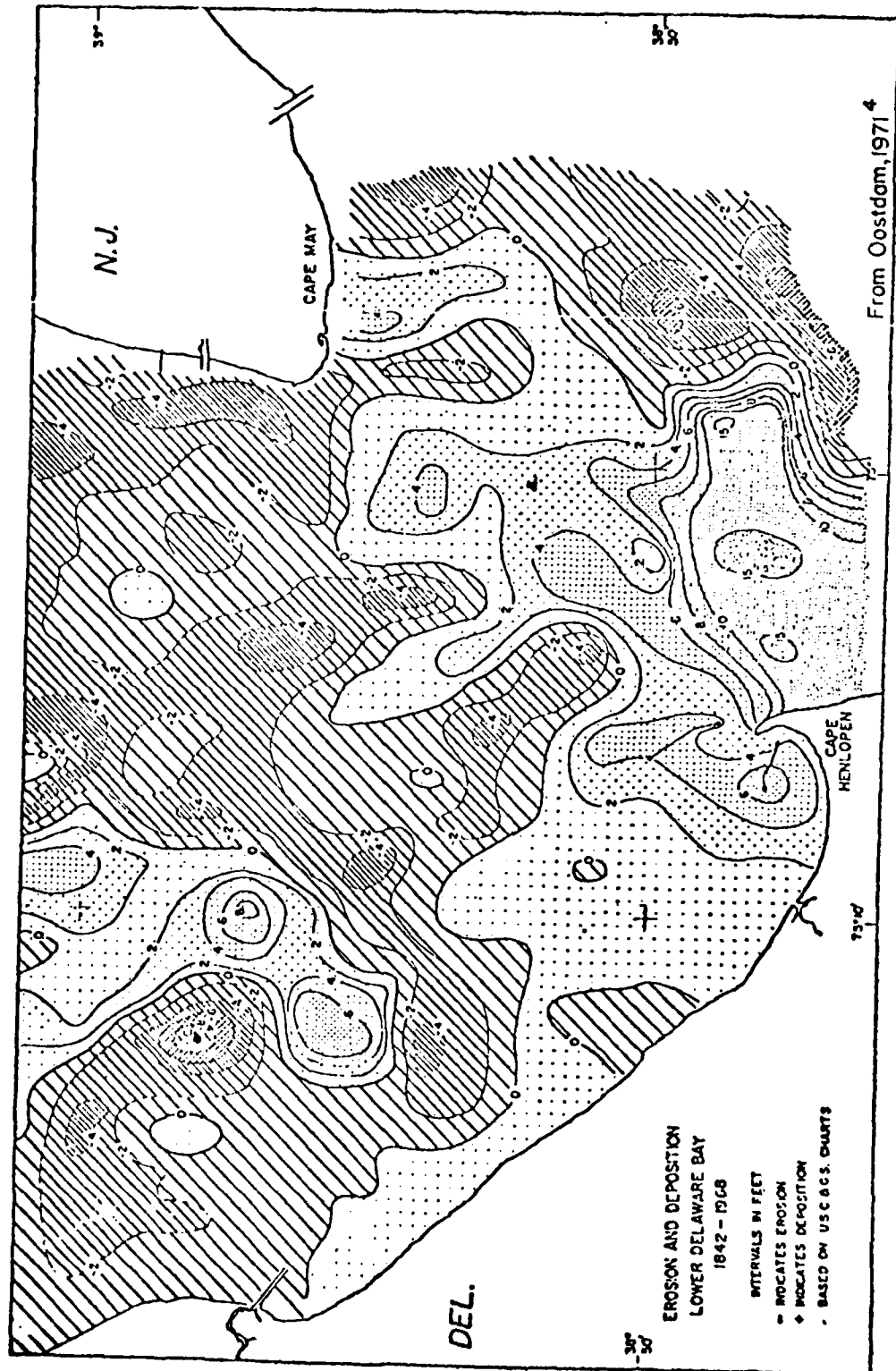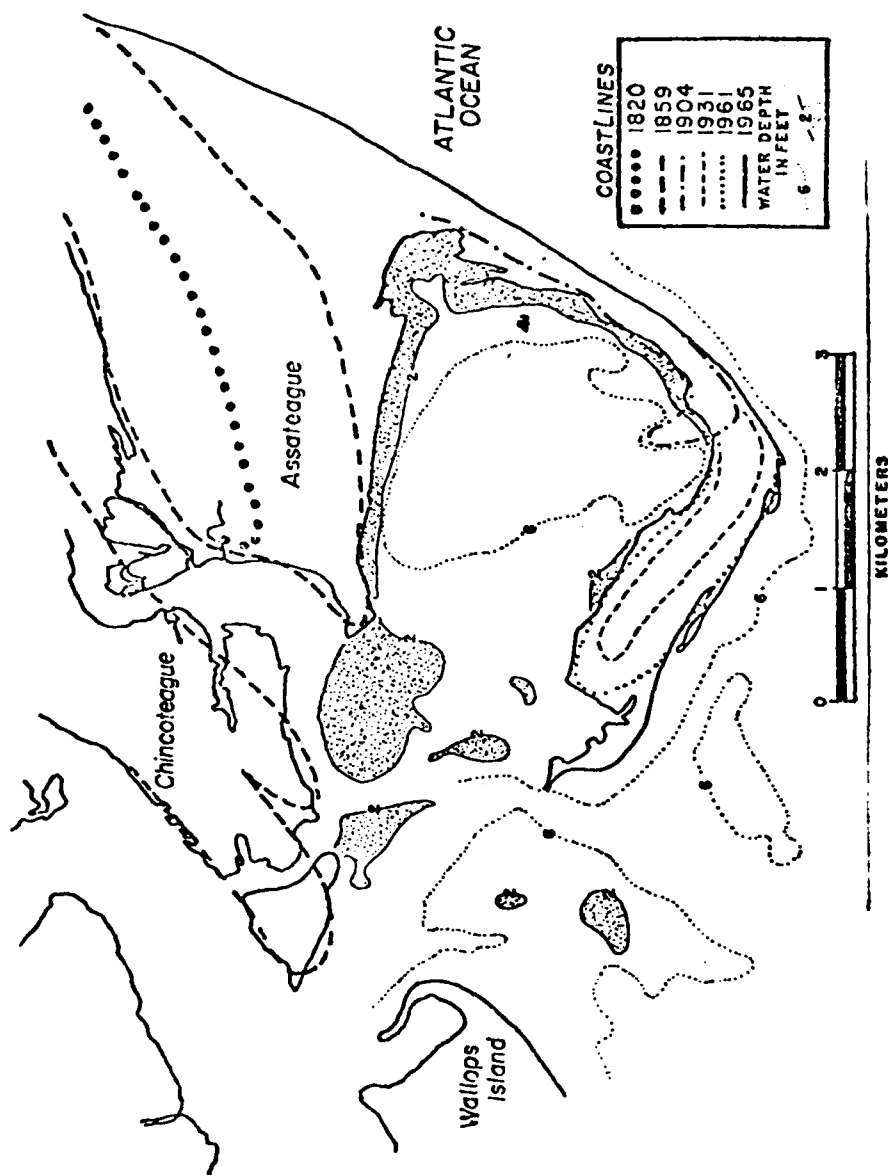
EROSION AND DEPOSITION
LOWER DELAWARE BAY
1842 - 1968

INTERVALS IN FEET

- INDICATES EROSION
+ INDICATES DEPOSITION
. BASED ON U.S.C.&G.S. CHARTS

From Oostdam,1971 [4]

Figure 1

Figure 2

2.0 INSTRUMENTATION

The AOL instrumentation required in the discussions to follow are included as an attached Appendix A.

3.0 TECHNIQUE AND PULSE RECOGNITION THEORY

During the course of performing a mission or preferably during each pass data is recorded over an area of water where the bottom is deep enough to be beyond the digitizing capability of the recording system or is at least optically thick so that no bottom returns are obtained within the recorded waveform. Data from this portion of the pass is used to develop a look-up matrix whose elements or arrays are averaged waveforms arranged in groupings keyed on the amplitude of the received surface return. Subsequently pulses obtained from shoaled water are individually corrected by subtracting a selected array from the look-up matrix again based on surface return amplitude. This technique yields a residual waveform which is "clean" in that the surface return portion of the waveform is reduced and flattened and effects of laser induced shot noise as well as electronic ringing from the high gain PMT are removed for the most part. The use of this technique aided by high SNR allows resolution of depth from waveforms even when the bottom return falls within the surface return region as will be demonstrated in the next section of this paper.

The pulses obtained over deep or optically thick water targets (and used to develop the above look-up matrix) contain Mie backscatter from particulate matter in the ocean volume in addition to the surface return which is primarily Fresnel reflection. The temporal extent of the latter should not exceed the approximate 7 ns pulse width of the nitrogen laser plus the additional time constant of the PMT and associated video amplifiers for a total width of approximately 10 ns. On the AOL system the nominally 4 ns analog-to-digital converters

effectively smear the specular surface return an additional 3 to 4 ns. All

considered the Fresnel component should be completely dissipated within six

channels or 15 ns of the centroid of the surface return. Beyond this sixth

channel any on-frequency received energy from deep water should be due to Mie

backscatter. By contrast a pulse striking a positive target would not have a

volume backscatter component and the total width of the received energy would

temporally not exceed the laser pulse width plus any system smearing and re-

sponse time. The energy from a laser pulse striking a flat positive target

devoid of foliage is spent entirely within the laser pulse width while con-

versely for a pulse striking a water target a portion of the energy is trans-

mitted downward into the water column. Therefore if waveforms from a "deep

water" look-up matrix are differenced from pulses obtained from land targets a

discernible amount of additional return energy should be present in the several

digitizer channels immediately beyond the peak surface return channel (normally

channel 3) and a deficit amount of return energy should be present in channels

15 ns from the peak surface return channel.

Figure 3 shows some waveforms taken from a "deep water" look-up matrix and

subtracted from their surface return amplitude counterpart obtained from a look-

up table similarly developed from pulses striking positive land targets. Note

that in all instances some additional energy is found beyond the peak return

channel 3. This data strongly suggests that pulses clearly striking land

targets should be recognizable from pulses clearly striking deep water targets.

Pulses striking very shallow water targets should not be as readily discernible.

However, in the next section results are presented which indicate that this

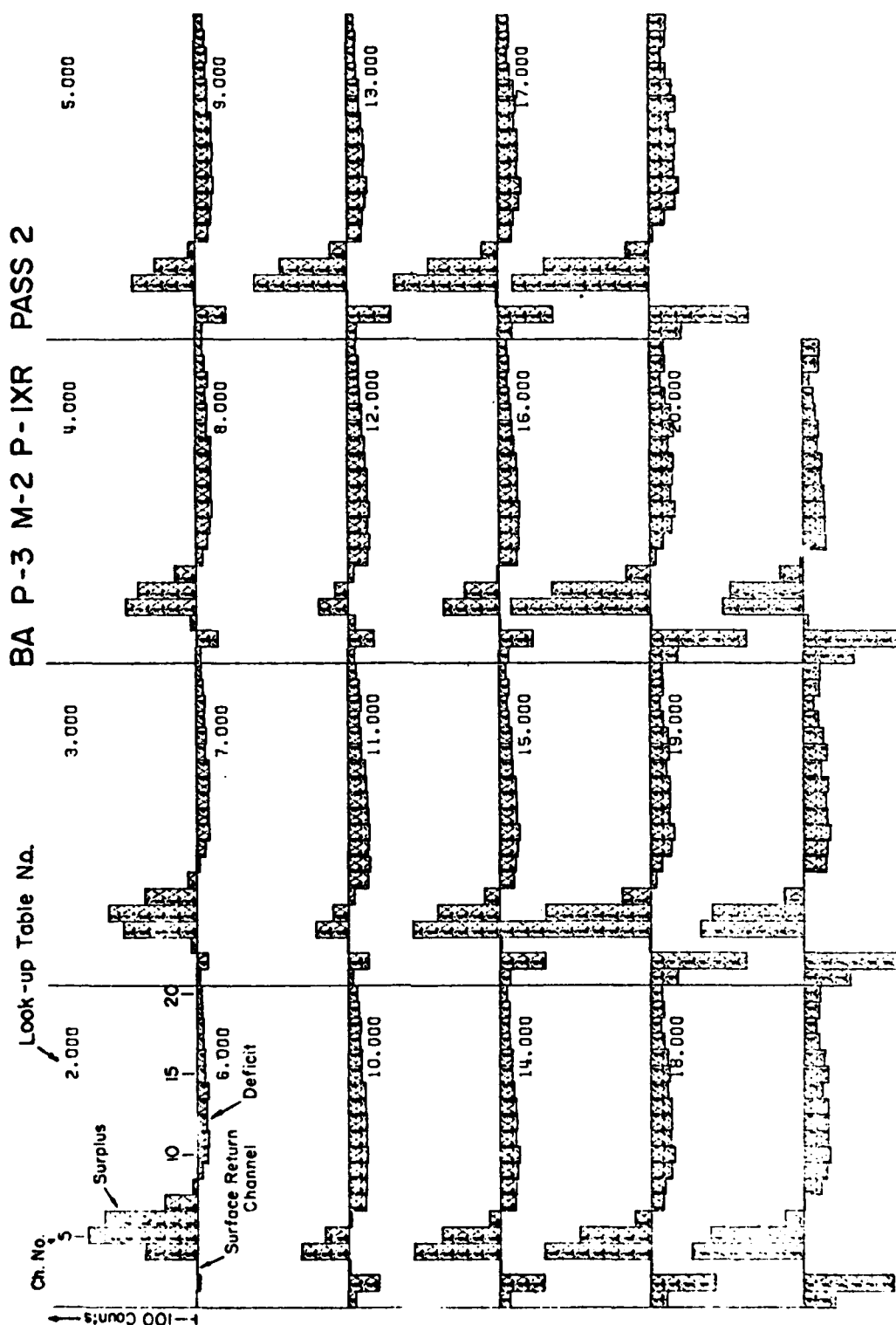technique may be applicable even to differentiating depths shoaler than 0.3 m.

Figure 3

4.0 RESULTS AND CONCLUSIONS

The joint NASA/NOAA/NORDA Airborne Laser Bathymetry Program flights were
conducted on two pre-selected test sites shown in Figure 4. The Atlantic Test
Site did not contain flightlines over shallow water therefore the analytical
work discussed in this paper was performed on data obtained on two flights over
the Chesapeake Test Site in the vicinity of Janes Island, Maryland. Figure 5
provides an enlarged view of the area under consideration and should be con-
sulted during the subsequent discussions.

A total of four passes from the 1977 Bathymetry Program were chosen for the
detailed re-examination. Two profiling passes taken under differing system
configurations and environmental conditions were chosen for detailed evaluation
of return waveforms from laser pulses striking in the vicinity of the land/water
interface. Two scanning passes were selected to demonstrate the feasibility of
performing shallow water bathymetry under scanning conditions. Pertinent infor-
mation on all of the above passes are given in Table 1.

During the following discussion all passes have been given a numerical
designation also given in Table 1 to facilitate easier reference. Raw data from
these passes was processed using the "deep water subtraction" technique described
briefly in the preceding section and a bottom tracking algorithm described in
more detail in References 1, 2, and 3. Pulses failing surface and bottom return
signal strength threshold tests were rejected. No attempt was made however to
alter the waveform processing of pulses known to have struck land targets in
order to demonstrate that these pulses can be recognized from their waveform
signatures Such recognition would be essential in processing scanning passes
taken near coastlines. Figure 6 is a plot of every fifth raw and residual
waveform from Pass 2 taken as the aircraft approached the Janes Island shore-
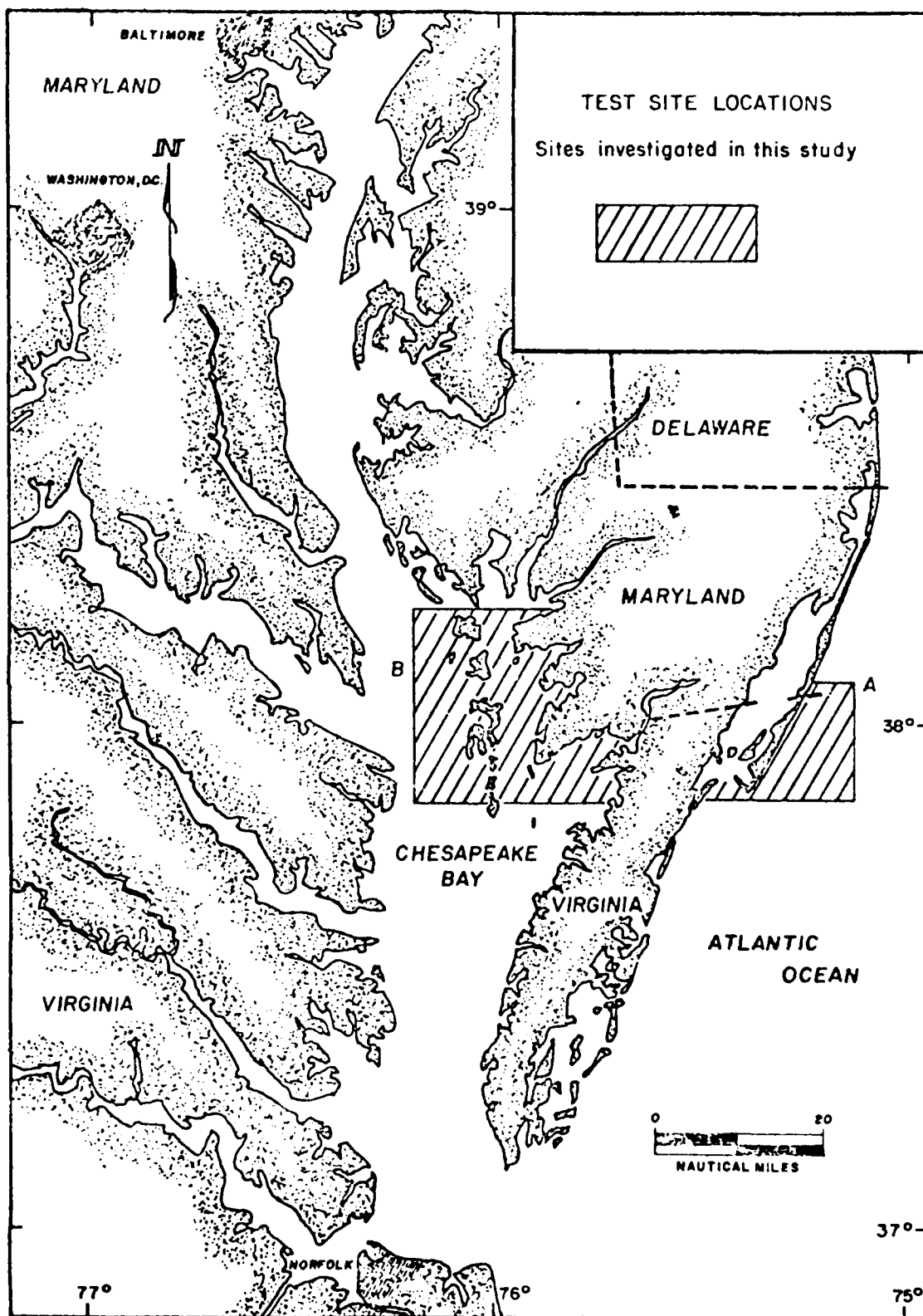line. The residual waveform has been amplified by plotting it on an expanded

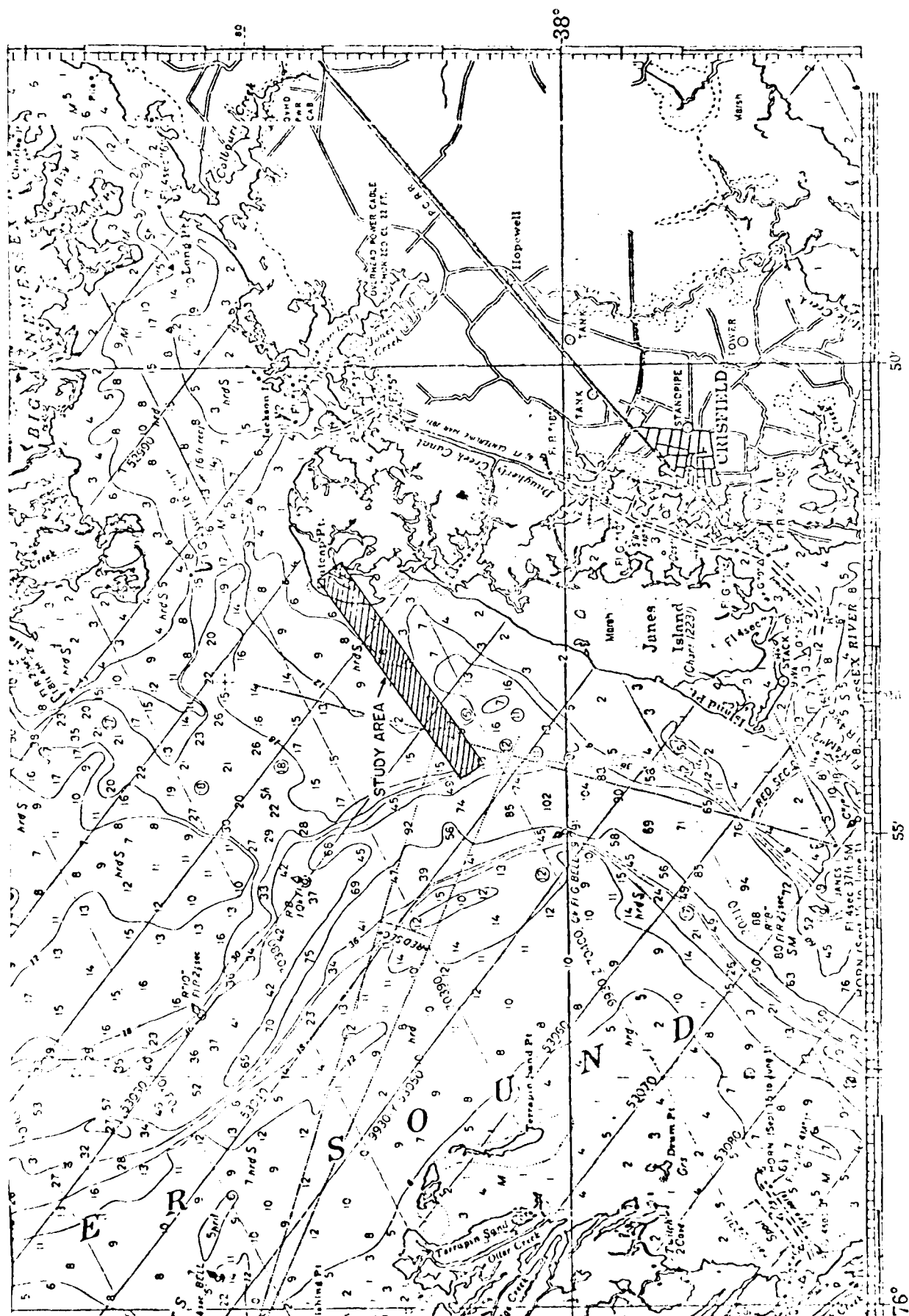TEST SITE LOCATIONS

Sites investigated in this study

Figure 4

Figure 5

TABLE 1

Phase/Mission	BA 2/2	BA 3/2	BA 3/2	BA 3/2	OM 2/2
Pass Number	TC-9	1XR	1	2	6-2
Designated Number	1	2	3	4	5
Date	10/25/77	12/15/77	12/15/77	12/15/77	4/2/80
Transmitter Divergence (mrad)	2	2	2	2	1
Laser Gas	Ne	Ne	Ne	Ne	N_2
Wavelength (nm)	540.1	540.1	540.1	540.1	337.1
Receiver					
Field of View (mrad)	20	20	20	20	5
PMT Voltage	1350	1350	1350	1350	1500
Scanner	OFF	OFF	ON	ON	ON
Nadir Angle (degrees)	10	15	15	15	15
Pulse Rate (pps)	200	200	200	200	200
Bathymetry Filter (center, nm)	540.1*	None	None	None	337.1**
Altitude (m)	160	320	480	480	360
Environment					
Waves (m)	0.3	0.2	0.2	0.2	0.8
Winds (knots)	5	2-3	2-3	2-3	12
Clouds	10%	Night	Night	Night	10%

*0.4 nm narrowband

**Corning CS7-37 UV transmitting filter
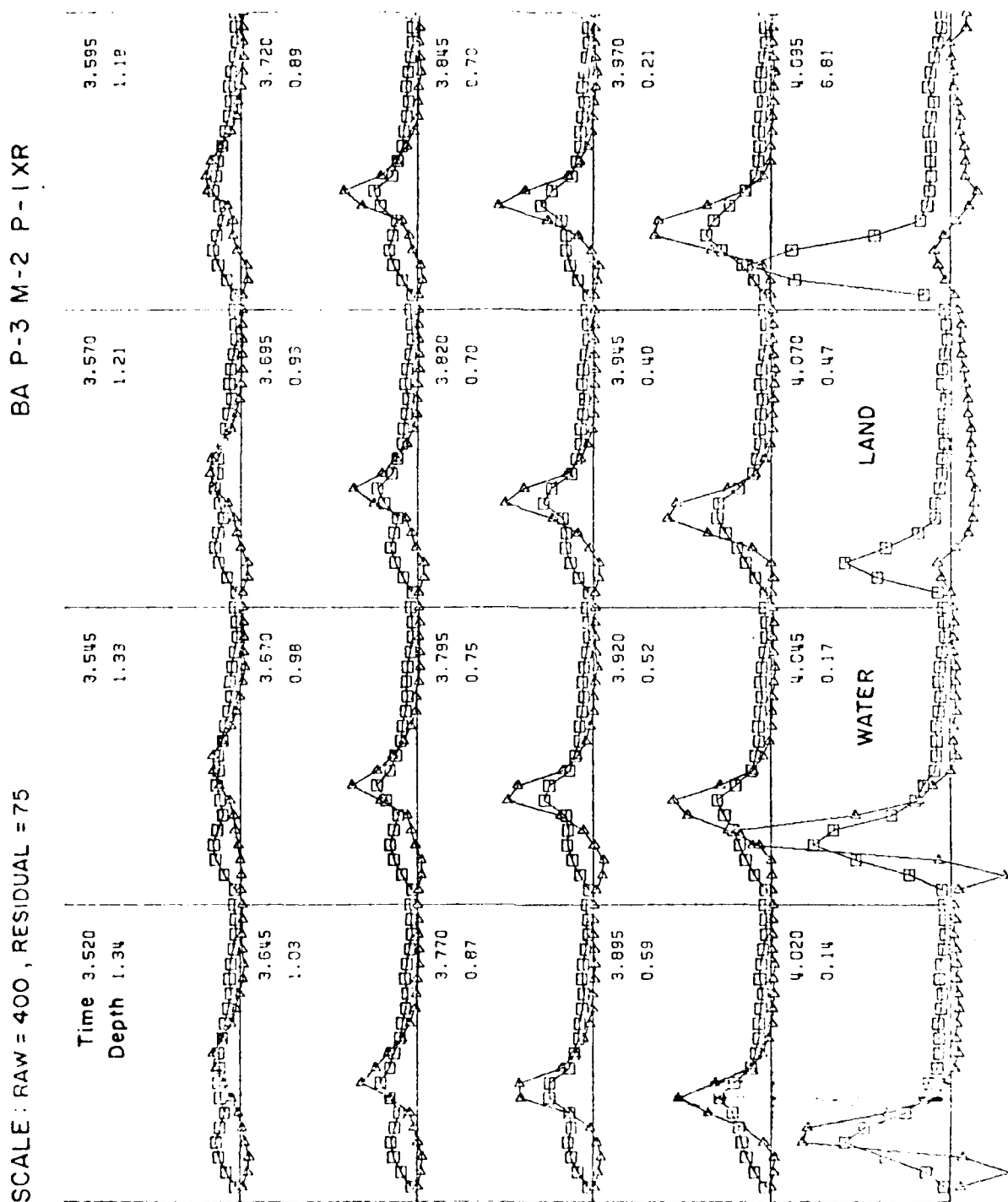
Figure 6

scale. Note the distinct shape of the bottom return pulse as the aircraft
approached the beach and the negative trend of the residual pulses after land
was encountered.

4.1 Profiling Passes

Profiling passes made normal to the trend of the beach and extending from
deep water well onto land are best suited for evaluating the potential of air-
borne laser measurements within the zone surrounding the land/water interface.
The data density at 200 pps is sufficient to establish unambiguous trends of
bottom and shoreline slopes needed to precisely define the land/water interface.
In the following discussions a number of time series plots of various parameters
are presented to allow contrasting changes between pulses striking land and
water targets. The purpose of this section is to determine the degree to which
the "deep water subtraction" can be applied to processing scanning data on a
pulse to pulse basis.

Profile plots of inverted range and depth plotted against time are shown in
Figures 7 and 8 for Passes 1 and 2 respectively. Differences in both range and
depth noise levels are quite apparent in contrasting Pass 1 obtained under
daylight conditions with Pass 2 obtained under darkness conditions. Aircraft
motion has not been removed from these passes as can be seen in the portion of
Figure 8 taken over water. Note that on both passes the bottom return is con-
sistently tracked to the point where the range profile is inflected upward
indicating a rise in relief as the beach is encountered. On both passes there
is a decrease in the depth (as derived by the depth tracking algorithm) over the
beach which fringes Janes Island and subsequently a return to a near zero
termination as laser reflections from the marsh behind the beach are
the sandy beach presents such a bright albedo that there is no match
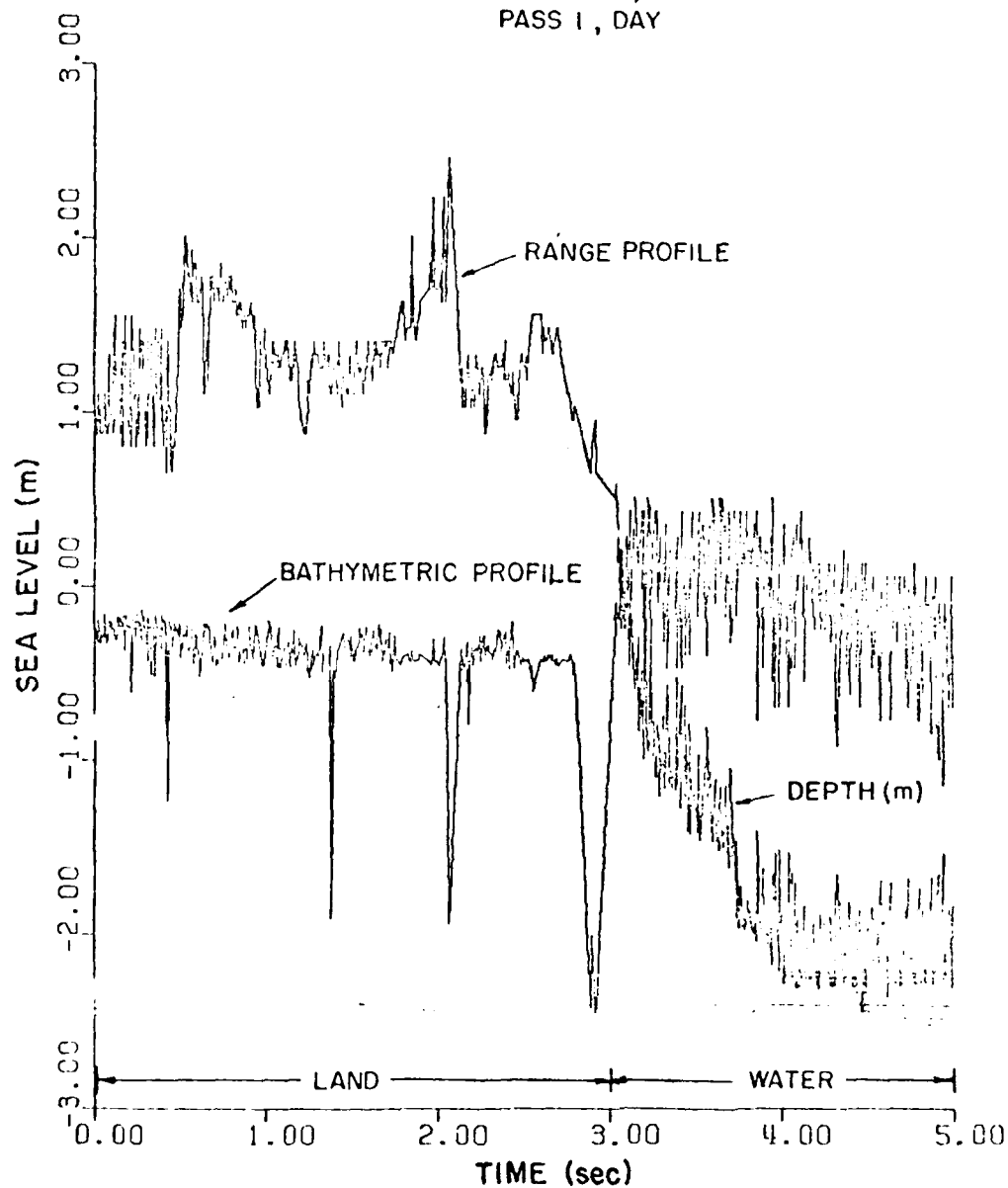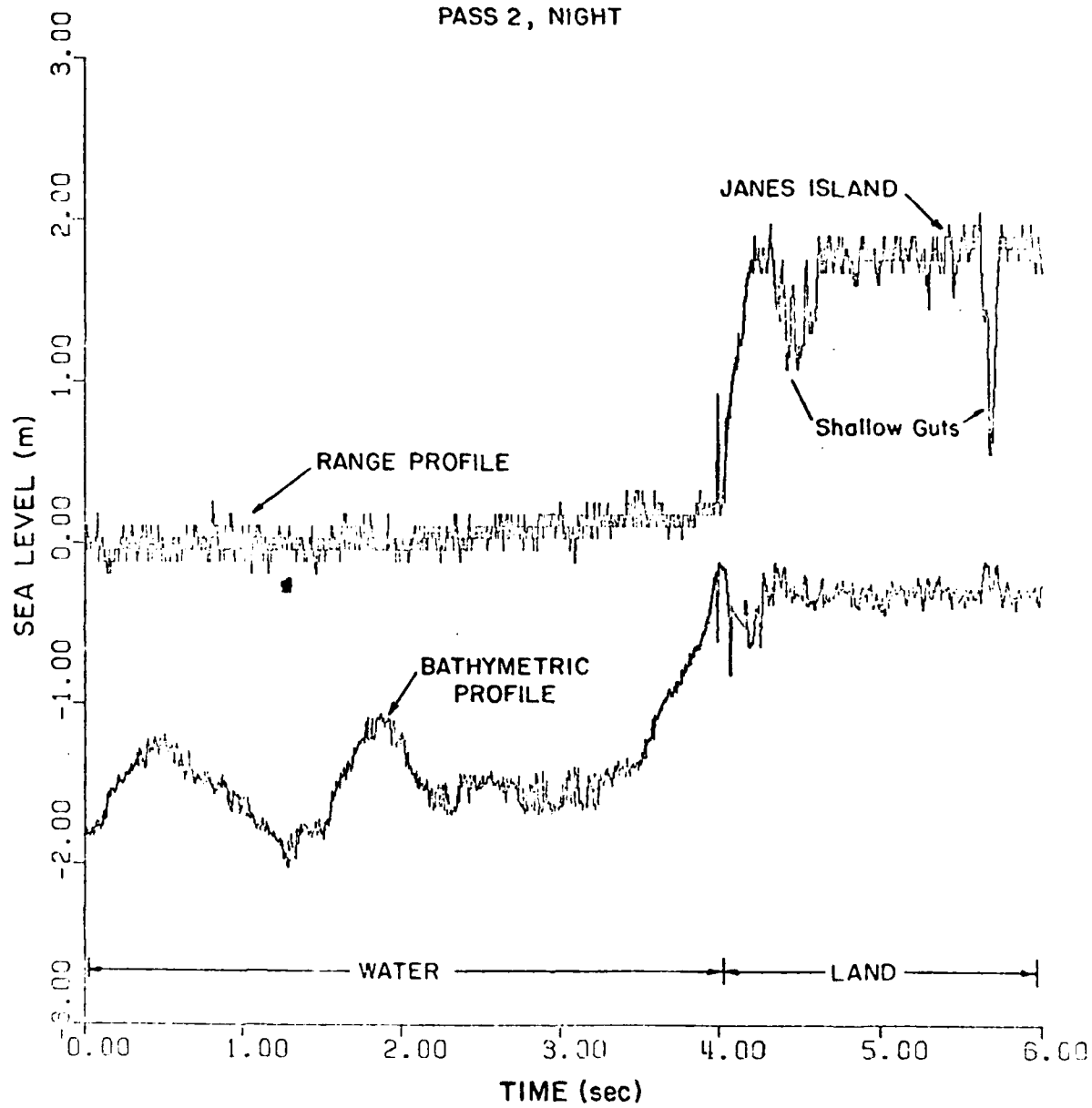
Figure 7

Figure 8

within the deep water look-up table for correcting the waveform. In the absence
of highly reflective sand the resolution of the waveforms from positive features
yields resolved depths similar to those obtained from nearshore shallow water
which poses a problem for differentiating between water and land targets in
processing scanning data.

Surface return amplitude is another potentially valuable tool for separating
pulses striking land from those striking water targets. Figures 9 and 10 are
profiles of surface return plotted against time for Passes 1 and 2 respectively.
Contrasting the surface return profiles of the two passes, the surface return
off water obtained on Pass 1 at 10° off-nadir is considerably more specular than
that obtained on Pass 2 taken at 15° off-nadir. The nearly constant return
shown at 15° off-nadir in the Pass 2 profile in fact does suggest that the
return surface signal strength alone could be used to determine whether the
pulse had hit a land or water target. More work under differing wind and wave
conditions will be necessary to ascertain how extendable the pass 2 results are
to all 15° off-nadir laser returns. The Pass 1 surface return profile clearly
indicates the dynamic range of signal strength between returns from land and
water targets remain too overlapped to serve as a means of recognition. In fact
the profile obtained over the marsh behind the beach is almost identical to that
obtained over the bay water.

Cross-sections of channels 5 and 10 of the residual waveform (after "deep
water subtraction") are presented in Figures 11 and 12 for Passes 1 and 2
respectively. Symbols have been used to separate channels 5 and 10 on the
noisier Pass 1 plot. Channel 5 is close enough to the surface return peak,
channel 3, to be within the nominal 10 ns total surface return width of the
received laser pulse (considering PMT response time and digitizer smearing)
while channel 10 is removed by some 14 to 16 ns and is outside the surface
return region of the return waveform. Notice in both passes, but especially in

Figure 9

BA P-3 M-2 P-1XR
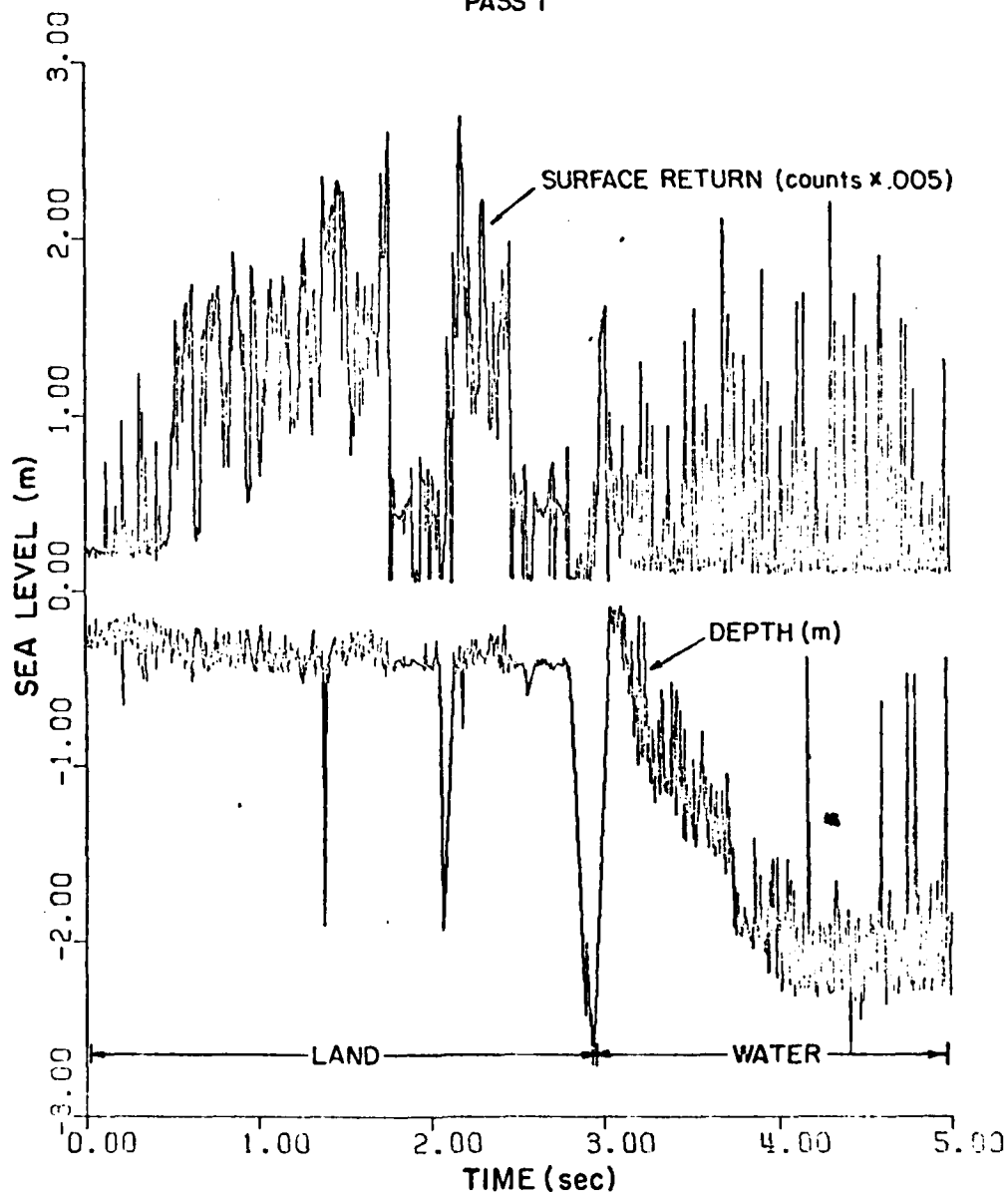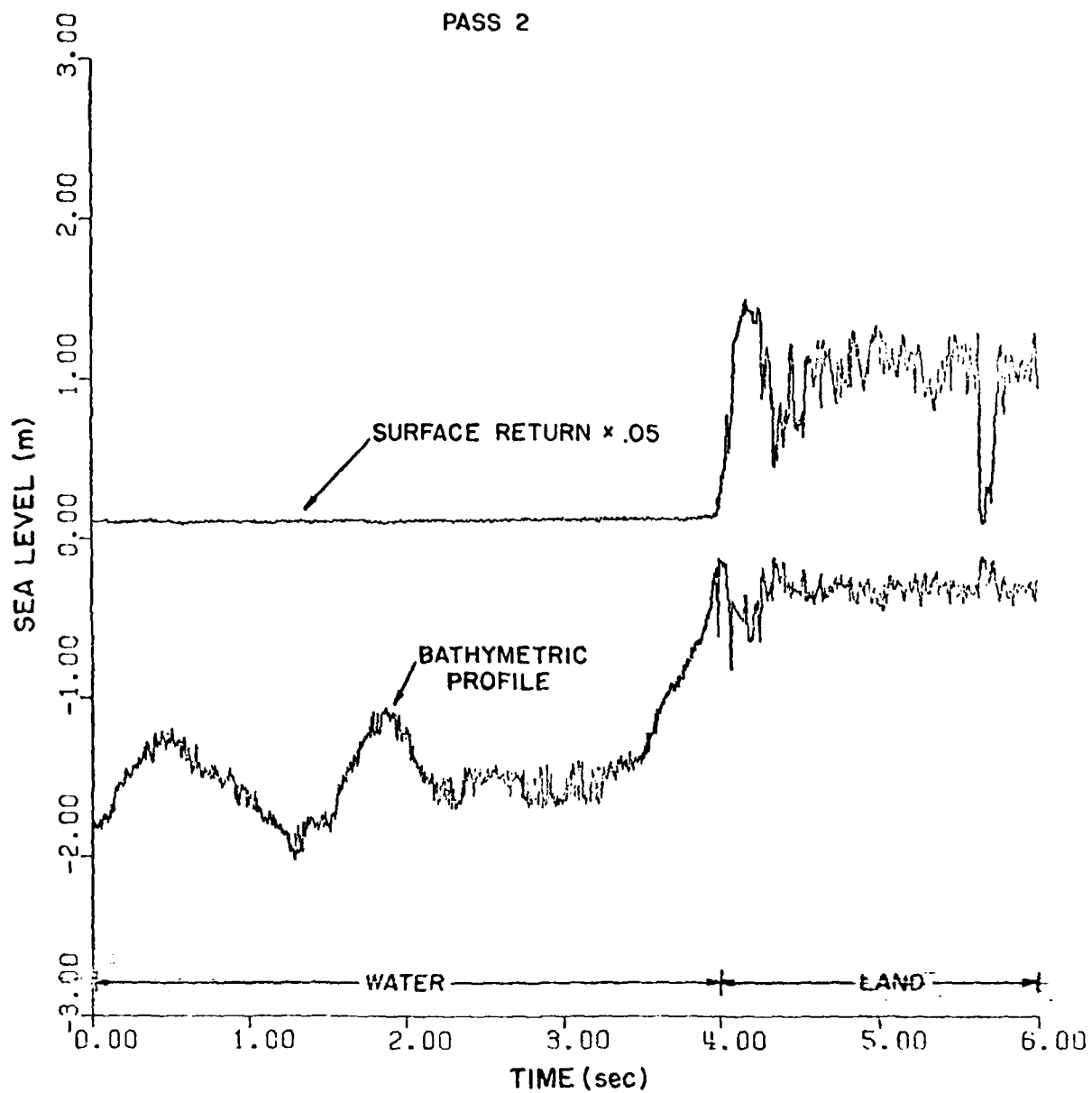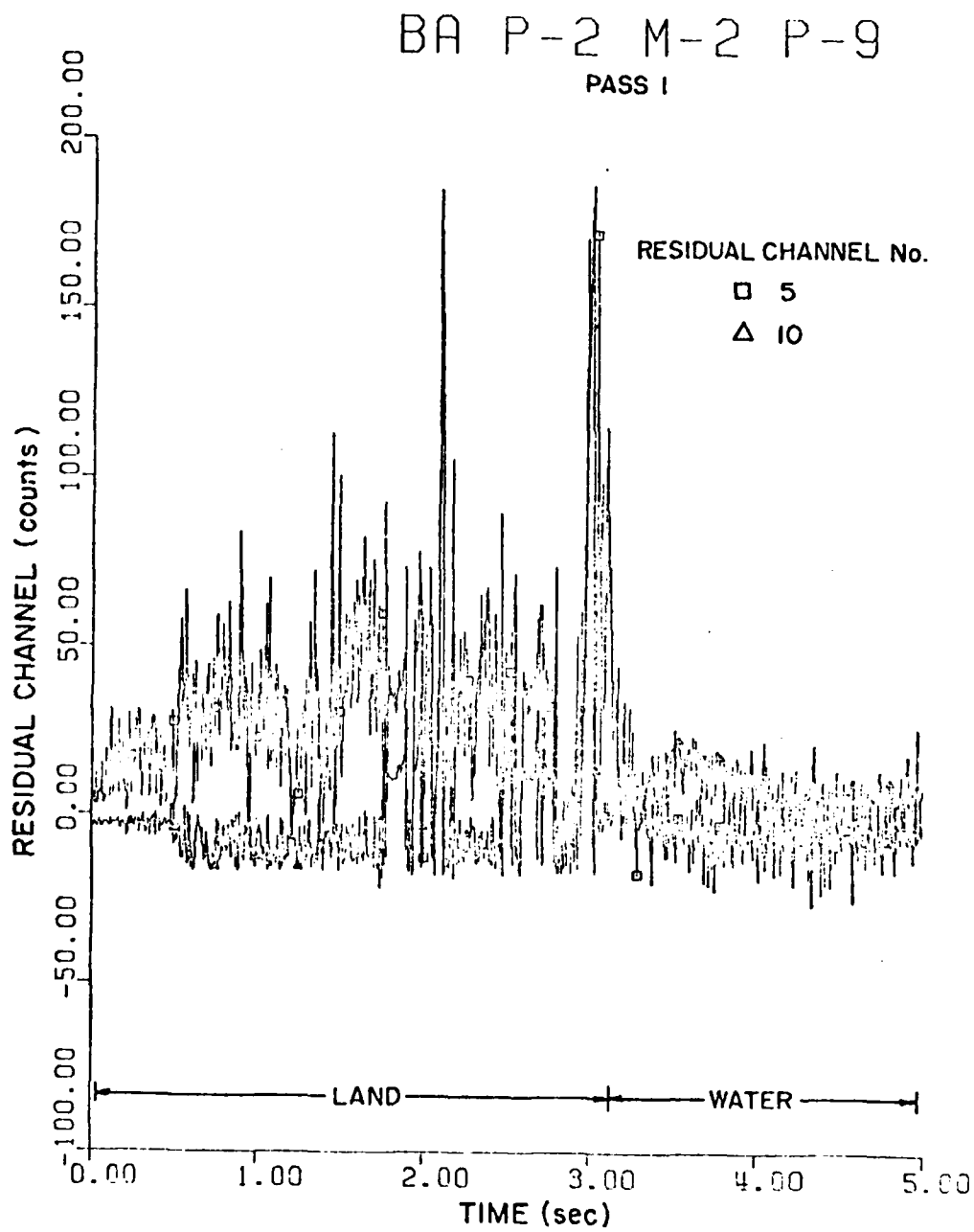
PASS 2

Figure 10
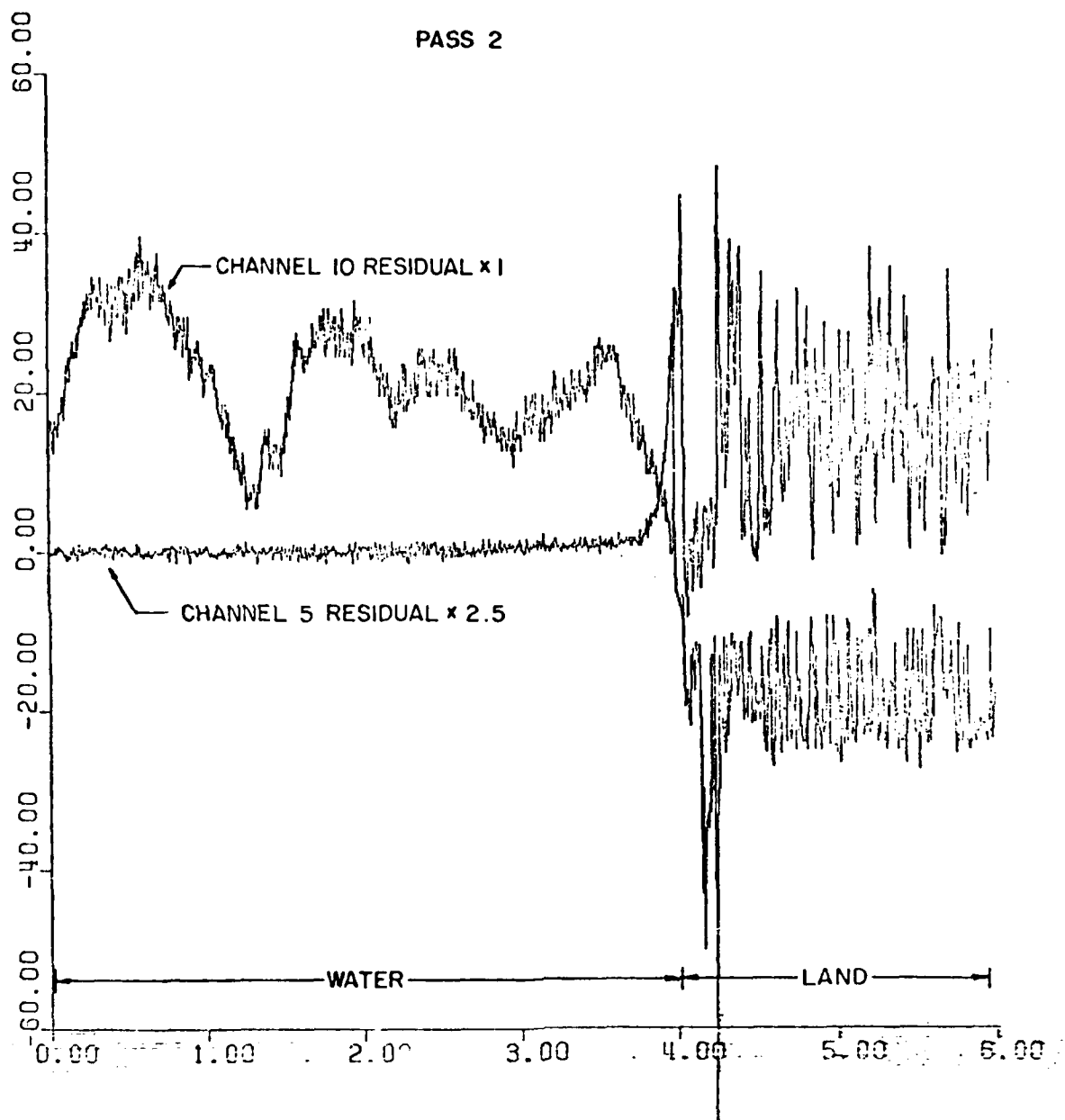
Figure 11

BA P-3 M-2 P-1XR

PASS 2

Figure 12

Pass 2, channel 10 is affected by bottom return signal strength in addition to
Mie backscatter from particulate matter in the water volume. The important
point is however that a strong inflection of both channels takes place at the
land/water interface. Note especially that the positions of channels 5 and 10
are reversed with respect to one another on either side of the inflection point.
This consistent relationship between the two pulses appears to be useable for
separating land and water laser returns irrespective of land types or the degree
of specular Fresnel reflection. Despite the fact that only two passes have been
presented herein we have noticed that the relationship is maintained consistently
throughout all of the available data sets with which we have worked analytically.
Another important outgrowth of this work is that the on-wavelength depth-resolved
Mie backscatter may also be separable from the Fresnel surface reflection in
spite of the wide variation in the peak return amplitudes. Thus, the extraction
of water column suspended sediment information from bathymetric type data now
appears more possible than ever before. Sophisticated deconvolution techniques
coupled with red-shifted, depth-resolved Raman backscatter may further enhance
the suspended sediment studies as well as aid the land-water identification
process. These techniques are of course recommended for future investigations.

4.2 Scanning Data

The collection of wide area laser hydrographic data with a conically
scanning laser system presents a number of geometric and processing problems
most of which are solvable in a straightforward manner. Although some advan-
tages are realized with a conical scan such as constant incidence angle, reduced
specular return over the entire scan, geometric solution of pitch and roll
independent of an onboard inertial system and others previously reported,[2] the
problem of separating land and water returns in shoaled areas and along beaches
and shorelines requires solution in order for laser hydrography to be of utility

in nearshore mapping to meet requirements of such agencies as the U.S. Army
Corps of Engineers and the NOAA National Ocean Survey. Figure 13 illustrates
the pulse recognition problem. Resolved depths from return waveforms are shown
in a cross-section plotted against time. The frequency modulation in depth at
the 5 Hz scan rate is apparent as the laser beam alternately strikes water and
land targets, finally striking only water targets of different depths as the
aircraft moves further offshore. Figure 14 is an expanded view of second 2.0-2.5
showing every pulse. The rise in depth between the scans onto the shoreline are
from a nearshore sand bar noticed on other scanning and profiling passes.

The two scanning passes identified in Table 2 have been processed as
described in the preceeding section and are shown on a contoured projection in
Figure 15 to demonstrate the feasibility of performing conical scanning laser
hydrography. Prior to computer contouring the scanning data was evenly gridded
through an inverse square of the distance (from each pixel) process which
invariably involves some smoothing not exceeding one pixel width around each
laser point. The pixel size for these projections are ~6 m and the contours are
39 pixels in width on the average. The small deviations are due to the effect
of roll changes. The dots within the projection are pixels which have received
a direct laser pulse and are a good indication of sample density. We are quite
encouraged by the agreement of depth for pulses falling over quite wide areas
demonstrating the internal consistency of the AOL system.

Unfortunately no passes were made parallel to the beach during the joint
Airborne Bathymetry Experiments thus a complete survey cannot be shown in which
the shoreline and adjacent beach were surveyed simultaneously. During a recent
ocean surface mapping experiment a beach survey conducted parallel to the
shoreline and above the beach/water interface was performed, however nitrogen
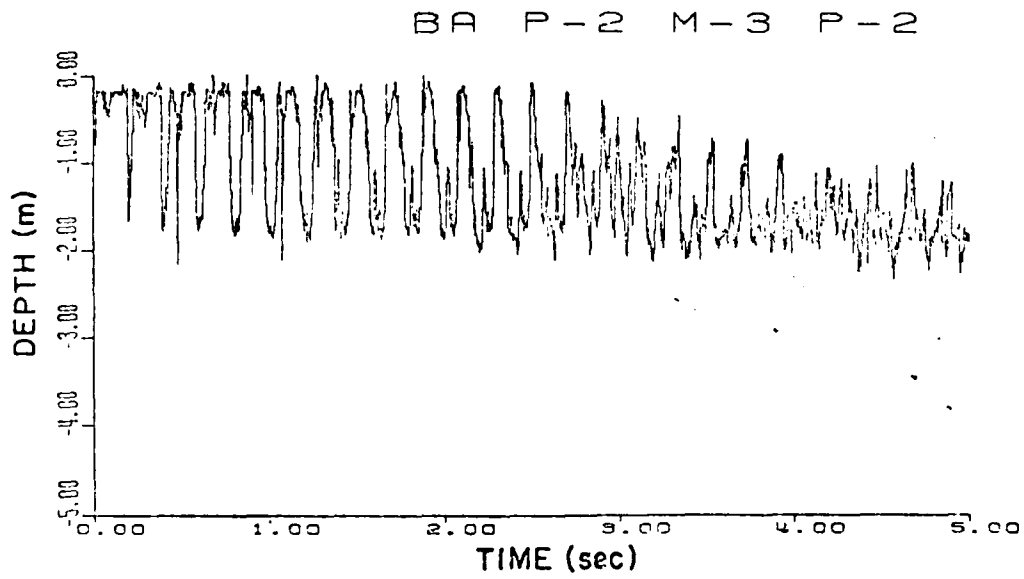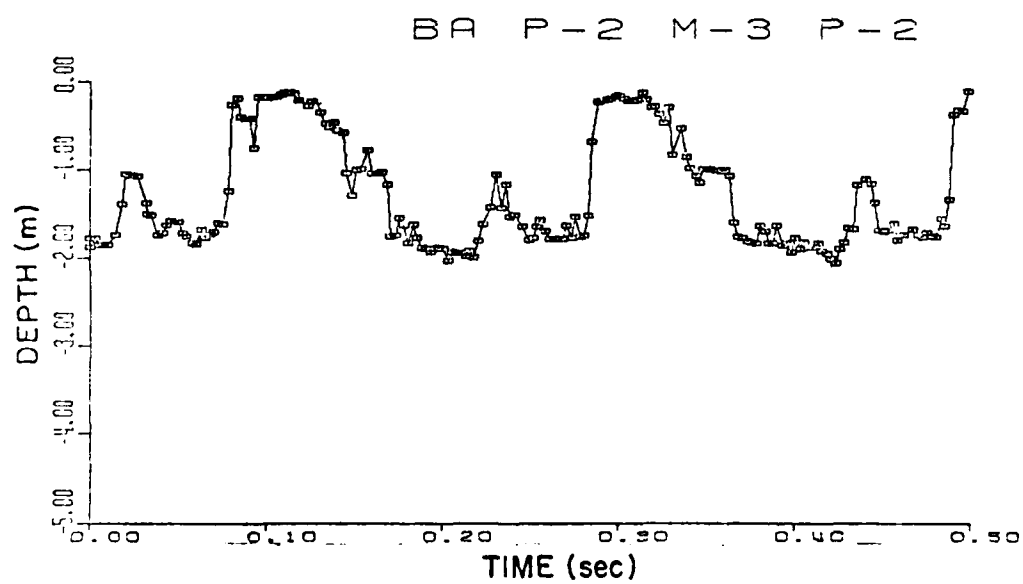gas was used in the AVCO C-5000 laser producing a 337.1 nm UV beam thus no

BA P-2 M-3 P-2

Figure 13

BA P-2 M-3 P-2

Figure 14

LASER DATA POINTS

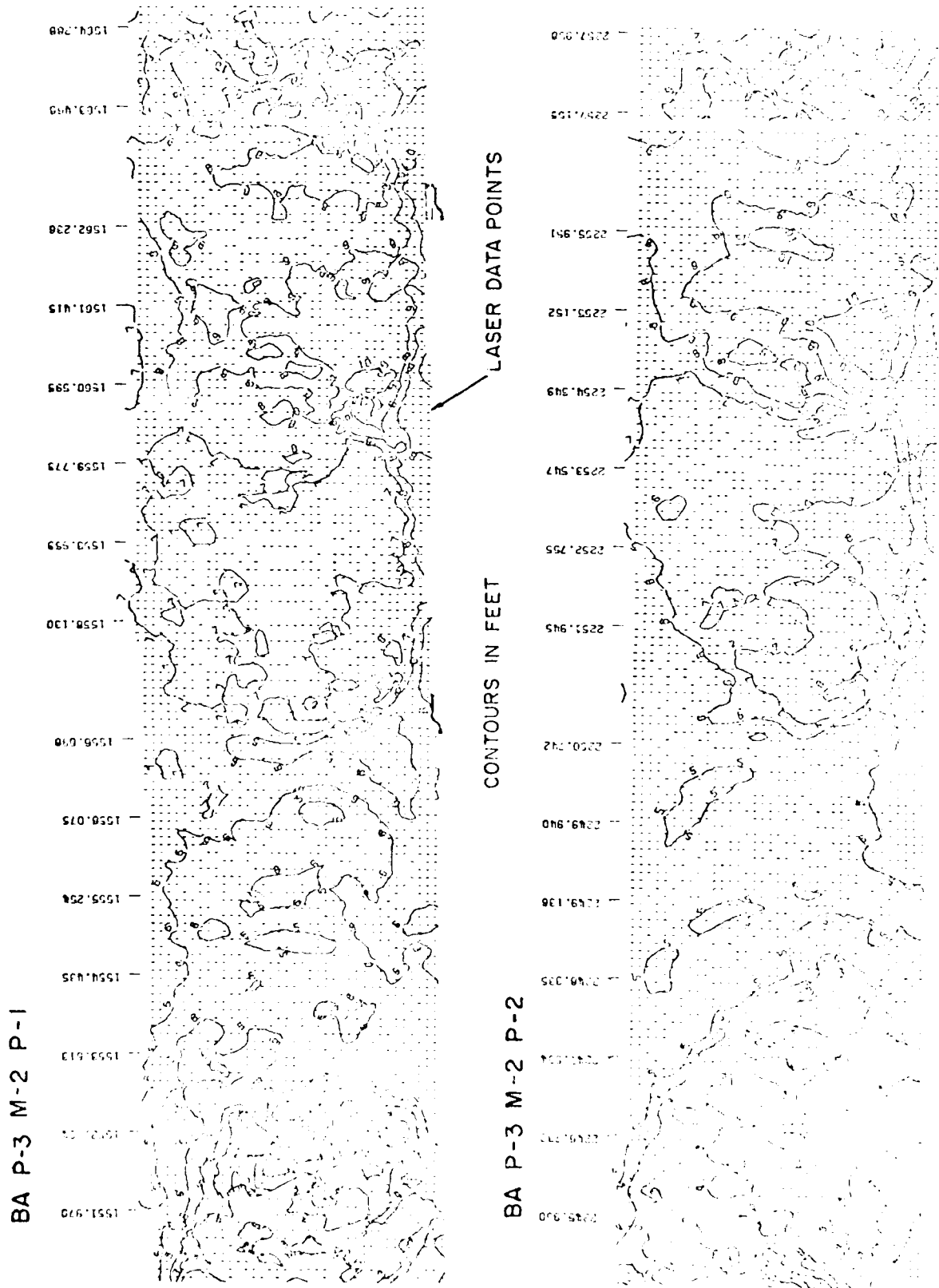CONTOURS IN FEET

BA P-3 M-2 P-1

BA P-3 M-2 P-2

Figure 15

depth data is available. The survey shown in a contoured projection i. given in Figure 16. Leveling has been accomplished using a vertical accelerometer and techniques described in another NASA publication.[3] A 1 m bias has been added to each laser point prior to contouring so tnat the 1 m contour represents the shoreline at the time of the survey. This pass was flown at mean low water therefore no tide correction is required. Coupled with the previously demonstrated depth resolving capability we believe that airborne mapping of the shoreline and adjacent shallow water is feasible.

4.3 Future Hydrography Related Work

The NASA WFC laser team is currently planning to perform experiments during FY 1981 designed to couple terrain mapping capabilities developed in an expanded program with the U.S. Army Corps of Engineers[3] with hydrographic capabilities developed in the joint Airborne Laser Hydrography Program to demonstrate the feasibility of extending these technologies to shoreline mapping. These experiments are expected to begin in December 1980.

5.0 ACKNOWLEDGMENTS

The authors wish to acknowledge the field and drafting efforts in behalf of this project by Earl B. Frederick and the typing of this manuscript by Helen Shirk.
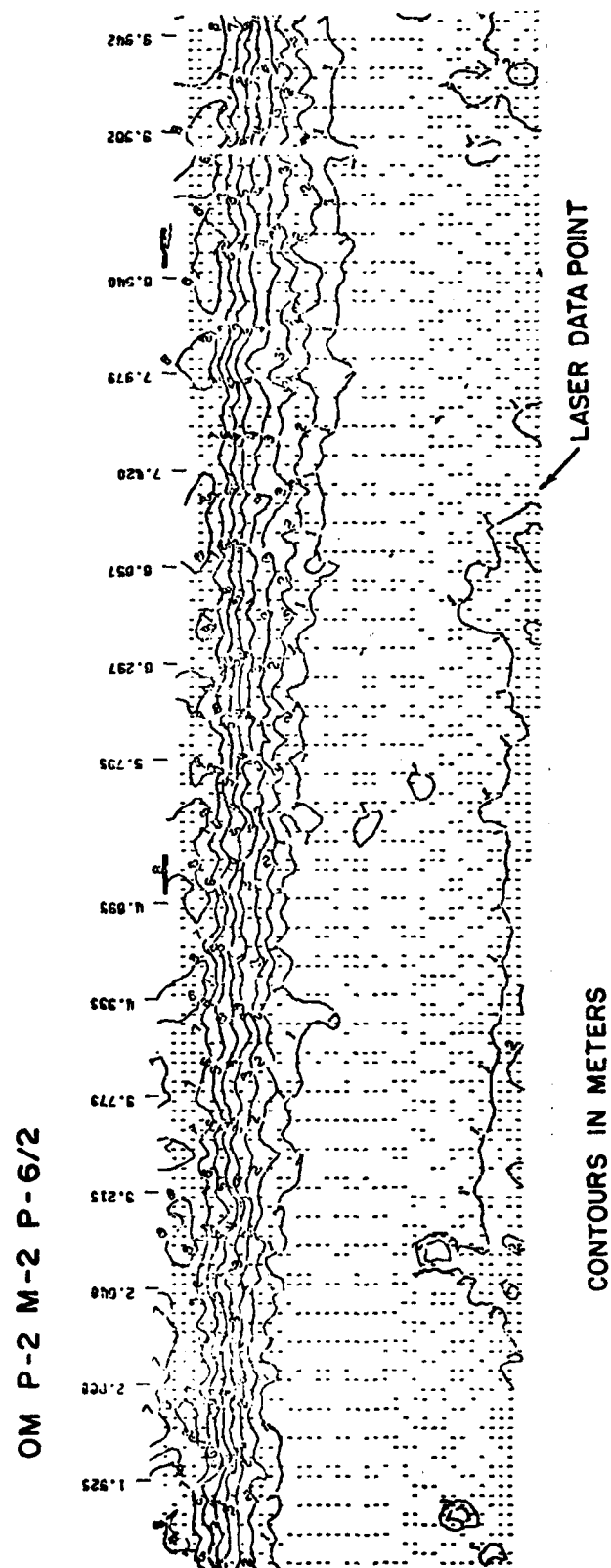
ERL-0193-SD

Figure 16

REFERENCES

1. R. N. Swift and L. R. Goodman, in Digest of Conference on Laser and Electro-optical System 1978 (CLEOS) (Optical Society of America, Washington, DC, 1978), paper THCC5, pp. 84-85.

2. F. E. Hoge, R. N. Swift and E. B. Frederick, Appl. Opt. 19, No. 6, 871 (1980).

3. W. B. Krabill, J. G. Collins, R. N. Swift, and M. L. Butler, NASA Technical Memorandum 73287, Wallops Flight Center, 1980.

4. B. L. Oostdam, Doctoral Dissertation, University of Delaware, College of Marine Studies, 1972.

APPENDIX A

AIRBORNE OCEANOGRAPHIC LIDAR SYSTEM DESCRIPTION

The Airborne Oceanographic Lidar (AOL) is a state-of-the-art conically scanning pulsed laser system designed primarily to perform field demonstration and technology transfer experiments for user agencies needing technology in the areas of airborne bathymetry and laser induced fluorescence. The AOL operates in either of the two above modes to respectively measure the depth of coastal waters or provide for the detection and resolution of water clarity, oil films, fluorescent dye tracers, and organic pigments including chlorophyll. In performing the above two functions the AOL system must always perform as a high précision laser altimeter, thus allowing the study of surface topography mapping as well. The timing electronics associated with the altimeter portion of the instrument further allows for depth stratification measurements. These vertical dimension measurements coupled with the airborne conical scanning capability of the optical portion of the system, allows wide area three-dimensional maps to be produced. Detailed horizontal resolution is provided by the 400 per second real-time data rate capability.

In the bathymetry mode a nominal 7 ns 2 kW neon laser pulse is transmitted to the water surface where, through Fresnel reflection, a portion of the energy is returned to the airborne optical receiver while the remainder of the pulse continues through the water column to the bottom and is subsequently reflected back to the receiver. The elapsed time interval between the received surface and bottom pulses allows determination of the water depth. Additional analysis of the amplitude and temporal decay characteristics of all the pulses allows resolution of sea state, surface reflectivity, water transmissivity, as well as bottom reflectivity.

The AOL optical system consists of a rigidly connected three tier optical table arrangement. This is seen in Figure A1. This construction technique affords good structural integrity while maintaining a quasi-laboratory situation for convenient and rapid adjustment, replacement or modification. The upper tier supports the laser transmitter, folding mirrors, beam forming or collimating optics while the intermediate tier carries the 30 cm receiving Cassegrain telescope coupled selectively to the bathymetry phototube detector or fluorosensor. The lowest tier is located beneath the aircraft floor in the cargo bay and supports only the folding flat and nutating mirror conical scanning assembly. A cut-away view of the AOL system as installed on the NASA C-54 aircraft is further provided by Figure A2.

In the bathymetry mode the AOL laser is filled with neon gas to yield an output wavelength of 540.1 nm. The 400 pps (or less) output is folded into the adjustable beam divergence collimating lens, directed downward through the main receiver folding flat onto the scanner folding flat finally striking the angle-adjustable 56 cm, round, nutating, scanner mirror which directs the beam to the earth's surface. The total ocean surface, volume, and bottom backscattered signals return through the same path but because of their uncollimated spatial extent are principally directed into the 30.5 cm Cassegrain receiving telescope. The horizontal and vertical fields of view of the receiving telescope are each separately controlled by a pair of remotely adjustable focal plane knife edges. The radiation is then collimated and focussed behind the face of the EMI D-279 PMT to avoid weak photocathode areas. The 45° folding flat and beam splitter between the collimating lens and the narrowband interference filter shown in Figure A1 are both used only in the fluorosensing mode.

The PMT analog output waveform is then routed through a multichannel 10X amplifier fanned-out or reproduced forty times and sent to charge digitizers
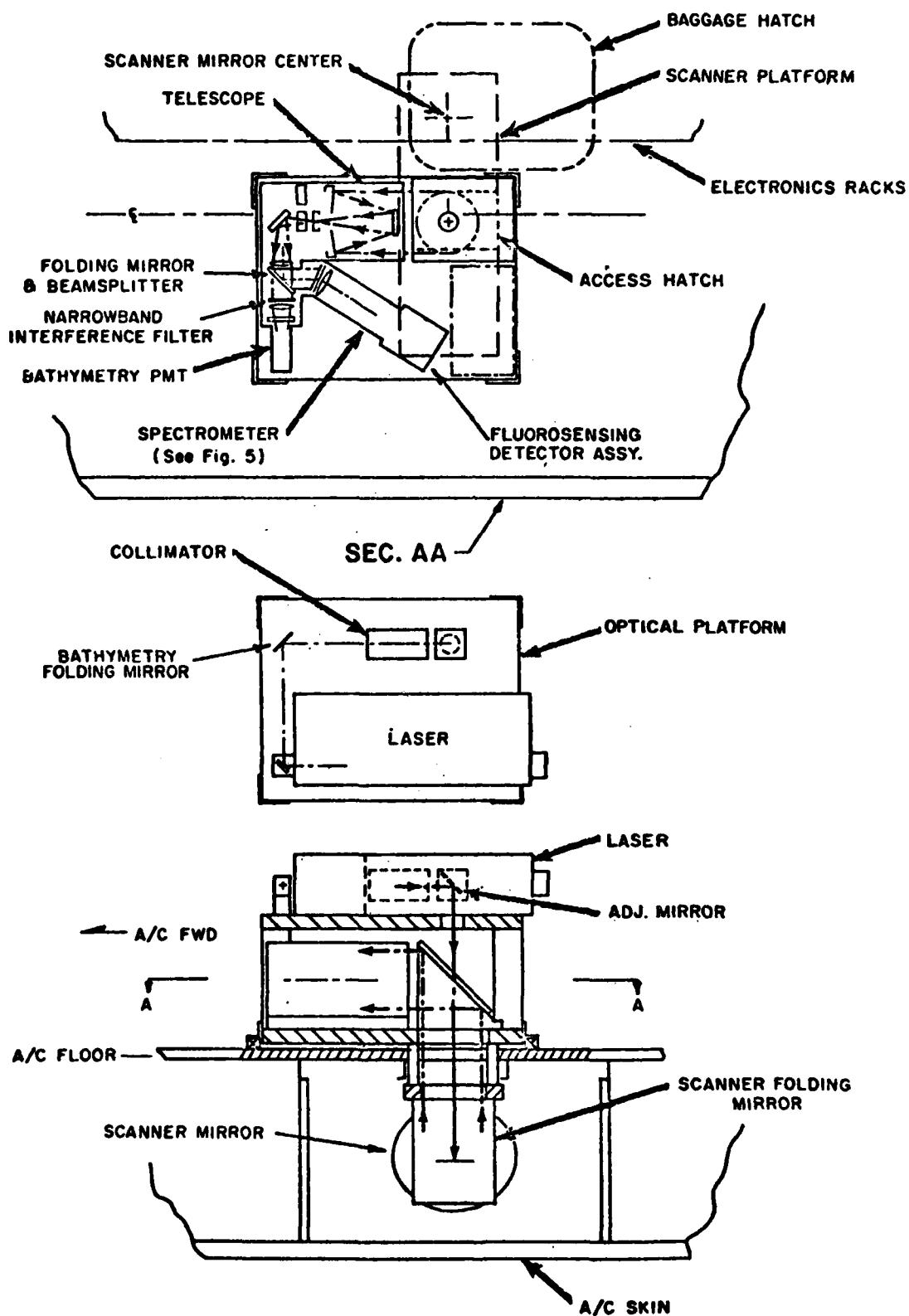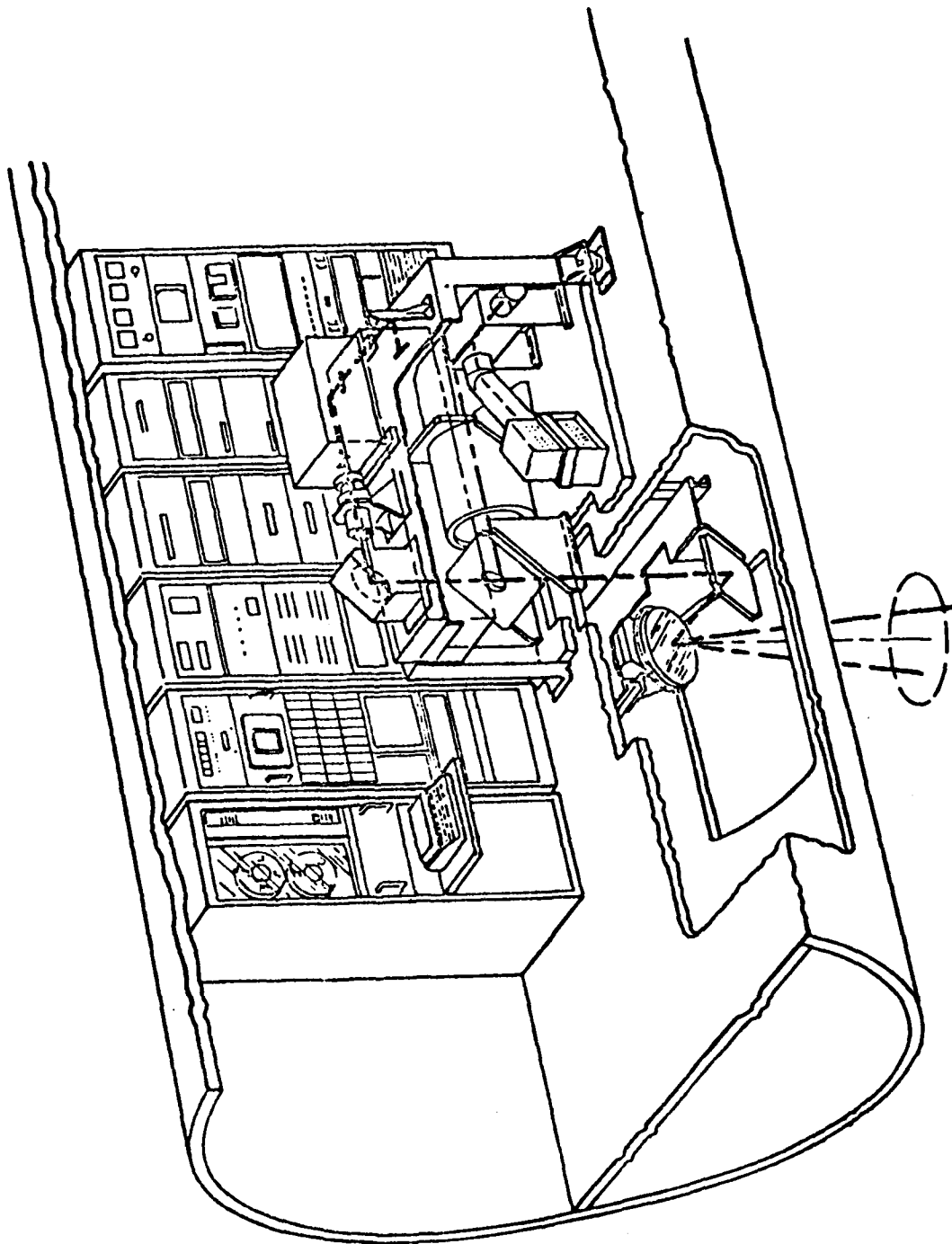
Figure A-1

Figure A-2

(CD). The 40 charge digitizers are gated "on" sequentially every 2.5 ns to obtain the proper segments of the waveform. Additionally, the CD's are held "on" for 4.0 ns. The center of each 4 ns gate remained spaced from its neighbor by 2.5 ns yielding a 0.75 ns overlap with both adjacent CD's.

PAPER 10

DEFENCE SCIENCE & TECHNOLOGY ORGANISATION

ELECTRONICS RESEARCH LABORATORY

SALISBURY, SOUTH AUSTRALIA.

WRELADS II TRIALS REPORT

RALPH ABBOT, WRELADS TRIALS COORDINATOR

The WRELADS II trials began with the installation of the equipment
in the aircraft in August 1979, and since then there have been 60 flights
totalling in excess of 200 hours. That time has been divided between testing
equipment, fault finding, calibration, evaluation of operational techniques
and recently, conducting small area surveys. Figure 1 shows the areas in
Australia in which trials have been conducted. Most of the trials have been
based in Adelaide in South Australian waters, however recently a four week
exercise was conducted from Townsville in Queensland, and that included a
very long trial to Thursday Island and Torres St. at the northern tip of
Queensland, returning via the Gulf of Carpentaria. One of the main reasons
for trials in Queensland is that most of Australia's shallow water is in
the Northern half of the continent; since a great deal of it is either
inadequately or not charted and carries a great deal of heavy shipping,
it is of considerable interest to the RAN Hydrographer.

The areas for the South Australian trials are shown in figure 2. They
were conducted mainly in the gulf waters: Gulf St Vincent adjacent to
Adelaide and Spencer Gulf, further to west and on which Port Lincoln is
located. The bulk of the work has been done in Spencer Gulf since the airspace
is less controlled than that in the Gulf St Vincent, and also because there
are a number of reefs and islands which offer rapidly changing depths. There
are very few rivers flowing into the gulfs and with the extremely dry year it
has been difficult locating high turbidity water except during and immediately
after storm conditions.

The area for the Townsville trials is shown in figure 3. The Great
Barrier Reef extends from shore out to about 60 km at Cairns in the north and
out to 100 km or so near Townsville in the South. One area selected for work
was that north of Dunk Island, on the basis that the RAN survey ship,
HMAS Flinders would be there for combined trials, but due to a refit that proved
not to be so. Our work area was then that south of Dunk Island, closer to
Townsville. The waters exhibited a wide range of turbidity of 100 to 1, from
beam attenuation coefficient, $c=0.05$ m^{-1} in the cleanest ocean waters near the
200 m contour line to $c=5$ m^{-1} or so in the band of very turbid waters running
right along the coast. Several small area surveys were conducted in the area.
Cape Sandwich, on Hinchinbrook Island was chosen as representative of the
extremely turbid areas, Britomart and Rib Reefs as typical of the inner to mid
reef areas with reasonably clean waters, and finally Myrmidon Reef which was
right on the 200 m contour line on the edge of the continental shelf, in clear
ocean waters.

In the WRELADS I trials in 1977 we were frustrated with both the necessity and the difficulty of having a boat to provide turbidity ground truth during trials, and almost all WRELADS I trials lacked that information. We have spent a lot of time evolving the techniques to remotely sense water turbidity. As shown in figure 4, we have used the exponential decay of the backscatter signal in the green return to provide k_b, the WRELADS backscatter attenuation coefficient. In figure 5 are shown two photographs used in such determinations. They are multiple exposures to superimpose a number of waveforms to help average the noise. The top photograph yields a $k_b = 0.057$ m^{-1} with the bottom signal just visible on the extreme right. The signal is just about buried in noise and the depth of 40 metres is just deeper than what we call extinction depth, d_e, with unity signal to noise ratio. To relate the system backscatter attenuation coefficient to water properties we have conducted joint trials with the boat measuring beam attenuation coefficient(c), using the DRCS transmissometer, and the relationship is shown in figure 6, giving a means of remotely sensing c on every flight.

A slightly different method of remotely sensing turbidity has involved measuring the amplitude of the backscatter return from a depth of 5.6 m, which corresponds with the depth at the first graticule line on the oscilloscope in the aircraft. The laser power and EHT are preset to 5 mJ and 2.1 kV respectively and the inner block in the receiver FOV removed. Figure 7 shows the calibration using this method (against beam attenuation coefficient as determined with the transmissometer). The curve determined from the 5.6 m depth readings rolls over in the more turbid water, since the laser energy is absorbed in the top few meters, and indeed, if the water is dirty enough there is no return at all from that depth! Ideally the backscatter amplitude would be measured at zero depth, however the presence of surface reflection prevents that. The technique evolved is for the exponential backscatter attenuation coefficient, k_b, to be determined (as previously explained) and used to back-project the backscatter amplitude to a shallower depth. The curve thus obtained at 2 m depth still shows a slight rollover at very high turbidities, but at a depth of 1 m the relationship is linear.

The relationships between several attenuation coefficients and the beam attenuation coefficient are shown in figure 8. The diffuse attenuation coefficient, K, was measured using an irradiance meter loaned by a research student at James Cook University in Townsville, and its relationship with c agrees reasonably well with the NADC data, although we were fortunate to encounter waters dirty enough to extend the data to very high c values. The backscatter coefficient, k_b, is plotted for comparison, and its slope is only one third that for K. The signal attenuation coefficient k_s was determined for WRELADS I in 1977, and that is also plotted, however we have not yet determined k_s for WRELADS II.

For all WRELADS trials the laser power is 5 mJ out of the laser, 5nS FWHM. The optical coupler, beam expander and 45° mirror assembly has 51% transmission and the scanning mirror surface, which has significantly degraded, has reflectivity of about 70% at present.

Hence our transmitted laser pulse is around 350 kW peak power. Nominal
operating altitude is 500 m, ±15° scan angle and 1 mR transmitted divergence.
We produce a rectangular scan pattern by driving a nodding mirror with two
orthogonally mounted scan actuators, which are loudspeaker type drivers. The
scan pattern shown in figure 9 is a Lissajous figure from the two scan
transducers, Z modulated by the laser Q-switch pulses. Although it's a
figure-of-8, the forward motion of the aircraft converts it to a rectangular
grid on the sea surface. The green return signal from the photomultiplier is
digitized in 6 bits at 2nS intervals and stored in memory, from which it is
replayed via a D/A at a 25 kHz rate for recording on an analogue tape recorder.
Some of the early signal returns recorded with this system are shown in
figure 10. A data logging system records a number of system parameters for
display on a monitor and for recording on digital channels on the tape recorder.
A sample of the data is shown in figure 11.

One of the major tasks in the Queensland trials was to determine the
WRELADS performance envelope. It was obtained on the very long flight path
from Townsville to Torres St. and return, on which there were numerous reef
crossings. At every crossing the extinction depth, d_e (at which the signal
disappeared into noise) was noted, together with the backscatter amplitude at
the 5.6 m depth. The extinction depths thus obtained are shown in figure 12,
and they range from 50 m in the clearest water to 5 m in the most turbid. The
beam attenuation coefficients determined from the backscatter amplitudes are
shown in figure 13, and the plot of one against the other in figure 14, giving
the WRELADS performance curve. The possibility now arises using this kind of
curve of predicting the depth to which a bottom could be sensed based on the
backscatter amplitude. Using this technique, in the areas in which the water
is too deep to obtain a bottom return, one may at least predict a minimum safe
depth, and provided this can be done reliably and accurately to useful depths,
then this method may be of great use to the Hydrographer.

Figure 15 shows the results of a survey flown in the Townsville area
in which the turbidity was remotely sensed using the above techniques. It
demonstrates the capacity to rapidly sample the water over a very large area.

The optimum field of view for the green receiver is of interest, and
with the ARGO navigation equipment it was possible to repeatedly return accurately
over the same selected area and record signal amplitudes for varying receiver
fields. The results of two such trials are shown in figure 16. The trial near
Port Lincoln was conducted with smooth glassy seas for depths of 10, 20, 30 and
40 m and the trial at Slashers Reef in Queensland in 30 m with rough seas. As
can be seen there is very little increase of signal with FOV (plotted as full
angle) for either sea state. If this is coupled to the background which increases
as the square of the FOV then the signal to noise ratio is decreasing with
increasing FOV, and the minimum FOV is optimum. This is not true of course at
night in a non-background limited situation, where the widest FOV is required
to collect every available photon.

The results of one small area survey is shown in figure 17. Its a portion of the lagoon in Britomart Reef which is situated midway between shore and the 200 m contour on the edge of the continental shelf. The depths have been hand plotted from those recorded by a simple threshold counter in the aircraft. There are two overlapping tracks, each of four seconds duration, and positions have been fixed as well as possible from video records, aerial survey photographs and the ARGO positions. Contours have been plotted, the deepest being 20 m. There is good agreement with the surface features on the survey photograph over which the depths have been plotted. Strong bottom signals were recorded from all parts of the lagoon, the maximum depth of which is around 20 m. The performance under limiting conditions is shown in figure 18, a similar plot over the outer edge of Britomart Reef. The dots on the left side indicate that bottoms were not recorded; the extinction depths here were just in excess of 35 m under bright daylight conditions.

Similar surveys were conducted at Cape Sandwich, chosen as a much more turbid area, and Myrmidon Reef, on the ocean edge of the Reef. Extinction depths around 18 m were measured at Cape Sandwich, indicating that the water was cleaner than it had been several days earlier when the boat there measured c values of 5 m^{-1}! At Myrmidon Reef out in the very clean ocean waters, extinction depths of 40 m on the ocean side and 45 to 50 m on the inshore lee side were recorded which was unexpected, as that, I thought, would have been slightly more turbid.

Of interest is the difference in performance, day and night. Figure 19 shows sequential waveforms recorded in the aircraft and re-recorded on a fibre-optic recording oscilloscope to produce hard copy. The laser beam is scanned side to side and hence if the water on one side of the aircraft is shallower than that on the other, then the depths in the waveforms will progressively become shallower and then deeper as the beam scans, and the traces of figure 19 show that. The lower waveforms were recorded at night off Britomart Reef, and show extinction depths around 48 m, whilst those at the top, taken the next day in the identical location, have extinction depths around 38 m. It is possible that turbidity had changed between the two trials, but our experience in the area during the whole trials period indicated that that was not likely.

Figure 20 shows shallow bottom returns in turbid water at Pickersgill Reef. The photomultiplier is working without variable gain control and there is no inner block in the receiver FOV. It illustrates the problem of bottom signals in turbid water where the bottom signal rides on the backscatter envelope. The design of the WRELADS receiver in its depth sounding mode is to pull down the backscatter envelope and expose the bottom signal for threshold detection.

Some unusual subsurface returns are shown in figure 21, where the bottom signal is extremely broad. We do not understand its cause - it may indeed be layers of turbid water or marine creatures swarming.

A sample of the computer printout of depths is shown in figure 22. There are three blocks, each of two seconds duration. Each block has 14 scans, with 12 spots, forming tracks 0(starboard) to 11(port).

At the moment the depth counter is recording zero for both very shallow water
and water in which no bottom is being detected (obviously to be changed) and
so one has to work out which are valid zeros.   There are a number of readings
around 5.3, 5.4 m which are unlikely to be valid depths. The depth counter
has a range gate which was set at that value during the trial, and if
because of roll errors the surface pulse occurred at that point then that
depth was recorded as a bottom.

        Figure 23 was the result of a confirmation exercise to ensure that
the depths we were recording from the depth counter in the air actually could
be tied back to the waveforms recorded on tape. The first waveform, at the
bottom, corresponds to the depth at the top right hand of the two second block
of depths. The successive higher waveforms have their depths recorded
successively to the left for the first scan, then to the right for the second
scan, and so on.

        I shall leave a detailed comment on ARGO to Doug Faulkner; suffice
it to say that we are very pleased with its performance and that after a five
hour sortie we can use ARGO to return to the navigation set point to within a
few metres.

        Rigorous depth calibration of WRELADS has not yet been attempted as
we are carrying several correctable equipment faults which lead to significant
errors which cannot be removed from the data. The rigorous exercise will be
conducted when those system faults have been corrected. Of course we have in
the joint exercises with boats obtained measurements which indicate that there
is nothing grossly wrong with the equipment and that we are nominally measuring
correct depths.

        In conclusion we are pleased that we have been able to demonstrate
reliable operation of the WRELADS II system and are looking forward to our
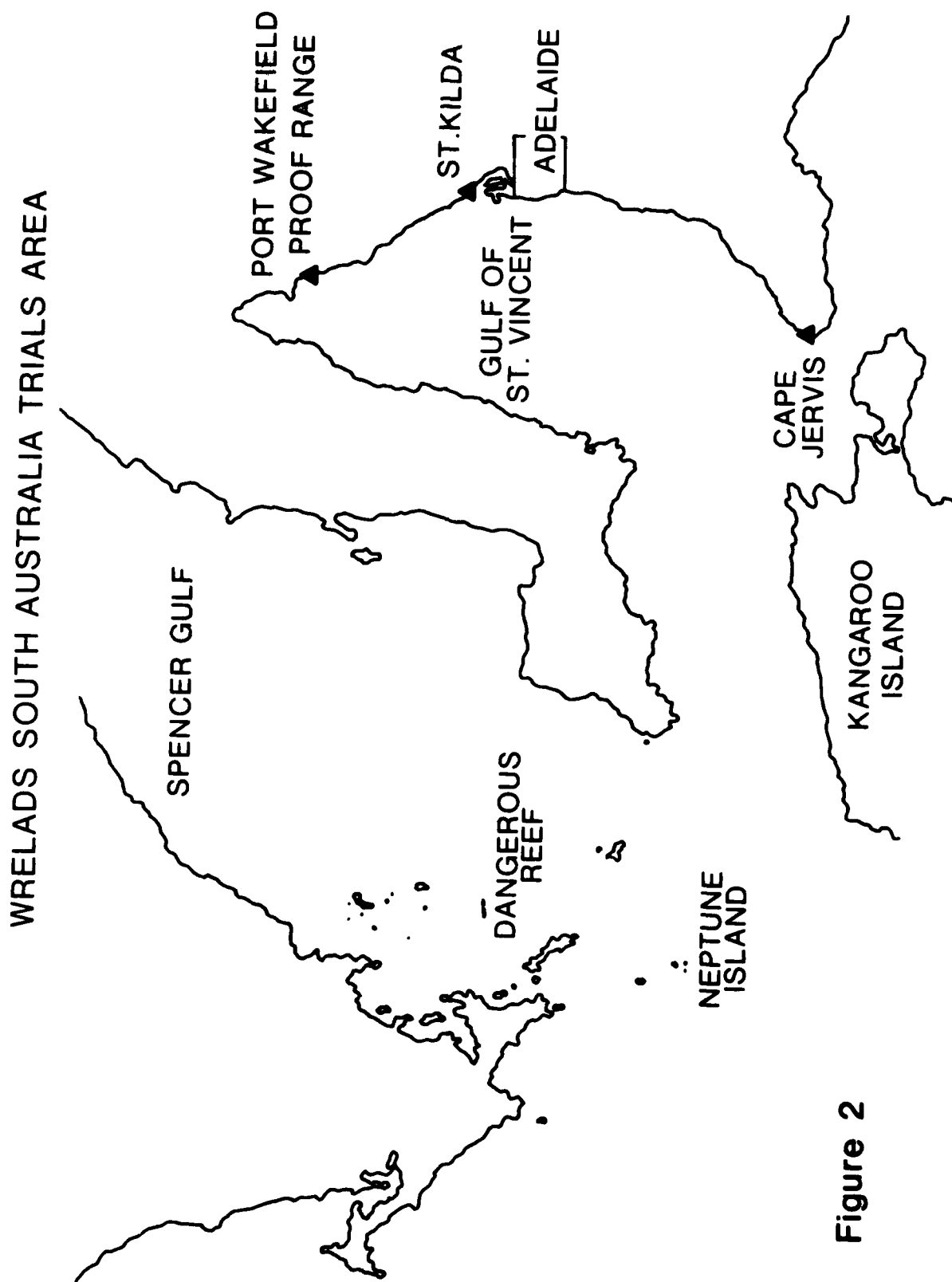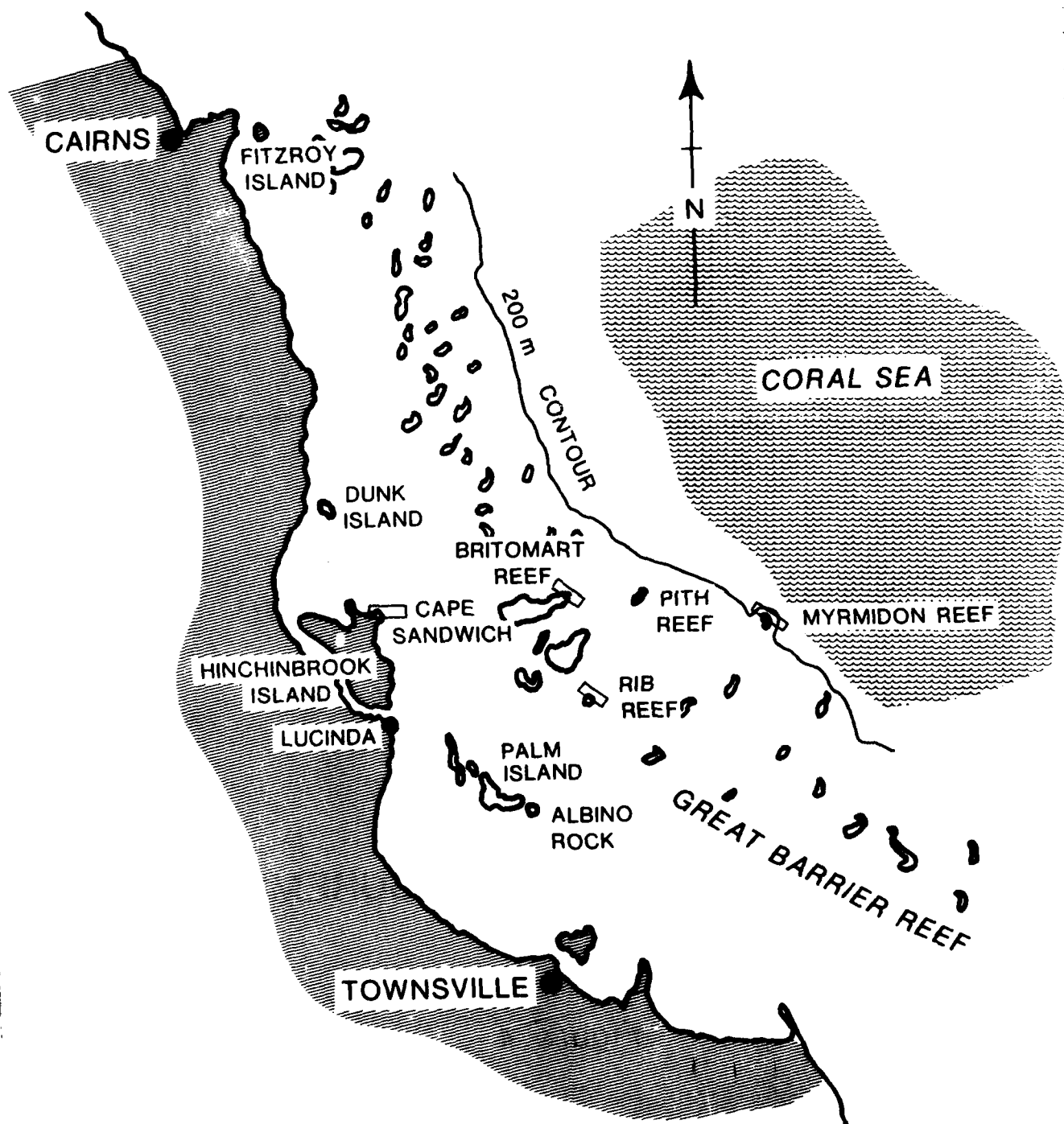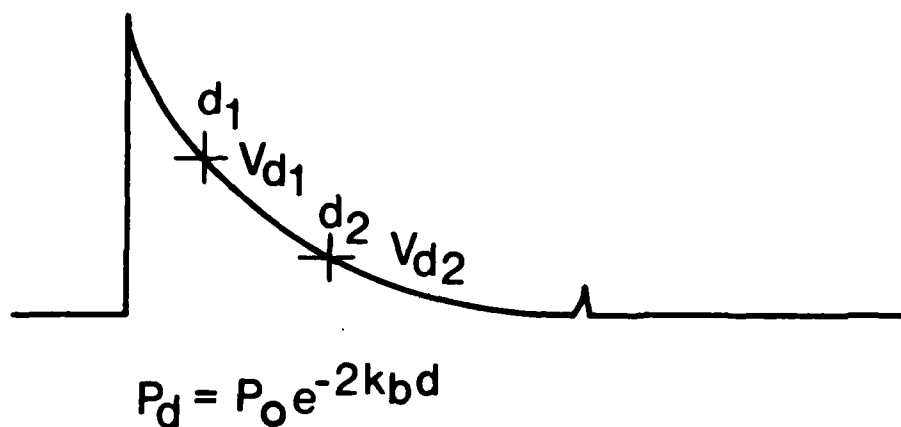next series of modifications and subsequent trials.

TORRES STRAIT

THURSDAY ISLAND

DARWIN

GULF OF CARPENTARIA

GREAT

BARRIER

REEF

TOWNSVILLE

NT

WA

QLD

SA

BRISBANE

NSW

PERTH

SYDNEY

PORT LINCOLN

ADELAIDE

VIC

MELBOURNE

TAS

Figure 1

WRELADS SOUTH AUSTRALIA TRIALS AREA

PORT WAKEFIELD
PROOF RANGE

ST.KILDA

ADELAIDE

GULF OF
ST. VINCENT

CAPE
JERVIS

KANGAROO
ISLAND

SPENCER GULF

DANGEROUS
REEF

NEPTUNE
ISLAND

Figure 2

WRELADS TOWNSVILLE TRIALS AREA

Figure 3

$$P_d = P_o e^{-2k_b d}$$

EXPONENT: $V_{d_2} = V_{d_1} e^{-2k_b(d_2-d_1)}$

AMPLITUDE: $V_{4.55m}$ or 5.56m

AIRBORNE TURBIDITY MEASUREMENTS

Figure 4

$\bar{k}_b = 0.057$
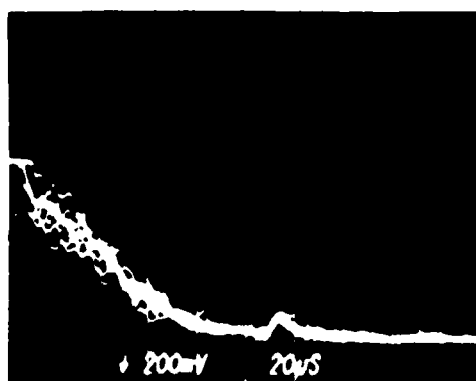$d_e \approx 40m$
F209

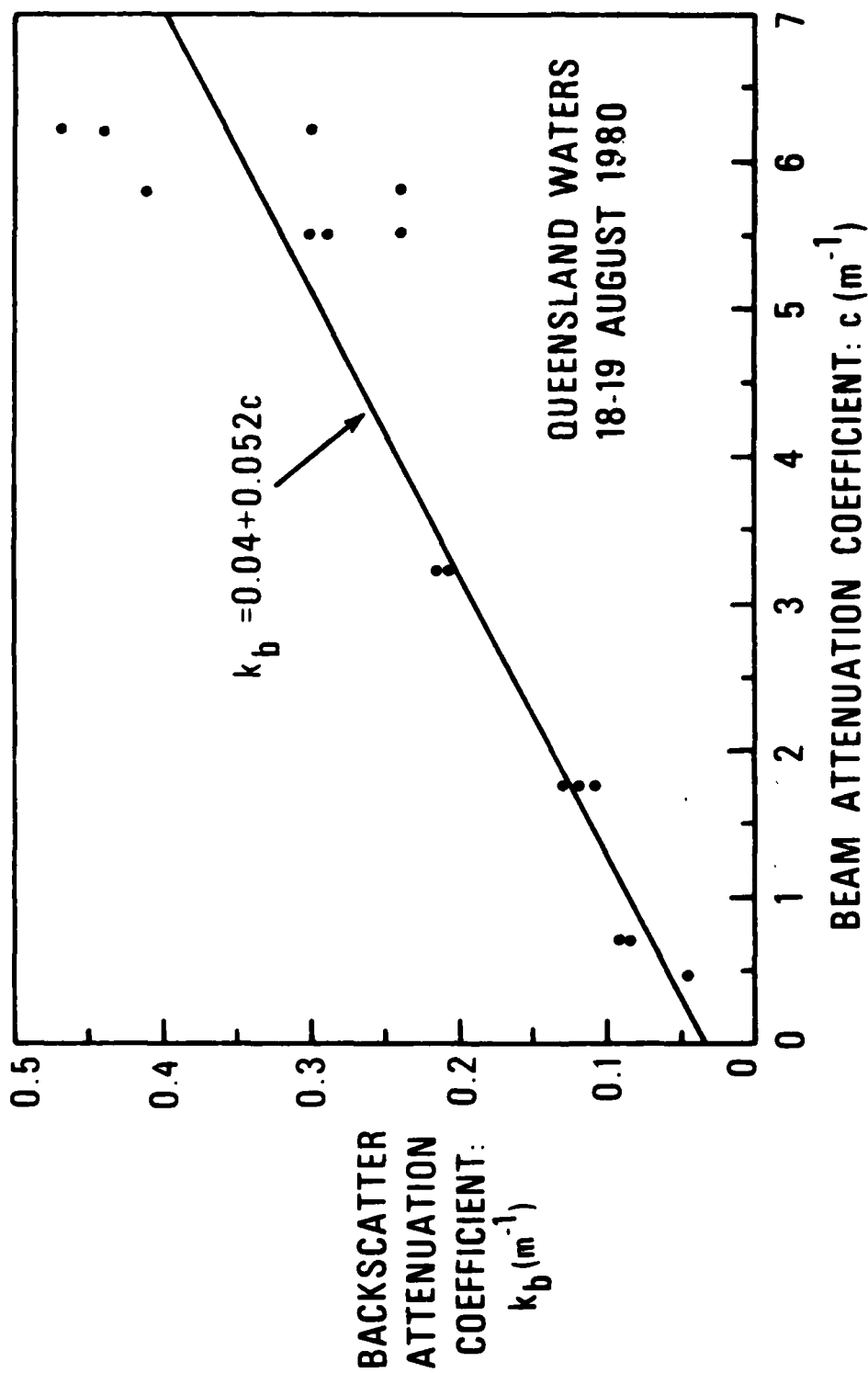| MID SPENCER GULF |
| EHT 2.4kV |
| $g_1 g_2$ off |
| 40mR FOV |
| NO BLOCK |

F 233/9
MINLACOWIE BAY

F 233/13
MID GULF ST VINCENT
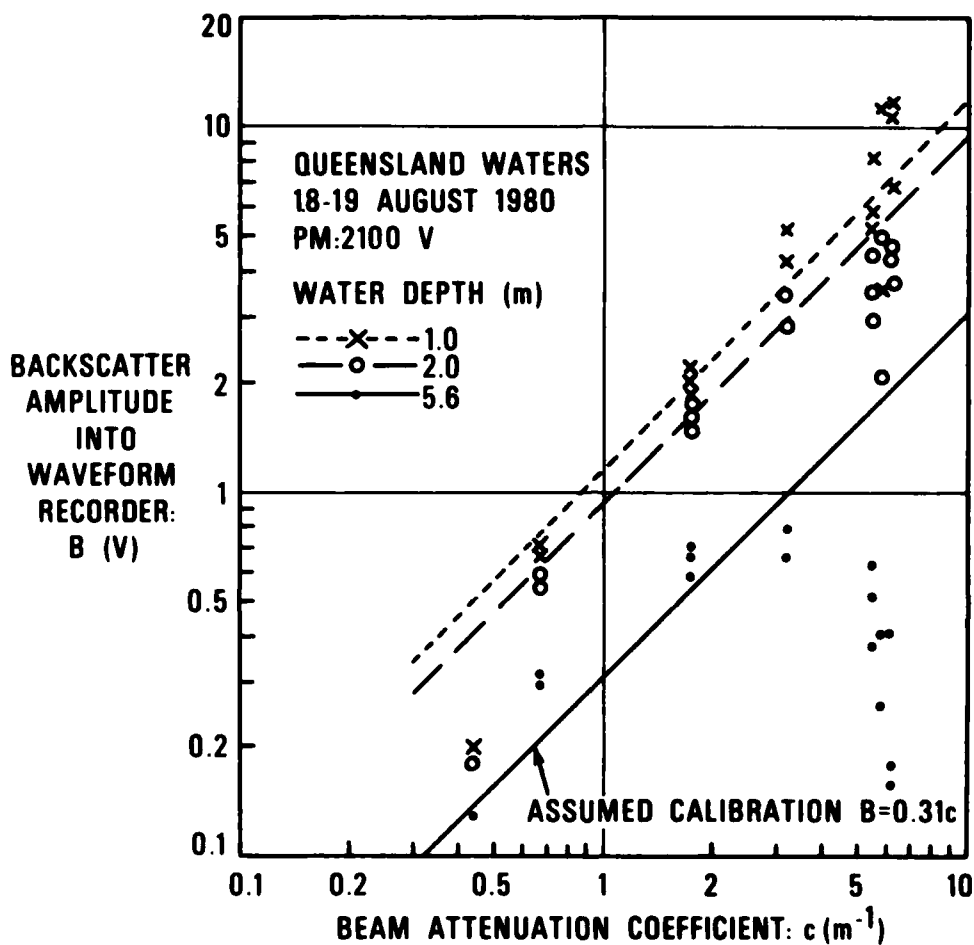$\bar{k}_b = 0.075$
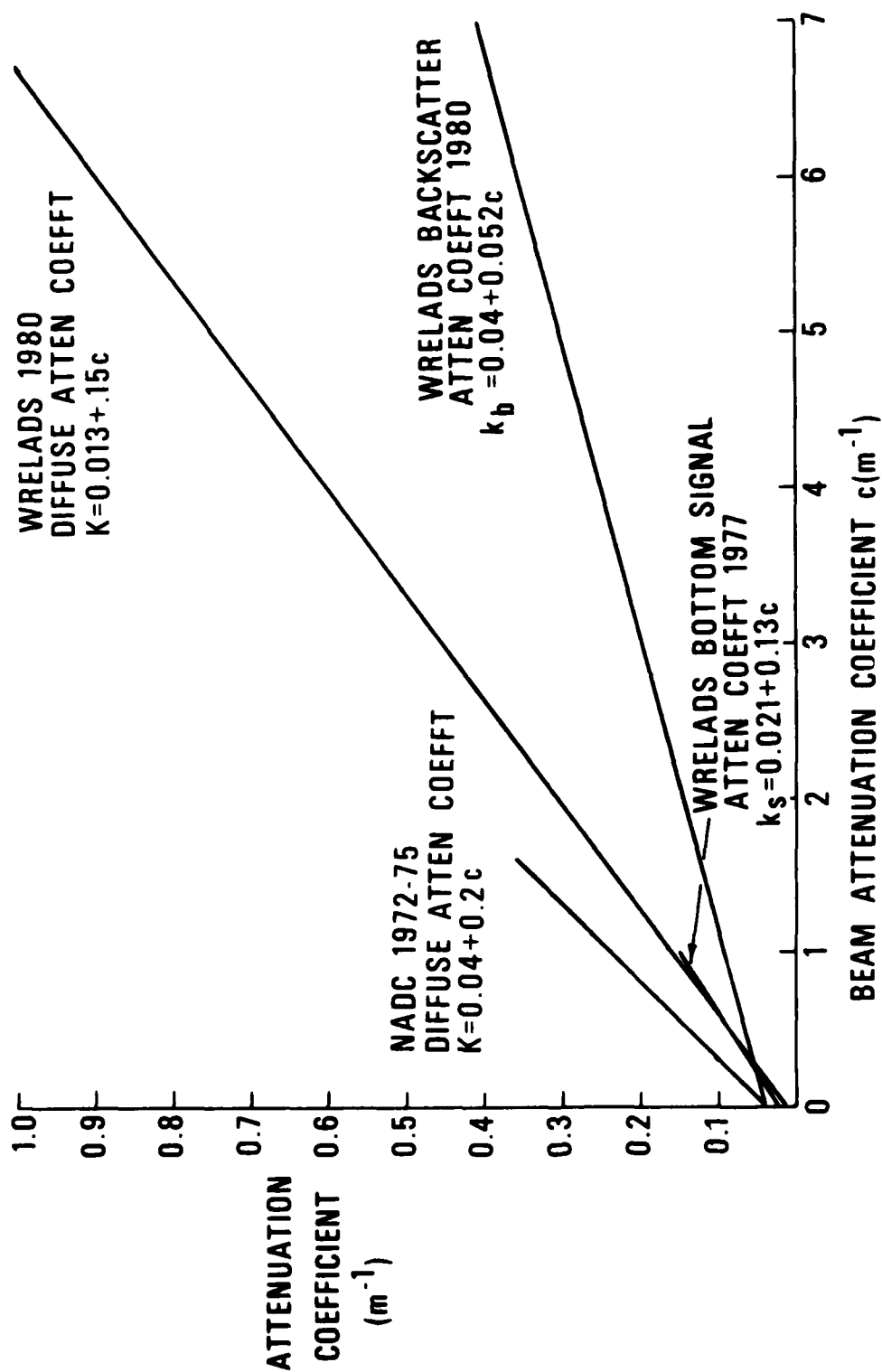$d_e \approx 27m$

BACKSCATTER MEASUREMENTS

Figure 5

RELATIONSHIP BETWEEN BACKSCATTER AND
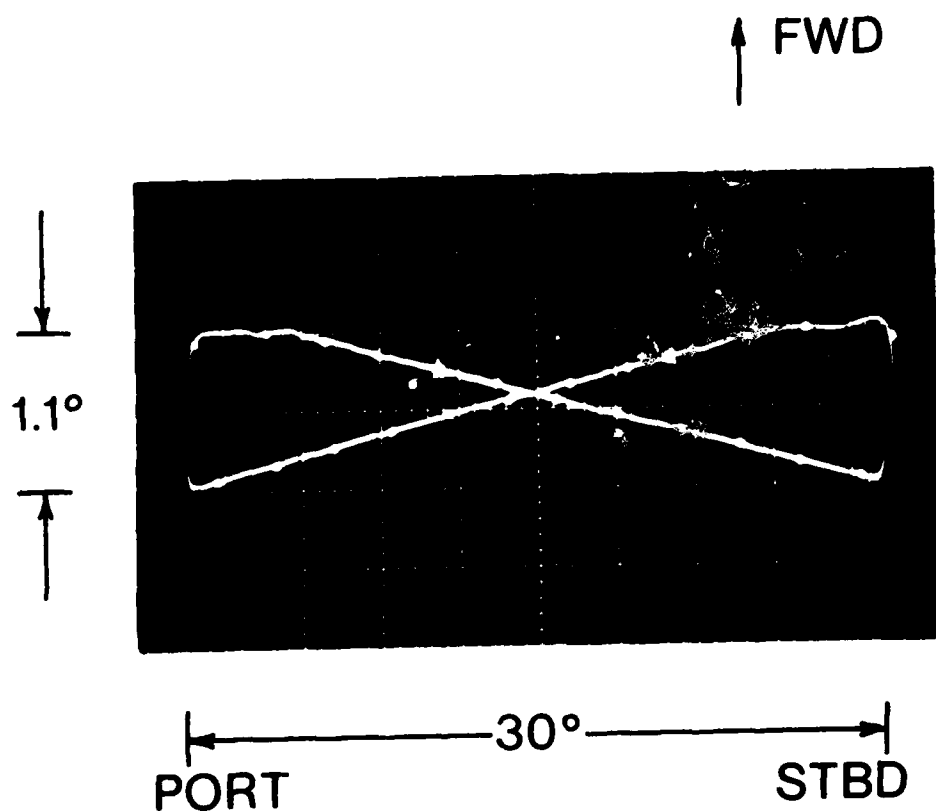BEAM ATTENUATION COEFFICIENTS IN WATER

Figure 6

RELATIONSHIP BETWEEN BACKSCATTER AMPLITUDE
AND BEAM ATTENUATION COEFFICIENT IN WATER
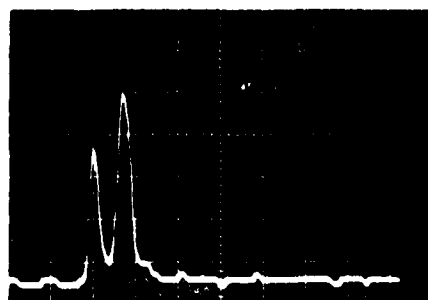
Figure 7

RELATIONSHIP BETWEEN WRELADS, DIFFUSE AND
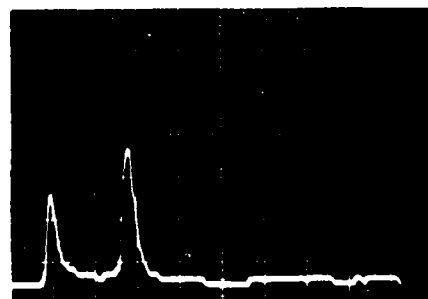BEAM ATTENUATION COEFFICIENTS
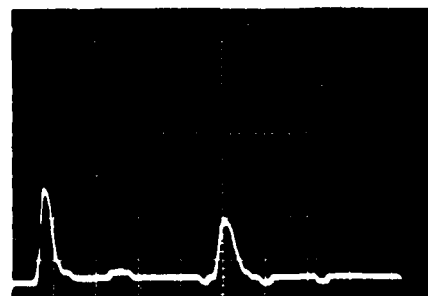
Figure 8

SCAN PATTERN

Figure 9

d=3m

d=9m
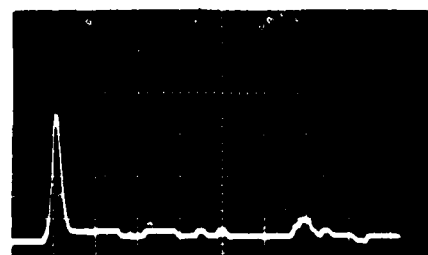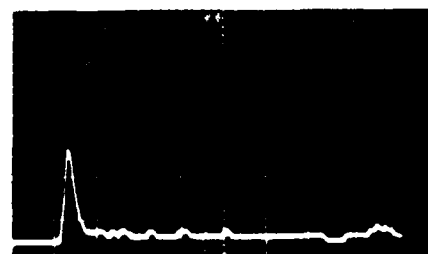
d=21m

SPENCER GULF
F 206
BEAM VERTICAL
EHT 2.4kV

d=29m

d=36m

WRELADS SUBSURFACE RETURNS

Figure 10

```
DATE      FLIGHT   ALT(M)      TIME
19.9.80    F256     4520       004952
AVIG  0114.55      0484.28    0532.88
SCAN    TEMP        GAIN        GYRO
J-  5.66  WT34.41  M 0        PT+ 0.07
N-  0.99  GF50.03  S 0.07     RL+ 0.00

PS AZ     ROLL(G)   EHT(KV)   BKPOS
3.73      + 4.87    2.06      0

X DIV     L2        L1        GFC  500
R50.03   GR 0.07   GR 5.76   GFD40.01
R 1.32   IR 0.07   IR10.03   IFD50.00

EN   THRESH   RANGE   BIOM    D(M)
     +011     +011    5       00000
```

DATA LOGGER PRINTOUT

Figure 11

PLOT OF EXTINCTION DEPTHS,
NORTH QUEENSLAND

Figure 12

TRIAL No.250T
10.8.80

TRIAL No.249T
9.8.80
ATTENUATION
COEFFICIENTS C
METRES^{-1}
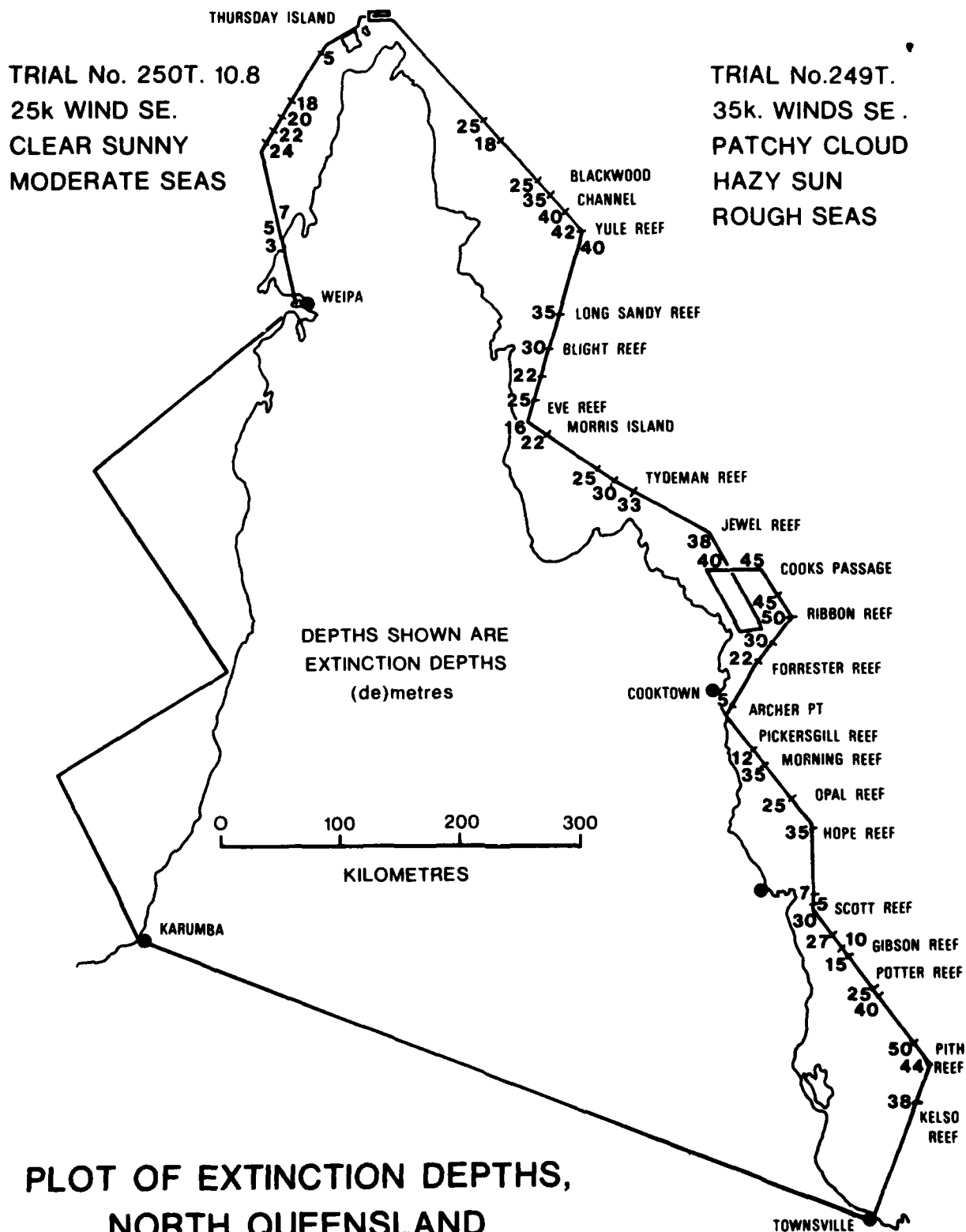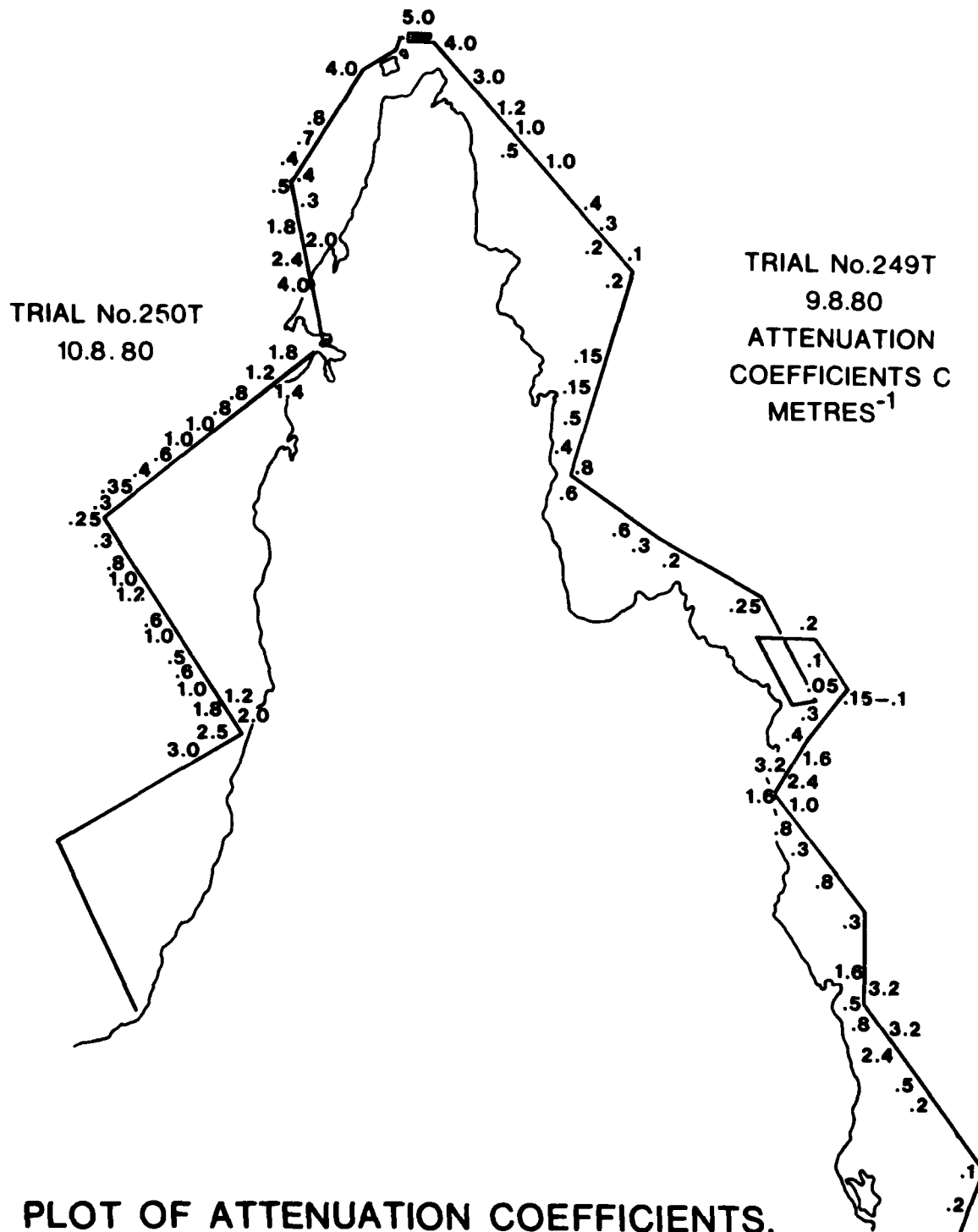
**PLOT OF ATTENUATION COEFFICIENTS,
NORTH QUEENSLAND**

Figure 13

DEPENDENCE OF EXTINCTION DEPTH ON WATER TURBIDITY

TRIAL 249T 9 AUGUST 1980
NORTH QUEENSLAND

Figure 14

FIGURES REPRESENT VALUES FOR
BEAM ATTENUATION COEFFICIENT (C,m⁻¹)
DERIVED FROM BACKSCATTER AMPLITUDE

F254T 18-8-80

TURBIDITY SURVEY - TOWNSVILLE AREA
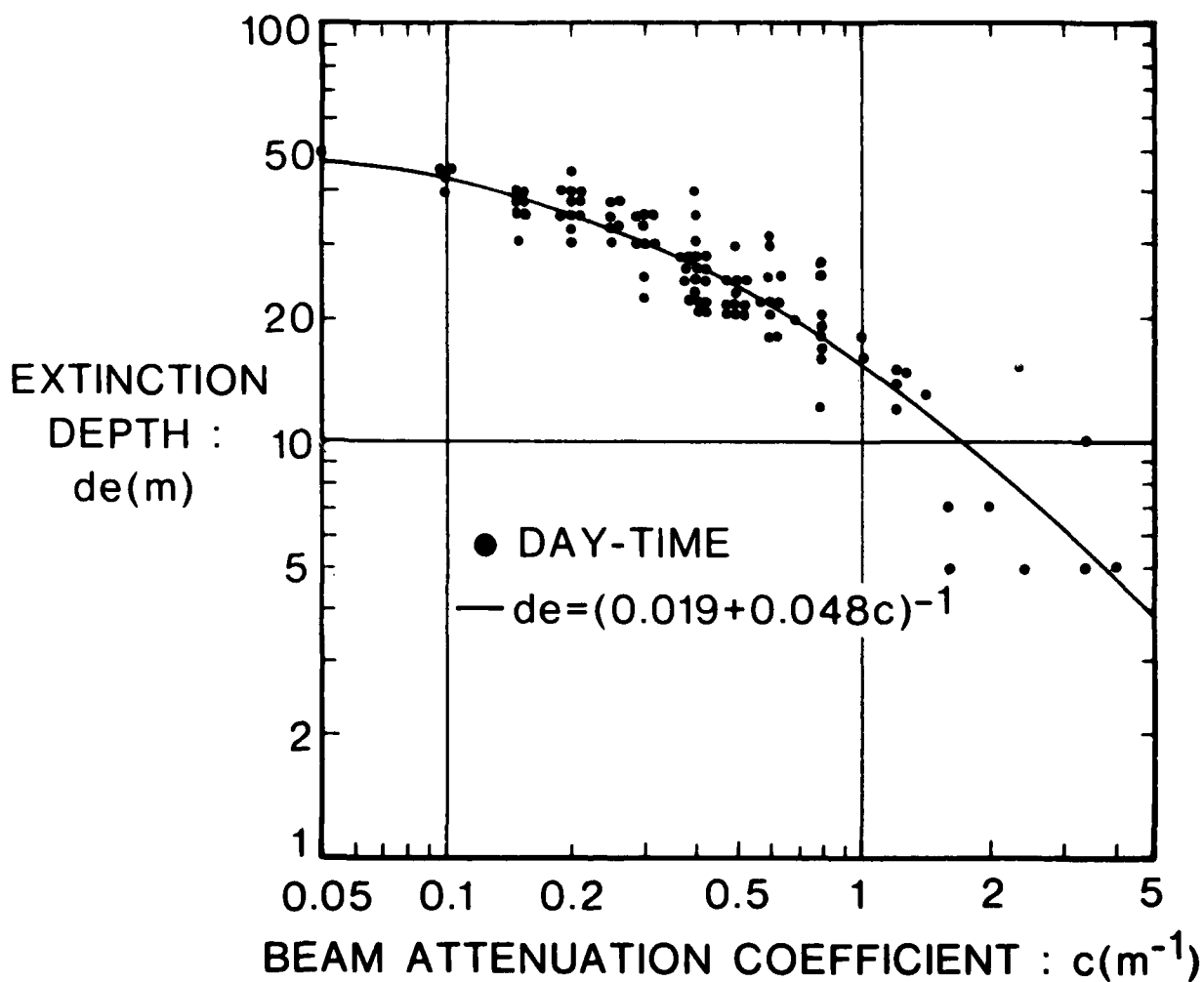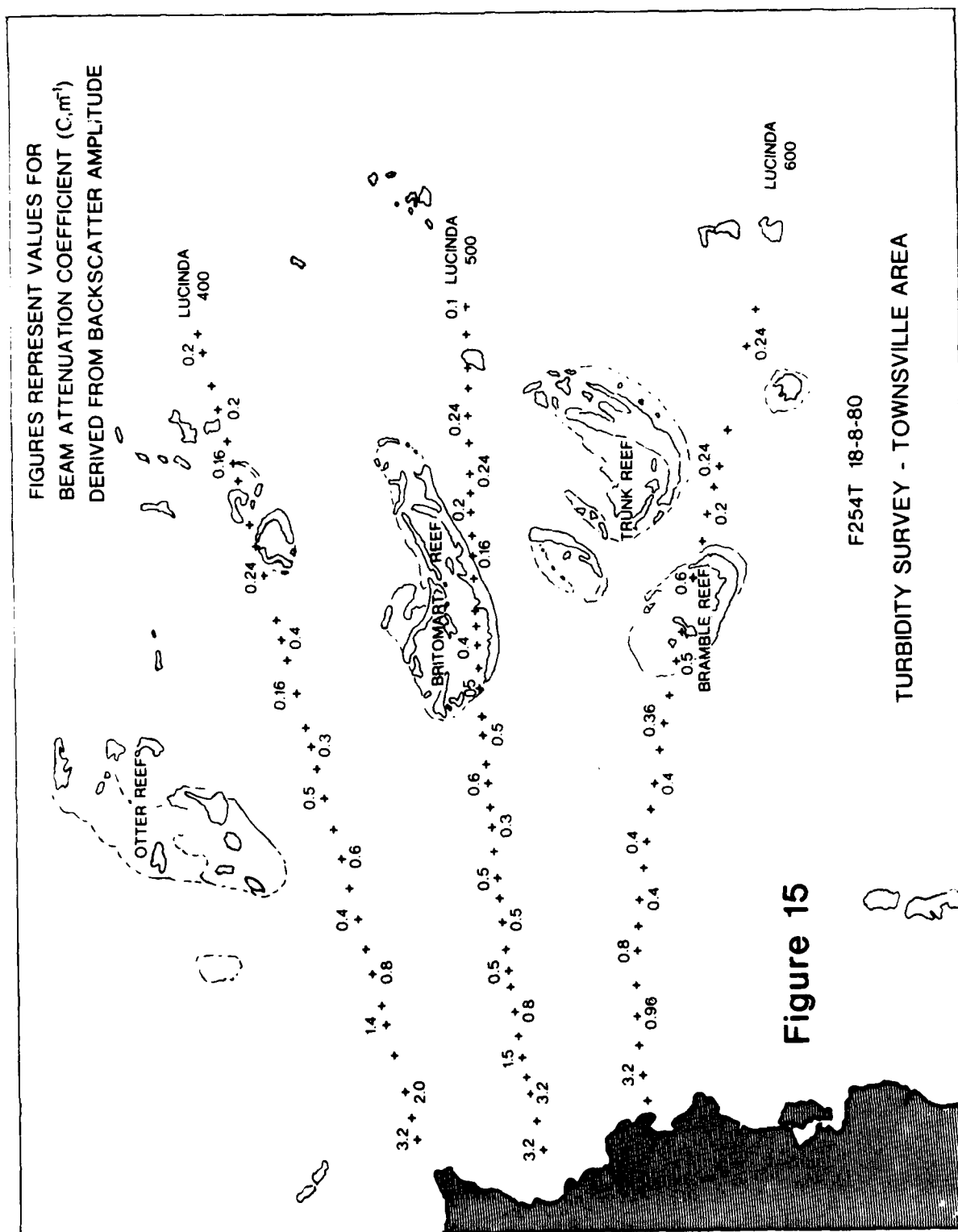
Figure 15

EFFECT OF GREEN RECEIVER FIELD OF VIEW
ON BOTTOM SIGNAL AMPLITUDE
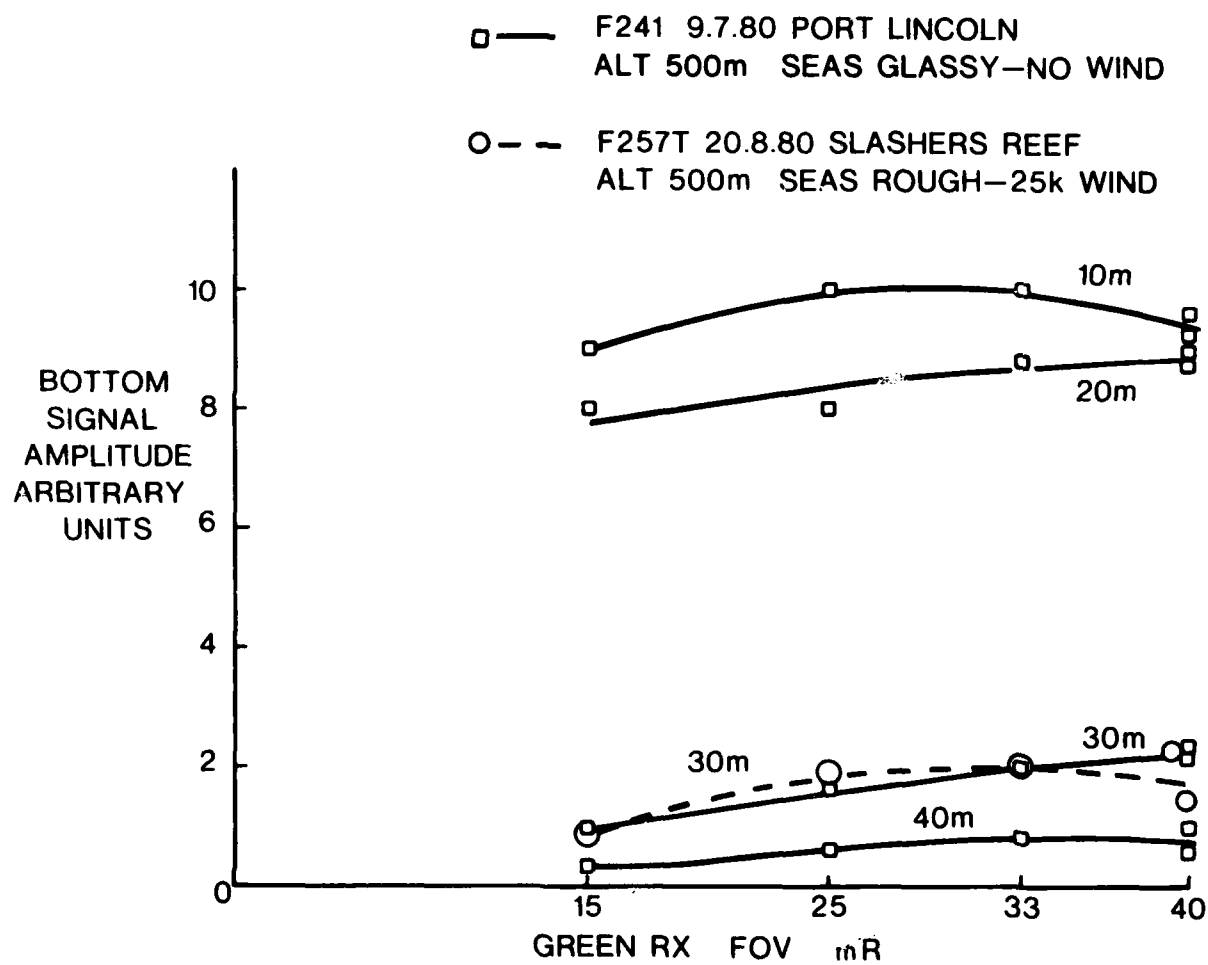
Figure 16
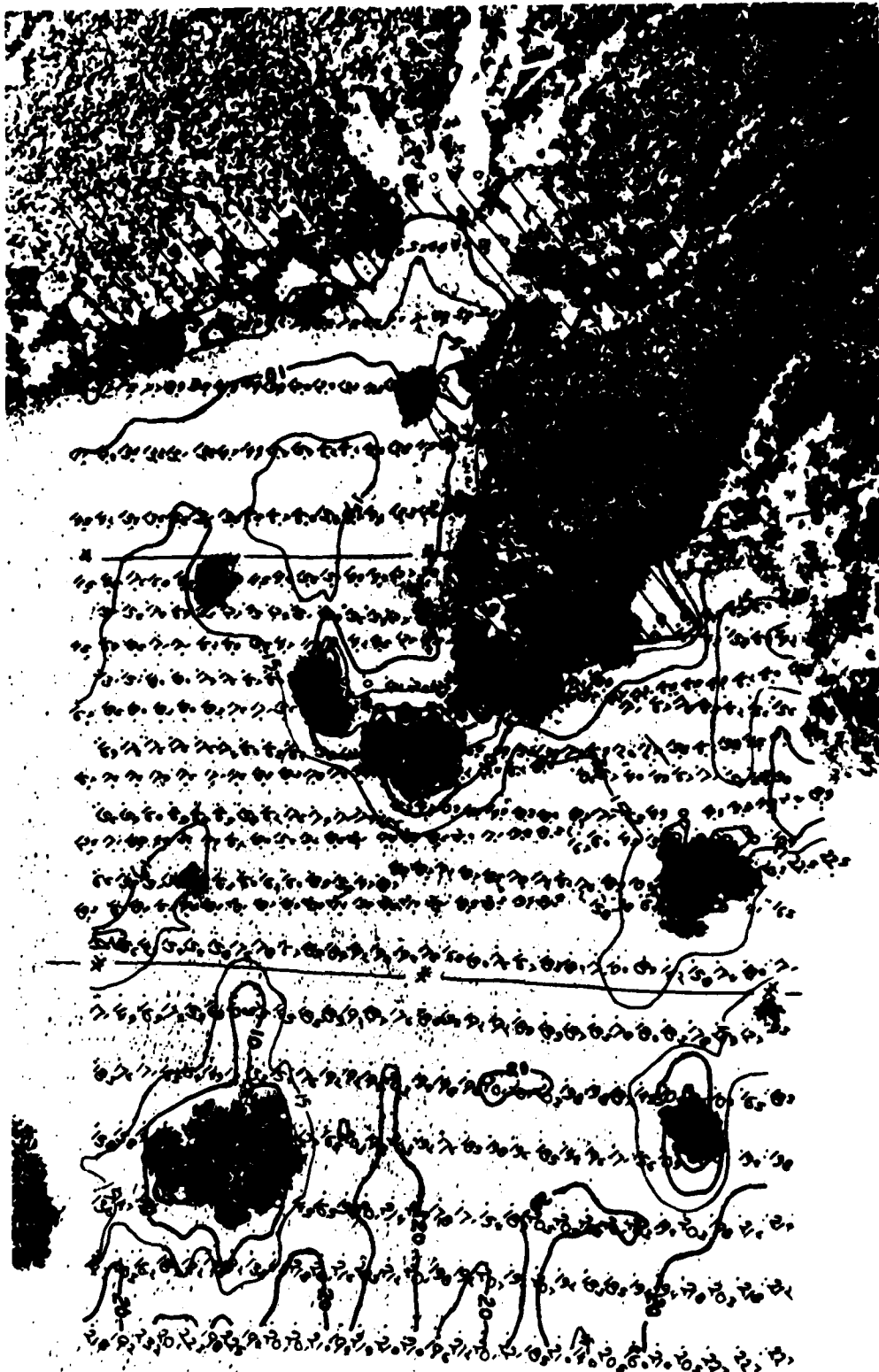
Figure 17 MICROSURVEY AT BRITOMART REEF: LAGOON
DEPTHS AND CONTOURS PLOTTED FROM TWO
TWO-SECOND OVERLAPPING PASSES
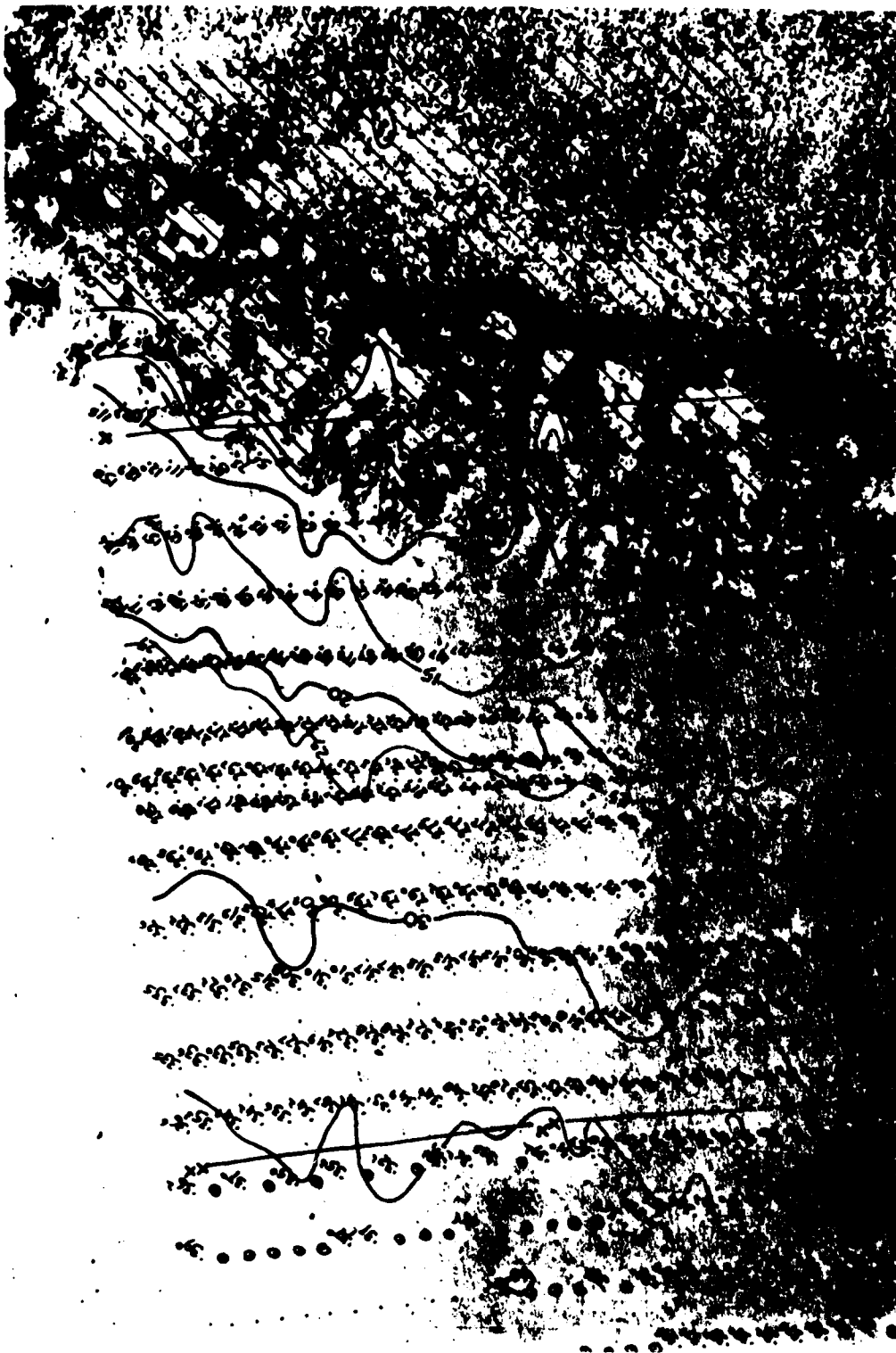
Figure 18

MICROSURVEY AT BRITOMART REEF: OUTER
OCEAN EDGE DEPTHS AND CONTOURS PLOTTED
FROM TWO TWO-SECOND OVERLAPPING PASSES
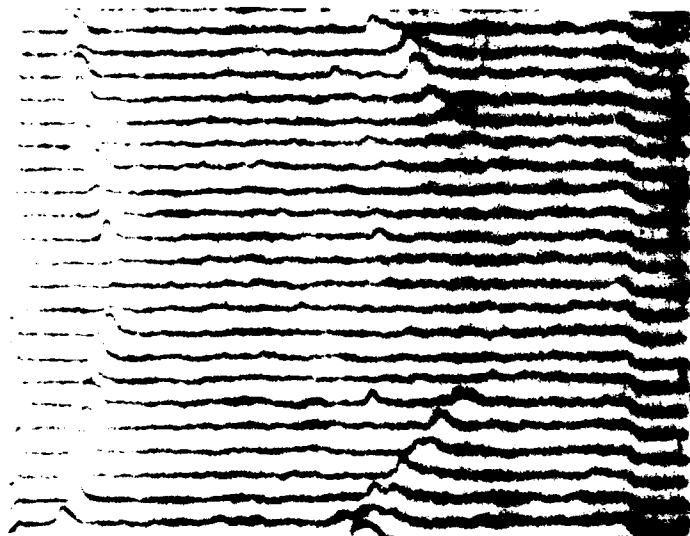
DAY

F257 20-8-80
BRITOMART REEF

RUN 6

ALT 468m
TIME 1.06.52
EHT 2.06 kV
BIOM 0.25 V
FOV 40 mR
BLOCK 4 mR
Tx 2.5 mJ
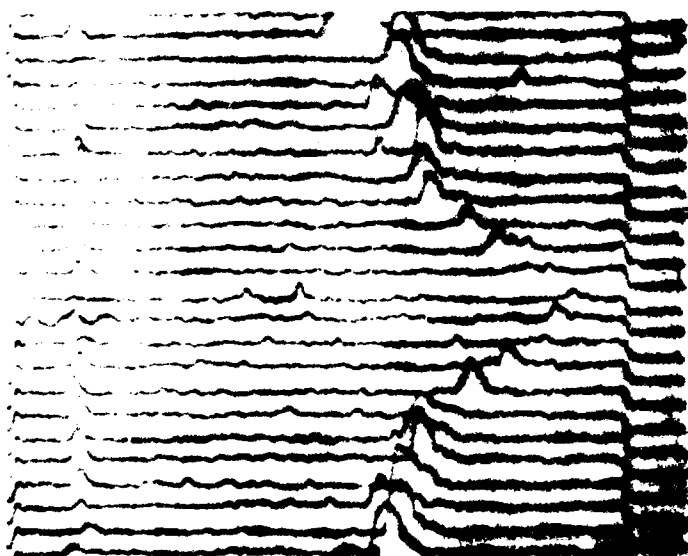
NIGHT

F256 19-8-80
BRITOMART REEF

RUN 6

ALT 492 m
TIME 1.12.20
EHT 2.35 kV
BIOM 1 V
FOV 40 mR
BLOCK 4 mR
Tx 2.5 mJ

SURFACE 10   20   30   40   50 m

COMPARISON OF DEEP WATER RETURNS
DAY AND NIGHT, BRITOMART REEF

Figure 19

0 5 10 15 20 m
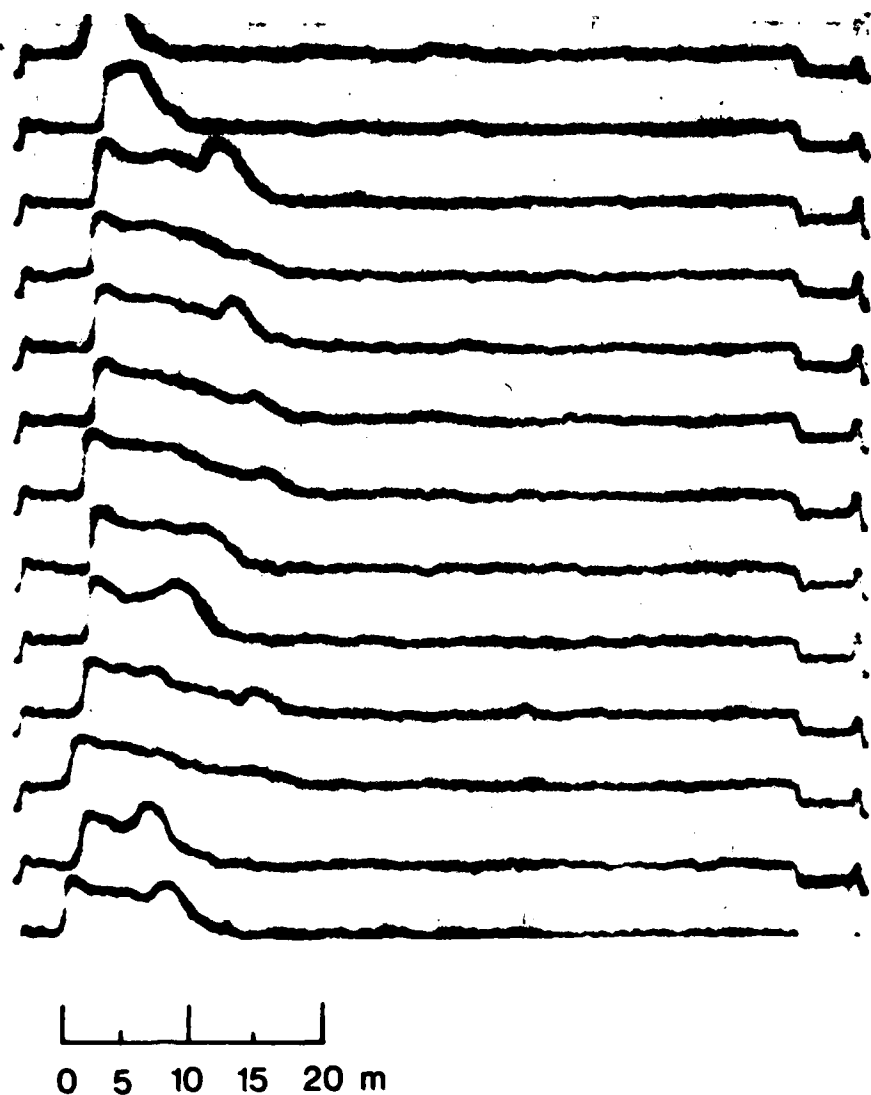
**SUBSURFACE RETURNS FROM SHALLOW
TURBID WATER PICKERSGILL REEF**

F249T 9-8-80

FOV 40 mR BLOCK 0 mR

NO VARIABLE GAIN ON PHOTOMULTIPLIER

Figure 20
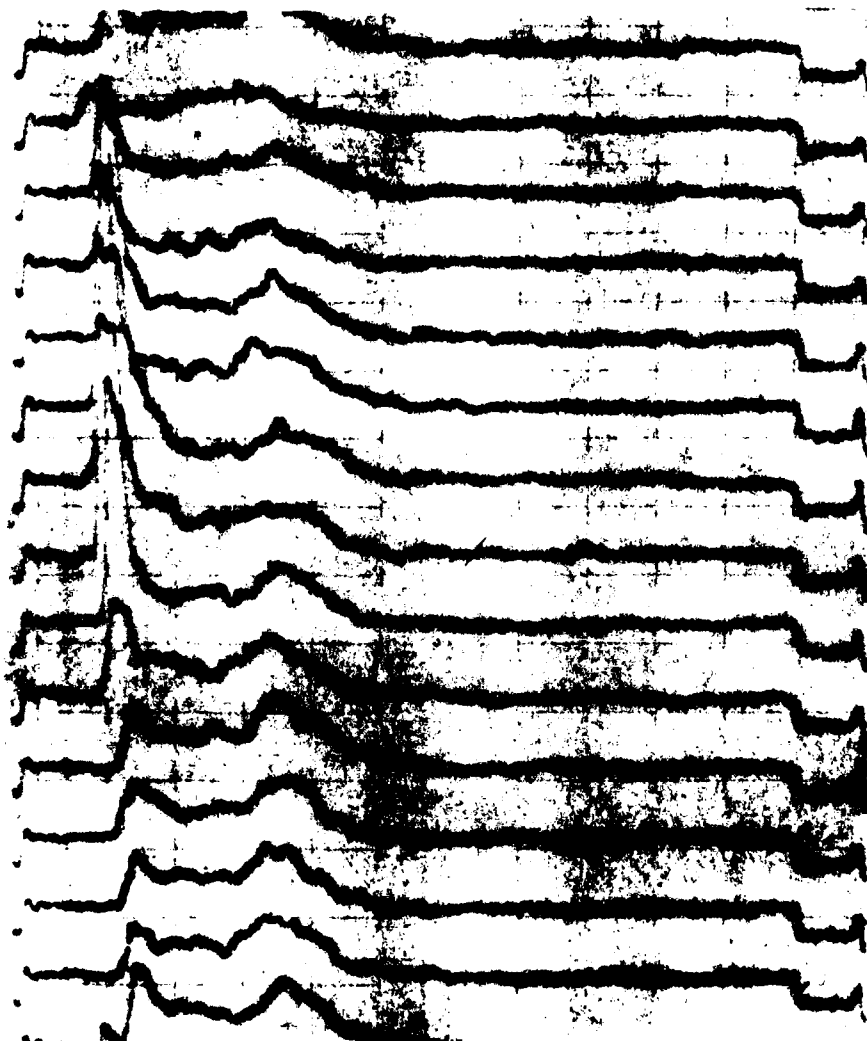
UNUSUAL SUBSURFACE RETURNS NEAR LUCINDA

F252T 00.15.20
FOV 40 mR BLOCK 0 mR
NO VARIABLE GAIN ON
PHOTOMULTIPLIER

Figure 21

COMPUTER PRINTOUT : BRITOMART REEF
20-8-80 F257T

DEPTHS IN METRES

TRACK 11 (PORT)	10	9	8	7	6	5	4	3	2	1(STBD)	0	SCAN
24.0	22.2	24.6	22.4	19.9	25.1	25.3	26.9	24.2	23.5	26.0	25.8	1
24.4	21.5	24.4	22.6	19.3	25.1	26.0	26.0	22.6	26.0	27.6	22.0	2
23.7	23.1	23.5	21.7	22.4	24.9	26.0	26.0	22.8	26.4	26.2	22.0	3
24.9	21.5	22.8	21.7	23.3	24.4	24.6	26.0	24.0	26.0	25.3	19.5	4
18.8	22.6	22.4	22.6	21.7	22.8	23.1	26.0	24.2	24.9	24.0	17.5	5
18.4	23.3	23.3	22.2	19.7	23.1	25.3	26.2	24.9	14.1	22.8	20.4	6
17.7	24.2	24.4	23.7	0.0	23.1	25.5	25.8	24.9	10.8	16.4	14.8	7
18.1	23.7	24.9	24.0	23.7	22.4	24.0	26.0	25.5	10.3	0.0	22.8	8
15.5	23.7	24.2	24.6	23.5	21.7	21.7	26.0	25.3	12.3	14.3	21.5	9
13.4	22.6	24.4	25.1	24.6	18.4	17.9	26.2	24.9	22.0	23.5	22.6	10
13.2	21.3	23.5	24.6	24.6	16.6	17.0	26.4	26.2	22.4	20.4	22.8	11
14.3	20.6	23.5	24.9	24.6	19.0	22.6	26.7	26.4	25.8	26.9	26.2	12
19.5	17.2	22.4	23.5	23.7	23.1	24.9	26.2	24.0	26.4	24.9	27.8	13
19.7	15.2	21.7	24.0	24.6	24.9	25.5	25.8	22.8	27.1	28.0	28.0	14

0140.04   0459.58   7944.95 **ARGO POSITION**

19.9	14.6	19.9	23.3	24.0	26.0	26.7	25.5	25.5	27.3	25.3	28.0
20.6	14.1	21.3	23.1	25.5	26.7	27.1	24.9	26.7	28.0	17.5	24.4
17.9	14.6	22.8	22.0	25.5	26.0	27.3	26.9	27.1	27.8	0.0	25.1
18.1	14.6	22.8	24.9	25.8	26.0	26.2	27.3	27.8	26.7	22.6	24.6
18.6	18.8	22.6	25.1	25.5	26.0	26.2	27.3	27.1	26.9	25.5	26.2
18.8	19.3	22.0	24.6	24.6	24.9	24.9	26.9	26.2	26.0	28.2	26.9
17.0	19.5	22.6	24.2	24.0	25.5	26.2	26.2	26.0	27.1	26.9	28.9
17.5	19.5	23.1	23.5	24.4	24.9	25.5	27.3	26.7	27.3	29.1	26.9
12.1	16.4	22.8	23.1	24.6	24.6	26.0	26.7	26.0	25.3	26.4	28.7
11.6	17.7	22.8	23.5	24.4	24.2	26.9	27.6	27.3	25.5	24.2	25.5
11.6	18.6	22.6	23.5	24.4	24.0	27.1	27.8	27.3	25.1	22.6	27.6
11.0	18.4	22.4	23.7	24.4	25.1	26.7	27.8	26.9	24.6	20.8	22.2
13.7	18.8	22.2	22.2	24.2	24.6	26.7	27.6	26.9	24.6	19.9	22.8
13.9	18.4	22.0	21.7	23.7	24.9	26.2	26.7	27.3	24.4	20.6	11.0

0140.03   0460.08   7945.35

12.3	16.8	21.7	22.0	23.3	25.5	26.0	25.8	26.9	24.4	20.4	11.0
12.5	16.6	21.5	21.7	23.3	24.9	25.5	24.9	26.7	25.1	24.6	9.6
9.4	10.3	19.7	21.1	22.4	24.0	25.5	24.6	26.7	25.8	24.6	0.0
8.5	10.1	19.9	21.3	21.1	23.7	25.1	25.8	26.7	24.9	24.6	19.3
0.0	11.9	17.9	20.2	16.1	24.2	24.6	26.0	26.2	26.0	24.2	19.9
0.0	13.0	17.2	19.9	15.0	23.3	24.9	25.8	25.5	26.4	23.7	22.2
0.0	11.4	16.6	19.9	15.0	23.7	24.4	24.4	25.5	26.4	22.6	23.1
5.3	11.9	16.6	19.5	19.3	23.1	24.6	24.4	26.4	26.4	24.9	16.6
0.0	5.3	14.8	18.6	21.3	23.3	23.5	24.4	26.2	26.4	23.5	15.0
0.0	0.0	15.2	18.1	21.3	22.6	23.1	24.2	26.4	27.1	20.6	16.1
5.4	5.4	12.8	17.5	21.1	22.8	23.3	18.6	25.5	27.1	24.2	22.6
5.3	0.0	12.3	17.2	20.8	22.0	23.1	19.7	23.3	27.1	25.8	23.1
5.4	5.6	9.6	9.9	19.3	19.9	22.4	21.7	24.4	26.9	26.0	26.0
5.3	6.0	9.6	5.6	18.8	19.9	21.7	20.8	26.0	26.9	27.6	26.0

0140.03   0460.57   7945.85

Figure 22

COMPUTER DEPTH PRINTOUT COUPLED TO WAVEFORMS
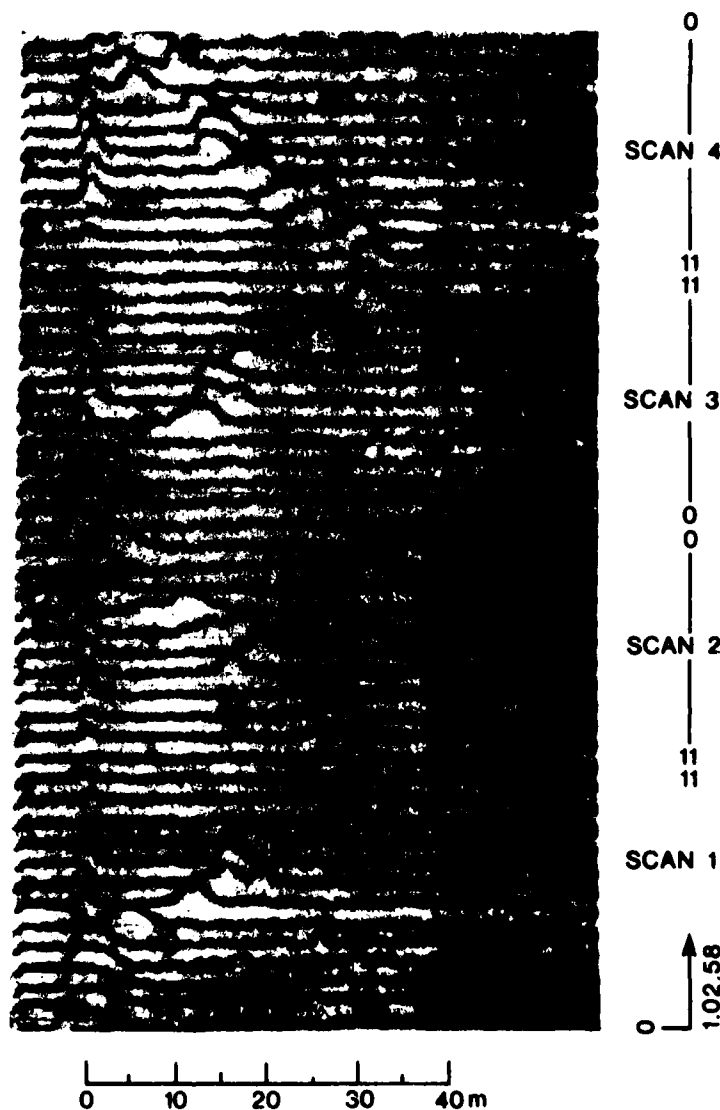
11	10	9	8	7	6	5	4	3	2	1	0	
31.1	31.1	29.1	19.5	16.6	16.8	12.5	5.6	0.0	0.0	0.0	0.0	1
30.9	0.0	28.2	26.7	17.0	20.4	17.9	11.9	0.0	0.0	5.3	0.0	2
31.4	30.9	25.8	26.4	17.9	14.3	14.1	12.8	0.0	0.0	0.0	0.0	3
31.6	30.7	25.8	0.0	18.4	14.1	13.9	12.3	5.6	5.4	5.3	0.0	4
32.0	31.6	25.8	22.4	23.3	23.3	15.7	17.5	8.1	5.3	0.0	0.0	5
0.0	30.9	0.0	0.0	19.9	15.9	14.3	12.1	12.5	7.2	7.4	0.0	6
0.0	32.0	30.9	24.0	21.5	15.9	14.8	13.2	11.6	7.2	6.0	0.0	7
0.0	31.1	30.7	24.4	19.7	17.7	16.4	13.4	12.3	11.6	7.4	27.6	8
0.0	32.5	31.1	30.2	26.'	26.2	17.0	13.7	12.8	12.8	8.7	0.0	9
0.0	31.8	31.1	29.8	0.0	23.3	16.4	15.5	13.4	12.8	8.3	5.3	10
0.0	33.4	32.0	29.6	29.1	21.5	17.5	15.9	13.2	13.2	10.5	5.4	11
0.0	32.5	31.8	30.2	29.1	26.9	25.3	20.2	14.6	15.9	14.8	6.9	12
0.0	34.0	32.7	31.4	30.2	28.0	24.9	18.6	15.0	16.4	13.2	9.2	13
0.0	33.4	32.5	0.0	29.8	27.8	25.3	21.5	24.4	16.4	16.4	0.0	14

0142.72   0460.72   7998.55

Figure 23

WRELADS Laser Development

B A See

SUMMARY

The development program for the laser for the WRELADS
system as described.

The program spanned four years of investigation in various
aspects of the problem of designing a high repetition
rate (168 Hz) laser capable of delivering the short
(5 nsec FWHM) pulses required.

The design proposed adopts a novel approach to the major
problem of thermal birefringence, no attempt is made to
compensate for this. A depolarising assembly is used to
spatially modulate the coupling and make the thermal
birefringence a perturbation rather than the dominant
effect.

INTRODUCTION

The specification of the laser required for the WRELADS
system is shown in Table 1. The specification is largely
determined by the operational requirements - aircraft
height, speed, spacing of data points and resolution.

The development program spanned some four years and
concentrated from the outset on a frequency doubled
Nd:YAG laser.

The problem areas in designing a laser to meet this
specification are listed in Table 2 along with possible
solutions.

   i)   The short pulse could be produced by a Pulse
         Transmission Mode laser or a short cavity design.

   ii)   At the outset a 75mm arc length lamp was selected
         to cope with the envisaged average power loading
         of some 2KW. Most of the work reported was
         therefore done on a 75mm long 6mm diameter YAG rod.

   iii) When it was attempted to run the lamps at 168 Hz,
         the current pulses were seen to be erratic in
         both amplitude and timing. The phenomenon is due
         to variations in the anode voltage in the post
         flash recovery. The solution was to increase the
         simmer current from the 50 mA level to between
         1 and 4 amperes. One could well be concerned over
         what effect this may have on lamp life. Subsequent
         limited experience indicates that it may prolong
         lamp lifetime. Lifetimes of 50 to 100 million
         flashes have been obtained, in excess of 100 hours
         at 168 Hz.

   iv)   Thermal lensing can be overcome by choice of
         mirrors or internal lenses.

v)   Thermal birefringence is the most difficult
     problem. At first the only option seen
     was to compensate but compensation techniques
     make the cavity physically longer. Hence the
     inital emphasis on finding an alternative
     approach for generating short pulses - the
     PTM laser.

vi) As it is difficult to design a laser having all
     the previous features and with low divergence,
     CD*A was recognised as being the preferred
     doubling material. Temperature tuning was
     considered but overseas experience seemed to
     indicate that damage could occur due to a phase
     change just above the phase match temperature.
     Angle tuning with CD*A still offered about
     twice the acceptance angle of KD*P and avoids
     the complications of temperature tuning.

THE PTM LASER

Early effort was concentrated on investigating the PTM
laser as a means of producing the short pulses. In this
laser the pulse width is essentially equal to the round
trip cavity time. Thus a 75cm cavity length gives pulses
of full width 5 nsec.

Before work could begin on the PTM laser an intensive
investigation of fast switching techniques was carried
out to develop the very fast double action Q switching
required.

An avalanche transistor circuit was devised using the
2N5192 which would reliably give the fast (5 nsec) dual
switching across a single Q switch (ref 1).

The pulses obtained from the PTM laser are shown in figure
1 with cavity length as a parameter. A 60 - 80 cm cavity
gave pulses of nearly ideal shape. The energy output was
however limited by gain saturation to less than 40 mj.

In a conventional laser, the drop in output due to
thermal birefringence at high average power is well known.
The techniques of thermal compensation are all based on a
rotation of the plane of polarisation by 90° on each pass
through the rod, effectively interchanging radial and
tangential components. The technique used for the PTM
laser is similar to a scheme used by Oettinger with a
ruby laser. The schematic of the laser is shown in
figure 2. For high rate operation it was found necessary
to introduce a second Q switch to prevent free running
laser action in the side arm.

The system is now quite complex and the energy output
was further restricted by saturation due to the double
pass cavity to $\sim$ 30 mj. (ref 2)

UTILISATION OF DEPOLARISATION

While studying the effects of thermal birefringence, an
alternative approach of utilising the phenomenon rather
than attempting to compensate, suggested itself.

The drop in output of a normal laser at high rates is due
to the depolarisation in the rod resulting in some energy
being rejected by the polarising prism. The total energy
extracted remains unchanged. In principle it would be
possible to close the cavity with 100% mirrors and make
the thermally depolarised component the output. At
low rates however, there would be no output. Introduction
of a $\lambda/4$ plate with variable azimuth allows the coupling
to be varied. Figure 3 shows the measured output from
such a laser. The output is indeed essentially constant
and independent of repetition rate. The minor variations
seen are thought to be due to thermal lensing, no attempt
was made to correct for lensing in this measurement.

There is a problem with such a configuration. The combined
effects of thermal birefringence in the rod and phase
shift in the $\lambda/4$ plate results in the coupling being variable
across the rod aperture. To study how the coupling varies,

a computer program was written to obtain contour plots
of the coupling and average coupling values. The program
computes the polarisation state of the light for an 80 x 80
grid of points using Jones calculus, with the waveplate
azimuth and rod thermal distortion as parameters. The
model is static and assumes a beam of uniform intensity
incident on the rod.

To obtain intensity distributions from this model the
dynamics of the laser would have to be taken into account.
Where the coupling is low, the laser would have a high
internal intensity, and low internal intensity where the
coupling is high. The contour plots thus represent
coupling and not the output intensity distribution across
the rod aperture. Figure 4 illustrates the contours
obtained for the laser of figure 3. From left to right
the waveplate azimuth changes from zero to 45°. From
top to bottom the rod thermal distortion changes from
$\lambda/4$ centre to edge to λ.

Despite the limitations of the static model the observed
output intensity distributions possessed the symmetry of
these contours. Where the coulping is high, laser action
tends to be suppressed. Where the coupling is low the
internal energy density becomes high which could lead
to damage.

The potential for damage could be avoided if one could
effectively depolarise the beam on a scale small compared
to the mode size so that the thermal birefringence became
a perturbation rather than the dominant effect.

To achieve depolarisation, a lens like wave plate was
fabricated where a radial variation of phase shift was
deliberatley introduced. Since one must compensate for
the lensing of the waveplate, a second lens of opposite
sign is required. This may be fabricated as an optical
rotator, a further lenticular waveplate or a simple
glass lens. Since one now has a pair of lenses it is
convenient to design these as a zoom assembly to also
correct for the thermal lensing in the rod. A patent

has been sought on the depolarising assembly.

The computer model for obtaining coupling contours was
extended to obtain contours of coupling with a lens like
waveplate plus the thermal birefringence of the rod.

Figure 5 (a) shows the contours obtained with a fixed
waveplate azimuth of 45°, rod thermal distortion varies
from zero to λ from top to bottom. The lens like
waveplate here has a 2λ phase variation from centre to
edge (of the laser beam). The numerical results from
the computer model give an average coupling value which
remains fairly constant at 40 to 50% but from the patterns
it is obvious there are still appreciable areas of the
rod where the coupling still is low and the internal
energy density could become high.

A depolarising zoom assembly was fabricated and tested
experimentally. The resultant intensity distribution
was made more uniform than for the flat $\lambda/4$ plate.
The areas of low coupling may not be a problem as the
mathematical model does not take into account the
astigmatic behaviour of both rod and waveplate.

Since the possibility of a problem still exists, further
investigation of means of removing these potential hot-
spots was undertaken.

THE CROSSED PORRO RESONATOR

The crossed porro resonator patented by both Ferranti and
ILS offers a means of smoothing the internal energy
distribution. This resonator is shown in figure 6.
The smoothing effect is obtained as on each pass through
the rod the beam is stepped across alternately by each
porro prism.

First, to see what effect a single Porro would have on
the coupling, contours were obtained with the rod
thermal distortion, and the single Porro prism.
These are shown in figure 5 (b) and rather resemble the
flat $\lambda/4$ plate with additional symmetry imposed by
the roof edge.

Figure 5 (c) illustrates the computed coupling contours
with the lens like waveplate, the single Porro prism and
the rod thermal distortion. These are considerably better
as the potential hot spots are smaller.

Finally to investigate the averaging effect of the crossed
Porro prisms the program was further modified to obtain
coupling contours using the two Porro prisms with the
coupling Porro at a fixed 45° azimuth and the other at
various azimuth angles. The modelling was becoming
increasingly complex and this last model did not
include the lens like waveplate. Figure 7 shows the
averaged internal energy densities between two Porro
prisms in the configuration described above. The coupling
Porro azimuth varies in 5°steps. The angle between roof
edges varies from 90°at the top left to 50° at the bottom
right.

Reasonable averaging is obtained in the range 55° to 80^0
with best averaging in the range 65° to 75°.

At the pump levels at which this laser operates, the
optimum coupling is around $\dot{}0\%$. For the angular range
given above coupling varies from 40% to 60%, i.e. about
optimum.

The laser design finally proposed for WRELADS adopts the
principle of utilising the thermal depolarisation rather
than attempting to compensate. It is referred to as the
Birefringence Coupled Laser (BCL).

The final design is shown in figure 7. A short cavity is used
to produce the short pulses. The depolarising zoom lens
assembly is used to depolarise and also compensate for

for thermal lensing.   The Porro prisms provide coupling
and averaging of the intensity distribution.

CONCLUSION

This system has been run at 168 Hz and with 8J pump energy
delivery   ∿ 70mj in the I.R. an average power output of
∿ 12 Watt.   With the zoom lens assembly divergence can be
held close to the low rate value of ∿ 3 mrad.   Using
angle tuned CD*A up to 25 mj of energy has been attained
in the Green.

Table 1.

W/RELADS Laser Specification.

Output Energy	9 mJ at 532 nm
Peak Power	1 MW at 532 nm
FWHM	5 nsec
P.R.F.	168 Hz.
Pump Energy	< 10 Joule.

TABLE 2

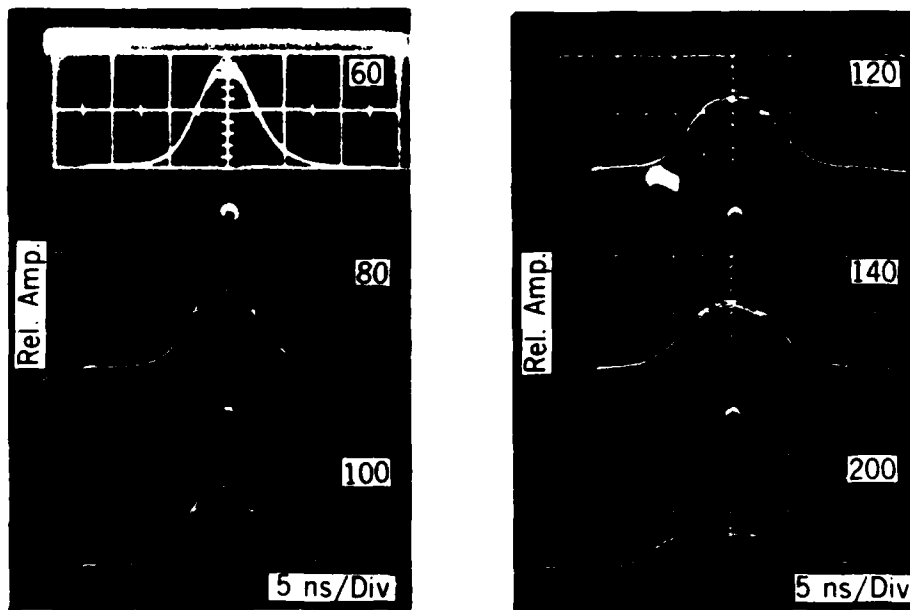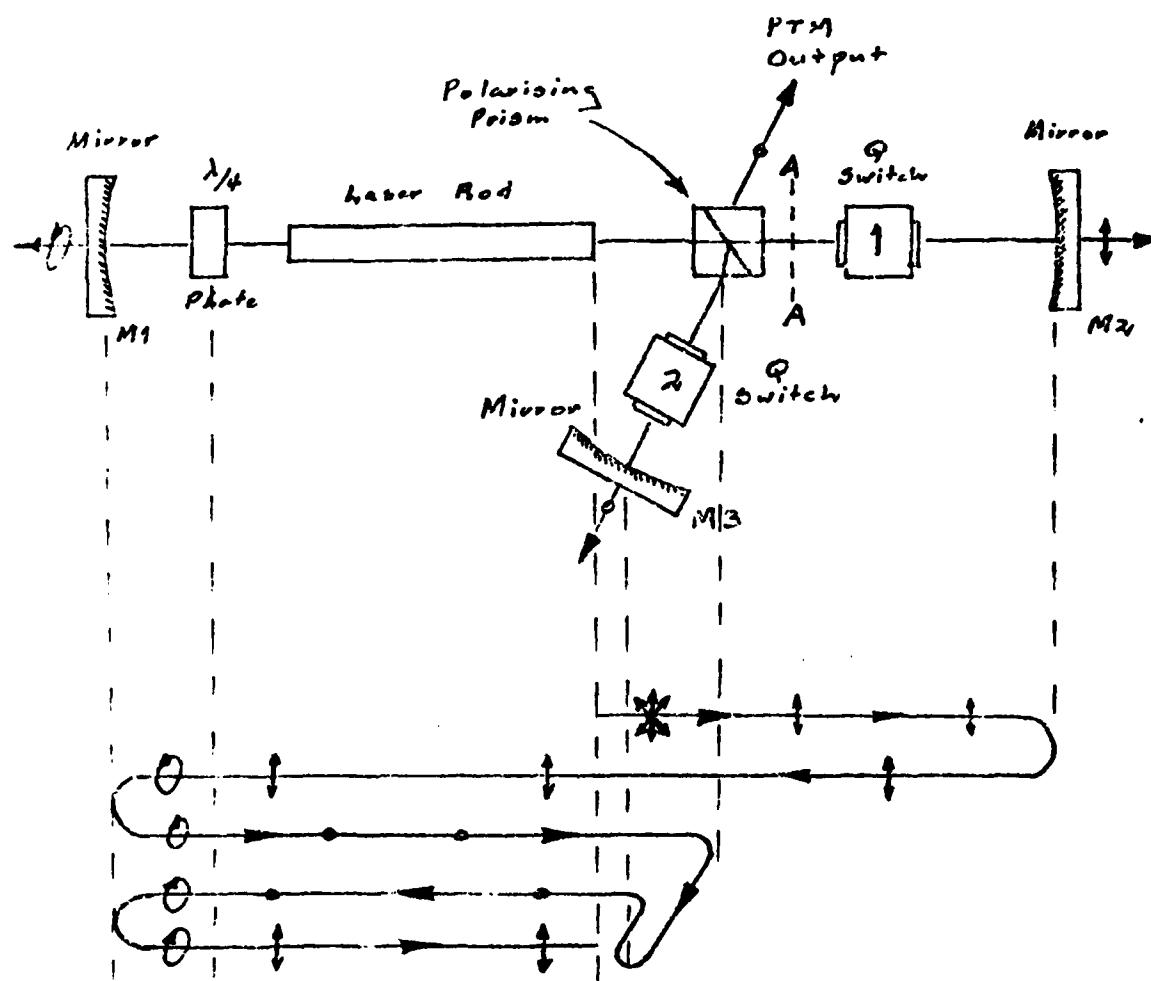| PROBLEM	POSSIBLE SOLUTION
SHORT PULSE	1. PULSE TRANSMISSION MODE (PTM) LASER 2. SHORT CAVITY
POWER DISSIPATION IN FLASHLAMP	LONGER LAMP (AND ROD)
ERRATIC LAMP BEHAVIOUR	HIGH SIMMER CURRENT
THERMAL LENSING	COMPENSATION
THERMAL BIREFRINGENCE	1. COMPENSATION 2. UTILISATION
HARMONIC GENERATION	CHOICE OF MATERIAL

Figure 1   PTM pulses

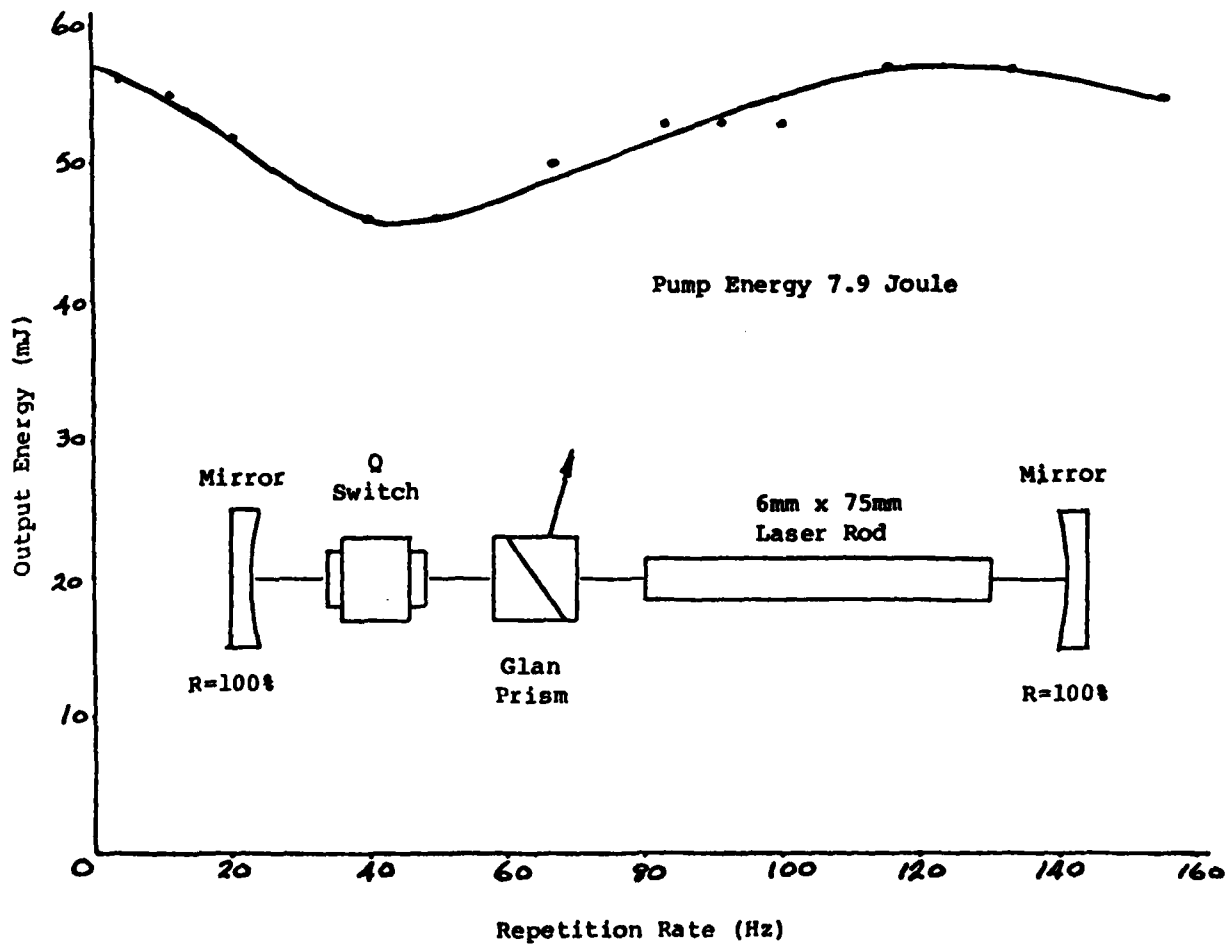Figure 2 : Folded Thermally Compensated Laser
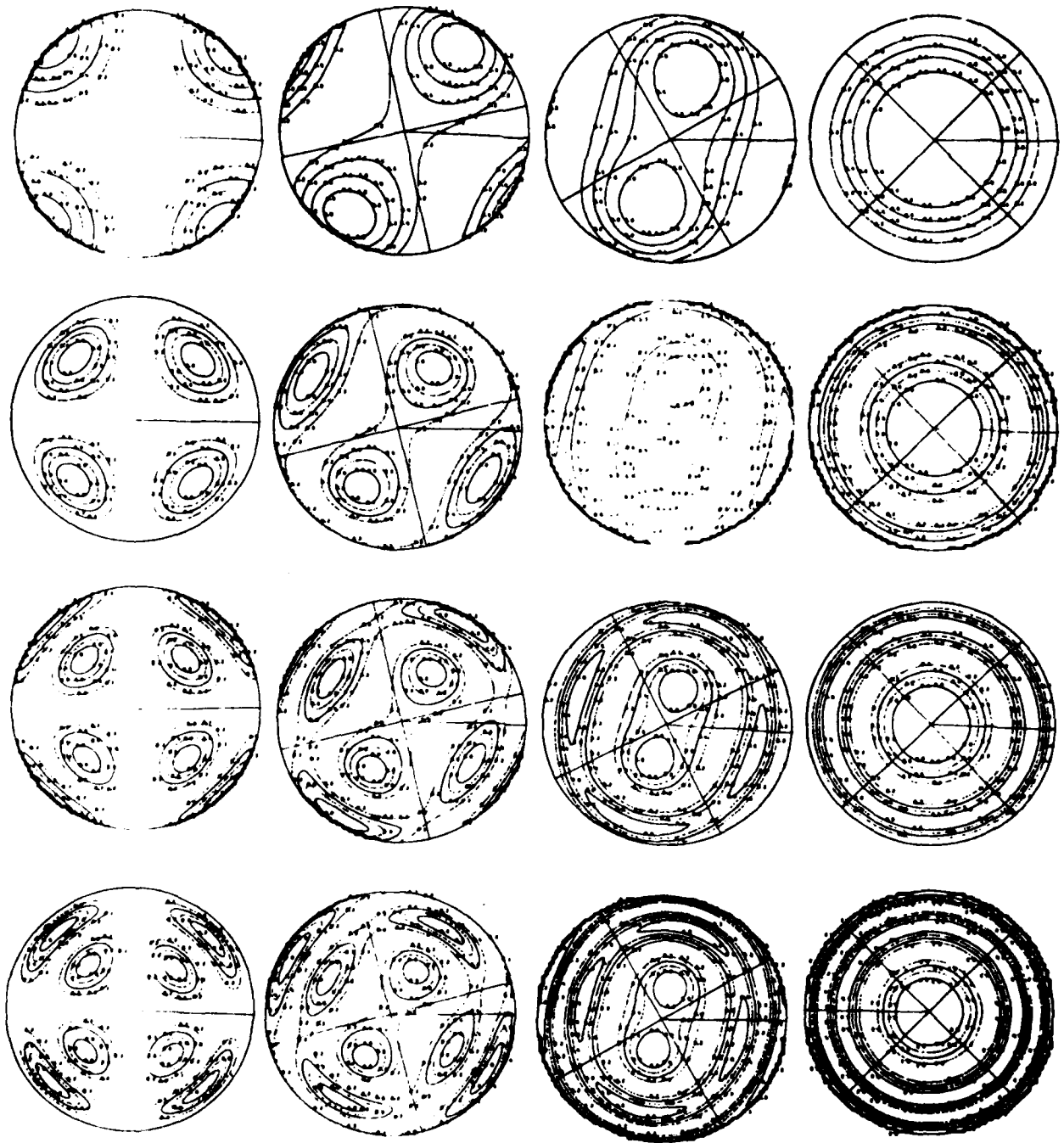
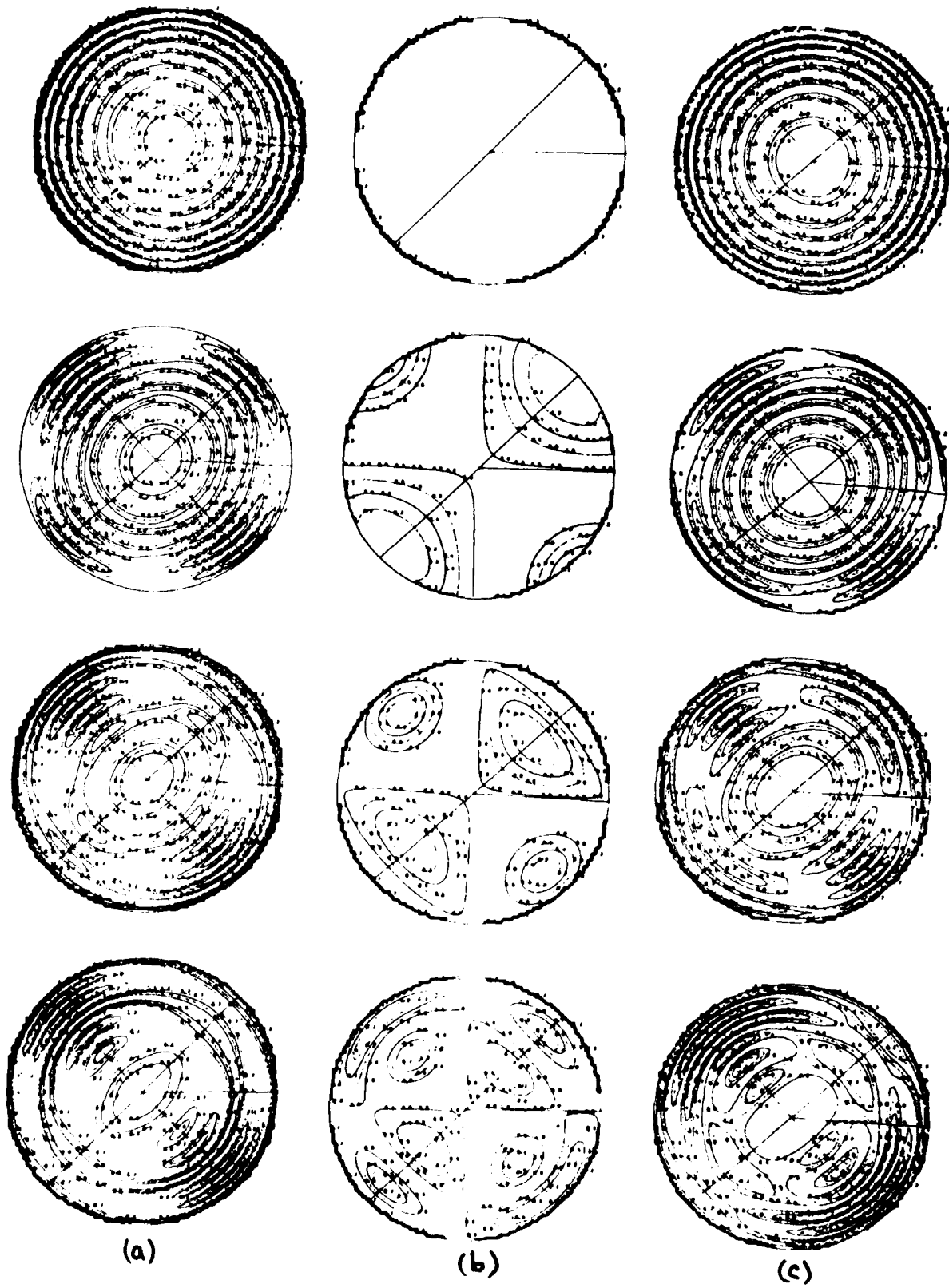Figure 3: Polarisation Coupled Laser

Figure 4 :
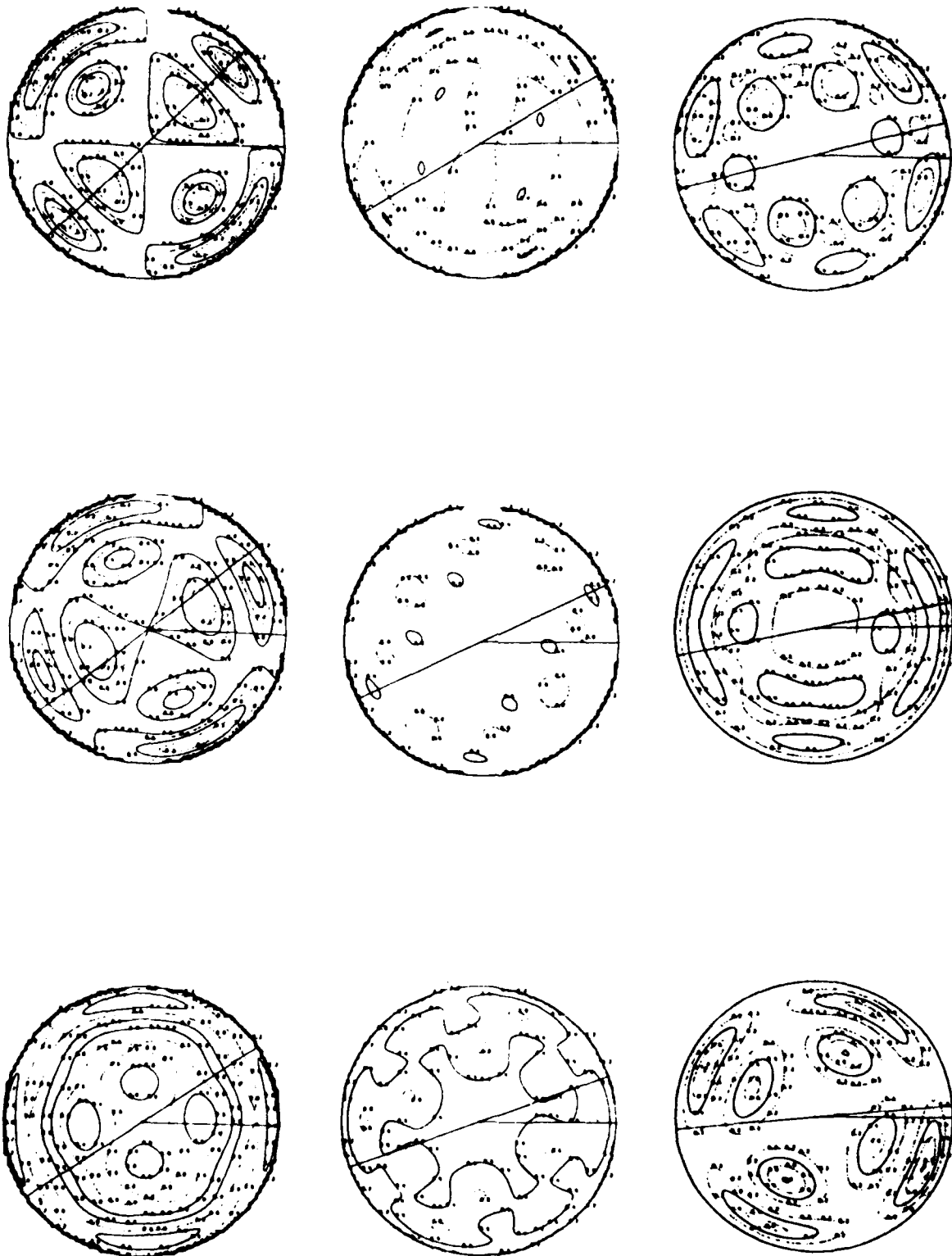
(a)　　　　　　　　　(b)　　　　　　　　　(c)
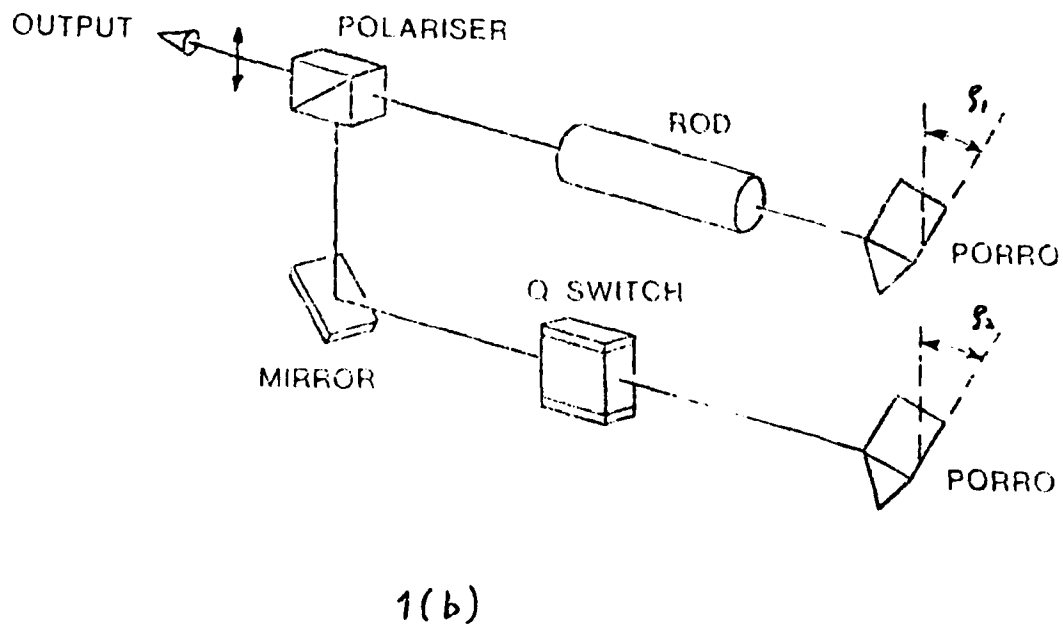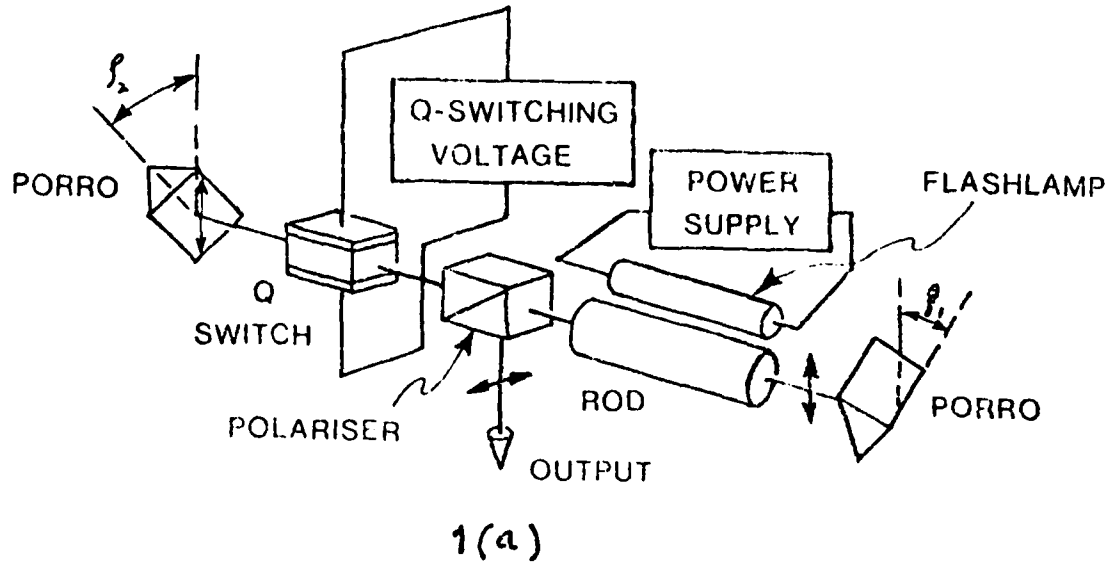
Figure 5:

Figure 6:

1(a)

1(b)

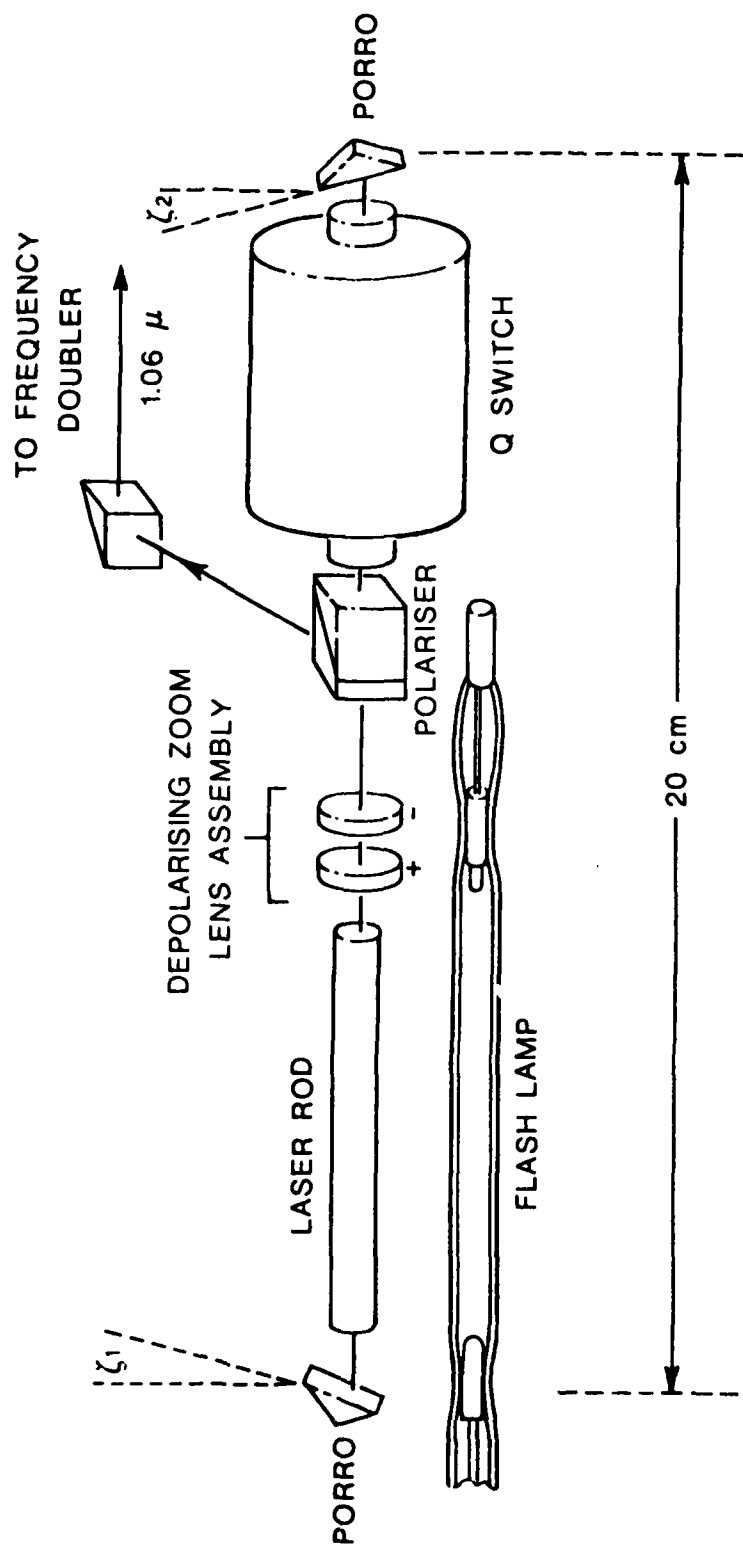Figure 1: In Line and Folded Crossed Porro Resonators.

Figure 8:   WRELADS LASER SCHEMATIC (TO SCALE)

HIGH REPETITION RATE FREQUENCY DOUBLED Nd:YAG LASER

FOR AIRBORNE BATHYMETRY

presented by

Dr Merlin Miller

To be published in Applied Optics.

Donna Northam
Mike Guerra
Mike Mack
Irv Itzkan
Charles Deradourian

September 1980

TABLE OF CONTENTS

I   INTRODUCTION

In 1977 the Airborne Oceanographic Lidar (AOL)[1] was developed
to explore the applicability of Lidar for shallow water bathymetry.
An extensive series of flight tests using the AOL demonstrated the
utility and confirmed the expected advantages of using an airborne
laser system for bathymetry[2].   Subsequently a study was conducted
to determine how an operational airborne bathymetry system might be
configured[3].   The laser was identified as a technology area re-
quiring additional development. The AOL system used a pulsed neon
laser which provides inadequate output energy for the operational
depths of interest and, which is too bulky and inefficient for heli-
copter deployment.   The required specifications for an operational
laser system are summarized in Table I.

Wavelength would fall in the range of 530-540 nm. Figure 1
shows the diffuse attenuation coefficient, K_d, measured in the
first 10 meters for various ocean waters as a function of wave-
length[4]. From this figure it can be seen that this wavelength
range brackets the optimum color for penetrating coastal waters.
Pulsewidth would be on the order of 3-10 nsec in order to obtain
adequate depth resolution. With suitable signal processing the
AOL achieved 20 cm resolution with a 7 nsec pulsewidth. Repeti-
tion rate would be on the order of several hundred pps depending
on aircraft speed, altitude and scan angle, in order for the
system to provide an adequate measurement point density for coastal
map making. Energy per pulse would be on the order of 1-2 mJ in

TABLE I

OPERATIONAL LASER REQUIREMENTS

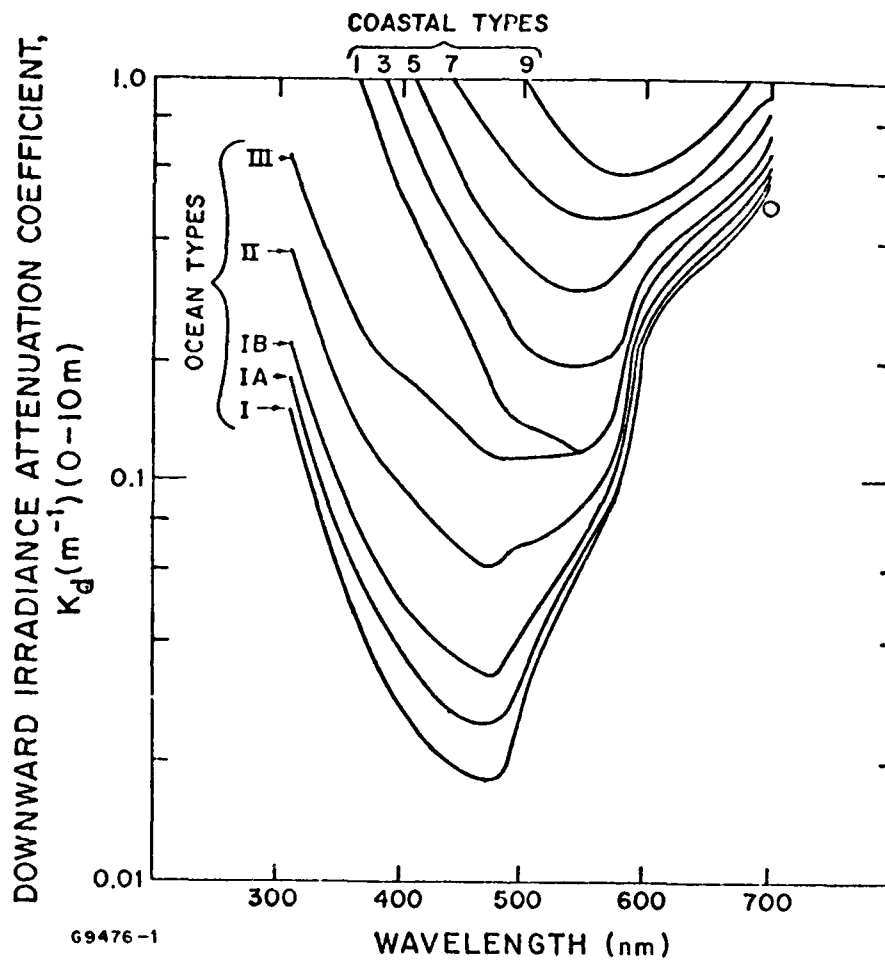|	
Wavelength	510 - 560 NM
Pulse Energy	$\geq$ 2 mJ
Pulse Duration	3 - 10 nsec
Beam Divergence	$\leq$ 3m Rad
Lamp Life	> 10^7 to 10% Degradation
Efficiency	> 0.05%
Volume	Minimum
Weight	Minimum

Fig. 1 Diffuse Attenuation Coefficient vs. Wavelength
        for Various Ocean Waters

order to provide adequate depth penetration in turbid waters. Other system parameters such as size, weight and power consumption should be minimized for aircraft operation.

An assessment of the state of the art in laser technology conducted in the bathymetry study[3], concluded that the requirements for an operational laser could most readily be met using a Nd:YAG laser. Ferguson and Rankin[5] demonstrated 400 pps operation in a prototype Nd:YAG laser operating in a Q-switched mode with a pulse width of 18 nsec. This laser has considerably higher pulse energy than required here and has been successfully operated in an airborne environment. The required short pulse duration could be met by modifying the resonator for a pulse transmission mode (PTM) operation[6].

In the course of developing a breadboard laser meeting all of the above requirements, several major technical areas were identified and addressed. These include flashlamp recovery time, thermal lensing, birefringence, Pockels cell switching and SHG damage threshold. In this paper we describe the laser system developed and the solutions arrived at in each of these problem areas.

II   LASER CONFIGURATION

The optical layout of the laser is depicted in Fig.2.   To
the right of the calcite rhomb two parallel beams of orthogonal
polarization propagate through the resonator.   These are recom-
bined by the rhomb and superimposed in the left hand side of the
resonator.   The adjustable telescope is used to compensate for
thermal lensing induced in the Nd:YAG rod by the high average
pump power.   The quarter wave plate between the telescope and
the end mirrors couples the two orthogonal polarizations.   The cylindri-
cal Nd:YAG rod (5mm diameter, 50mm length) is pumped by a single
flashlamp in a commercial silver coated, water filled, elliptical
pump cavity.   In this cavity the rod and flashlamp are displaced
from the faci to compensate for pump non-uniformity due to direct
illumination of the rod.   A transverse flow baffle divides the
center of the pump cavity to assure an adequate flow velocity for
the water cooling flow about the rod and flashlamp. The flashlamps
have an arc length of 4.5 cm, a bore of 0.3 cm and are fabricated
of stabisil quartz.   The output coupler is a 100% reflecting
mirror with a central hole through which the laser beam passes
during the high feedback portion of the cycle.   The Pockels cell/
quarter-wave plate combination serves as an electro-optic switch.
The half-wave plate in the doubler section rotates the direction
of polarization of one beam so that both have the same polariza-
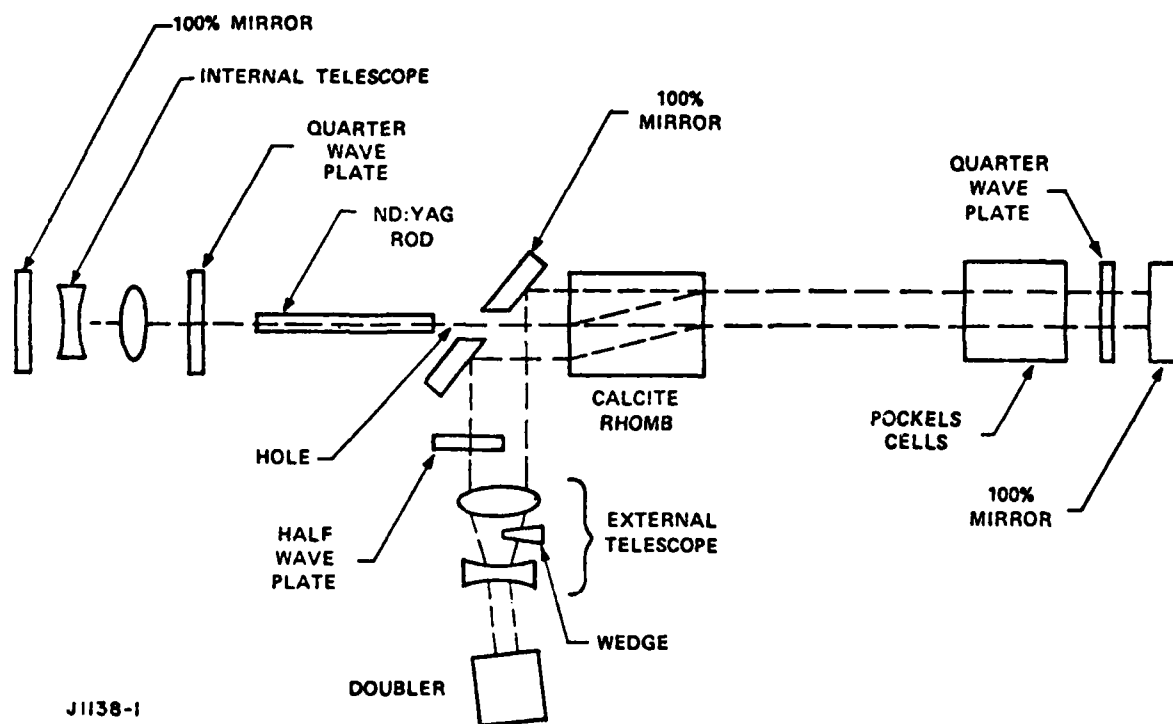tion.   The external telescope is used to increase the energy

Fig. 2 Optical System

J1138-1

density in the SHG (second harmonic generator) for greater
doubling efficiency. The SHG is a CD*A (cesium dideuterium
arsenate) crystal cut for optimum phase match at an angle of 85°.
It is housed in an oven and maintained at a temperature of 55°C.
This resonator is similar to a short pulse resonator design
developed by Ferguson and Rankin[7].

PTM Q-switching operation was chosen to achieve a narrow
pulse width with maximum output energy. The sequence of events
is depicted in Fig. 3. Initially, when the flashlamp is fired
the optical resonator is maintained in a low Q condition and
energy is stored in the laser rod. When the population inver-
sion in the rod has reached a maximum, the optical resonator is
switched to a high Q allowing the optical flux to build up.
When the flux reaches its maximum, the resonator is switched
open, gating the flux out of the resonator via the output
coupling mirror. The pulse width is uniquely determined by
the optical cavity length (assuming a negligible switch time).

AMPLITUDE

a. FLASHLAMP PULSE   TIME

TOTAL
INVERVSION

b. INVERSION (STORED ENERGY) t_1 t_2 TIME
   IN LASER ROD

V_0

VOLTS

c. POCKELS CELL VOLTAGE t_1 t_2 TIME

RELATIVE
POWER

d. OPTICAL POWER IN RESONATOR   TIME

Δt

e. LASER OUTPUT   TIME
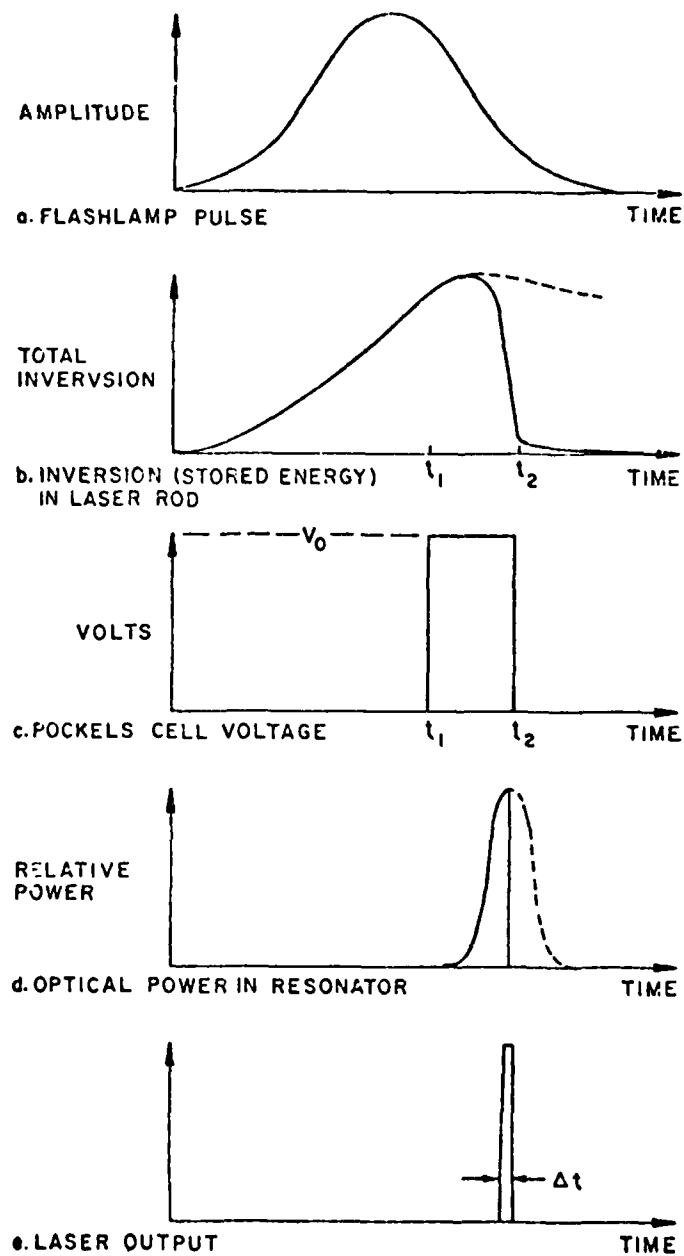
J1139

Fig. 3   PTM Q-Switching Pulse Generation-Timing Sequence

III FLASHLAMP OPERATION

The flashlamp is operated by an SCR gated resonant charging/ discharging circuit as shown in Fig. 4. · A 100 ma D.C. simmer current is maintained in. the flashtube, to provide a low discharge path impedance. The Jennings vacuum switch is used to protect the SCR from overvoltage during the initial triggering of the simmer discharge. The 130 µhy discharge circuit inductance combined with the 27 µf discharge capacitance gives a flash duration of approximately 110 µsec (FWHM). If the series inductance is not used, the flash duration is significantly reduced, and the arc no longer has sufficient time to expand and fill the bore of the flashlamp. This results in arc wander, which produces an undesirable jitter in the peak laser output. The shorter flashlamp pulse duration also reduces lamp lifetime.

The advantage in spectral matching to Nd:YAG of krypton over xenon flashlamps at low power densities has been recognized since 1967[8]. A quantitative comparative study was given by Noble et al[9]. The traditional difficulty with krypton flashlamps has been the inability to operate them at high repetition rates.

                      The source of this limitation is the relatively slow recovery time of the krypton plasma. Figure 5 shows time histories of lamp voltages for three lamps with differing gas fills. In Fig. 5a the lamp is filled with 1500 torr of krypton. In Fig 5b the fill gas is 450 torr of xenon. The
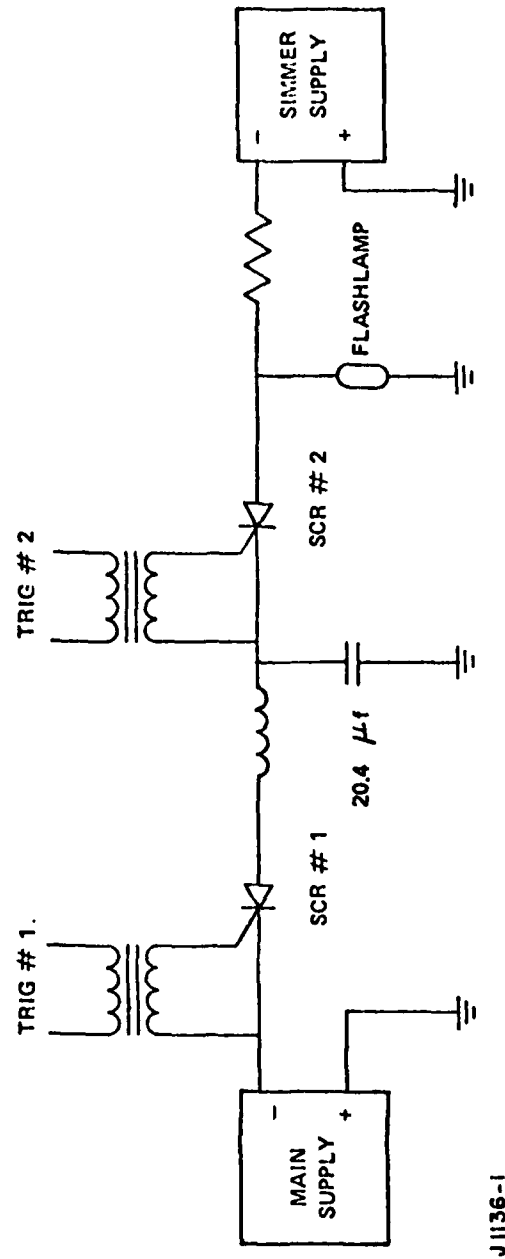
Fig. 4   Flashlamp Driver

lamp impedance during the discharge is characterized by the formula[10].

$$V = \pm K_o \, |i|^{1/2}$$

$$K_o = kl/d$$

Where k is a gas constant, dependent on pressure and type, l is the flashlamp arc length, and d is the discharge diameter.

For both lamps K_o is approximately 29.2 (volt/amp$^{1/2}$); however, the time history of the voltage traces differ. In particular, the xenon lamp voltage returns smoothly to the simmer level in approximately 1 ms while the krypton lamp voltage recovery time exceeds 10 ms implying a repetition rate limit of the order of 100 pps. In order to reduce this recovery time to less than the 2.5 ms required for 400 pps operation without radically changing circuit parameters a small amount of xenon was added to the krypton gas fill. This reduces the recovery time while maintaining the favorable spectral match of the krypton. Figure 5c illustrates the voltage recovery of a lamp filled with 700 torr of a 90% krypton/10% xenon mix. At 440 the pps measured laser efficiency operating normal mode (i.e. using a two mirror resonator without switching) with 10% output coupling (in both cases) was 0.31% for the zenon lamp and 0.42% for the krypton/zenon lamp.

200V   KRH.3   VCAMP   5.3.79
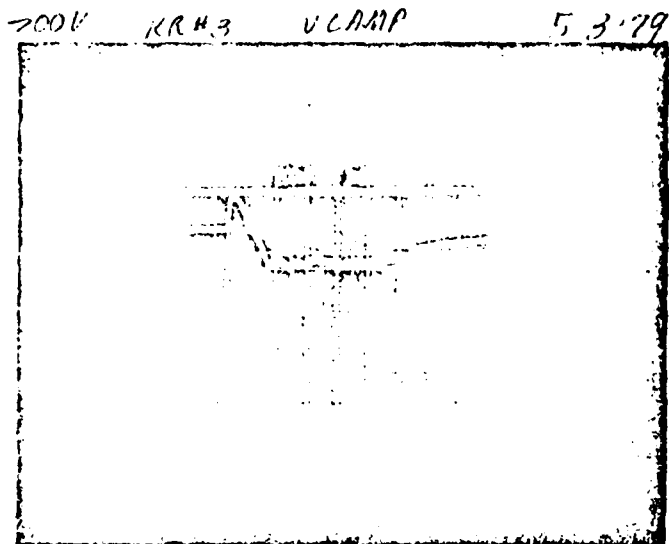
a. 1500 TORR
    KRYPTON

    LAMP VOLTAGE 200 v/DIV

    1 ms / DIV
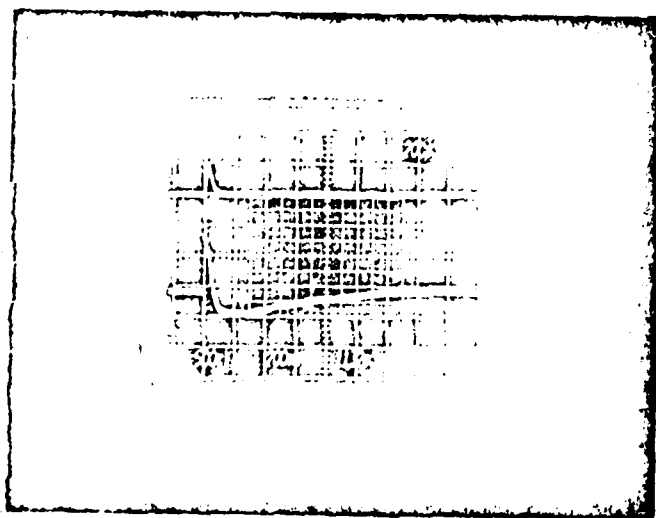
b. 450 TORR
    XENON

    UPPER: LAMP CURRENT

                        200 V/
    LOWER: LAMP VOLTAGE
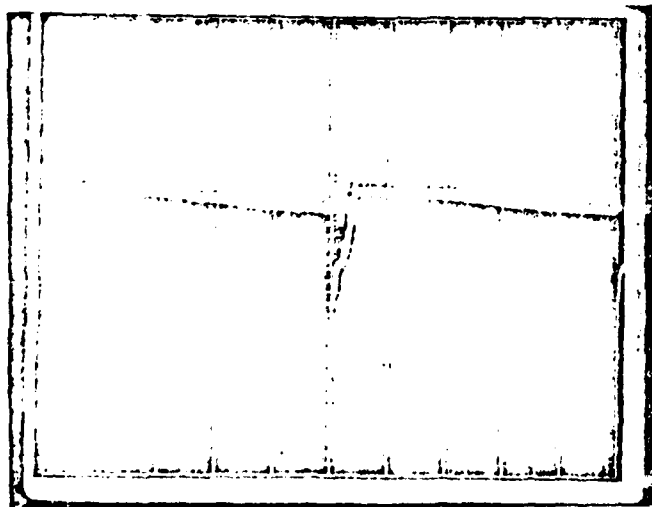   (INVERTED)
    0.2 ms / DIV

c.   1500   torr

    90 % KRYPTON / 10% XENON

    LAMP VOLTAGE 200 v/D

    0.5 ms / DIV

Fig. 5   Flashlamp Voltage Recovery

IV   THERMAL EFFECTS

An excellent review of thermal effects in laser rods includ-
ing both lensing and birefringence has been given by Koechner[11].
In order to compensate for thermal lensing we elected to use an
adjustable internal telescope, since the required wavefront cor-
rection varied with average power. The birefringence compensation
is somewhat more complex.

The Pockels cell, which performs the electro-optic switching
required in the PTM Q-switching mode of operation, is polarization
sensitive. Any mixing of polarization caused by thermally induced
birefringence in the rod must be eliminated. This is accomplished
by using a calcite rhomb to separate the beam into two parallel
but orthogonally polarized beams. Because of the thermal bire-
fringence and the quarter wave plate, energy is transferred between
the two polarizations on alternate passes. Prior to switching,
both polarizations pass without loss through the center hole in
the output coupler. Once switched, the two polarized beams are deflected
by the rhomb both above and below the center hole and are reflected
out of the resonator.

V   POCKELS CELL

The Pockels cell utilized in this system was a Lasermetrics 1058 FV with index matching fluid, FC 104. For successful PTM Q-switched operation the Pockels cell switching time must be rapid. If the switching time for low Q to high Q is slow, energy leaks out of the cavity ahead of the main laser pulse and peak cavity flux is reduced. Ideally, the switching time should be fast compared to the resonator cavity decay time. The switching time from high Q to low Q should be short compared to the cavity round trip time (~7ns), or the output pulse is broadened in time. Conventional krytron tube circuits provide adequate switching times but are limited by tube recovery to repetition rates of a few hundred hertz. Avalanche transistor circuits can meet both repetition rate and switching time requirements but have unacceptably short lifetimes. A hydrogen thyratron switching circuit potentially capable of meeting all three requirements had been developed by Plourde et al [12]. A slight modification of this circuit was used to drive the Pockels cell. Minimum thyratron switching time is achieved by using the highest hydrogen pressure consistent with voltage holdoff.

VI   SECOND HARMONIC GENERATION

CD*A was selected as a second harmonic generator because
of its expected high conversion efficiency at the available flux
levels of the fundamental. The required temperature for 90° phase
matching is 112°C. This is relatively close to the phase transi-
tion temperature of 125°C. Crystal heating due to laser energy
absorption can result in crystal damage under these circumstances.
In order to avoid this problem, the angle insensitivity of 90°
phase matching was sacrificed in favor of a crystal cut for 85°
phase matching at the lower temperature of 55°C. With the lower
temperature crystal the flux limiting element in this system was
found to be the antireflection coating on the SHG oven windows.
Damage of these surfaces occurs at power levels above the normal
operating point and may have been caused by dust or other con-
taminant.

VII RESULTS

The laser configuration described above produces a laser output of 5.8 mJ per pulse at 1060 nm $\stackrel{with}{\Lambda}$ a 4.8 J flashlamp input energy independent of pulse repetition rate over the range from 100 Hz to 400 Hz, the current limit of the present power supply. At this level of input, the infrared could be doubled to the green with 40% efficiency, giving 2.3 mJ at 530 nm. The laser output pulses are shown in Fig.6. Because the external telescope separation was displaced from the collimating position, the frequency doubling conversion efficiency was different for the two beams. Two corrective measures are possible in this instance. Either the focal lengths of the lenses can be altered for a greater intensification and the lenses set for collimation, or a wedge can be inserted into the path of one of the beams to bring it into collimation with the other beam. Preliminary results with a non-optimal wedge, increased total 530 nm output to more than 2.8 mJ.

The doubler crystal has been operated for over 50 hours at high repetition rate without damage. In addition, flashlamp lifetimes in excess of 10 million shots have been achieved again at high repetition rate and full input loading. Pulse to pulse amplitude stability is within ± 10%. This is entirely acceptable for bathymetric applications.
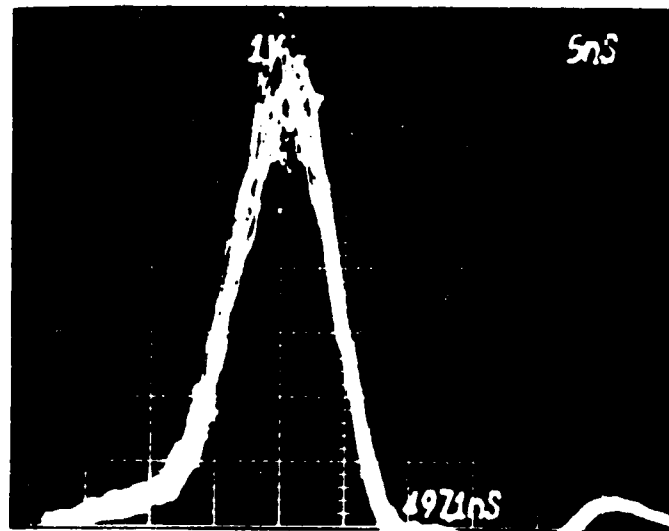
100 MHz DETECTOR BANDWIDTH

J4837-1

Fig. 6 Laser Pulse. The pulse energy at 530 nm was 2.3 mJ at a laser repetition rate of 400 pps.

ACKNOWLEDGEMENTS

REFERENCES

1. F. E. Hoge, R. N. Swift and E. B. Fredrick
Water Depth Measurement Using an Airborn Pulsed Neon Laser
System, Applied Optics 19, pg 871-883 (1980).

2. G. C. Guenther and L. R. Goodman, Laser Applications for
Near Shore National Charting, SPIE Vol. 160, Ocean Optics V,
pg 174-183 (1978).

   see also Digest of Conference on Laser and Electro-optical
   Systems, 1978 (CLEOS) (Optical Society of America, Washington,
   D.C. 1978), pater THcc4, and THcc5.

3. "Airborne Hydrography System Limited Design Report",
Contract 7-35373, U.S. Dept. Commerce, National Oceanic and
Atmospheric Administration, National Ocean Survey, Jan. 1978.

4. N. G. Jerlov, "Marine Optics", Elsevier Scientific Publishing
Co., N.Y. (1976). Figure 1 is a plot of the data on pg 135.

5. G. D. Ferguson, "Blue-Green Laser Investigation for Naval
ASW Applications", Independent Research and Independent
Exploratory Development Annual Summary, Report Control
#NAVMAT 3920.1.

6. A. A. Vuysteke, "Theory of Laser Regeneration Switching",
J. Appl. Phys. 34, 1615 (1963)

7. M. B. Rankin and G. D. Ferguson, "A Short Pulse-Width Laser
for Underwater Applications," SPIE 150, Ocean Optics V,
pg 67-73 (1978)

8. J. H. Goncz, W. J. Mitchell: J. Quant. Elect. QE-3, 330 (1967).

9. C. Noble, J. Moffat, L. Reed, J. Richter: Optical Pumps
for Lasers Final Report TR-ECOM-0035-F, U.S. Army Electr.
Comm., Fort Monmouth, N.J. (1971).

10. J. P. Markiewicz and J. L. Emmett, "Design of Flashlamp
Driving Circuits," IEEE J. Quant. El-ctr., QE-2,1I (1966).

11. W. Koechner, Solid State Laser Engineering, (Springer-Verlag,
New York, 1976).

12. B. E. Plourde, M. E. Mack and E. Verro, "Simple, Fast Rise
Time, High Repetition Rate Pockels Cell Driver", Rev. Sci.
Instr. 51, pg 549-550 (1980).

NAVAL AIR DEVELOPMENT CENTER
WARMINSTER, PENNSYLVANIA 18974

A PTM ND:YAG LASER FOR AIRBORNE HYDROGRAPHY

1 October 1980

Michael B. Rankin, Nelson J. Hall, Gerald D. Ferguson

ABSTRACT

Airborne optical radar systems using pulsed green lasers as trans-
mitters can perform coastal hydrographic surveys quickly and accurately.
The frequency-doubled Nd:YAG laser, operated in pulse transmission mode
(PTM), can provide the required performance characteristics (wavelength,
pulse duration, and repetition frequency) for this application. This paper
describes a PTM Nd:YAG laser operating reliably at pulse repetition fre-
quencies (PRF) of up to 400 Hz. Technical problems encountered include
thermal effects in the laser rod, design of suitable Q-switch driving
circuitry, and the problem of doubler lifetime. A stable resonator
designed to correct thermal lensing and birefringence is described. A
differential Q-switch driver for high PRF operation is described. A power
output of 2.4 watts at 1.06 micrometers was obtained in PTM operation,
at 400 Hz. Frequency doubling in DCDA at 400 Hz produced 0.176 watts at
532 nm. Thermally induced birefringence in the index-matched Q-switch
imposed a limit on the average power of the PTM laser.

INTRODUCTION

The frequency-doubled Nd:YAG laser, operating in pulse transmission
mode (PTM), can meet the required performance characteristics of a laser
transmitter for airborne coastal hydrography.[1] The important laser charac-
teristics are wavelength, pulse energy, pulse width, and pulse repetition
frequency (PRF). A wavelength that matches the underwater transmission
window for coastal waters is required.[2] A pulse energy of a few millijoules
at this wavelength is necessary to penetrate depths up to six fathoms. To
provide depth resolution of approximately one foot a pulse width of a few
nanoseconds is required. A PRF of several hundred hertz is needed to provide
sufficient area coverage.

This paper discusses the theory, design and operation of a PTM Nd:YAG
laser suitable for airborne coastal hydrography. Correction for the thermal
effects in the laser rod at high PRF, Q-switch driving circuitry, and
frequency doubling are discussed. Experimental results obtained with this
laser are presented and discussed.

BASIC PRINCIPLES OF PTM OPERATION

PTM Q-switching was first suggested and studied by Vuylsteke,[3] and
has been applied to Nd:Glass and Nd:CaWO$_4$,[5] CW-pumped Nd:YAG[6] and ruby.[7]
Kay and Waldman,[8] and Weidler et al[9] have studied the theoretical modeling
of PTM laser operation. The topic has been reviewed by Koechner[10] with
many references.

Comparison with Conventional Q-switching

PTM Q-switching differs from conventional Q-switching in the method of
coupling the optical field out of the resonator and in the resulting output
pulse width. In both cases energy is stored in the laser rod in the form of a
population inversion during flashlamp pumping with the resonator in the low
Q state. When the resonator is switched to the high Q state an optical field
forms as the energy is extracted from the laser rod. In conventional

Q-switching, output coupling of the optical field is provided by a partially reflective mirror. During the entire time of field buildup and decay a portion of the field is coupled out of the resonator. The output mirror affects the resonator efficiency and output pulse width. Minimum pulse widths of 10 to 20 nanoseconds have been obtained with conventionally Q-swtiched Nd:YAG resonators. In PTM, variable output coupling of the optical field is employed. The optical field is first allowed to build up in the resonator with ideally no output coupling. When the field reaches a maximum the output coupling is rapidly switched to a maximum (ideally, 100% output coupling) to extract the field from the resonator as rapidly as possible. Minimum output pulse widths of a few nanoseconds, limited by the resonator roundtrip time, can be obtained by this method.

Basic Nd:YAG PTM Resonator

A basic Nd:YAG PTM resonator is shown in figure 1. The resonator cavity has a 100% reflective mirror at each end. The dielectric thin-film polarizer, quarter wave plate and Pockels cell Q-switch together function as a voltage controlled, variable output coupler. The optical field in the resonator is polarized by the polarizer. With zero bias voltage applied to the Q-switch the output coupling through the polarizer is a maximum and the resonator Q is a minimum due to the birefringence of the quarter wave plate. With quarter wave bias voltage applied to the Q-switch the bire-fringence of the quarter wave plate is cancelled and the output coupling is minimized while the resonator Q is a maximum. The sequence of events leading to the generation of a PTM laser pulse is shown in figure 2. Figure 2a indicates that the resonator Q is kept at a minimum for approxi-mately the first 100 microseconds of flashlamp pumping. As in conventional Q-switching this allows the population inversion in the laser rod to build up (figure 2b). At time t_1 the population inversion reaches a maximum. Quarter wave bias voltage is applied to the Q-switch. Lasing occurs and the intra-resonator optical field builds up to a maximum at time t_2. Typically, $t_2 - t_1$ ranges from 50 to 300 nanoseconds. At time t_2 the quarter wave bias voltage on the Q-switch is rapidly switched to zero to switch the output coupling through the polarizer from a minimum to maximum

and the optical field is extracted from the resonator in the form of a narrow pulse. The pulse width is determined by the resonator roundtrip time or the optical switching time of the Q-switch, whichever is longer. The resonator roundtrip time represents the minimum pulse width that can be obtained. For a resonator 75 cm long the minimum pulse width is 5 ns.

Design Considerations

The important considerations in the design of a Nd:YAG PTM laser are resonator cavity length, thermal effects in the laser rod, the damage thresholds of the resonator optical components and the Q-switch voltage driver. The cavity length determines the minimum pulse width. Thermally induced birefringence and thermal lensing in the laser rod will limit resonator efficiency and compensation for these effects is required for operation at high PRF and average power. The thermal effects will limit the energy stored in the resonator optical field by increasing the resonator losses. The damage thresholds of the optical components will place a limit on the amount of energy that can be stored in the optical field. The Q-switch voltage driver is required to apply high voltage pulses to the Q-switch to raise the Q of the resonator on the leading edge of the pulse and to couple the optical field out of the resonator on the trailing edge. The fall time of the trailing edge of the pulse must be short enough to produce an optical switching time in the Q-switch that is less than the resonator roundtrip time to obtain the minimum PTM laser output pulse width.

400 Hz PTM LASER DESIGN

The requirements of high average power, high PRF operation affect all the major components of the laser. This section describes the resonator, pump cavity, and Q-switch driver used in the high PRF experiments.

Resonator Design

The PTM resonator shown in figure 3 includes compensation for thermally induced lensing and birefringence in the laser rod. Mirror M1 and lens L1

provide compensation for the thermal lens in the laser rod. Two configurations were used, as shown in figure 3; M1 having a radius of curvature of $\pm$50 cm with L1 a -40 cm negative lens, and M1's curvature +10 m with L1 not in the resonator. The calcite rhomb and half-wave plate compensate for the thermally induced birefringence in the rod. This birefringence tends to depolarize a linearly polarized beam passing through the laser rod. The rhomb separates the beam into ordinary and extraordinary beams orthogonally polarized. The half-wave plate in the extraordinary beam then rotates its polarization so that it reflects from the dielectric polarizer rather than passing out of the resonator as a loss. Two parallel beams with the same polarization pass through the Q-switch wing of the resonator, and are modulated by a single Pockels cell, a Lasermetrics model 1058 FV with either FC-43 or FC-104 as an index matching fluid. The quarter wave plate "a" can be rotated to provide a variable amount of birefringence and is used to equalize the energy distribution between the two beams. Mirror M2 is flat so that the wavefront curvature in the Pockels cell will be nearly plane, and to facilitate the simultaneous alignment of the two beams.

Figure 4 shows the pump cavity used in this resonator. The reflector is a pyrex cylinder with a clamshell cross-sectional profile and a vacuum-deposited silver coating on its outside surface. The silver coating is overcoated with chromium for durability. The clamshell shape was chosen from ray-trace studies for uniform pumping of the laser rod. The 0.25 in. diameter by 3.0 in. long Nd:YAG rod is pumped by a fully simmered ILC L-2893 flashlamp with a 4 mm bore and 2.5 in. arc length. A 20 µf capacitor and 20 µh inductor compose the discharge network. The interior volume of the pump cavity is flooded with coolant (distilled water in these tests) and separate coolant flow paths are provided for cooling the lamp and the rod. High velocity flow is provided over the lamp electrode regions. A 9 mm I.D. uranium-doped glass flow tube channels the coolant flow closely around the rod. The uranium-doped glass absorbs ultraviolet light from the flash-lamp and has some fluorescence near the visible wavelength (500 - 600 nm) Nd pump bands. Overall coolant flow rate through the pump cavity was 1.8 gallons per minute, about equally divided between flashlamp and laser rod.

Q-SWITCH VOLTAGE DRIVER

Driver Requirements

The function of the Q-switch voltage driver is to produce rectangular high voltage pulses across the Pockels cell Q-switch. The important pulse characteristics are amplitude, width, pulse width jitter, rise and fall times and PRF. A pulse amplitude sufficient to induce quarter wave retardation in the Q-switch is required. This amplitude is approximately 4000 volts for a KD*P Pockels cell at a wavelength of 1.06 micrometers. A pulse width in the 50 to 300 nanosecond range with pulse width jitter below one nanosecond is required. The required pulse width is the time between the leading edge of the voltage pulse and the time the resonator optical field reaches a maximum value (times t_1 and t_2, respectively, as shown in figure 2b). This time interval depends on the flashlamp pump energy and it is desirable that the Q-switch voltage driver provide the capability to vary the pulse width easily during laser operation for operation at different flashlamp pump energies. Low pulse width jitter is required to minimize the pulse-to-pulse instability in the PTM laser output caused by pulse width jitter in relation to the time at which the resonator optical field reaches a maximum. Fast rise and fall times are required. These times control the pulse's growth. The trailing edge of the voltage pulse in particular must have a fall time short enough to produce an optical commutation time in the Q-switch that will allow PTM laser pulses of minimum width to be obtained. The 10% to 90% optical commutation time of a Pockels cell Q-switch is approximately 74% of the 10% to 90% voltage fall time across the Q-switch.[11] In order to approach the minimum 5 nanosecond PTM laser pulse associated with the roundtrip time of a 75 cm resonator a 10% to 90% voltage fall time of 6.8 nanoseconds or less is required. The Q-switch driver must be capable of operating at the PRF of the laser. At high PRF, a limitation on the types of high voltage switches that can provide both the required rise and fall times and high reliability is encountered.

Driver Circuit

A circuit diagram of the Q-switch voltage driver used with the PTM
resonator described in this paper is shown in figure 5. Two hydrogen
thyratrons are used as high voltage switches to apply a rectangular high
voltage pulse differentially across the Q-switch. The thyratrons are
triggered in sequence with the delay between triggering determining the
pulse width. The thyratrons are triggered with avalanche transistor
circuits to minimize jitter and delay times. The delay between triggers
is produced by digital delay circuitry. The delay is easily varied during
driver and laser operation to allow manual adjustment of the high voltage
pulse width. An advantage of this type of Q-switch driver over the type
that uses a transmission line as the pulse forming network is that the
pulse width is not fixed by a length of transmission line. The hydrogen
thyratron was chosen as the switch because it provides high reliability
for high PRF, kilovolt switching compared to the krytron, spark gap and
avalanche transistor. The avalanche transistor appears to be much more
reliable when used to switch several hundred volts for thyratron triggering
compared to its use for kilovolt switching at high PRF. A design tradeoff
between fast voltage switching time and reliability was made because the
thyratron cannot switch voltage quite fast enough to allow the production
of PTM laser pulses with a width that approaches the 5 nanosecond resonator
roundtrip time. Table 1 lists the voltage pulse characteristics produced
by this driver circuit with the Lasermetrics 1058 FV KD*P Q-switch.

TABLE 1.   Q-SWITCH DRIVER VOLTAGE PULSE CHARACTERISTICS

Characteristic

Pulse amplitude	0-5 kV
Pulse width	30-300 ns
Pulse width jitter	less than 1 ns
Rise time (10%-90%)	12 ns
Fall time (10%-90%)	8 ns
PRF	0-500 Hz

EXPERIMENTAL RESULTS

Tests have been conducted on the PTM resonator to evaluate the thermal lensing and birefringence compensation, PTM operation at PRF's ranging from 10 to 400 Hz, and frequency doubling efficiency.

Resonator Evaluation

The resonator was run in long pulse mode at PRF's from 10 to 400 Hz and flashlamp energies from 3.6 to 4.9 J. Output coupling was provided by either rotating the $\lambda/4$ plate ("b" in figure 3) or applying a DC bias voltage to the Pockels cell. With either method, an output coupling transmission of about 30% gave maximum output power. Tests were run with the Pockels cell in and out of the resonator, and both mirror configurations were used at the M1 end of the resonator. Results are shown in figure 6. Without the Pockels cell, the output pulse energy remained nearly constant from 10 to 400 Hz. When the Pockels cell was inserted, this condition no longer held true; pulse energy decreased as PRF increased. Additional measurements indicated that birefringence was induced in the Pockels cell assembly by the intra-resonator circulating power. Other researchers[12,13] have observed similar effects with index-matched Pockels cell Q-switches in high average power Nd:YAG lasers. This birefringence is not directly controlled by the voltage applied to the Pockels cell electrodes, and represents a serious obstacle to high average power PTM operation. We observed similar effects with three different Pockels cells, and with the index fluids FC-43 and FC-104. The onset of these thermal effects appears to set a limit on the average power at which such a resonator can operate.

The Pockels cell also affected the shape and stability of the laser's output beam. At low PRFs the beam was round, about 5 mm in diameter. As the PRF increased, this shape became progressively flatter, reaching a height of 2.5 mm and a width of 5 mm at 400 Hz. The shape of the beam also fluctuated more severely as PRF increased. These effects were observed with a Varo model 9902E IR viewer. Neither effect was observed when the resonator was tested without the Pockels cell.

The beam divergence of the resonator was measured at 10 Hz with the +10 m mirror at M1, and at 400 Hz with both sets of optics. At 10 Hz, the beam divergence was 1.7 mr. At 400 Hz, the beam divergence was 5 mr with +10 m mirror at M1, and less than 2 mr with the lens/mirror combination.

PTM Operation at 1.06 Micrometers

The PTM resonator was first operated at 10 Hz in order to study it in the absence of extreme thermal effects. Table 2 describes the 10 Hz performance of the resonator in optimally coupled long pulse mode and with PTM Q-switching.

TABLE 2.   10 Hz PTM OPERATION

Flashlamp Energy [J]	Long-Pulse Energy [mJ]	PTM Output Energy [mJ]	Pulse Width [ns]	Peak Power [MW]
3.6	8	7	6.5	1.08
4.23	12	11	6.5	1.69
4.9	17	16	6.5	2.46

Pulse energies were calculated from average power as measured with a Coherent Radiation Model 201 Thermopile Detector. Pulse shapes were observed with an ITT Biplanar Photodiode with a risetime of 0.75 nanoseconds or a Lasermetrics Model 3117 Photodiode with a risetime of 150 ps and fall time of 250 ps. A Tektronix Model 485 oscilloscope with 350 MHz bandwidth was used to display the pulses.

For a given flashlamp energy, we found that the PTM pulse contained at least 87% of the energy available from the resonator in long-pulse, optimally coupled operation. Pulse widths were consistent with the switching time of the high voltage bias on the Pockels cell, typically 8 nanoseconds, and with the 5 ns roundtrip time of the 75 cm resonator. A Q-switch driver pulse amplitude about 10% higher than the DC quarter wave voltage gave the maximum output pulse energy. This ratio is consistent with the relative magnitudes of the direct and indirect electro-optic effects in KD*P.[14]

High PRF operation was studied at a flashlamp energy of 4.23 joules/
pulse, and at PRF's from 10 to 400 Hz. Figure 7 shows the optimally
coupled long-pulse energy and the PTM pulse energy over this range of PRF.
The stability of pulse energy was $\pm 10\%$ at best at 400 Hz, and degraded
rapidly if flashlamp energy was increased. Pulse width remained in the
6 to 7 ns range. For these measurements, the +10 meter 100% mirror was
used at M1. As the PRF was increased above 10 Hz, a progressively smaller
fraction of the long-pulse energy was available in the PTM pulse. This is
attributed to the thermally induced birefringence in the the Pockels cell,
which acts as a non-linear (field-dependent) resonator loss. Since the
induced birefringence is not controlled by the bias applied to the Pockels
cell, control of the resonator's Q in both high-Q and low-Q states is
reduced.

Frequency Doubling Tests

The output of the PTM laser was frequency doubled with a DCDA crystal
at 10 and 400 Hz. The crystal, supplied by Quantum Technology, Inc., was
highly deuterated but was cut for critical phase matching rather than the
noncritical phase matching orientation normally used with DCDA. This
choice lowers the phase matching temperature of the crystal, and reduces
the probability of surface damage due to localized heating of the crystal
faces. Maximum conversion efficiency was obtained from this crystal at a
temperature of 80° C. The 12 mm x 12 mm x 20 mm crystal was enclosed in an
oven housing filled with dry nitrogen. Entrance and exit windows of the
oven were uncoated. Table 3 gives the frequency doubling results.

TABLE 3. FREQUENCY DOUBLING MEASUREMENTS

PRF Hz	Pulse Energy mJ	Pulse Width ns	Peak Power Density MW/cm^2	SH Energy mJ	Conv Eff %
10	10	6	23.6	0.79	7.9
10	14	6	33	2.65	18.9
400	6.7	5.5	21	0.44	6.8

Figure 8 shows pulse shapes observed during the 400 Hz measurements.
Figure 8a shows the fundamental pulse, and figure 8b shows the resulting
second harmonic pulse shape. Exposure time for the photographs was
60 seconds. The width of the second harmonic pulse in figure 8b is
between 4.5 and 5 ns on the average. Theoretically, a triangular funda-
mental pulse with a full width at half maximum [FWHM] of 6 ns should
produce a second harmonic pulse with a 4.2 ns FWHM. The pulse widths
observed are consistent with theory.

The conversion efficiencies observed are close to those obtained by
Kogan et al[15] in noncritically phase matched DCDA. Damage to the crystal
was observed in one instance, resulting from a severe imbalance in pulse
energy in the two output beams of the PTM laser. The conversion efficiency
at 400 Hz may have been lower due to temperature gradients in the DCDA
caused by the 2.4 watt average power throughput at 400 Hz.

CONCLUSIONS

The PTM laser described here satisfies several requirements of coastal
hydrography systems. The resonator design operated efficiently in the
presence of appreciable thermal lensing and birefringence in the laser rod.
At 10 Hz, 532 nm pulses with energy of 2.65 mJ and width of 4.5 ns were
obtained. At 400 Hz, pulse energies of 0.44 mJ were observed, again with
4.5 ns pulse widths.

Thermal effects in the Pockels cell present the most significant
obstacles to efficient, stable high average power operation of this laser
design. The individual contributions of the index matching fluid and the
KD*P crystal have not yet been studied in this investigation. If the
effects occur primarily in the index fluid, a dry KD*P Q-switch will
modulate the resonator loss properly for PTM operation. However, the
insertion loss of uncoated KD*P (4% per surface) will reduce the effi-
ciency of the laser. Unlike KD*P, $LiNbO_3$ can be coated with damage-
resistant AR coatings. This feature provides a low insertion loss without
index fluids, and $LiNbO_3$ Q-switches can be used within limits set by damage

threshold and photoelastic effects. Thermally induced birefringence in the
Q-switch crystal will limit the average power for either material. The
magnitudes of absorption coefficients, elastic and elasto-optic coefficients,
temperature coefficient of refractive index, and power density in the Q-switch
will determine this limit.

ACKNOWLEDGMENTS

REFERENCES

1.   Guenther, Gary C., and Goodman, Lowell R., "Laser Applications for
     Near-Shore Nautical Charting," Proc SPIE, Vol 160, pp 174-183 (1978)

2.   Ferguson, G. D., "Blue-Green Lasers for Underwater Applications,"
     Proc SPIE, Vol 64, p 150 (1975)

3.   Vuylsteke, Arthur, JAP, Vol 34, (6), 1615 (Jun 1963)

4.   Rankin, Michael B., and Ferguson, G. D., Proc SPIE, Vol 160, p 67 (1978)

5.   Hook, W. R., Hilberg, R. H., and Dishington, R. P., Applied Physics
     Letters 9 (3), p 125 (Aug 1966)

6.   Baldwin, G. D., IEEE Journal of Quantum Electronics, Vol QE-7, (6),
     p 220 (Jun 1971)

7.   Rundle, W. J., IEEE Journal of Quantum Electronics, Vol QE-5, (6),
     p 36 (1969)

8.   Kay, R. B., and Waldman, G. S., Journal of Applied Physics, Vol 36, (4),
     p 1319 (Apr 1965)

9.   Weidler, R. C., Jr., Burkhalter, J. H., and Vuylsteke, A. A.,
     J. Applied Physics, Vol 38, (11), p 4510, (Oct 1967)

10. Koechner, Walter, Solid State Laser Engineering, Springer Verlag, NY,
     p 441 (1976)

11. Johnson, B. C., Guinn, K. R., Martin, W. E., and Fountain, W. D.,
     "Optical Risetime Measurements on KD*P Transmission-line Pockels Cells,"
     J. Applied Physics 49 (1), p 75 (Jan 1978)

12. Erickson, Edward G., Private Communication

13. Hume, Gilbert, J., Private Communication

14. Sliker, T. R., and Burlage, S. R., "Some Dielectric and Optical
     Properties of KD_2PO_4," J. Applied Physics, Vol 34, pp 1837-1840 (1970)

15. Kogan, T. R., Pixton, R. M., and Crow, T. G., "High Efficiency Frequency
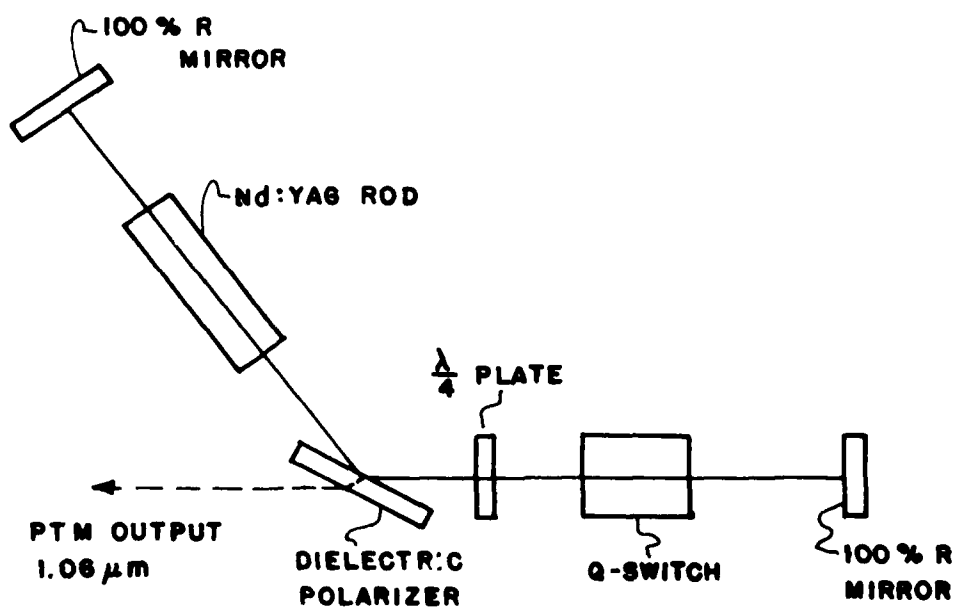   Doubling of Nd:YAG," Optical Engineering, Vol 17, (2), pp 120-124 (1978)

FIGURE 1 - BASIC Nd:YAG PTM RESONATOR

RESONATOR
LOSS FACTOR

POPULATION
INVERSION

INTRA-RESONATOR
OPTICAL FIELD

LASER OUTPUT

TIME t_1 t_2

~50 - 300 n SEC

MINIMUM PULSE
WIDTH : $\frac{2L}{c}$

(b) PTM PULSE GENERATION

FLASHLAMP
CURRENT

RESONATOR
LOSS FACTOR

t_0 $t_1 t_2$ TIME

~100μ SEC
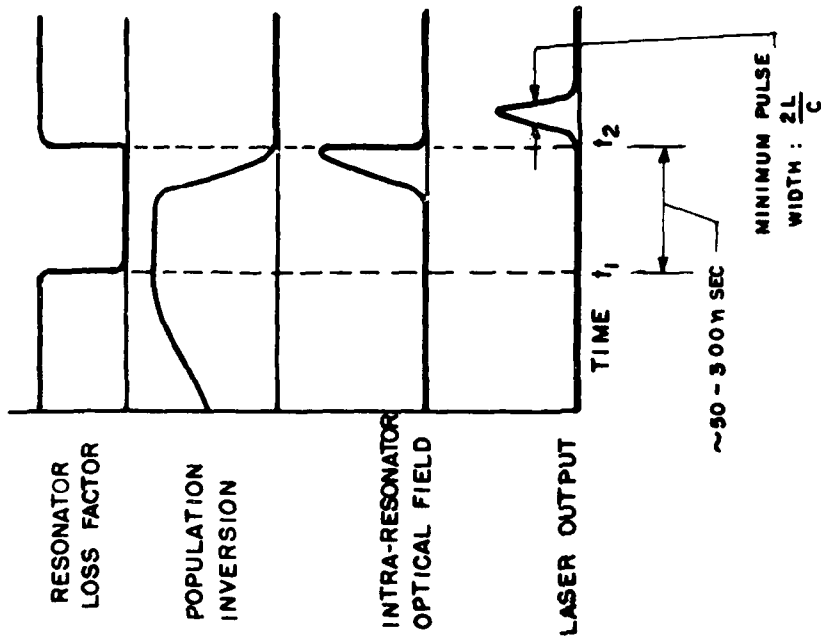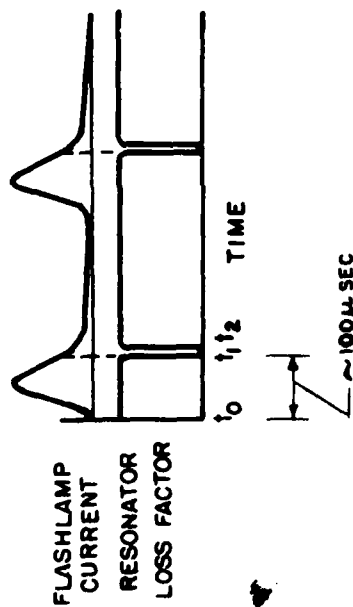
(a) FLASHLAMP TIMING
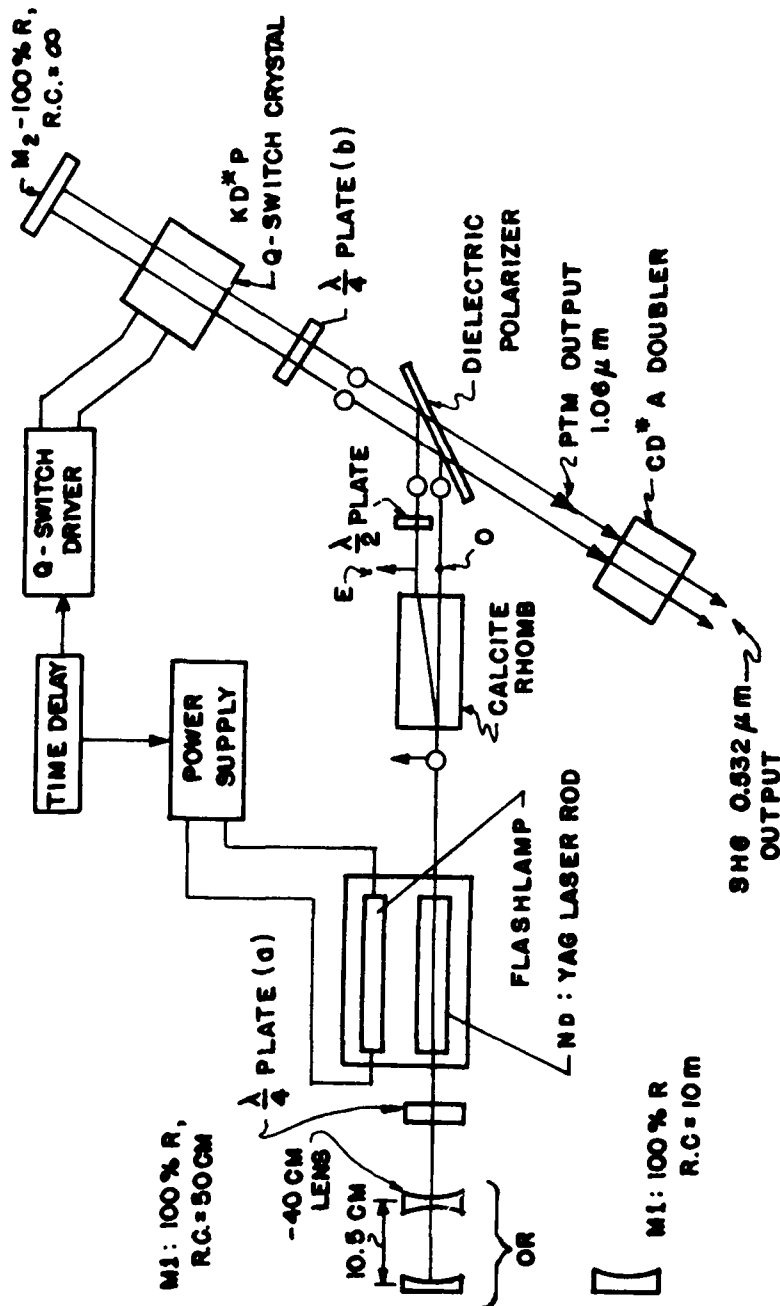
FIGURE-2   PTM Q-SWITCHING SEQUENCE OF EVENTS

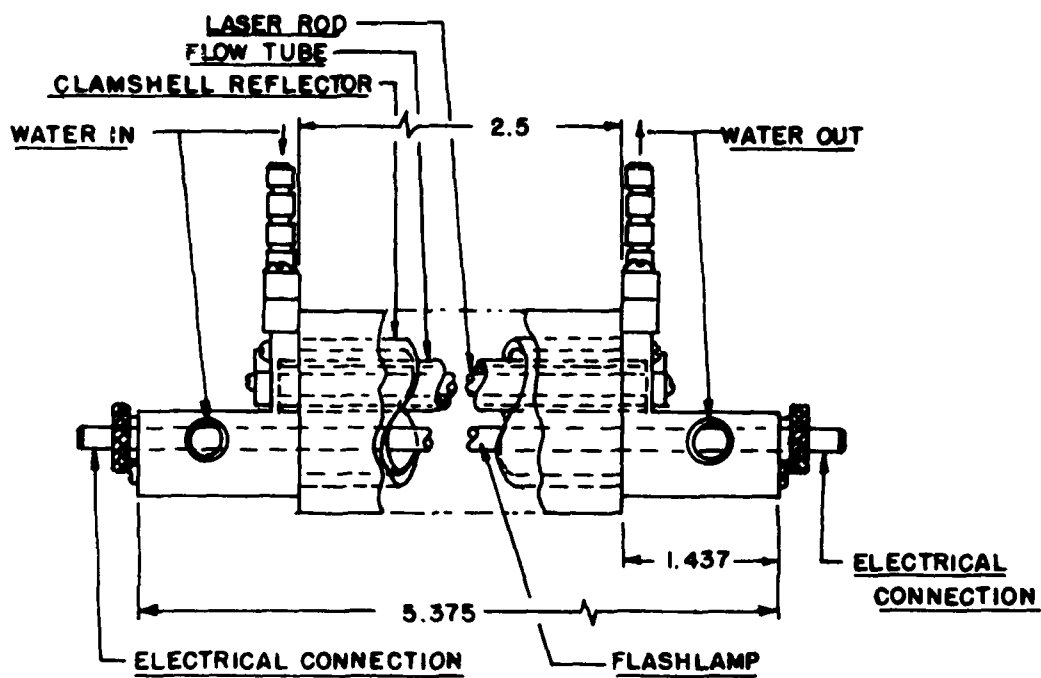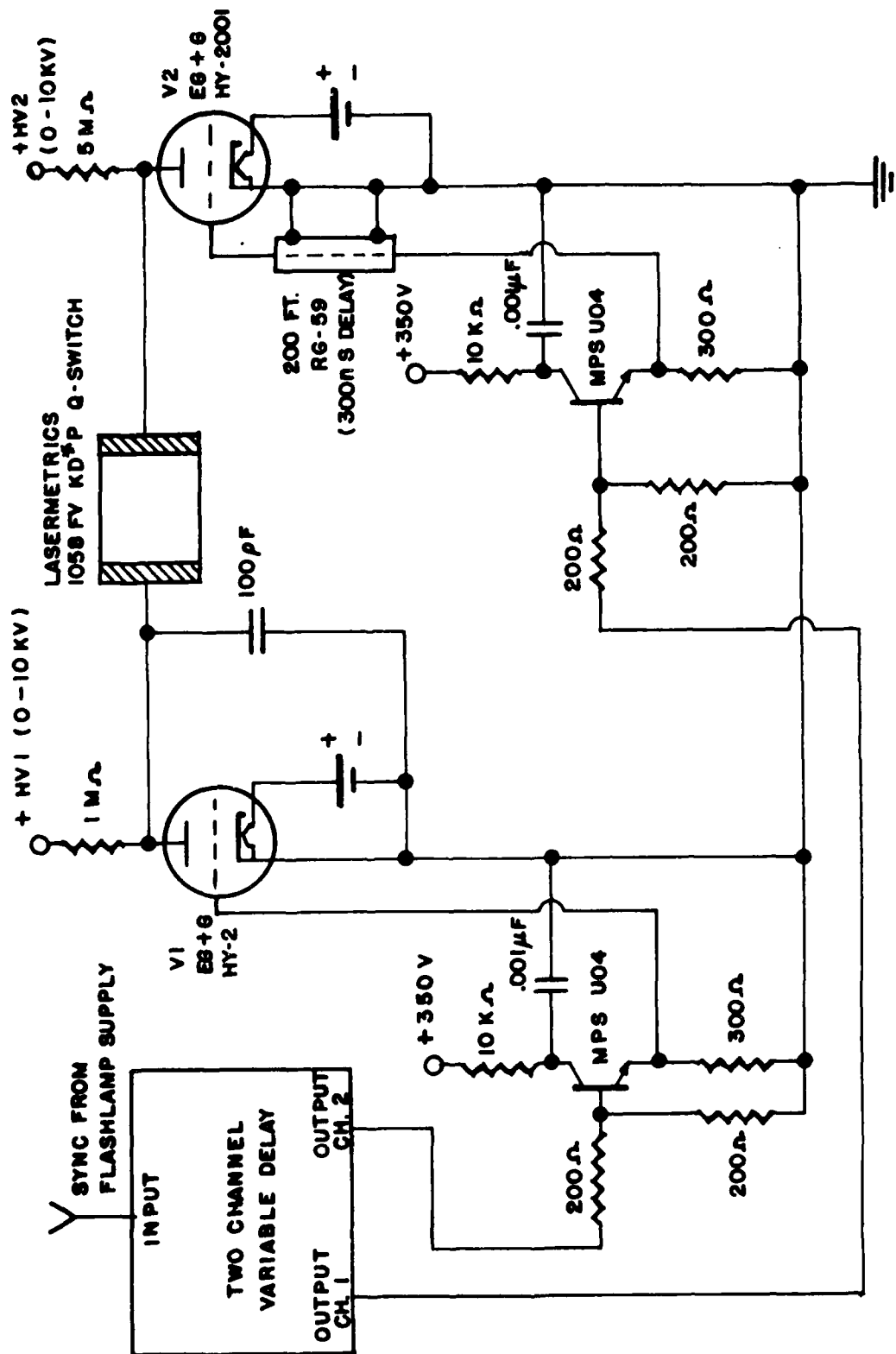FIGURE - 3 HIGH PRF PTM RESONATOR

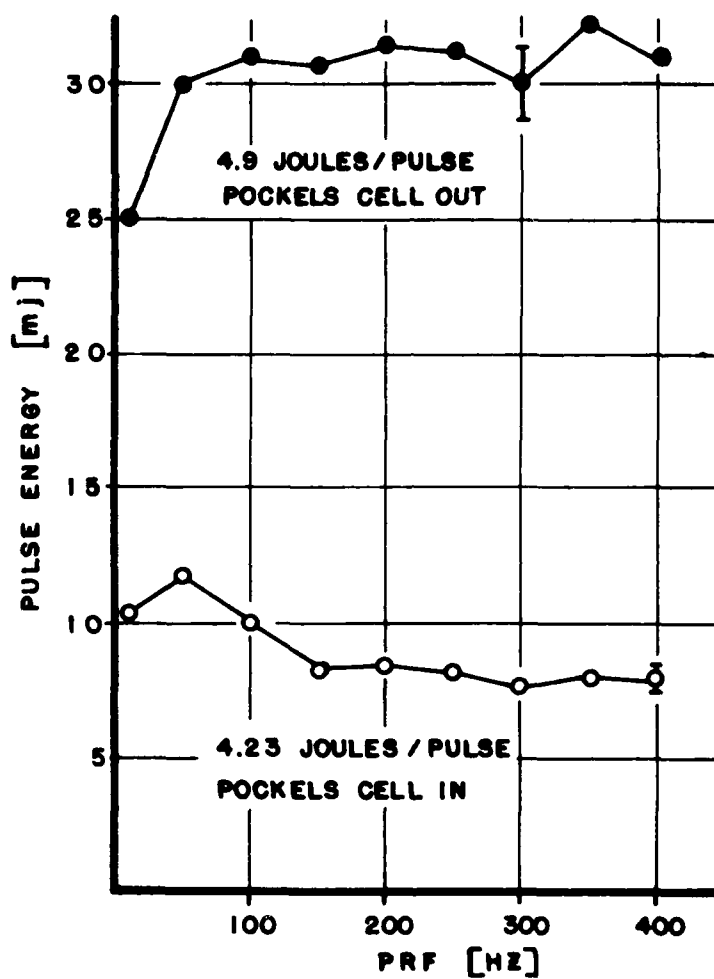FIGURE-4 PUMP CAVITY

FIGURE - 5   Q - SWITCH VOLTAGE DRIVER

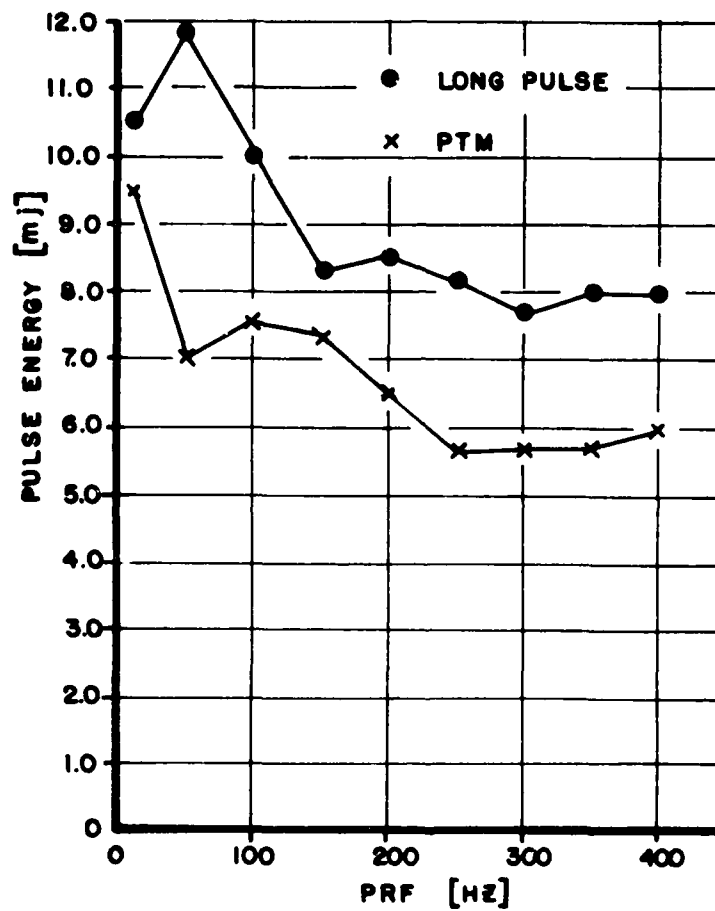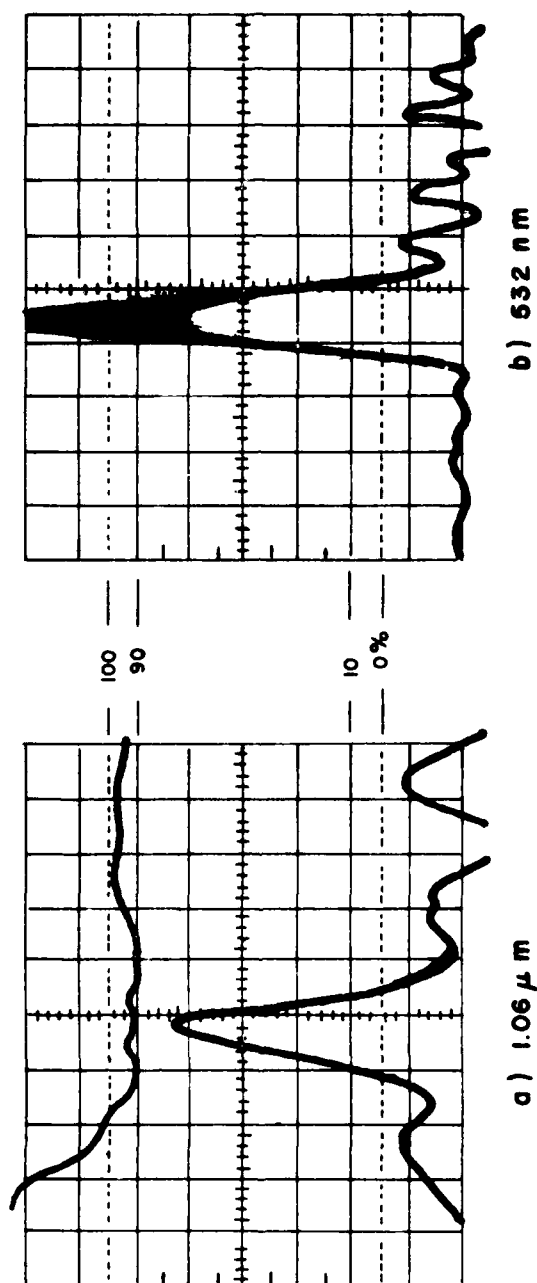FIGURE 6 - LONG PULSE ENERGY VS PRF

FIGURE-7 PTM PULSE ENERGY VS PRF

100
90

10
0 %

a) 1.06 μ m

b) 532 nm

FIGURE - 8   400 Hz PTM PULSES - 5 nsec/DIV

PAPER 14

Future Hydrographic Lasers
M. B. White, Office of Naval Research
Eastern/Central Regional Office

Introduction

Laser sources for hydrographic applications must produce short, 3-5 nsec green output pulses at pulse-repetition-rates ranging from a few hundred Hz to over 10kHz. Pulse energy is generally limited to a few millijoules, either because of eye damage considerations or because of electrical power limitations on airborne platforms. A wavelength in the 480nm-550nm range is required.

Hydrographic laser requirements differ significantly from those generally associated with other ocean-optics applications in that both the average power and pulse-length are one-to-two orders-of-magnitude smaller, and the preferred operational wavelength is green to yellow-green rather than blue-green. Never-the-less many of the new, promising laser concepts that have been under vigorous exploritory development in the U.S. over the last few years for underwater communication, ranging and detection, and illumination, could in principle, be directly adapted for hydrographic use on a 2-5 year time scale. Also, there is a small, but active ongoing basic/applied research effort in the U.S. that is specifically directed toward hydrographic laser development.

Some of the most promising future hydrographic laser possibilities are discussed below. These candidates all appear capable of satisfying hydrographic radiation output requirements in small, light weight, highly reliable configurations of a type suitable for aircraft mounting.

Copper Vapor Laser

Future development of the copper vapor laser snows great promise of providing a significant near-term advancement in the hydrographic laser state-of-the-art. In its usual mode of operation, this device produces 20-40 nsec output pulses at pulse-repetition-frequencies between 1 and 15 KHz. The output normally contains spectral components at 511nm and 578nm, with about 2/3 the energy in the 511nm line.

In the early 1970's two alternative types of electrica. discharge excited Cu vapor lasers were pursued with about equal vigor. One type uses pure metalic copper as the active lasing material, while the other uses a copper halide such as CuCl or CuBr. The pure copper device has the advantage of higher output energy-per-unit-volume but has to operate at 1500°C, where common discharge tube fabrication materials and sealing techniques cannot be used. On the other hand, the copper halide laser can operate at temperatures where simple fused silica discharge tube technology is applicable (400°-600°C) but is limited in its volumetric energy density and PRF capabilities. By operating in a mode where waste heat from the electrical discharge is used to vaporize the Cu or Cu halide, both type copper lasers can routinely achieve "wall-plug" electrical-to-optical energy conversion efficiencies of over 1%.

The operational lifetimes of copper vapor lasers are normally limited by seal integrity and/or diffusion of the Cu or Cu halide out of the hot active-gain region of the discharge tube. This is a particularly severe problem with the metalic copper laser because of its very high operation temperature. Never-the-less, metalic Cu systems have been operated in the U.S., for over 700 hrs., by using a slow gas flow to compensate for seal leakage. Over 3000 hrs. of continuous sealed off operation has been achieved in the Soviet Union by employing a high buffer gas pressure to impede the diffusion of Cu atoms out of the discharge region. Because Cu halide devices generate at temperatures where an "all hot" quartz configuration is premiseable, it is fairly straightforward to realize a simple, He-Ne laser type design which is much less plagued by seal and gas diffusion problems. Such devices have been operated, sealed-off, for several hundred hours with no measureable decrease in output power.

Primarily because of the energy/pulse requirements of most systems applications, recent U.S. copper laser development efforts have for the most part concentrated on the use of pure metalic copper. Over 100 such lasers, with the following output specifications, have been sold by the General Electric Company: Average Power = 5Watts, Pulse Energy = 0.8 mJ, Pulse Repetition Rate = 6kHz, Pulse Width = 20 nsec. A 15 watt average power device is also offered commercially by G. E., and a laboratory laser that delivers 40Watts has been demonstrated.

Longitudinal discharge, low pressure copper vapor lasers, such as are offered commercially by G. E., are generally limited to volumetric output energy densities of $\sim$ 10 μJ/cc/pulse. However, by converting to a higher pressure gain medium and transverse discharge pumping, both higher energy density and higher electrical efficiency appear to be possible. Soviet scientists report that, using this approach, they have demonstrated energy densities of 640 μJ/cc/pulse and efficiencies of 2.5%. An experiment aimed at achieving similar results using a small, transverse excited CuBr device will be carried out in the near future by the U.S. Westinghouse Research Laboratories.

As is implied by the discussion above, already demonstrated copper vapor laser technology would be nearly ideal for high-data-rate hydrographic sounding applications, if the 20-40 nsec pulse-widths that normally characterize such lasers were about an order-of-magnitude shorter. In view of this fact, a U.S. Navy supported research program was initiated about a year ago at the G. E. Applied Sciences Laboratory to try to devise a simple technique for obtaining short pulse copper vapor laser output. The goal of the program was to demonstrate a metalic copper vapor laser with the following output characteristics: Pulse energy = 200 μJ, pulse length = 3 nsec, PRF = 15 kHz, Electrical Power Input = 1 kW. The following characteristics were recently demonstrated at the G. E. Laboratories: Pulse Energy = 500 μJ, pulse length = 5 nsec, PRF = 15 kHz, Electrical Input = 3 kW.

The initial approach followed by G. E. involved the use of a short copper "laser" with only one cavity mirror. It was found that although this double-pass amplified flourescence configuration was capable of producing the requisite pulse-width and energy-per-pulse, the angular divergence of the resulting light beam was too large for the intended hydrographic sounding application. Subsequently, the output characteristics listed above were obtained with low ($\sim$ 1 mrad) beam divergence by using a two-mirror true laser configuration and carefully adjusting the copper density, buffer gas pressure, and drive voltage. It is interesting to note that, for the laser configuration used by G. E., the observed 5 nsec pulse length corresponds approximately to the time necessary for light to travel one round-trip through the cavity!

A contract to deliver a ruggedized version of the G. E. hydrographic copper laser for airborne field experiments is presently being negotiated.

Near-Atmospheric-Pressure Molecular Gas Lasers

Over the last several years an entirely new class of UV and visible near-atmospheric-pressure molecular gas laser (MGLs) has been under rapid development in the U.S. and elsewhere. These lasers all require short, very high voltage electrical pulses for transverse excitation and all require U.V. preionization of the gas mixtures involved for stable operation. The molecular-chemistry/electron-kinetics involved in the operation of these lasers is generally very complex, and entails a multiplicity of electron excitation/ionization and molecular energy exchange processes. In all cases the lower laser state is unstable because of molecular recombination and/or dissociation. Hence, an automatic population inversion results. Because of the very short lifetimes of the excited molecular levels involved, all MGLs operate only in the pulsed-mode, with pulse lengths ranging from 10's to 100's of nsec. UV producing MGLs are available commercially from a number of manufacturers. These typically provide 40-50 nsec, 50-100 mj pulses at 10 Hz PRF's.

Mercury Bromide Dissociation Laser

Of all the MGLs, the mercury bromide dissociation laser is probably the most promising candidate for hydrographic applications. The upper laser level for this device is an excited state of the HgBr molecule, which is formed as a result of electrical discharge dissociation of (stable) $HgBr_2$. After stimulated emission, the resulting HgBr ground-state molecule quickly recombines with a free bromine atom to reform the original $HgBr_2$ molecule. During this cyclic molecular process, the lower laser level is rapidly depleted so that the population inversion necessary for laser operation can be achieved. Also, since all dissociated $HgBr_2$ is ultimately reconstituted, the possibility for long-life sealed-off laser operation exists.

The mercury bromide laser normally operates simultaneously at several wavelengths, between 490nm and 510nm. However, through the use of an intracavity frequency selecting component (eg. a prism or a grating), it is possible to operate at any one of a great multiplicity of wavelengths within that range. In order to achieve the required $HgBr_2$ vapor pressure for laser

operation, the system must be held a temperature exceeding 170°C.
It has been demonstrated that this temperature can be maintained quite
easily by using waste heat from the discharge, in the same manner as was
described above in connection with the copper vapor laser. U.S. Navy
researchers at NOSC have operated a sealed off "self heated" mercury
bromide laser for 10^5 pulses at 100 pps. Five watts of average power
were achieved at 0.5 percent efficiency.

Low pulse-repetition-rate mercury bromide lasers have been operated with
nearly one percent wall plug electrical-to-optical energy conversion
efficiency and output energy densities of 500 µJ/cc/pulse (400 mJ from 800 cc).
There does not seem to be any inherent reason why "scaling down" to the 1mJ/
pulse required for hydrography should present any particular problem. As is
the case with all MGLs, the presence of highly reactive gases in the mercury
bromide laser discharge makes it very difficult to avoid chemical reactions
with the electrodes and other metalic parts of the system. This, in turn,
could make it extremely difficult to achieve the very long ($\approx 10^9 - 10^{10}$ shot)
operational lifetimes required for some military applications. However, in
the case of hydrographic sounding, where the laser can be serviced every few
hours, these slow chemical degradation effects should not constitute a serious
problem.

It should be noted that although most mercury halide laser development work
has concentrated upon the mercury bromide laser (because its output wavelength
is appropriate for penetration of clear ocean water) there is every reason to
believe that the mercury chloride dissociation laser could be further developed
to provide performance that equals or surpasses that achieved with mercury
bromide. It is therefore very likely that most of the rapidly accruing
mercury bromide laser technology could be directly transfered to produce a
mercury chloride laser with output in the 555nm-565nm wavelength range.
Such a laser might prove very useful for hydrographic measurements in murky
coastal waters.

Raman Downshifted Xenon Chloride Laser

The xeonon chloride MGL, which produces an ultra-violet output wavelength of
308nm, is probably the most highly developed of all MGLs. This device has
been operated at a 1kHz pulse repetition rate to produce 210 watts of average
power at over one percent efficiency. A continuous lifetime of 10^7 shots has
been obtained from a sealed-off laser with rapid gas recirculation, and a
wavelength tuneability of 100 Å has been demonstrated. Output energy
densities of several mJ/cc/pulse are readily achieved. A program is presently
underway in the United States to development a XeCl laser which produces
several hundred watts of average power and is capable of very long operational
lifetime.

The reason for the great interest in (and therefore, the rapid development of)
the xeonon chloride laser is that its 304nm output wavelength fortuitously
coincides with an atomic resonance transition of Pb. This coincidence allows
the Stimulated Raman Effect to be used to very efficiently downshift the UV
laser output wavelength to the blue-green (459nm) region, where it can be
advantageously used for ocean-optics applications (such as hydrography).

Using a simple experimental arrangement in which 50mJ output pulses from a
XeCl laser were focused into a heated cell containing lead vapor, workers
at the U.S. Naval Research laboratory have achieved 50 percent energy con-
version efficiency from the UV to the blue-green. There is little doubt
that a scaled down version of this arrangement could provide a useful low
prf blue-green source, with lifetime capabilities consistent with hydro-
graphy mission length requirements.

Because of the highly corrosive nature of hot lead vapor, the development
of a lead vapor Raman Effect wavelength converter with a very long opera-
tional life could prove to be a very difficult technical problem. For this
reason, there is an effort in the United States to develop UV-to-blue-green
Raman Effect downshifting techniques that involve less corrosive room
temperature gases. These techniques all involve multiple Raman Effect down-
shifts in one or two molecular gases contained either in one cell or in se-
quential cells. Multiple shifts are necessary because, for molecular gases,
the wavelength change for a single shift is too small to convert from the
UV to the green. For example, three Raman Effect downshifts of XeCl laser
output in hydrogren gas produce green radiation at 500nm, while two down-
shifts in hydrogren and one in deuterium provide blue-green radiation at
472nm. Since a multiplicity of non-resonant Raman Effect shifts is involved,
the overall efficiency of the molecular gas downshifting process is not ex-
pected to be as high as what could be obtained using a single resonant Raman
Effect downshift in atomic lead (30 percent max. Vrs 50 percent observed).
However, the molecular process has the advantage of providing a potentially
long lived system, and of allowing some selectivity of the final wavelength
(through choice of the Raman Effect downshifting gases). This selectivity
could be of considerable significance for hydrography.

Ultra-violet Molecular Gas Laser Pumped Lasers

For many years UV gas laser pumped dye lasers have been commercially available
from many manufacturers and have been widely used as tuneable visible sources
for spectroscopic measurements. Use of coumarin and rhodamine dyes allows
these systems to be tuned through the entire yellow and green regions of
the spectrum, with 30-50 percent UV-to-visible energy conversion efficiency.
The output pulse length is determined by that of the pump laser. It can
range from 5-15 nsec, for a nitrogen laser pump, to continuous wave, for rare-
gas ion laser pumps.

The primary reason that UV gas laser pumped dye lasers have not been used
for field applications, such as hydrographic sounding, is that the very low
electrical efficiencies of available UV pump lasers precluded such utilization.
For example, the commonly employed UV nitrogen laser is characterized by an
electrical-to-optical energy conversion efficiency of only a few one-
hundredths of one percent. With the emergence of UV molecular gas lasers
with potential efficiencies of several percent, renewed attention is being
given to the use of UV laser pumped dye lasers for field applications.
There are apparently a number of applications where the wavelength agility
afforded by such devices trades off favorably against the added complexity
of a compound laser source.

In addition to being potentially useful for pumping green dye lasers, UV MGLs are also strong contenders for pumping green and blue-green gas and solid-state lasers. for example, the first mercury bromide dissociation laser was photolytically pumped using UV output from an ArF MGL, and a program has just been initiated in the United States to optically pump a Xe_2Cl laser (λ = 478nm) using 304nm UV output from a XeCl MGL. Furthermore, it has been demonstrated that the Tm:YLF solid-state laser (λ = 452nm) can be optically pumped, very efficiently, using output from a 351nm XeF MGL. Sixty percent UV-to-visible energy conversion efficiency appears to be possible using this approach.

Short Pulse Operation Of Molecular Gas Lasers

Molecular gas lasers generally produce pulses with lengths ranging from 30 to 100 nsecs. Therefore, for hydrographic applications, special techniques must be used to reduce the normal pulse length to the 3 to 5 nsec range.

There is every reason to believe that the "cavity dump" approach that has been used to obtain short pulse output from solid-state and dye lasers could be equally well applied to gas lasers. Attempts to demonstrate this experimentally with the mercury bormide and the copper vapor laser are in the planning stage at NOSC and NADC, respectively. With the "cavity dump" approach, the laser radiation is stored in a high "Q" resonant cavity until peak intracavity intensity is reached, and is than dumped out, using a fast electrooptical shutter. Theoretically, an output pulse length equal to twice the laser cavity length should be achievable. In fact, the pulse length is usually determined by the frequency response of the electrooptical shutter drive circuit.

Another technique that can be used to extract short-pulse output from an MGL is to utilize a master-oscillator-power-amplifier (MOPA) configuration, with the oscillator electrooptically short pulse gated and the amplifier traveling-wave excited. Since most of the final output energy is extracted from the amplifier, the energy that is thrown away in gating the oscillator output pulse has a minimum effect on overall system efficiency. By using traveling-wave electrical excitation of the amplifier to create an amplifier population inversion that is temporally sycronized with passage of the pulse from the oscillator, optimum short pulse amplifier extraction efficiency is obtained with minimal loss to superfluorescence. This MOPA approach has been used successfully with the He-N_2 charge-transfer gas laser, and it is presently under investigation for the XeF MGL. Furthermore, similar MGL MOPA configurations are under study at a number of United States laboratories, since the use of such configurations appears necessary for solving high energy MGL frequency selection and beam control problems.

A very promising short pulse MGL configuration, that is under development at the United Technologies Research Center in East Hartford, Connecticut, appears to be particularly well suited for hydrographic sounding applications. In this configuration, the active laser gas is contained in small capillary tube ($\approx$ 30cm long, .5-1mm bore) and is longitudinally excited using a pulsed capacitive discharge. Because the discharge tube is so small, system inductance is naturally very low and short pulse output is easily achieved.

The system is inherently simple and compact, and would appear to lend it-
self very well to operation from a small airborne platform. Although
the small capillary discharge volume limits output to ≳1mJ/pulse, this
output energy is large enough for most hydrographic sounding applications.

So far, the UTRC capillary discharge configuration has been used to ob-
tain laser action from four different MGL species, including xenon
chloride and mercury bromide. Best results have been obtained using KrF
(λ = 248nm), where 50 uJ, 3 nsec pulses were obtained from a 0.04cc gas
volume with 1.5 percent efficiency. An attempt to optimize and theore-
tically analyze the operation of the mercury bromide system is just getting
underway.

Green Solid-State Lasers

In addition to the highly developed frequency-doubled Nd:YAG laser, which
represents the state-of-the-art in hydrographic laser technology, there are
a number of advanced solid-state laser options that show great promise. In
particular, several solid-state laser candidates that directly provide out-
put in the green are in the early phases of development. Use of such
lasers would eliminate the need for a frequency doubler, thereby greatly
decreasing the complexity and increasing the reliability of optical hydro-
graphic systems.

Measurements of the 550nm stimulated emission cross section of liquid
nitrogen cooled Er:YLF have just been completed at MIT. The results of
these measurements strongly indicate that efficient green laser operation
should be possible using that material. An attempt to experimentally
verify this conjecture is planned for later this year. Since a well
engineered liquid nitrogen cooled infrared solid-state laser is commer-
cially available, packaging of a, very similar, 77°K Er:YLF laser for
airborne hydrographic applications is not expected to constitute a
difficult problem.

Strong theoretical evidence exists that the use of Ce:ThO$_2$, in a laser con-
figuration similar to that commonly used for Nd:YAG, should result in an
efficient room temperature solid-state laser that is tuneable through the
entire green region of the spectrum. U.S. Navy supported programs to
grow laser-quality samples of this material are ongoing at MIT and North
American Philips.

The great strides that the fiber optics communications community has made
in improving the performance and reliability of near infrared diode lasers
has stimulated U.S. Navy interest in developing frequency-doubled diode
laser arrays for ocean-optics applications. Continuous operational
lifetimes of 100-1000 years are projected for continuous wave devices
that deliver 10 mW of average IR power at 30 percent efficiency. It is
reasonable to speculate that pulsed operation with similar lifetimes,
average powers, and efficiencies can be obtained.

In the case of diode lasers, the output pulse length is determined entirely by the drive circuit, so that the 2-5 nsec pulses required for hydrography should be readily achievable. Furthermore, it is very probable that by properly choosing diode composition, any frequency-doubled output wavelength in the 480-550nm can be obtained.

The main technical problem associated with developing a frequency-doubled diode laser source for hydrography (or for any other ocean-optics application) is that a detector array containing a great many elements must be used to obtain the requisite output energy/pulse. Also, the outputs from many (perhaps a hundred) elements must be phase-locked in order to achieve the power densities necessary for efficient frequency-doubling. For example, in order to realize a hydrographic laser source with 160 kW peak power, an array containing over 10^4 of the best pulsed laser diodes currently available would be required. While the fabrication of such an array appears to be within the state-of-the-art of integrated circuit technology, it is certainly non-trivial! Also, only a few laser diodes have ever been phase locked, hopefully because there has never before been any motivation to phase lock hundreds.

A program to investigate the fundamental technical problems associated with frequency-doubled diode laser array development is just getting underway at MIT. It is anticipated that within two years basic feasibility will have been established (or ruled out) so that design and fabrication of a modest sized (10^3 - 10^4 element) green radiation source can be initiated.

Summary

This paper briefly describes a number of advanced green laser sources that appear suitable for hydrographic sounding. The discussion ranges from the short pulse copper vapor laser, that is about to be configured for airborne utilization, and delivered for field hydrographic tests, to green solid-state lasers and frequency-double diode laser arrays, that have not yet been demonstrated in the laboratory. Much of the discussion is centered around a new class of near-atmospheric-pressure molecular gas lasers that is being rapidly developed for a multiplicity of ocean-optics applications. "Scaled down" versions of both green and frequency-downshift-ultra-violet lasers of this type show great promise for future hydrographic systems.

It is reasonable to assume that most, if not all, of the future hydrographic lasers discussed in this paper could be developed for field utilization on a 2-5 year time frame.

FUTURE HYDROGRAPHIC LASERS

Type Laser	Wavelength (nm)	Stage of Development for Hydrog.
Metalic Copper	511, 578	Ready for Aircraft-Mounting/Field Use
Copper Halide	511, 578	Demonstrated in the Laboratory
Mercury Bromide	490 - 510	Under Rapid Development
Mercury Chloride	555, 565	Ready for Aircraft-Mounting/Field Use In 1 - 3 Years
Raman Down-Shifted XeCl	490 (with Pb) 472, 500,...(with mol. gases)	
UV MGL Pumped Dye	Tuneable in Green	
XeF Laser Pumped Tm:YLF	452	
XeCl Laser Pumped Xe$_2$Cl	478	Under Laboratory Investigation
Cooled Er:YLF	550	
Room Temp. Ce ThO$_2$	Tuneable in Green	Ready for Aircraft-Mounting/Field Use In 2 - 5 Years
Freq.-Doubled Diode Array	Green	

HYDROGRAPHIC LASER REQUIREMENTS

· ENERGY PER PULSE = 1 - 10 mJ

· PULSE LENGTH = 3 - 5 NSEC

· PULSE REPETITION RATE = 0.1 - 10 KHz

· EFFICIENCY = 1%

· WAVELENGTH = 500 NM - 600 NM

· SMALL - LIGHTWEIGHT FOR AIRCRAFT MOUNTING

     COPPER VAPOR LASER (511 NM, 578 NM)

· UNDER DEVELOPMENT SINCE MID 1960's
    1-15 KHz, 20-40 NSEC, 1% EFF. SELF HEATED

· METALLIC COPPER AND COPPER HALIDE VARIANTS PURSUED
    1500°C VRS 500°C OPERATION TEMP.
    10 μJ/CC VRS 1 μJ/CC OUTPUT ENERGY DENSITY
    MOST WORK DONE ON METALLIC COPPER SYSTEM

· LIFETIME LIMITED BY SEAL FAILURE AND COPPER DIFFUSION
    700 HRS WITH SLOW FLOW IN USA - LOW PRESSURE
    3000 HRS SEALED-OFF IN USSR - HIGH PRESSURE

· MANY LASERS PRODUCED IN USA WITH 0.8 mJ PULSES @ 6 KHz
    HIGH PRESSURE, TRANSVERSE EXCITATION → 640 μJ/CC, 2.5% EFF. IN USSR

· PROGRAM TO DEMONSTRATE SHORT-PULSE HYDROGRAPHY LASER JUST COMPLETED
    GOAL - 200 μJ, 3 NSEC, 15 KHz WITH 1 KW ELECT. IN
    ACHIEVED - 500 μJ, 5 NSEC, 15 KHz WITH 3 KW ELECT. IN

NEAR ATMOSPHERIC PRESSURE MOLECULAR GAS LASERS

- New Class of Efficient UV and Visible Lasers

- Short High-Voltage/High-Current Pulsed Electrical Excitation

   Transverse Discharge with UV Preionization

- Complex Excitation Kinetics; Unstable Lower Laser Level

- Ultra-Violet MGLs Available from Several Manufacturers

   50-100 mJ/Pulse, 10 Hz, 40-50 nsec

- Vigorous Development Program Underway in USA

MERCURY BROMIDE DISSOCIATION LASER (490 nm - 510 nm)

- Most Promising/Highly Devel. Green MGL

- 500µJ/cc/Pulse, nearly 1% Eff. Demonstrated (400 mJ from 800 cc)

- 5 W Ave Power @ 100 Hz Achieved "Self Heated" to 170°C
   Cyclic Kinetics + Long Life Possible

- HgBr Laser Technology Directly Applicable to HgCl (555 nm - 565 nm)

RAMAN DOWN-SHIFTED XENON CHLORIDE LASER (308 nm → GREEN)

· XeCl LASER MOST HIGHLY DEVELOPED OF ALL MGLs

    210 W AVE POWER, 1 kHz, 1% EFF.

    10^7 SHOTS WITH GAS RECIRCULATION/CLEAN-UP

    SEVERAL mJ/cc/PULSE

· RESONANT RAMAN EFFECT IN PB VAPOR → 459 nm WITH 50% EFF.

    CORROSIVE HOT METAL VAPOR → POTENTIAL LIFETIME PROBLEMS

· MULTIPLE RAMAN SHIFTS IN MOLECULAR GASES → LONGER LIFE + MANY WAVELENGTHS

    3 SHIFTS OF XeCl LASER IN H_2 → 500 nm

    2 SHIFTS IN H_2 + 1 SHIFT IN D_2 → 472 nm

· NON-RESONANT, MULTIPLE MOLECULAR RAMAN EFFECT LESS EFF.

    30-50% EFF. POSSIBLE FOR 308 nm → 500 nm IN H_2

    12% EFF. ACHIEVED SO FAR

ULTRA-VIOLET MGL PUMPED GREEN LASERS

· UV LASER PUMPED DYE LASERS EXTENSIVELY USED FOR SPECTROSCOPY

    TUNEABLE THROUGH GREEN

    CONVENTIONAL UV PUMP LASERS VERY INEFFICIENT

    UV MGLs COULD ALLOW FIELD UTILIZATION

· UV MGL PUMPED GAS AND SOLID-STATE LASERS → GOOD FUTURE POSSIBILITIES

    XeCl LASER PUMPED Xe_2Cl GAS LASER → 478 nm

    XeF LASER PUMPED Tm:YLF SOLID-STATE LASER → 452 nm

SHORT PULSE MGLs

- 50-100 nsec MGL Pulses Too Long for Hydrography
  Special Pulse Compression Techniques Required

- Cavity Dump Technique Applicable
  Used Successfully With Nd:YAG and Flash-Lamp Pumped Dye Lasers
  Copper Vapor and HgBr Laser Experiments Planned @ NADC and NOSC, Resp.

- Pulse-Gated MOPA Approach Being Studied @ UTD Using XeF Laser
  Related MGL MOPA Experiments @ Several US Laboratories

- Capillary Waveguide MGL Very Promising Approach
  Small Discharge Tube → Low Inductance → Short Pulse Operation
  1.2 mJ/cc, 3 nsec Pulses Obtained from 20 cm long, 0.5 mm bore KrF Laser (248 nm)
  Lasing Achieved with HgBr; Optimization Underway

GREEN SOLID-STATE LASERS

- Cooled Er:YLF Laser (550 nm)
  Stimulated-Emission X-Section Measured; 77°K Operation not Difficult
  Laser Quality X-Tal Grown; Laser Experiments Underway

- Room Temp. Ce:ThO$_2$ (Tuneable through Green)
  Theoretically Promising; Two Labs Attempting X-Tal Growth

- Frequency-Doubled Phase-Locked Diode Laser Array (Green)
  100-1000 Year Continuous Lifetime Projected for 10 mW CW IR Device
  22% Eff. Demonstrated in IR; 50% Doubling Eff. Reasonable
  Pulse-Width Determined by Drive Circuit; 3 nsec No Problem
  Phase-Locking Many Diodes for Doubling Eff. → Main Technical Problem

PAPER 15

WRELADS POSITION FIXING AND NAVIGATION

D.W. Faulkner

Defence Science and Technology Organisation
Electronics Research Laboratory
Salisbury   South Australia

LEUT M.F. Gale, RAN

(attached) Defence Science and Technology Organisation
Electronics Research Laboratory
Salisbury   South Australia

The Royal Australian Navy have purchased the ARGO DM-54 position fixing system for use in their ongoing hydrographic survey program. Elements of that system have been allocated to the Defence Research Centre Salisbury for use with the WRELADS development. The system originally supplied by Cubic Western Data of the United States had four operational formats each permitting both range-range and hyperbolic use with lane identification available on demand for the range-range user. In conjunction with Cubic Western, a new format has been devised for use with WRELADS which is specifically dedicated to hyperbolic operation.

The basic operation of the system in hyperbolic mode requires a master and a slave transmitter respectively located at separated but known points. The master, at power on, commences to transmit a timing pulse and a succession of interrogation pulses within a basic two second time frame. The slave, following power on, goes into search, and when timing is acquired it recognises the interrogation pulse from the master and transmits its reponse pulse. A receiver, somewhere in the area covered by the master-slave pair, when powered on also searches for and acquires the local system timing. The receiver then recognises both the interrogation and response pulses, makes a phase difference measurement and produces an output based on that measurement. If the receiver is then moved such that the output remains constant the locus of successive positions is a hyperbola as shown by the solid line in figure 1. This is but one of a family of hyperbolae stretching between the the master and slave; the dotted lines are two further hyperbolae, one on each side of the example hyperbola and on which the output of the receiver would be identical with that on the solid line. There is a succession of these constant output hyperbola stretching from the master to the slave and these form a family of hyperbola upon any of which the receiver may be located. To determine a position fix, another slave is added to form a basic chain as in figure 2. There will now be two outputs from the receiver, each representing a family of hyperbolae between the respective master and slaves. These two families of hyperbolae will have multiple intersections and the ambiguity is removed in practice by initialising the receiver at a known position prior to determining actual position fixes.

The ARGO system operates in the HF band and transmits on 1700 kHz and 1870 kHz, one of sixteen switch selectable frequency pairs available. Figure 3 shows the basic ARGO time frame of 2 seconds which is subdivided for WRELADS to provide a timing pulse and a further 8 time slots. Slots 1, 2, 4, 5, 7 and 8 each contain interrogation and response pulses at 1700 kHz leading to a maximum of three hyperbolic outputs for each slot. Time slots 3 and 6 have interrogation and response pulses at 1870 kHz which provide for lane identification. This particular format, developed for WRELADS, provides a high data output rate necessary because of the relative high aircraft velocity compared with the usual marine environment for which ARGO was designed.

A feature of the ARGO system is the ability of the equipment to operate
for relatively long periods of time without the need for operator inter-
vention. This feature has been utilised in the chain of stations set up
in South Australia for use with WRELADS. The stations are fuelled with
liquified petroleum gas (LPG) and each station consumes 68 kg of LPG each
week. The gas is burnt catalytically in thermal generators which provide
the electrical supply to run the station. A float battery pack provides
the high peak current demand when the station transmits. Each station
contains an ARGO Range Processing Unit (RPU), an ARGO Antenna Loading
Unit (ALU), two thermal generators, float battery pack and four 45 kg LPG
bottles. All these items are contained within a substantial steel cabinet
with the 27 ft top hat antenna mounted as shown in figure 4. Each station
installation also has incorporated within it a series inductor and ball
spark gap for lighting protection, is well grounded to a deep driven earth
stake and utilises the supplied radial earth mat only where conditions demand
its use. This has provided a reasonably vandal and theft resistant solution
to the problem of the desirable remote unmanned station in that the stations
need be visited once only each two weeks for LPG replenishment and a general
check.

The aircraft navigation system consists of a number of elements as shown
in the block diagram of figure 5. The central element is a PDP11/03 computer
which obtains a number of inputs as shown. The principal output for airborne
navigation are the current position in Australian Map Grid (AMG) co-ordinates
(Transverse Mercator Projection), cross track error, delta height (departure
from the chosen mission altitude) and drift angle. These are continuously
displayed to the Hydrographer who is in charge of the survey. The cross
track (X TRACK) error, turn information and delta height (ΔH) are also fed
to the Pilot Navigation Monitor (PNM).

The PNM is a 10 cm video screen mounted in the instrument cluster in the
cockpit. The form of the display is as shown in figure 6. The aircraft is
situated at the centre of the display as indicated by the fiducial lines.
The diamond, the centre of which represents the desired track for the mission
is deflected horizontally in response to XTRACK data and vertically with ΔH.
The arrow indicates the direction of the next turn. The pilot flies the
aircraft towards the diamond and thereafter maintains the diamond at the
centre of the screen.

Before the system can be used for accurate work in the field the system
must be calibrated. An ARGO system is calibrated when its hyperbolic out-
puts agree with the lane counts calculated using the usually accepted value
of phase velocity for over the sea propagation. The difference between the
calculated value and the actual value (the result of a real phase difference
measurement by ARGO) is the calibration factor - sometimes called the range
offset or locking constant. This calibration factor is in general a function
of position and must therefore be determined at a number of points through-
out the survey area. Each pattern (i.e. the output from each master-slave
pair) will have a calibration factor and in general these are all different
in value at any given location and may also change by different amounts at
different locations in the survey area.

Calibration for WRELADS is effected by visually overflying a fixed point
with known AMG coordinates as shown in figure 7. A vertically pointing
camera is used to photograph the fixed point during the overflight. Orienta-
tion of the photograph is obtained from knowledge of the track made good

(TMG) and drift angle determined from the navigation system. These data permit the precise position of the aircraft to be correlated with the ARGO outputs at the time the photograph was taken and hence lead to the calibration factors for each of the ARGO patterns in use. Once these calibration factors for the survey area are known, those for the local area can be preset into the ARGO receiver and then the ARGO receiver only requires initialisation with inputs being the integer whole lane counts for each pattern at a fixed point.

There are three basic methods by which ARGO can be initialised.

The first relies on the airfield being within the area covered by the ARGO chain of stations. The aircraft is taxied to a fixed point on the airfield and the lane counts for that point are inserted. Provided the aircraft is accurately positioned at the fixed point on each occasion, this process is in reality a calibration of the system and so provides a sortie by sortie check on stability of the calibration factor as well as initialising the ARGO receiver. This method of initialisation has been in use now for some months during trials of the WRELADS system in South Australian waters.

In many survey situations the airfield may not be conveniently located within the field coverage of the ARGO chain of stations. For these cases the ARGO system must be initialised within the survey area. The second method of initialisation therefore closely parallels that of airborne calibration described earlier. The aircraft, is flown over the fixed point in the operational area and (provided the calibration factors have been preset) the integer whole lanes are input to the ARGO receiver as the aircraft overflies the fixed point. This technique is satisfactory provided the aircraft is within approximately $\pm$ 0.5 a fine lane of the correct position at the instant the integer lane counts are input. The special WRELADS format provides also for input of the calibration factor for the LID and in this case, the aircraft need be within approximately $\pm$ 2.5 fine lanes of the fixed point. For this latter variation, immediately following initialisation with the integer values the LID is interrogated to determine any errors in the fine lanes, and these are removed by incrementing or decrementing the lane count by means of the ΔR function of ARGO. The initialisation is then checked by flying the aircraft back over the initialisation point under computer control and photographing the overflown point.

The third initialisation technique makes use of base line extensions. Along a base line extension, the lane count for a master-slave station pair takes a constant value; zero (by definition) along a base line extension through the master and a fixed maximum value along the extension at the slave station. By flying the aircraft in the vicinity of the base line extension an appropriate value of lane count may be entered into the ARGO receiver. This technique is most useful at the master where all patterns can initialised. At a slave only that pattern generated by the particular master-slave combination can be initialised using the extended baseline. The remaining patterns may however be initialised by using the ARGO antenna as a fixed point whose coordinates are known and hence using the second technique described above.

When the ARGO receiver has been correctly initialised the task of laser depth sounding can be commenced. Three distinct mission types have been identified which should enable the objectives of any sortie to be realised. These missions have a definite purpose and each constitutes a precise mathematical track along which the aircraft is to be flown in order to maximise the data acquisition on each sortie. The mission types, as shown in figure 8, are described as follows:

Mission 1. Purpose: Overflight of any chosen fixed point in the
                        ARGO field. The principal use of this mission
                        is to verify that the ARGO lane counts are
                        correct. The verification is achieved when the
                        target point is seen to be satisfactorily over-
                        flown (photographed) while the aircraft is being
                        flown under computer/PNM control.

Mission 2. Purpose: To permit laser depth sounding along any speci-
                        fied straight line in the Australian Map Grid.
                        The principle use of this mission is to carry out
                        a single 200 m wide swath of depth soundings along
                        any specified line and therefore facilitates flying
                        chosen lines to sample a survey area at the commence-
                        ment of the survey task. Mission 2 would also be
                        used to cover any gaps in sounding coverage which
                        may occur during general data gathering.

Mission 3. Purpose: To permit area survey by means of parallel tracks
                        with modified procedure turns at each end enabling
                        the aircraft to return on a reciprocal track off-
                        set by the working swath width (200 m). This
                        mission is the general purpose area coverage
                        mission which permits large scale surveys to be
                        covered in an efficient manner.

The mission types described above are contained in software which is now
ready to be included in the aircraft computer. The work to date however has
been accomplished by flying along a chosen ARGO lane number in either pattern I
or pattern II; departures from the chosen line are determined and displayed
to the pilot as XTRACK error on the PNM.

Figure 9 is a performance graph from the monitor station at DRCS for a
24 hour period, namely the 2nd of June of this year. The pattern I and II
lanecounts have been plotted for this period and at the monitor station
location the lane expansion is such that 0.01 lane is approximately equal
to 1 metre for both patterns. The distance between each of the dashed lines
corresponds to about 5 metres so the noise in the ARGO output appears as an
apparent movement of the monitor station about some mean position in each of
pattern 1 and pattern 2. When both results are combined this represents an
apparent movement in total position. The cause of the two spikes in
pattern 1, at about 0700 and 0830, is unknown, but comparison with other
days of records show they are not typical deviations. Discounting these
two spikes, we see that the maximum variation from each mean is about 0.05
lane, or 5 metres; for pattern I there was also a slow drift in the lane
count over the period. For our trials in northern Queensland, we had a
similar monitor, but in this case, in a quite different locality with
respect to the total chain. The ARGO chain consisted of a master station
at Dunk Island, and slaves at Fitzroy Island (north of Dunk Island) and Lucinda
(south of Dunk Island), this giving an almost linear north-south chain. The
monitor station was situated further south again, in Townsville, about
200 miles to the South of Fitzroy Island and 60 miles from the most southerly
station (Lucinda). Figure 10 shows the output from this monitor on the
8th of August. The distance between the dashed lines corresponds to about
70 metres in this case, because of gross lane expansion at Townsville. As was
previously mentioned, the station was in an area of much reduced signal
strength; this is borne out by the significantly greater "jitter" about the
respective mean positions. It was also noted that lanes were invariably
gained or lost at the monitor station each night between sunset and sunrise.
Nevertheless while in Townsville, two night trials were flown using ARGO. The

ARGO receiver was initialised well within the effective ARGO pattern and
it was found that lane counts were maintained within the working area.
However during the transit back to Townsville, lane slippage was observed.
The reason is believed to be progressively weaker signals, combined with
sky-wave activity.

An idea of the performance with regard to track keeping, again in north
Queensland, can be gained from Fig.11. The pilots were using the monitor as
it appears in the top right hand corner of the diagram, with the diamond being
deflected to the left or right only, in response to XTRACK information, no
delta-height information being supplied at that time. The solid line across
the centre of the diagram represents the desired track, the total length of
which was 40 Km. Analysis of the actual tracking data, represented by the
wavy line, gave a standard deviation of 8 metres, and a maximum distance
off-track of 24 metres; a performance which is quite adequate for WRELADS.
The pilots did comment that track-keeping using this small monitor was
fatiguing.

Figure 12 shows track keeping during a "micro-survey" mentioned in an
earlier paper by Mr Abbot. For this survey, over a reef in northern
Queensland, the aim was to fly 7 parallel tracks, approximately 205 m apart,
and 1.5 km in length. The total width of the micro survey was approximately
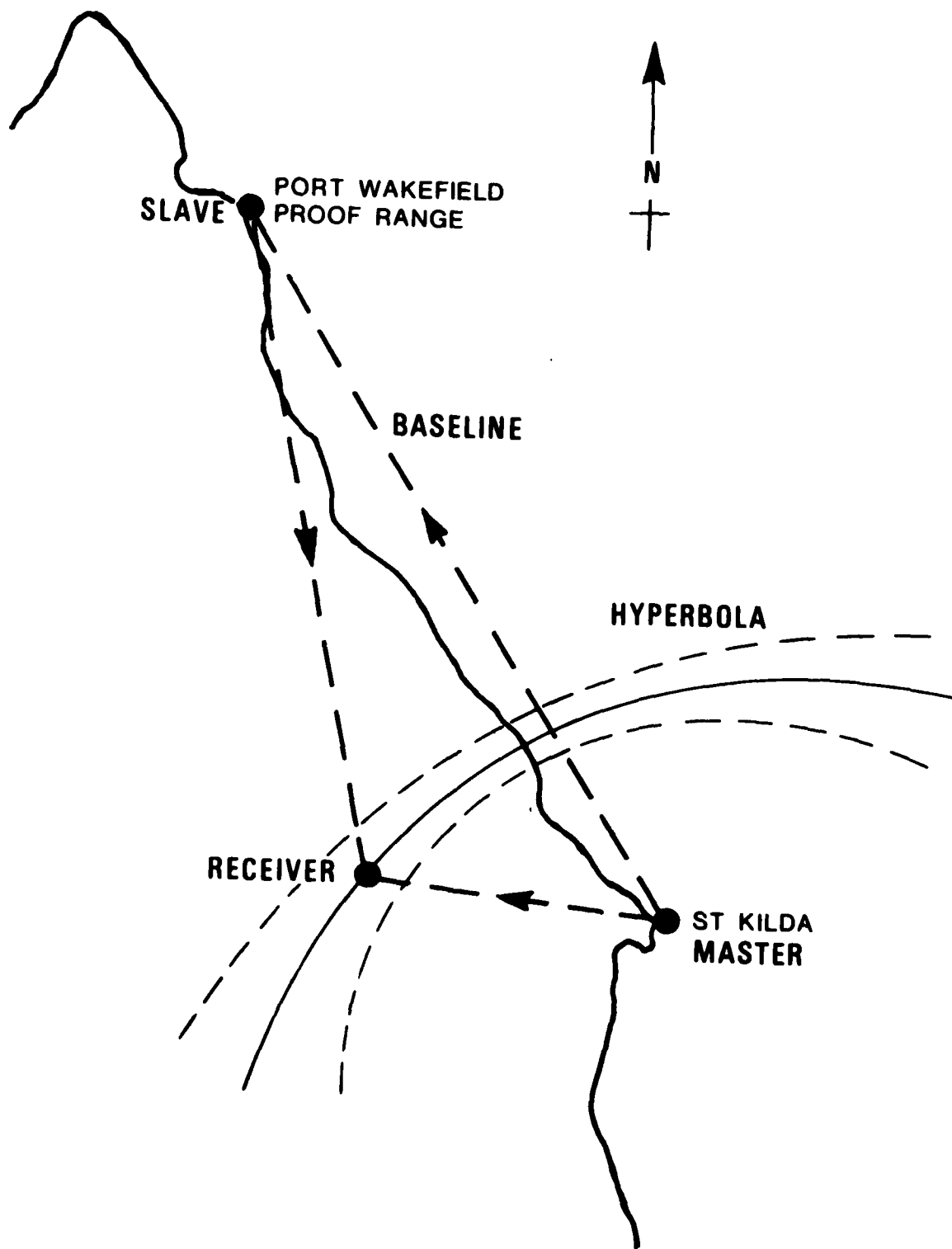1.4 km. The maximum off-track error for this survey was 56 m.
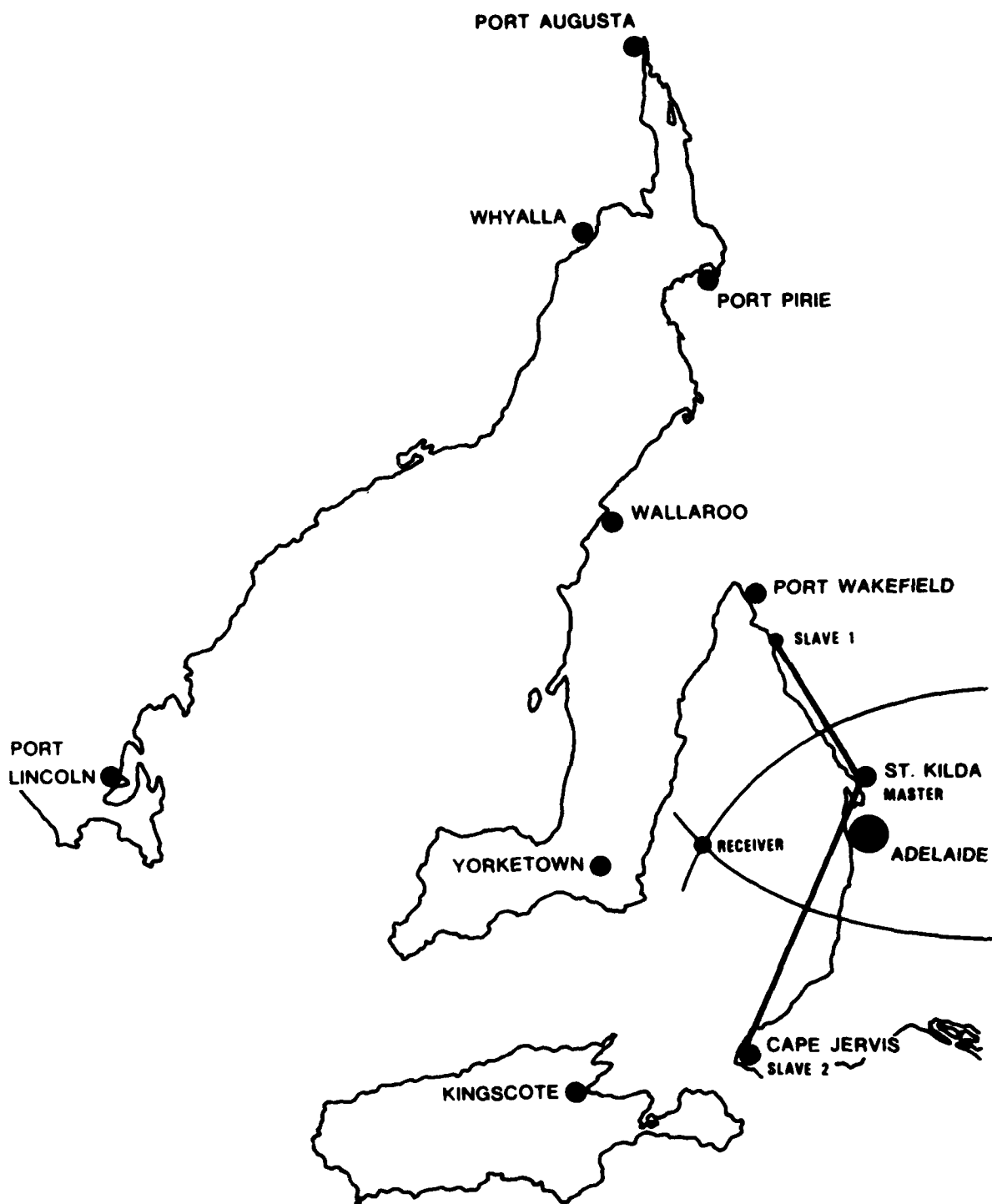
Figure 1 ARGO - OPERATING PRINCIPLE
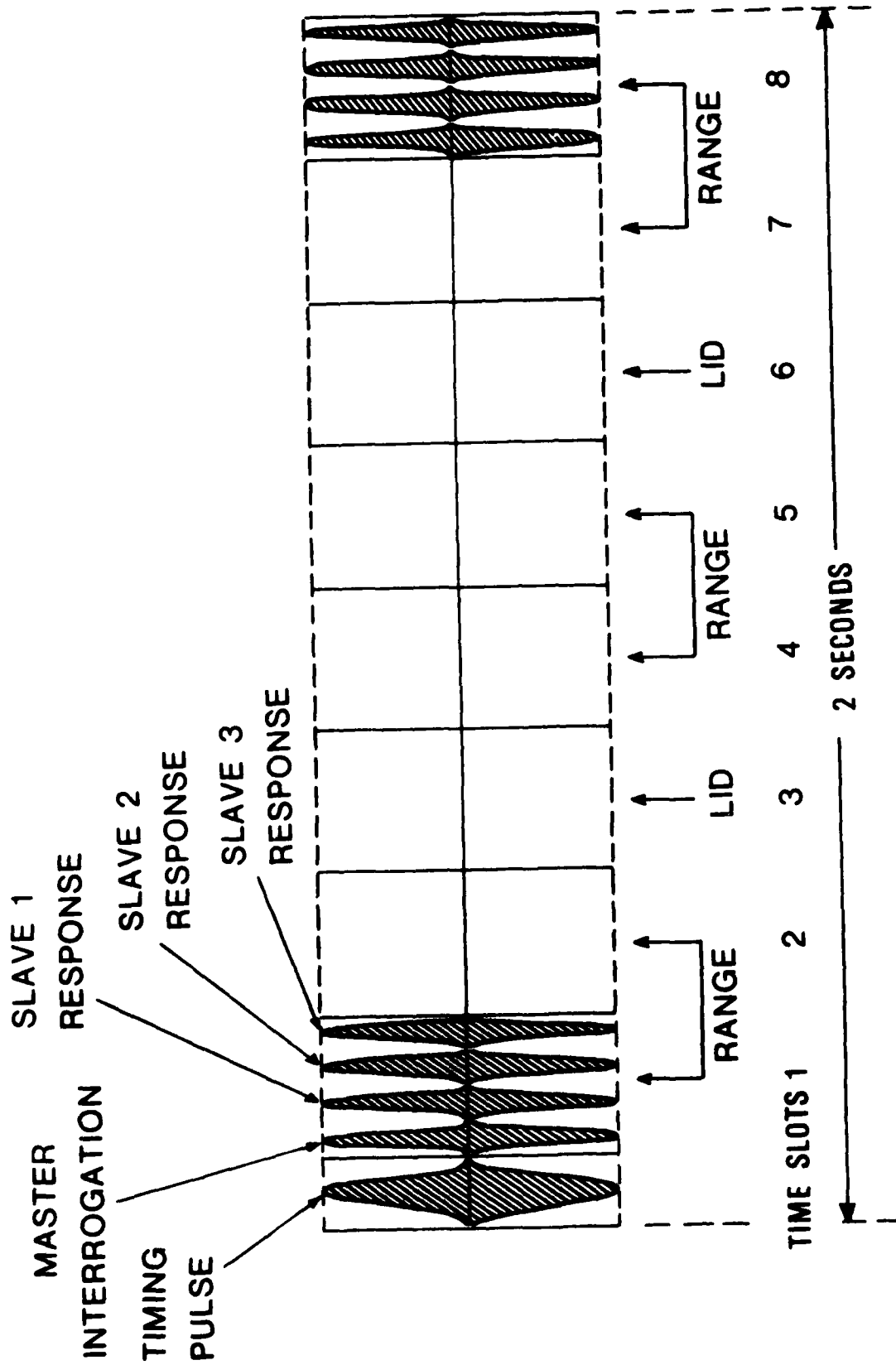
Figure 2   ARGO - OPERATIONAL HYPERBOLIC CHAIN

ERL-0193-SD
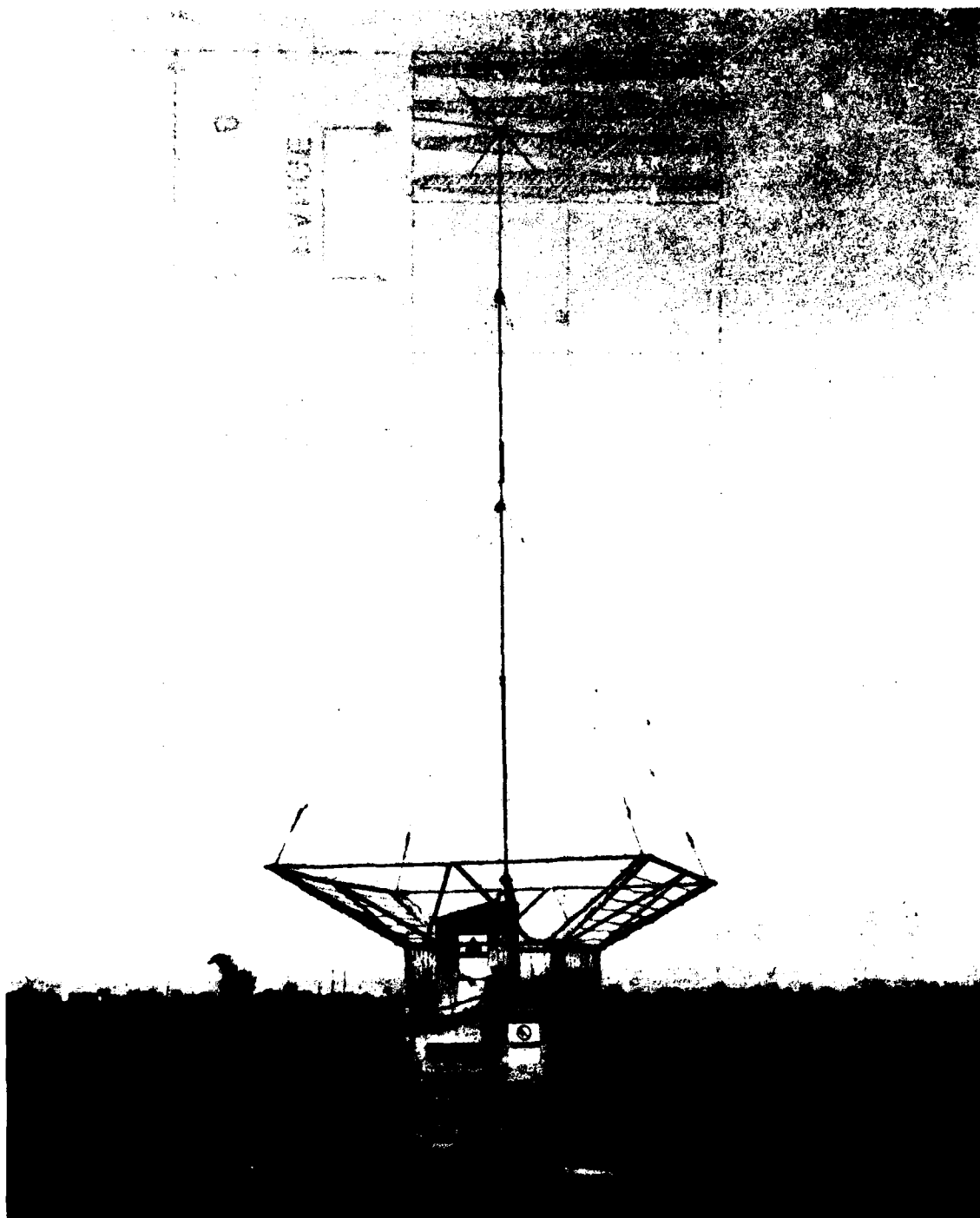

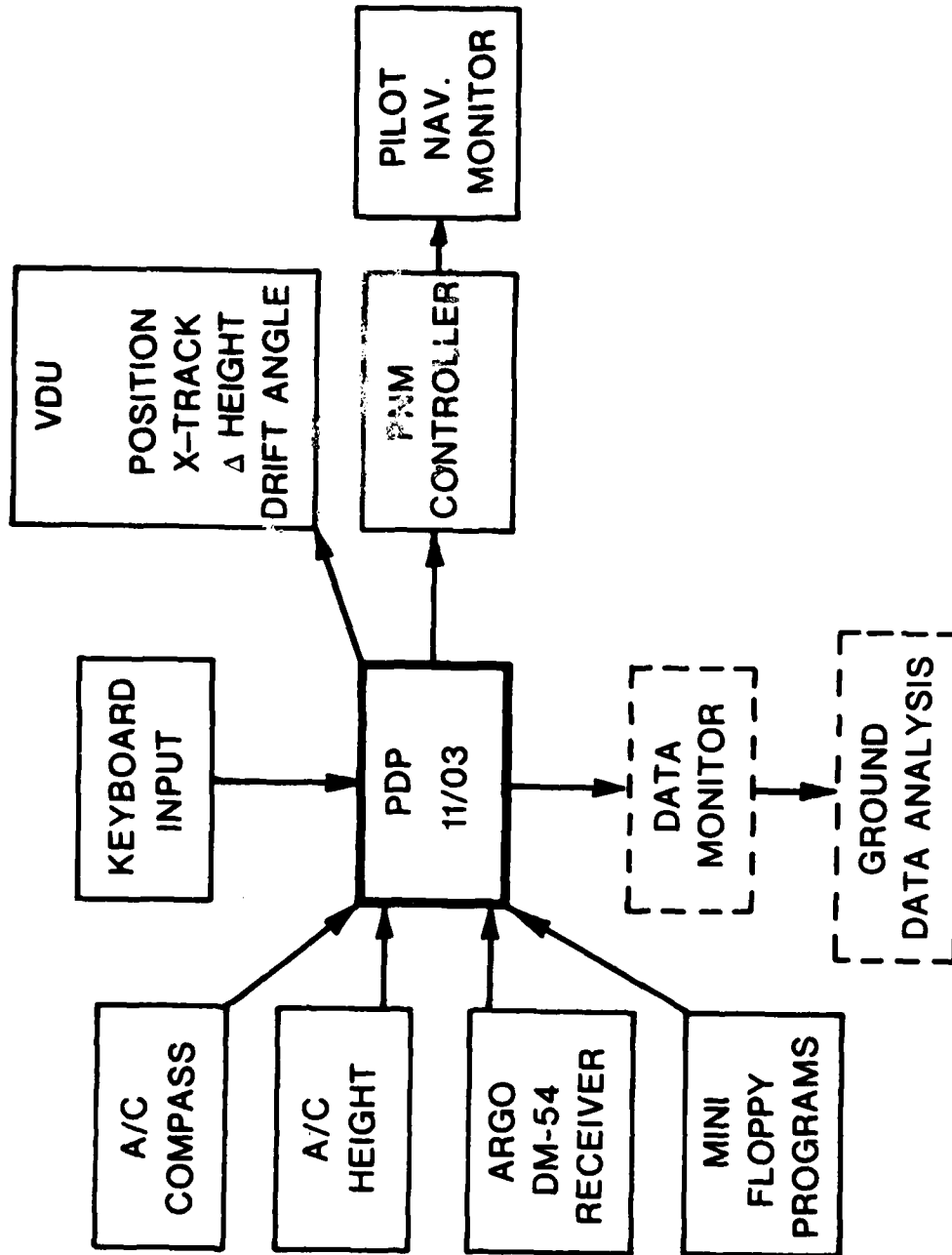Figure 3 ARGO - WRELADS FORMAT

Figure 4   ARGO STATION

Figure 5   WRELADS - BLOCK DIAGRAM AIRCRAFT NAVIGATION
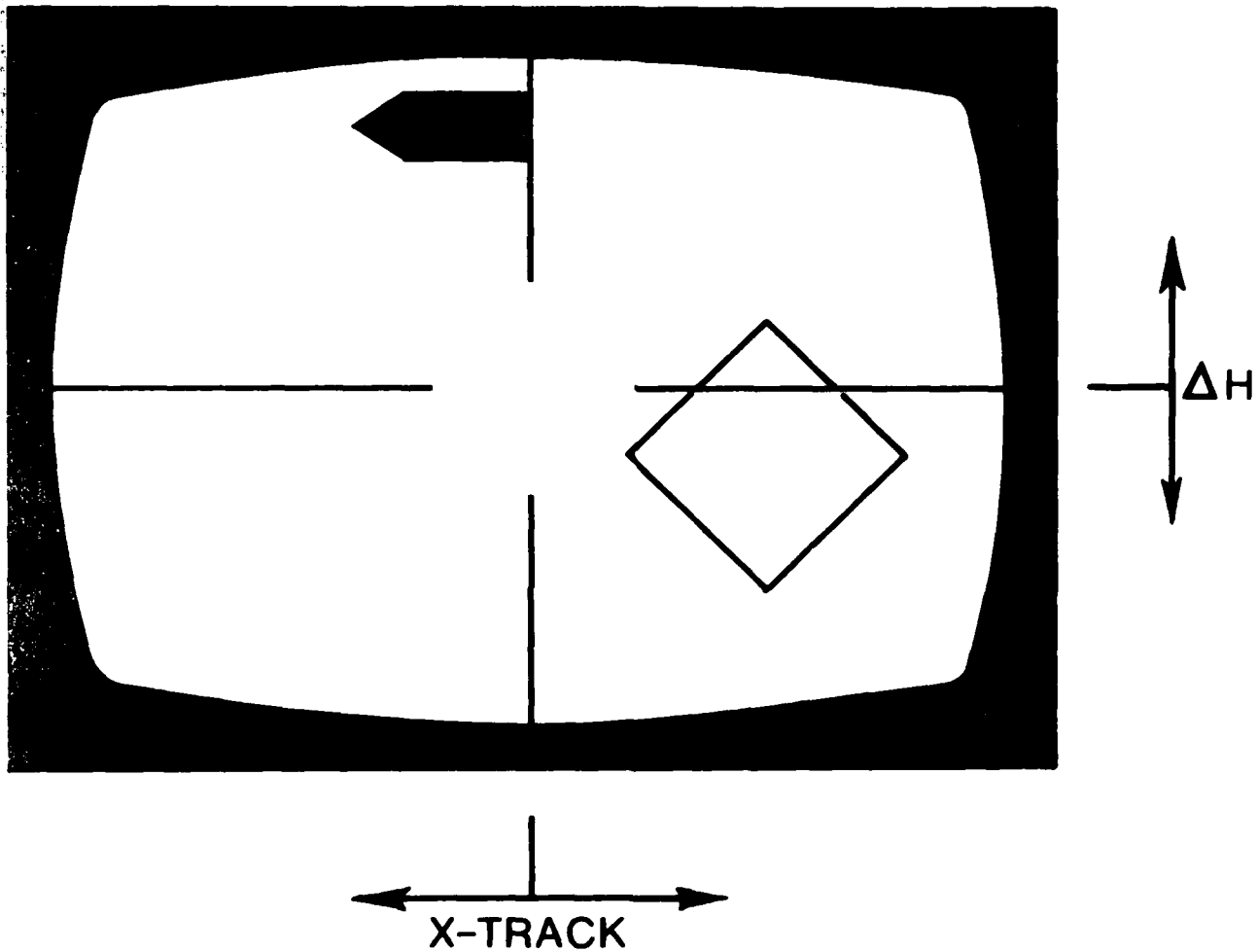
Figure 6   WRELADS - PILOT NAVIGATION MONITOR

OPERATIONAL
ALTITUDE
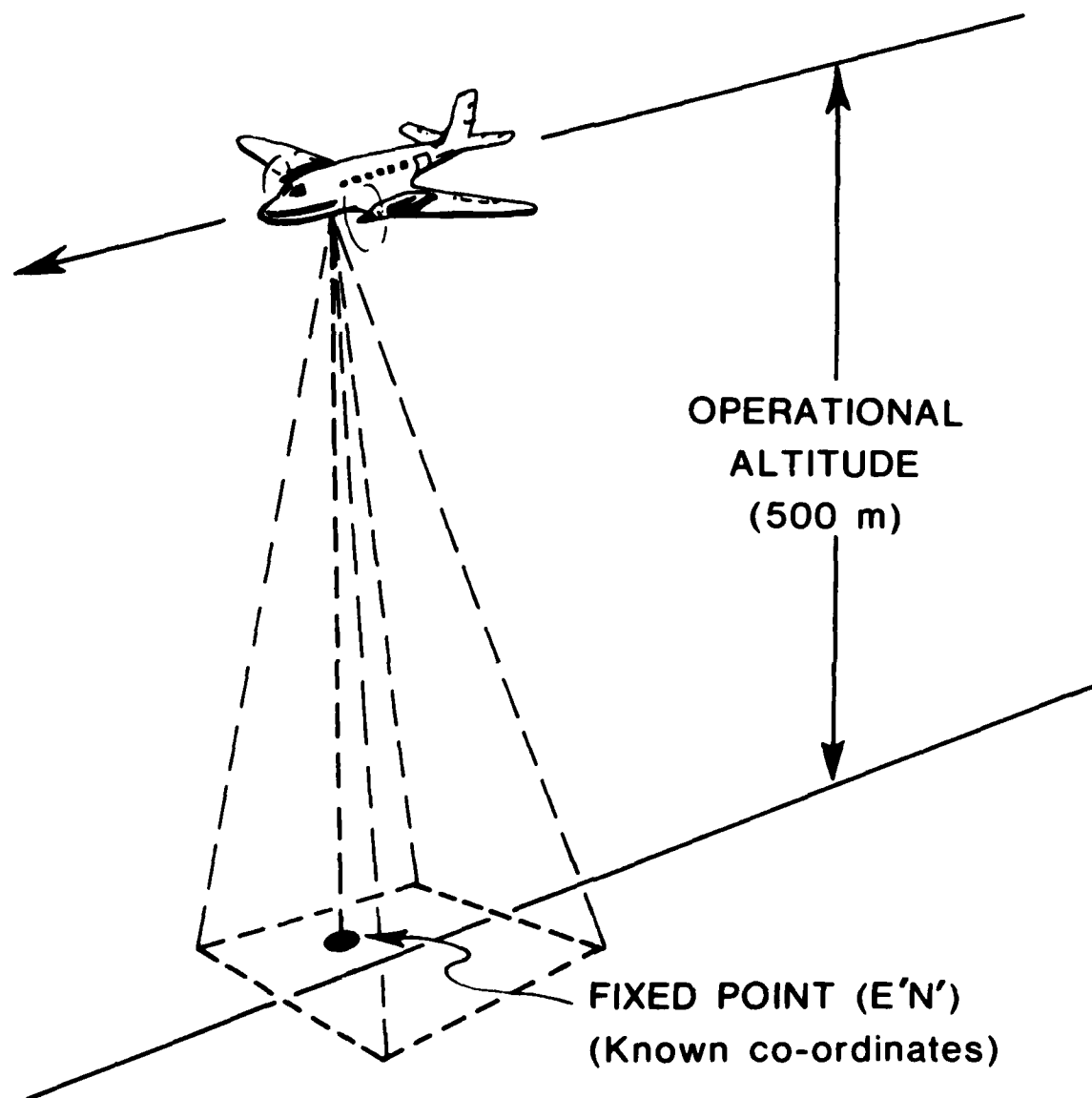(500 m)

FIXED POINT (E'N')
(Known co-ordinates)

Figure 7   WRELADS - ARGO CALIBRATION

1 FIXED POINT OVERFLIGHT

2 SINGLE SWATH LASER DEPTH PROFILE

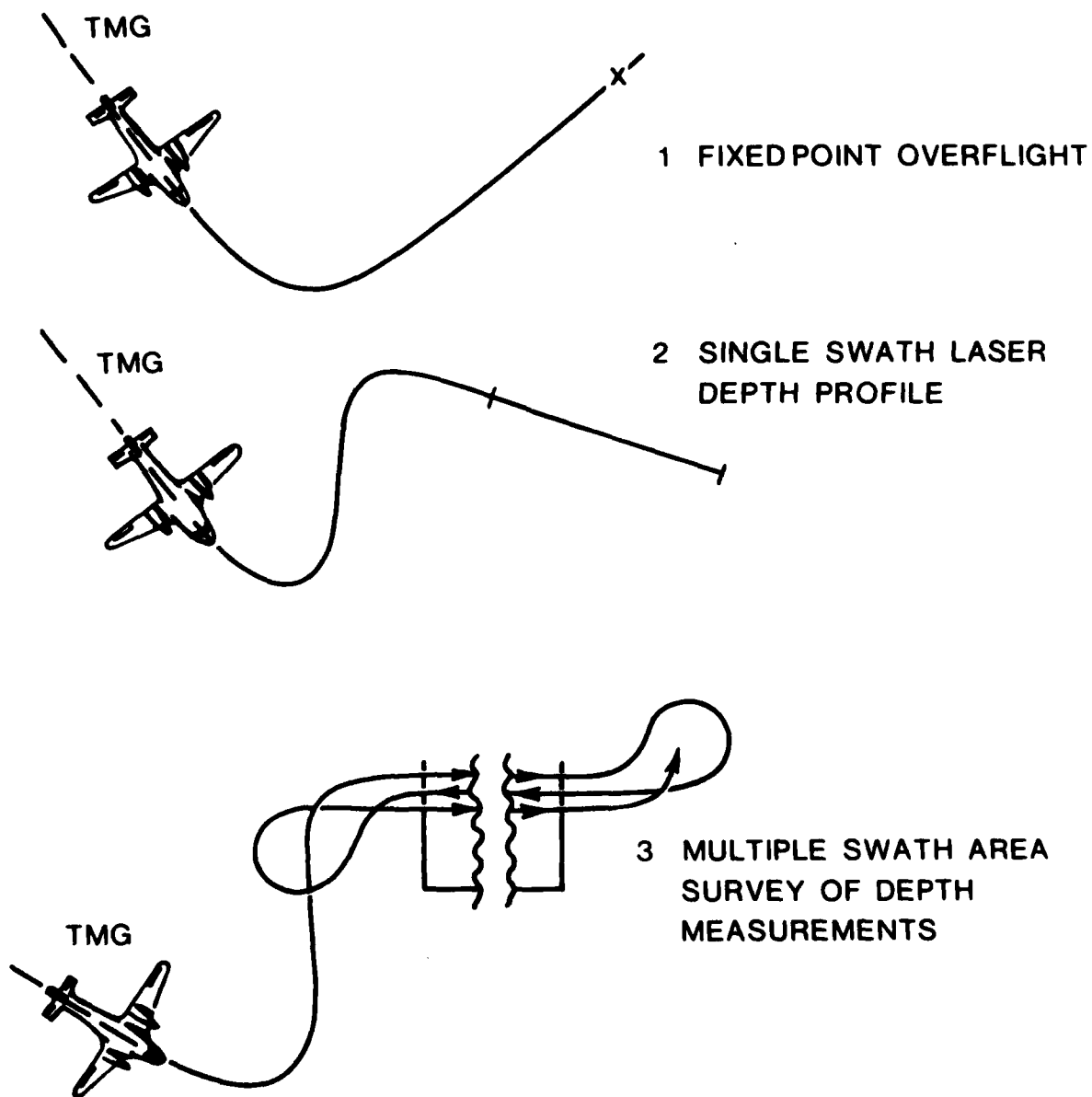3 MULTIPLE SWATH AREA SURVEY OF DEPTH MEASUREMENTS

Figure 8   WRELADS - MISSION TYPES
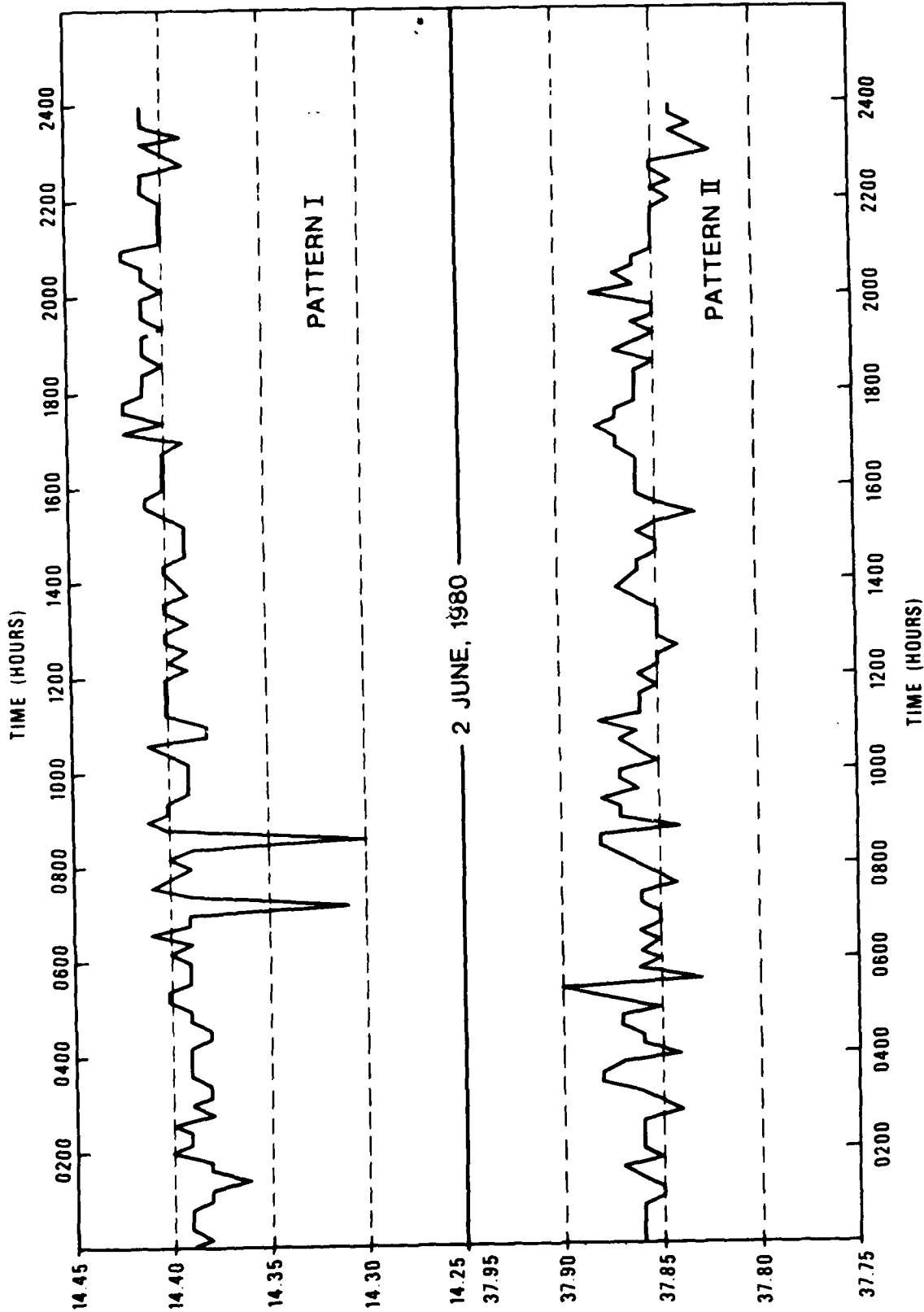
Figure 9 DRCS MONITOR STATION RECORD
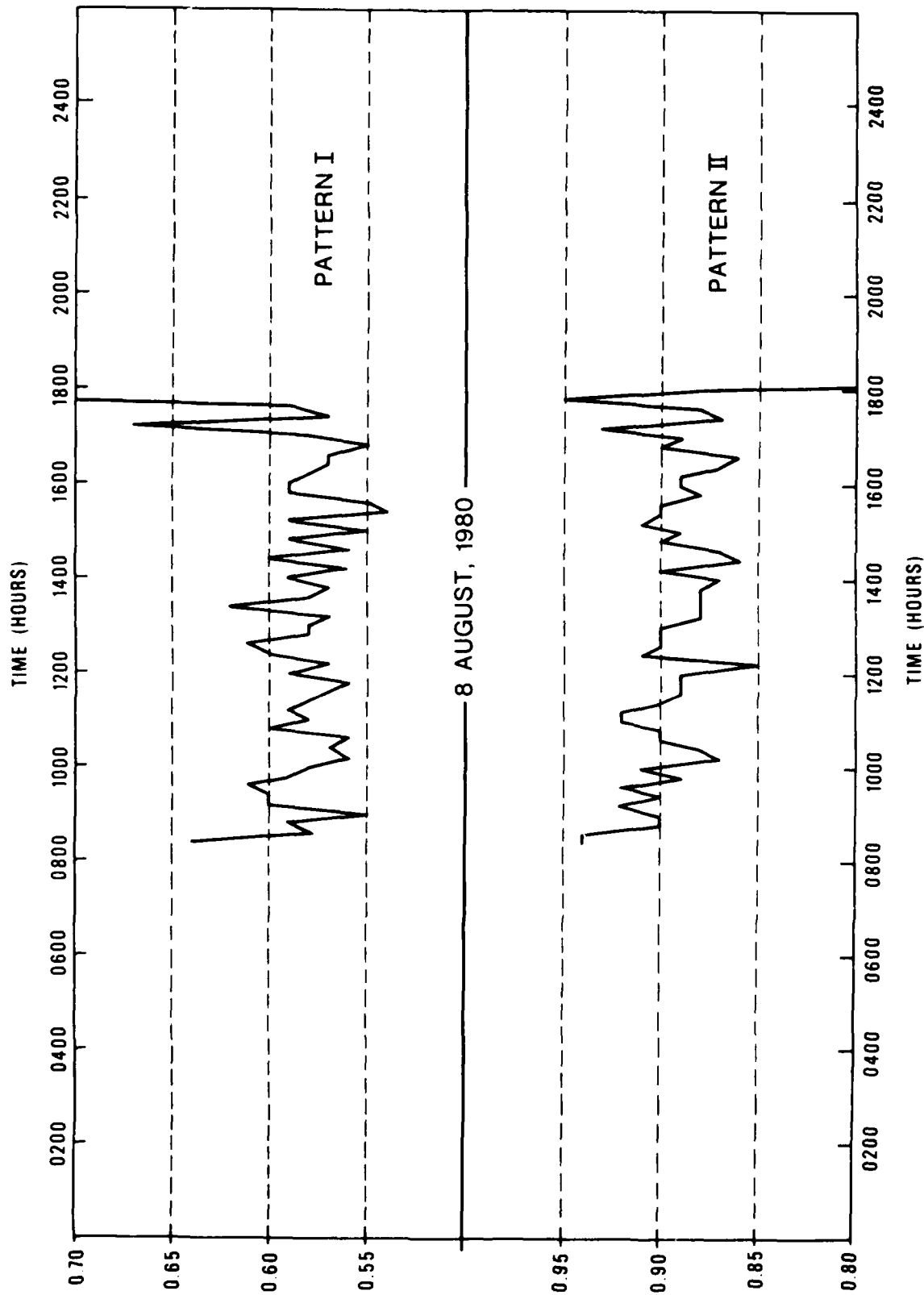
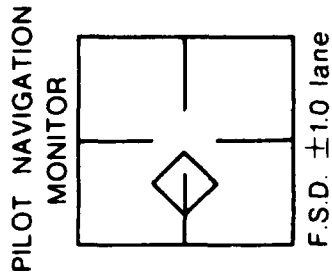Figure 10 MONITOR STATION RECORD - TOWNSVILLE
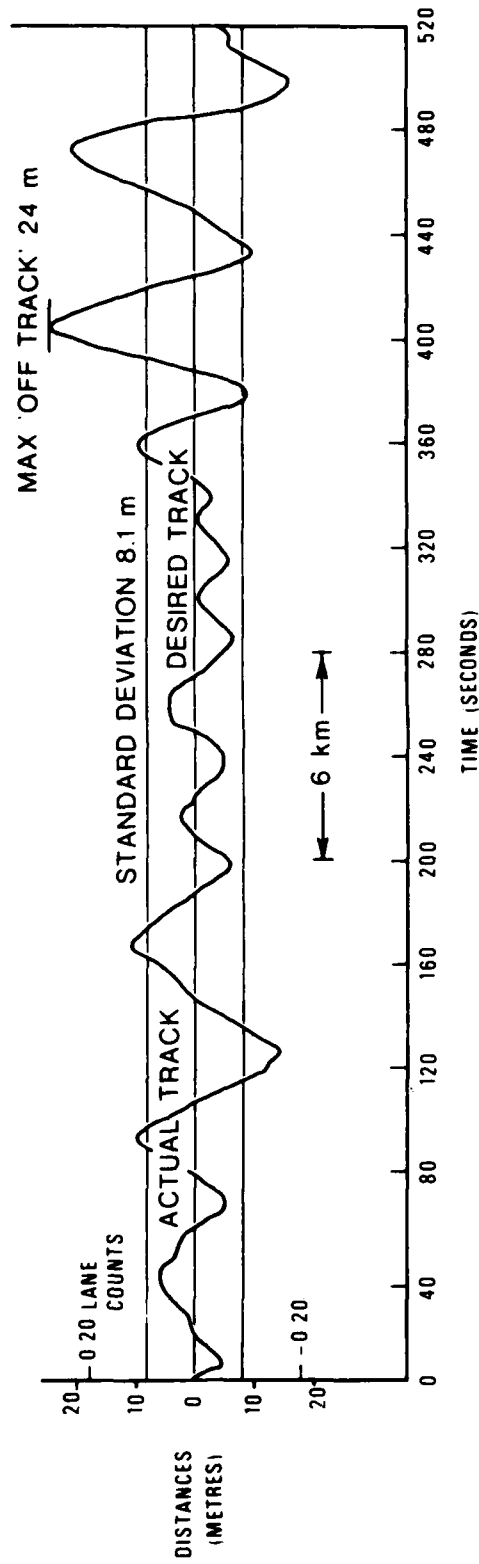
Figure 11 EXAMPLE OF TRACK KEEPING
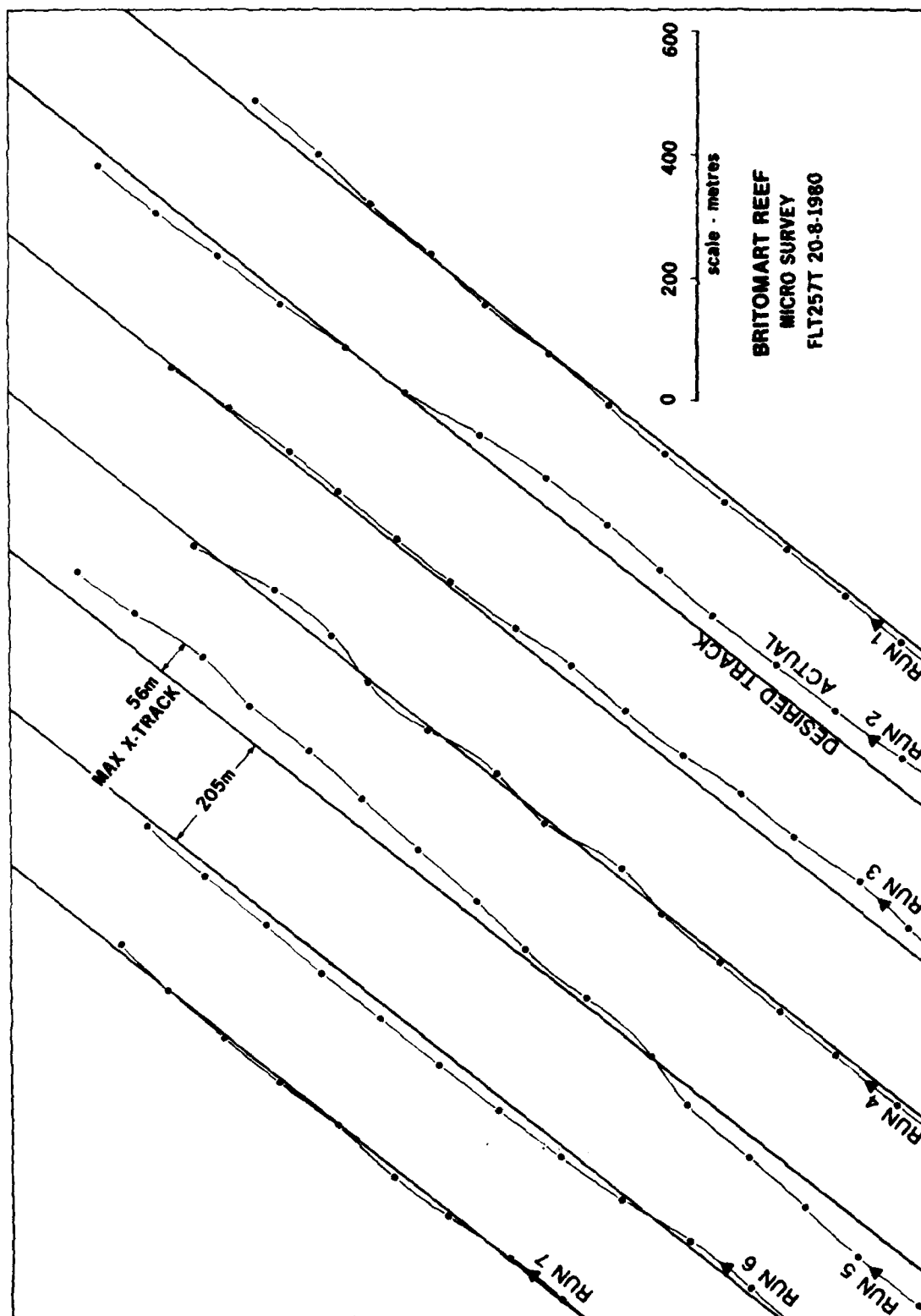
Figure 12   MICRO SURVEY - AN EXAMPLE OF TRACK KEEPING

BRITOMART REEF
MICRO SURVEY
FLT257T 20-8-1980

scale - metres

0   200   400   600

DESIRED TRACK

ACTUAL

RUN 1

RUN 2

RUN 3

RUN 4

RUN 5

RUN 6

RUN 7

56m
MAX X-TRACK

205m

PAPER 16

AN ACTIVE/PASSIVE MULTISPECTRAL SCANNER

FOR AIRBORNE HYDROGRAPHY

Michael T. Cooper
Naval Coastal Systems Center
Panama City, Florida 32407
USA

ABSTRACT

A technique for high-speed, wide-area, high-resolution airborne hydro-graphic survey using a hybrid active/passive scanner is described. The scanner collects data in several passive channels in the blue-green and near infrared. The effect of the optical characteristics of the water and the bottom on the depth determination process is established by use of a pulsed blue-green laser, which is bore-sighted with the passive scanner. The calibration established permits derivation of quantitative data on water depths from the passive data. The technique has been successfully tested in several locations in and near the U.S. Design studies indicate that an operational version of the scanner can be built using off-the-shelf technology.

BACKGROUND

The Defense Mapping Agency has a large backlog of hydrographic chart revision work which cannot be eliminated using assets and techniques currently available. A significant portion of this backlog is of shallow water areas which can be charted by means of active and/or passive electro-optic sensors mounted on airborne platforms. The high speed and large swath width obtainable using airborne sensors make it possible to chart more quickly and less expensively than alternative means over wide areas of interest.

Attempts have been made to use data collected by airborne passive multi-
spectral scanners to determine water depth over the area scanned.[1]
Passive scanners have the advantage that the data collection rate is extremely
high, making possible wide area coverage, high resolution coverage, or some
desirable combination of the two. It should be possible, using these scanners,
to make full use of the relative stability and speed of a fixed-wing aircraft
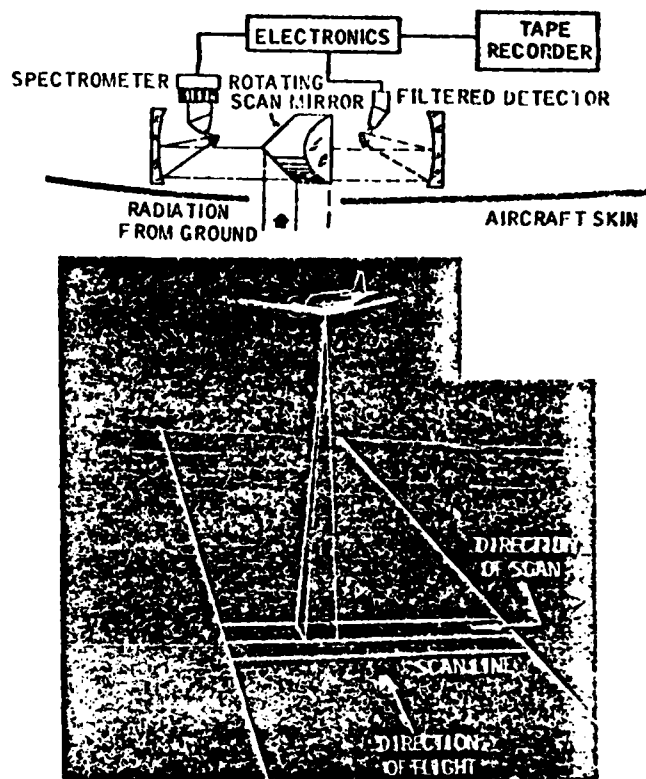(Figure 1).

FIGURE 1.   PASSIVE MULTISPECTRAL DATA COLLECTION OPERATIONS

Passive multispectral scanners have been in use for many years to gather
environmental data for a broad variety of uses. Basically, the scanners
all work on the same principle: light is gathered from a picture element,
or "pixel" of the scene below the aircraft by a rotating scanning mirror.
The light is directed into passive optical components which decompose the
beam into its constituents, each of a narrow frequency band. The constituent

Figure 1 ARGO - OPERATING PRINCIPLE

beams are then directed into photomultiplier or photometer receivers which convert
the light into electronic signals, which are then digitized and recorded on
high density digital magnetic tape for subsequent analysis.

The use of sensors such as this for bathymetry depends on the physics
expressed in the following equation:

$$V_T = V_D + g \rho e^{-fkd} \tag{1}$$

where V_T represents the light signal at a given wavelength received in
the scanner

V_D represents the signal received from the water surface

g and f are instrument and geometric constants and atmospheric factors

ρ is bottom reflectivity

k is the diffuse attenuation coefficient of water, and

d is water depth.

This means that if a logarithmic plot of the net radiance vs. depth d is made,
and if two depth points are known, depth can be determined in principle for
all points on the scanner image.

The problem with passive scanning is that passive data alone is not
sufficient to determine water depth. Not only is it usually necessary to
know the depth at two or more points in the scene in order to calibrate the
data, but also the presence of different optical bottom types or of non-
uniformity in water turbidity can complicate the calibration.

It has become apparent that much of the difficulty can be resolved by the
incorporation of a pulsed blue-green laser into the scanner, along with the
development of methods of analysis which can make use of the additional data
provided by the laser.

DESCRIPTION OF ACTIVE/PASSIVE SCANNER

Figure 2 is a schematic diagram of the M-8 active/passive multispectral
scanner. This device was developed by the Environmental Research Institute
of Michigan (ERIM) for the NASA Advanced Applications Flight Experiment
program.[2] The scanner was conceived as a modification of the all-passive
ERIM M-7 multispectral scanner.[3] As may be seen in Figure 2, a single mirror
is mounted at either end of the drive motor. A fixed folding mirror in front
of one scan mirror directs two laser beams onto the scan mirror. The second
scan mirror is used for reception of the surface return, and is separated from
the first by 24" in order not to receive atmospheric backscatter of the trans-
mitted beams. Canting of the mirrors is adjusted to focus them on a common point
1000 feet distant. Torsional displacement of 1 mrad compensates for the time
delay as the laser beam travels to the scene and back.
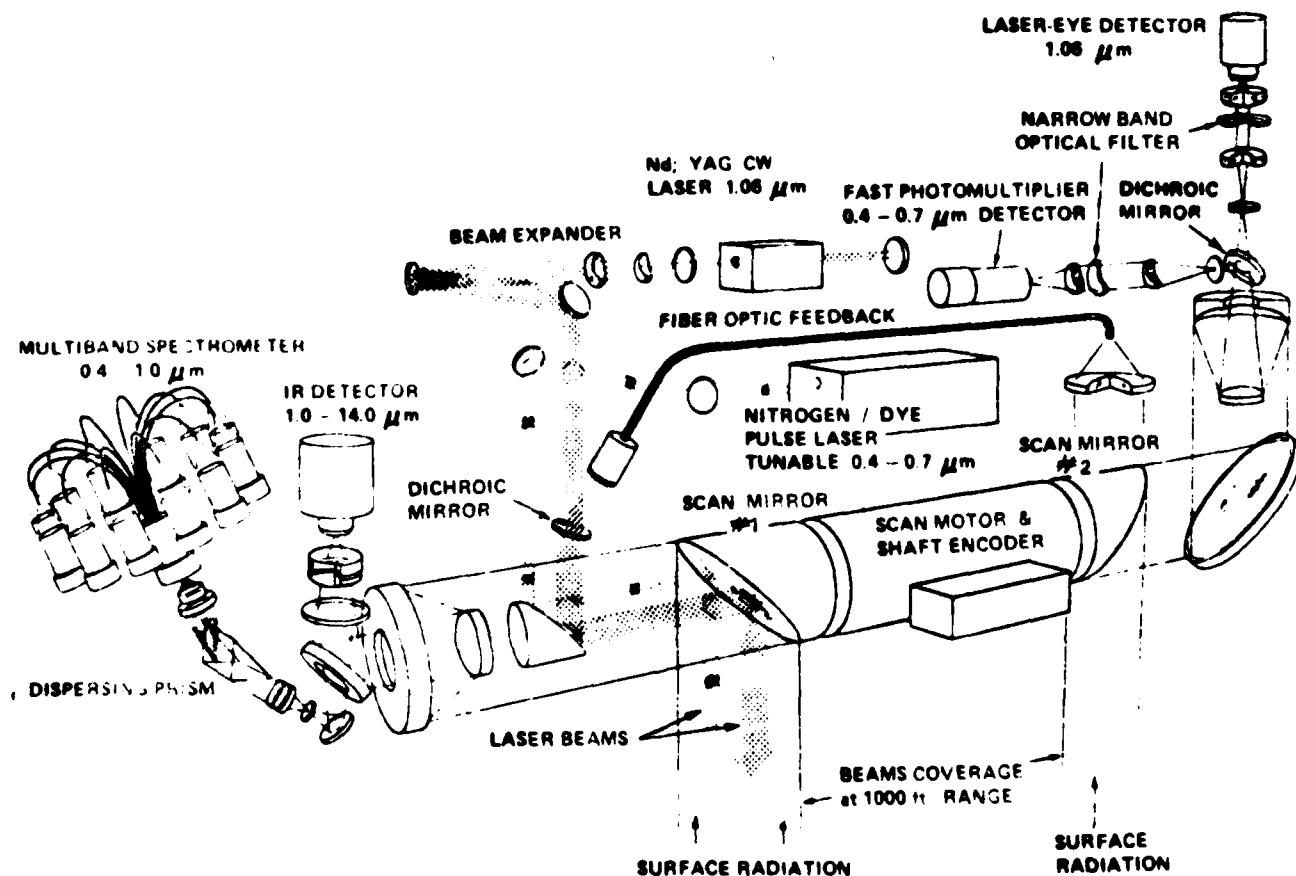

FIGURE 2. OPTICAL SCHEMATIC OF ACTIVE/PASSIVE MULTISPECTRAL SCANNER

Incoming passive radiation is reflected by the scan mirror on the left into a beam divider which diverts the radiation into an IR detector and a multichannel spectrometer. The IR detector can be configured to cover any one of several bands in the range of 1.1 to 13.5 μm. If the 1.5 to 1.8 μm band is selected, a cooled filter for that band is used together with a liquid nitrogen cooled InSb detector. Thermal bands use an uncooled external filter with a liquid nitrogen cooled HgCdTe detector.

The radiation from 0.4 to 1.0 μm passes through a glass prism into a set of photomultiplier detectors. Up to nine bands ranging from the ultraviolet to the near infrared can be chosen. Common radiation reference sources consisting of a dark level, a point source calibration lamp, one ambient temperature blackbody plate, and two temperature-controlled blackbody plates are emplaced where they can be viewed by each detector for calibration purposes during the internal portion of each scan. The operator sets lamp brightness and the temperature of two of the plates to approximate surface conditions.

The effective aperture of the optics is 106.4 cm^2. The instantaneous field of view of the passive optics is 2 mrad, leading to a 2 foot pixel at the design altitude of 1000 feet. The total field of view is $\pm$ 45° about nadir, leading to a swath width twice the aircraft altitude. The scanner is normally mounted in a DC-3 aircraft which travels at 200 ft/sec during runs. A revolution rate of 100 Hz provides contiguous data at 1000 feet. A rate of 60 Hz is selectable for higher altitudes. Signal gains and offsets are operator-selected prior to data runs.

The M-8 scanner possesses a Nd:YAG continuous wave laser operable at 1.06 μ which can make a laser-illuminated image of the scene. Calibration for bathymetry data is provided by a Molectron Spectroscan 10 Nitrogen-pumped pulsed dye laser operated at a center wavelength of 0.52 μm. The laser radiation scattered from the surface is received by the scan mirror on the right. The

active detectors have a 3 mrad IFOV because of slight changes in alignment as scan angle and range varies.

The Molectron laser emits about 100 pulses per second with a pulse width of 4.5 nanoseconds and a peak power of 18 kw. The laser is usually operated at nadir, but can be operated out to $\pm$ 24°. The return pulses are recorded in registration with the passive data. This is an extremely important point, because it permits analysis of the active and passive data as a unified set. Only 5 pulses per second, or one pulse every 12 scan lines at 60 Hz are actually digitized and recorded, due to the limitations of the signal handling electronics. Depth is determined via laser by multiplying the time difference between the surface return pulse and the bottom return pulse by one-half the velocity of light in sea water.

The output of the passive detectors is a set of analog electrical signals. These signals are pre-amplified at the scanner and postamplified at the operator console to a 0-3 volt level. The signals are then digitized and recorded on 8-bit (256 level) high density digital magnetic tape (HDDT). The laser pulses are digitized using a Tektronix Model 7912 transient digitizer. The digitized waveform is stored in a semiconductor memory and then read out to two channels of the HDDT tape recording. Current limitations of this system permit only 5 pulses per second to be   recorded.

In summary, the M-8 active/passive multispectral scanner is capable of making imagery at a rate of about 40 nmi^2/hr in 9 passive and one active band from the ultraviolet to the infrared. It can also take five laser calibration pulses per second. Resolution of the raw passive imagery is one point every four square feet. The alignment of the scanner is tolerant of variations in speed and altitude as circumstances require.

The scanner was designed as a general purpose instrument and has been made available to federal, state, and local government institutions and private

customers for a wide variety of experiments. It is not optimized for hydrography.

Research in hydrographic applications of the scanner is normally carried out by operating the scanner over a selected area of shallow water, processing the data for water depth and bottom classification, and comparing the depths so determined with depths obtained by survey teams on the ground. Some examples will be given in a later section.

DATA ANALYSIS FOR HYDROGRAPHY

The unique feature of analysis of active/passive scanner data for hydrography is that the blue-green laser data, collected in registration with the passive data, is used to establish the effect of the optical characteristics of the water and of the sea bottom on depth determination and to establish a valid calibration of the data. This analysis is still evolving.[4-5] The following is a discussion of the analysis as it is now carried out. The figures are taken from References 4 and 5, also.

A typical data set will consist of several hundred lines of scanning data, in all bands. Normally two channels will be selected for processing. In addition to this, the pulsed blue-green laser has fired at random into the scene, as far as bottom types are concerned. The laser pulses yield depth immediately. It is known in what pixel the laser/depth data was taken. Therefore, several tens of thousands of geographic points are viewed, for several dozen of which the depth is known.

A flow chart of the processing is shown in Figure 3. The first step is to create a computer-compatible tape with those data channels most likely to be needed for processing. Then, separately, the laser pulse returns are displayed and depths extracted.
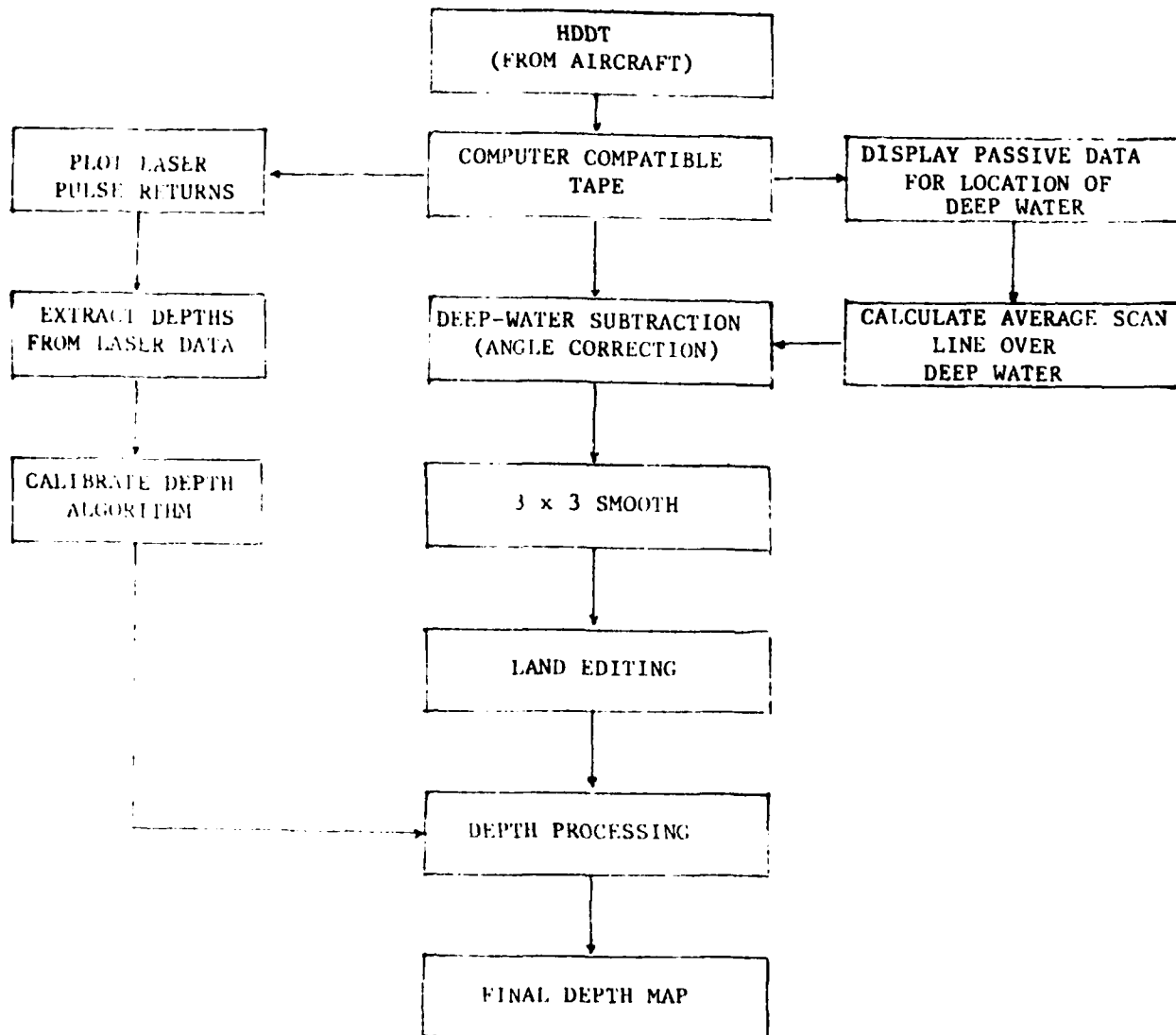
```
                    ┌─────────────────────┐
                    │        HDDT         │
                    │  (FROM AIRCRAFT)    │
                    └─────────────────────┘
                               │
                               ▼
┌─────────────────┐ ┌─────────────────────┐ ┌─────────────────────┐
│   PLOT LASER    │◄│ COMPUTER COMPATIBLE │►│ DISPLAY PASSIVE DATA │
│  PULSE RETURNS  │ │        TAPE         │ │   FOR LOCATION OF    │
└─────────────────┘ └─────────────────────┘ │     DEEP WATER       │
         │                     │            └─────────────────────┘
         ▼                     ▼                        │
┌─────────────────┐ ┌─────────────────────┐ ┌─────────────────────┐
│ EXTRACT DEPTHS  │ │ DEEP-WATER SUBTRACTION│◄│ CALCULATE AVERAGE SCAN│
│ FROM LASER DATA │ │  (ANGLE CORRECTION) │ │      LINE OVER       │
└─────────────────┘ └─────────────────────┘ │     DEEP WATER       │
         │                     │            └─────────────────────┘
         ▼                     ▼
┌─────────────────┐ ┌─────────────────────┐
│ CALIBRATE DEPTH │ │     3 × 3 SMOOTH    │
│    ALGORITHM    │ └─────────────────────┘
└─────────────────┘           │
         │                     ▼
         │          ┌─────────────────────┐
         │          │    LAND EDITING     │
         │          └─────────────────────┘
         │                     │
         │                     ▼
         │          ┌─────────────────────┐
         └─────────►│  DEPTH PROCESSING   │
                    └─────────────────────┘
                               │
                               ▼
                    ┌─────────────────────┐
                    │   FINAL DEPTH MAP   │
                    └─────────────────────┘
```

FIGURE 3.   BATHYMETRY PROCESSING FLOWCHART

Total radiance, V_T, consists of two components,

$$V_T = V_D + \Delta V \qquad\qquad (2)$$

at all frequencies. V_D represents that fraction of the radiation scattered
from the surface. ΔV is net radiance reflected from the bottom. It is first
necessary to isolate ΔV. This is done by making part of the data run over deep
water, where $\Delta V = 0$. The deep water signal is typically a function of scan
angle, because of longer atmospheric paths and sun glint. To estimate this
function for each spectral band, the passive signals in that band for all
pixels, at a given scan angle, in a set of lines representative of deep water
are averaged. This "average scan line" is then subtracted pixel by pixel
from the data taken over shallow water. Areas where the net bottom radiance is
zero are treated as water too deep to analyze.

The next step is to smooth, or spatially filter the data in order to
improve the signal-to-noise ratio. This must be done with care, in order not
to obscure features of interest such as, for example, coral heads. Typical
practice in the experiments described here is to replace each pixel value by
the average of the pixel radiance and its eight nearest neighbors. This will
improve the signal-to-noise ratio by a factor of three.

Land area, if any, can be edited out by deleting all pixels with a radiance
above a pre-selected threshold in a near-infrared band, (1.5-1.8μm). This is
possible because signal levels in this band are very low over water as compared
with those over land.

The fact is now used that for several dozen of the points, depth and
passive radiance are known simultaneously.

The first-order physics, as stated in Eqn. (1), says that when net radiance
at a given frequency is plotted vs. depth, the points should arrange themselves
along one or more determinable straight lines, depending upon the number of
bottom types present. The intercept of the line at zero depth will be higher
or lower as the bottom is more or less reflective in that frequency band. The
slope of the line will be more or less steep as the water is more or less turbid.
A regression analysis will result in lines which assist in determining water
and bottom optics. If significant penetration is achieved at two wavelengths,
λ_1 and λ_2 a multiple regression of the form

$$d = a + b\,x_1 + c\,x_2 \qquad\qquad (3)$$

where $x_1 = \ln \Delta V_1$, net radiance at wavelength λ_1

$x_2 = \ln \Delta V_2$, net radiance at wavelength λ_2

may be used. Calculation of the associated correlation coefficients is
performed to choose the band or band combination which best determines depth.
Figure 4 shows an example of a single bottom-type case from data taken over the
Gulf of Mexico.

In the case of a uniform bottom, this is all that need be done, and this
is all that is done if only passive data and a few ground points are available.
Each net radiance value is mapped onto the corresponding depth as determined by
the regression analysis.

The situation is complicated if water turbidity or bottom reflectivity
or both are non-uniform. Work to date at NCSC has been with data sets taken over
areas of uniform water turbidity. It should be possible by interactive means
(i.e., by a light pen and a display of one channel) to segregate areas of
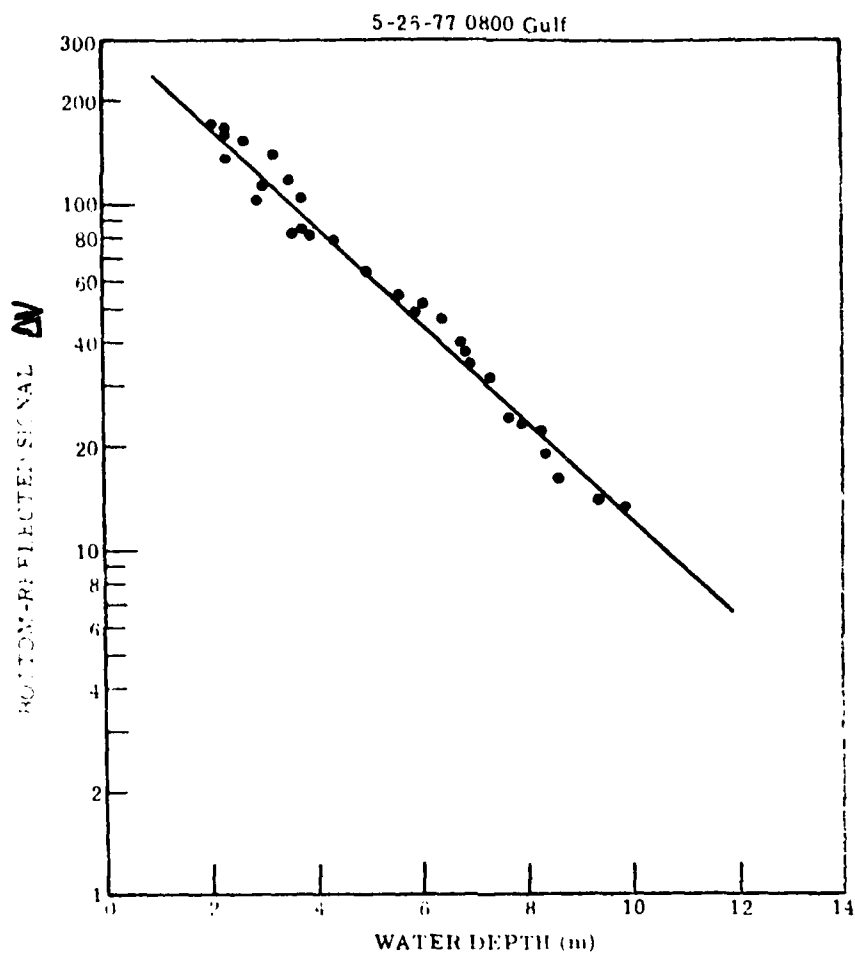relatively uniform turbidity. The computer can be directed to re-plot points

FIGURE 4.   PLOT OF PASSIVE SIGNALS IN BAND 3 (.50-.54 μm) VERSUS
            DEPTHS FROM LASER PROFILER, FOR GULF TEST SITE

as in Figure 4 for laser points lying within the area enclosed by the light pen.
Uniform turbidity is established by visually ascertaining that the calibration
points arrange themselves along one or more straight lines, with the same slope
for all bottom types, slope being determined by turbidity. A multiple line case,
reflecting the presence of different bottom types, is shown in Figure 5. This
data was collected over St. Andrews Bay in 1977.

For areas such as the Panama City test area, recognition of a uniform-
turbidity/multiple bottom type case may be virtually instantaneous. It may not
be so clear-cut for other areas. Figure 6 shows a more ambiguous case, taken
off Puerto Rico in 1979.[(6)] To resolve uncertainties it may be necessary to
exclude points of low signal-to-noise ratio, or study footprint camera photo-
graphs (or color reconstitutions of the image data). As will be seen later,
one design objective of a dedicated hydrographic scanner would be to make a
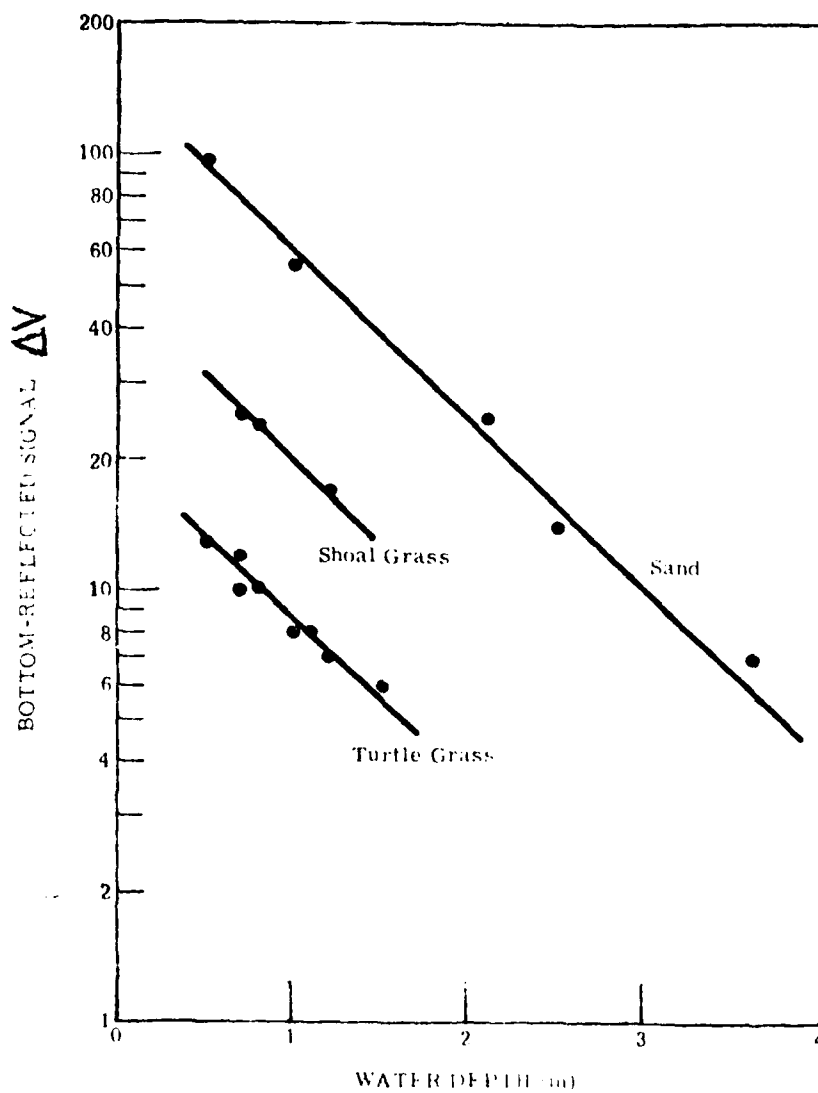
FIGURE 5.   PLOT OF PASSIVE SIGNALS IN BAND 4 (.52-.57 μ m) VERSUS
            DEPTHS FROM LASER PROFILER, FOR ST. ANDREW BAY TEST SITE

scanner whose capabilities could assist in resolving processing uncertainties
with a minimum of analytical work.

In a multiple-bottom case it must be decided which of several calibration
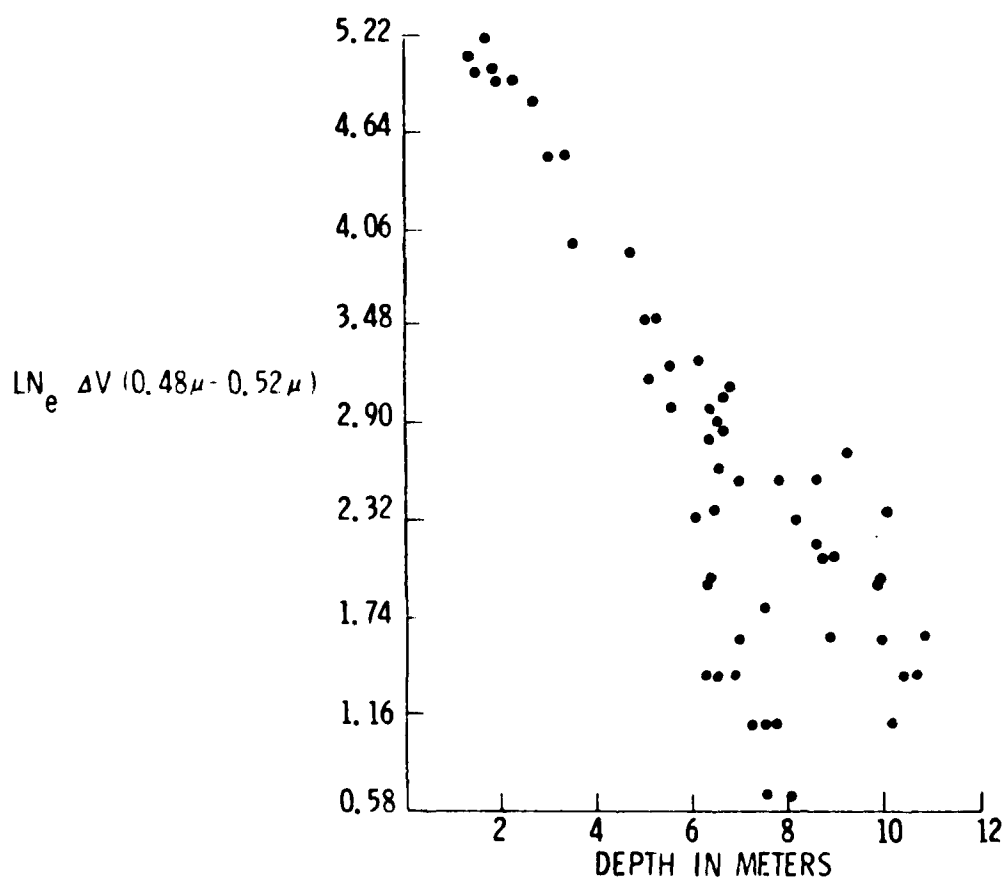curves a given passive point must be assigned to.   If the bottom types are

FIGURE 6.   LASER-DETERMINED DEPTHS VS. NET RADIANCE FROM
SEA BOTTOM, λ = (0.48 - 0.52$_\mu$), 15 MAY 1979

distinct this can be done by plotting the passive points, (along with those
for which laser-determined depths are available) in the amplitude space of the
$(X_i = \ln \Delta V_i)$. A two-band example is shown in Figure 7. The points tend to
arrange themselves in clusters, as they do in data taken over land. The clusters
tend to be elongated in the direction of less radiance, since the points are
collected over water columns of varying depth. Correspondence between laser
points in a given calibration curve and in a given cluster serves to indicate

X_5
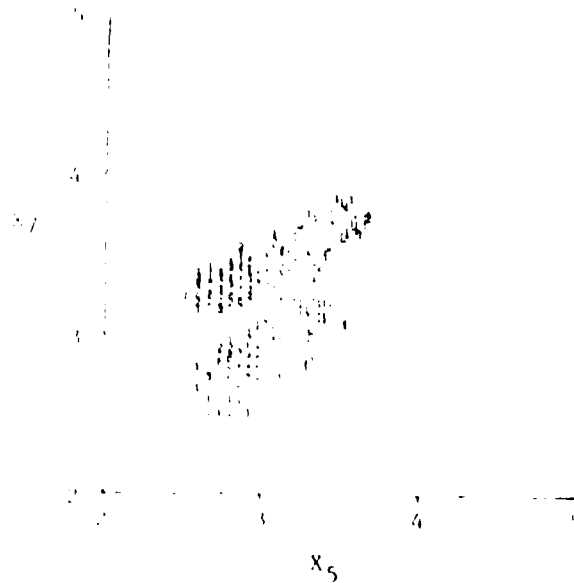
FIGURE 7.   PLOT OF PASSIVE SIGNALS IN AMPLITUDE SPACE

which cluster should be assigned to which calibration curve. Analysis has
shown that errors will arise in this procedure from incorrect classification of
points. In addition, difficulties will arise when bottom types are not sharply
distinct.

A more general procedure is suggested by noting that Eqn. (1) is true for
all wavelengths   which penetrate the water:

$$V_{T_i} = V_{D_i} + g_i \rho_i \, e^{-fk_i d} \qquad (4)$$

using Eqn. (2) this may be rewritten as

$$X_i = \ln \Delta V_i = \ln(g_i \rho_i) - fk_i d \qquad (5)$$

and a set of such equations exist, one for each of the λ_i of interest.

It can be shown that the N X_i coordinates can be transformed by a rotation
into a new coordinate system Y_i

$$Y_i = \sum_{j=1}^{N} a_{ij} X_j \qquad (6)$$

for i = 1....N

characterized by the fact that all but one of the Y_i are independent of depth
and dependent only on the optical bottom characteristics. For N = 2, the
rotation is throught the angle $\tan^{-1}\left(\dfrac{K_2}{K_1}\right)$. Furthermore, Y_N is of the form

$$Y_N = \sum_{j=1}^{N} a_{Nj} X_j \qquad (7)$$

where $a_{Nj} = K_j / \left(\sum_{L=1}^{N} K_L^2\right)^{\frac{1}{2}}$ a k.. wn

dependence on the turbidity characteristics of the water.

It can further be shown that the relation of Y_N to d is of the form

$$d = \alpha + \beta Y_N \qquad (8)$$

where β is a function of water attenuation and α is a function of bottom reflectance. It is possible to select a cluster, characterized by Y_i, $i = 1$ to N-1, and an appropriate value of α, and then solve for d, using Eqn. (8). This was done in Reference 4, on data taken in St. Andrew Bay. However, in order to allow for mixtures of bottom types, α must vary continuously. It has been found that α is approximately a linear function of the Y_i variables, for $i = 1....$N-1. This implies that depth itself can be written as a linear combination of the Y_i variables, therefore, of the X_i variables. Equation (3) is then valid for mixed bottom types, and the general procedure is to perform a regression analysis and correlation coefficient calculation using that equation. Explicit recognition of the bottom type is no longer necessary.

It is evident that the physics says that the X_i and Y_i are parametrically dependent on d. Because of this, contours of uniform depth, isodepth contours, must exist. A large number of calibration points may make possible a purely empirical procedure, where isodepth contours would be established and depth determined by an interpolation procedure. Data sets with enough calibration points to justify formulating and testing such a procedure are not yet available.

EXPERIMENTAL RESULTS

This technique has been tested in several experiments carried out in the USA.[4,6] Figure 8 shows a color graphic of the results of a run carried out over the Gulf of Mexico near Panama City, Florida. The aircraft flew from south to north at an altitude of 1000 feet. The flight track is the vertical through the center of the graphic. Because of the volume of data, it is convenient to color code the results, dividing the depth scale into increments and assigning a color to each. For each point the digitally-controlled color CRT is directed to display the colors of the increment in which the calculated depth falls.

Legend

>12 m

11-12 m

10-11 m

9-10 m

8-9 m

7-8 m

6-7 m

5-6 m

4-5 m
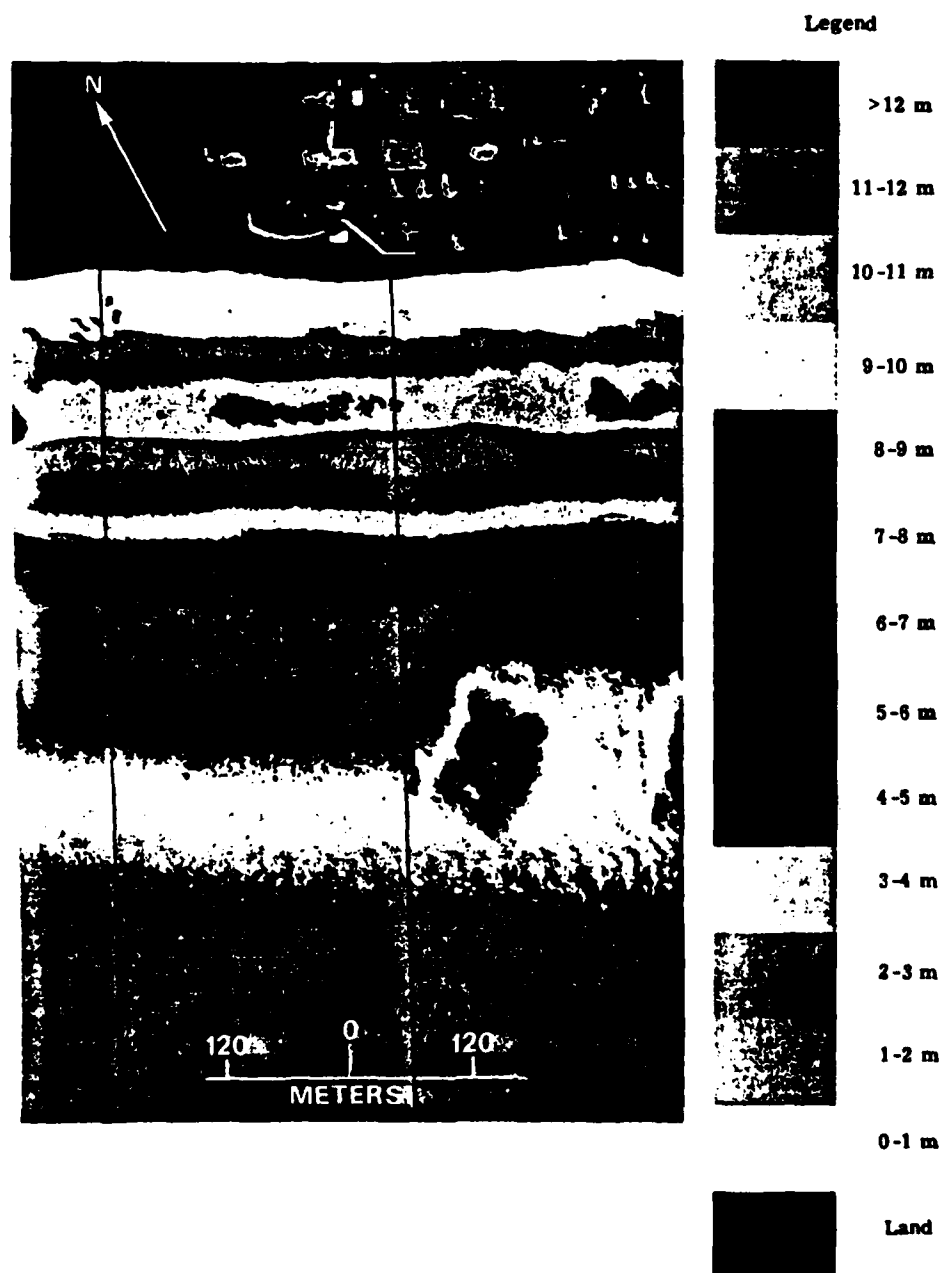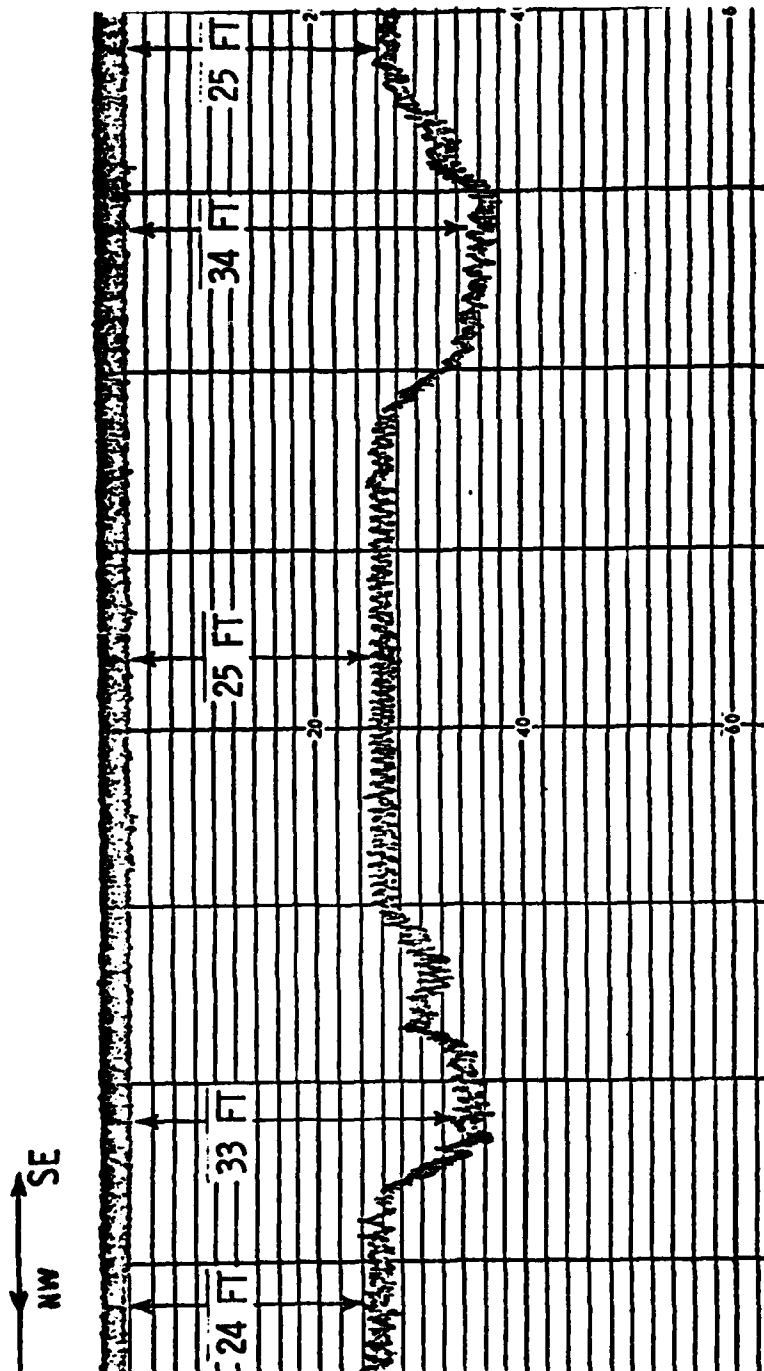
3-4 m

2-3 m

1-2 m

0-1 m

Land

FIGURE 8.   BATHYMETRY OF THE GULF OF MEXICO, 26 MAY 1977

The laser point distribution for this run, shown in Figure 4, indicates
a uniform bottom type. The large holes in the lower right actually exist,
as verified by fathometer data taken later. (Figure 9) It is the result of
dredging operations to restore the beaches after a hurricane.

TRACK IS AT GULF OF MEXICO TEST SITE
PARALLEL TO BEACH AT 24-25 FT. CONTOUR

FIGURE 9.   FATHOMETER PROFILE OF GULF BOTTOM ANOMALY

Figure 10 shows the results over a mixed bottom in St. Andrews Bay. The
black lines indicate fathometer transects. The ground surveys were conducted by
NCSC personnel. The results were compared at NCSC with the contractor-generated
bathymetry map. (Figure 11)
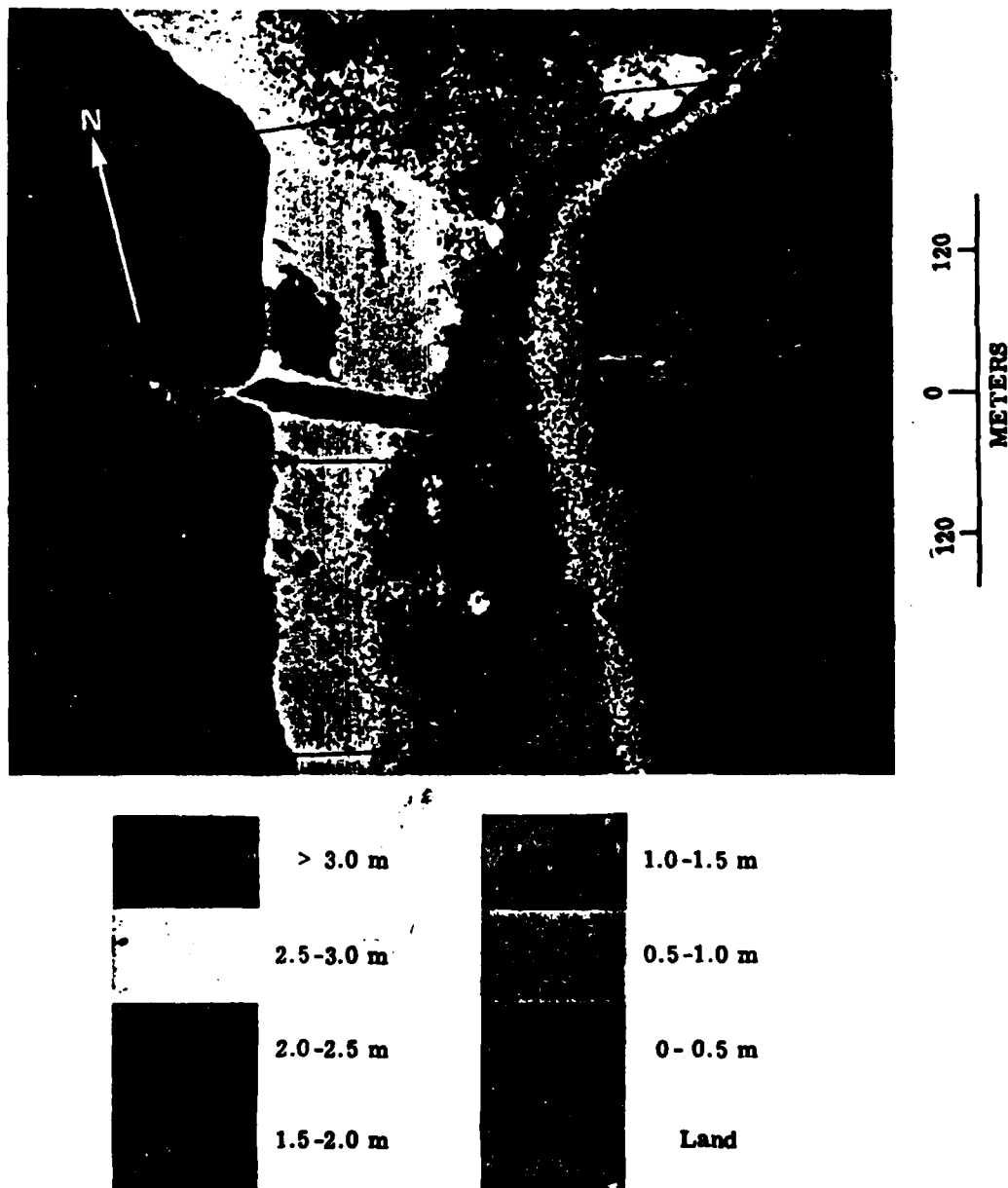
FIGURE 10. BATHYMETRY MAP OF ST. ANDREWS BAY, 26 MAY 1977
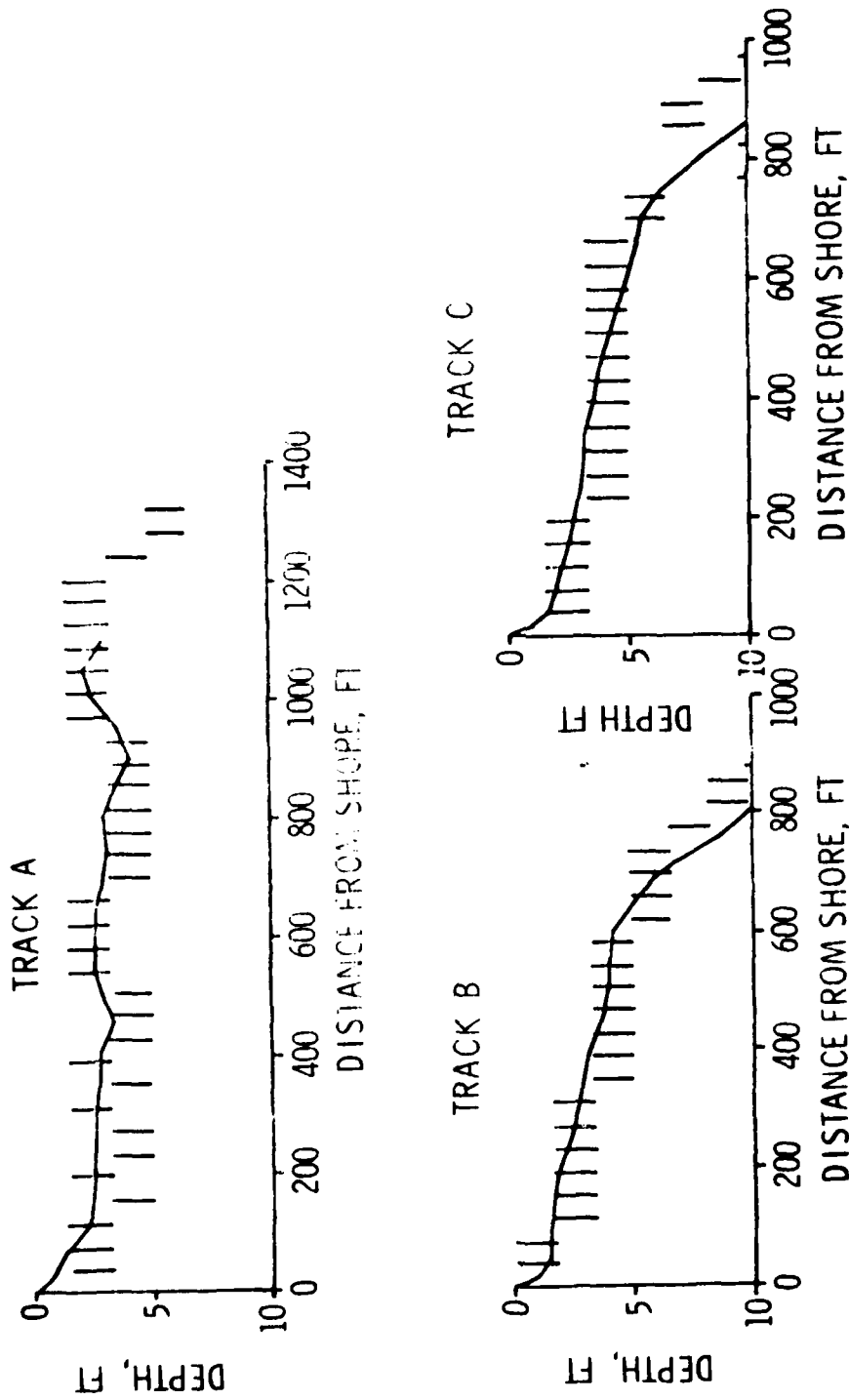
FIGURE 11.   COMPARISON OF FATHOMETER PROFILES WITH REMOTELY
SENSED RESULTS, ST. ANDREWS BAY, 26 MAY 1977

Figure 12 shows a bathymetry map generated from data taken over the
Bahia de la Chiva in Vieques, Puerto Rico on 15 May 1979. [6]

DEPTH IN FATHOMS

- Land
- 0-0.5
- 0.5-1.0
- 1.0-1.5
- 1.5-2.0
- 2.0-2.5
- 2.5-3.0
- 3.0-3.5
- 3.5-4.0
- 4.0-5.0
- 5.0-6.0
- Over 6.0

Scale in feet

FIGURE 12.   BATHYMETRY MAP FOR BAHIA DE LA CHIVA, 15 MAY 1979,
             SCANNER ALTITUDE 600 FEET

Concurrently with this survey a ground team generated the depth map
shown in Figure 13. Depth is in feet. The black lines on Figure 12
show the bounderies of the ground survey.

FIGURE 13.   DEPTH CHART PREPARED FROM GROUND SURVEY,
             BAHIA DE LA CHIVA, 15 MAY 1979

The two sets of survey results were compared in detail at NCSC using computer printouts of the airborne survey results. Using the known scales, the beach markers located on both products, and aircraft velocity and altitude, the position of each point of the ground survey was determined on the airborne product, and the depth values compared.

Figures 14-17 exhibit comparisons between the depth values and profiles determined by the ground survey and those determined by the airborne survey along the lettered transects perpendicular to the shore in Figure 13. The rms difference between the two sets of numbers is indicated beside each graph.
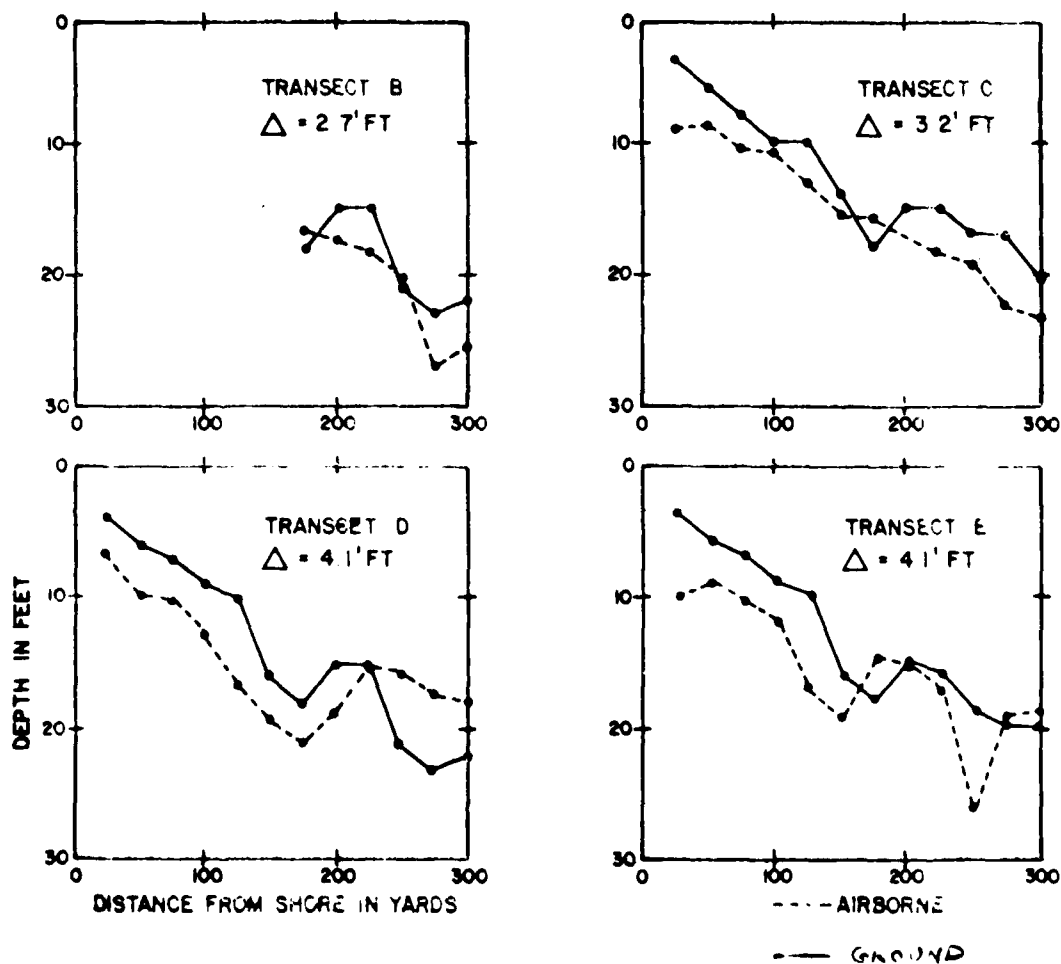
FIGURE 14.   COMPARISON OF DEPTH PROFILES DETERMINED BY GROUND
             AND AIR SURVEY, BAHIA DE LA CHIVA, 15 MAY 1979 - I
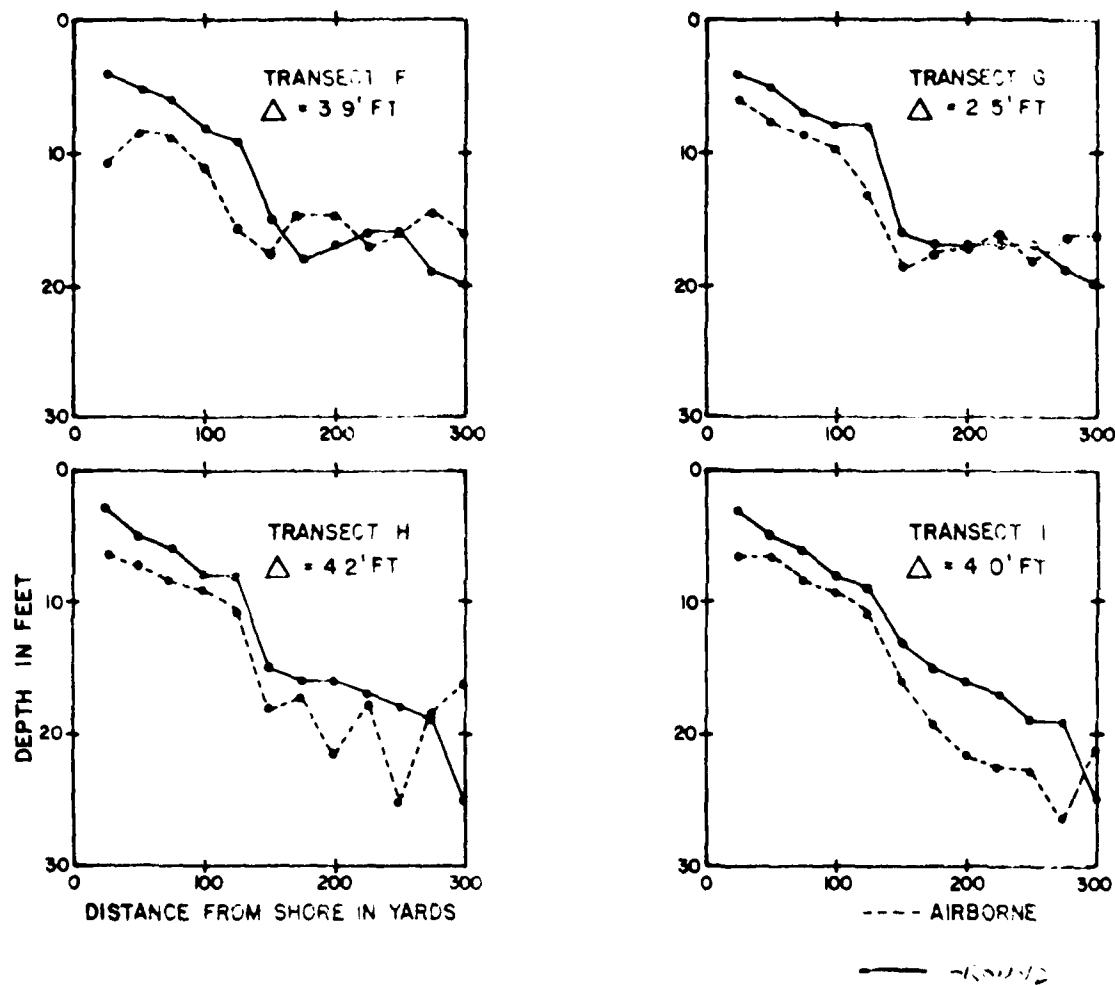
FIGURE 15.   COMPARISON OF DEPTH PROFILES DETERMINED BY GROUND
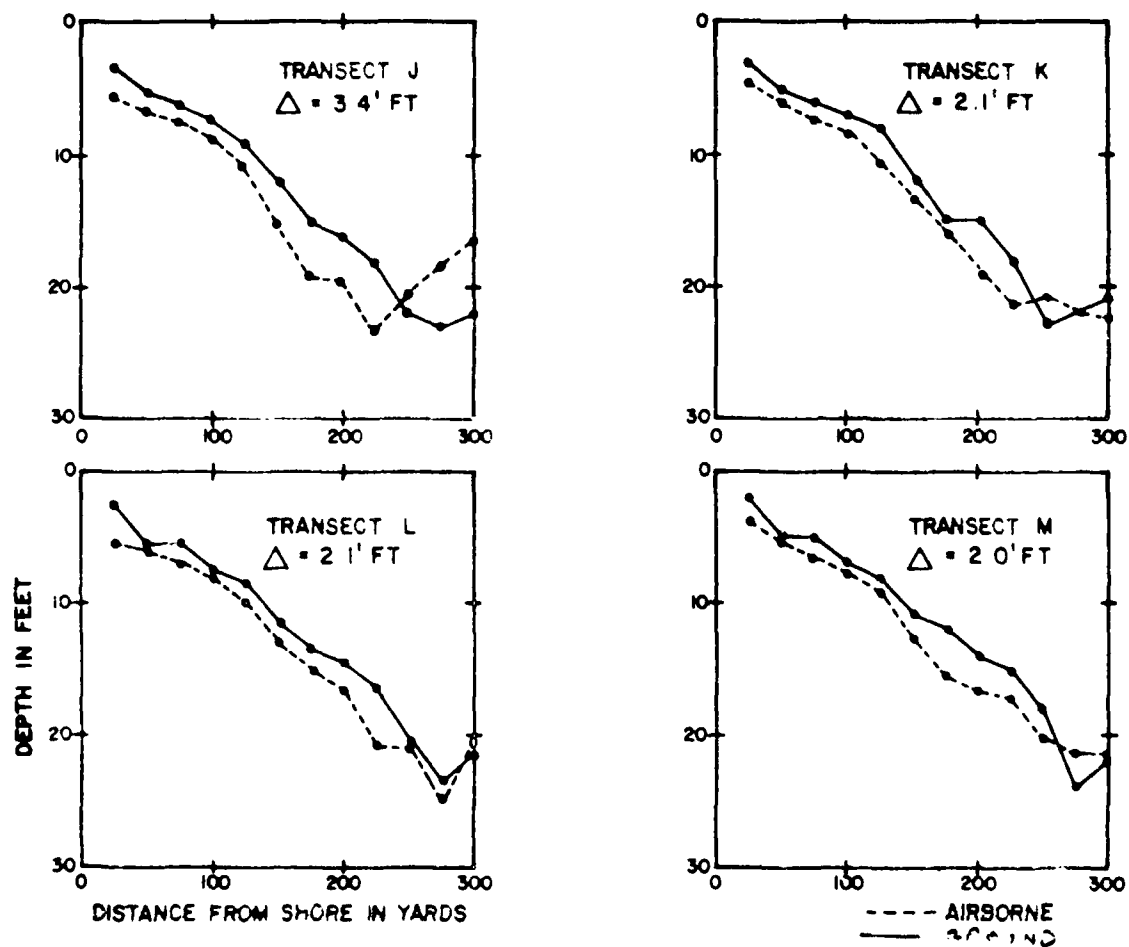AND AIR SURVEY, BAHIA DE LA CHIVA, 15 MAY 1979 - II

FIGURE 16.   COMPARISON OF DEPTH PROFILES DETERMINED BY GROUND
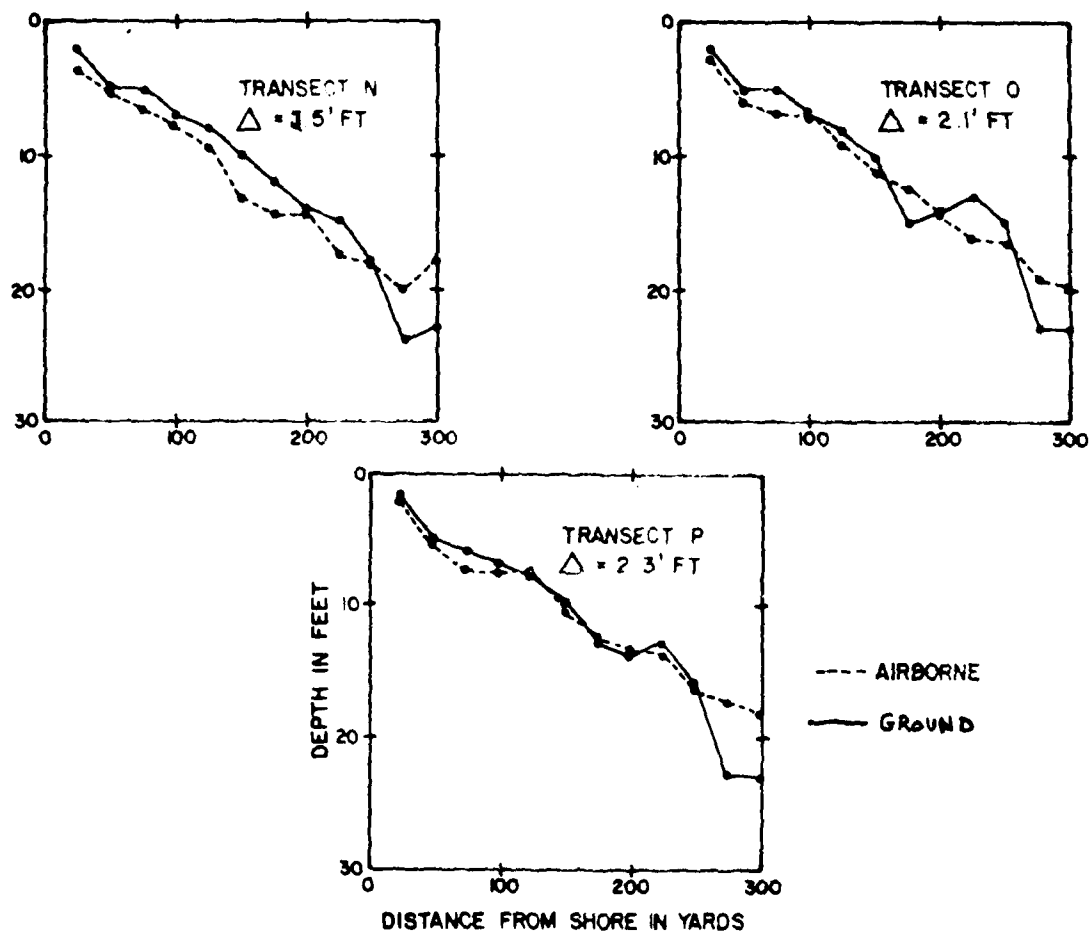AND AIR SURVEY, BAHIA DE LA CHIVA, 15 MAY 1979 - III

FIGURE 17.   COMPARISON OF DEPTH PROFILES DETERMINED BY GROUND
AND AIR SURVEY, BAHIA DE LA CHIVA, 15 MAY 1979 - IV

In Figure 18, the depth values of Figure 13 have been replaced by the
absolute magnitude of the difference, in feet, between the ground and air surveys.
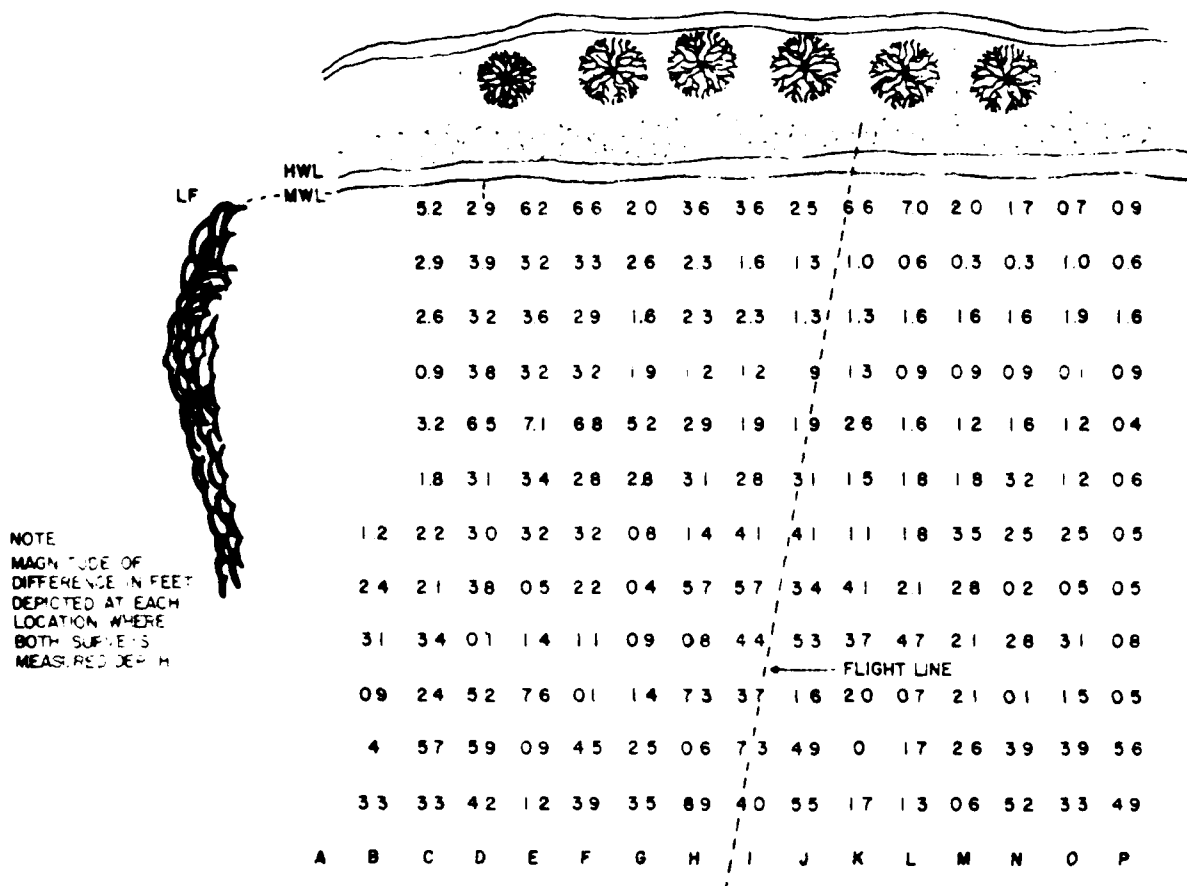

FIGURE 18.   LOCATION OF DEPTH DIFFERENCES BETWEEN GROUND AND
AIRBORNE SURVEYS, BAHIA DE LA CHIVA, 15 MAY 1979

Figure 18 indicates a significant asymmetry   in magnitude of the depth

errors, depending on which side of the flight line data was taken. Since the

sun was to the right of the flight line, this indicates that areas which are

more stongly illuminated will be characterized by a higher optical signal-to-

noise ratio, and more accurate results. Figures 14-17 indicate that the depth

differences between the ground and air surveys have a systematic character,

with the air-determined depths generally greater than the ground-determined

depths. Resolution of discrepancies such as this will be the subject of

further analysis.

DESIGN OF OPERATIONAL HYDROGRAPHIC SCANNER

Currently studies are being conducted to determine whether a scanner can

be built using currently available off-the-shelf equipment and technology.

Initial conclusions are that this is possible. The currently existent M-8 [7]

scanner could be modified in the following fashion:

The Molectron nitrogen-pumped dye laser could be replaced with an

International Laser Systems NT-90 doubled Nd:YAG laser with 1.5 Mw peak pulse

power, 8 nanosecond pulse width, and 20 pps repetition rate. The laser firing

and return pulse digitization could be controlled by microprocessors. The

CW Nd:YAG laser would be removed.

The number of passive bands in the scanner would be reduced to five.

Four blue-green bands at $0.45-0.5\mu m$, $0.5-0.52\mu m$, $0.53-0.55\mu m$, and $0.55-0.57\mu m$

would be obtained by a grating spectrometer. A separate detector/filter

combination would supply near IR coverage necessary for water/land boundary

editing.

The instantaneous field of view would be adjusted to secure 4m linear ground resolution at a nominal operating altitude of 2000 feet. Data will be taken at up to 25-30° off nadir, at least for passive channels. An option will exist to collect data at higher altitudes for merger with data taken at lower altitudes. These adjustments, along with simplification of the optical paths, will make possible a significant increase in passive signal-to-noise ratio over the present design.

It was recommended that the data be collected with 16 bit A/D conversion in order to eliminate gain control in the passive channels. It is believed that the Tektronix 7912 transient digitizer could be upgraded to allow laser pulse capture at 20 pps vice the current 5 pps. (It is also very possible that technology currently being developed under the HALS project could be used both for laser pulse capture and automatic depth determination.)

This system is best used in conjunction with the NAVSTAR Global Positioning System now under development. Aircraft attitude information would be recorded using an inertial navigation system such as the Litton LTN-51.

Issues now being taken up are:

(1) Is it feasible to define a new type of chart product which would give depth range, or minimum depth with a satisfactorily low probability of error?

(2) Can the immense amount of data collectible by such a system be processed in a timely fashion using a special-purpose interactive, parallel processing computer?

(3) Should a dedicated scanner be a variant of the M-8 or should a new scanner be designed and built? Should high resolution capability be built into the system to look for underwater obstacles such as coral heads?

These, and other issues such as a precise definition of the errors inherent in this technique will be the subject of future work. At this point, however, it can be said that the technique of high speed, high resolution, determination of shallow water depths has been demonstrated. If developed into an operational system, it would assist in reducing the large chart revision backlog that now exists.

REFERENCES

1. D. Lyzenga and F. Thomson, "Data Processing and Evaluation for Panama City Coastal Survey: Bathymetry Results," Environmental Research Institute of Michigan Report No. 121400-1-T, August 1976

2. P. G. Hasell, et.al., "Active and Passive Multispectral Scanner for Earth Resources Applications: An Advanced Applications Flight Experiment," Environmental Research Institute of Michigan Report No. 115800-49-F, June 1977

3. P. G. Hasell, Jr., et.al., "Michigan Experimental Multispectral Mapping System, A Description of the M7 Airborne Sensor and Its Performance," Report No. 190900-10-T, Environmental Research Institute of Michigan, Ann Arbor, Michigan, January 1974

4. R. A. Schuchman and D. R. Lyzenga, "Active-Passive Scanner Bathymetry and Land Feature Classification Results - Panama City, Florida, 1977," Environmental Research Institute of Michigan Report No. 128500-4-T, March 1978

5. D. R. Lyzenga and J. Livisay, "Documentation of Computer Software for Multispectral Bathymetry Analysis," Environmental Research Institute of Michigan Report 148900-1-F, April 1980

6. Cooper, M. T., "Airborne Hydrographic Survey During READEX 1A-79," Naval Coastal Systems Center Technical Note TN498, June 1979

7. F. Thomson, et.al., "M-8 Scanner Design Modifications for Bathymetry Mapping," Environmental Research Institute of Michigan Report No. 144600-2-F, April, 1980

PAPER 17

EFFECT OF WATER TURBIDITY ON
LASER DEPTH SOUNDING PERFORMANCE

D.M. Phillips

Defence Science and Technology Organization
Electronics Research Laboratory
Salisbury   South Australia

Water turbidity can be defined and measured in a variety of different ways. During trials of the WRELADS system, measurements of the beam and diffuse attenuation coefficients have been made from boats and measurements of backscatter amplitude and signal attenuation with depth have been made from the aircraft. Empirical relationships between these parameters have been established.

The most reliable measure of turbidity has proved to be the beam attenuation coefficient measured with a transmissometer developed in the Electronics Research Laboratory. The usefulness of this instrument is restricted by the need to operate it from a boat.

Large scale surveys of water turbidity become possible when relevant parameters can be measured from an aircraft. Experimental measurements of the amplitude and attenuation of the backscatter signal show that both are linearly related to the beam attenuation coefficient.

Using an empirical relationship between backscatter amplitude and beam attenuation coefficient, the depth measuring performance of the WRELADS system has been determined as a function of water turbidity.

The Measurement of Water Turbidity

Figure 1 illustrates four different measures of turbidity that I have calculated from experimental observations in some way. I have taken the empirical approach of measuring many different parameters and looking for relationships between them.

The beam attenuation coefficient, denoted here by c in accordance with the international convention (also commonly called α in U.S.A.) is a very exclusive parameter. It describes the attenuation of a parallel beam of light due to any departure from that parallel transmission: all scattered and absorbed light is excluded. It has the advantage of being an intrinsic property of the water.

Another parameter, which is probably more appropriate for describing attenuation of the laser pulse in a depth sounding system, is the diffuse attenuation coefficient K. It is determined by measuring the irradiance due to ambient light as a function of water depth. Strictly, it is not an intrinsic property of the water because it depends on whether the ambient light is dominated by directional sunlight or diffuse skylight.

Two attenuation coefficients have been measured with the WRELADS system. The signal attenuation coefficient, denoted by k_s, describes the attenuation of the signal reflected from the water bottom. In principle, it is determined by measuring the signal amplitude as a function of water depth, when the bottom reflectivity and water turbidity remain constant.

The backscatter attenuation coefficient, denoted by k_b, describes the attenuation of the backscatter envelope. This coefficient could be different from k_s because of the different processes involved. Close to the surface the laser light is highly directional and the strong forward scattering is directed downward. At a greater depth, the laser light becomes less directional and a greater proportion of the light may be scattered upward. This would result in k_b being smaller than k_s.

The beam attenuation coefficient is derived from measurements of transmittance made with a transmissometer designed and constructed at D.R.C.S. A schematic diagram of the instrument is shown in Figure 2. An incandescent lamp provides two beams of light. One beam passes through the water to a photodiode detector. The other beam provides a reference signal, used to maintain a constant lamp brightness. A rotating shutter is used to separate signal, reference, and background light.

We have adopted the beam attenuation coefficient as our preferred indicator of water turbidity, because it is derived from transmittance measurements made with our most reliable and accurate turbidity instrument: the transmissometer.

Simultaneous measurements of the diffuse and beam attenuation coefficients were made during trials in August 1980 near Townsville. The irradiance meter used to obtain the diffuse attenuation coefficient was kindly made available by the James Cook University of North Queensland. The results of these measurements are presented in Figure 3. The range of turbidity covered by this data is from typical coastal water ($c = 0.5m^{-1}$) to very turbid water ($c = 6m^{-1}$). Rough seas on the days of the trial prevented measurements in the clearer water expected further from the shore ($c = 0.1m^{-1}$). The results indicate an approximately linear relationship between the two coefficients. Differences of about 20% are evident between the NADC data and the present results; these are probably not significant compared with the errors associated with the instruments used to obtain the data.

Figure 4 shows some measurements of the signal attenuation coefficient obtained during combined aircraft and boat trials in 1976 and 1977. The amplitudes of the laser pulses reflected from the bottom were recorded in the aircraft while transmittance measurements were made in a boat. The range of turbidity (from $c = 0.1$ to $0.5m^{-1}$) is much smaller than in the previous figure and corresponds to relatively clear water. The regression line fitted through the data is close to the line fitted to the diffuse attenuation coefficient data in Figure 3. Thus, within the limitations of the data, the diffuse attenuation coefficient describes the attenuation of the laser signal.

The backscatter attenuation coefficient was calculated by fitting a regression line to the logarithm of the backscatter decay curve recorded in the aircraft. The results are shown in Figure 5. Apart from the scatter of points corresponding to the very turbid water, the regression line fits the data well. The slope of this line is very much smaller than those in the two previous figures. Hence, the backscatter appears to decay more slowly than the signal, especially in turbid water.

The above results are limited by both the ranges of turbidity covered and by scatter of the data. However, if the trends are correct, the signal to noise ratio deteriorates as the water depth increases.

Measured Distribution of Turbidity

Having looked at the various turbidity parameters, let us now look at some of the surveys we have done to try to understand the distribution of turbidity in water. Figure 6 shows St. Vincent Gulf, where we have carried out several boat trials.

The results shown in Figure 7 were derived from measurements alon the line of buoys. The contours in the lower graph show the variation in the beam attenuation coefficient. It is noteworthy that the contours of equal attenuation coefficient are almost vertical, which suggests that there is strong vertical mixing, particularly in the shallower water. The signals obtained in the aircraft along the same buoy run at the same time are reproduced at the top of Figure 7. It can be seen that the amplitude of each bottom return (taking account of the photomultiplier voltage) is closely related to the turbidity of the water at that point. For example, the water depth does not change much between returns (a), (b) and (c) but the amplitude of bottom return (b) is greatly reduced because of the turbid water there.

Having gain confidence that the water turbidity generally did not change greatly with depth, we did a horizontial survey of St. Vincent Gulf by boat and the results are shown in Figure 8. By taking a large number of measurements we were able to produce contours of equal turbidity. Turbid water was found along the coast line on both sides of the gulf, where the water is shallow and wave action can agitate bottom sediment. However there is also a patch of turbid water in the centre of the gulf where the water is relatively deep. The explanation for this is not clear.

Another series of measurements was made in water off the Queensland coast near Cairns (see Figure 9). Close to Arlington Reef the water was clear because it originated in the Pacific Ocean. Close to False Cape, on the other hand, the water became very turbid. This can be seen in Figure 10 which presents the data obtained along the line from False Cape to Arlington Reef. Again the contours of equal turbidity are almost vertical. The corresponding waveforms at the top of Figure 10 again shows the relationship between water turbidity and bottom signal amplitude. Waveforms (a), (b), (e) and (f) show bottom returns of about the same amplitude but depth increases as the water becomes clearer.

Effect of Turbidity on Performance

The relationships between the amplitude of the backscatter signal and the beam attenuation coefficient was investigated in a combined aircraft and boat trial. The backscatter amplitude at different depths was obtained by first fitting a regression line to the logarithm of the backscatter decay curve. The results are presented in Figure 11. The range of turbidity covered was restricted to relatively turbid water for the reasons given above. A linear relationship fits the data well at a depth of 1m. At 2m depth, the backscatter amplitude falls above about $c = 5m^{-1}$. At 5.6m depth, the backscatter amplitude reaches a peak at about $c = 3m^{-1}$. The fall in turbid water is due to attenuation of the beam.

One trial in August 1980 was flown around Cape York Peninsula along the
route shown in Figure 12. On the northbound leg the aircraft travelled a
zig-zag track from the mainland to the outer reef. The return track covered
parts of the Gulf of Carpentaria. At intervals during the flight, estimates
of the beam attenuation coefficient were made from the observed backscatter
amplitude using the assumed calibration shown in Figure 11. The resulting
values of c are plotted along the track in Figure 12. It can be seen that the
coefficient covered two orders of magnitude: from $0.05m^{-1}$ in the clearest
ocean water to $5m^{-1}$ in the turbid Torres Strait.

During this flight estimates were made of the "extinction depth" which is
the maximum depth at which a bottom return pulse can be recognised above the
noise. These data were used to produce Figure 13, which defines the performance
of the WRELADS system in water of different turbidities. It can be seen that
while the beam attenuation coefficient increases by two orders of magnitude
from 0.05 to $5m^{-1}$, the extinction depth reduces by one order from 50 to 5m.
The emphirical relationship given in Figure 13, which is based on a regression
line fitted to a plot of $1/d_e$ against c, was found to fit the data well.

Given the performance curve in Figure 13 it is important to know how
frequently Australian coastal waters will be within depth sounding capability
of the system. Some information about this was obtained during a boat trial,
when the beam attenuation coefficient was determined with the aid of the
transmissometer while the depth was measured with the boats echo sounder.
The results are presented in Figure 14. Points lying below the performance
line should be within the capability of the WRELADS system.

These results show that a majority of the locations included in the survey
could not have been sounded by WRELADS. However the conditions were most
unfavourable, with 35kn winds and rough seas. Others who have studied water
turbidity in the area report that much clearer conditions occur in calm
conditions. Quantitative descriptions of those favourable conditions must
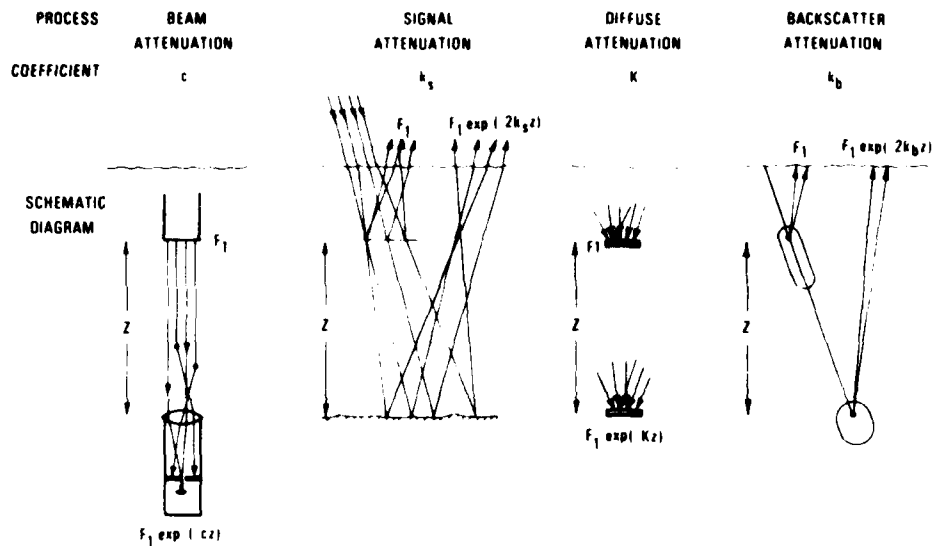await further trials.

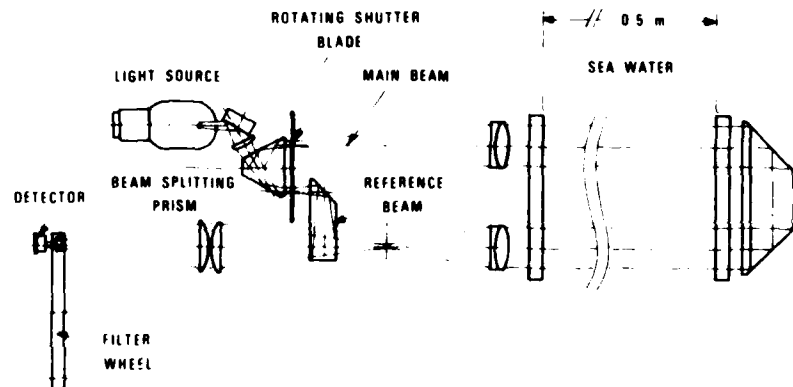Figure 1 SOME ATTENUATION COEFFICIENTS

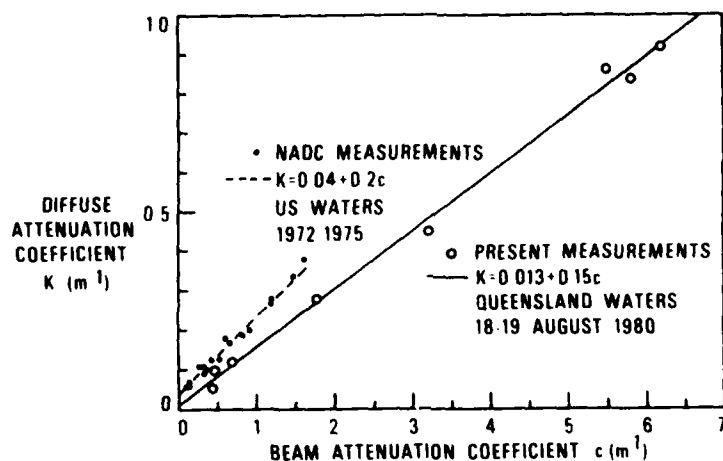Figure 2 DIAGRAM OF THE UNDERWATER TRANSMISSOMETER

Figure 3   RELATIONSHIP BETWEEN DIFFUSE AND BEAM
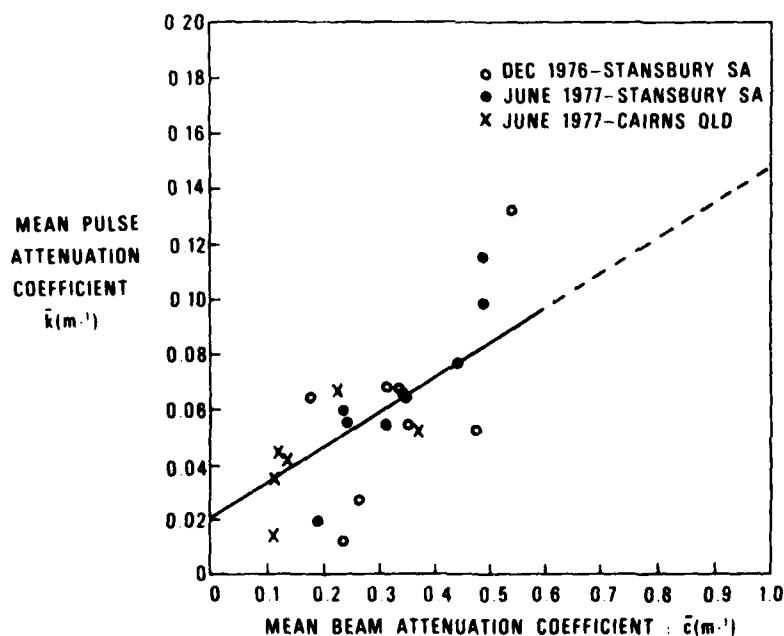ATTENUATION COEFFICIENTS IN WATER

Figure 4   DEPENDENCE OF MEAN PULSE ATTENUATION
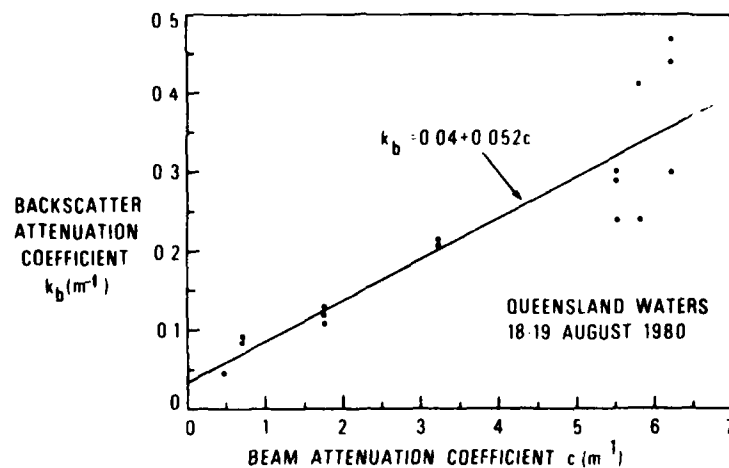COEFFICIENT ON MEAN BEAM ATTENUATION
COEFFICIENT

Figure 5   RELATIONSHIP BETWEEN BACKSCATTER AND
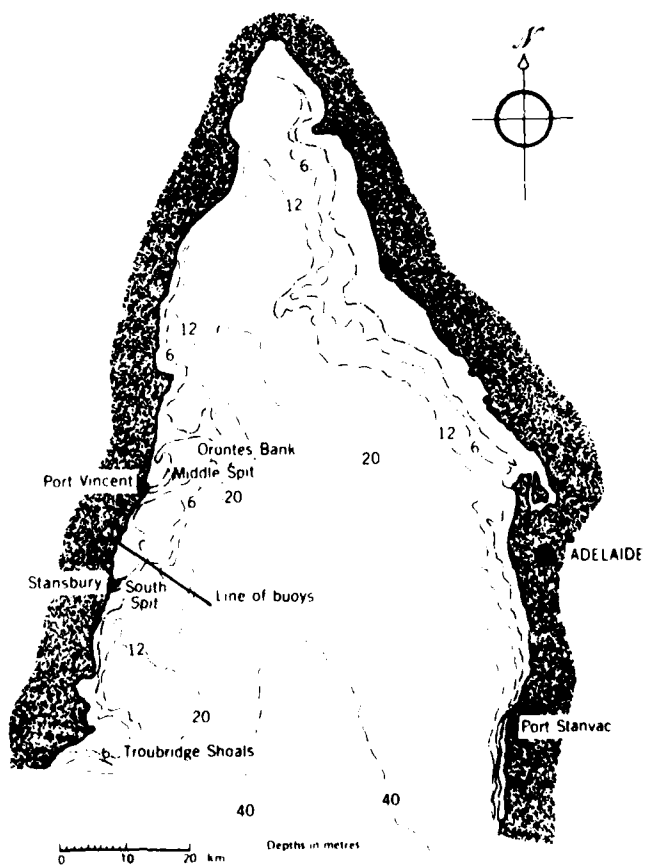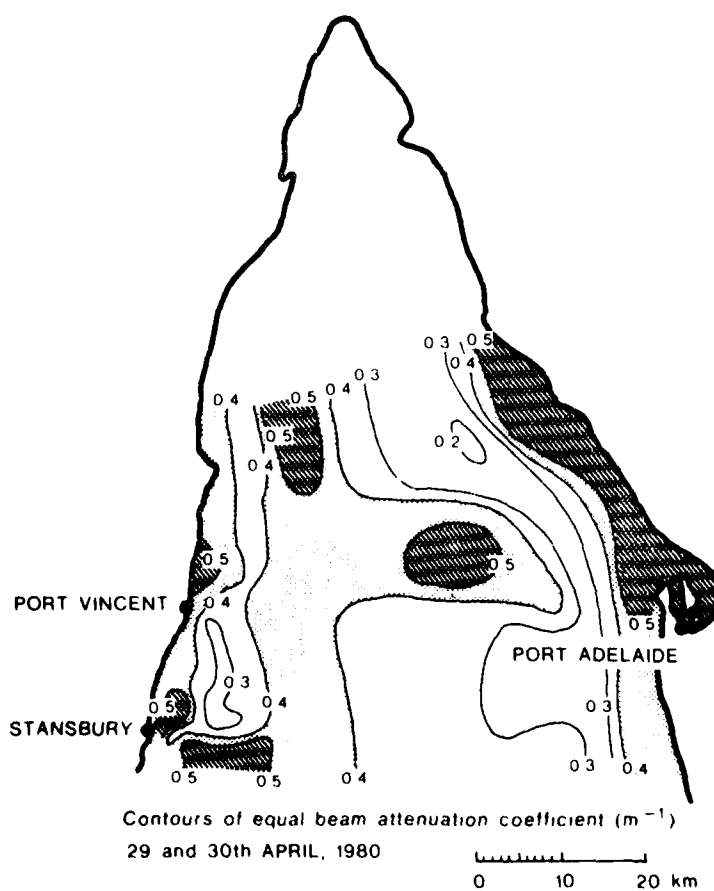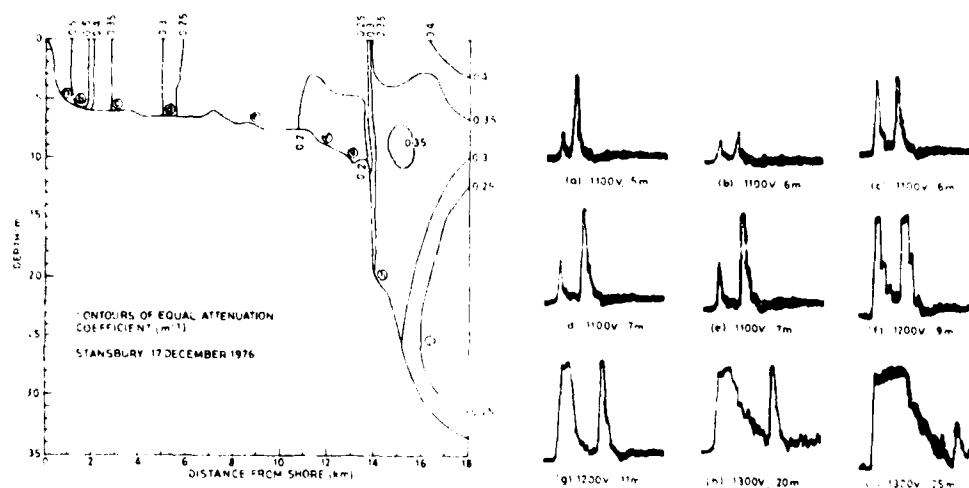BEAM ATTENUATION COEFFICIENTS IN WATER

Figure 6   CHART OF GULF ST VINCENT SHOWING
THE LINE OF BUOYS NEAR STANSBURY

Figure 7 MEASURED DISTRIBUTION OF BEAM ATTENUATION COEFFICIENT
OF THE WATER AND AIRBORNE LASER RETURN SIGNALS
ALONG THE STANSBURY LINE OF BUOYS ON 17 DECEMBER 1976

Contours of equal beam attenuation coefficient (m^{-1})
29 and 30th APRIL, 1980

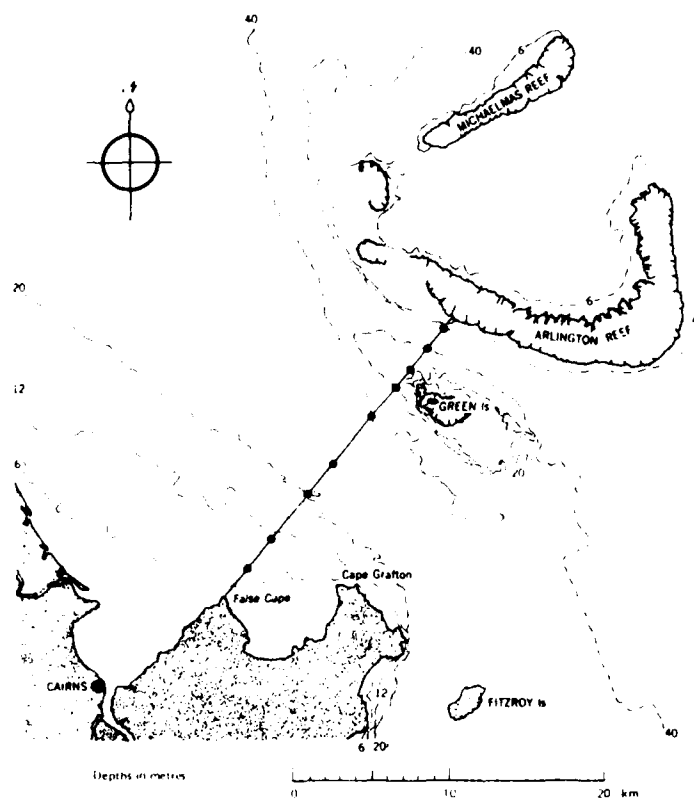Figure 8 TURBIDITY OF SURFACE WATER ACROSS GULF ST VINCENT

Figure 9   CHART OF CAIRNS WATERS SHOWING
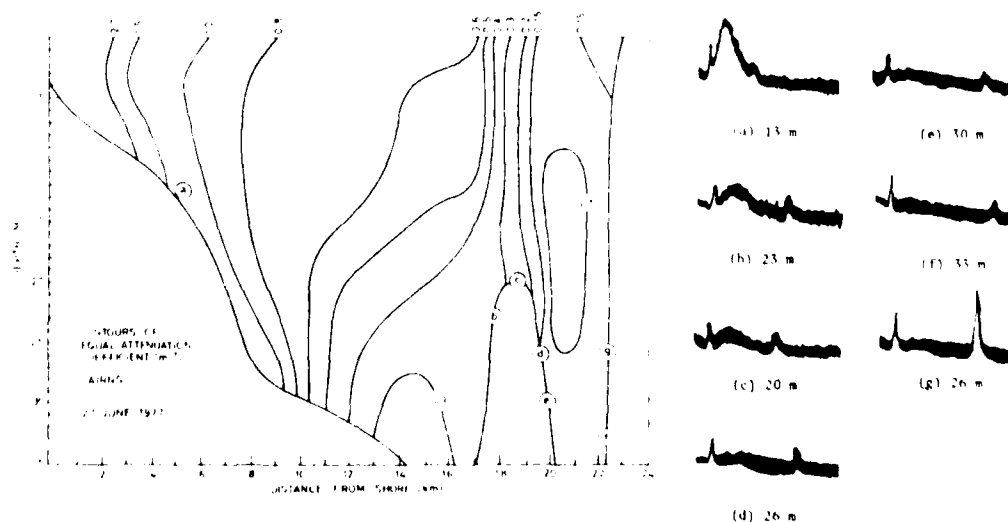LOCATIONS OF TRANSMITTANCE
MEASUREMENTS

Figure 10   MEASURED DISTRIBUTION OF BEAM ATTENUATION COEFFICIENT
OF THE WATER AND AIRBORNE LASER RETURN SIGNALS NEAR
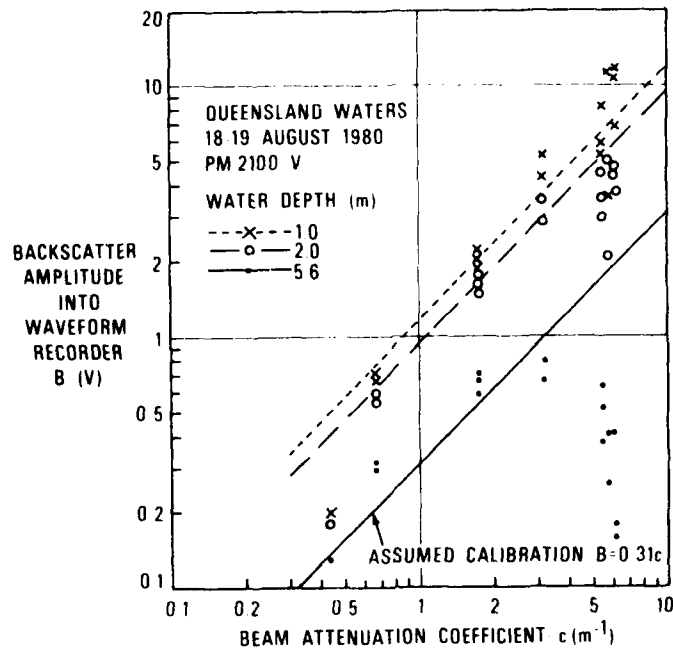CAIRNS ON 27 JUNE 1977

Figure 11   RELATIONSHIP BETWEEN BACKSCATTER
AMPLITUDE AND BEAM ATTENUATION
COEFFICIENT IN WATER

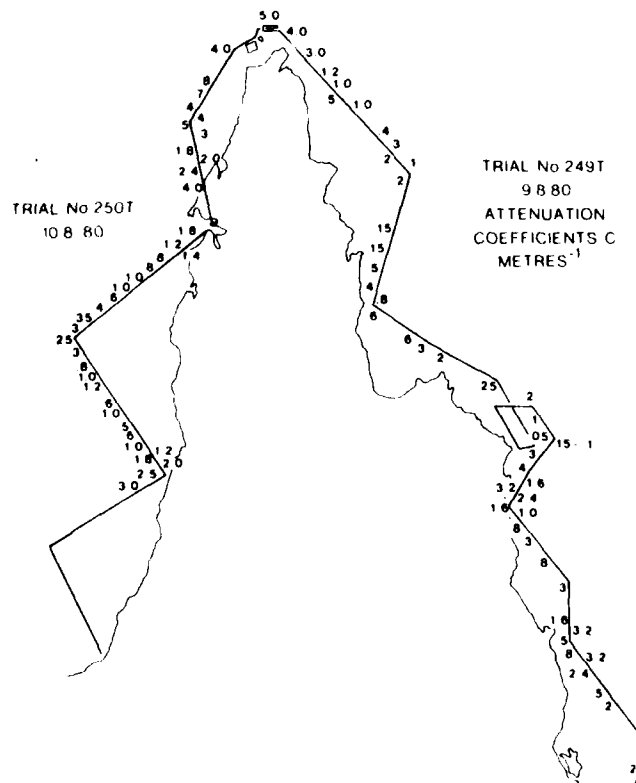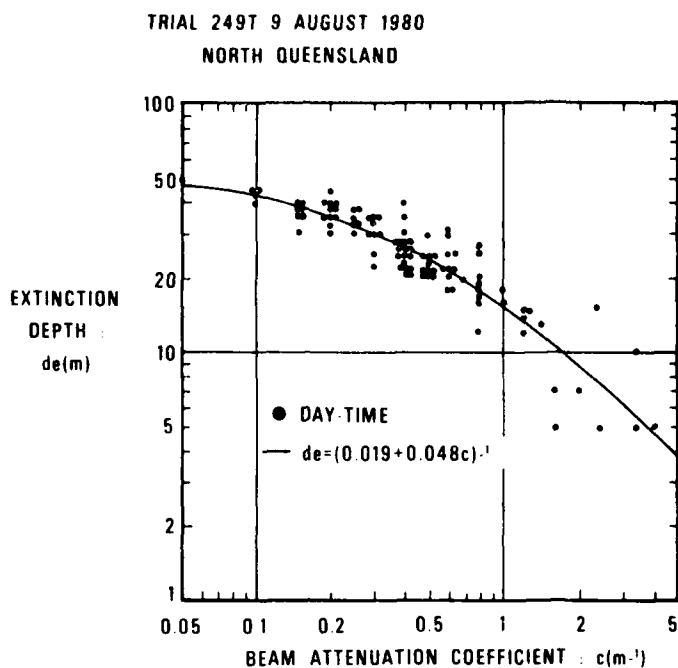Figure 12   MEASURED WATER TURBIDITY AROUND
CAPE YORK PENINSULAR

TRIAL 249T 9 AUGUST 1980
NORTH QUEENSLAND

Figure 13   DEPENDENCE OF EXTINCTION DEPTH ON WATER
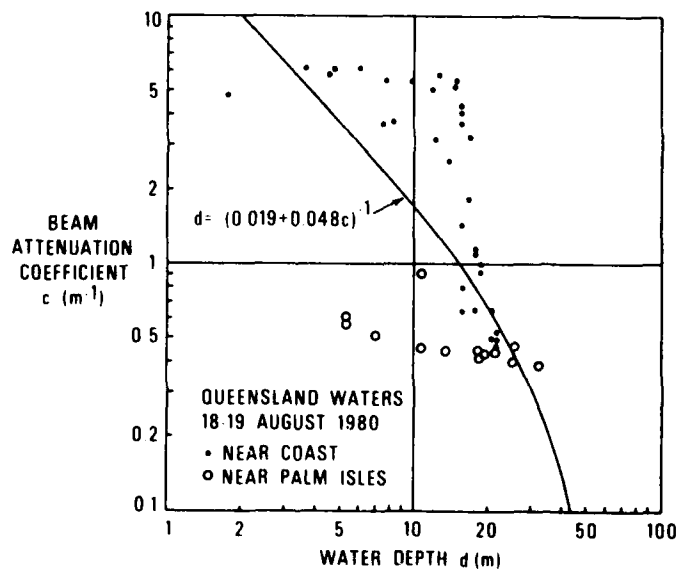   TURBIDITY

Figure 14   STATISTICAL VARIATION OF TURBIDITY
            WITH WATER DEPTH

PAPER 18

SIGNAL PROCESSING AND DATA PROCESSING: WRELADS

G.J. Watts
ELECTRONICS RESEARCH LABORATORY

1. INTRODUCTION

In this field of Laser Hydrography, we no longer have a simple well
defined instrument producing depth data which can be processed directly, rather
do we have a sophisticated, complex machine which records a very large amount
of different information about the environment over which and through which it
passes. This recording is then processed on the ground and various complex
calculations need to be performed. This paper discusses the airborne proces-
sing and the ground processing; both feature analogue signal processing, and
numerical processing of digital data. The rather artificial distinction
made here is that signal processing is used to describe all manipulation of
signals and data to produce the best depth estimates, while data processing
is used to describe the manipulation to the depth data necessary to provide
data in a form suitable for the Hydrographer.

2. AIRBORNE SIGNAL PROCESSING

2.1 General

Figure 1 shows the various components of the signal processing
with the exception of the optical components and photo-multiplier.
These components are described in more detail in other papers, however,
as signal processing starts at the moment green photons enter the
receiving telescope, a short description is given.

2.2 Telescope and Photo-multiplier

The aim at this stage is to reduce the dynamic range of the signal
(which is several orders of magnitude), to within the range of the
waveform recorder. In the telescope, spatial filtering (by means of a
variable, central block in the field of view), is used to attenuate the
surface reflection. In the photo-multiplier, the gain is varied in a
logarithmic manner, from a low value at a time prior to the surface

signal, to a maximum at a time corresponding to 10 to 20 metres. The

maximum gain is au' matically controlled to maintain a maximum back-

ground noise level, while the minimum gain and slope are currently

manually adjusted to suit the water conditions.

2.3 Signal Recording

The green signal is then digitized in the waveform recorder. WRELADS

uses the BIOMATION 6500 transient recorder, which has a 500 MegaHertz

sampling frequency, and 6 bit resolution. The waveform recorder is

triggered by the infra-red (I.R.) surface pulse, which is always vertical.

Figure 2 illustrates how the green signal appears in memory for a vertical

green signal, and a 15° skewed signal which arrives later in time due to

the additional air path. The digitized signal is then clocked out at a

25 KiloHertz rate through an analogue to digital converter. This read-

out of the waveform is controlled by the waveform converter.

The waveform converter is an Intel 8085 micro-computer based controller

which performs the following functions:

(i)   calculates the nominal air path connection for the skewed

(scanning) green beam, from the height counter and scan angle

information.

(ii) calculates the aircraft to water surface time interval of the

next green pulse, and generates a presurface trigger for the

programmable photo-multiplier gain control.

(iii) as mentioned above, clocks out the waveforms.

These waveforms have the air-path correction applied, so that the surface

pulses of all green signals coincide. This serves several purposes:

(i)   the bandwidth required for recording the analogue waveforms

on magnetic tape is reduced

(ii) viewing the waveforms on the oscilloscope is much simpler.

The analogue signal also goes via the signal enhancer (an adjustable

low frequency filter) into the depth counter. The depth counter has an

adjustable range-gate and threshold (which are superimposed on the wave-

form display), and is used to provide an in-flight indication of depth
and system performance. While this depth is recorded, it is intended that
the final depth determinations will be from the waveform data.

3.   GROUND-BASED SIGNAL PROCESSING

The magnetic tapes received from the aircraft contain:

(i) Analogue waveforms

(ii) Digital data - height, plus various system operating parameters.

The analogue waveforms are then digitized, for processing by computer.
The choice for recording the signals in analogue form on instrumentation tape,
was made on the basis of tape capacity. An all digital system generates
approximately 140 Megabytes of data each hour. As 1600 BPI magnetic tapes
have a capacity of only about 40 Megabytes, only 15 minutes of recording per
reel would be achieved. In comparison, the analogue solution provides for
over an hour per reel. It is intended, however, to convert WRELADS to an all
digital system.

The calculations to be performed are:

(i)   filter waveforms

(ii)   calculate the turbidity and maximum depth capability

(iii)   apply the bottom detection algorithms

(iv)   calculate system errors and correct the depths.

3.1 Filtering the Waveform

None of the waveform data from WRELADS II has yet been analysed.
Previous data from WRELADS I (the non-scanning proto-type) has been
processed to a limited degree. Most of the work concentrated on
determining the filter characteristics most suitable for suppressing
the backscatter envelope. Filters with zero phase shift are most
suitable, and such a filter is incorporated in the airborne signal
enhancer. Ground filtering will concentrate not on the backscatter,
but on improving the signal/noise ratio.

3.2 Turbidity Calculation

Water turbidity and the expected maximum depth capability is
determined from the amplitude of the backscatter component of the
signal and is described in detail in other papers.

3.3 Bottom Detection Algorithms

Figures 3 through 6 are a selected set of WRELADS signals, which
cover the range of various types of signals and have been classified
into several groups. The purpose of classification is to enable the
most suitable bottom detection algorithm to be applied. The main
classes are:

(a) Shallow water - where the bottom return is large and
superimposed on the backscatter.

(b) Signals with good signal levels, but smaller than the
surface pulse, and high backscatter amplitudes.

(d) No-backscatter, but good signal/noise ratio.

(e) Poor signal/noise ratio.

Current planning for WRELADS is to scan the waveforms after
filtering to determine the number and position of the peaks. Generally,
the last peak will be the bottom. Figure 3b, however shows a 3 metre
deep signal return where this is not the case. Here a multiple reflec-
tion has occurred, and in fact the 2nd peak is the bottom. This appears
to only occur over a very limited depth range, and the fact that the
third peak is at twice the depth is a fairly clear indication.

It is intended initially to use $\frac{1}{2}$ peak amplitude as the reference
point for meas rement. Measurement of depth less than 1.5 metres is
limited as at 1.5 metres the base of the bottom signal is barely
detectable, superimposed on the surface signal (see figure 3a).

3.4 Signal Averaging

In deep water, as illustrated in figure 6, the signal at 38 metres
can be seen just above the quartizing noise of the waveform recorder.
I expect that depending on the type of bottom, signal averaging will
improve the signal/noise ratio. Signal averaging over a cluster of

nine points is similar to providing a large laser pulse 30 metres

diameter and almost an order higher power. In these circumstances,

we expect to get an extra attenuation length in depth capability.

The disadvantage is that the spatial resolution is decreased. For

example, a detectable 35 metre signal could result from the above

procedure, but there may be a number of isolated holes deeper than

this throughout the data.

3.5 Qualification of Data

If a bottom is not detected, then additional information is

necessary. Bottom trend data will indicate whether the bottom is

not detected because of being too shallow or too deep. Turbidity

calculations will indicate the expected maximum depth capability.

Data provided to the Hydrographer will therefore be qualified in the

following ways:

(i)   depth less than 2 metres

(ii) no bottom detected at x metres, depth greater

(iii) bottom detected at x metres

(iv) bottom detected at x metres, reduced spatial resolution.

3.6 System Errors and Corrections

The major sources of error in the WRELADS system are:

(i)   geometric errors due to the scanning geometry

(ii) digitizing error

(iii) wave height errors

(iv) stable platform roll errors.

Figure 7 shows the geometry of the scanning beam. The first

component to be corrected is the air path slant range. The waveform

converter in the aircraft has already corrected the slant range, but

only to the accuracy to which the waveform recorder can be controlled,

that is, to one sample interval, or 0.2 metres. As we can calculate

the airborne correction, we can recalculate the slant path to higher

accuracy, eliminating this possible source of error. The water path

slant range correction is a maximum of 0.6 metres, and can also be easily

applied at this stage.

The wave height error is ± 0.3 times the wave heir :. Mr Gary
Guenther in a previous paper described correlating aircraft to surface
distance and aircraft to bottom distance, to extract wave height
information. In WRELADS, the information is available which would
enable similar corrections to be applied.

Stable platform roll errors are currently the largest errors in the
system, and contribute ± 0.6 metres for ± 0.25 degrees roll error (the
gyro limit). The aircraft slant range to the green surface reflection
can however be used to determine the error in the stable platform.

3.7 Hardware

The system being used for signal processing is shown in figure 8.
The analogue waveforms are digitized and read into the PDP11. Filtering
will be done initially in the PDP11, until the proceedures are sufficiently
well-defined to implement them in hardware which will speed up the
processing. Such hardware filters would still be digital and controlled
by the computer.

3.8 Outputs

The output of the signal processing phase will be:

   (i) blocks of soundings comprising depth and quality information

   (ii) time

   (iii) aircraft height and position in ARGO lanes.

4. GROUND DATA PROCESSING

4.1 Data Input and Calculations

The data processing phase will have inputs the above information,
and in addition:

   (i) ARGO station co-ordinates

   (ii) Tidal information.

From the information on the ARGO Station co-ordinates, and the
recorded positions for the start of each block of soundings must be
converted to Australian Map Grid (A.M.G.) co-ordinates. The next

calculation is to correct the horizontal position of each sounding as
a function of aircraft height and the water depth (refer again to
figure 7). The reason that this geometric correction is not done in the
previous signal processing phase, is that the quantity of data expands
enormously, due to the necessity of adding the position of each sounding
to the data file. The calculations involve the interpolation of each
sounding position in the block of soundings, according to the known
scan pattern, and then applying the individual corrections due to depth.
Tidal connections must then be applied, and finally, unwanted data
discarded, such as that during aircraft turning etc.

4.2 Output for the Hydrographer

The output produced will be a magnetic tape containing for each
sounding

   (i)   position (A.M.G. co-ordinates)

   (ii) depth

   (iii) classification or quality information pertaining to the
         depth value.

5. CONCLUSION

It is apparent that the large amount and complex nature of the airborne
data generated in a depth recording system such as WRELADS requires considerable
processing to obtain the depth information. In addition the large amount of
depth information produced necessitates the development of new methods for
assessing the data in the field, and for editing the data before use by the
Hydrographer.

All of these will require a high degree of automation and will add a new
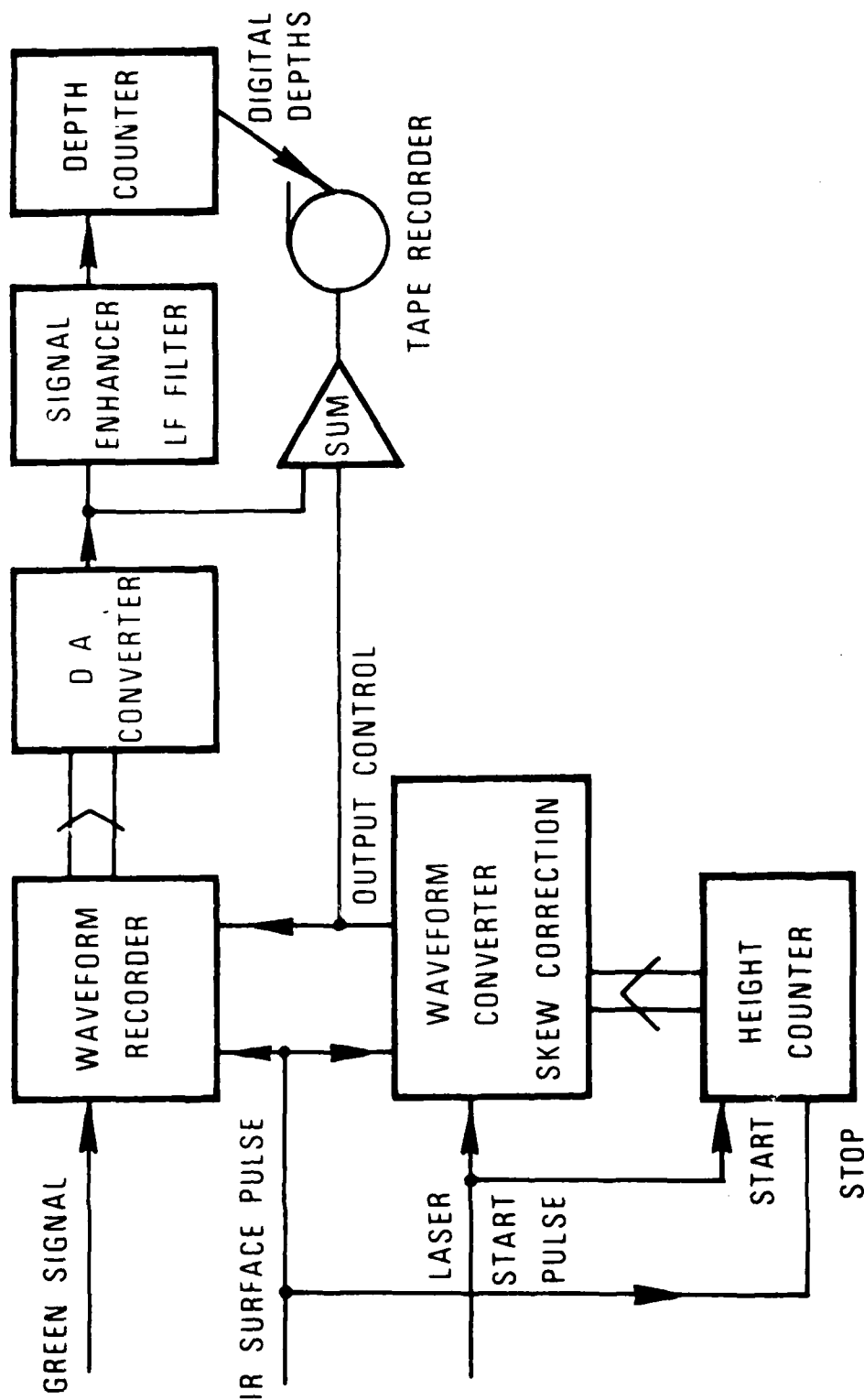dimension to the responsibility for chart production.

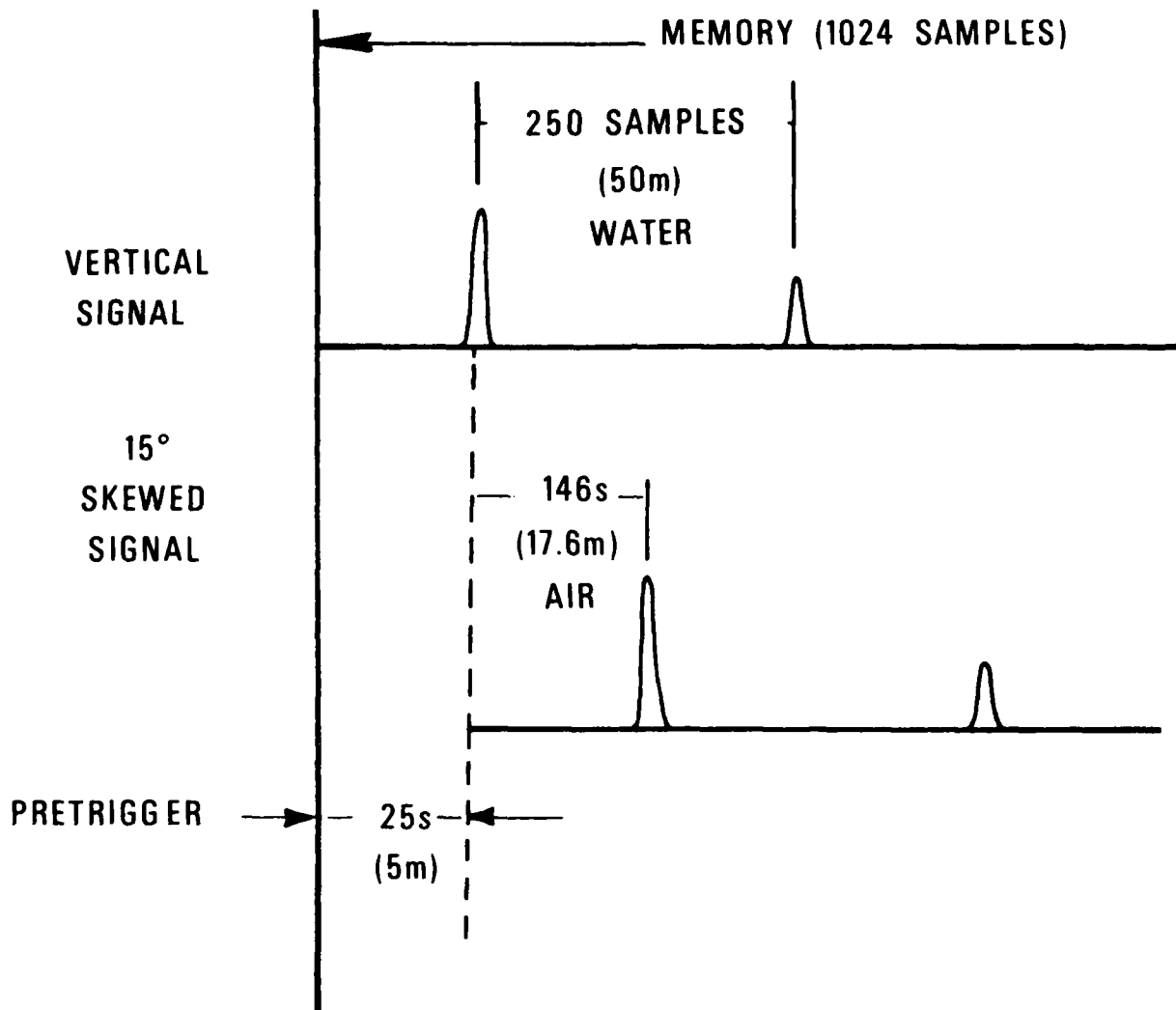Figure 1   AIRBORNE SIGNAL PROCESSING

Figure 2   WAVEFORM RECORDER—SIGNAL STORAGE

Type A — Shallow water

1.5m

3m

4m
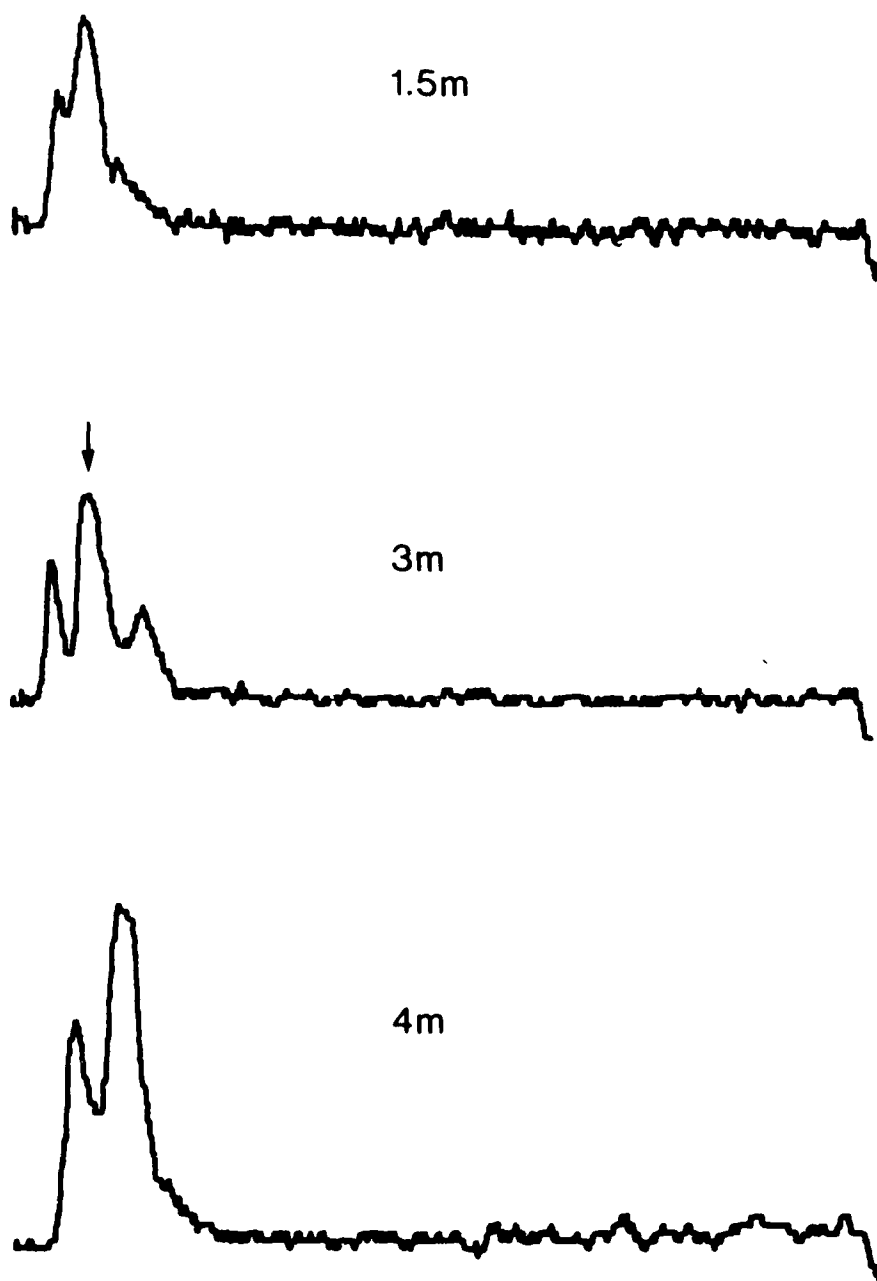
Figure 3   SIGNAL RETURNS

Type B — Large backscatter
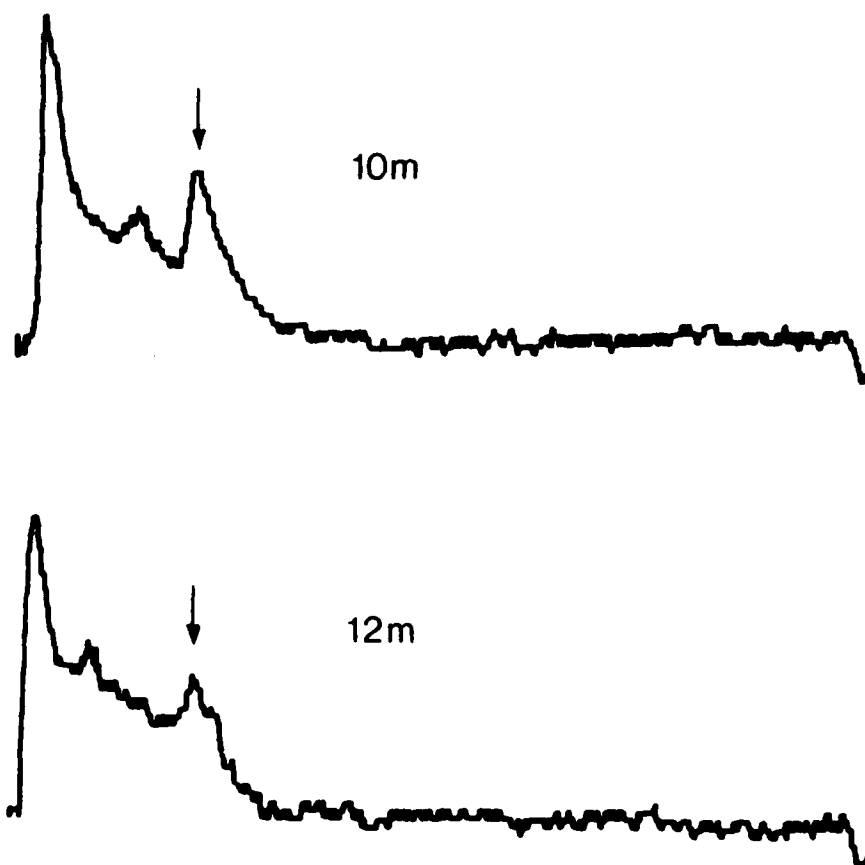## good signal/noise

Figure 4 SIGNAL RETURNS

Type C — No backscatter
good signal noise

7m

12m

18m
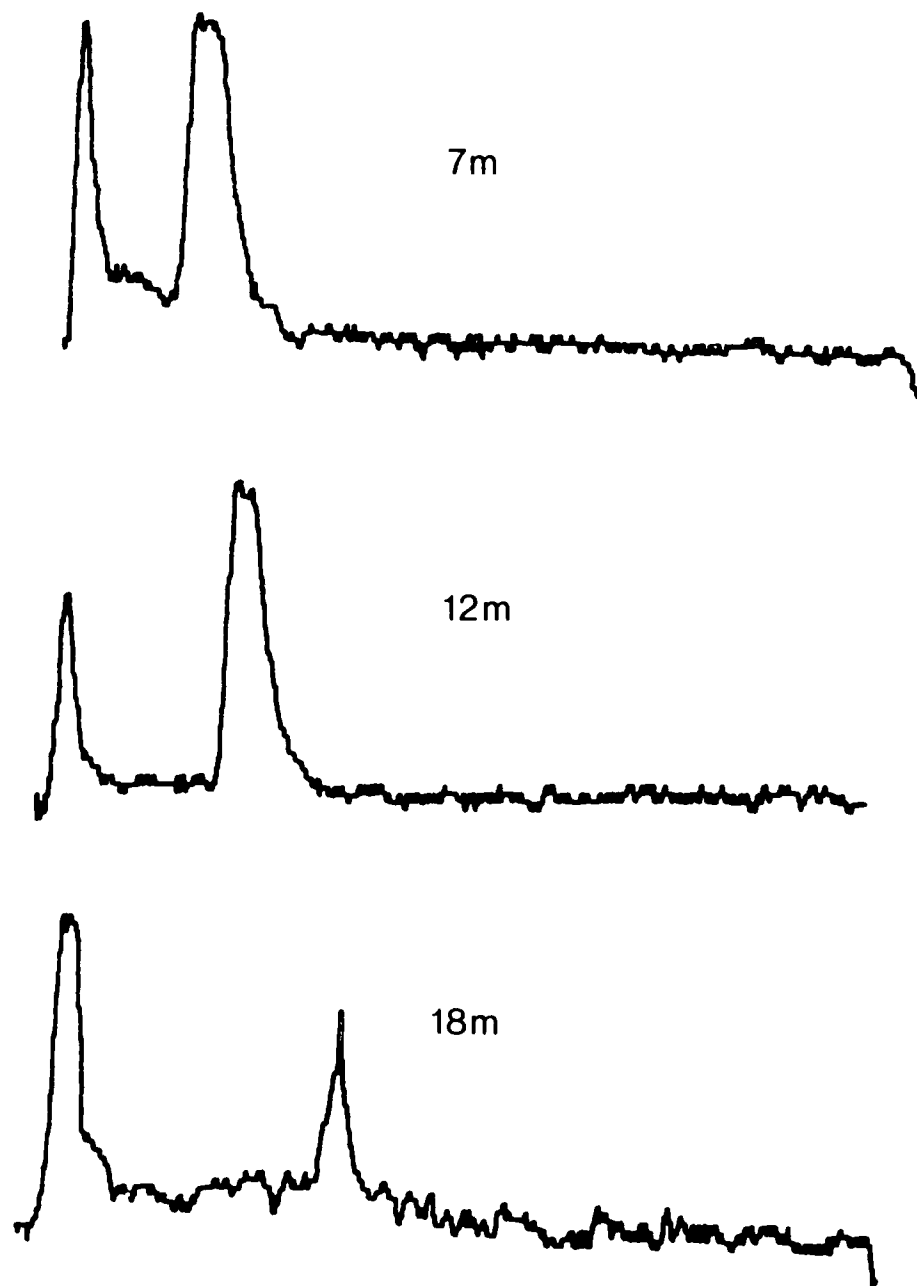
Figure 5   SIGNAL RETURNS

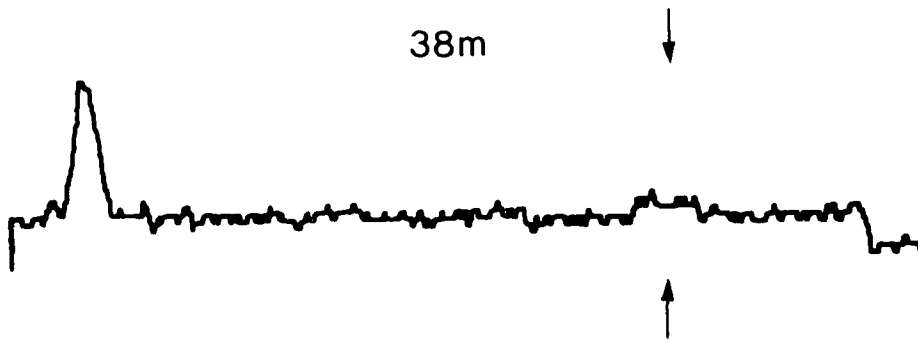Type D — Poor signal/noise

38m

Figure 6   SIGNAL RETURNS

θ MAX=15°

H

H=500m

SEA SURFACE

ΔH

ΔD

θ

D

L

SEA BOTTOM
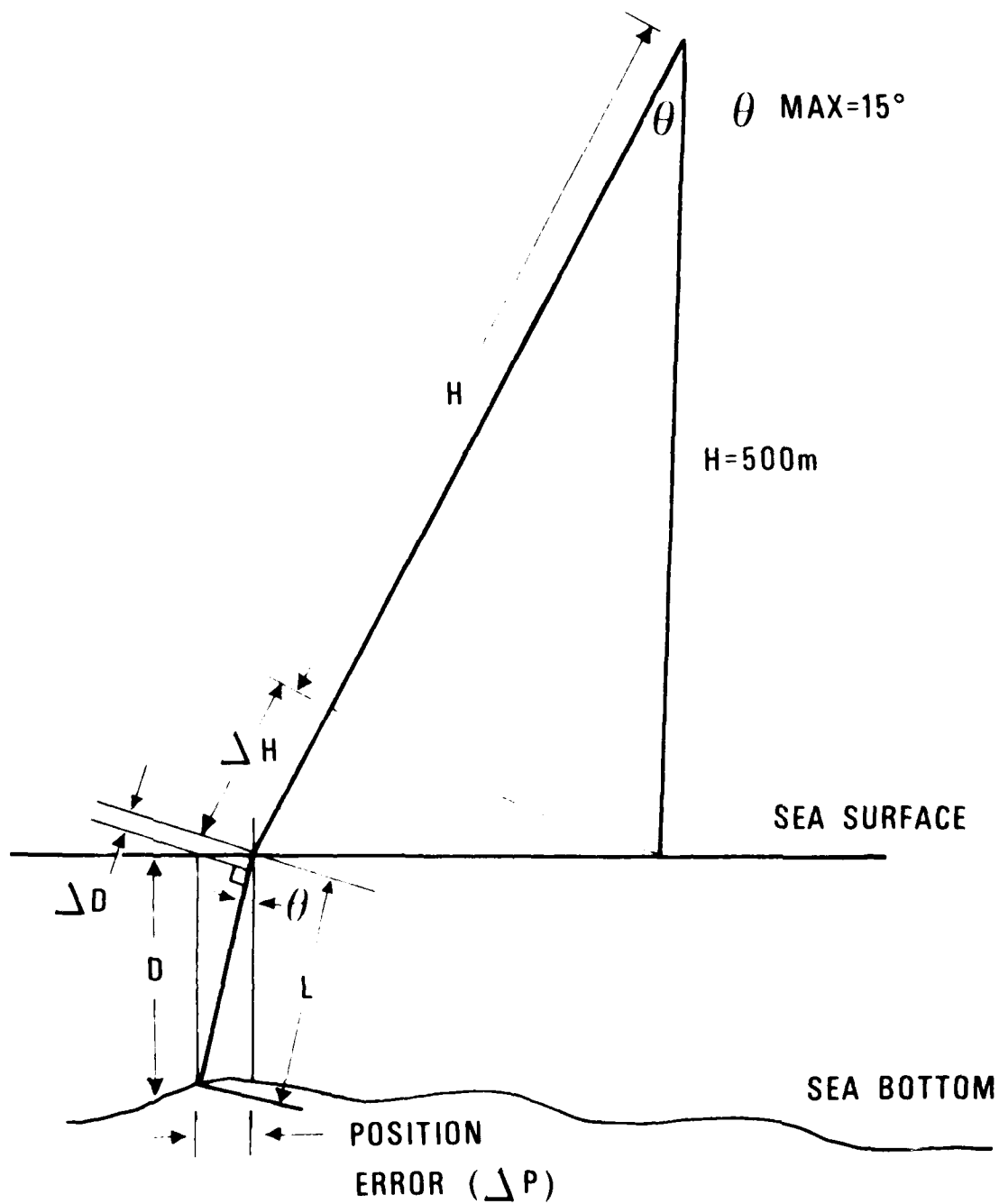
POSITION
ERROR (ΔP)
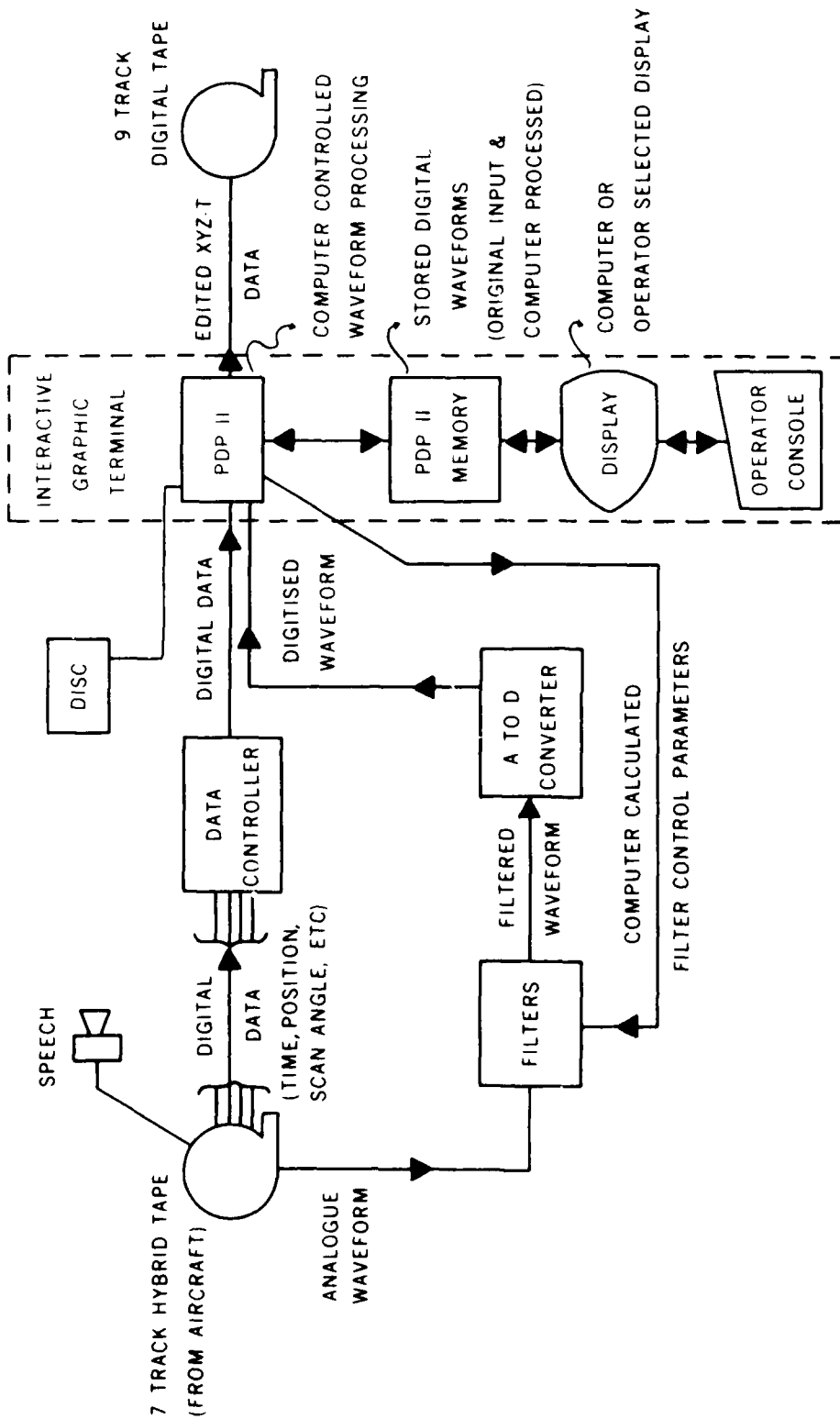
Figure 7   SCAN GEOMETRY

Figure 8   GROUND PROCESSING FACILITY

PAPER 19

ERROR ANALYSIS OF PULSE LOCATION ESTIMATES FOR
SIMULATED BATHYMETRIC LIDAR RETURNS

Gary C. Guenther

Engineering Development Office, OA/Ocean

Technology and Engineering Services, NOAA

Rockville, Maryland   20852

Robert W.L. Thomas

EG&G/Washington Analytical Services Center, Inc.

Riverdale, Maryland   20840

ABSTRACT.   A Poisson count simulator has been exercised to
generate precision and offset results for the estimated
temporal location of quantum limited laser pulses.   Pulse
sizes, shapes, and charge integration times are varied over
appropriate ranges.   A number of location estimators
including variations on peak, centroid, and threshold
detectors are examined.   Comparisons with experimental
results are presented.   Hardware and software design
parameters for an airborne lidar hydrography system are
discussed.

INTRODUCTION

The utilization of an airborne, scanning, pulsed lidar system for
acquiring bathymetric data from coastal waters, bays, and lakes has been
extensively studied in this decade (Guenther and Goodman et al. 1979).
Experimental programs with second-generation hardware are currently
underway in Canada and Australia as well as in the United States. This
technique is destined for implementation and integration into the
spectrum of existing bathymetric systems.

The ultimate operational feasibility of airborne lidar hydrography
depends on a number of physical, economic, and logistical factors. The
results of several cost studies (i.e., Enabnit and Goodman et al. 1978)

have indicated that the augmentation of existing sonar capabilities in "shallow" water with a single airborne laser system should result in substantial savings in operational costs, and the acquisition costs would be recovered in less than two years. Logistical requirements such as navigation, positioning, water clarity forecasting, tide control, data reduction, etc., are being actively studied and are not expected to provide any major barriers.

The two basic physical constraints on a system utilizing this technology are depth measurement "accuracy" and maximum "penetration" depth. The accuracy of depth measurements encompasses several concepts such as precision, repeatability, and comparability with independent standards. Penetration implies not just the capability to detect but also to accurately locate a return signal which has traversed the water column, been reflected from the bottom, again traversed the water column, and arrived as a distant receiver. Useful penetration is limited, therefore, not by detection, but by the accuracy requirement. Accuracy is the paramount concept upon which the design of such a system must be predicated.

The basic accuracy standard in the United States for hydrography in "shallow" water (less than 20 m) is ±30 cm. This is the total permissible error accumulated from all sources including random error, bias, tide control, positioning, waves, etc. It is estimated that a maximum of roughly half this error budget, ±15 cm, should be allocated for "precision," i.e., lack of short-term (pulse to pulse) repeatability. This is equivalent to ±1.3 nanoseconds (ns) of round-trip time in water. In this domain (gigahertz frequency) it may be perceived that extremely stringent requirements are incumbent on the receiving electronics system and the processing algorithms - particularly in view of the fact that a practical laser pulse is expected to be emitted with a "half width" (FWHM) of no less than about 5.0 ns and will be further stretched as it propagates through the water. Complementary approaches have been invoked in a comprehensive study of the errors associated with airborne lidar bathymetry over a range of depth and water clarity conditions: the field test of a research instrument - NASA's Airborne Oceanographic Lidar system (Guenther and Goodman 1978), a derivation of pulse stretching and return

power based on scattering and diffusion theory (Thomas and Guenther 1979), a Monte Carlo propagation simulation (Guenther and Thomas 1981), and the computer simulation described in this report to predict, verify, and extrapolate experimental results for "random" error.

The detailed design of a prototype airborne lidar bathymetry system (consisting of a laser transmitter, scanner and receiver optics, data acquisition electronics, data recording, analysis, and control computer, and integrated attitude, navigation, and positioning electronics) is extremely complex and involves a number of difficult hardware tradeoffs at a state-of-the-art level. It is absolutely vital that no hardware configuration be selected before a careful analysis is performed to determine the impact of that design on the inherent accuracy potential of the instrument.

The purpose of this study is to provide a standard upon which such judgements can be based. The simulations herein described have been conducted with algorithms and parameter ranges consistent with advanced state-of-the-art laser and electronic hardware in such a way that the effects on the accuracy of algorithm or parameter trade-offs can be explicitly resolved. In this way, development programs for unavailable components can be prioritized not only by their cost but by their cost-effectiveness. Furthermore, pulse location techniques, whether implemented in hardware or software, analog or digital, may be selected to provide the optimum balance between precision and bias errors over a typical range of operating conditions. This will permit the selection of the best of possible alternatives within the constraints of resources, technology, and operational restrictions.

DESCRIPTION OF THE SIMULATION

Concept

The concept to be simulated consists of an input pulse waveform sampled by a series of discrete, temporally adjoined quantum accumulation intervals which, in effect, integrate charge from adjacent time slices across the superimposed pulse. In practice, this could be the results of sampling a pulsed lidar signal from the output of the

photocathode of a photomultiplier tube with an a/d converter. (The simulation is performed at the output of the photocathode since this location represents the lowest signal level and thus dictates the limiting signal-to-noise ratio for the system. The resultant output is a series of cardinal numerals representing the time sampled amplitude variation if the input pulse. These integer values are subject to Poisson statistics; that is to say, for any fixed mean input signal or "rate" in a time slice, the distribution of output values from that time "bin", over a number of pulses, will be Poisson. The optional selection of Gaussian statistics instead of Poisson statistics in data set generation has been included in the code for its ability to save computer time when large mean rates are involved.

The simulation process consists first of generating a large number (typically 100 or more) of digitized pulse waveforms, or "data sets", with Poisson distribution about a specified mean signal. A given set of pulse location estimation "procedures" are then applied to each data set. For the laser bathymetry application, eight procedures have been applied; these consist of center of peak bin, centroid of a specified band of bins surrounding the peak, and frontwards- and backwards-looking proportional thresholds at the 20%, 50%, and 80% levels (illustrated in Fig. 1). The mean location, standard deviation, standard error in the mean, and success probability (fractional number of location determinations compared to the number of attempts) for the ensemble of data sets are calculated for each procedure. A bias may be obtained for each procedure by noting the difference between the calculated mean location and the "true" or expected location.

The simulation is performed over the ensemble of data sets to determine pulse location statistics for a single pulse, but a bathymetric measurement is based on two independent pulses: the surface return and the bottom return. The "precision" or standard deviation of a simulated bathymetric measurement is then the root sum of squares (RSS) of the standard deviations for two independent pulses, and biases are summed algebraically to obtain the bathymetric bias for the procedure. The probability of a successful depth measurement is the product of the individual success probabilities.

Data Synthesis

Consider a continuous waveform representing an analog pulse superimposed arbitrarily on a time axis which has been divided into a number of adjacent "increments" or time slices of equal width. In each increment, or "bin", the analog signal is integrated and normalized to yield a single value which is displayed as a constant output level for the duration of that bin. The shape of this digital representation will depend strongly on the location of the input rate peak with respect to the edges of the time bins as seen in Fig. 2. It is clear that if random noise is added to the pulse, a peak location solidly in the center of a time bin will generally remain in that bin, but a peak location near the edge between two bins will appear to jump back and forth between the two. The standard deviation of the estimate of a pulse location procedure can rightfully be expected to be larger for the latter case -- by an amount which depends on the procedure, the pulse width, and the bin width.

In an operational situation, the actual pulse locations may generally be assumed to be uniformly and randomly distributed over the space from the bin edge to bin center. Simulations must be performed in which mean rate input pulses are placed at a number of equally spaced locations between bin edge and bin center and the output standard deviation of the location estimate averaged over all cases. This is a very taxing procedure. The results obtained indicate that for relatively symmetric pulses and moderate signal levels, a good approximation to the calculated result for the average variance can generally be obtained from the algebraic mean of the variances obtained for the two extremes -- the input mean rate pulse centered at the edge of a bin and in the middle of a bin. (For a peak detector, these results will not be complete but will provide a lower bound on the expected variance.) Results are considered invalid if the difference between the mean locations for the two cases is greater than the mean standard deviation. More difficult circumstances which involve high signal strengths and highly asymmetric pulses requiring additional data or techniques beyond the scope of this report are discussed in a NOAA Technical Memorandum which is available upon request.

While the simulator possesses the capability to generate a broad range of pulse shapes, the specific mean rate distributions, f(t), considered here are generally of Gaussian character (recall Fig. 1). (This temporal pulse shape is completely different from and should not be confused with the probability distribution involved.) The asymmetric shapes utilized to simulate arriving laser pulses consist of a Gaussian leading edge of a given width combined with a Gaussian trailing edge with a different (longer) width. Pulse shape and width will henceforth be denoted by listing the one standard deviation (1σ) leading- and trailing-edge widths (in nanoseconds) separated by a colon, i.e., 3:5 or 5:20. Triangle shaped pulses have also been examined.

All pulse location procedures to be tested are applied to the same ensemble of data sets; this insures that observed differences are due to the procedures and not statistical anomalies in data set generation. Random errors in the output statistics for pulse location procedures due to the particular random number sequences involved in data set generation can be constrained to any desired level by selection of a sufficiently large number of data sets per ensemble. A minimum value of 100 data sets per ensemble was used; this provides an expected standard error in the estimate of the standard deviation of pulse location (for a given procedure) of $1/\sqrt{2n} = 1/\sqrt{200} \sim 7\%$.

Bathymetric lidar is intended for daytime use as well as night. Under daylight conditions, the lidar return pulses are superimposed on the additive background level of the volume reflected solar background. In the simulator, a selectable constant mean background rate is added to all bins in the mean rate input pulse data prior to generation of the probability tables and data sets. This mean rate, having exerted its influence on the distribution of Poisson counts, is then subtracted from all data sets prior to pulse detection/location in order to simulate a realistic system in which this would be accomplished (either by ac-coupling or digital data processing) to remove any pulse location bias which could caused by an uncorrected background level. Negative values generated by this subtraction are set to zero.

The gain of the system and the number of bits in the digitizer act to truncate certain ranges in the number of photoevents into a discrete "count." For example, if 10 photoevents are required to produce a single count, then both 21 and 29 photoevents will produce 2 counts, while 30 photoevents will produce 3 counts. This truncation effect can alter counting statistics, and hence the number of photoevents per count is included in the simulation as an input variable.

Pulse Location Estimators

The first step in pulse location is pulse detection. In the simulator, a pulse is "detected" at the site of the maximum integer in the data set or the first of equal maxima. The location and magnitude of the detected peak are stored for use in the pulse location procedures. Three basic types of pulse location procedures have been analyzed: these are center of peak bin, centroid of a region linked to the peak bin, and threshold. If we were to base our pulse location estimation on only a selected count, i.e., the peak, we would have to assign the pulse location to an arbitrary point within the corresponding time bin. With no further information, we could do no better than choose the middle of the time bin to be the required location. In reality, pulse peaks will be distributed uniformly across the bin width. The _minimum_ RMS error for a peak detector is thus the bin width divided by the square root of twelve (the standard deviation of a uniform distribution). A procedure which allows a location estimate anywhere within a bin would therefore be preferable. With little a priori knowledge of the return pulse shape, curve fitting estimators appear to be overambitious; we have thus considered centroid and threshold estimators.

Centroid based locators are defined by choices of the length of the centroid region, whether the length is fixed or variable (depending on the pulse width), and of the relative location of the peak within the region (i.e., a centroid of only the leading edge, one balanced symmetrically or asymmetrically on the peak, or one encompassing the entire pulse energy). Results have been determined for slightly asymmetric centroids (matched to pulse shape) of various lengths "centered" on the peak bin.

Threshold based locators can be categorized as fixed level or fractional (to peak height), and they can be frontward searching or backward searching (in time). The performance of any of these variations depends strongly on the specific threshold level selected. In the simulation, the exact threshold location is selected by identifying the bin in which the specified level is passed and interpolating to a fractional location between that and the previous bin based on the amplitudes involved.

RESULTS

Prediction of AOL Performance

This pulse location estimation (PLE) simulator was originally conceived for the purpose of predicting the limiting precision (random depth measurement error as a function of bottom return signal strength) imposed by the hardware in the NASA/AVCO Airborne Oceanographic Lidar (AOL) system which was being test flown for NOAA in the bathymetry mode. Without this information, there would have been no way of allocating the measured random errors between basic design constraints and unknown causes which would require further investigation. As seen in Fig. 3, the system precision (for calm sea conditions) and the simulation results are in excellent agreement. Not only did this give us confidence that the AOL was performing to its design limits, but it also, in turn, verified the performance of the simulation for further predictive purposes.

The simulation also produced a rather surprising result: fractional threshold algorithms (among others) applied to single asymmetric pulses yield offsets (compared to the "true" location) toward the tail of the pulse with magnitudes as large as 15 cm for the cases studied. It is important to note, however, that, in a two pulse measurement, these offsets will be self cancelling to the extent that the two pulses have the same shape and duration. For a "stretched" bottom return, a net depth measurement bias in the deep direction will result as the difference between the offsets for the two single pulse cases. The offsets (and hence resultant bias) are very small for small (20%) threshold fractions and can become large for high (80%) threshold

fractions. For example, given a 2.5 ns bin width and a 20 photoelectons per nanosecond (pe/ns) peak rate, a pulse stretching from 3:5 ns to 5:20 ns would exhibit a 2 cm bias with a 20% threshold, a 7 cm bias with a 50% threshold, and an 11 cm bias with an 80% threshold.

Sensitivity Studies

In a shot-noise limited system, the performance (measurement accuracy) depends not only on the return signal strength to ambient background ratio; but on the absolute magnitudes of these two individual components. Simulations have been conducted for two diverse conditions: low absolute rates (consistent with AOL performance) and high absolute rates (consistent with the design parameters of the Hydrographic Airborne Laser Sounder (HALS) presently being designed by AVCO for the U.S. Navy). The distinction arises not from different environmental conditions (such as night versus day), but rather from different tranceiver configurations (output power, optics, etc.). Only the low rate results are included in this limited report; the high rate results may be obtained upon request.

When photon arrival rates are low, counting statistics and the resulting shot-noise level are very sensitive to factors which cause changes in the rates. Such factors as pulse width, integration time (bin width), and amplifier gain (truncation in digitization) are important because they will have larger effects here than in high rate systems. Simulations were performed for all combinations of the parameter sets listed in Table 1.

Table 1. Simulated Parameters and Procedures

Pulse width: 1:2 ns, 3:5 ns, 4:10 ns, 5:20 ns (as defined in Fig. 1)

Bin width: 1.5 ns, 2.5 ns, 5.0 ns

Algorithms: centroid (a 6 bin window with the peak in bin 3 denoted "6C3"), center of peak count (denoted "PK"), and frontward- and backward-looking fractional thresholds at 20%, 50%, and 80% of the peak amplitude (denoted F20, F50, F80, B20, B50, and B80).

For the AOL case, the mean peak rate was varied from 2 photo-electrons per nanosecond (pe/ns) to 20 pe/ns in steps of 2 pe/ns. The solar background for daytime operation was estimated to be 8 pe/ns, while the dark current of the PMT was estimated to be 2 pe/ns for nighttime operation. Truncation levels of 1, 4, and 8 pe/"discrete" count were exercised. Sample results appear in Figs. 4 through 18.

The effect of the pulse location algorithm is examined for the case of a typical unstretched pulse at night in Figs. 4 and 5 which present mean pulse location and the standard deviation about that mean (as function of the peak signal strength) for various algorithms. (Notation used in identifying the algorithms on the plots is listed in Table 1). The nominal location of the peak signal is at 25 ns into the data set. Note that an error of 11.25 cm in depth measurement will accrue for every nanosecond of timing error.

It can be seen in Fig. 4 that as the peak signal strength is reduced, the mean pulse location remains constant and stable for all algorithms except F20 until about 4 pe/ns (a peak signal to mean background ratio of S/B=2). The F20 result (i.e., for a forward-looking 20% threshold searching from the beginning of the data set) becomes unstable for peak signals of less than 14 pe/ns. This is indicated by the drop in the mean F20 pulse location below its (correct) high signal strength value. This drop is caused by shot-noise induced false early detections generated in the region between the start of the data set and the true 20% threshold location.

This results, as clearly evidenced in Fig. 5, in a very large standard deviation for the F20 algorithm below a peak signal strength of 14 pe/ns. The remaining algorithms produce pulse location precisions (with magnitudes related to the algorithm) which do not increase significantly until the peak signal rate drops below about 6 pe/ns (S/B=3). It can be seen that, for this parameter set, the best performance (lowest asymptotic standard deviation at high peak rates) from a threshold detector is about 7 cm at 20 pe/ns derived from B20, F50, and B50; while F80 and B80 are slightly noisier at 8.5 cm; and peak detection at 13 cm is much noiser and yields a result twice as large as that for the preferred algorithms. The 6-point asymmetric centroid is,

in this case, well matched to the pulse and hence offers the lowest
standard deviation of 4 cm. This will not always be the result,
however, because the precision of a centroid-based pulse location
estimate depends strongly on the "matching" of the size and location of
the centroid window to the given pulse. The high standard deviation
associated with the peak location i.., however, as will be seen, a
general result.

A similar set of results is presented in Figs. 6 and 7 for a
stretched (e.g., by underwater propagation) return pulse. It is seen in
Fig. 6 that the results for the means are similar to but subtly
different from those for the previous "nominal" pulse. The peak
location is biased above its actual 25 ns location by the high
probability of detecting a peak (caused by noise spikes) on the long,
slowly-decaying trailing edge of the pulse. As the peak signal rate is
reduced, several of the fractional threshold derived means rise slightly
(rather than fall as in the previous example) for the same basic
reason. The F20 algorithm again becomes unstable below 12 pe/ns due to
early detections in the noise preceding the pulse.

Most precision results for this case, as seen in Fig. 7, are
qualitatively similar to the former case, but quite different
quantitatively. One major qualitative difference is the relative
performance of the centroid detector whose standard deviation of 28 cm
(at 20 pe/ns) falls far above that for the 20% and 50% thresholds and
just below that of the peak detector at 34 cm. This occurs because the
6 bin window is no longer large enough to encompass the entire pulse,
and the centroid result "jitters" with the movement of the peak detector
to which it is tied. In addition, the B80 at 30 cm is not as good as
the F80 at 20 cm due to the flatter shape of the top of the pulse. The
F50 and B20 at 10 cm are again preferred; the F20 is lost in the noise,
and the B50 is still feeling the effects of the elongated pulse shape
(as evidenced by unusually prolonged elevated values at middle-sized
peak signal rates).

It is very important to note the effect of the increased pulse
width on the limiting precision of the various algorithms. In the
field, the bottom return pulse width will increase more than linearly

with increasing depth (Guenther and Thomas 1981). It would not, therefore, be appropriate to select an algorithm whose basic precision limitation is strongly sensitive to pulse width. The aforementioned limiting precision results are compiled in Table 2.

Table 2. Effect of Pulse Width on Limiting Precision
(at 20 pe/ns) for Various Algorithms

Algorithm*[†]	Limiting Precision (cm) Pulse width		Ratio ($\frac{5:20}{3:5}$)
	3:5 ns	5:20 ns	
6C3 centriod	4	28	x 7.0
PK (peak)	13	34	x 2.6
B20 threshold	6	10	x 1.7
F50 threshold	7	10	x 1.4
F80 threshold	8.5	20	x 2.4
B80 threshold	8.5	30	x 3.5

It is clear that the B20 and F50 algorithms not only produce some of the lowest standard deviations for unstretched pulses but also are the least sensitive to pulse stretching. This is further illustrated in Fig. 8 which compares the performance of a peak detector against F50 for increasing pulse widths.

The choice of the "optimum" threshold fraction (defined in terms of the lowest standard deviation) depends to a certain extent on both pulse width and bin width as seen in Fig. 9. Here we see the value of the mean peak signal strength required to reduce the standard deviation of the pulse location estimate to 10 cm or less as a function of the threshold fraction.

---

* for notation see Table 1
† F20 and B50 are excluded due to poor performance as describe in the text

For narrow (1:2 ns) pulses fairly large threshold fractions are preferred. As the pulse width increases to 3:5 ns, a minimum forms at a threshold fraction of about 0.5. As the width increases to 5:20 ns, the required signal becomes larger and higher threshold fractions become increasingly undesirable, particularly for narrow bin widths. The increase in required signal is due to the decreasing slope at the detection point. The increasingly poor performance for narrow bins is a result of the classic struggle between resolution and accuracy. As the bin size is decreased, the resolution improves, but the encompassed signal decreases, and the counting statistics cause the overall accuracy to degrade. Over a range of pulse widths, it can be seen in Fig. 9 that the optimum threshold fraction lies in the range from 0.3 to 0.6. For the cases illustrated, the wider 5.0 ns bin results in slightly better performance for pulse widths of 3:5 ns and greater. This bin size effect will be illustrated again after a few other sensitivities are examined.

Figures 10 and 11 illustrate the effect of raising the background rate to 8 pe/ns to simulate the effect of daytime operation. A comparison of these curves with Figs. 5 and 7 indicates that results for most algorithms are remarkably similar in shpae and limiting value (at high signals) and that the curves are basically shifted toward higher peak rates with the "knees" occuring at about 10 pe/ns (P/B ~ 1.2). An exception is F20 which can be seen (in Fig. 10 at the upper right corner and mid-group in Fig. 11) to have been made even worse than before (as might be expected). The effect of the increased (solar) background on the F50 algorithm is seen directly in Fig. 12 for nominal and stretched pulses. For peak signal strengths beyond about 10 pe/ns the differences are reasonably small compared to the desired error budget.

Because of its demonstrated performance, the F50 algorithm will be used as a standard for the remaining sensitivity analyses.

The effect of truncation of counts by the digitizer is demonstrated in Fig. 13 for the F50 algorithm. It is clear that this effect is small compared to many others, and the "standard" value of 4 pe/ns which has been used in previous comparisons will be continued.

The effect of bin size for an F50 algorithm applied to nominal and stretched pulses is seen in Figs. 14 and 15 to be quite small and not worth discussing except to note that decreasing the bin width slightly increases, rather than decreases, the random pulse location error due to the previously mentioned effect of counting statistics. (This will not be the case for a high rate system.)

The effect of pulse width for three bin widths is presented in Figs. 16 through 18. It can be noted that for an F50 algorithm, the reduction in precision due to moderate pulse stretcing is only about 3 cm and is not significant.

CONCLUSIONS

The effects of pulse shape and duration, integration time, pulse location algorithm, signal level, background level, and digitizer truncation on the pulse location estimation accuracy for quantum limited returns have been studied via a Poisson count simulator utilizing Monte Carlo techniques. Experimental pulse-to-pulse precision data obtained with the NASA/AVCO Airborne Oceanographic Lidar (AOL) system were consistent with predictions for that specific configuration.

The following conclusions are drawn from simulations of a "low-rate" system such as the AOL but are felt to be generally applicable.

The pulse location algorithm is very important in determining both the limiting precision at high signal rates and the signal rate at which the precision drops to an acceptable level. The latter is most strongly influenced by the absolute peak signal and background rates and must be examined individually for each specific case of interest. Centroid-type pulse locators require interactive decisions on window size and placement and result in large biases on stretched pulses. Correlation or matched-filter locators are not appropriate for application to propagation stretched pulses. Peak detectors are inherently noisy due to both their discrete nature and detection in a zero slope region. They exhibit disastrous loss of precision with increasing pulse width and are also prone to a deep bias for asymmetric pulses. Fractional

threshold detectors with interpolation between adjacent time bins offer the best overall performance. The optimum threshold fraction depends to a certain extent on the other parameters, but of all algorithms examined, those preferred were the frontward-looking 50% threshold (F50) and the backward-looking 20% threshold (B20). These offer low bias, high limiting precision, and a rapid approach to limiting precision with increasing signal rates.

Results from the propagation simulation (Guenther and Thomas 1981) indicate that selection of the threshold fraction as a function of nadir angle may provide a tool for constraining the magnitude of propagation-induced depth measurement biases.

For well-chosen fractional threshold pulse locators, such as F50, the effects on precision of digitizer truncation and integration time (bin width) are minimal. The effects of pulse width and shape are small for F50 and, for the simulated parameters, fall within the desired error budget. This is advantageous because it implies that there is no need to struggle with state-of-the-art hardware to eke out the last possible nanosecond of performance.

ACKNOWLEDGEMENTS

We wish to thank Lowell R. Goodman whose drive and dedication to airborne laser hydrography spurred the metamorphosis from technological toy to inescapable destiny. We also thank Rodney McJimpsey who patiently performed the tedious data reduction necessary for the presentation of these results.

REFERENCES

Enabnit, D.B., Goodman, L.R., Young, G.K., and Shaughnessy, W.J., 1978: The cost effectiveness of airborne laser hydrography. NOAA Technical Memorandum NOS26, National Oceanic and Atmospheric Administration, U.S. Department of Commerce, Rockville, MD., 56 pp.

Guenther, G.C., and Goodman, L.R., 1978: Laser applications for near-shore nautical charting. SPIE Ocean Optics V, 160, 174-183.

Guenther, G.C., Goodman, L.R., Hoge, F.E., Swift, R.N., Thomas, R.W.L.,
and Bright, D., 1979: AOL bathymetric field test program. Airborne
Laser Hydrography Symposium III October 5-6, 1977, U.S. Department
of Commerce, National Ocean Survey, Rockville, MD., 62-103.

Guenther, G.C., and Thomas, R.W.L., 1981: Monte Carlo simulations of
the effects of underwater propagation on the penetration and depth
measurement bias of an airborne laser bathymeter. NOAA Technical
Memorandum OTES 01, National Oceanic and Atmospheric Administration,
U.S. Department of Commerce, Rockville, MD., 144 pp.

Thomas, R.W.L., and Guenther, G.C., 1979: Theoretical calculations of
bottom returns for bathymetric lidar. Proceedings of the
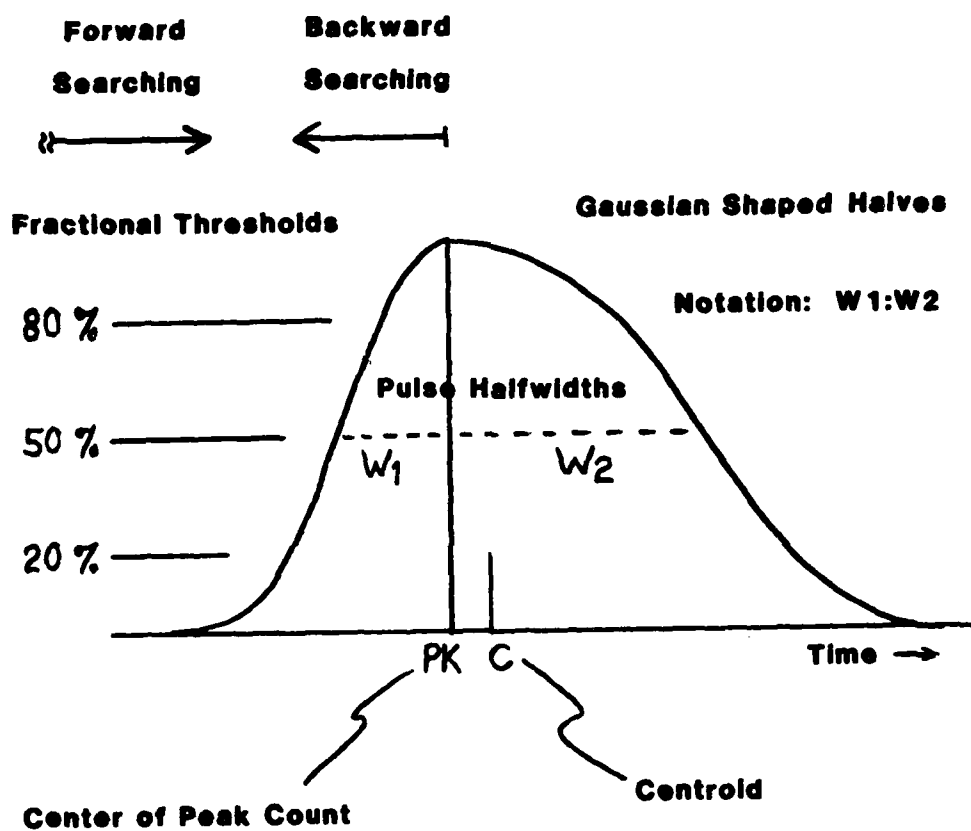International Conference on Lasers '78, Orlando, Fla., 48-59.

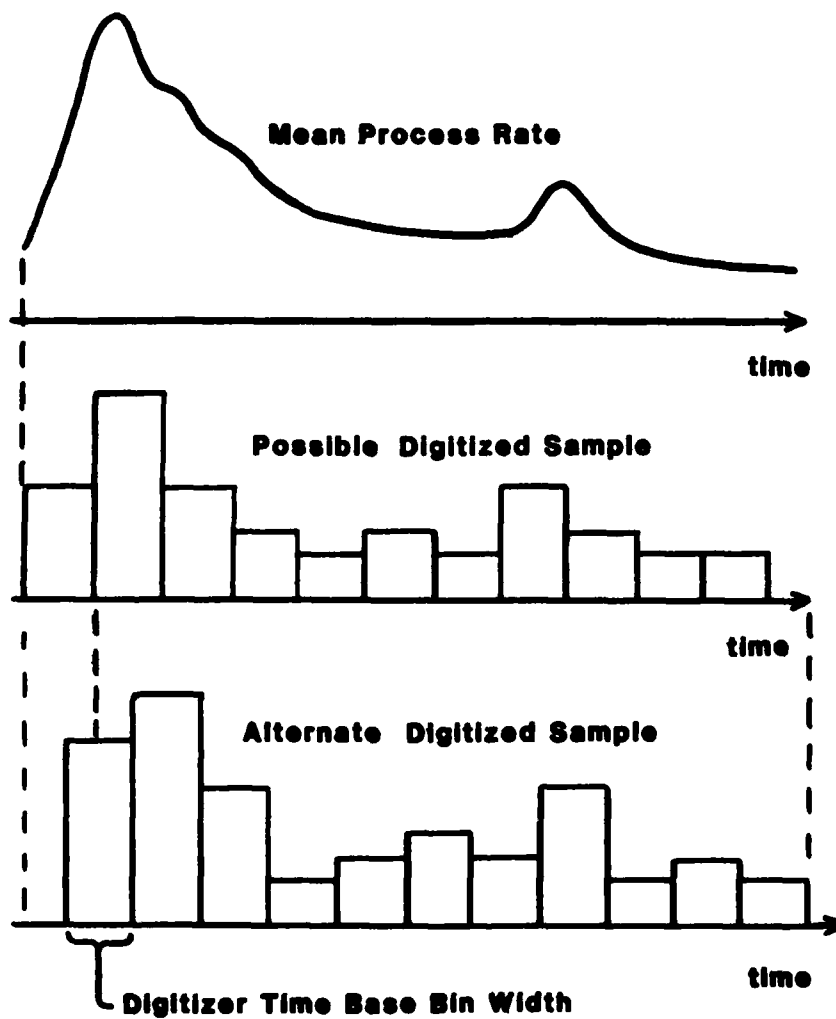Figure 1. Input Pulse Shape and Pulse Location Algorithms

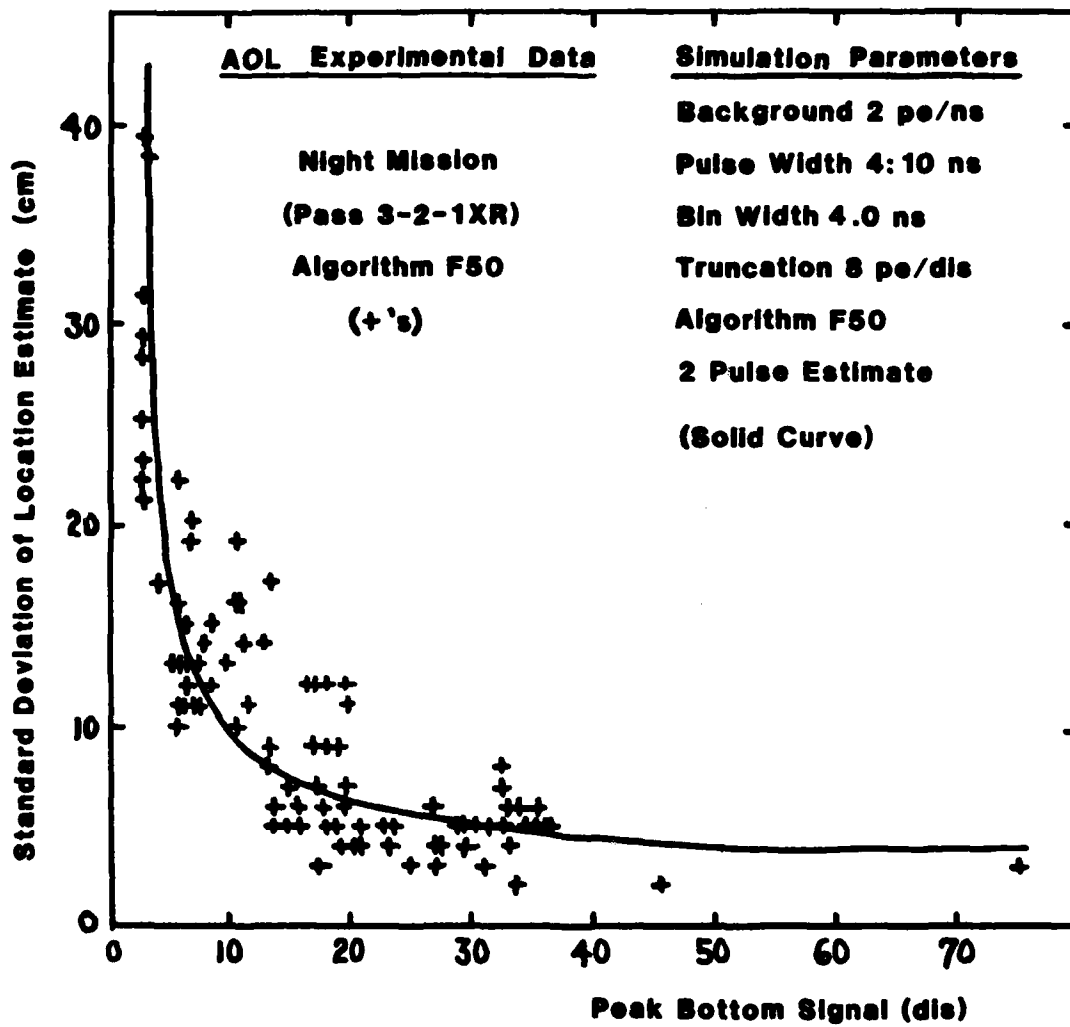Figure 2. Illustration of Digitization Timing

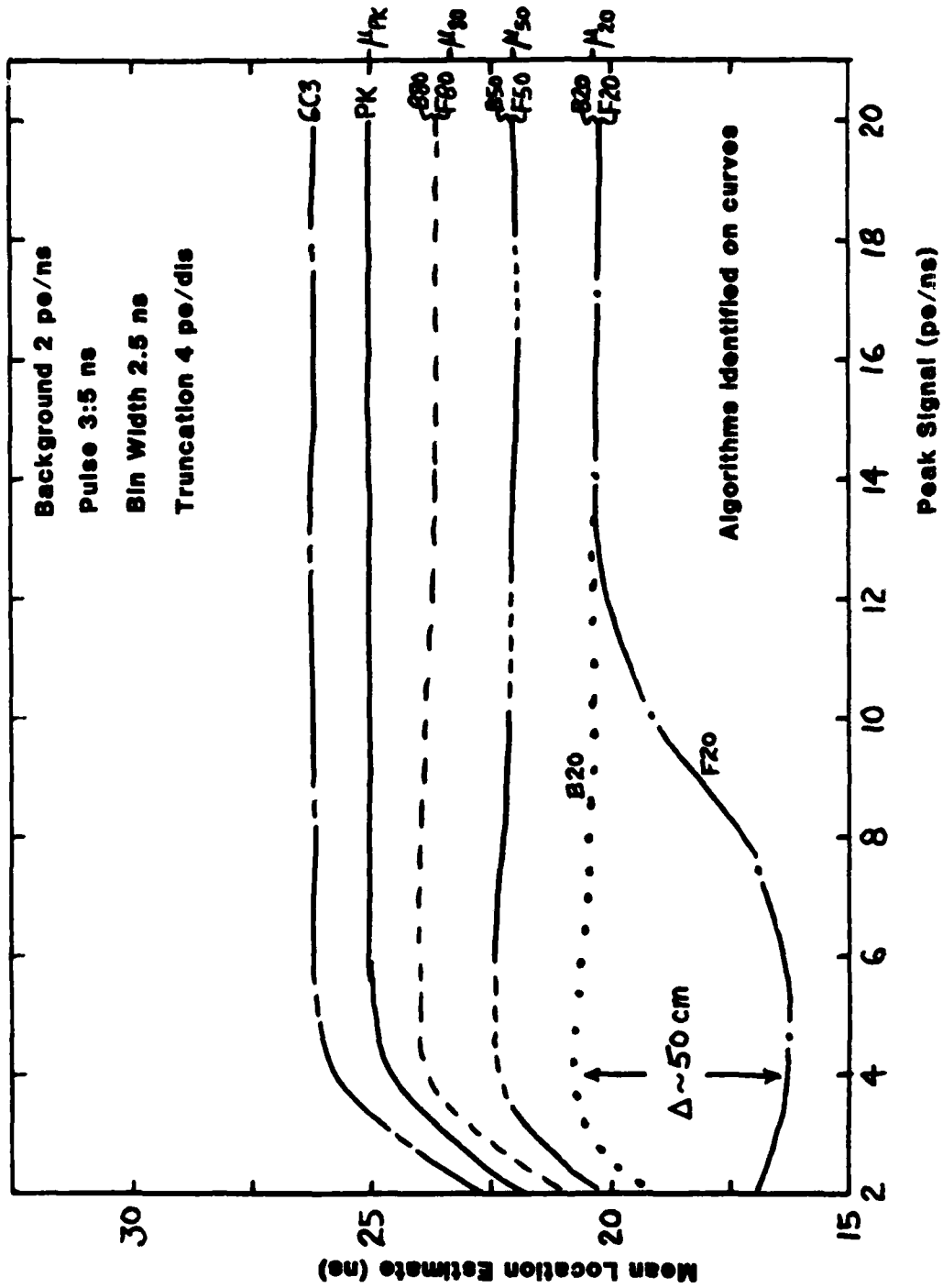Figure 3. Comparison of Experimental Data with Simulation Prediction

Figure 4. Mean Pulse Location for Nominal Pulse at Night

Figure 5. Precision for Nominal Pulse at Night
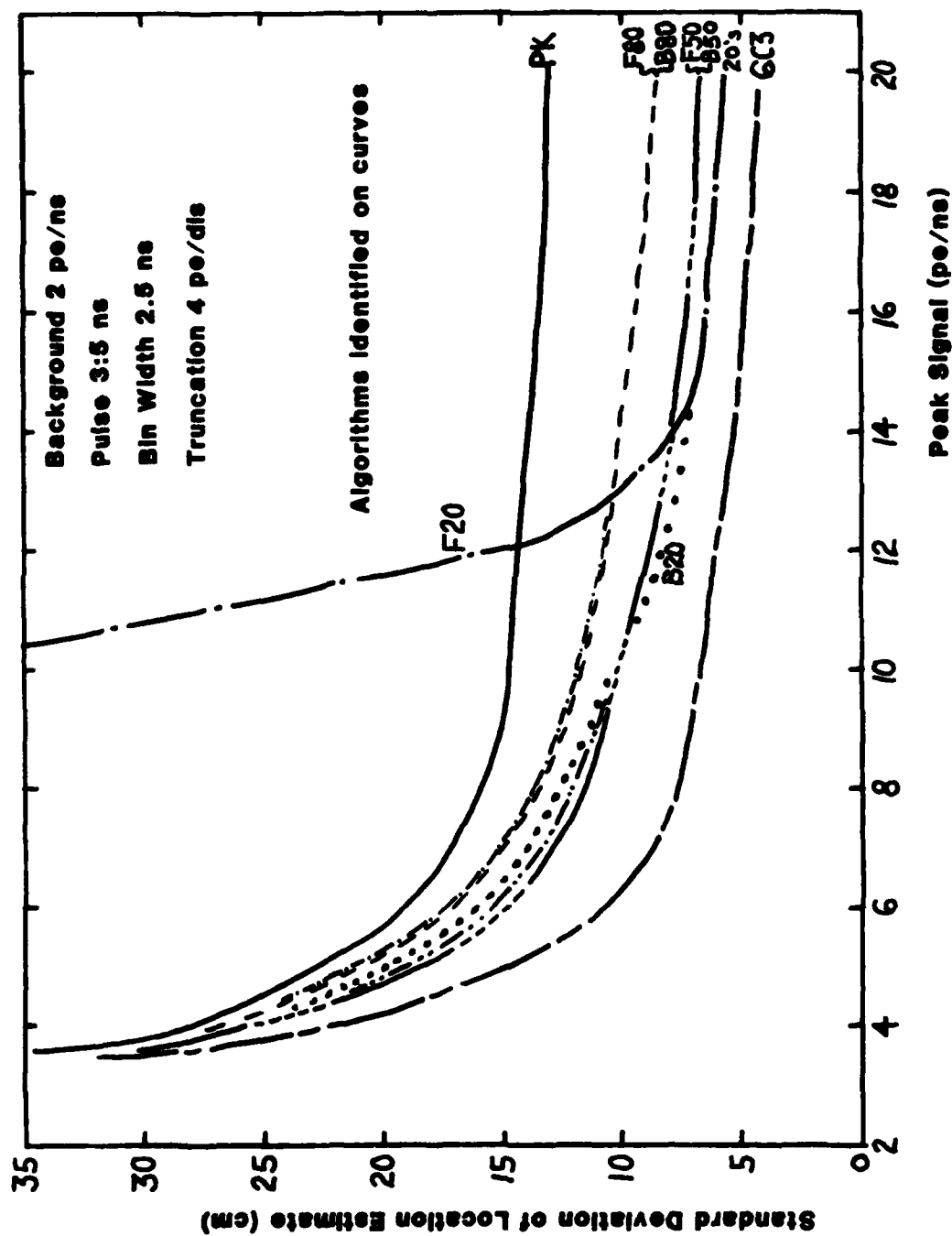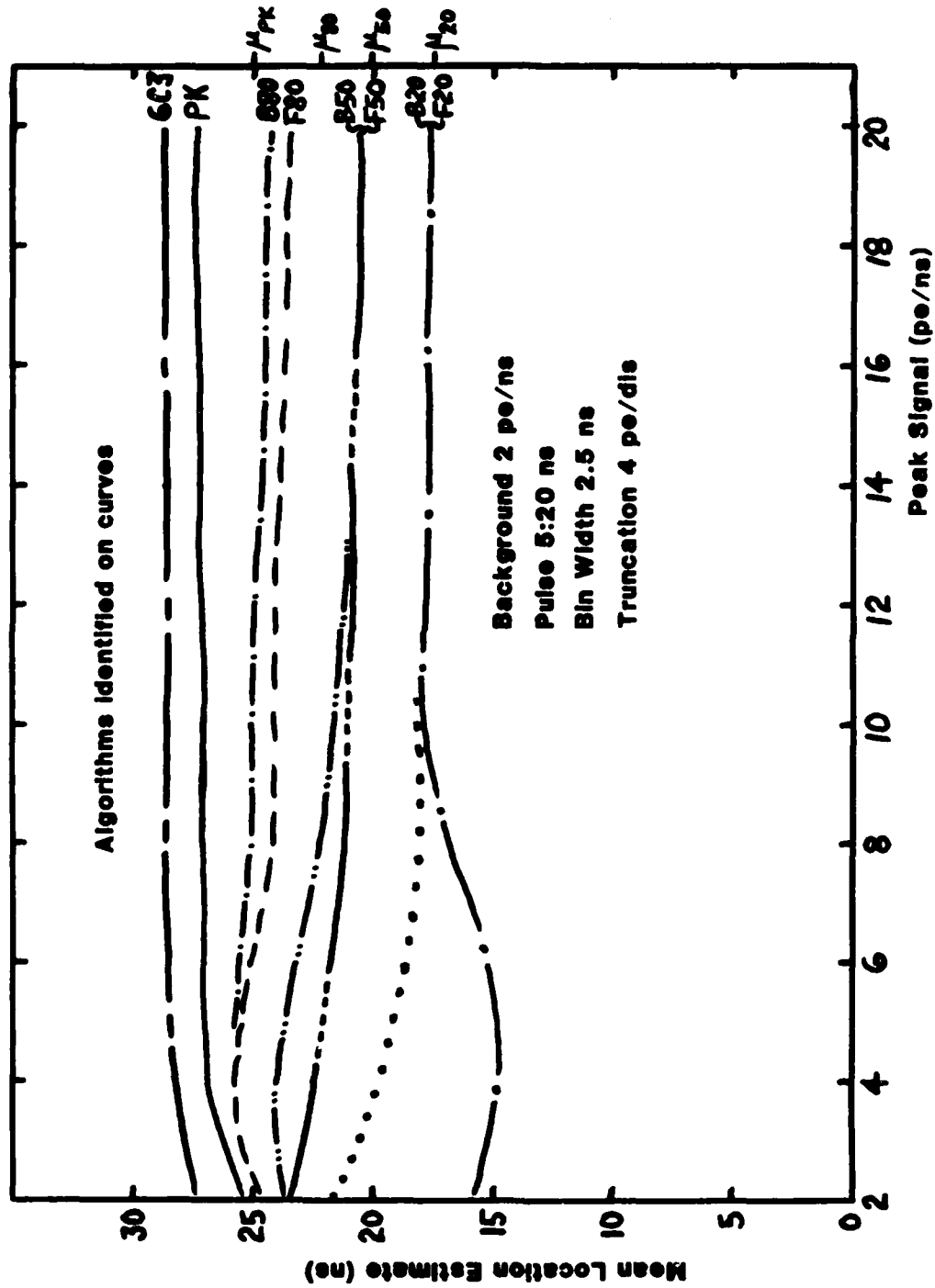
Figure 6. Mean Pulse Location for Stretched Pulse at Night
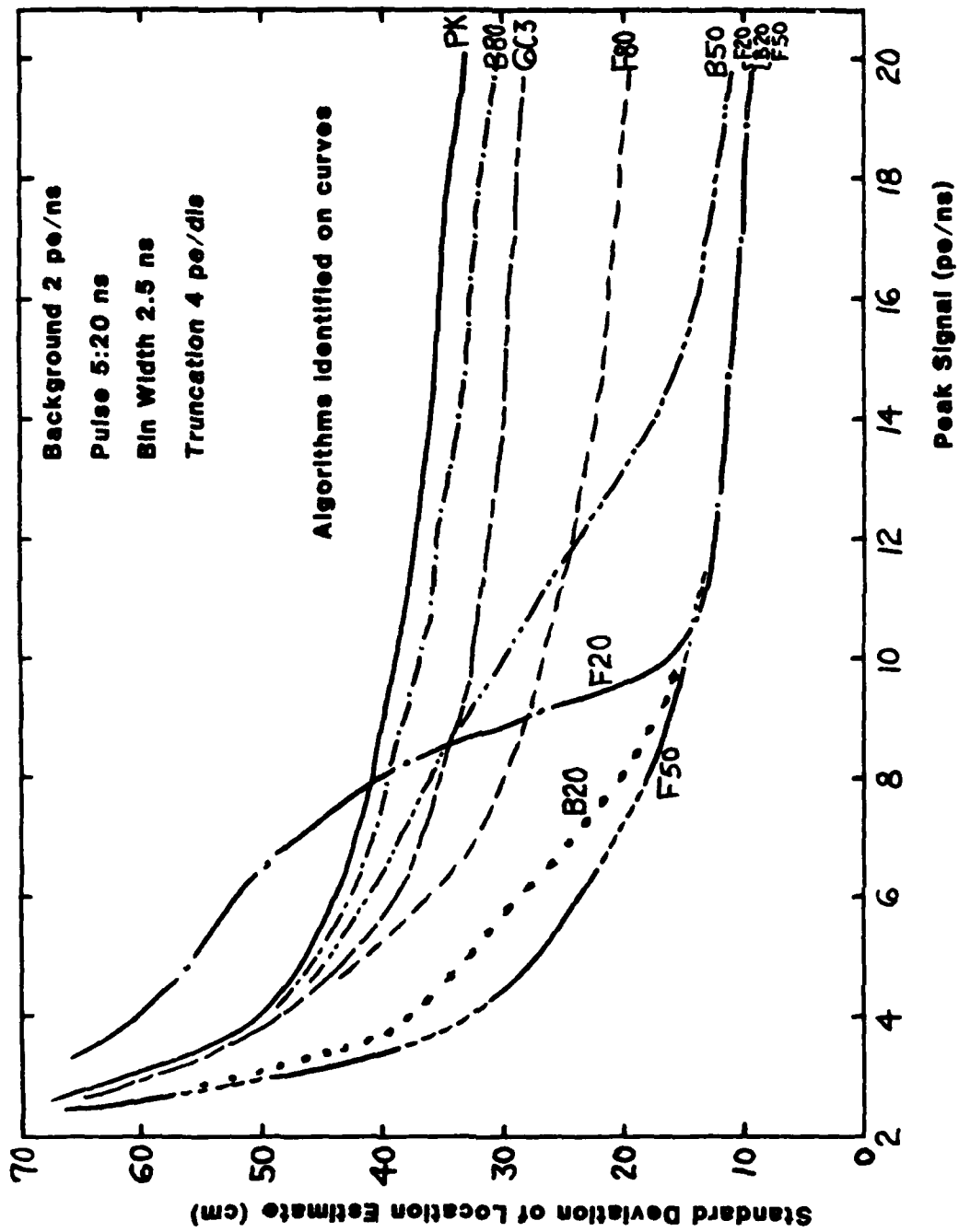
Figure 7. Precision for Stretched Pulse at Night
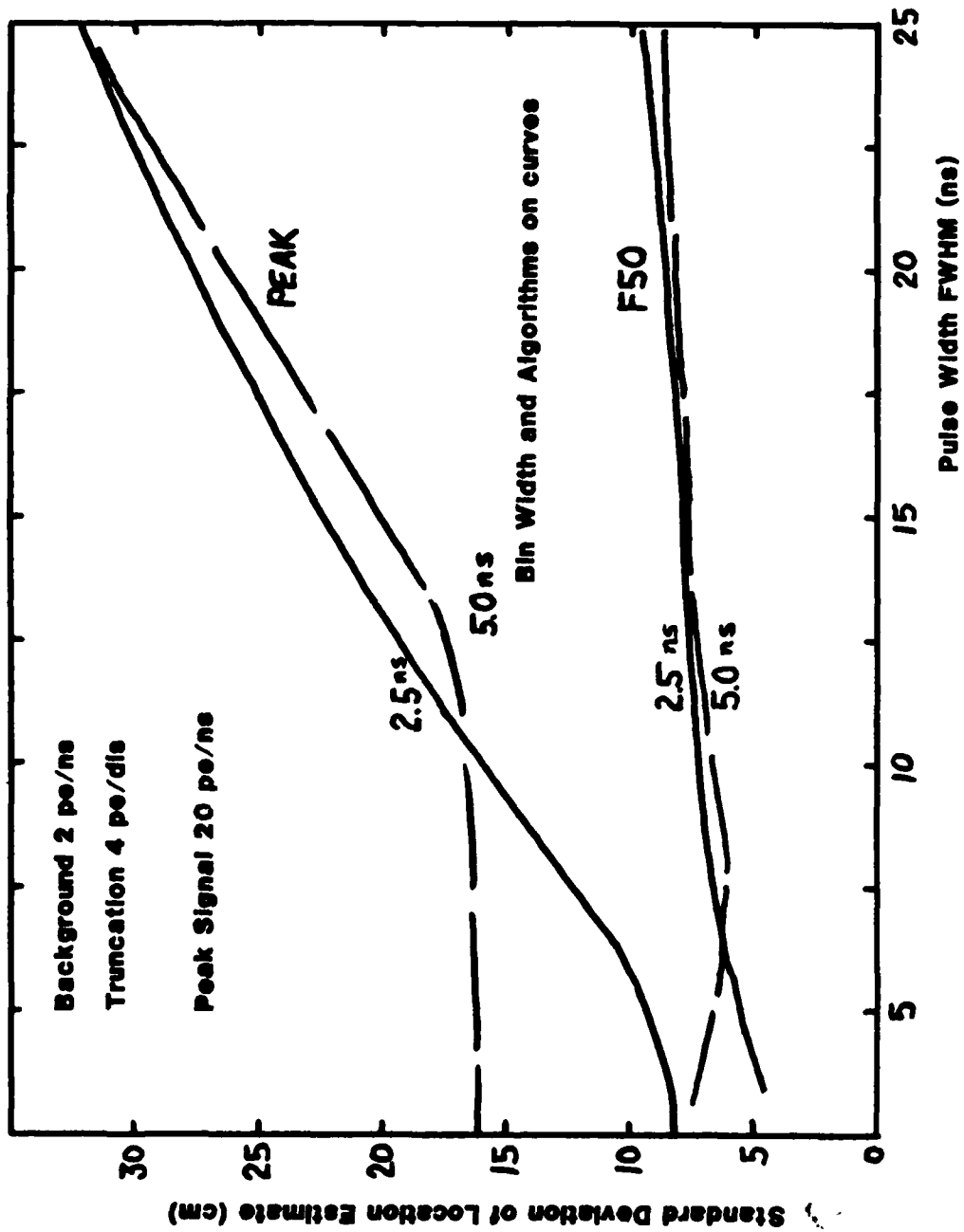
Figure 8. Effect of Pulse Stretching for Two Algorithms
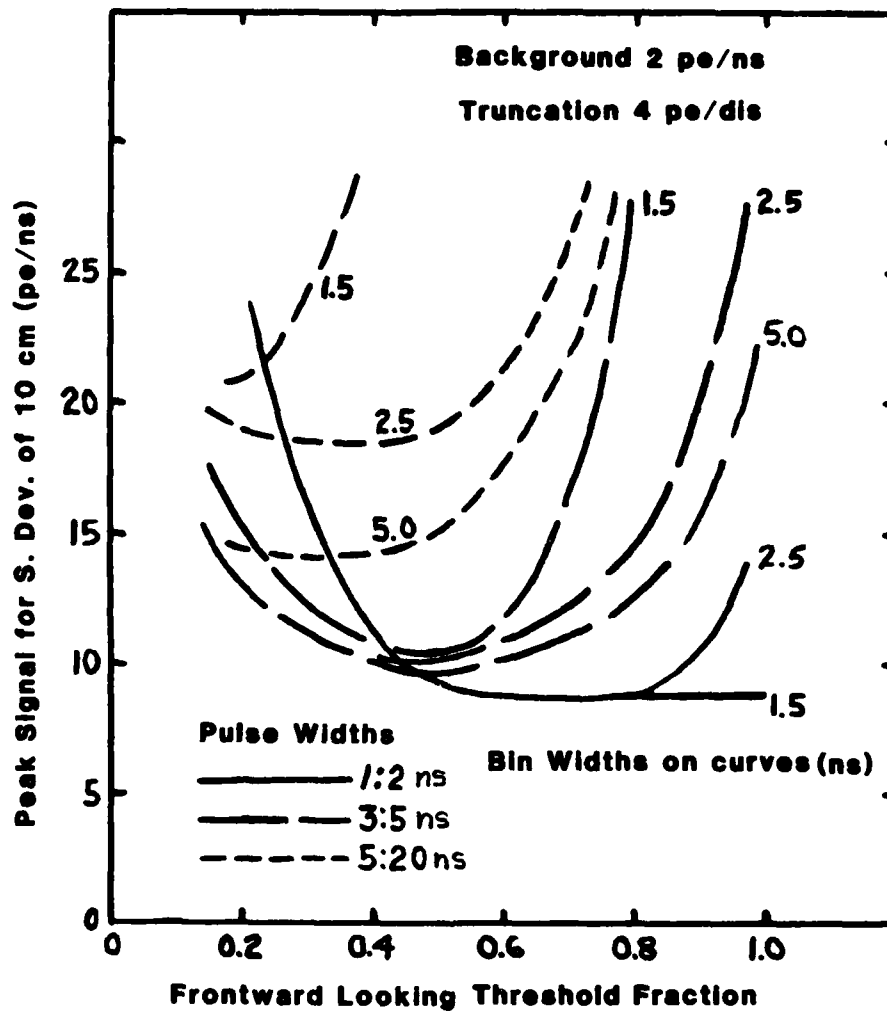
Figure 9. Effect of Threshold Fraction on Signal
Required for 10 cm Precision
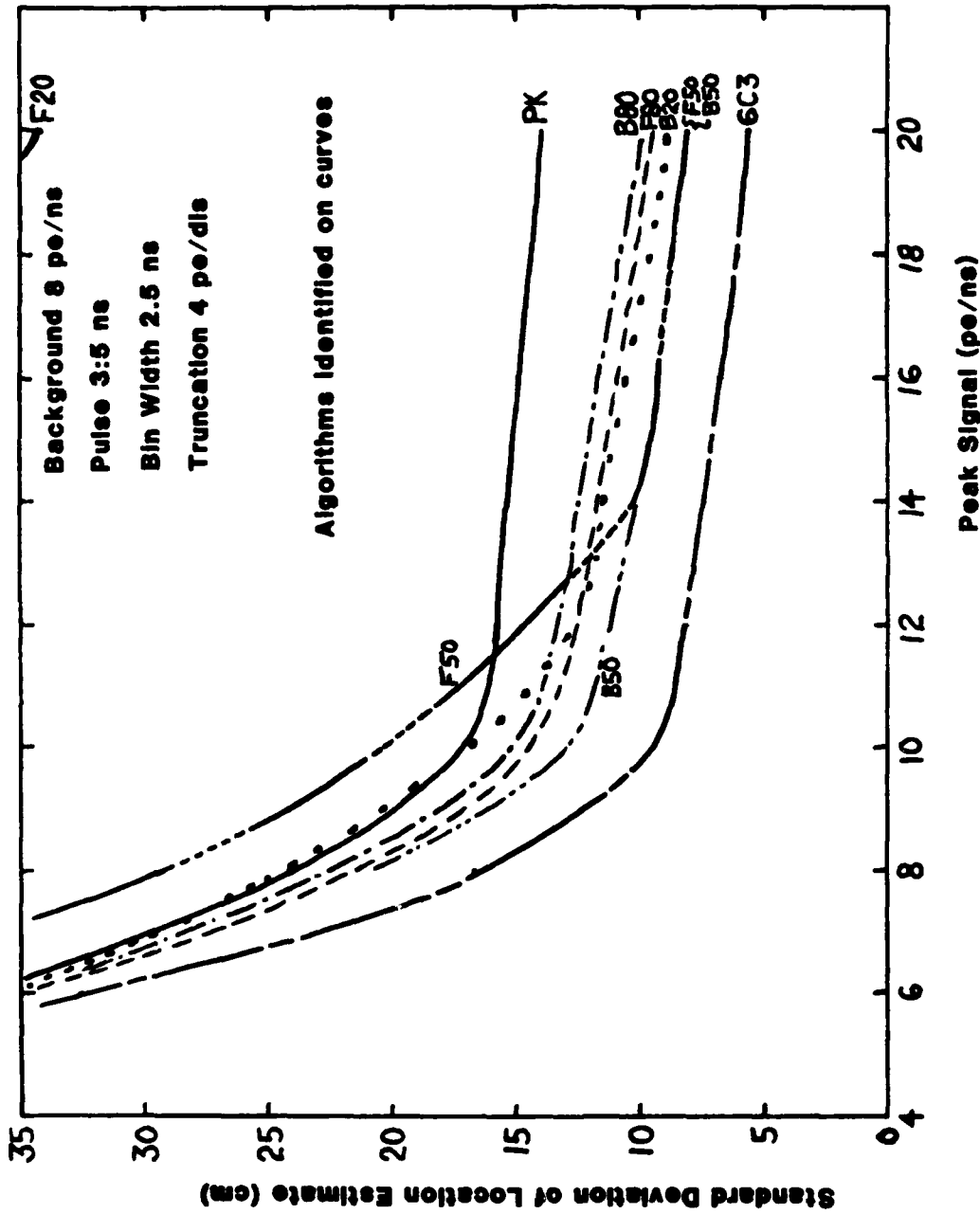
Figure 10. Precision for Nominal Pulse in Daylight
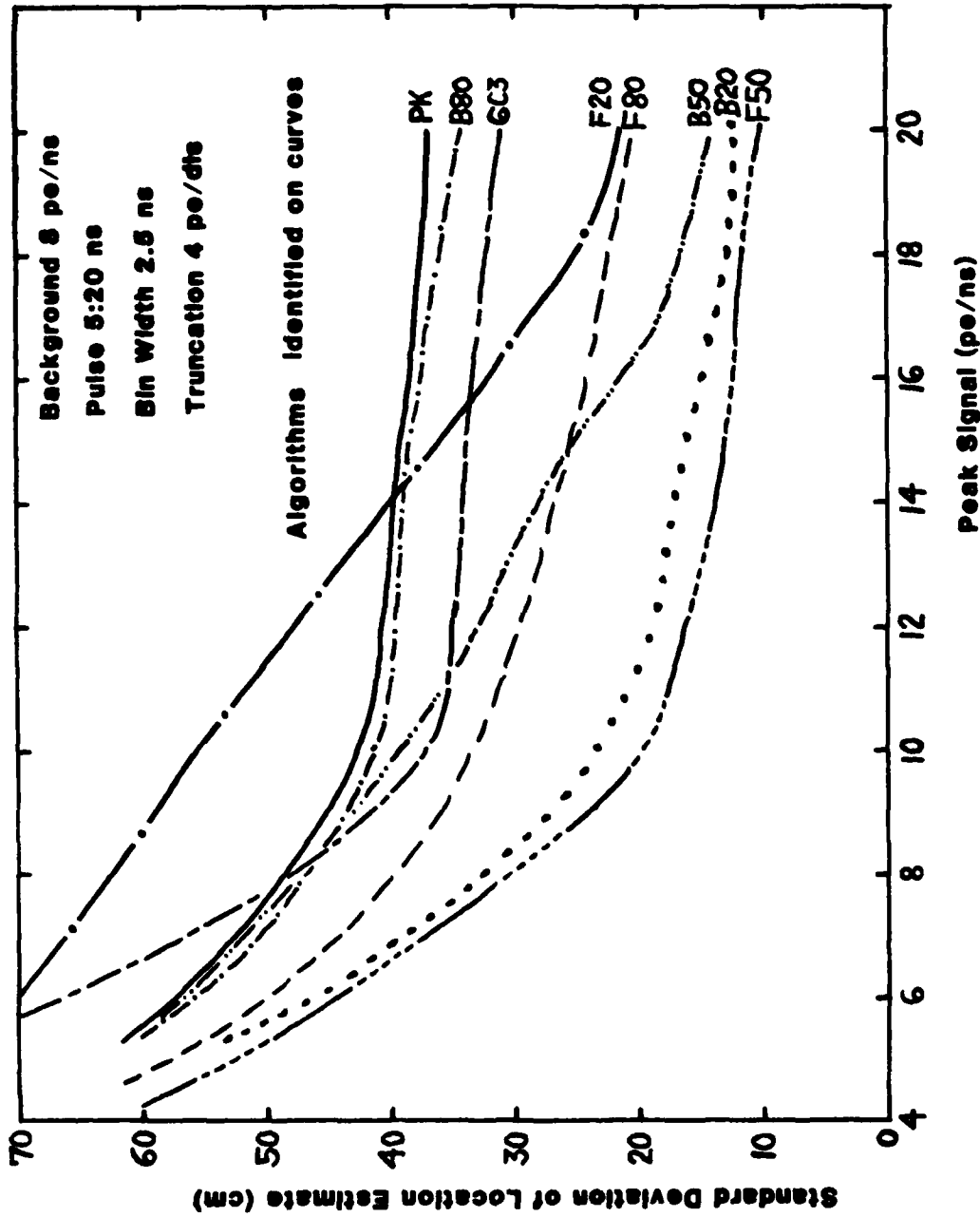
Figure 11. Precision for Stretched Pulse in Daylight
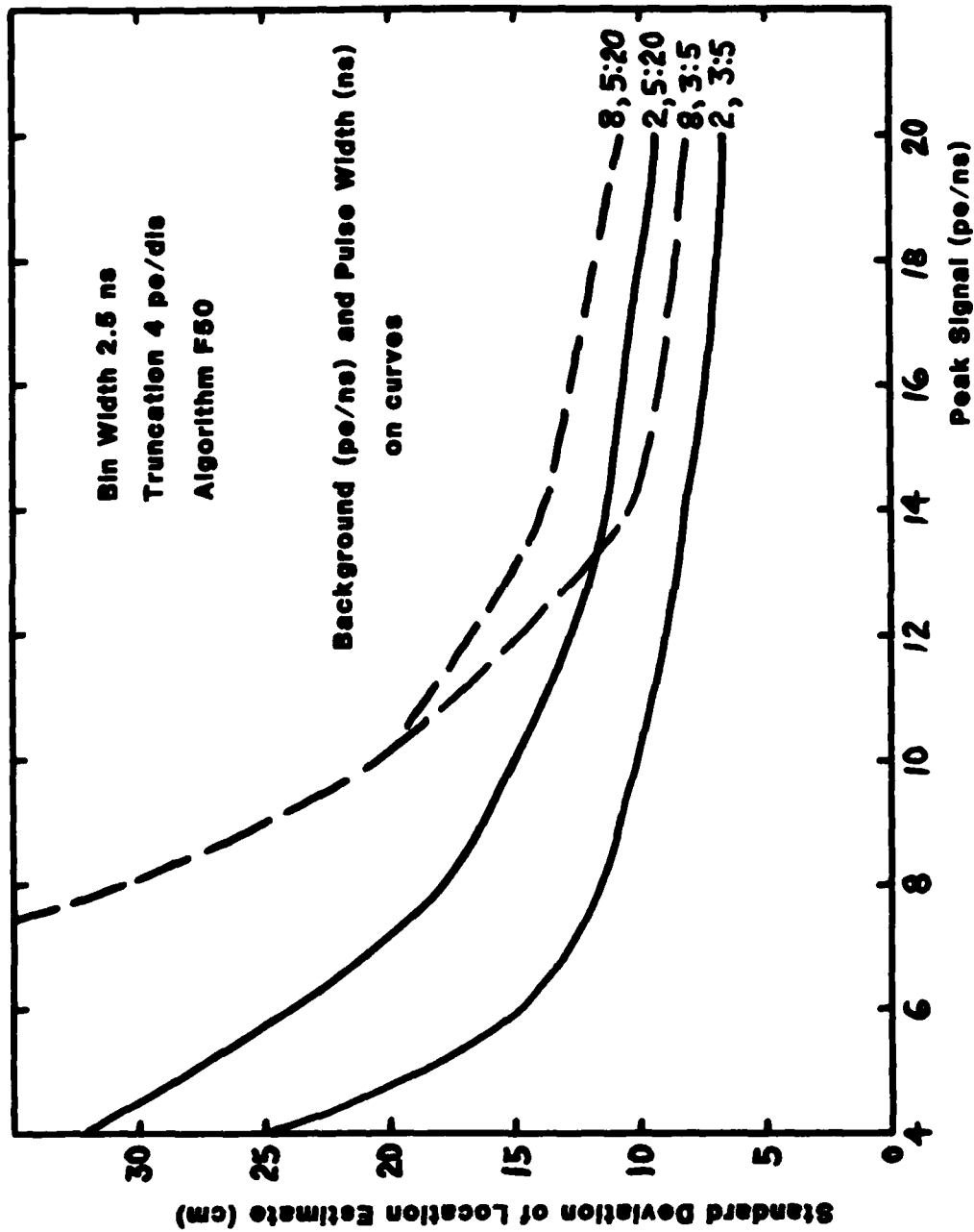
Figure 12. Day vs. Night Effect
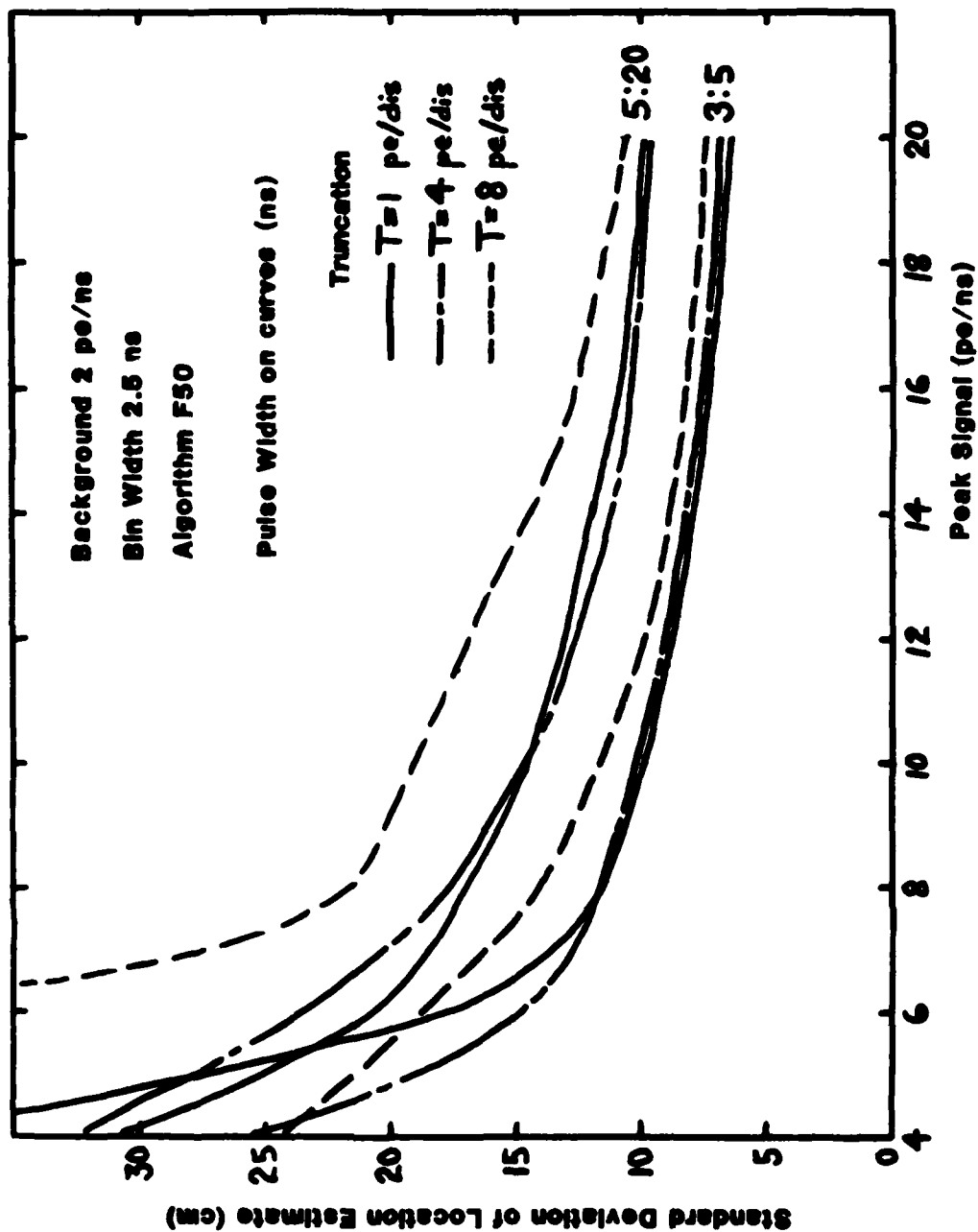
Figure 13. Truncation Effect
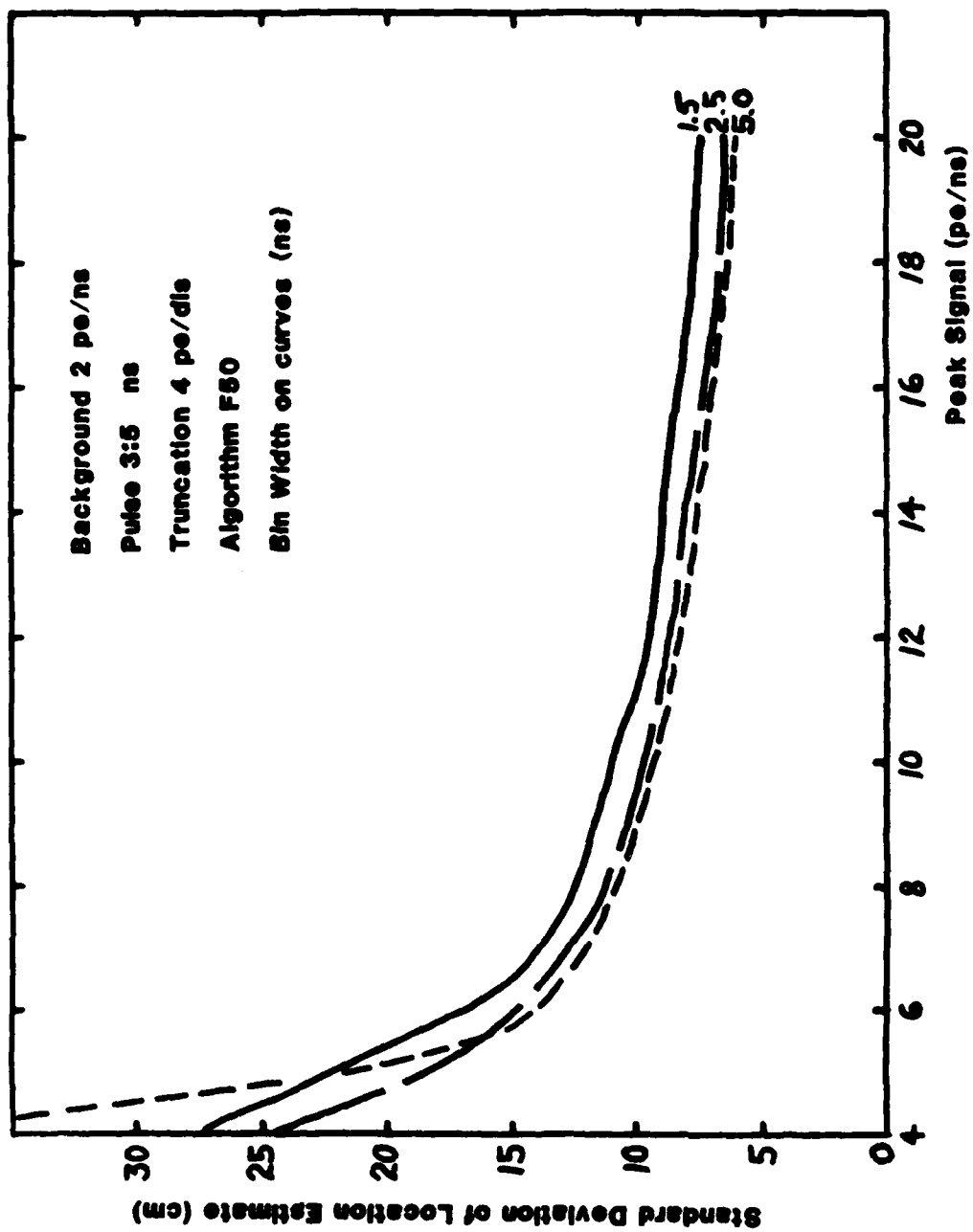
Figure 14. Bin Width Effect for Nominal Pulse
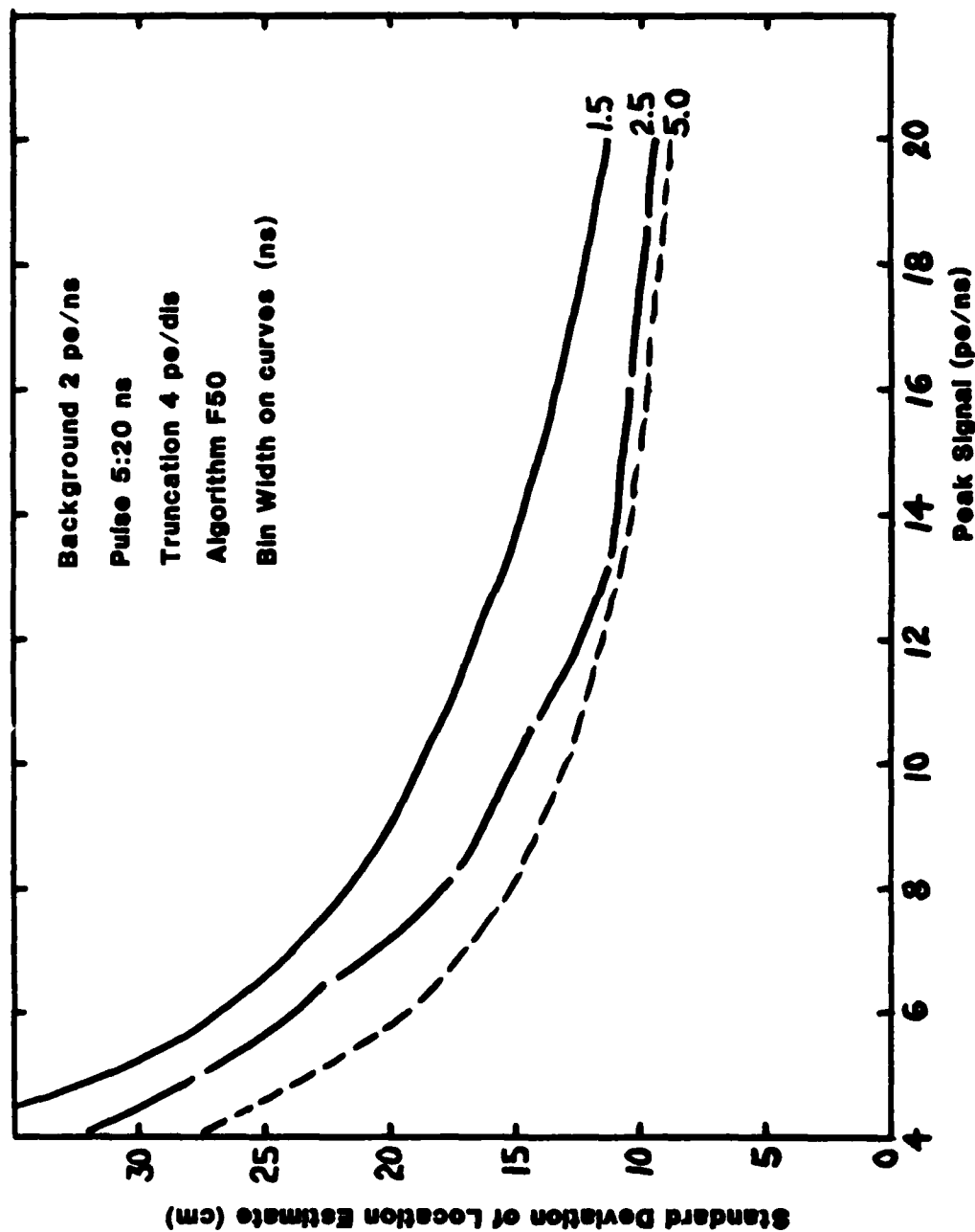
Figure 15. Bin Width Effect for Stretched Pulse
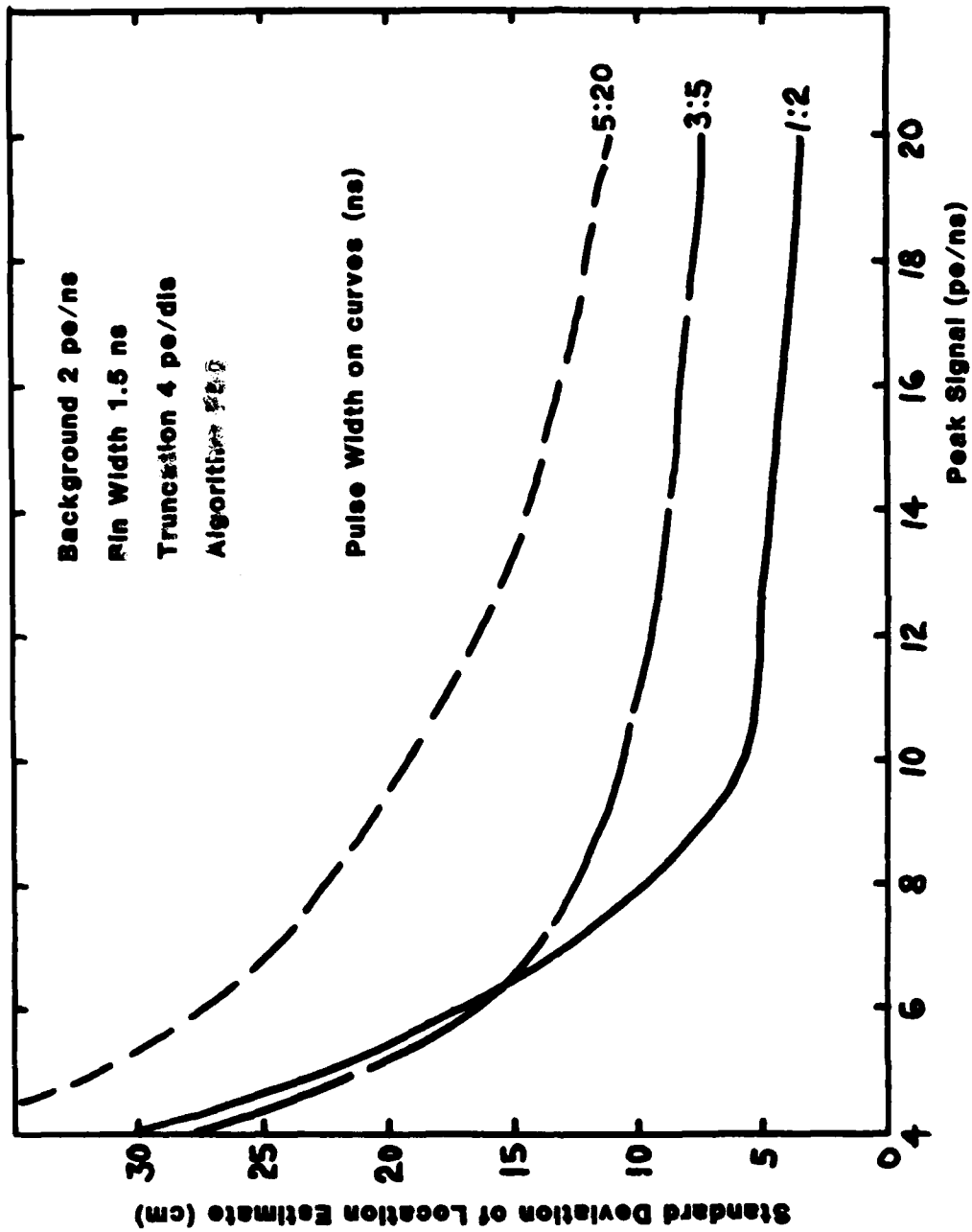
Figure 16. Pulse Width Effect for Small Bin
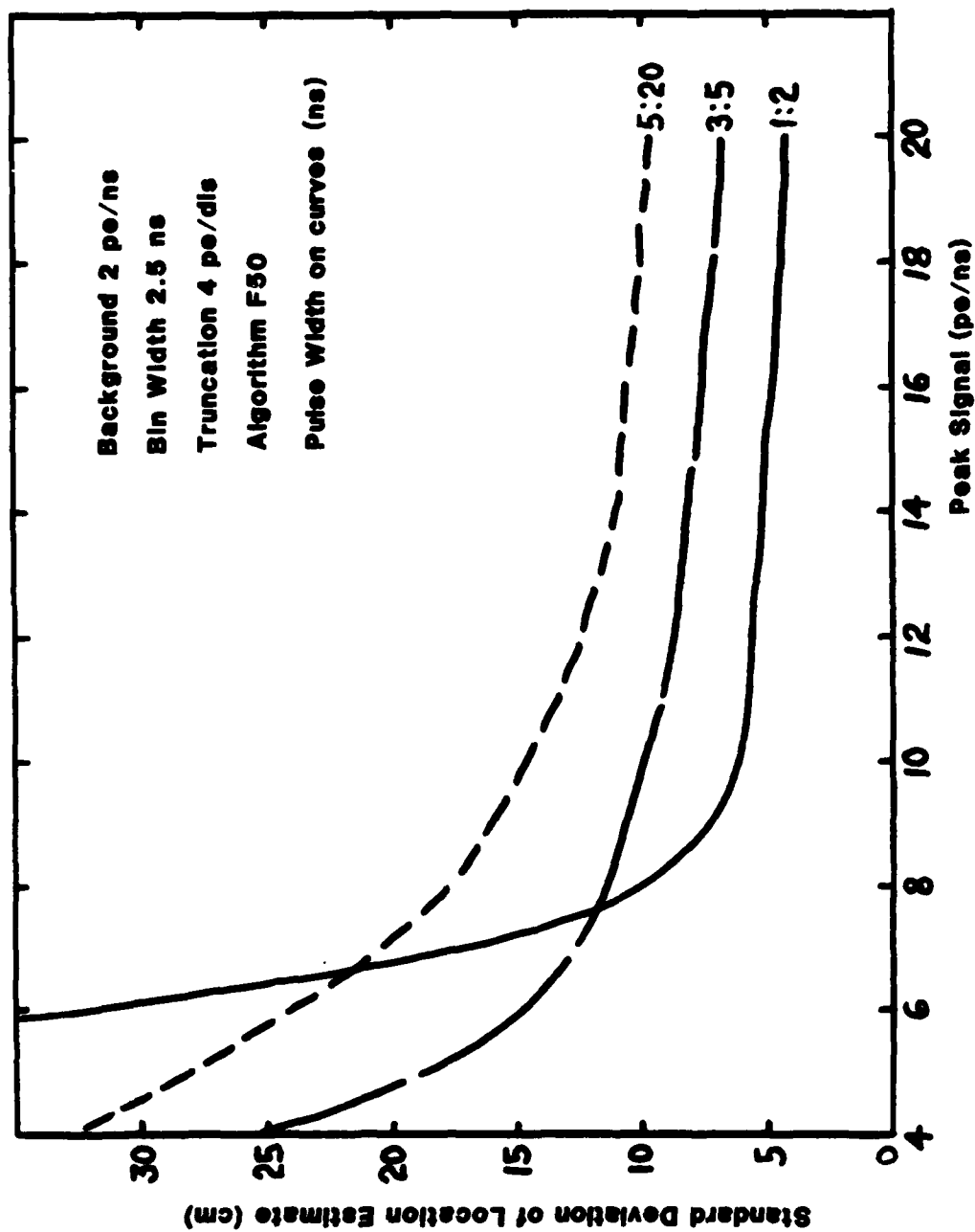
Figure 17. Pulse Width Effect for Nominal Bin
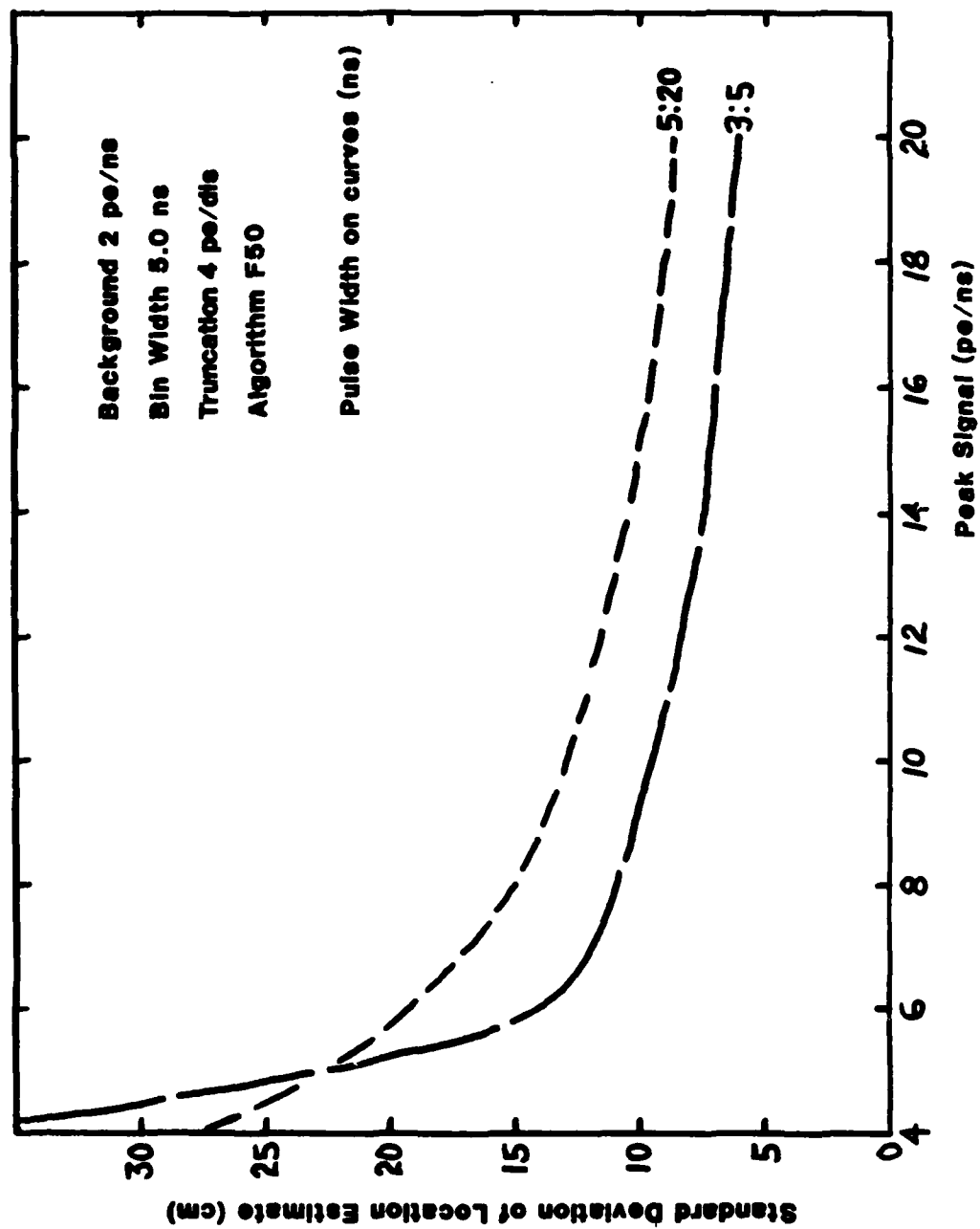
Figure 18. Pulse Width Effect for Wide Bin

Real Time Laser Hydrography Data Processing[*]

M.G. Miller and R.E. Lang

Avco Everett Research Laboratory, Inc.

2385 Revere Beach Parkway

Everett, Massachusetts, U.S.A.   02149

Abstract

The Hydrographic Airborne Laser Sounder (HALS) includes a real time analog data processor designed to provide estimates of slant altitude and depth on a pulse to pulse basis. Key elements in this processor include logarithmic data compression, signal differencing and constant fraction discrimination. The characteristics of this system, when combined with propagation phenomenon and noise statistics, establish system performance. Errors incurred include both random effects and biases which are expected to change slowly with time and operational conditions. A detailed analysis of error sources has been carried out in order to identify critical design parameters, anticipated system performance and off-line data processing requirements. A summary of this analysis, including numerical predictions, is given in this paper.

The Hydrographic Airborne Laser Sounder (HALS) has been designed to provide a routine operational capability for rapidly collecting substantial amounts of bathymetry data of utility for the generation of coastal hydrographic charts.[1] A requirement placed on the system is to provide a real time measurement, on a pulse by pulse basis, of slant altitude to the water surface and slant depth. The benefit of such a real time processor is that it avoids the necessity of recording, with high resolution, the entire return pulse. This results in a significant reduction in the amount of data that must be recorded yielding a major increase in the endurance of available flight qualified tape recorders.

Several environmental effects must be dealt with in the design of the real time processor.[2] These include daylight background, water backscatter and input aynamic range. The first of these causes the fundamental limiting noise which governs daytime operation. Because background can vary due to meteorological and operational conditions, the processor must be capable of responding to a high bandwidth signal (water and bottom return) riding on top of a nominal dc return (background) which can vary over several orders of magnitude. Water backscatter yields a generally exponentially decreasing signal which prohibits the use of simple thresholding. Because of the magnitude of typical surface returns and water attenuation, the processor must respond to signal levels which can differ by many orders of magnitude. These general characteristics of the observed signal are shown in Figure 1.

GENERAL CHARACTERISTICS OF RETURN SIGNAL
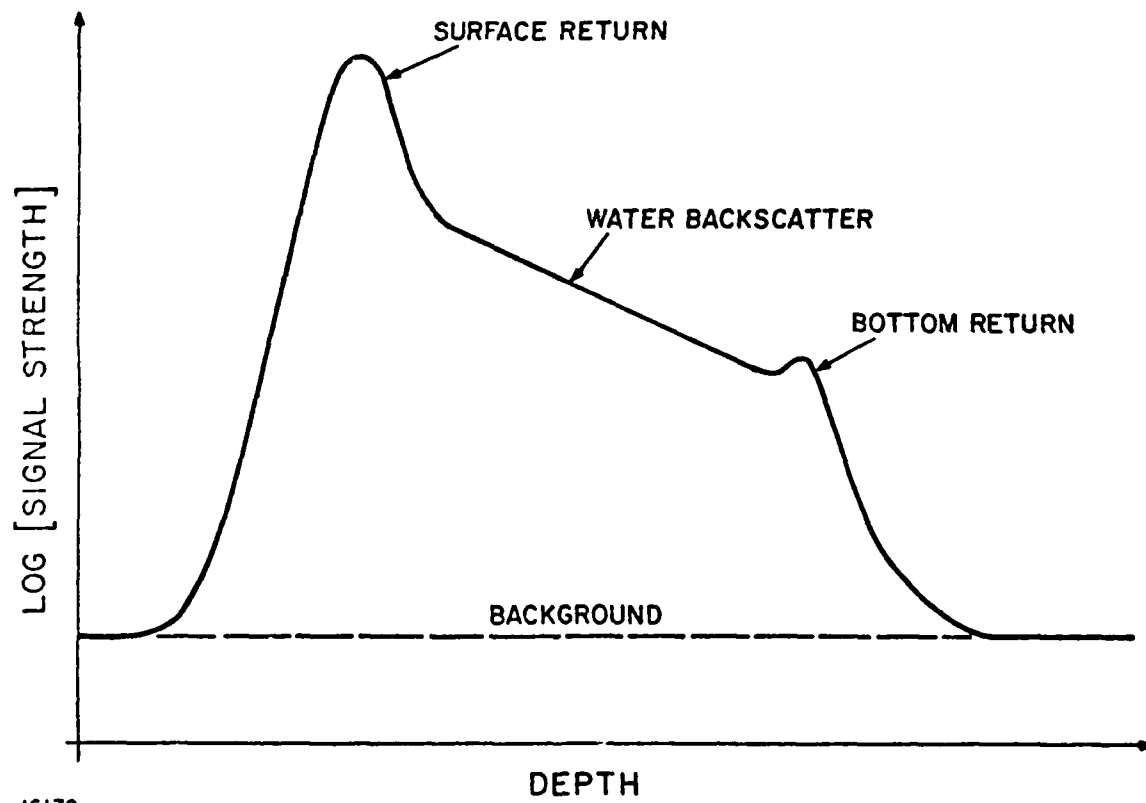
J6I72

Fig. 1

The basic philosophy of the real time processor developed
for HALS is to differentiate the return signal (Fig. 1) and
measure the time delay between the peaks corresponding to the
surface and bottom returns. (A similar procedure is used for
slant altitude.) This signal is shown in Figure 2.

As can be seen from this figure, differentiation deals
with the background and water backscatter characteristic in
such a manner that simple thresholding can be implemented.
However, the anticipated returns will not be as simple as
shown in Figure 2. In reality, it is possible that multiple
peaks will be seen in the signal differential due to variations
in water backscatter and background noise. Consequently, the
processor must determine which peak corresponds to the surface
and bottom, respectively. This is done by using first pulse
and last pulse discrimination logic. The system is initialized
by observing the output laser pulse with the system detector. The
next return above some reference level is assumed to be the
surface return. This, in turn, triggers a depth measurement
system which counts down to the next signal peak. If multiple
peaks are observed, the counters are automatically reset until
the last pulse within a defined time window is observed. The
allowed time window is determined by prior bottom detections.

While differentiation deals with the problem of water
backscatter, it does not substantially decrease the dynamic
range requirement. This is done by a combination   PMT (de-
tector) gating and signal compression via a high bandwidth
logarithmic amplifier. The former provides several orders of
magnitude of compression by control of the grid bias, whereas

DERIVATIVE DETECTION
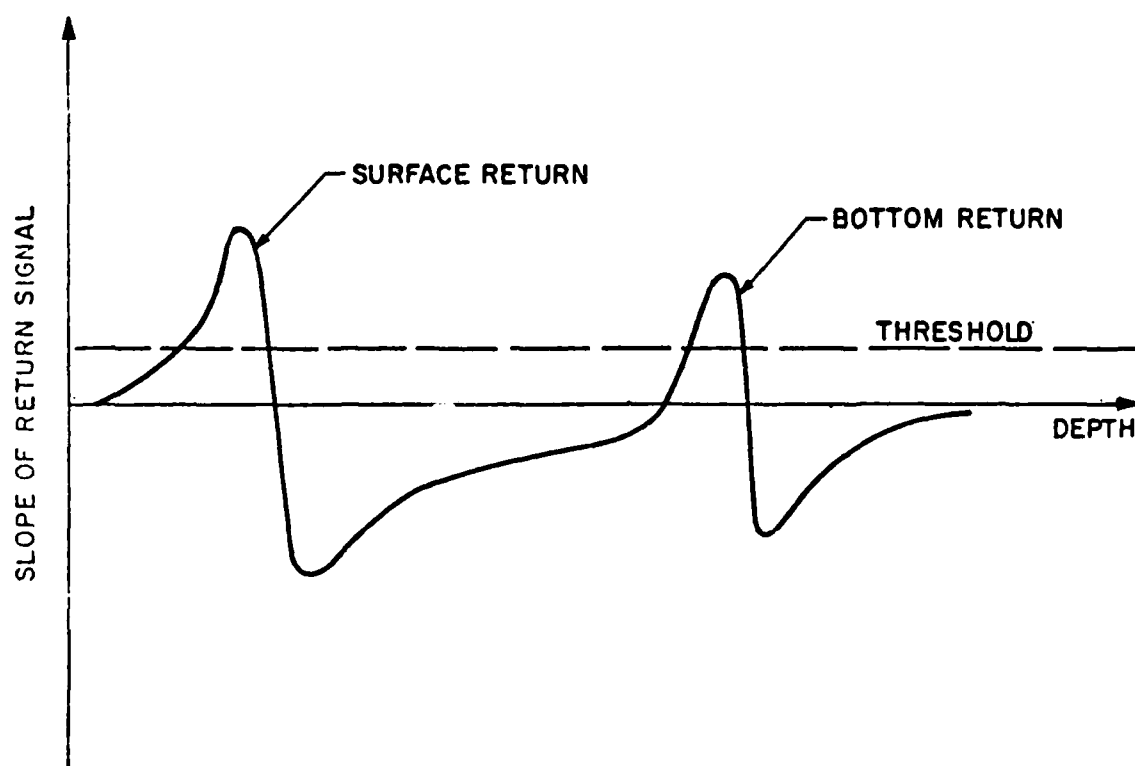
J6169

Fig. 2

the latter compresses four orders of magnitude of signal down
to a dynamic range of 300. The resulting signal can then be
adequately processed by a variety of existing, high speed
electronics and detectors.

A block diagram of the detection electronics is shown
in Figure 3. The output of the PMT is first compressed by
the log amplifier to provide the required decrease in dynamic
range. Approximate differentiation is implemented by sub-
tracting a delayed version of the log amplifier output from
the primary signal. The time delay, τ, is chosen to be longer
than the anticipated pulse rise time in order to avoid compro-
mising signal to noise (above the obvious doubling of background
noise) and shifts in peak location associated with a true
derivative. Detection is accomplished by use of a commercially
available Constant Fraction Discriminator (CFD). The Time
Interval Meter (TIM) contains the first/last pulse logic and
interpulse timing.

The operation of the CFD, EG&G Ortec Model 934, is shown
in Figure 4. This device combines the detection function with
threshold arming which establishes the desired false alarm
rate. Detection is accomplished by observing the difference,
$X(t)$, between a delayed (Δ) and attenuated (α) version of the
input signal, $S(t)$. In response to a peak in the input signal
(Fig. 2), $X(t)$ is initially negative. As $S(t)$ increases, $X(t)$
crosses zero with a positive slope. This crossing is detected
by the zero crossing detector which generates a timing pulse
which activates the time interval meter. However, for this to
occur, the zero crossing detector must be armed via a signal

DETECTION ELECTRONICS

$$V_{OUT} = V_S \log [V_{IN} / V_o]$$

$$S(t) = V_{OUT}(t) - V_{OUT}(t - \tau)$$

J6171
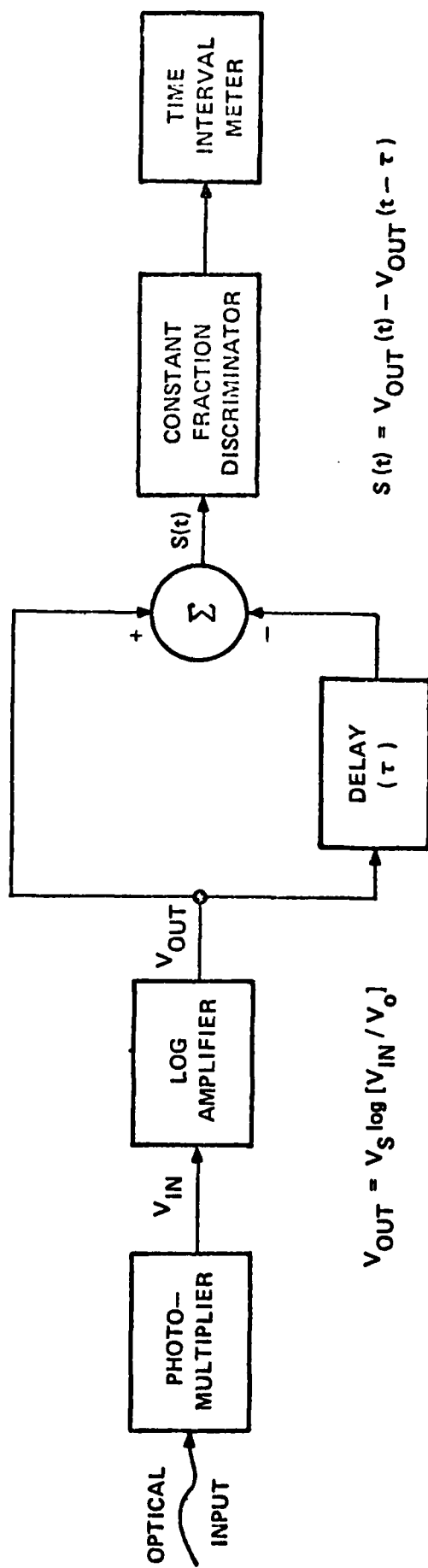
CONSTANT FRACTION DISCRIMINATOR
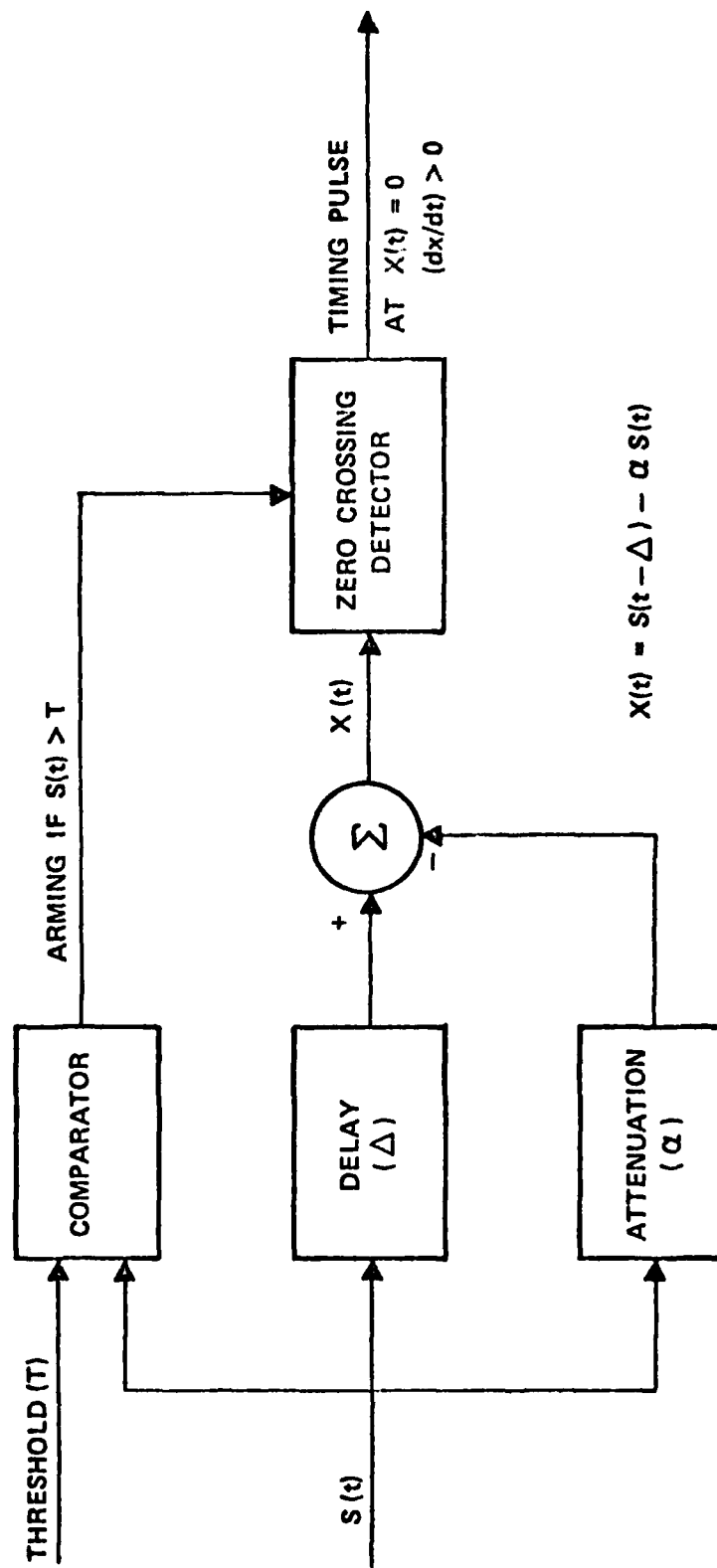
Fig. 4

J6170

from the comparator (C) which is generated only if the input (S)
is greater than the selectable constant value, T. Proper sel-
ection of this value controls the probability of false alarm
which can occur in the absence of a true bottom return.

The detection system described above is of utility for
measurements of water depths in excess of several meters.
Shallow water will not yield positive responses because of
the finite width of the laser pulse. Due to pulse overlap,
shallow water returns will exhibit broadening rather than
distinct peaks. For this reason separate shallow water pro-
cessing electronics, based on pulse width measurements, are
included in the processor.

The prior discussion briefly summarizes the HALS real
time detection electronics. As a result of the hardware imple-
mentation as well as several phenomenological effects, various
types of errors are inherent in its operation. Two basic types
are of concern: biases and random. Bias errors are defined as
those expected to vary slowly in time and, hence, be correlated
from pulse to pulse. Random errors are primarily statistically
independent from pulse to pulse and have zero mean when averaged
over many pulses. By virtue of this classification, the non-
zero mean value of any truly statistical error is considered
to be a bias. The identified and analyzed errors for each type
of measurement is given in Table I. The letters in parenthesis,
B or R, indicated type, i.e., bias or random.

Processor bias arises from the combination of log com-
pressing, constant fraction discrimination and variations in
the amplitude of the background, water backscatter and bottom/

TABLE I - SYSTEM ERRORS

- SURFACE RETURN

  - PROCESSOR (B)
  - SURFACE/BACKSCATTER (B)
  - RANDOM NOISE (R)
  - CFD TIMING (R)
  - TIM TIMING (R)
  - TEMPERATURE (B)
  - PULSE STRETCHING (B)

- BOTTOM RETURN

  - PROCESSOR (B)
  - RANDOM NOISE (R)
  - CFD TIMING (R)
  - TIM TIMING (R)
  - TEMPERATURE (B)
  - PULSE STRETCHING (B)
  - BEAM STEERING (R)

- SHALLOW WATER

  - PULSE WIDTH (R)
  - TIMING (R)

surface returns. It results from the fact that the input to the
CFD is the log of the linear return and, hence, has a shape
which depends on relative signal strength. Furthermore, the
input to the CFD in the absence of bottom return will not be
identically zero due to the water backscatter. This bias simply
reflects the fact that any constant fraction discriminator will
change its detection point in response to variations in pulse
shape or non-zero input level.

Random noise errors are the result of noise-inspired early
(or late) detection in the CFD zero crossing detector. This is
the conventional error referred to as range accuracy in radar
system.[3]

CFD and TIM timing errors reflect the timing jitter in-
herent in these two devices. The operating temperature range
of the system causes drifts in the electronics and CFD set
points. While the majority of these effects cancel out because
the same electronics are used to time both pulses in each dif-
ferential measurement, small residuals remain due to the differ-
ent amplitudes of the two pulses.

The surface/backscatter error refers to the fact that for
the system scan angles of interest, the "surface return" may,
in fact, be due to volume backscatter rather than a hard reflec-
tion.[4] These two types of returns will yield different pulse
shapes and hence, different CFD timing outputs. If the type of
return is unknown, an error results.

Pulse width measurement errors occur in the shallow water
detection electronics due to the relative amplitudes of the sur-
face and bottom contributions to the total pulse. Timing jitter
also occurs in these electronics.

Pulse stretching refers to the effect of off-nadir inci-
dence of the laser beam on the water surface or bottom and
multiscatter in the water. Beam steering refers to the random
refraction at the ocean surface due to wave slope. These
propagation errors are discussed elsewhere[5]

Each of the system errors included in Table I have been
subjected to extensive analysis. The numerical results are
given in Table II. In the case of several of the biases,
two values are given. The first in the total bias associated
with the full range of parametric variation over the anticipated
system operational range. The second (and smaller) values
reflect the amount these errors can be reduced by post-process-
ing using system derived information. The anticipated source
of this information is first a measure of signal amplitude at
point of detection on a pulse by pulse basis and secondly, a
high bandwidth recording of the complete return pulse using a
waveform analyzer operating at low repetition rate (≤ 10 Hz).
Together they provide the data necessary for dividing the full
range of bias into several subintervals. The last entry in
Table II is the root-sum-square of all the individual error
sources. As such it represents the anticipated performance
of the system before propagation errors are added. When the
latter[5] are added, the resulting maximum values
are a bias of 10 cm and a random error (one sigma) of 29 cm
for a single pulse measurement. Multipulse processing can
reduce the random error, but not the bias because it is ex-
pected to be approximately the same for all pulses within a
data set of any reasonable size.

TABLE II - DEPTH ACCURACY

EFFECT	BIAS	RANDOM
PROCESSOR		
Surface	$\pm$ 8CM; $\pm$ 4CM	--
Bottom	$\pm$ 16CM; $\pm$ 4CM	--
RANDOM NOISE		
Surface	--	2CM
Bottom	--	14CM
PULSE STRETCHING - SURFACE	--	3CM
TIMING		
CFD	--	1CM
TIM	--	1CM
TEMPERATURE	3CM	--
TOTAL (RSS)	6CM	18CM
SHALLOW WATER	--	9CM

References

1. A complete description of the Hydrographic Airborne Laser
    Sounder is given by M. Houck, Laser Hydrography Symposium,
    Adelaide, Australia, 1980.

2. The operation of Laser Hydrographic Systems has been dis-
    cussed in several previous papers. See, for example,
    G.C. Guenther and L.R. Goodman, Laser Applications for
    Near-Shore Nautical Charting, Proc. SPIE 160, 174 (1978);
    F.E. Hoge, R.N. Swift and E.B. Frederick, Water Depth
    Measurement Using an Airborne Pulsed Neon Laser System,
    App. Optics 19, 871 (1980).

3. M.I, Skolnik, Introduction to Radar Systems (McGraw-Hill,
    New York, 1962), 462.

4. Data obtained by the Naval Air Development Center indicates
    that the true surface return may become very small for scan
    angles in excess of 15°. K.J. Petri and R.F. Starry,
     Experimental Results of a Continuous Wave Laser Radar
    System, Symposium on the Use of Lasers for Hydrographic
    Studies, NASA, Wallops Island Virginia, September 1973.

5. G.C. Guenther, Laser Hydrography Symposium, Adelaide,
    Australia, 1980.

REAL TIME LASER HYDROGRAPHY DATA PROCESSING

M. G. MILLER AND R. E. LANG

- REQUIREMENTS

- TECHNIQUE

- ELECTRONICS

- ERRORS

- ACCURACY

J6433

REQUIREMENTS & TECHNIQUE

GENERAL CHARACTERISTICS OF RETURN SIGNAL

SURFACE RETURN

WATER BACKSCATTER

BOTTOM RETURN

BACKGROUND

LOG [SIGNAL STRENGTH]

DEPTH

DERIVATIVE DETECTION

SURFACE RETURN

BOTTOM RETURN

THRESHOLD

SLOPE OF RETURN SIGNAL
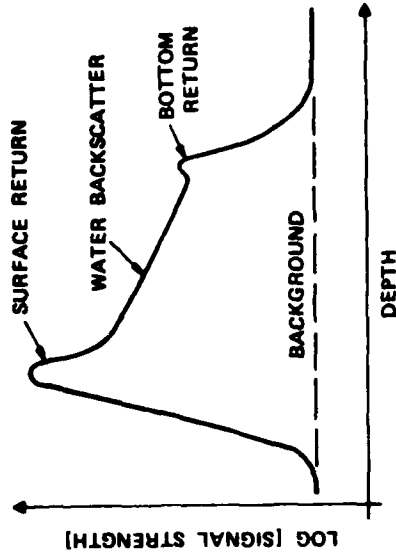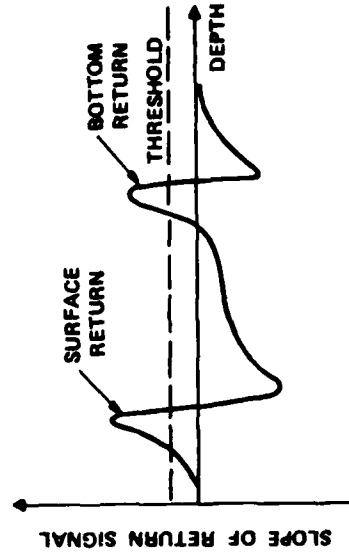
DEPTH

- ● PULSE BY PULSE MEASUREMENT
  - – SLANT ALTITUDE
  - – SLANT DEPTH

- ● ACCURACY
  - – ALTITUDE: $\pm$ 10 cm
    - $\pm$ 0.05%
  - – DEPTH: $\pm$ 28 cm ; D $\leq$ 20 m
    - $\pm$ 1 m ; D > 20 m

- ● HARDWARE
  - – DERIVATIVE DETECTION
  - – PULSEWIDTH MEASUREMENT
  - – WAVEFORM RECORDER

J6436

DETECTION ELECTRONICS
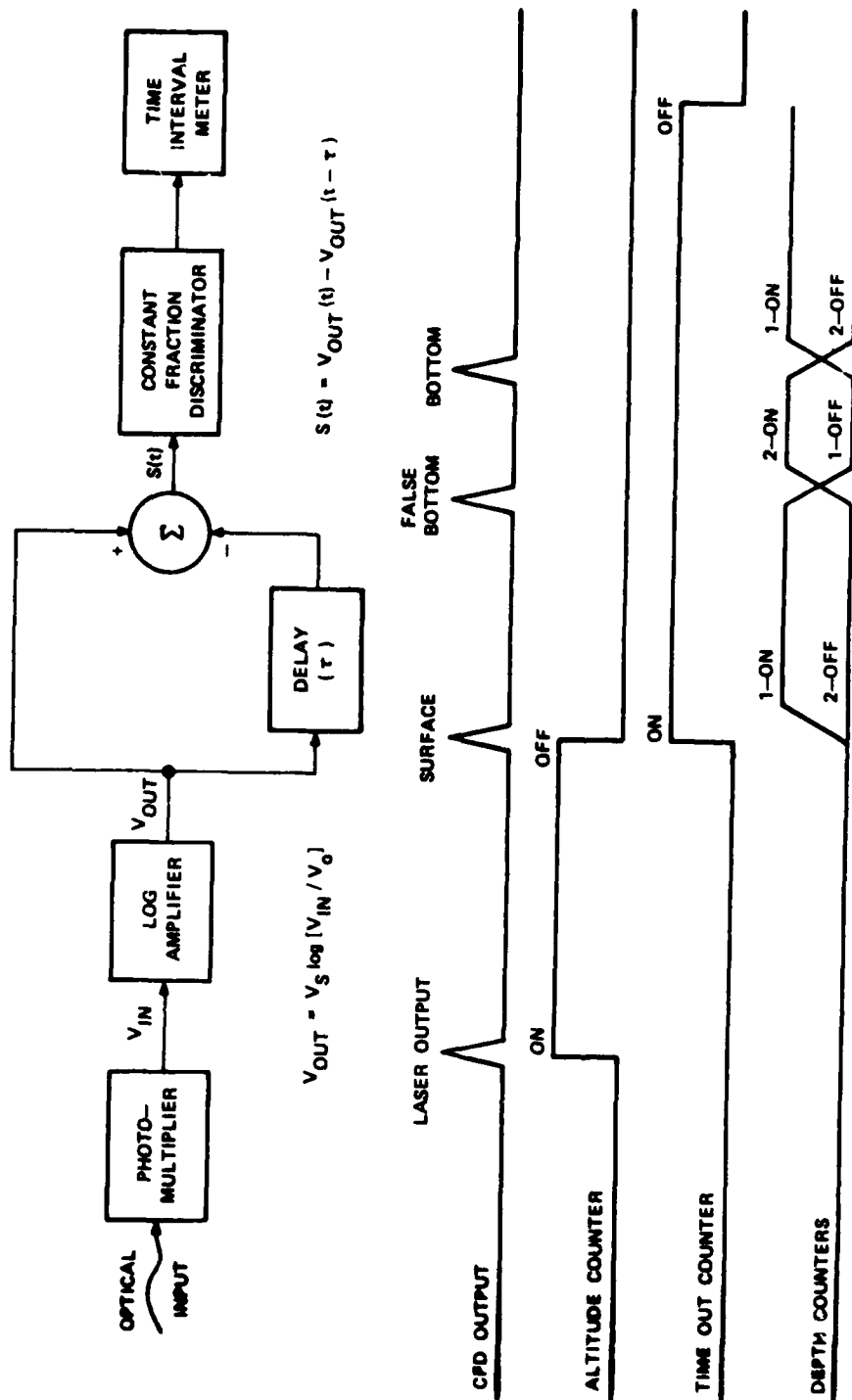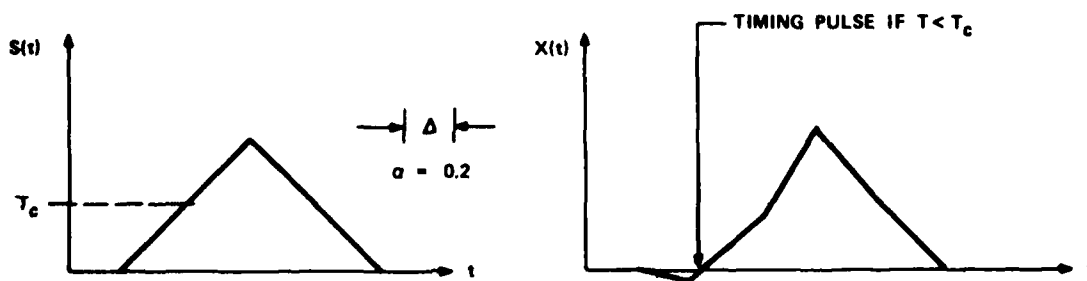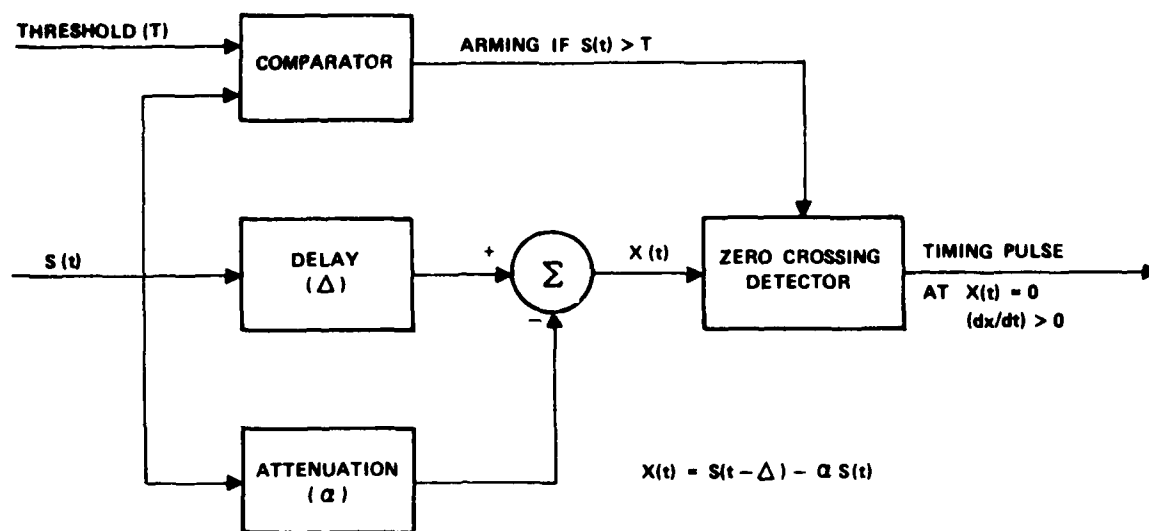
$V_{OUT} = V_S \log [V_{IN}/V_o]$

$S(t) = V_{OUT}(t) - V_{OUT}(t - \tau)$

J0171-1

CONSTANT FRACTION DISCRIMINATOR

THRESHOLD (T) ──────────▶ | COMPARATOR | ── ARMING IF S(t) > T ──────┐

S(t) ──────────▶ | DELAY (Δ) | ──── + ───▶ (Σ) ──── X(t) ──▶ | ZERO CROSSING DETECTOR | ── TIMING PULSE
                                                                              AT X(t) = 0
                                                                              (dx/dt) > 0
                                           | ATTENUATION (α) | ──── −

$$X(t) = S(t - \Delta) - \alpha\,S(t)$$

S(t)   ├─ Δ ─┤
                                       $\alpha = 0.2$

T_c

TIMING PULSE IF $T < T_c$

X(t)

J6170-1

SYSTEM ERRORS

- SURFACE RETURN
  - PROCESSOR (B)
  - SURFACE/BACKSCATTER (B)
  - RANDOM NOISE (R)
  - CFD TIMING (R)
  - TIM TIMING (R)
  - TEMPERATURE (B)
  - PULSE STRETCHING (B)

- BOTTOM RETURN
  - PROCESSOR (B)
  - RANDOM NOISE (R)
  - CFD TIMING (R)
  - TIM TIMING (R)
  - TEMPERATURE (B)
  - PULSE STRETCHING (B)
  - BEAM STEERING (R)

- SHALLOW WATER
  - PULSE WIDTH (R)
  - TIMING (R)

B = BIAS ERROR
R = RANDOM ERROR

J6435

PROCESSOR BIAS

BACKGROUND LIMITED OPERATION
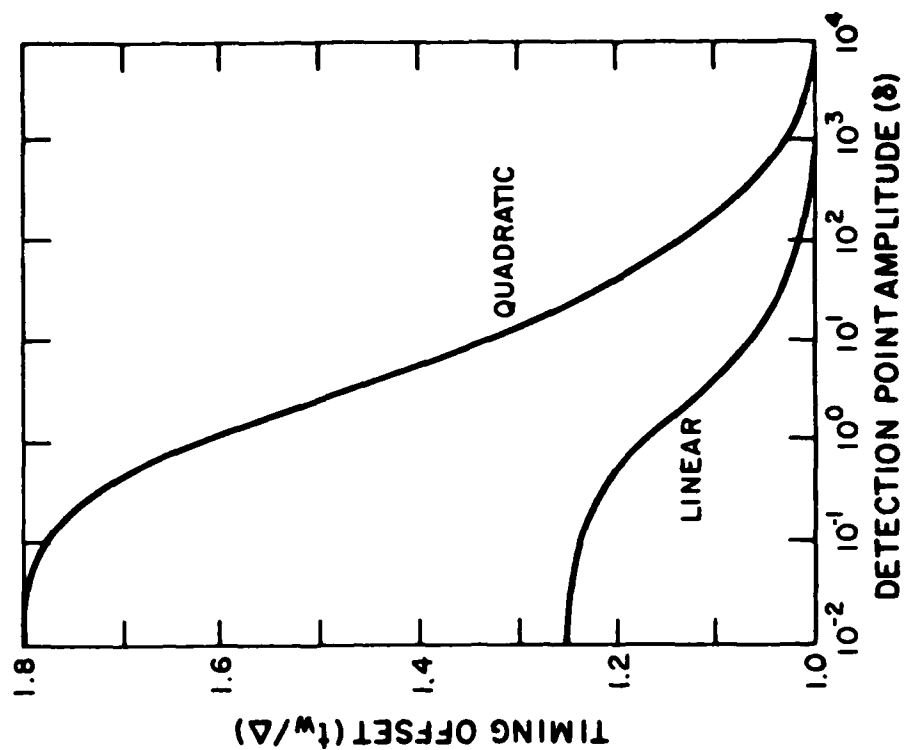
- $S(t) = LN[(P_M/B) P_N(t) + 1]$

- $P_N(t-B) = \dfrac{[(P_M/B) P_N(t) + 1]^\alpha - 1}{(P_M/B)}$

- A VARIABLE TIMING BIAS OCCURS WHICH IS A FUNCTION OF

  - PROCESSOR DELAY
  - PULSE SHAPE
  - DETECTION POINT AMPLITUDE

  $\gamma = (P_M/B) P_N(t_D)$

J6556

SURFACE / BACKSCATTER BIAS

- **SURFACE RETURN DOMINATES AT SMALL SCAN ANGLES**

- **VOLUME BACKSCATTER IS FUNCTIONS OF ATTENUATION COEFFICIENT**
  - PEAK DELAY
  - RISE TIME
  - REFLECTIVITY

- **PROCESSOR BIAS LARGER FOR VOLUME BACKSCATTER**

- **IF NATURE OF RETURN IS UNKNOWN, MINIMUM CFD DELAY MUST BE USED**

J6957
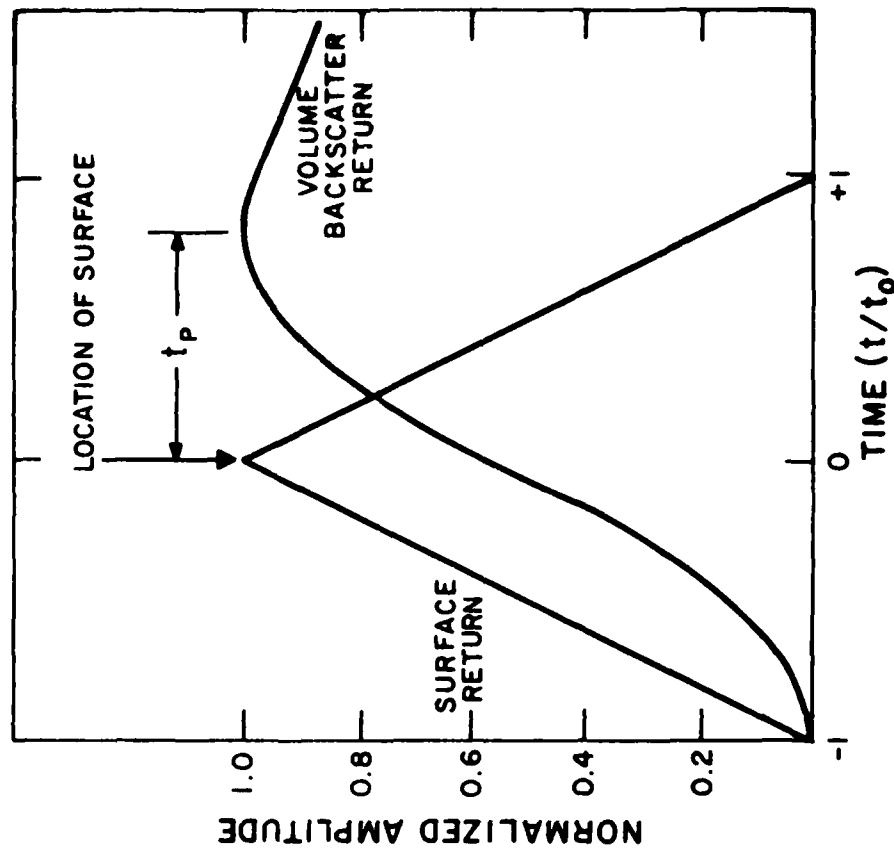
SYSTEM ACCURACY

EFFECT	ALTITUDE	DEPTH	SHALLOW WATER
PULSE SHAPE	$\pm$ 2 cm	$\pm$ 6 cm	7 cm
RANDOM NOISE	2 cm	14 cm	6 cm
CFD TIMING	2 cm	2 cm	–
TIM TIMING	1 cm	10 cm	–
TEMPERATURE	$\pm$ 2 cm	$\pm$ 3 cm	–
SURFACE PULSE STRETCHING	3 cm	3 cm	3 cm
TOTAL			
BIAS	$\pm$ 3 cm	$\pm$ 6 cm	–
RANDOM	4 cm	18 cm	10 cm

J6434

THIS IS A BLANK PAGE

PAPER 21

LASER BEAM REFLECTION FROM THE SEA

D.M. Phillips

Defence Science and Technology Organisation
Electronics Research Laboratory
Salisbury South Australia

The reflection of a short laser pulse from a sea surface depends on the wavenumber spectrum of that surface and on the diameter of the spot illuminated by the laser.

The mean water level within the illuminated area determines the delay between the time of transmission of the laser pulse the time of detection of the peak of the reflected pulse. The variation of water level within this area determines the temporal spread of the reflected pulse.

Similarly, the mean water slope within the illuminated area determines the direction of the strongest reflection. The slope variation within this area governs the angular spread of the reflection.

The theoretical treatment of laser beam reflection from an ocean surface by Swennen (Ref. 1) takes no account of the wavenumber spectrum of the sea surface. That is equivalent to assuming the beam has infinite diameter.

The theoretical model outlined below assumes a finite diameter for the laser spot on the sea surface.

The Significance of Beam Diameter

The diameter of a laser beam has a significant influence on its reflection from a transmission through a sea surface.

Figure 1 illustrates the influence of sea-state, swell and aircraft roll on the reflection of a laser beam from the sea surface. The three diagrams on the left show how the highly directional reflecting from a calm sea can cause problems. While the laser beam is vertical and the water is horizontal the strong reflection will return to the aircraft. However, when a slow swell produces a slope on the water surface or when the aircraft rolls, the reflection misses the aircraft and is not detected.

When wind ruffles the surface, as illustrated on the right side of Figure 1, the reflection is more diffuse and is not affected greatly by swell and aircraft roll.

In calm conditions the reliability of detecting the surface can be improved by increasing the diameter of the laser spot. A larger spot provides a greater probability of including water facets of the correct orientation to reflect some light back to the aircraft.

A large spot, however, introduces wave height and slant height errors - as illustrated in Figure 2. Consequently, it should be possible to define an optimum diameter for sea surface detection with an airborne laser.

The laser spot diameter is a parameter that can significantly affect the detection of the water bottom in a laser depth sounding system. This is illustrated in Figure 3. The upper diagrams show a coral head rising from the bottom. Mariners want the minimum water depth for safe passage of their boats. A small spot combined with calm seas could produce a low fractional coverage of the bottom that could leave some coral heads undetected. A wind-ruffled surface or a larger beam diameter would not present this problem.

The optimum field of view of the receiving telescope is expected to be a function of sea-state. The lower diagrams in Figure 3 show how the reflected signal will be concentrated in a small area in calm seas but will extend over a wider region in wind-ruffled seas.

The diameters of the areas of the sea surface illuminated by the laser beam and observed with the receiving telescope are significant variables in the design of an airborne depth sounding system. In order to include diameter in a theoretical model of reflection or refraction of a laser beam at a water surface it is necessary to consider the length of the waves that produce a given rms slope.

The Theoretical Model

As the theoretical model is described more fully in Reference 2, only a brief outline will be given here.

There is a reasonable amount of published data suggesting that the wave-number spectrum of water slope, $S(k)$, is inversely proportional to the wave-number k, when the waves are in equilibrium with the wind. It follows that $kS(k)$ is a constant between two cutoff wavenumbers: k_0 and k_1 as shown in

Figure 4. The lower cutoff wavenumber, k_0, which corresponds to the longest waves present, is governed by the swell. As the swell becomes larger, k_0 becomes smaller. The upper cutoff wavenumber, k_1, describes the smallest

ripples present. The stronger the wind blows, the more ripples it generates and the higher k_1 becomes.

The whole of the present theory depends on the two parameters k_0 and k_1

between which the wavenumber spectrum of water slope is assumed to be constant. How accurate a description of the sea surface this provides is not known at present. Nevertheless, it represents an advance on previous models which ignore wavenumber altogether.

A two-dimensional spatial autocorrelation function is used to describe the sea surface. Using two-dimensional Fourier transform techniques it is possible to calculate the roughness of the water surface within a circle of radius R. If the total variance of the sea-slope is designated $S(0)$ and the variance of the mean slope within a circle of radius R is called $S_R(0)$,

then the relative variance of the mean slope is given by the ratio $S_R(0)/S(0)$.

This is shown in Figure 5 as a function of the dimensionless radius of the illuminated spot: k_0R.

It can be seen that, as the spot shrinks to a point $(k_oR \rightarrow 0)$, the variance of the mean slope of the area approaches the total variance of the water surface slope $(S_R(0) \rightarrow S(0))$. This is necessary, because no averaging can be achieved with a vanishing by small spot.

The parameter k_1/k_o defines the spectral range of slopes present. When $k_1/k_o = 1$, only one wavelength is present, for example if the sea surface were a function. Under these conditions the variance of the mean slope falls rapidly when $k_oR \rightarrow \pi$, that is when the diameter of the spot is exactly one wavelength.

The average amplitude of the reflection from the water surface (in relative units) is shown in Figure 6 as a function of several parameters. The abscissa is the roll angle $(\emptyset_o)$ of the aircraft and hence the inclination of the axis of the laser beam to the vertical. The parameter σ is the rms slope of the surface within the illuminated area expressed in radians. It is assumed that the mean slope of this area of the surface is zero.

It can be seen that, in calm conditions ($\sigma = 0.02$ rad) the average reflected signal strength is very sensitive to aircraft roll, particularly if the transmitted beam has a small divergence. On the other hand in rough seas ($\sigma = 0.2$ rad) the reflected signal strength is relatively insensitive to both aircraft roll and beam divergence. Figure 6 quantifies the trends expected from general arguments.

If a threshold detector is used to recognize the surface reflection, then the threshold required to achieve a given reliability can be calculated. Figure 7 shows the threshold (in relative units) needed to achieve a reliability of 99.9% (or a failure probability of 0.1%). The abscissa is the rms residual slope within the illuminated area (radians). The parameter $\bar{\sigma}$ is the mean slope of the area (radians).

The curves for a horizontal mean water surface ($\bar{\sigma} = 0$) show that a steadily decreasing threshold, that is a more sensitive detector, is required as the surface becomes rougher. This is because rough water produces a more diffuse reflection, that has a smaller vertical signal strength. As the swell increases (larger $\bar{\sigma}$) it becomes increasingly difficult to achieve reliable detection in calm conditions (σ' small).

Figure 7 assumes a knowledge of the mean and residual rms slopes, without any assumptions about the form of the wavenumber spectrum. When the spectrum is assumed to be saturated between two cutoff wavenumbers (as in Figure 4), the results can be expressed as shown in Figure 8. Each point in the (k_o, k_1) plane corresponds to a particular sea state. The small lower cutoff wavenumbers to the left of the graph correspond to the long wavelength swell of the open ocean, while the right of the graph represents the small waves of restricted water such as rivers and bays. On the vertical axis, the large upper cutoff wavenumbers at the top of the graph represent the small ripples generated in a strong wind, while the lower part of the graph represents smooth waves that occur in calm air. A variety of sea conditions can therefore be represented by an area of the graph.

For a given threshold and diameter, the failure probability is below 0.1% to the right of the corresponding curve. For a threshold of 10 sr^{-1}, reliable detection is achieved only when the saturated range of wavenumbers k_1/k_0 is less than 30. As the spot diameter is increased, reliable detection is achieved in the presence of longer swells. The effect of reducing the threshold (for example with a more sensitive detector) is to achieve reliable detection when the wave spectrum is saturated over a greater range of wavenumbers. If reliable detection is required over a wide range of upper cutoff wavenumbers and with lower cutoff wavenumbers as low as 0.1 m^{-1}, a diameter between 1 and 10 m is required together with a threshold less than 2 sr^{-1}.

The main hindrance to the immediate application of these results is the lack of measurements of the two parameters on which the theory is based. It is not known, therefore, what area of Figure 8 corresponds to commonly encountered sea conditions.

Port Stanvac Wave Monitoring Station

In order to provide the necessary data some equipment has been designed, made and installed on the Port Stanvac wharf (some 20 km south of Adelaide). An illustration of the equipment is given in Figure 9. The main instrument is the wave slope monitor. It is attached to a floating rig that is free to move up and down with swell and tide. A small hut houses a micro-processor controlled data recording system. Other meteorological and oceanographic equipment forming part of the station include 2 anemometers and wind vanes, a wave staff that measures wave height, a transmissonmeter, and a current meter. Data from all these instruments will be automatically recorded at regular intervals.

A schematic diagram of the wave slope monitor is given in Figure 10. A He-Ne laser produces a beam that is chopped and sampled for synchronous detection before being sent down a submerged sealed tube. The beam travels vertically upward through the water until it is refracted at the surface. A neutral density filter located in the image plane of the primary lens attenuates the beam by an amount that depends only on the water slope and not on the height of the water (to a first approximation). A second recording channel is used to compensate for any changes in the power of the beam.

Laboratory tests have shown that the wave slope monitor has a frequency response of nearly 100 Hz. When data from this instrument are combined with power frequency data from the wave staff, it should be possible to measure spectra over a wide frequency range. A transformation from frequency to wavenumber spectra should then provide relevant information for the theoretical model described earlier.

References

1. Swennen, J.P.J.W. (1968) J. Opt. Soc Am. 58, 47.

2. Phillips, D.M. (1979). Aust. J. Phys. 32, 469-89
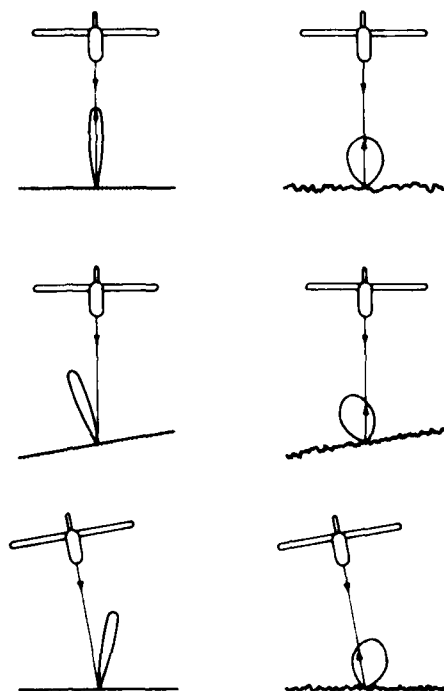
Figure 1 INFLUENCE OF SEA-STATE, SWELL
AND AIRCRAFT ROLL

WATER   SLANT
HEIGHT   HEIGHT
ERROR   ERROR
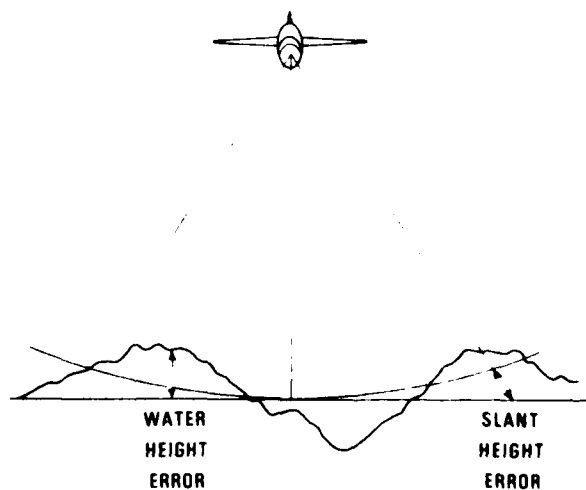
Figure 2 SLANT AND WATER HEIGHT ERRORS
OVER A LARGE SPOT

INFLUENCE OF SEA STATE AND SWELL ON SEA BOTTOM ILLUMINATION

INFLUENCE OF SEA STATE AND SWELL ON SEA BOTTOM RETURN
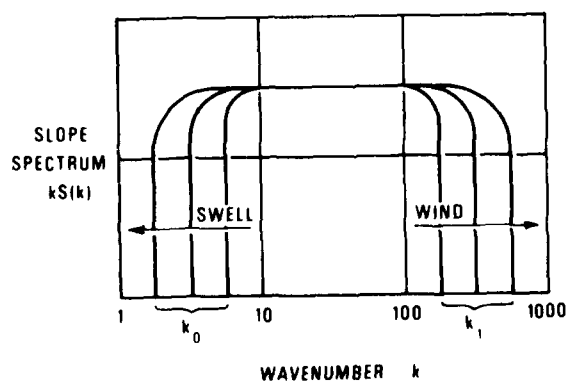
Figure 3

Figure 4   ASSUMED WAVENUMBER SPECTRUM OF
WATER SLOPE
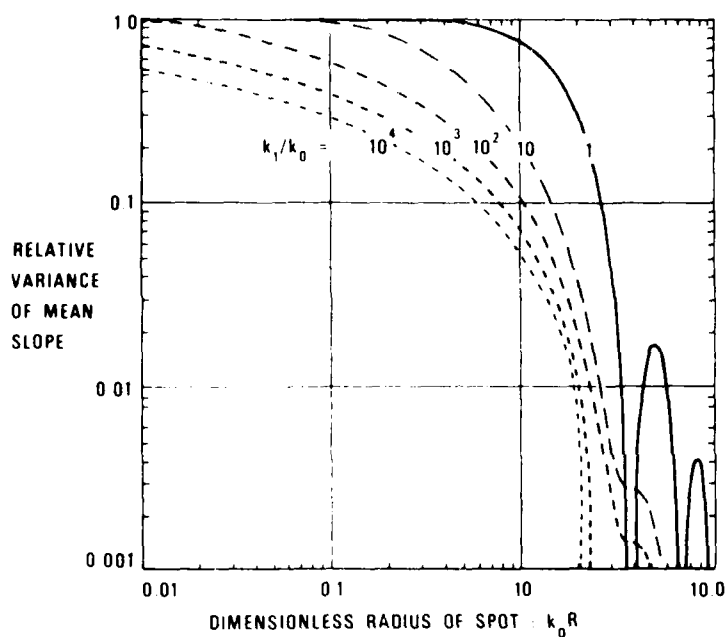
Figure 5   VARIATION OF MEAN WATER SLOPE
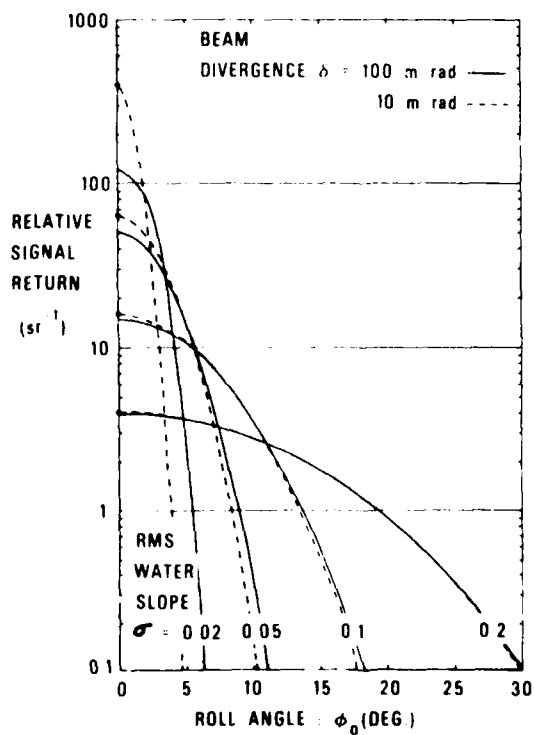
Figure 6   AVERAGE AMPLITUDE OF REFLECTED
SIGNAL
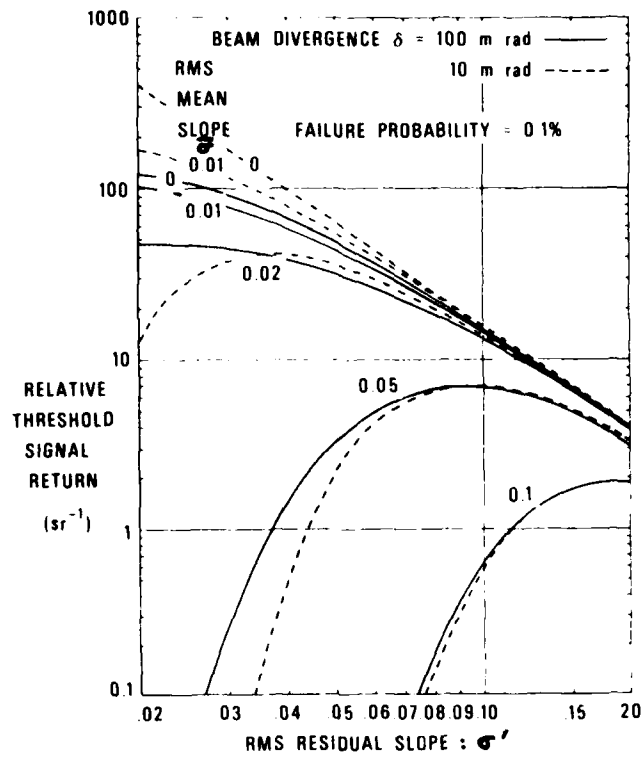
Figure 7   DETECTION THRESHOLDS IN THE
PRESENCE OF SWELL
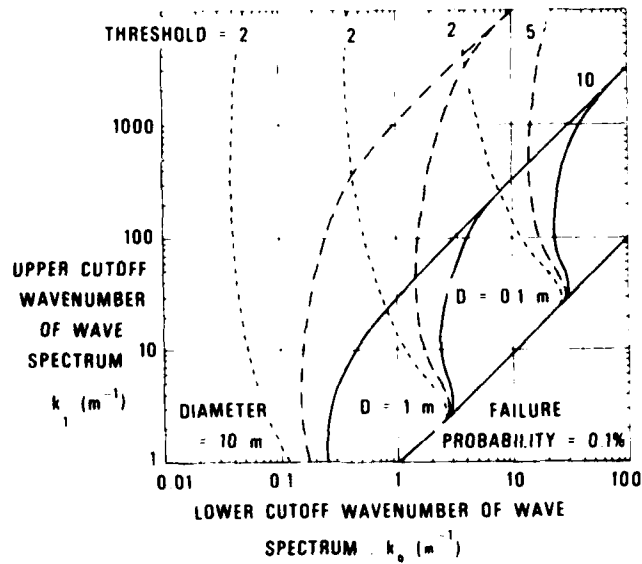
Figure 8   INFLUENCE OF SEA STATE ON
DETECTION THRESHOLDS
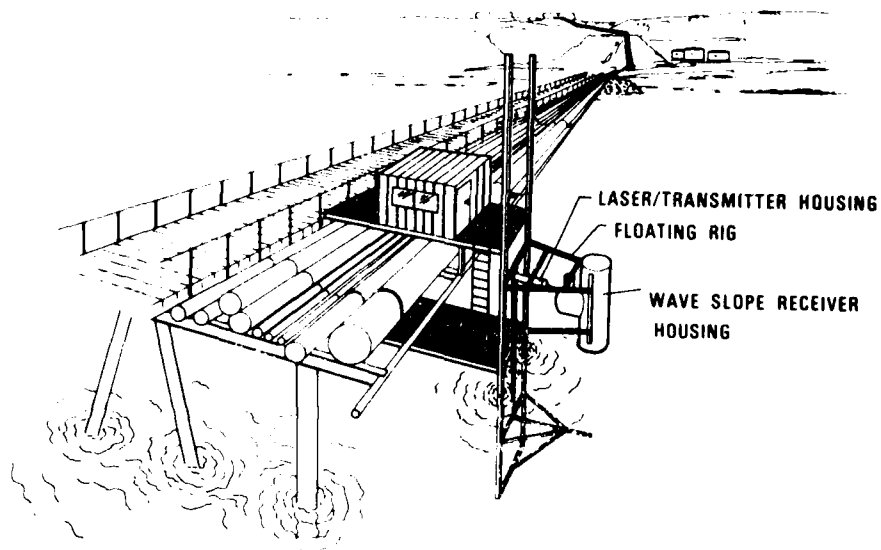
Figure 9   WHARF STRUCTURE AT PORT STANVAC
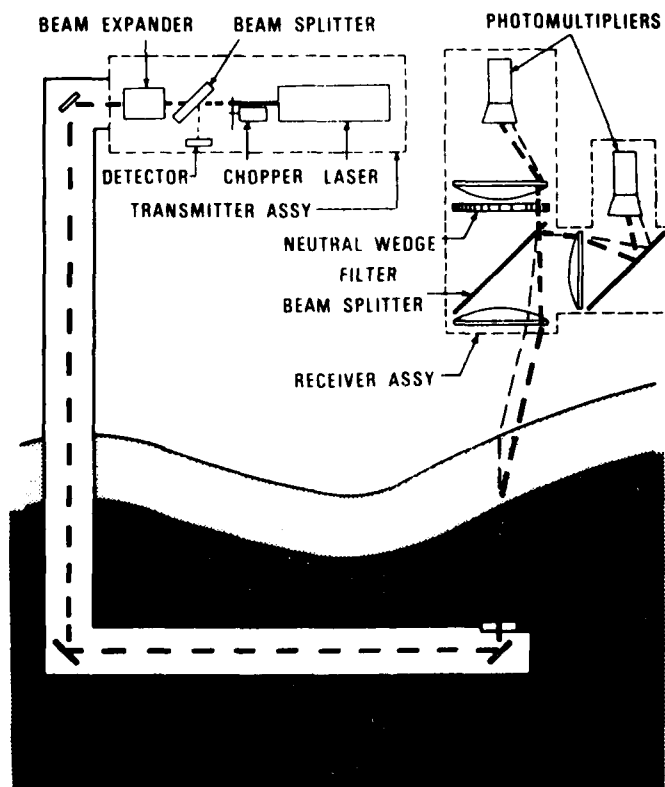
Figure 10   SCHEMATIC DIAGRAM OF SEA SLOPE
MONITOR

PAPER 22

DEPTH MEASUREMENT BIASES FOR AN AIRBORNE LASER BATHYMETER

Gary C. Guenther
Engineering Development Office, OA/Ocean
Technology and Engineering Services, NOAA
Rockville, Maryland   20852

Robert W.L. Thomas
EG&G/Washington Analytical Services Center, Inc.
Riverdale, Maryland   20840

ABSTRACT.   A Monte Carlo simulation program has been
developed and exercised to model airborne lidar depth
measurement biases caused by radiative transfer processes
for impulse laser inputs to a homogeneous water column. The
water parameters and systems constraints of the computation
are appropriate to airborne laser hydrography systems
presently under consideration for use in coastal waters.

INTRODUCTION

Earlier analytical computations by Thomas and Guenther (1979) have
indicated the possibility of a significant bias toward greater depths
for operations of the system at nadir.   This bias arises from the
multipath transport mechanism by which the laser radiation penetrates
the water and is subsequently reflected back through the water to the
receiver.   This is the so-called "pulse stretching" effect.   The impact
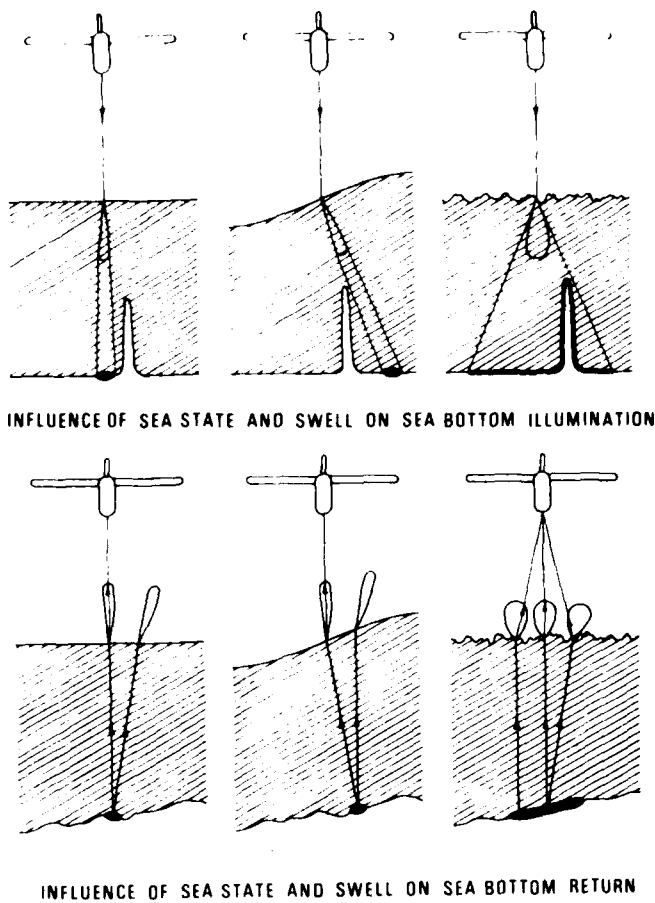of this effect on the estimated depth is influenced both by the temporal
profile of the incident laser pulse and the return pulse processing
electronics, but the key to the quantification of the effect is the
generation of a set of response functions for the medium which
characterize the temporal history of radiation reaching the receiver for
an impulse input.   Monte Carlo simulation is the only practical method
of generating these impulse response functions.

Depth measurement bias predictions are parameterized on inherent
water properties (such as beam attenuation coefficient and single-
scatter albedo) and system constraints. If these parameters are known
or can be estimated, the bias predictions obtained from the simulation
can be suitably modified to account for depth dependence and system
electronics and applied to field data as "bias correctors" to reduce the
magnitude of the raw biases in post-processing. This technique is
considered mandatory if international hydrographic accuracy standards
are to be met. Estimation of the relevant inherent water parameters for
ancillary airborne lidar data poses a serious problem which will
strongly impact system data processing requirements.

SIMULATION MECHANICS

In the Monte Carlo approach we model the transport of
representative photons through a homogeneous water column to the
bottom. A schematic diagram of the simulation geometry is given in
Fig. 1.

Traditionally, the mean free path for radiation transport through
water has been described through a parameter called the "narrow-beam
attenuation coefficient" (α). The narrow-beam attenuation is comprised
of two components: scattering and absorption. If "s" is the scattering
coefficient and "a" is the absorption coefficient, then

$$\alpha = a + s. \tag{1}$$

If a beam of intensity, I_0, is incident on a column of water, then the
amount that remains unscattered and also not absorbed after travelling a
distance L is $I_0 \exp(-\alpha L)$. Thus the mean free path, q, is equal
to α^{-1}. The vertical "optical depth" of the medium, defined as the
number of mean free path lengths required to vertically traverse the
medium to the bottom for a depth D, is D/q which is thus equal to αD.

The "albedo for single scattering," ω_0, is defined as the average fraction of the incident energy at any scattering event that is not absorbed; i.e.,

$$\omega_0 = \frac{\alpha - a}{\alpha} = \frac{s}{\alpha} \ . \tag{2}$$

For typical coastal waters, ω_0 is believed to range from about 0.55 to 0.9. In the simulations, photons are not actually eliminated by absorption as they might be in the real world. Rather, we represent the behavior of a photon ensemble by retaining a photon weight (initially unity) and multiplying it by the single-scattering albedo, ω_0, at each scattering event. In this way we can conveniently accumulate results for several values of ω_0 at the same time.

Photons are considered to change direction at all scattering events. The scattering angle θ from the incident direction is generated according to the "phase function", $P(\theta)$, which defines the probability that the photon will scatter into a unit solid angle between θ and $\theta + d\theta$. Since the solid angle between θ and $\theta + d\theta$ is $2\pi\sin\theta\,d\theta$, the probability of occurance of θ in θ to $\theta + d\theta$ is

$$p'(\theta)\,d\theta = 2\pi\sin\theta\,P(\theta)\,d\theta \ . \tag{3}$$

Typical phase functions for water exhibit a very strong forward scattering effect (Petzold 1972). The phase functions increase by a factor of more than 1,000 as the scattering angle diminishes from 10° to 0.1°. The physical reason for this phenomenon appears to be the proximity of the refractive index of the scattering agent to that of the ambient water (Gordon 1974). (Note that if the refractive indices were identical there would be no scattering, and the phase function would be a delta function at zero degrees.)

The value of each scattering angle, θ_k, is generated by solving the equation

$$\int_0^{\theta_k} p'(\theta)\,d\theta = 4\pi\,\rho \ , \tag{4}$$

where ρ is a rectangularly distributed random number between 0 and 1. This equation is solved by linear interpolation within a look-up table of the value of the integral as a function of θ_k. For this work, we considered two phase functions designated "NAVY" or "clean" (Fig. 2) and "NOS" or "dirty". Note that the "volume scattering function" is simply the phase function normalized to existing water conditions by multiplying by $\omega_0 \alpha$.

The parameters, αD, ω_0, and $P(\theta)$ are the "inherent" description of the transport medium characteristics required for the simulation. The relationships between these parameters and the parameters governing the "apparent" properties of the medium have been discussed by Gordon, Brown, and Jacobs (1975). The most important apparent parameter is K, the so-called "diffuse oceanographic attenuation coefficient," which is defined as the fractional rate of decay of the downwelling flux as the depth is increased. For small depths, K depends on both the depth itself and the angle of incidence of the radiation at the surface; but for larger depths these dependences become very small. K is properly measured at or corrected to nadir entry. The ratio, K/α, is a monotonically decreasing function of ω_0, which has a value of unity when ω_0 is zero and which decreases towards zero as ω_0 tends to unity. There is a small dependence on the phase function, but this is not significant for realistic coastal waters.

The lengths of the photon paths for photons reaching the bottom are summed to allow an evaluation of the associated time delay. The minimum time of transit to the bottom is

$$t_w = \frac{D}{c_w} , \tag{5}$$

where c_w is the velocity of light in water. The "time delay" for paths of length L_i is then computed as

$$t_D = \frac{1}{c_w} \left(\sum_{i=1}^{n} L_i - D \right) . \tag{6}$$

By repeating this computation for a large number of downwelling photons we can compute the <u>downwelling</u> impulse response function $d(t_D)$ as a histogram representing the probability distribution of arrival times of incident photons at the bottom.

An important gain in the information content of the results arises from the realization that, for given values of αD and ω_0, all temporal results scale linearly with the depth, D. This is illustrated in Fig. 3 where we show representative photon paths for two cases with the same αD but with different values of D. The photon paths for the two cases are geometrically "similar" so that the <u>fractional</u> time delays t_D/t_w, are identical. Therefore the <u>absolute</u> time delays <u>scale</u> linearly with D, and one set of simulated results can be used to determine absolute results for all depths.

The receiver response function is computed using the principle of reciprocity (Chandrasekhar 1960) which states that the <u>statistical</u> description of the upwelling paths to a distant receiver for photons reflected at the bottom is identical to that for the downwelling paths from a co-located transmitter. This is not a declaration that the downwelling and upwelling paths are physically the same, but rather that the simulated downwelling photon tracks can be regarded as respresentative for both cases to obtain the impulse response at the receiver. The computed impulse response $d(t_D)$ for downwelling transport is convolved digitally over a similar upwelling distribution $u(t_D)$ computed by multiplying the weights of photons reaching the bottom by the cosine of their arrival nadir angles. The last step assumes Lambertian-type reflection as opposed to isotropic reflection (which would be characterized by simply substituting $d(t_D)$ for $u(t_D)$).

The act of convolving the functions d and u is an integration, and, as such, it has the effect of reducing the magnitude of statistical noise in the resulting function. It has been found that the result, $r(T)$, is acceptably reproducible for simulations of as low as 10,000 photons when the program is rerun with different starting random numbers; this adds confidence to the results.

Although a specific receiver field of view is not directly applied
in the simulation, an effective field-of-view restriction is caused by
the truncation of paths which have been judged to be excessively long
(to save computer time). This restriction applies only to photons which
would have arrived in the trailing edge of the impulse response and in
no way affects the leading edge or the peak power. Thus, the effective
field of view is large but considerably less than unlimited. The effect
of restricting the field of view to an infinitesimal area around the
entry point of the incident beam has been calculated to bound the
problem. Results indicate that, in general, the bias cannot be removed
(or even necessarily reduced) by reducing the receiver field of view.

BIAS ESTIMATION

The depth measurement bias errors are estimated by applying
fractional threshold detectors to the computed receiver impulse response
function, $r(T)$. The "reference time," T_R, for this computation is the
time delay for radiation travelling unscattered (at the refraction
angle ϕ) to the bottom and then being reflected back along the same
path. This time delay is

$$T_R = 2t_w (\sec \phi - 1). \tag{7}$$

For the nadir case, of course, ϕ is zero, so that T_R is zero. Thus
only positive (deep) errors in depth estimates can be contributed by
propagation effects in this case. For the off-nadir cases, however,
both positive and negative errors can occur. Negative (shallow) errors
arise from a favoring of shorter paths closer to vertical, since these
are the ones for which absorption is less likely to occur. This is the
so-called "undercutting" effect where the majority of bottom reflected
energy falls predominantly "beneath" the unscattered ray (closer to the
aircraft), and a significant amount of energy is returned before the
reference delay time, T_R, as illustrated in Fig. 4.

We can gain approximate estimates of the potential biases by
applying a linear fractional threshold detector to the impulse
responses. In this method we compute the time, t_f, at which the impulse
response rises through a given fraction, f, of the peak response. Since

our simulation results are referenced to unit depth and unit velocity of light, we must convert to a specific depth in the real world by multiplying by t_w, the depth transit time. Thus we compute the time bias as

$$T_B = t_w \cdot t_f - T_R, \tag{8}$$

and, using Eq. (7), we have

$$T_B = t_w [t_f - 2 (\sec \phi - 1)]. \tag{9}$$

In most of our presentations we have assumed a depth of 20 m, since this is the greatest depth at which the International Hydrographic Bureau (Special Publication No. 44, 1968) requires an accuracy of one foot (30 cm). In this case, t_w is 88.7 ns.

Note that in the analysis of the impulse responses, the <u>fractional</u> *depth error is independent of the true depth. This is because the two-* way transit time for unscattered light is $2t_w \sec \phi$ so that the fractional error is given by

$$F(f) \equiv \frac{T_B}{2t_w \sec \phi}, \tag{10}$$

which, by Eqs. (8) and (7) becomes

$$F(f) = (t_f/2 + 1) \cos \phi - 1 . \tag{11}$$

It is not possible to relate the biases computed by these formulas in a simple way to that associated with an input pulse of finite duration. For very short laser pulses these bias correctors will be accurate. For long input pulses, the bias may be larger or smaller than the value given -- with a greater potential for error in the corrector as the input pulse duration increases. This particular aspect of the problem is being studied as part of an on-going investigation.

OUTPUT

For each of the two phase functions, we performed five simulation
runs (with nadir angles in air ranging from 0° to 45°) for a total of
ten runs. In general, both αD and ω_0 are larger for the more "turbid"
or "dirty" water. Nevertheless, to insure comprehensive results sets
for the two phase functions, we performed simulations over full sets
of αD and ω_0 values for the two cases. Eight values of both
parameters were employed in each simulation run so that 64 sets of
results were generated in each run.

The listed output includes the following for all cases: (1) The
impulse response function for downwelling radiation reaching the bottom;
(2) The impulse response function for upwelling radiation reflected
from the bottom; (3) The convolution of functions (1) and (2)
representing the response at the receiver; and (4) The spatial (radial
and Cartesian) distribution of downwelling radiation at the bottom.

While the complete impulse response and depth measurement bias
results are far too voluminous to present or describe in this report,
representatve samples are displayed in Figs. 5 through 12. (Note: the
block of information describing the parameters for the curves in the
bias plots contains (in order) the values for phase function, nadir
angle, threshold fraction, and single-scattering albedo.)   These
presentations are designed to illustrate the effects of varying
combinations of key parameters against a typical background of those
remaining fixed. It can be seen that the phase function and albedo for
single scattering have relatively small effects, while the optical
depth, nadir angle, and threshold fraction exhibit rather large
effects. A complete description of the simulation and a full set of
results and conclusions have been produced and may be obtained upon
request. A data base containing 640 impulse response functions has been
archived for future work.

CONCLUSIONS

We have succeeded in developing a technique for investigating the impact of underwater light propagation mechanisms on laser bathymetry measurements. A Monte Carlo simulation program has been suitably adapted to yield the impulse response function (i.e., the shape and size of the return pulse for a very brief input pulse) at an airborne receiver. This calculation has been performed for a range of conditions valid for coastal waters.

The actual lidar bottom return pulses will vary considerably in shape and arrival time depending on the water depth, the scanner nadir angle, the incident laser pulse width, the optical properties of the water, the airborne system signal processing electronics, and the depth determining algorithm or procedure. These perturbations of the return signals will cause depth measurement biases which can be considerably larger than the International Hydrographic Bureau shallow water accuracy requirements.

In general, bias error predictions can be used as bias error correctors which, when applied to the raw depth measurements during post-flight processing, will significantly reduce the magnitude of the errors. The first step in the estimation of these errors is the determination of the impulse response functions of the medium for various permutations of the relevant optical parameters. An output data set consisting of 640 impulse response functions has been generated which provides the basic results of this phase of the investigation.

We have determined that the shapes of the impulse response functions are sensitive to the nadir angle and that the width of the response (particularly the tail, or trailing edge) always increases with increasing nadir angle. The dependence on the phase function, which describes the redistribution of energy at scatterings, is not very significant, provided we specify phase functions within a reasonable range. The width of the impulse response functions increases both with increasing αD, the vertical optical depth of the water column, and increasing ω_0, the albedo for single scattering.

The characteristics of the impulse response function cannot be directly estimated from the parameter, KD, the product of the diffuse oceanographic attenuation coefficient and the depth. This fact is explained in terms of the behavior of the ratio of K to the narrow-beam attenuation coefficient, α, as the single-scattering albedo, ω_0, changes.

For non-zero nadir angles, the leading edge of the impulse response function behaves approximately as a power law with an exponent of 3.5 to 4.5; i.e., the receiver power varies from $t^{3.5}$ or $t^{4.5}$, where t is the time since the earliest possible return.

Example bias predictor/correctors have been calculated from the impulse responses alone. These predictors are strictly valid only for the case where the impulse response temporal width is very long compared to the incident laser pulse width (i.e., deep water) and where the signals are processed linearly with a fractional amplitude threshold for the depth determining algorithm. They are expected, however, to also be fair estimates for the actual case of a finite incident pulse. These predictors have been reported and discussed for a wide range of nadir angle, optical depth, single-scattering albedo, and the depth algorithm threshold fraction in a separate report which is available upon request.

We have found that the biases are not very sensitive to the phase function. For non-zero nadir angles and small fractional thresholds an underestimate in depth is caused which increases towards a limit as αD reaches six or eight. This limit increases with increasing nadir angle. The biases for nadir angles of 35° and 45° are very large and cannot be predicted to acceptable accuracy because of the practical uncertanties in ω_0 and αD. Hence, unless reliable predictions of the inherent ocean optical properties can be found, operations at nadir angles above 25° should not be undertaken. The bias is not very sensitive to ω_0 over most of the conditions considered. With larger fractional thresholds, the biases are small for αD values of eight or less, but the use of peak detection is not recommended because of an adverse impact of statistical noise. The computed biases scale linearly with the true depth, and, for small depths, the results show that a correction may be unnecessary.

In order to calculate bias predictors (and hence correctors) generally valid in all cases for a specific lidar system, one must first convolve a selected impulse response with the intrinsic laser pulse shape to obtain a prediction for the actual bottom return pulse. This signal must be "processed" in a manner consistent with the signal processing which takes place in the electronic hardware and, finally, operated upon by the depth determining algorithm to be used with actual field data. The convolution/non-linear processing/depth algorithm steps planned for the U.S. Navy's Hydrographic Airborne Laser Sounder (HALS) are the basis of on-going work, and specific results will be reported at a later date.

The bias predictors are necessarily parameterized on their driving, inherent optical properties (i.e., beam attenuation coefficient and single-scattering albedo). Neither of these optical properties will be directly measured in the field as part of a typical airborne survey. It is thus necessary to provide continuous estimates of their values based solely on specially processed, ancillary flight data. A preliminary discussion of the required data and how one might make these determinations has been given in the associated report. We have also considered alternative and/or supporting bias estimation procedures that do not require knowledge of the inherent properties. This subject is being studied further as part of the on-going effort.

REFERENCES

Chandrasekhar, S., 1960: Radiative Transer. Dover Publications, New
    York, N.Y., 385 pp.

Gordon, H.R., 1974: Mie theory models of light scattering by ocean
    particulates. Suspended Solids in Water. Plenum Press, Ed. Ronald
    J. Gibbs, 73-86.

Gordon, H.R., Brown, O.B., Jacobs, M.M., 1975: Computed relationships
    between the inherent and apparent optical properties of a flat
    homogeneous ocean, Appl. Opt., 14, 417-427.

Petzold, T.J., 1972: Volume scattering functions for selected ocean
    waters. SIO Ref. 72-78, Scripps Institution of Oceanography, San
    Diego, Ca., 79 pp.

Thomas, R.W.L., and Guenther, G.C., 1979: Theoretical calculations of
    bottom returns for bathymetric lidar. Proceedings of the
    International Conference on Lasers '78, Orlando, Fla., 48-59.

INCIDENT BEAM (δ —FUNCTION)

ψ → AIR NADIR ANGLE

FLAT SURFACE

WATER NADIR
ANGLE
(SNELL'S LAW)

φ

L_1

Θ_1

L_2

UNSCATTERED RAY
(TIME REFERENCE
FOR BIASES)

Θ_2

DEPTH D

L_3

Θ_3

L_4

RADIAL DISTRIBUTION

FLAT
BOTTOM
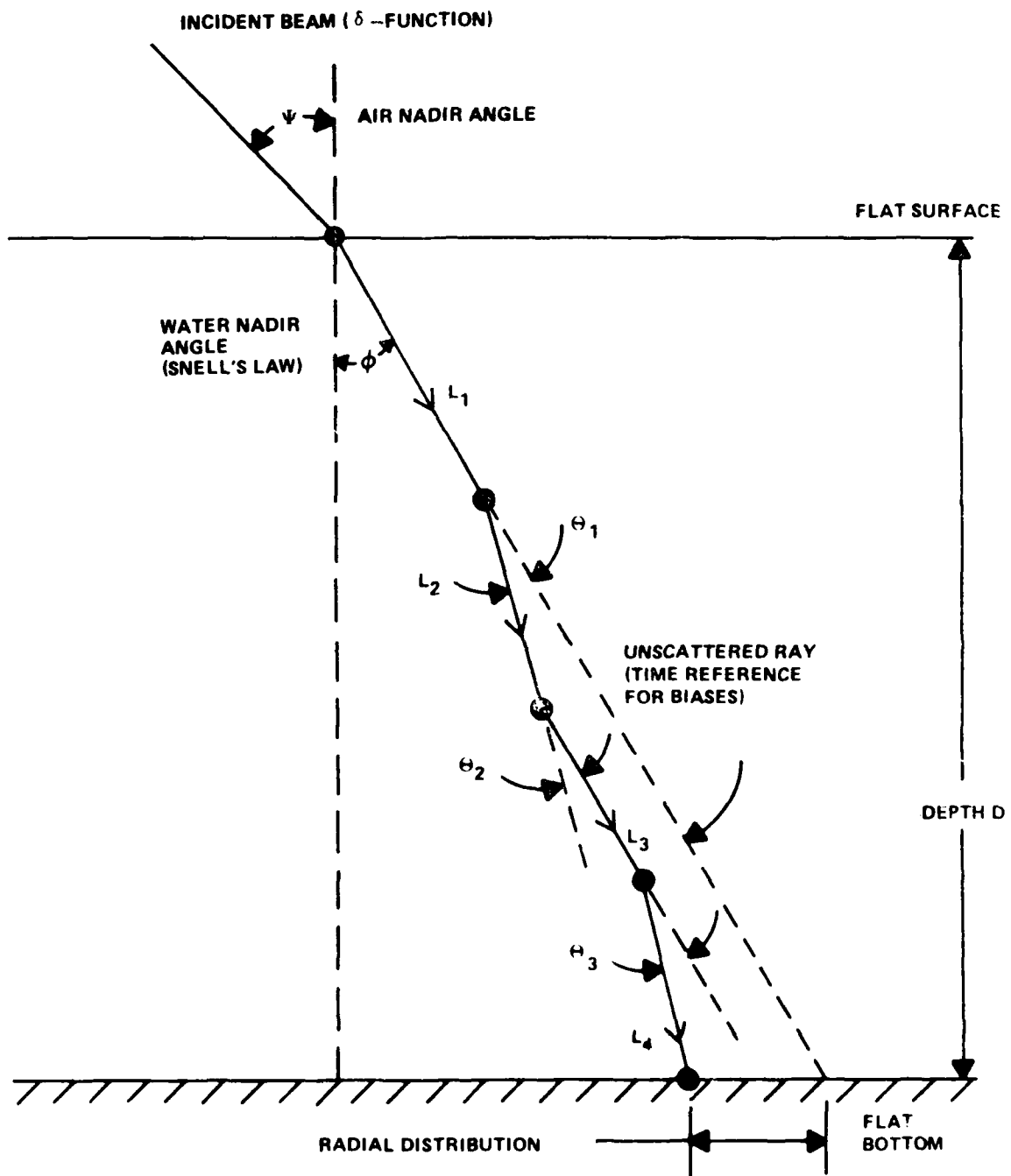
$$\text{DELAY TIME T} = \frac{1}{c_W}\left[\sum_i L_i - D\right]$$

FIGURE 1. PROPAGATION SIMULATION GEOMETRY

"NAVY WATER"

α = 0.47 m^{-1}	SLOPE	=	-1.546 @ $0.1°$
ω_0 = 0.585	VSF $(0.05°)$	=	5700
B = 0.014	$\overline{\cos \theta}$	=	0.9466
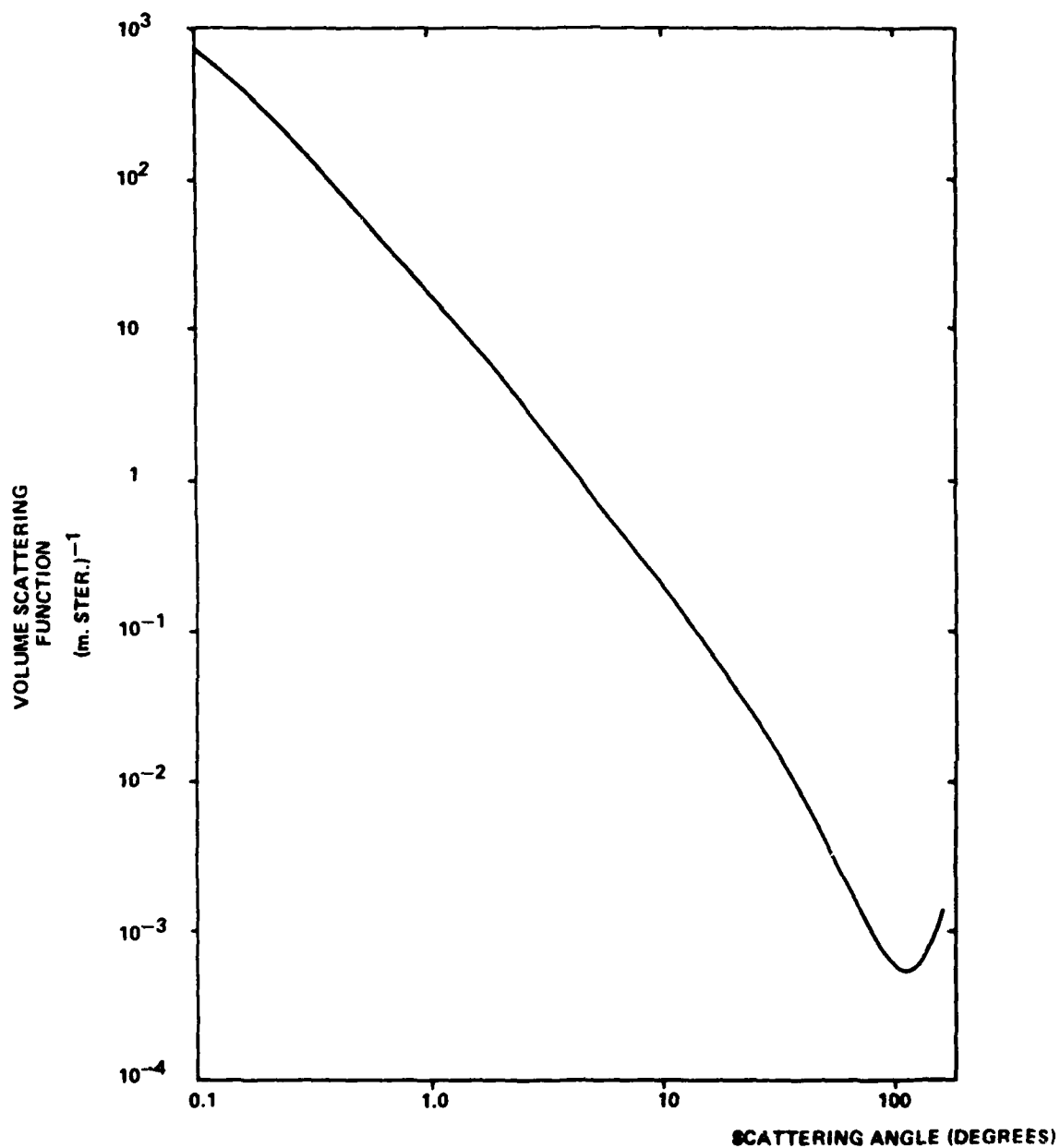
FIGURE 2. VOLUME SCATTERING FUNCTION FOR 'CLEAN' OR 'NAVY' WATER

FIGURE 3. ILLUSTRATION OF SCALING RULE FOR ESTIMATIONS APPROPRIATE TO DIFFERENT DEPTHS
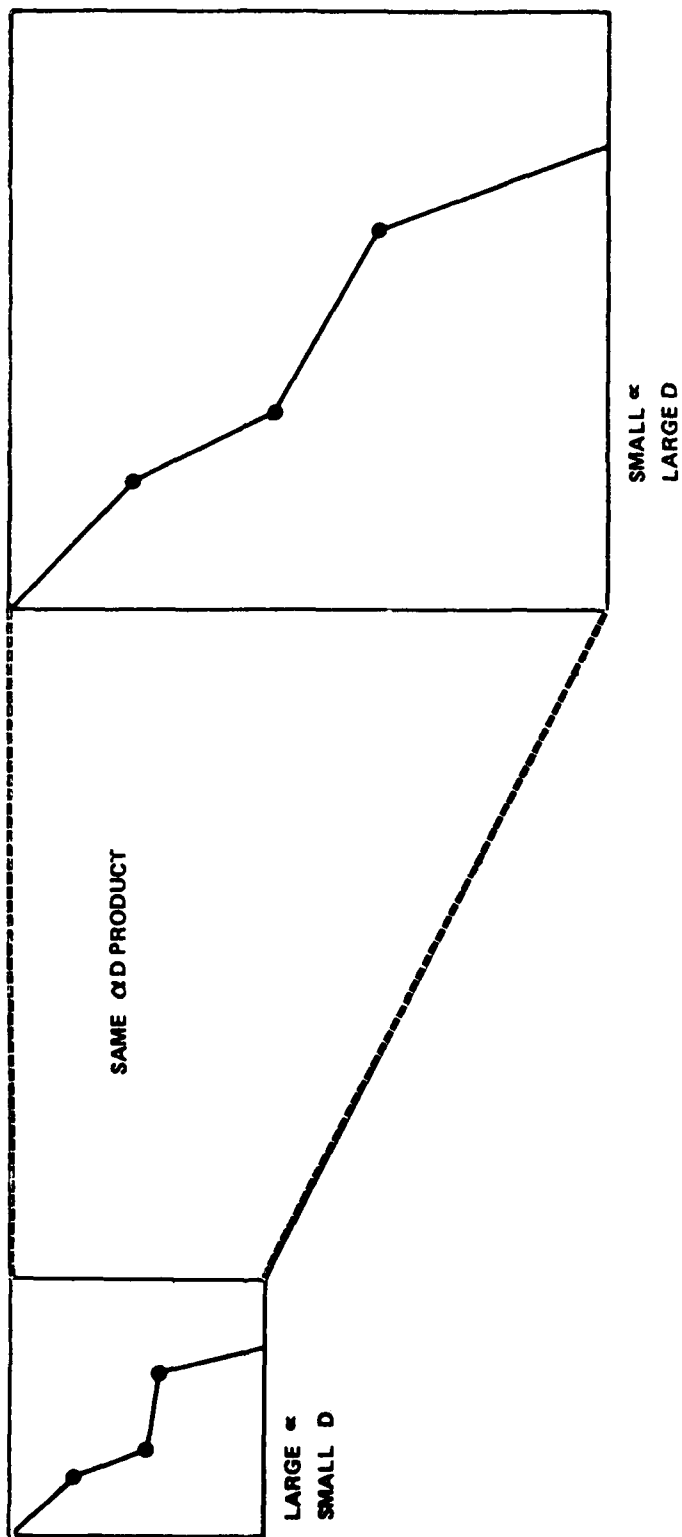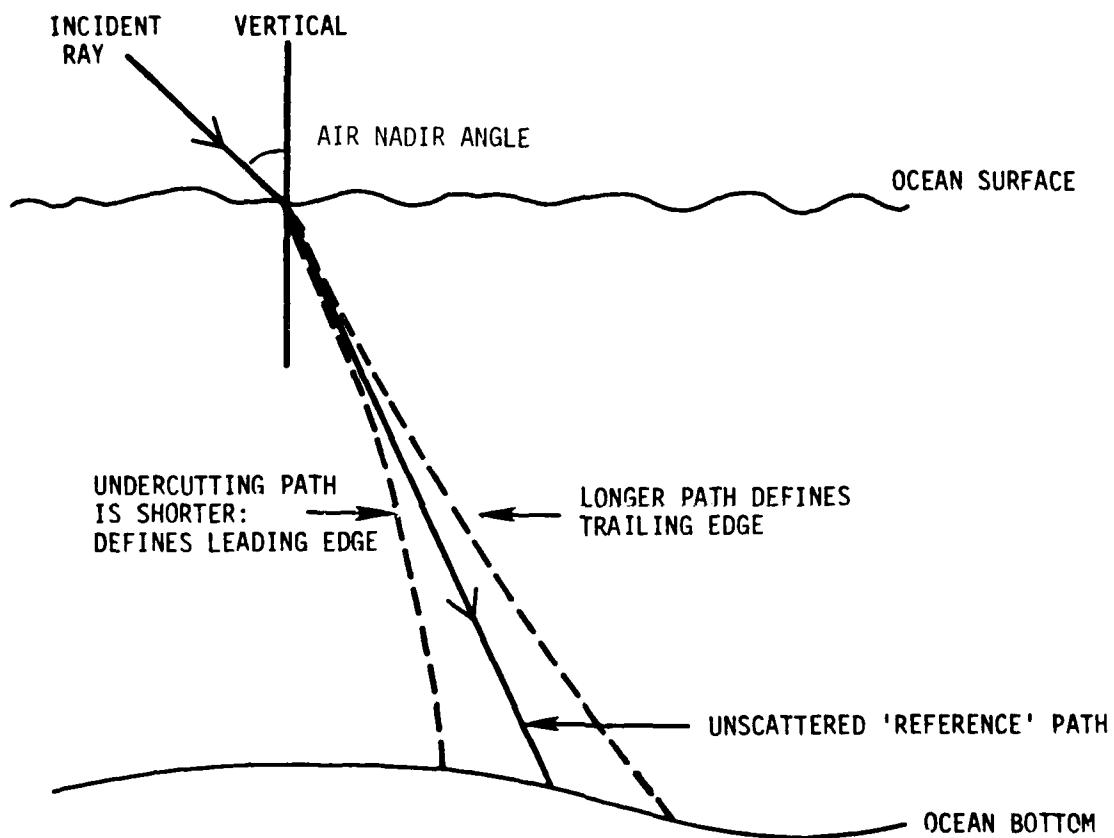
FIGURE 4.   GEOMETRICAL RELATIONSHIPS AFFECTING IMPULSE
            RESPONSE FUNCTION
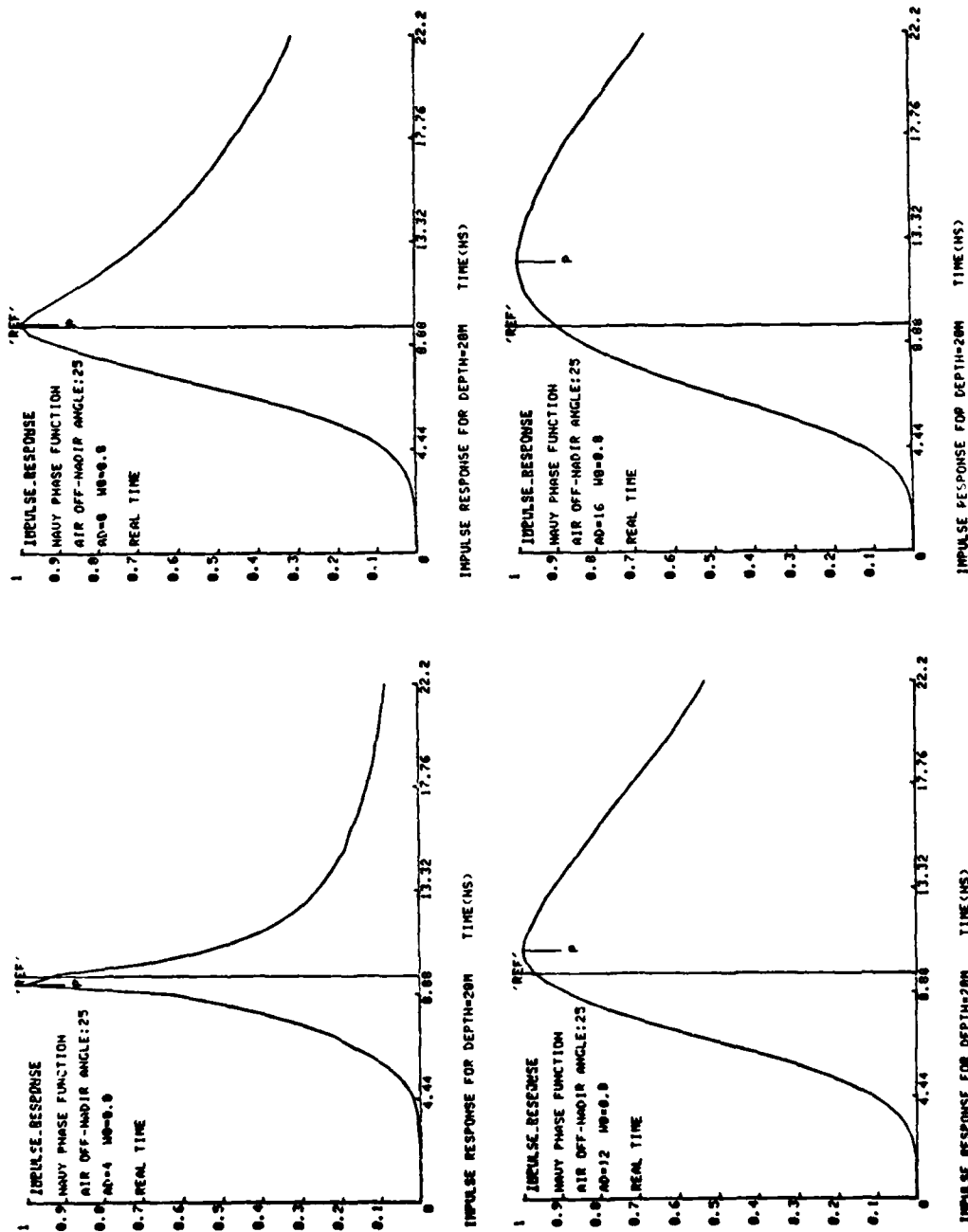
FIGURE 5. SENSITIVITY TO QD
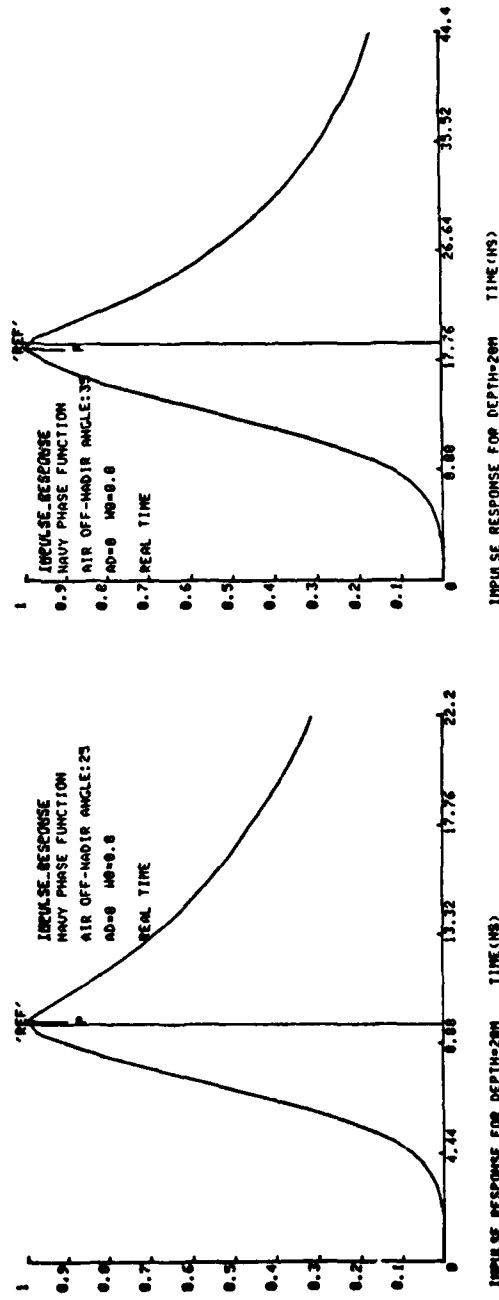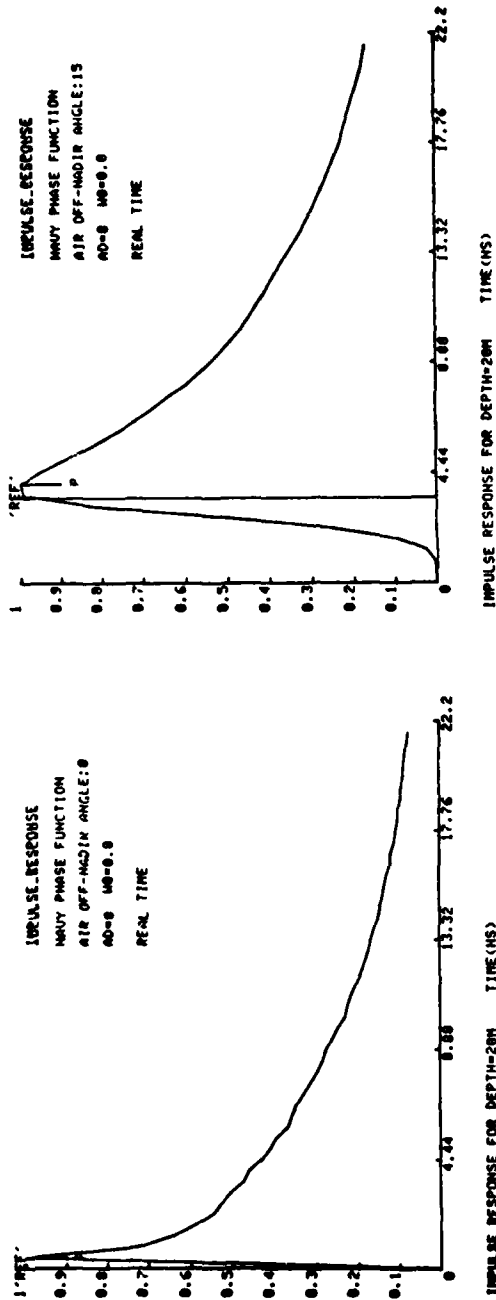
FIGURE 6. SENSITIVITY TO NADIR ANGLE

IMPULSE RESPONSE FOR DEPTH=20M   TIME(NS)
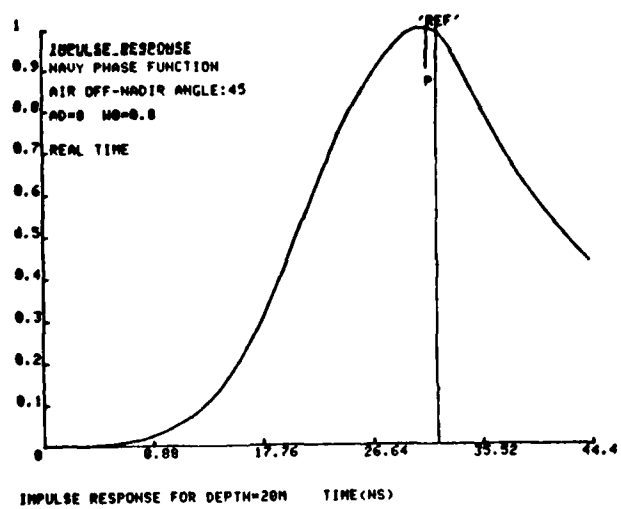
FIGURE 8A. SENSITIVITY TO NADIR ANGLE
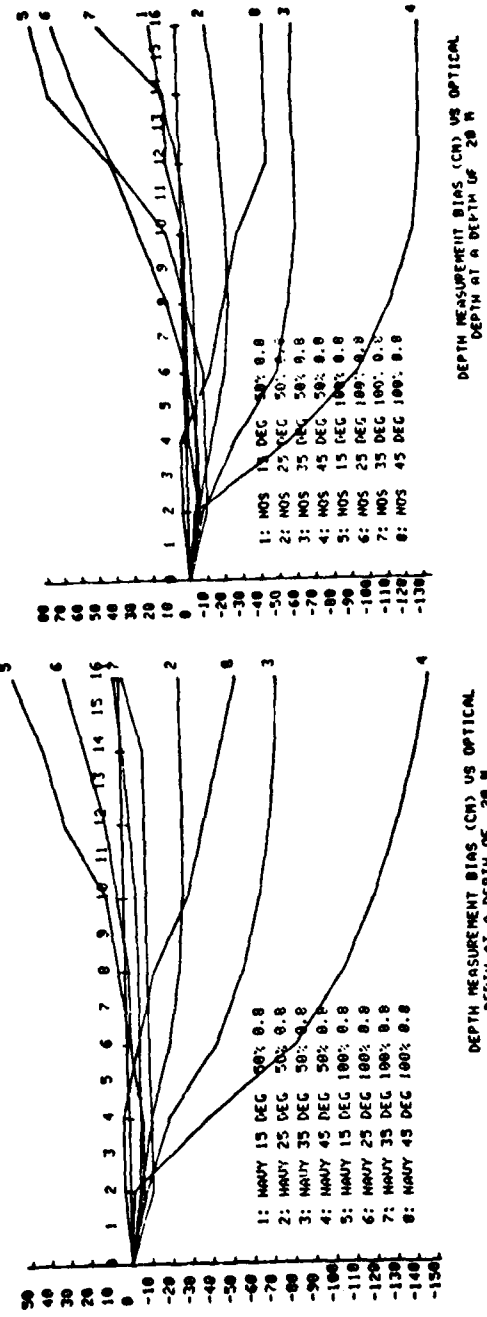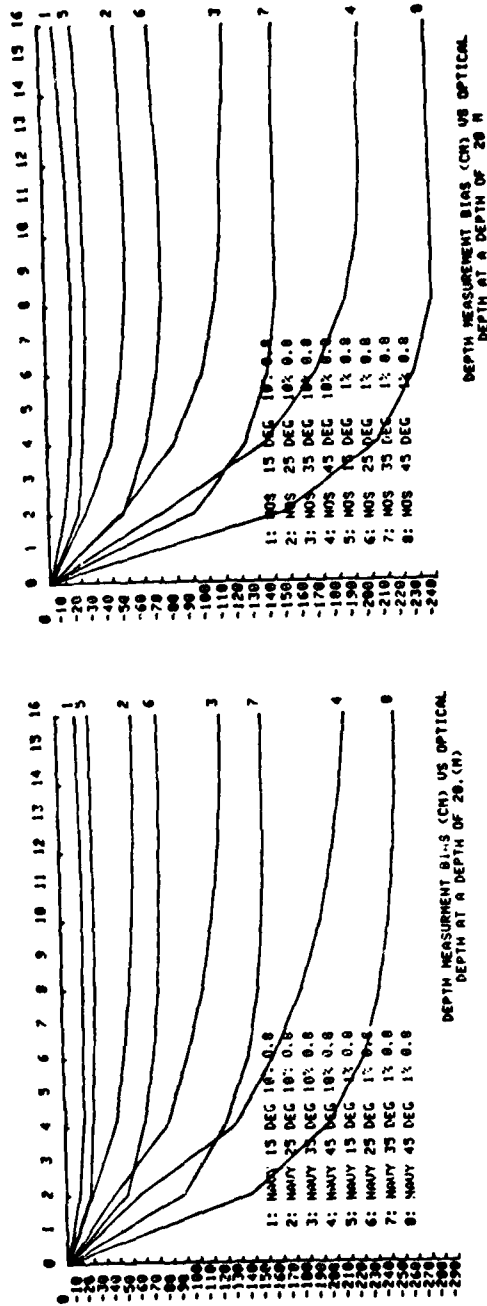
FIGURE 7   SENSITIVITY TO NADIR ANGLE
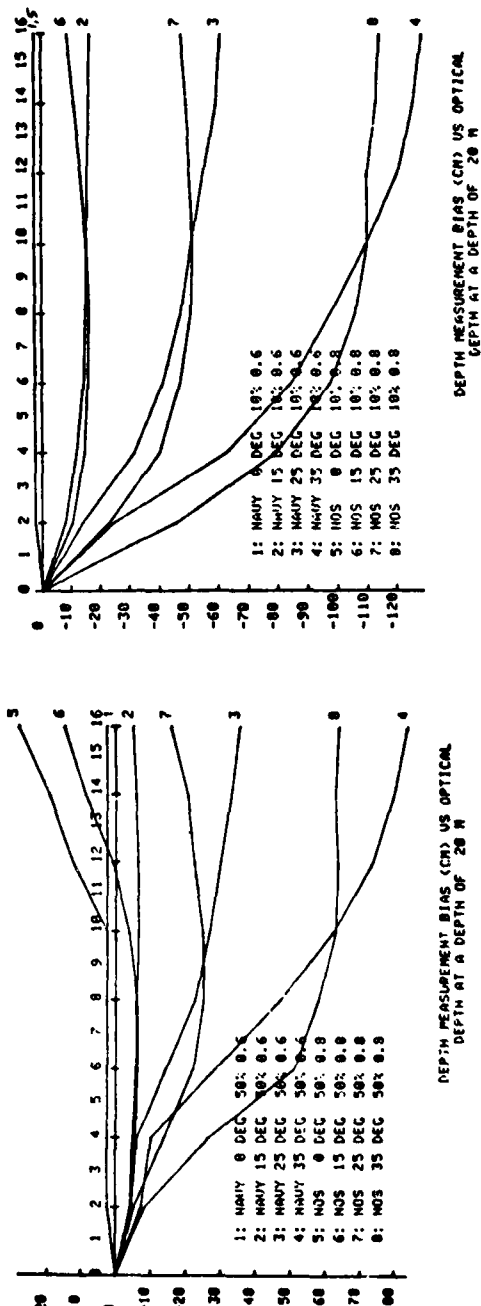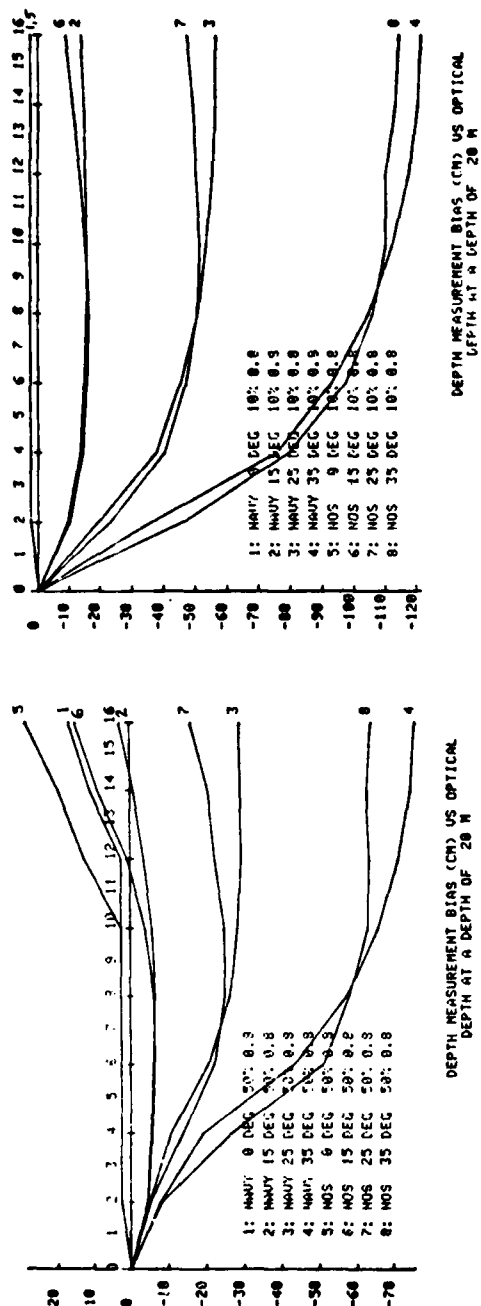
FIGURE 8. SENSITIVITY TO PHASE FUNCTION
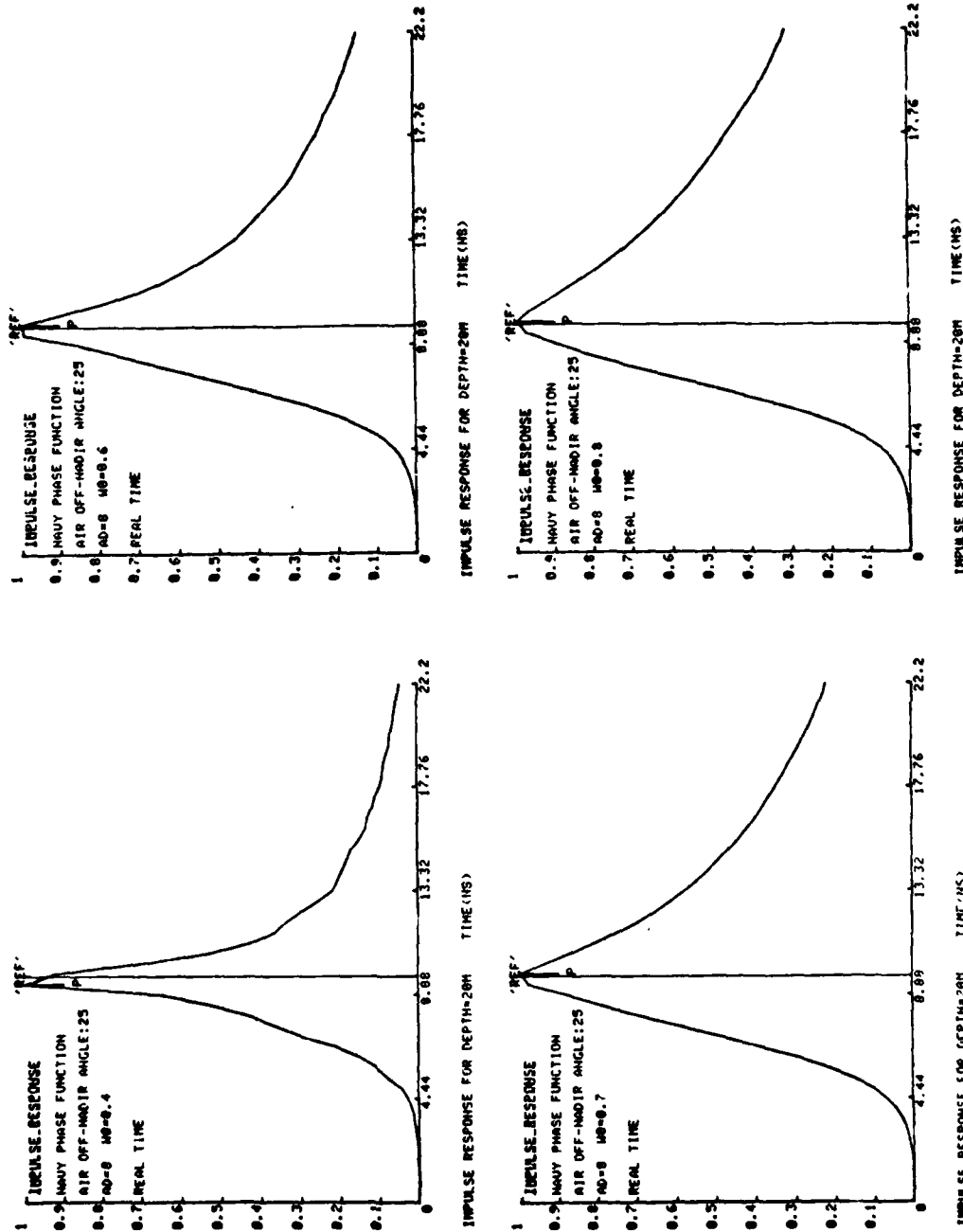
FIGURE 9. SENSITIVITY TO ALBEDO FOR SINGLE SCATTERING
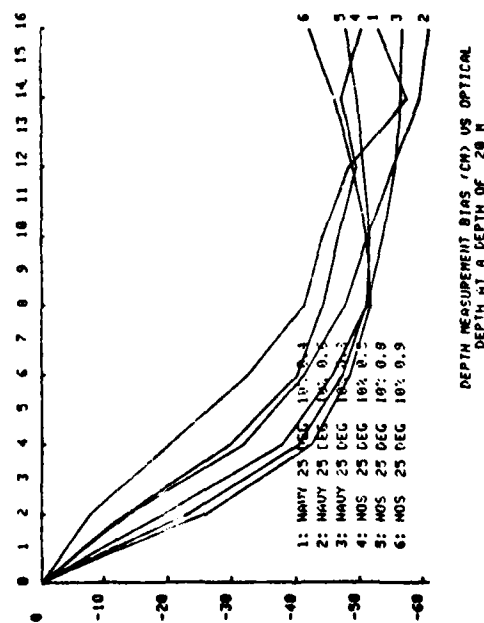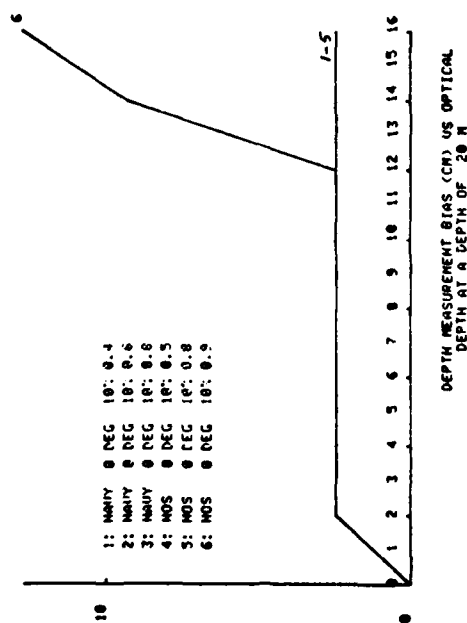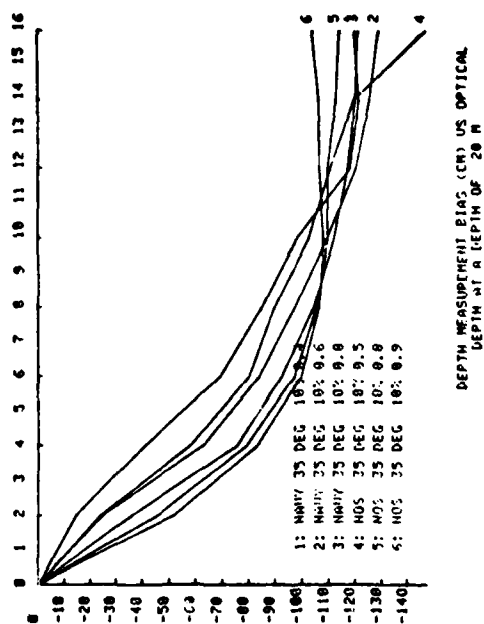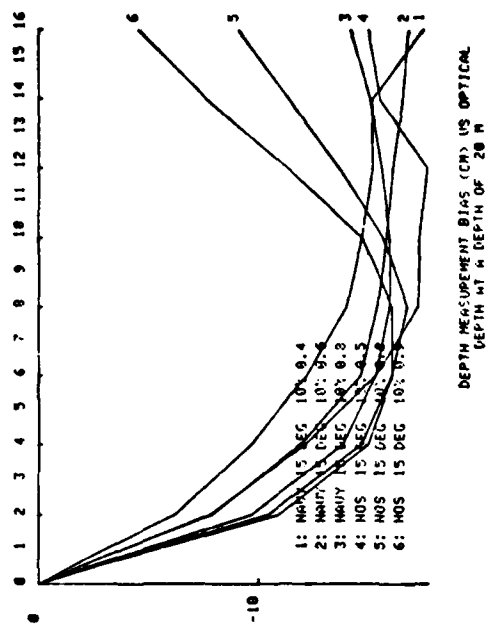
FIGURE 10. SENSITIVITY TO ALBEDO FOR SINGLE SCATTERING
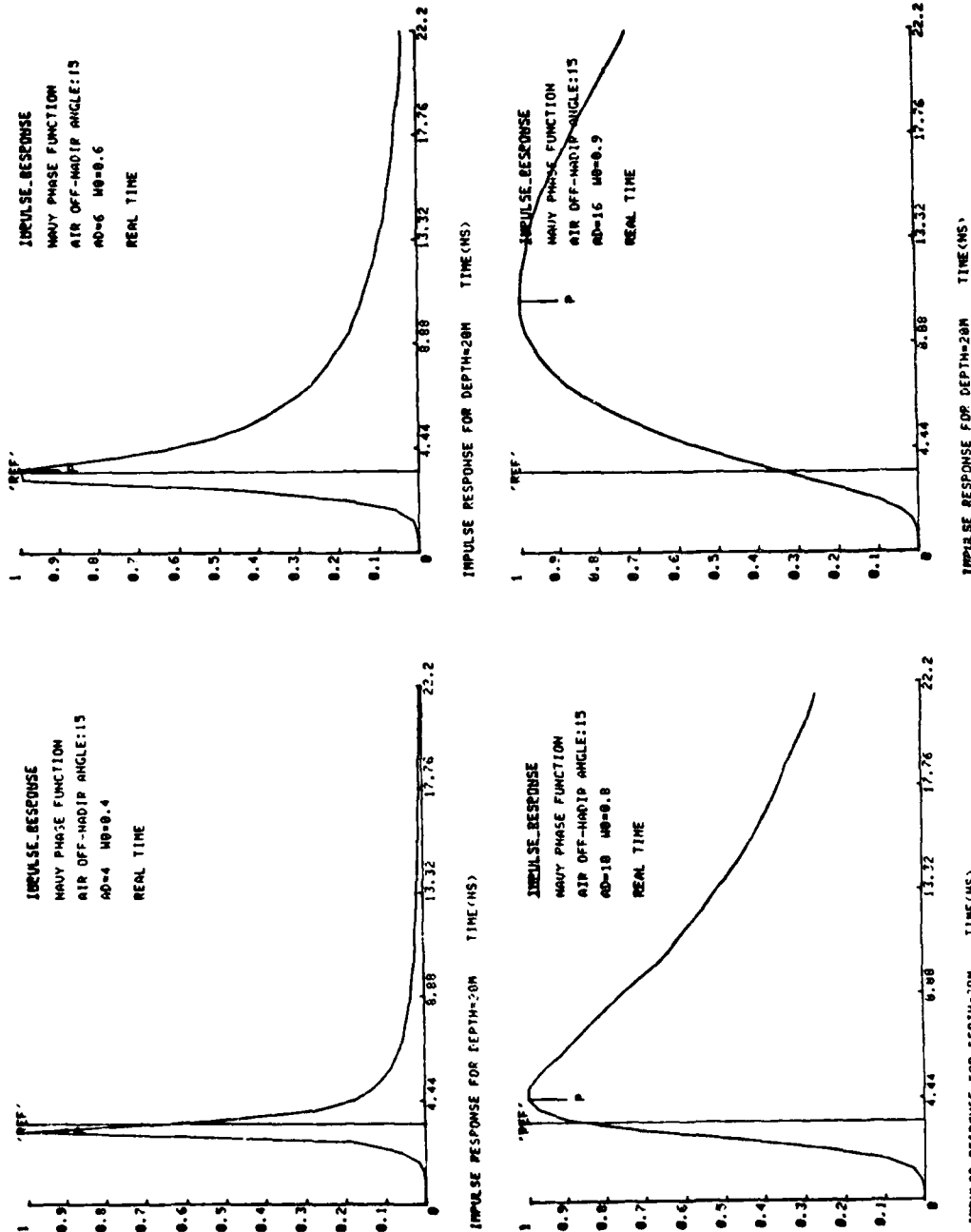
FIGURE 11. VARIABILITY AT CONSTANT KD (=3)
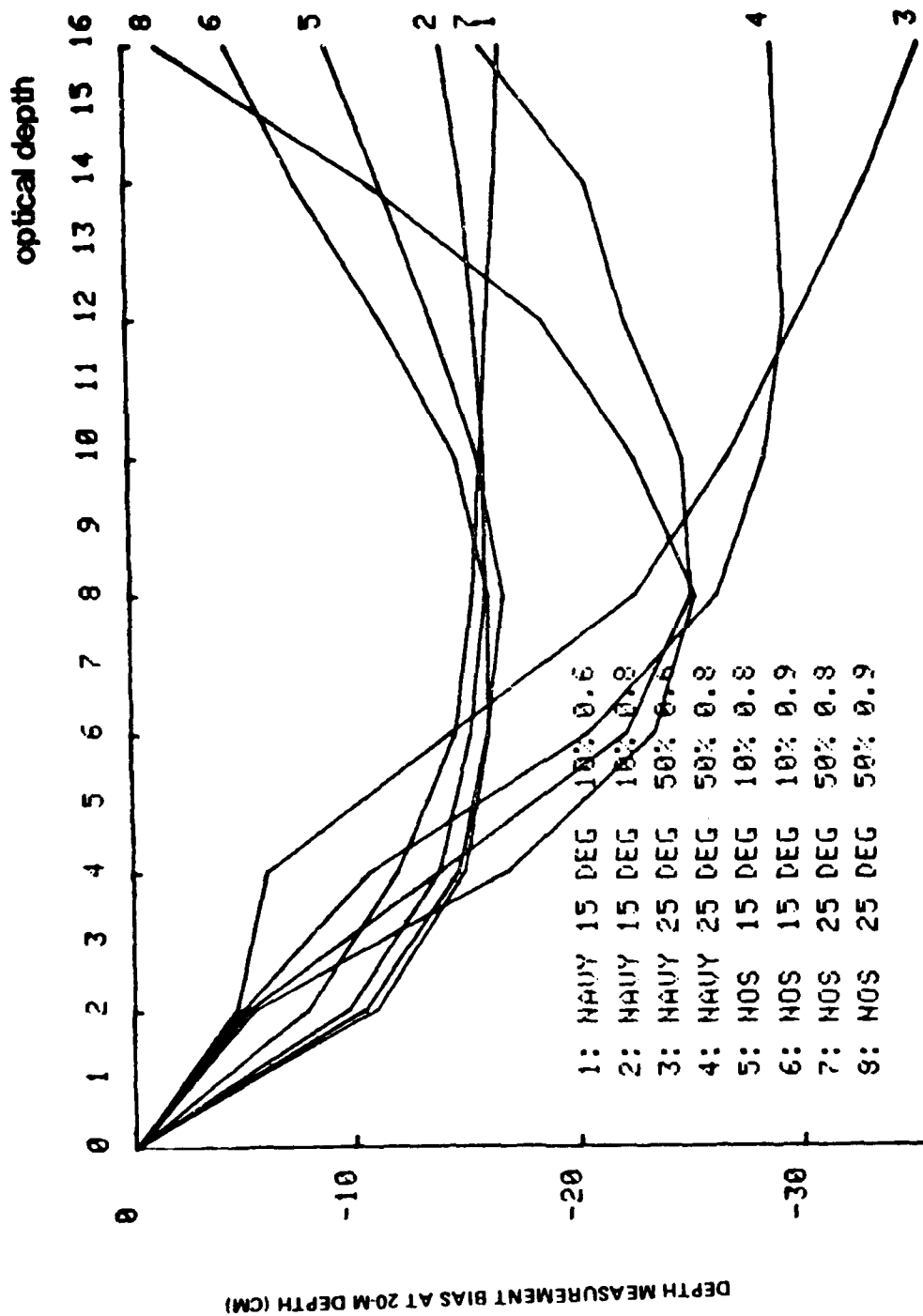
FIGURE 12. DEPTH MEASUREMENT BIAS (CM) VS. OPTICAL DEPTH AT A DEPTH OF 20 M

PAPER 23

THE LASER AIRBORNE DEPTH SOUNDER
AND CHARTING IN AUSTRALIA

by Mr. K.G. Burrows, Chief Cartographer

During 1979 the Hydrographic Office RAN introduced automated charting with the acquisition of the Autochart System. This initial acquisition was the first phase of a total project which will provide a specialised sea resources data bank. The system will provide management control over all hydrographic information for defence and maritime interests.

The initial programme establishes the cartographic capacity and specialised operations necessary for chart production. Current system operation permits the semi-automated compilation of charting information into a chart data base and the fully automated output of reproduction material for printing. The management capacity in the data base provides:

(i)   Time separation of detail to facilitate chart revision.

(ii)   Data structuring to facilitate derivative charting and multi-product extraction.

(iii) Special management of selected areas of interest to support rapid revision and auxiliary publications. e.g. A navigation light file automatically updates any chart and provides for the publication of a Light List.

Subsequent system development in applied cartography will enhance cartographic editing and product versitility.

The other arm of the Autochart project services the primary need for control over all hydrographic field information. The Hydrographic Data Base is being developed to control the accelerated increase in survey information arising from an increase usage of digital data acquisition systems. Specifically, it will be necessary to manage the flow of information generated by Laser Airborne Depth Sounder equipment.

Information arising from field operations will have been processed for signal comparision, position, tides, etc and consist of serial data in the form of x y z and classification. In order that a detailed area evaluation beyond the limits of individual or adjacent scans may be undertaken by a hydrographic surveyor, the serial information will be structured into area files on the Hydrographic Data Base. Facilities will then exist to support the surveyor in his evaluation and comparison with existing surveys, particularly in shoal or dangerous water.

System processor capacity necessary to evaluate ultra high data volume, precludes detailed evaluation in the field. The software necessary to evaluate the field results, is essentially the same as that required for general hydrographic information management on the Hydrographic Data Base. Information arising from other digital field systems will also be incorporated into the base. A program exists to transfer existing source information held in the traditional manual form, into the Hydrographic Data Base, despite the current technological limitations in this field. However, the rate of field acquisition with the Laser Airborne Depth Sounder may negate the necessity to incorporate much of the manually produced surveys.

The Hydrographic Data Base will provide the management capability over the continually growing volume and variety of field information. The manipulation of this basic information into the traditional navigation chart, and the growing demand for new and specialised cartographic products related to the sea will be a function of data base extraction and processing through the Autochart cartographic and publication facility.

Today this office does not simply produce charts, it manages the information on our sea environment and supplies an information service to the defence, scientific and maritime communities. Indeed, all organisations having a common interest in the sea and its resources will benefit from the expertise developed by the Hydrographer of the Royal Australian Navy.

HYDROGRAPHIC OFFICE
ROYAL AUSTRALIAN NAVY

CHART PRODUCTION ON THE AUTOCHART SYSTEM

SOURCE MATERIAL

LISTINGS   DIGITAL   TOPOGRAPHIC   HYDROGRAPHIC

DATA INPUT PHASE

Keyboard Entry

Direct Processing and Reassignment of Data Tags

Manual Digitizing and Data Tagging

Associated Data File

(Linked Address)

Allied productions (publications etc.)

Input Data Files

Verification Plot

DATA MANIPULATION PHASE

TRANSFORMATIONS – Adjust for projections and changes to horizontal/ vertical control

MERGING – Brings together all source models into the one file

DATA REDUCTION – Optimises the number of data points stored relative to largest scale requirement

DATA GENERALIZATION – Degradation of symbol detail relative to the scale of output document

TRANSFORMATION

MERGING

REDUCTION

GENERALISATION

OUTPUT PHASE

This is a sample of the final verification plot of the amalgamated models in the chart data base. This is used for editing purposes before the final cartographic quality plot is made.

FINAL EDITED PLOT

Sample of final cartographic product produced from reproduction material which is 100% automated

DATA BASE

Foul
Pearce Ful
Bay
Bay
Herring R?
Irwin Point
(82)

CARTOGRAPHIC PRODUCTS FROM THE AUTOCHART SYSTEM

DATA BASE

An objective of the Autochart system is 100% automation of graphic output. To achieve this objective the philosophy has been adopted that all symbology, linework, text and graticule required for charting will be software generated. Allowances can be made for automatic selection of detail for the final plot and for different cartographic output from the same data bank and file input.

PLOT CONTROL SOFTWARE

FEATURE SELECTION FACILITIES

MASTER LIBRARY

FEATURE SELECTION

WINDOW INCLUDE

WINDOW EXCLUDE
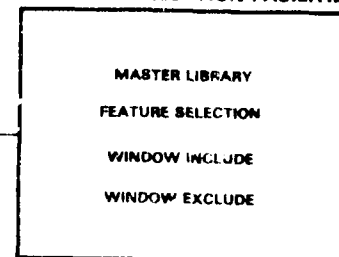
This facility permits the selection of specific groups of data concepts within or outside of defined geographical areas. The Master Library contains stored listings of standardised groupings which permits identification for output requirements. The Feature Selection option permits operator overruling of Master Library references - thus permitting flexibility to meet variations in the cartographic requirement.

SYSTEM DIRECTORY FACILITY

FEATURE TABLE

ASSOCIATED DATA FILE

This facility controls the system address for entry into the Symbol Generation Facility directly through the Feature table or indirectly through the Associated Data File.

The Associated File provides the information for cartographic output as well as management requirements and other derived products such as publications etc. This facility also permits the software generation of a variety of thematic mapping.

SYMBOL GENERATION FACILITY

SYMBOL TABLE

MATRIX TABLE

Symbol Product No 1
No 2
No 3
No 4
No 5
etc

Melbourne

Cape Otway

Wilsons Promontory

BASS STRAIT Kent Group

King I

Furneaux Group

TASMANIA

Sample Cartographic output requiring no manual intervention

Tr (Red I ts) (305)

Tr (Red I ts) 1/45

NORTH SYDNEY North

CITY OF SYDNEY

This facility permits all plotter instructions in relation to data position and according to final product type required through the Symbol Set facility. Thus a particular feature can be symbolised in many ways e.g. a lighthouse on a navigational chart is the conventional star symbol while the same feature when plotted for aircraft use may be a large dot.

To facilitate 100% automation of symbology all symbols are software defined on a matrix base which avoids the negative aspects of symbol aperture plotting. Simple round apertures are used to photo draw all software defined matrices permitting complete user flexibility in symbol definition. Autochart currently uses some 60% stored symbols including cartographic quality text.

A B C D E F G H J K L M N
O P Q R S T U V W X Y Z
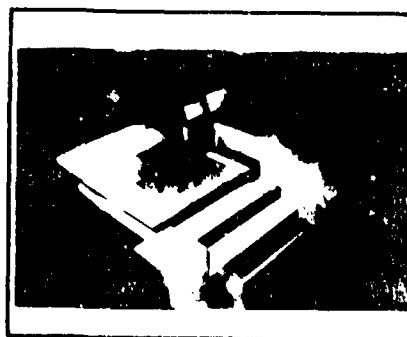
Sample of Matrix Generated Symbology

PAPER 24

SYSTEM CONCEPT AND RESULTS OF THE CANADIAN
AERIAL HYDROGRAPHY PILOT PROJECT *

D.B. Reid

Philip A. Lapp Ltd.
Toronto, Ontario, Canada

A.J. Dow

Canadian Hydrographic Service
Ottawa, Ontario, Canada

S.E. Masry

University of New Brunswick
Fredericton, New Brunswick, Canada

J. R. Gibson

Canada Centre for Remote Sensing
Ottawa, Ontario, Canada

ABSTRACT

The Canadian program for obtaining hydrogra-
phic data by aerial methods consists of merg-
ing laser bathymeter data with photogrammet-
ric depth data. The main deficiency of the
photogrammetric approach for bathymetric mea-
surements is that incomplete stereomodels can
occur in areas where little or no land appears.
This problem is overcome by using an inertial
navigation system (INS) hardmounted to the
aerial camera to provide the orientation para-
meters of position and attitude for each photo-
graph. In order to meet the high accuracy re-
quirement the INS and other complementary na-
vigation data is processed through a post
mission track recovery software package. The
photogrammeric depths are further improved by
merging them with the water-line height infor-
mation and the laser bathymeter depths using
a least-squares adjustment algorithm. The
photogrammetric compilation, depth measure-
ments, shoreline plots and laser bathymeter
integration is done in an analytical stereo-
plotter. This instrument provides an on-line
refraction correction necessary because of
the two media mode of operation. Results of a
recent pilot project indicate that the inte-
grated system is capable of depth accuracy in
the 0.5 to 1.0 meter range with horizontal
positioning accuracy of 1.0 meter or better.

1. INTRODUCTION

A new hybrid coastal mapping system has been
developed under the recent Canadian Aerial
Hydrography Pilot Project [1]. The system
combines laser radar (lidar) and photogrammet-
ric methods with precise aircraft track re-
covery techniques to obtain bathymetric plots
of shallow coastal and inland water areas.
The Pilot Project, which was initiated in

February 1979 and completed in August 1980,
was conducted by Philip A. Lapp Ltd. (PALL)
and a number of subcontracting companies for
the Canadian Hydrographic Service (CHS).
Project support, in the form of aircraft, sen-
sors and computer facilities was provided by
the Canada Centre for Remote Sensing (CCRS).

Aspects of system operation and performance
are reviewed in the following sections.
Section 2 provides an overview of system struc-
ture and its principles of operation. The
methods used to integrate the photo and laser
components of the system are reviewed in some
detail in Section 3 and a brief description of
a recent field trial is presented in Section 4.
Field trial results and a summary of conclusions
drawn from these results are given in Sections
5 and 6, respectively.

2. SYSTEM STRUCTURE AND PRINCIPLE OF OPERATION

The prototype coastal mapping system developed
in this project is a hybrid of the CCRS photo
bathymeter sensor package and the CCRS profi-
ling laser bathymeter. The system is made up
of 3 major subsystems (Figure 1):

- airborne subsystem for the acquisition of
  bathymetric and navigation sensor data

- main-frame computer and software for post-
  mission track recovery and reduction of
  laser bathymeter data

- analytical plotter for compilation of
  stereomodels and the measurement and plotting
  of water depths.

The structure and operation of the three sub-
systems are outlined in the following para-
graphs.
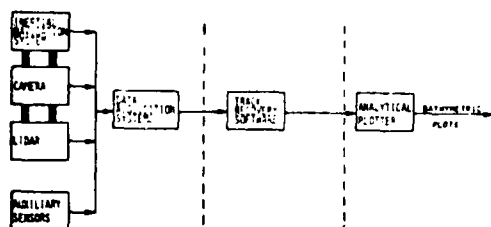
FIGURE 1 - STRUCTURE OF THE AERIAL
HYDROGRAPHY SYSTEM

2.1 Airborne Component

The airborne component consists of the CCRS
pulsed lidar bathymeter, a Litton LTN-51
inertial navigation system (INS) hardmounted
to the top of a Wild RC-10 aerial survey ca-
mera, and a number of auxiliary positioning
sensors including a barometric altimeter and
a microwave ranging system. The camera/INS
assembly and laser bathymeter are connected
by a rigid truss structure designed to reduce
dynamic deflections of the camera and laser
optical axes caused by airframe flexure and
vibration (Figure 2). The INS, camera and
auxiliary sensor set are each interfaced to
the CCRS airborne data acquisition system
(ADAS), and together make up the airborne
segment of the photo bathymetry system.
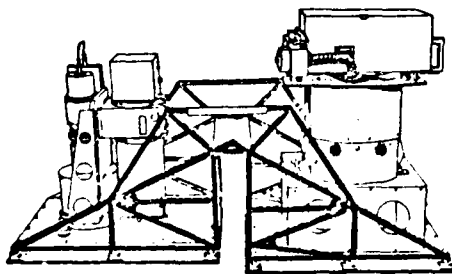
FIGURE 2 - LIDAR, SURVEY CAMERA AND INS

The RC-10 survey camera is equipped with an
f/4 Universal-Aviogon II wide-angle lense having
a calibrated focal length of 153 mm. The camera
produces 9" x 9" colour imagery of the survey
area, corresponding to a ground area of approx.
5 km^2 at a flying height of 1500 m (AGL).

The laser transceiver measures water depth and
slant range to the water surface at discrete
points along the aircraft track. The system con-
sists of a pulsed laser transmitter, two optical/
electronic receivers and a data recording sys-
tem. The transmitter is an International Laser
System NT-462 frequency - doubled Nd: YAG laser
which delivers up to 10 MW peak pulse power at
532 nm wavelength (green) and 15 MW pulse power
at 1064 nm (infrared). The output pulse power
width is 5 ns and the maximum pulse repetition
rate is 10 Hz. The 532 nm receiver, employed to
acquire depth data, consists of a 20 cm apera-
ture refracting telescope, a grid-gated photo-
multiplier tube (PMT) and a logarithemic ampli-
fier for compression of the dynamic range of
the PMT output signal. The 1064 nm receiver em-
ploys a photodiode detector to acquire returns
from the water surface (slant range). The two
receivers were designed and integrated with the
receiver by Optech Inc. Further details concer-
ning the operation of the CCRS laser bathymeter
can be found in [2].

The gimballed LTN-51 inertial navigator is
employed to measure the position and attitude
of the camera and laser sensors in real-time.
The CCRS system has been modified to provide
direct access, through the system's test port,
to navigation parameters stored in the compu-
ter memory. In addition, the gimbal synchros
which are normally supplied with this system
have been replaced with high-resolution dual-
speed resolvers which enable platform-indica-
ted attitude (roll, pitch and azimuth) to be
read to a resolution of 5 arc seconds and an
accuracy of better than 60 arc seconds.

The data provided by the INS are employed to
establish the orientation parameters of the
aerial photography for compilation of stereo-
models on the analytical plotter and to define
the geographic coordinates of the measured
photo and lidar depths on bathymetric plots.
The INS is not by itself sufficiently accurate
for this purpose. Consequently, a number of
auxiliary sensors are employed to provide
complementary position and attitude data for
correction of the INS-generated camera orienta-
tion parameters. These sensors include:

- precise barometric altimeter (Garrett AFTS-
  23), which provides auxiliary altitude data
  for damping of the INS vertical channel

- photo resections: Prior to a mission, widely-spaced clusters of photo-identifiable targets are deployed along the shores of the waters to be charted and surveyed to third-order or better accuracy. Following a mission, photos containing 3 or more targets are processed using photogrammetric resection methods to compute precise fixes of camera position and attitude [3]. These fixes are used to update the position and attitude parameters computed by the INS and so 'tie' the INS data into local control.

Since the survey and deployment of target clusters is time-consuming and expensive and, moreover, since the reliance on targets to obtain fixes can impose undesirable constraints on aircraft flight profile, the feasibility of using a microwave ranging system to reduce dependence on target clusters was investigated in this project. The particular microwave system employed was the Tri-sponder manufactured by Del Norte Technology Inc. This system determines the line-of-sight distance (slant range) from a master station installed in the aircraft to one or more remote transponders deployed at widely-space surveyed points on the ground by measuring the round trip times of pulsed, 9 GHz signals transmitted between the airborne and ground-based stations. The maximum range of the system is approximately 85 km.

2.2 Track Recovery

Following a mission, the airborne tapes containing recorded navigation and laser sensor data are transferred to CCRS's PDP-10 computer facility where the recorded data are stripped from the tapes and written to disc for subsequent processing. The recorded lidar returns are displayed, manually edited and then processed to produce a disk file containing time, slant range and slant depth measurements for each laser firing.

The position velocity and attitude data obtained from the inertial navigation system are processed with the auxiliary sensor data sets - including baro, laser, Trisponder and resection fixes - to remove time-correlated errors from the inertial data, and thereby generate precise estimates of the in-flight position and attitude parameters of the camera and laser sensors. An extensive track recovery software (TRS) package was developed to perform this function. This package implements recursive, optimal estimation algorithms - a Kalman filter and optimal smoother (see e.g. [4]) - which compute minimum-variance estimates of the inertial

system error state using a high-order mathematical model of the sensor error characteristics. Features of this package include:

- a data compression algorithm to enable high-rate input data to be processed at low filter/smoother cycle rates with minimum information loss

- implementation of the U-D factorized form of the Kalman filter and the modified Bryson-Frazier form of the optimal smoother. These algorithms provide significant advantages in numerical stability and efficiency over conventional filter/smoother mechanizations [5]

- complete flexibility in selection of the combination of sensor data sets to be processed, and the number and type of error parameters to be estimated in a given run of the package.

Further details concerning the structure and operation of the TRS package can be found in [1, 11].

Three data files constitute the principal outputs of the TRS package:

1. Flight Profile Parameter File, containing the time-histories of aircraft position, velocity and attitude parameters.

2. Camera File, containing the position and attitude of the RC-10 camera at each firing time referenced to an earth-fixed (geodetic cartesian) coordinate system.

3. Lidar File, containing selected lidar spot depths corrected for slant angle and re-fraction effects, and the geographic coordinates of each depth.

On the completion of the track recovery process, the camera and lidar files are transferred on magnetic disc to the analytical plotter where they are used in the generation of bathymetric plots.

2.3 Analytical Plotter Facility

The analytical plotter comprises a stereo-viewing instrument and a plotting table (flatbed plotter) each interfaced to a common control computer (Figure 3). The operation of the plotter in the aerial hydrography mode is summarized below.
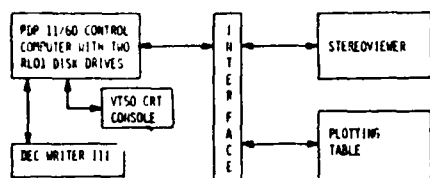
FIGURE 3 - HARDWARE COMPONENTS OF ANALYTICAL
           PLOTTER SYSTEM AT UNB

The camera file generated by the TRS package
is input to the system's computer to provide
control data for orientation of over-water
photography and positioning of measured water
depths. Pairs of overlapping photographs
acquired during a mission are placed, one pair
at a time, on the film carriages of the ste-
reoviewer. Each photo pair is then positioned
automatically under computer control to form
a stereo image and corresponding analytical
stereomodel of the bottom topography, where
the carriage coordinates for each photo and
the earth-referenced coordinates for each
stereomodel are determined from the appropri-
ate camera orientation parameters contained
in the TRS camera file. The depths of bottom
features appearing in each model are measured
by the instrument operator, and corrected in
real-time for the effect of refraction of the
imaging rays at the air/water interface [12].
The measured depths are adjusted (corrected)
off-line in the computer, as described in Sec-
tion 3, using redundant depth/height informa-
tion provided by the lidar depth samples (TRS
lidar file) and water-line points contained
within the stereomodel. In the final process-
ing stage the lidar and adjusted photo depths
are plotted automatically at the required
scale on the flatbed plotter to produce bathy-
metric plots of the survey area.

The plotter facility utilized in this pro-
ject is located at the University of New
Brunswick. This system was acquired from
OMI of America and was originally configured
with a special-purpose delay line memory
computer. During the initial stages of the
project, the computer was upgraded to a
general-purpose PDP 11/60 . ` a new inter-
face and associated photog.ammetric and
controlling software were acquired from OMI
and integrated with the system. Following
system integration, a number of new software
routines were developed specifically for the
coastal mapping application. These include:

- Transformation Software: used to compile
  a stereomodel on the plotter from the
  TRS-generated camera orientation para-
  meters

- Automatic Plotting Software: used to plot
  UTM grid coordinates and measured photo. and
  lidar depths at user-specified scale

- Depth Adjustment Software: for correction
  of measured photo depths using redundant
  information contained within a stereomodel.

3. SYSTEM INTEGRATION

An important result of the Pilot Project was
the successful integration of the photo and
lidar bathymeter systems to produce a hybrid
system which capitalizes on the complementary
characteristics of its two components.Comple-
mentary features of the systems include:
- Coverage and Spatial Resolution

  The lidar, being a pulsed profiling sensor,
  provides relatively poor depth coverage and
  spatial resolution. For an aircraft ground
  speed of 75 m/s and a pulse repetition rate
  of 10 Hz, the lidar will acquire spot depths
  at a spacing of 7.5 m along the aircraft
  track. On the other hand, the photo system
  provides broad, essentially continuous co-
  verage within the field of the stereo pho-
  tography. The coverage of each stereomodel
  is approximately 3 km^2 at a flying height
  of 1500 m and a photo overlap of 60%.

- Altitude Data

  The lidar slant range measurements, after
  appropriate transformations are made for
  aircraft roll and pitch, provide precise
  information on aircraft height above the
  water surface. The photo system requires
  precise altitude data for measurement of
  water depth.

- Sensitivity to Attitude Errors

  Roll and pitch data from the inertial system
  are employed both to establish the orienta-
  tion parameters of stereomodels on the ana-
  lytical plotter and to transform the mea-
  sured lidar depths into the local vertical.
  As the lidar provides a direct measurement
  of depth and since its optical axis is main-
  tained within a few degrees of the vertical
  on all flight lines, the accuracy of the
  transformed lidar depths is, to first order,
  independent of small errors in the INS-
  indicated attitude parameters (cosine re-
  lationship). On the other hand, depths mea-
  sured by the photo system contain error
  components which are directly proportional
  to (a) the horizontal distance of each depth
  sample from the origin of the stereomodel,
  and (b) the magnitude of roll and pitch
  errors - or tip and tilt - of the model
  with respect to the local horizontal (sine
  function). For example, a roll error of

only .05° will produce a depth error of about 1 m at the across-track extremities of a stereomodel for a flying height of 1500 m.

Integration of the photo and lidar system was achieved through development of the 3 major integration functions described below.

3.1 Camera/Lidar Boresighting

The camera/INS assembly and laser transceiver, mounted in adjacent bays in the CCRS DC-3 aircraft, were connected by a specially developed structure (Figure 2) designed to maintain the relative deflections of the optical axes of the lidar and camera within 1 arc minute. No attempt was made to physically align - or boresight - the optical axes of the two sensors. Instead, camera/lidar boresighting was performed analytically through software implemented in the TRS package. Here, estimates of the relative misalignments of the sensor optical axes were employed to correct the measured lidar slant ranges, lidar depths and computed depth coordinates to account for boresight misalignment effects. The required boresight misalignment angles were obtained by the method outlined below.

The analytical boresighting technique is based on the fact that the image of a lidar footprint will always appear in the same location in the camera focal plane irrespective of aircraft attitude and terrain topography, provided (a) the camera and lidar optical axes have a fixed orientation with respect to each other and (b) the relative displacement of the optical centers of the two sensors is small in relation to aircraft altitude. Under these conditions, a distinct, unambiguous image of the lidar footprint can be obtained by flying the camera/lidar assembly over dark terrain, jamming the camera shutter open and firing the lidar for a period long enough to ensure that the total energy reflected from the terrain is sufficient to expose the film. The coordinates of the centroid of the lidar footprint image with respect to the photo fiducial center can then be measured from the exposed film and used to compute the fixed misalignment angles of the two sensor axes using the simple geometric relationships shown in Figure 4.

A mission was flown on the night of July 9, 1979 over the Ottawa River to acquire data for camera/lidar boresighting. Mission altitude was approximately 1500 m (AGL). Atmospheric conditions were good but not excellent with the moon visible through a strong haze. The camera, loaded with high-speed black and white film, was operated with the shutter

$$\theta_x = \tan^{-1}\left[\frac{-r_x}{\sqrt{f^2 + r_y^2}}\right]$$

$$\theta_y = \tan^{-1}\left[\frac{r_y}{f}\right]$$

(f = camera focal length (153mm))
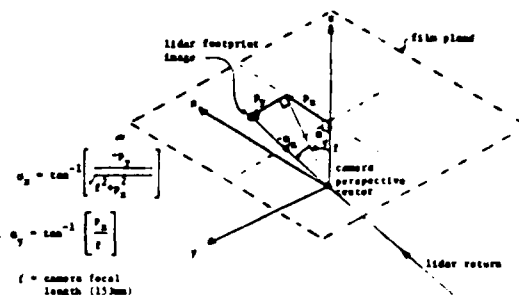
FIGURE 4 - LIDAR/CAMERA BORESIGHTING CONCEPT

open during the entire mission. The laser beam divergence angle was set to 2 milliradians and the pulse repetition rate was 10 Hz at 10 MW peak pulse power. A set of 7 photos were selected post-mission for analysis and measurement; the exposure times of these photos ranged from 3 seconds to 60 seconds (average of 20 seconds). An elliptical laser spot with a long tail, caused by reflection off the atmospheric aerosol, appeared in each of the selected photos (Figure 5). Measurements taken on these photos yielded average boresight misalignment angles of

$$\bar{\alpha}_x = 4.8 \text{ min}$$

$$\bar{\alpha}_y = 66.7 \text{ min}$$

These values were used in processing all lidar data acquired in the subsequent hydrography mission described in Section 4.
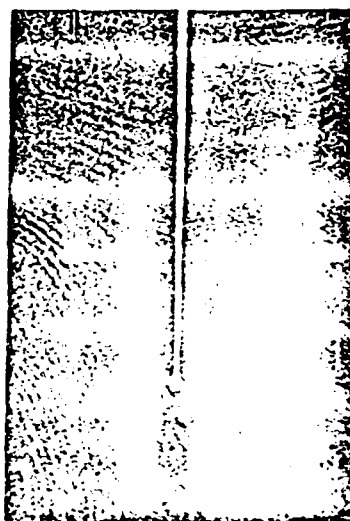
FIGURE 5 - PHOTOGRAPH OF LASER FOOTPRINT AND TAIL

3.2 Track Recovery Integration

In addition to the boresighting function performed by the track recovery package, a number of additional integration functions are carried out in the TRS software. These include:

- Lidar slant range data are employed to damp the vertical channel of the inertial system to provide precise estimates of camera altitude.

- The angle of incidence of each lidar pulse at the water surface is computed using the camera orientation parameters derived from inertial data, and is employed to resolve each lidar depth into the vertical accounting for refraction at the air/water interface.

- The geographic coordinates of each lidar depth are determined from the computed camera position vector and the computed lidar slant range vector.

All computations performed on lidar data were taken with respect to the camera coordinate system centered at the camera perspective centre (Figure 4).

3.3 Depth Adjustment

Three major factors contribute to the errors in the depths measured from a stereomodel on the analytical plotter. These are:

- error in knowledge of camera height above the water surface

- absolute errors in roll and pitch parameters computed by the TRS for the stereo photo pair

- residual relative errors in the model orientation parameters which remain after clearing of Y-parallax.

The first error source will produce a bias in the measured depths, the second will cause the stereomodel to be 'tipped' or 'tilted' with respect to the local horizontal producing depth errors which vary as linear functions of the position coordinates, and the third will generate depth errors which vary as quadratic functions of the position coordinates. Thus, the errors in measured depths can be represented by a function of the form [6]:

$$\delta d = a_0 + a_1 X + a_2 Y + a_3 X^2$$
$$+ a_4 XY + a_5 Y^2 + \nu \qquad (1)$$

where
$\quad \delta d$ is the depth error

$\quad a_i$ is a constant coefficient (i=0 to 5)

$\quad Y, X$ are the UTM northing and easting coordinates of the measured depth respectively

$\quad \nu$ is the random measurement error

Three additional sources of depth/height information which occur in a stereomodel are used to reduce or eliminate the depth errors caused by the factors described above. These are:

- water-line points at water/shore interface (water height is measured by tide gauge at the time of survey)

- heights of surveyed control points

- lidar depth samples

The procedure which has been implemented on the plotter to combine this additional information with the measured photo depths is outlined below.

First, the heights of water-line points and control points, where available in a stereomodel, are measured and stored on the system. Next, the measured photo depths which lie within a radius of 100 m of each lidar depth are interpolated to each lidar point as a function of distance and angle to the point. The distance interpolating function is of the form

$$\overline{d} = \sum_{i=1}^{m} (d_i / r_i^2) / \sum_{i=1}^{m} (1/r_i^2) \qquad (2)$$

where $\overline{d}$ is the interpolated depth, d_i is a measured photo depth sample and r_i is its radial distance from the lidar depth point.

When interpolation is complete, the measured heights of water-line and control points are differenced with the corresponding surveyed heights and, similarly, the interpolated photo depths are differenced with the corresponding lidar depth measurements to generate a vector of n depth difference samples:

$$\underline{\delta d} = [\delta d_1, \delta d_2, \delta d_3, \ldots \delta d_n]^T \qquad (3)$$

where superscript T indicates the vector transpose.

The depth difference samples are then processed by a weighted least-squares estimation algorithm to estimate the coefficients a_0 through a_5 of equation (1). The estimation algorithm

is of the form [7]:

$$\hat{\underline{a}} = [H^T R^{-1} H]^{-1} H^T R^{-1} \underline{\delta d} \qquad (4)$$

where superscript -1 indicates the matrix inverse, and

R = nxn diagonal matrix of weighting factors

$\hat{\underline{a}}$ = the 6x1 vector of estimated coefficient

$= [\hat{a}_0, \hat{a}_1, \hat{a}_2, \hat{a}_3, \hat{a}_4, \hat{a}_5]^T$

H = nx6 matrix which relates the coefficient vector $\underline{a}$ to the observed depth differences vector $\underline{\delta d}$

$$= \begin{bmatrix} 1 & X_1 & Y_1 & X_1^2 & X_1 Y_1 & Y_1^2 \\ 1 & X_2 & Y_2 & X_2^2 & X_2 Y_2 & Y_2^2 \\ \cdot & \cdot & \cdot & \cdot & \cdot & \cdot \\ \cdot & \cdot & \cdot & \cdot & \cdot & \cdot \\ 1 & X_n & Y_n & X_n^2 & X_n Y_n & Y_n^2 \end{bmatrix}$$

In the final step, all depths measured from the model are corrected as a function of their position coordinates using equation (1) and the coefficients estimated in (4). That is; a photo depth d having coordinates X, Y is corrected as

$$d_c = d - (\hat{a}_0 + \hat{a}_1 X + \hat{a}_2 Y + \hat{a}_3 X^2 + \hat{a}_4 XY + \hat{a}_5 Y^2) \qquad (5)$$

where d_c is the corrected depth.

The above procedure is performed on the plotter's control computer after all measurements have been taken from a given stereomodel. The full sequence is repeated for each model.

In the absence of control points (which are generally not available), the accuracy of the adjustment process, will depend primarily on the distribution of water-line points, and/or the number, distribution and accuracy of the lidar spot depths within the model. In particular, if little or no land is visible, the adjustment will rely entirely on lidar data. In this case, maximum adjustment accuracy would be achieved if lidar depth samples were to occur along the outer edges of the model as well as along the model centerline. This condition can be realized if the mission flight

lines are configured to provide more than 50% sidelap of the photography.

4. AERIAL HYDROGRAPHY MISSION

The aerial hydrography system was flown over a 20 km reach of the St.Lawrence River in southern Ontario on July 20, 1979. In parallel with this mission the CHS carried out a conventional survey of the area by launch and echo sounder to acquire reference data for evaluation of system performance. Three clusters of targets, at a nominal spacing of 7.5 km, were deployed along the river shore for purposes of photogrammetric resection, and two Trisponder remote stations were located approximately 15 km inland at a baseline of 23 km to provide auxiliary positioning information.

The aircraft flight profile consisted of a grid/racetrack pattern comprising a total of nine 20 km lines at a spacing cf approximately 600 m. The principal flight lines are shown in Figure 6, and were flown in the following sequence: 1E, 4W, 2E, 5W, 3E, 6W, 1E, 1W, 2E. Aircraft ground speed during the mission was approximately 75 m/s. Aircraft altitude (AGL) was 1500 m on the first 7 legs (1:10,000 scale photography), 2250 m on the 8th leg (1:15,000 scale) and 1000 m on the 9th leg (1:7,000 scale). The total mission duration was approximately 90 minutes, including a period of 10 minutes between lines 5W and 3E in which ADAS flight tapes was changed.

The RC-10 camera was loaded with Kodak 2445 colour film and fired at intervals of approximately 7 seconds corresponding to 80% along track overlap between contiguous photos. (The line spacing of 600 m provided approximately 75% sidelap). Camera aperature and exposure time were set to f 5.6 and 1/200th of a second, respectively. The lidar was fired at its maximum rate of 10 pulses per second with beam divergence angle set to 2 mr, providing one pulse every 7.5 m along-track and a footprint diameter at the water surface of approximately 3 m. Laser power was 4 MW peak pulse power.

Following the mission, photos containing 3 or more targets, well distributed throughout each image, were resected to produce a total of 51 fixes on camera position and altitude for track recovery processing and assessment of TRS performance.
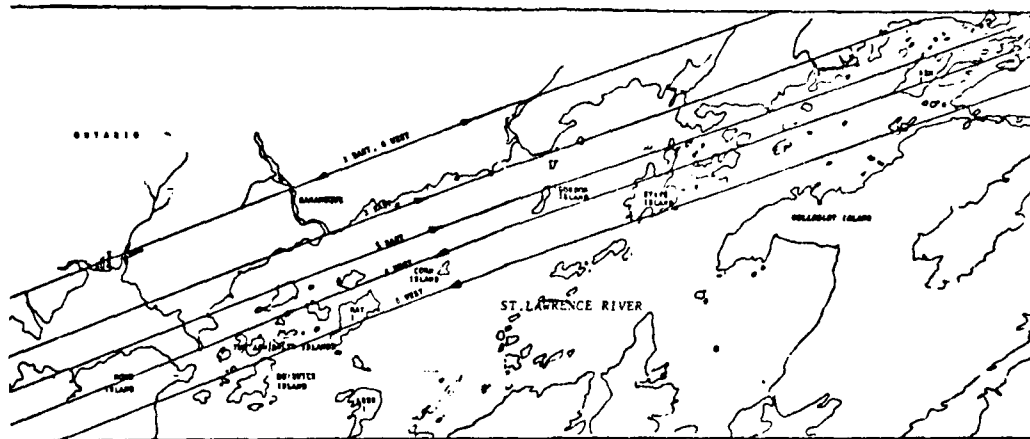
FIGURE 6 - FLIGHT LINES FOR AERIAL HYDROGRAPHY MISSION

5. RESULTS

A total of nine milar 1:5000-scale bathymetric plots were compiled from the St.Lawrence data set on the UNB analytical plotter (Figure 7). Each plot corresponds to a single 1:10,000-scale stereomodel having 60% overlap and covers an area of approximately 3 km^2. Photo and lidar spot depths were plotted on each sheet at a nominal spacing of 5 mm together with shoreline detail and the appropriate UTM coordinate grid. All plotted photo depths were adjusted via the least-square adjustment algorithm using available waterline and lidar depth information to remove systematic errors caused by residual orientation errors of the stereomodels. TRS position and attitude data obtained by processing INS, baro, lidar and Trisponder data and two resection fixes per line (average spacing of 15 km/line) were employed to compile the stereomodels on the plotter.

The performance cf the system is described in the following paragraphs in terms of coverage and penetration, depth accuracy and positioning accuracy.

5.1 Coverage and Penetration

A high level of water turbidity and extensive, dense weed growth in the survey area at the time of the flight trial severely limited the coverage and depth penetration of the system. Water transmission measurements taken by transmissometer gave an average value of 2 m^{-1} for the water attenuation coefficient,

compared to .5 to 1 m^{-1} for clearer Arctic and coastal waters. The CHS field party, which performed the conventional hydrographic survey of the test area, also experienced problems with weeds which, as described by R.C. Lewis in [8], tended to mask the true bottom from their echo sounders in areas of dense growth.

The maximum depth plotted by the system, which was consistent with CHS ground truth, was 4.4 m. This reading was taken by the laser bathymeter. The maximum depth acquired photogrammetrically was 4.2 m. Coverage at the nominal 5 mm depth spacing varied from plot to plot from a minimum of about 2% of total water area to a maximum of 40%. While penetration and coverage of the system were limited by poor water conditions, other experiments have shown that the system has a much greater depth capability. Previous tests carried out in Canada and the United States in clearer waters have demonstrated that depths exceeding 10 m can be sounded using photogrammetric methods [9, 10]. In a flight trial performed by CCRS in August 1979 over the Magdalen Islands in the Gulf of St. Lawrence, the lidar bathymeter measured depths up to 20 m or more in waters having an attenuation coefficient of .7 m^{-1} [2].

5.2 Depth Accuracy

Each of nine milar plots produced by the system were placed on a light table overlaying the corresponding CHS field sheets. Following registration of grid coordinates, depth soundings were selected at random in each plot and

compared with the corresponding reference depths obtained from the field sheets. A total of 357 valid depth differences were computed. It should be noted that since measured and reference depths did not generally coincide, it was necessary to interpolate the field sheet depths surrounding the measured depths to obtain a reference depth reading at the measured depth point. This interpolation was done by simple 'eyeballing' rather than by computational methods.

A statistical analysis showed that the observed depth differences were to first order, unbiased over the 9 plots having a standard deviation/RMS value of approximately .65 m. This statistic is a conservative measure of depth accuracy in that the reference depths used in computing the difference samples can themselves contain significant errors. Error sources which affect the accuracy of the reference depths include echo sounding errors, positioning errors of the echo soundings, and errors in interpolation of field sheet depths. Assuming an RMS error of .5 m in the reference depths due to these factors, an estimate of the actual RMS error in the measured depths

is computed as

$$\text{RMS Error in Measured Depth} = \sqrt{(.65)^2 - (.5)^2}$$

$$= .42 \text{ m}$$

A plot of the cumulative distribution of difference samples against sample magnitude is given in Figure 8. This plot defines the number of depth differences - expressed as a ratio of the total - whose magnitudes are less than or equal to a specified value. For example, Figure 8 shows that

- 68% of the depth differences have magnitudes $\leq$ .5 m

- 90% of the depth differences have magnitudes $\leq$ 1.0 m

- 95% of the depth differences have magnitudes $\leq$ 1.5 m

These results suggest that the distribution of depth differences can be approximated by a Gaussian or normal distribution function having zero-mean and a standard deviation of about .65 m.
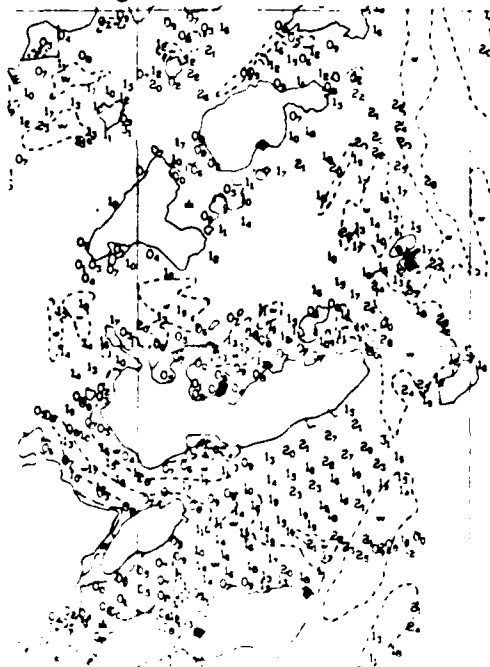
FIGURE 7 - PORTION OF DEPTH PLOT PRODUCED BY SYSTEM

(All depths reduced by .9 m to sounding datum)
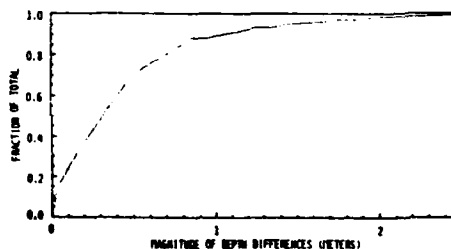
The majority of the plotted spot depths were obtained photogrammetrically,   that the accuracy figures given above app., by-in-large to the photogrammetric component of the system and are not necessarily indicative of the performance of the laser bathymeter. An in-depth quantitative analysis of lidar performance has not been carried out. However, the results of a limited error analysis and the experience gained in 'picking' spot depths from the lidar returns suggest that, overall, the performance of the lidar was not quite as good as the photo system. There are two reasons for this:

1. Due to the high level of water turbidity, the bottom returns appearing in the lidar traces tended to be rather indistinct and spread out causing degraded resolution.

2. In areas of dense growth, weeds could mask the true bottom from the lidar pulse causing the measured depths to fall short of the mark.

A sample of approximately 100 lidar spot depths was compared to reference depth information taken from the CHS field sheets. Approximately 56% of the depths were found to be corrected to within .5m, and 72% correct to within ± 1.0 m.

5.3 Positioning Accuracy

The accuracy achieved by the system in determining the geographic coordinates of plotted depths was analyzed on the plotter by measuring the coordinates of control points (targets) appearing in selected stereomodels and comparing the measured coordinates with those obtained by ground survey. A set of 8 different models were selected from 3 flight lines for analysis. These models were chosen so as not to coincide with the resection fixes processed by the track recovery system. After the models were set with the TRS-computed camera orientation parameters, the coordinates of the control points appearing in the models were measured and differenced with the corresponding surveyed coordinates. A total of 9 measurements were taken on 5 different targets to generate the 9 sets of difference samples given in Table 1.

MODEL NUMBER	FLIGHT LINE NUMBER	CONTROL POINT NUMBER	OBSERVED DIFFERENCES			
			EASTING (M)	NORTHING (M)	VERTICAL (M)	RADIAL LEVEL (M)
5868-5869	2E	27	.62	-.05	.23	.62
5869-5870	2E	27	.55	.45	-.02	.71
5869-5870	2E	28	.51	.61	-.15	.80
5870-5871	2E	28	.48	.11	.13	.49
5693-5695	5E	113	-.21	-.34	-.28	.40
5704-5706	5E	27	-.32	-.05	-.22	.32
5719-5721	5E	37	.85	.63	.62	1.12
5524-5526	4W	311	.32	.87	.57	.93
5525-5527	4W	311	-.18	.87	.34	.89
RMS OF SAMPLES	--	--	.49	.54	.34	.74

TABLE 1 - DIFFERENCES IN MEASURED AND SURVEYED COORDINATES OF CONTROL POINTS

Table 1 shows that the system is capable of very high precision in positioning ground points. In all cases, the measured northing, easting and vertical coordinates of the targets fell within ± 1 m of the corresponding surveyed values. The total horizontal (radial level) deviation of each measurement was typically less than 1 m with a maximum error of 1.12 m occuring in one model. The RMS deviations of the measurements taken over the set of 9 samples were less than .55 m per axis and .75 m total horizontal.

While this analysis is not fully comprehensive, these results, supported by the results of other accuracy tests presented in [1], indicate that the accuracy of the system in determining the coordinates of measured depths and ground points is better than 1 m RMS for a flying altitude of 1500 m. This corresponds to an RMS error of .2 mm at the plot scale of 1:5000.

With respect to plotting accuracy, the error in plotting the measured depths and shoreline detail on the bathymetric plots is a function of both the error in the measured coordinates and the positioning or pointing error of the flatbed plotter. Tests have shown that the maximum total pointing error of the UNB plotter is approximately .25 mm. Thus, the maximum RMS plotting error - computed as the root-sum-square of the RMS coordinate and pointing errors - is estimated to be less than .35 mm.

6. CONCLUSION

A fully-operative prototype system has been developed for aerial coastal mapping applications. Test results show that this system can measure and position water depths to a precision which is comparable to the bathymetric standards accepted by the CHS and the international community. Further, a study performed during the course of the Pilot Project demonstrated that the system can be both a cost-effective and a time-effective complement to conventional bathymetric methods for shallow water surveys [1]. Based on these results, Canada now plans to proceed with a program aimed at re-engineering and 'productionization' of the hybrid coastal mapping system. Elements of the program include:

- follow-on projects for assessment of system performance in clearer waters and for evaluation of certain system functions which would aid in the definition of a production system configuration

- formation of a industrial project team which would proceed with the build of a basic production system and apply the system to surveys of a commercial nature.

Although it will take some time before a production system is in place, the existing system prototype could be used, with the support of the Canada Center for Remote Sensing and other Canadian government agencies, for international demonstration missions and limited commercial surveys.

REFERENCES

[1] Aerial Hydrography Pilot Project, PALL Rept. # 5/F/80, prepared for the CHS, July 1980.

[2] Ryan, J.S., and O'Neil, R.A., "Field Trials of an Airborne Lidar Bathymeter", 19th Annual Canadian Hydrographic Conference, March 18-20, 1980.

[3] Thompson, M.M., ed., Manual of Photogrammetry, Third Edition, American Society of Photogrammetry, Falls Church, Va., 1966.

[4] Gelb, A., ed., Applied Optimal Estimation, MIT Press, 1974.

[5] Bierman, G.J., Factorization Methods for Discrete Sequential Estimation, Academic Press, New York, 1977.

[6] Masry, S.E., Report on Aerial Hydrography Project, Part I, prepared for the CHS, June, 1977.

[7] Sage, A.P. and Melsa, J.L., Estimation Theory with Applications to Communications and Control, McGraw Hill, 1971.

[8] Lewis, R.C., "The Weed Dilemma", 19th Annual Canadian Hydrographic Conference, March 18-20, 1980.

[9] Tewinkel, G.C., "Water Depths from Aerial Photographs", Photogrammetric Engineering, Volume XXIX, Number 6, Nov. 1963.

[10] Polier, M., "NOS Study of Applied Photobathymetry", Marine Geodesy, Volume 1, No. 3, 1978.

[11] Reid, D.B., Gesing, W.S., McWilliam, B.N., and Gibson, J.R., "An Inertially-Aided Aircraft Track Recovery System for Coastal Mapping", Position Location and Navigation Symposium, Atlantic City, N.J., December, 1980.

[12] Masry, S.E., and Konecny, G., "New Programs for the Analytical Plotter", Photogrammetric Engineering, Vol. XXXV, No. 12, Dec. 1970.

PAPER 25

The Hydrographic Software/Data Processing Subsystem
of the NOS Airborne Laser Hydrography System

David B. Enabnit
Engineering Development Office
National Oceanic & Atmospheric Administration
United States

The planned NOS Airborne Laser Hydrography system is heavily dependent on data processing. An enormous amount of processing will be required to compute accurate depths and positions and to maintain data quality control. Interactive data processing will be needed to allow a meaningful, manual examination of the data by skilled NOS hydrographers while still at the survey site. Finally, a sophisticated data management scheme will be required to control the approximately 6×10^5 sounding records gathered during a nominal four-hour survey mission.

To perform the required data processing, a Hydrographic Software/Data Processing (HS/DP) Subsystem will be built as an integral part of the NOS Airborne Laser Hydrography System (figures 1 and 2). This ground-based, trailered subsystem will provide the necessary hardware and software to process raw survey data through to final, certified, survey results.[1]

A preliminary description of functions to be performed by the HS/DP subsystem has been prepared as the first step in its development. This paper will list those functions, give some constraints on their performance, and present comments on how they might be implemented. Additionally, a brief description will be given on one means under consideration for dealing with the large number of soundings gathered by an Airborne Laser Hydrography System.
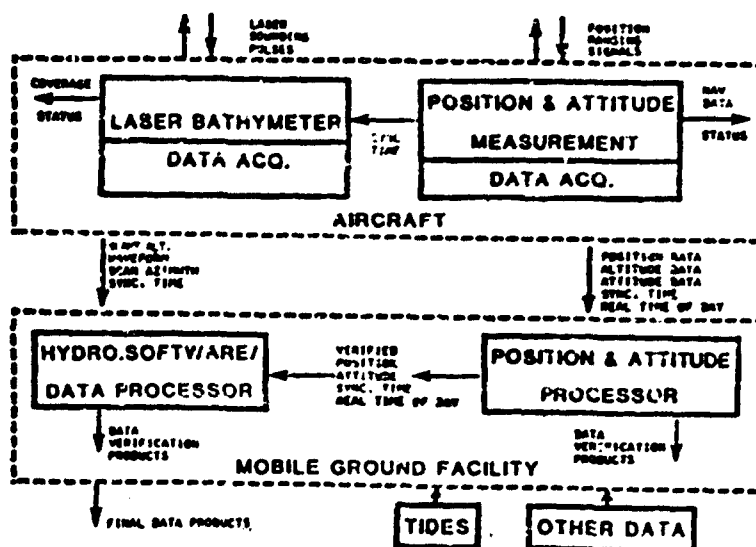
Figure 1. NOS Airborne Laser Hydrography System

---

[1] The aircraft position and attitude will be computed by the Position and Attitude Measuring Subsystem (PAMS) and provided to the HS/DP for use in computing the position of each laser sounding.
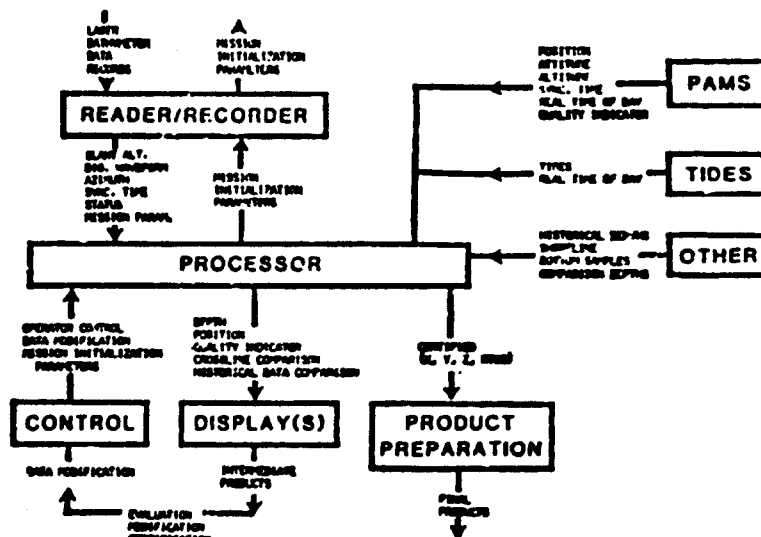
Figure 2.   Hydrographic Software/Data Processing Subsystem

The Hydrographic Software/Data Processing Subsystem has been separated into three configuration items which are capable of being developed simultaneously. Those configuration items are the preliminary, intermediate, and final processing. Preliminary processing will start with the raw, digitized, laser return waveforms, compute depth and depth correctors, merge depth and position, and perform some quality control functions. The preliminary processing will be fully automated and will operate using only properties of the data set itself. The intermediate processing is a quality control phase in which the survey party examines the data for completeness and accuracy. Intermediate processing is interactive and takes advantage of the hydrographer's experience. Final processing prepares the output products of the survey. The functions performed in each configuration item are discussed in the following paragraphs.

Configuration Item: Preliminary Processing (pre-flight)
Function: Flight tape initialization
Discussion: Performed in the Mobile Ground Facility with initialized tape hand
     carried to the aircraft. Initialization parameters are tape number, survey
     identification number, survey site, and Julian date. System and operating
     parameters (laser power, scan angle, field-of-view,...) will be recorded
     by the laser bathymeter on the flight tape and provided to the air crew in
     a written flight plan.

Configuration Item: Preliminary Processing (post flight)
Function: Flight tape duplication
Discussion: Immediate duplication of raw data tapes is a standard precaution at
     NOS. Duplicate tapes will be stored at a separate location until submission
     of the final survey results. The duplicates will then be recycled and the
     originals archived.

Configuration Item: Preliminary Processing (post flight)
Function: Accept preliminary processing setup parameters
Discussion: Reads manually input computing parameters. Present list of
    parameters includes:

> 1. All depth computing parameters not directly measured and
>   recorded by the laser bathymeter (e.g. % threshold, off
>   nadir angle, ...).
>
> 2. All depth corrector information not computed from the raw
>   data (e.g. table of depth correctors as a function of
>   bottom pulse width, ...).
>
> 3. Quality control editing parameters (acceptable S/N ratio,
>   acceptable % successful returns, acceptable pulse width, ...).

Access to these parameters will be limited, in most cases defaulting to pre-
established values. Such limited access is necessary to maintain consistency
in processing results and to defeat ad hoc changes by personnel who do not
realize the implications, for example, of the pulse detection threshold on bias.

Configuration Item: Preliminary Processing (post flight)
Function: Read laser bathymeter preflight calibration data, perform calibration
    calculations, and compute system based correctors.
Discussion: Calibration data is only on the first part of the first tape for each
    mission. Examples of preflight calibrations being considered are:

> 1. radiometric calibration,
>
> 2. ground-based differential range measuring to simulate depth,
>
> 3. optical alignment to assure accurate sounding positioning,
>
> 4. depth measuring stability test,
>
> 5. system noise,
>
> 6. laser power monitor calibration,
>
> 7. calibration of internal calibrator pulse,
>
> 8. gain calibration, and
>
> 9. digitizer calibration.

Results should be available for manual review before processing continues
and included in the final report of the survey.

Configuration Item: Preliminary Processing (post flight)
Function: Read raw laser bathymeter data in blocks
Discussion: The total amount of data from the laser bathymeter will be too great
    for the computer memory (10^{10} bits per four-hour mission). Reading,
    unpacking, and processing will be done in blocks where each block is one
    laser survey swath or an integer number of swaths.

Configuration Item: Preliminary Processing (post flight)
Function: Edit unacceptable returns
Discussion: Edits will be performed frequently to continually reduce the amount
      of processing that must be done in subsequent steps. Editing will be done
      by flagging rather than erasure so that edited data may be examined for
      required system modifications. Simple statistics will be kept on each edit
      to determine how often and why the edits were invoked. Such statistics will
      be included in the final survey report. Presentation of edited pulses and
      statistics will be an option. The edit criteria at this step are:

      1. low laser power,

      2. incomplete data record

            a. no synchronization time,
            b. no (or partial) waveform
            c. no slant altitude,
            d. no scanner azimuth,

      3. other, out-of-bounds housekeeping parameters.

Configuration Item: Preliminary Processing (post flight)
Function: Identify and process internal calibrator pulses and apply correction
Discussion: Every x pulses, the laser bathymeter will generate a calibration
      waveform instead of a sounding pulse. Characteristics of this waveform
      will be measured to monitor system performance or to provide correctors.
      Statistics on the calibration waveform will be compiled and documented.

Configuration Item: Preliminary Processing (post flight)
Function: Compute pulse locations on bathymetric waveforms
Discussion: Determines surface and bottom return pulse locations using predefined
      algorithms to find the correct pulses and compute their effective location.
      Finding the correct pulses will be done using the depth from previous
      soundings and pulse characteristics such as width. Computing their
      effective location will probably be done with a proportional threshold.

Configuration Item: Preliminary Processing (post flight)
Function: Zero depth test and computation
Discussion: In very shallow water, the surface pulse and bottom pulse will
      overlap. This case must be identified and flagged so that it will not be
      edited by the next function. A special algorithm using the width or
      amplitude of the combined pulses will be used to compute depth.

Configuration Item: Preliminary Processing (post flight)
Function. Edit unacceptable waveforms
Discussion: Edits by flagging those cases where a surface and/or bottom pulse
      could not be found and where zero depth test was failed. Statistics on the
      editing will be kept and documented in the survey report. Presentation of
      edited pulses and statistics for manual examination will be an option.

Configuration Item: Preliminary Processing (post flight)
Function: Compute waveform-based parameters
Discussion: Computes properties of waveform that will be used to determine depth
      correctors and quality indicators. Examples are: pulse amplitude, effective
      diffuse attenuation coefficient (K) from volume backscatter, background noise,

and pulse width. Some of these parameters, such as K, might have to be averaged over several pulses. Simple statistics on these parameters will be kept and documented in the final report. The statistics will be used to help monitor system performance and verify theoretical models of laser hydrography.

Configuration Item: Preliminary Processing (post flight)
Function: Edit unacceptable waveforms
Discussion: Edits by flagging those returns whose waveform based parameters exceed preestablished limits. Statistics on the editing will be kept and documented in the survey report. Presentations of edited waveforms and statistics for manual examination will be an option.

Configuration Item: Preliminary Processing (post flight)
Function: Compute apparent depth
Discussion: Differences time location of surface and bottom pulses; converts to depth.

Configuration Item: Preliminary Processing (post flight)
Function: Compute and apply depth correctors
Discussion: Uses waveform based parameters, apparent depth, and processing set-up parameters. All correctors will be temporarily kept as part of the record of each sounding. Depth must be corrected here before applying the wave corrector. Statistics will be kept on depth and correctors to help monitor system performance and verify theoretical models of laser hydrography.

Configuration Item: Preliminary Processing (post flight)
Function: Compute slant altitude
Discussion: Uses laser pulse time-of-flight from aircraft to sea surface. Location of the sea surface return pulse must be determined by the same means as was used for depth.

Configuration Item: Preliminary Processing (post flight)
Function: Edit unacceptable slant altitudes
Discussion: Edits by flagging those sounding records whose slant altitude is indeterminate or exceeds preestablished limits. Simple statistics on the editing will be kept and documented in the final report. Presentation of edited pulses and statistics for manual examination will be an option.

Configuration Item: Preliminary Processsing (post flight)
Function: Accept positioning data
Discussion: Reads verified aircraft position, attitude, synchronization time, real time of day and quality indicators from Position and Attitude Measurement Subsystems (PAMS). PAMS contractor will provide data and an algorithm such that accurate position and position can be computed by the HS/DP at the time of each sounding.

Configuration Item: Preliminary Processing (post flight)
Function: Compute and apply wave corrector
Discussion: Predicts slant altitude using true aircraft altitude and attitude from PAMS plus scan pattern parameters. Subtracts predicted from measured slant altitude. The difference is the wave height. Local mean sea level is computed as a short term, running average of wave heights. The difference between each wave height and local mean sea level is added to measured depth as the wave corrector. Statistics on wave height will be kept to estimate random, beam steering errors in depth.

Configuration Item: Preliminary Processing (post flight)
Function: Compute laser sounding position
Discussion: Merges depth and position record. Combines aircraft position and
     attitude with laser pointing direction to compute geographic coordinates
     of laser soundings.

Configuration Item: Preliminary Processing (post flight)
Function: Edit unacceptable roll and pitch records
Discussion: Edits by flagging those sounding records for which the aircraft
     exceeded preestablished values of roll and pitch. Large values of roll
     and pitch will cause unacceptable errors in depth and sounding
     position. Statistics on the editing will be kept and documented in
     the survey report. Presentation of edited records and statistics for
     manual examination will be an option.

Configuration Item: Preliminary Processing (post flight)
Function: Correct depth based on attitude
Discussion: Uses attitude, waveform based parameters, apparent depth, and set
     up parameters to compute a depth corrector. Statistics on the corrections
     will be kept and documented in the final survey report.

Configuration Item: Preliminary Processing (post flight)
Function: General edit
Discussion: Edit by flagging those soundings which:

   1. are outliers according to a preset, quantitative criteria
       (e.g., greater than 3 sigma from a local average).

   2. $Depth_i - Depth_{i+1} >$ a preset criteria.

   3. Soundings were taken over land.

   4. Running precision $\geq$ a preset criteria

   5. % successful returns $\leq$ a preset criteria

Configuration Item: Preliminary Processing (post flight)
Function: Read, edit, and correct tides data
Discussion: Tides data will be gathered by the Tides Measurement Subsystem (TMS).
     Existing TMS has frequent errors of data omission. Manual examination will
     be necessary to correct these errors. Record of corrections will be kept.

Configuration Item: Preliminary Processing (post flight)
Function: Compute and apply tide corrector
Discussion: Interpolates time, location, and tide among stations to compute
     depths at mean low water.

     End of preliminary processing. The result is a data set which has been
accepted on its own properties and involves no hydrographic knowledge. Each
sounding record is an extensive collection of depths, waveform characteristics,
correctors, positions and so forth. There is also a large body of statistical
summaries. All this data from each block (swath) under examination will be carried
forward into the Intermediate Processing.

Configuration Item: Intermediate Processing
Function: Intraswath sort
Discussion: Deconvolves the scanning pattern of the swath to a rectangular
        array.

Configuration Item: Intermediate Processing
Function: Intraswath data evaluation and edit
Discussion: Allows for manual evaluation of soundings. Displays depths in
        their proper, relative positions and draws simplified contours. Allows
        retrieval of the entire sounding record of any sounding chosen by the
        hydrographer. Computes and displays simple statistics on data being
        examined such as distribution of interpulse depth changes. Allows
        editing of sounding by flagging. Keeps statistics on editing for final
        report.

Configuration Item: Intermediate Processing
Function: Process next block (swath)
Discussion: Process a second block (swath) of data up to and including the
        immediately preceding step.

Configuration Item: Intermediate Processing
Function: Interswath data comparison and edit
Discussion: Allows for comparison and manual evaluation of two data sets in
        their region of overlap. Displays depths in their proper, relative
        positions and draws simplified contours. Distinguishes between soundings
        from different swaths. Allows retrieval of the entire sounding record
        of any sounding chosen by the hydrographer. Computes and displays
        statistics on the comparison such as distribution of depth differences
        at common locations. Allows editing of soundings by flagging. Keeps
        statistics on comparison and editing for final report.

Configuration Item: Intermediate Processing
Function: Purge
Discussion: Purges all data from the sounding record of one swath except the
        following: X, Y, D, RTOD, tide corrector, and swath identifier. The data
        to be purged is from the "older" of the two swaths being compared. Purges
        entire record of all soundings edited by flagging. This record is sufficient
        to produce the final survey product or to help locate any soundings if its
        entire record must later be recomputed. Quality indicators will be compiled
        for the final report. This purge is performed to reduce the amount of
        information being stored.

Configuration Item: Intermediate Processing
Function: Examine all data and edit
Discussion: Allows for manual evaluation of all depth/position data at once.
        Displays depths in their proper, relative position. Allows subsections
        to be enlarged until the scale is such that depths are printed for all
        soundings being displayed. Draws simple contours. Allows editing by
        flagging and keeps statistics on edited soundings for the final report.
        This evaluation is for completeness of coverage, anomalous features,
        and large scale errors (e.g., systematic tidal errors or swell).
        Position of gaps in coverage must be made available in order to schedule
        resurveys. All swaths must be processed before this step can be performed.

Configuration Item: Intermediate Processing
Function: Read and compare shoreline
Discussion: Shoreline will be provided digitally. A comparison will be made
      between the provided shoreline and the computed zero depth curve at mean
      low water. Manual evaluation will be allowed. Statistics will be com-
      puted and displayed on the comparison and included in the final report.
      Editing by flagging will be allowed.

Configuration Item: Intermediate Processing
Function: Read and compare historical data
Discussion: Historical depths and positions will be provided digitally. Automated
      comparison and manual evaluation of the two data sets will be performed.
      Will be able to enlarge subsections of the data until the scale is such
      that depths are printed for all soundings being displayed. Statistics on
      the comparison will be computed and displayed. Soundings may be edited
      by flagging and statistics will be kept.

Configuration Item: Intermediate Processing
Function: Read and compare contemporary comparison data
Discussion: The first laser hydrography systems will be undergoing "acceptance"
      throughout their useful lives. In order to build confidence in their
      performance, it is anticipated that a small test patch within a survey area
      will be sounded using sonar or lead lines as a check on laser performance.
      Automated comparison and manual evaluation of the two data sets will be
      performed. Statistics on the comparison will be computed, displayed, and
      documented in the final report. Will be able to enlarge subsections of
      the data until depths are printed for each laser sounding.

Configuration Item: Intermediate Processing
Function: Crossline comparison
Discussion: Crosslines are laser soundings gathered in swaths perpendicular
      to main scheme survey lines. They will be processed like all swaths of
      laser data. Automated comparison of crosslines will be made with the main
      scheme lines they cross. Manual evaluation of the overlap will be possible
      and statistics on the comparison will be computed, displayed, and reported.
      Editing by flagging will be allowed.

     Most of the examinations and comparisons in the Intermediate Processing are
quite similar, but operating on different data bases. It is hoped that only one
set of software will need to be developed for all of them. Those comparisons
and examinations are conceptualized as the graphic display of a pseudo three-
dimensional representation of the bathymetry or perhaps the difference in depth
measurement of two data bases. Using, for example, a light pen, subsections
could be selected for successive enlargement until actual depths are printed for
the displayed soundings. Selection of a specific depth (sounding) would then
present the entire record for that sounding.

     A consistent effort is planned to present simple statistics describing each
display. These statistics would be used by the hydrographer to locate those
displays that require his attention. For example, when comparing the overlapping
area of adjacent swaths, a histogram of the depth differences at locations common
to both swaths would be shown. If good agreement is indicated, then the hydro-
grapher can immediately proceed to the next section of compared data without
examining areas of good agreement. Without such a preselection tool, there would
be only 3-6 seconds to manually examine each displayed section of the bathymetry.

End of Intermediate Processing. The result is a data set which has been accepted on the basis of a hydrographic evaluation. The soundings which remain are considered as "certified."

Configuration Item: Final Processing
Function: Hydrographic sounding selection
Discussion: Reduces the total number of soundings by a factor of 100 or more. This selection chooses the minimum number of soundings needed to create a final cartographic product as nearly identical as possible to that which would have been created using the entire data set. Statistics will be computed on how well the reduced set approximates the total set. Statistics will be included in the final report.

Configuration Item: Final Processing
Function: Examination of the set of selected soundings
Discussion: Allows manual examination of the set of selected soundings. Allows exchange or insertion of non-selected soundings into the final set. Computes and displays depth curves. Prepares statistics on final, altered data set.

Configuration Item: Final Processing
Function: Prepare final survey products
Discussion: The final survey products are:

1. Digital tape of selected soundings (X, Y, D, RTOD, tides, swath ID).

2. Statistical summaries

3. Archival flight tapes

4. Survey results (area surveyed, density of soundings, final written report, ...).

Hydrographic sounding selection is performed to reduce the number of soundings that NOS must store in its digital data bank. It also reduces to a manageable number the soundings that the cartographers must deal with. The intent of this selection will be to preserve the final charting product. This means that a chart produced from the reduced set of soundings should be nearly identical to a chart produced from the total set of soundings.

NOS is presently developing an automated cartographic system. Among other things, this system will draw depth curves for charts and select the soundings to be printed. The implementation of a hydrographic sounding selection would thus be simple in principal: the cartographic sounding selection and depth curve program would be run on the total data set; soundings will be intelligently discarded and the cartographic selection and depth curve program run on the reduced set; the two sets of depth curves and selected soundings would then be compared. If the results were sufficiently similar, the process is finished. Clearly there are some poorly defined terms such as "intelligently discarded" and "sufficiently similar" which will determine how easy this principal is to implement.

The approach proposed above has several advantages:

1. It preserves the final charting product.

2. It honors the actual soundings.

3. One can quantitatively determine the distortion in the final product which is caused by the hydrographic sounding selection.

4. The cartographic sounding selection and depth curve algorithms are being developed by someone else and will be "officially approved" by NOS.

Other approaches for hydrographic sounding selection have been proposed such as optimal smoothing (the Navy/DMA approach) or local averaging. These were determined to be unacceptable for the following reasons:

1. They do not honor the actual soundings.

2. They will average actual changes in depth as well as system noise.

3. They will produce an unknown distortion in the final product.

4. They provide no advantages other than simply reducing the number of soundings.

It must be remembered that "optimal" techniques are only optimal in some narrowly defined mathematical sense such as minimum variance. They are not necessarily optimal for the production of nautical charts.

THE HYDROGRAPHIC AIRBORNE LASER SOUNDER

DATA PROCESSING

H. J. Byrnes
D. C. Bright
L. Greczy
M. W. Houck

U.S. Naval Ocean Research and Development Activity

Bay St. Louis, Mississippi

Presented at the

LASER HYDROGRAPHY SYMPOSIUM

Salisbury, South Australia

1 October 1980

THE HYDROGRAPHIC AIRBORNE LASER SOUNDER

DATA PROCESSING

H. J. Byrnes
D. C. Bright
L. Greczy
M. W. Houck

U.S. Naval Ocean Research and Development Activity

Bay St. Louis, Mississippi

ABSTRACT

The Naval Ocean Research and Development Activity (NORDA) has
been given the responsibility for formulating data collection
rationale, developing post-mission data reduction techniques and
preparing data processing software for the Hydrographic Airborne
Laser Sounder (HALS) system which is being developed by NORDA
under the sponsorship of the Defense Mapping Agency (DMA).
Stringent vertical accuracy requirements, coupled with large errors
inherent in the HALS measurements, preclude individual laser ob-
servations from standing alone as depth measurements. Consequently,
statistical processing is required; and statistical processing
implies frequency response. The ability of the HALS system to de-
tect submerged objects will be a function of the size of the object
and the spatial distribution of the laser observations. Careful
planning will be required to ensure that data is collected and
processed at the proper frequency response to guarantee detection
and delineation of all features of interest. Laser slant range
measurements acquired by the system will be contaminated by biases
and random errors which must be removed or minimized to assure
final product accuracy. The magnitudes of spatially and/or tem-
porally correlated biases will be estimated and/or calculated and
removed mathematically leaving predominantly random errors. A
two-dimensional optimal filter capable of dealing with horizontal
positioning and depth errors simultaneously will be used to handle
the random errors. The optimal solution uses data redundancy to
accept or reject individual observations on a statistical basis.
The filter will analyze slant depth measurements, weight the data
in favor of the shallowest depths and process the observations into
an equally spaced grid of depths. The depth grid will be accompanied
by a grid of data quality designators which will define the end
product accuracy. Tidal corrections will be applied to the gridded
data during shipboard processing. Data verification and evaluation,
final editing, and smooth sheet plotting will also be done on board
the survey ship. Error analyses were performed and data processing
routines were exercised to determine the expected raw measurement
and end product accuracies. The magnitudes of the raw measurement

errors were found to be quite large but were reducible to accept-
able levels by applying bias corrections and performing multipulse
processing.

INTRODUCTION

The Naval Ocean Research and Development Activity (NORDA)
is currently being funded by the Defense Mapping Agency (DMA) to
develop a Hydrographic Airborne Laser Sounder (HALS) capable of
collecting depth information in shallow coastal waters. The HALS
development involves not only design and fabrication of hardware,
but also the formulation of data collection rationale, the develop-
ment of post-mission data reduction techniques and the preparation
of data processing software. It is these aspects of the program
that are discussed in this paper.

The individual laser observations acquired by the HALS system
will have large magnitudes of uncertainty associated with them due
to certain biases and random errors inherent in the collection
hardware and in the laser measurement. This fact, coupled with the
stringent vertical accuracy requirements of the system, precludes
individual laser observations from standing alone as depth measure-
ments. The combination of these factors establishes the need for
some type of statistical processing where redundancy is the key to
meeting the accuracy requirements. Consequently, optimal filter
techniques will be applied to the HALS data processing whenever pos-
sible.

The initial version of a model for processing laser survey data
entitled "Model for Optimal Laser Surveying," was developed in 1977
by S. L. Fagin Associates. It contained all the major processing
elements required to reduce raw laser slant range observations to
a grid of depths. Processing of simulated survey data with this
m .el indicated that the computational load would be too great for
the NAVOCEANO shipboard computer. To facilitate computational speed,
the optimal model was broken down into two submodels. One portion of
the model deals with resolving laser slant ranges from the aircraft
to the sea surface. The other deals with resolving slant ranges
from the surface to the bottom, i.e., determining depth. The portion
of the model dealing with the aircraft to sea surface slant ranges
has been tested with real field data acquired by the National Aero-
nautics and Space Administration's (NASA) Airborne Oceanographic
Lidar (AOL). The results of those tests and more details about the
modeling are reported in Byrnes and Fagin, 1978, and Byrnes, 1979.

DATA COLLECTION RATIONALE

The primary application of the HALS system will be for charting
shallow coastal waters and shoal areas. However, the system will
also be expected to detect small hazards and obstacles to naviga-
tion. A question thus arises as to the optimum data density for a
HALS survey. Since the purpose of the survey is to ensure safety
of navigation, the shoalest depths in an area should always be
recorded. Davis, 1974 discussed the selection of the optimum spacing
for survey track lines. He indicated that data density should be
controlled by the amount of expected bottom variation and the amount
of tolerable sample error. Therefore, the HALS data collection
density should be determined by expected bottom roughness, the size

of the smallest targets to be detected, and the amount of sample
error that can be tolerated.

The ability of the HALS system to detect submerged objects
is a function of the size of the object and the spatial distribu-
tion of the laser soundings. These two factors define the fre-
quency response (i.e., sensitivity) of the system. The spatial
distribution of the observations is dependent on the off nadir scan
angle, the pulse repetition rate, the aircraft altitude, and the
aircraft forward velocity. Since the maximum laser pulse repeti-
tion rate is limited to 400 Hz, the only methods of making the
HALS survey more sensitive to small bottom features are: (1) nar-
rowing the swath width of the survey, (2) flying at a lower altitude,
and (3) flying at a slower speed. The size of the bottom features
is important in defining frequency response because individual
laser observations cannot stand alone as depth measurements. Con-
sequently, the HALS survey data must be reduced by applying appro-
priate statistical processing techniques to take advantage of data
redundancy. However, statistical processing implies a minimum
frequency response for the processing which, in turn, implies non-
sensitivity to bottom features smaller than a given size. These
factors, in combination with some knowledge of expected bottom slope
and probability of submerged obstacles, must be considered during
mission planning.

The versatility of the HALS system is significantly enhanced
by having these multiple controls over the frequency response
during both the data collection and the data reduction process.
The only comparable method available to soundboats for adjusting
frequency response is by varying survey line spacing. It thus
becomes apparent that HALS "swath" surveying is an important step
forward compared to soundboat "profile" surveying. However, care-
ful planning of HALS surveys is imperative to ensure optimum utiliza-
tion of, and maximum benefit from, the system.

DATA PROCESSING

During a typical HALS survey mission, laser slant range informa-
tion, positioning information, heading and attitude information, and
general housekeeping information will be recorded on tape cartridges.
Upon completion of a survey, the data tapes will be removed from the
helicopter for post flight data reduction on the Naval Oceanographic
Office (NAVOCEANO) shipboard computer. A flow chart outlining the
post flight data reduction procedure is shown in Figure 1. The
initial step of the data reduction process is to read and deblock
the data tape and merge the laser slant range information with
external environmental inputs. At this point the HALS observations
contain errors from multiple sources. These sources include: (1)
errors in the determination of the aircraft's true position, altitude
and attitude, (2) inaccuracies in determining the true shape of the
sea surface, and (3) contamination of the laser slant range measure-
ments by various environmentally caused biases and random errors. In
order to deal with these multiple error sources, optimal filter tech-
niques are applied to the data to isolate each of the errors. The op-
timal solution deals with depth and horizontal position errors simul-
taneously. However, before the optimal filter can be applied, the
environmentally caused biases must be removed from the laser observations

Provisions have been made in the HALS hardware to digitize
complete laser return wave forms at low pulse repetition rates.
(2 - 10 Hz). These wave forms will be examined to determine system
amplitude response and environmental correction parameters. The
amplitude response and environmental correctors will be used in
conjunction with the observed incidence angle to form bias correc-
tion estimates which will be applied to the laser slant ranges.
Since these are fixed or slowly varying temporal and/or spatial
biases, the sparsely sampled bias correctors can be applied to
all the rapidly sampled undigitized laser observations in the im-
mediate space/time domain. Initially, the bias estimators will be
interpolated from a stored table which has indexes relating to water
clarity, depth, and incidence angle. The table will be collated
from empirical data gathered early in the HALS calibration phases.
This portion of the processing is expected to change as more is
learned about the nature of the biases and about the system response
to the environment. In this regard, a contract has been let with
EG&G in Washington, D.C. for the purpose of studying, via simulation,
the expected HALS system response to the environment. The results
of the studies are expected to lead to the development of bias cor-
rection equations. When the bias correction equations can be shown
to, or can be adjusted to fit an adequate amount of empirical data,
the table/interpolation process will be replaced by a direct calcula-
tion method. The advantage of bias correction equations will be
greater applicability to changing environmental conditions which
exceed those conditions for which empirical data is available.

After removing the bias from the laser slant ranges, the measure-
ment from the aircraft to the surface of the water is processed in a
minimum variance solution. The purpose of this process is, primarily
to determine wave corrections and altitude above the mean sea surface,
and to statistically reject observations which contain excessive
error. This is the first application of rejection criteria in the
processing. When an observation fails the "aircraft to sea surface"
criteria, the accompanying depth measurement is also rejected because
an acceptable wave correction cannot be calculated for that particular
observation.

The minimum variance solution is in the form of an optimal filter
with state vectors representing aircraft altitude, roll, pitch, and
sea surface. Projection equations are executed for a given situa-
tion of roll, pitch, and altitude to provide an estimated slant
range from aircraft to sea surface. The estimated slant range is
subtracted from the observed slant range, and the result becomes
an observation. The observation is then processed through error
propagation equations updating the roll, pitch, and altitude at each
laser return. The system can be modeled to provide roll and pitch
directly from the laser measurements (Byrnes and Fagin, 1978) or
can be modeled to track error in roll and pitch of an inertial unit.
The major advantage of using an inertial attitude measurement unit
is that the attitude information derived from it is more reliable
when a portion of the HALS survey pattern falls over land.

Basic assumptions included in the model are that aircraft motion
varies very slowly while the state vector representing waves varies

rapidly because of the sample pattern generated via the scanning HALS mirror. This separation in correlation time is a very important factor in the separation of the waves from the other vectors of the system. The minimum variance solution on the "aircraft to sea surface" slant ranges will also provide an excellent detection system for any systematic errors generated by misalignments occurring in the manufacture of the scanner. Misalignment errors will show up as oscillations correlated with scan rate.

Upon completion of the "aircraft to sea surface" slant range processing, a wave correction is applied to each slant depth, and a position on the sea surface relative to the aircraft is supplied. The slant depth, still contaminated with random error as well as residual bias, is used to compute a somewhat noisy position on the sea floor. A two dimensional optimal filter which deals with both depth error and horizontal position error simultaneously is now applied. This optimal filter takes the form of a grid where all the laser depth observations within the four immediately adjacent cells are used to calculate depth estimates at grid intersections. The optimal gridding is conceptually similar to polynominal surface fitting, except that we can select any grid interval we wish and can impose any bottom slope restrictions without changing the computer processing load. (The spacing of the grid and the imposed bottom slope control defines the frequency response of the processing). For any given swath of data, the post processing frequency response can be increased merely by assigning smaller values to the grid interval. The penalty for this, though, is a reduction in accuracy since accuracy is a function of the total number of observations incorporated into any given grid estimate.

As with any processing based on optimal filter theory, a co-variance matrix is the integral element which governs the weighting and incorporation of individual observations into the data set. Each grid estimate is represented by a diagonal term of the co-variance matrix all the way through the grid processing. At the end of the process, the covariance matrix reflects the number and proximity of observations incorporated into the individual grid estimates and can be used as data quality indicators. A grid of quality designators accompanies the grid of depth estimates and can be used to evaluate the overall survey quality and/or the degree to which agreement can be expected between depths derived from sound boats and depths determined by HALS. The covariance matrix comes into play in establishing rejection criteria when incorporating data into a grid. As more data is incorporated into the grid, the standards for incorporating the next observation become more strin-gent, and a new observation must be more closely in agreement with the bottom which has been established or it will be rejected. The evaluation takes into account bottom slope, position error, and depth measurement error, all simultaneously. Depth measurements which have been rejected will be analyzed to determine if any pat-tern of rejection exists. If many rejections occur in some particular location, the area may require resurveying at a higher frequency response (Byrnes, 1979).

Once the depth grid is generated, tidal corrections will be applied to the gridded data. The data will be evaluated for agreement between HALS survey lines and HALS cross-check lines. The HALS data will be further verified by comparing it to overlapping ship or sound boat data to determine if any residual biases exist. Final editing will be performed, and smooth sheets will be produced on the shipboard plotters. (Bourquin and van Norden, 1980)

DATA REDUCTION ANALYSIS AND RESULTS

The final accuracy of the HALS depth measurements will be dependent on the precision with which the HALS hardware can make slant range measurements, on the magnitude of the various environmentally caused errors, and on the ability of the data reduction algorithms to isolate and reduce/remove these errors. In an effort to define the expected system accuracy, several error analyses (Miller, 1980, and Guenther and Thomas, 1980) were performed to determine the contribution of various error sources to the overall HALS error budget. In addition the proposed data processing routines were exercised by NORDA (using real and simulated data) to determine how well the optimal process can handle the various errors. The results of these error analyses and tests were combined to form a projected HALS error budget which is summarized in Table 1.

There are two basic types of errors which comprise the HALS error budget; they are: biases and random errors. Biases are fixed and/or slowly varying errors which can be spatially and/or temporally correlated. The magnitude of the raw biases can be quite large, but can be reduced to acceptable values by applying appropriate estimates and processing techniques. The residual biases listed in the error budget result from an inability to completely correct for displacements from the true datum. Analysis of the bias sources indicates that they can be corrected to $\pm$ 10.7 cm after processing. The errors listed in the error budget as random errors vary rapidly through time and/or in space and can be treated with "normal distribution" statistics. The magnitude of the raw random errors was computed to be 29.3 cm (RSS), but results of tests using the optimal processing technique indicate that these errors can be reduced to 5.6 cm by multipulse processing. The magnitudes of the errors listed in the error budget were computed for a maximum water depth of 20 meters, a scan angle of 25 degrees, and average wave conditions encountered in sea state 3. It should be noted that the magnitudes of the raw errors decrease while the ability to correct for errors improves as the water depth, scan angle and wave height decrease.

The optimal filter processing algorithms were exercised to determine how much benefit could be derived by the multipulse processing/gridding approach. Figure 2 shows the quality of information that can be expected from the optimal gridding routine for various grid intervals and scan angles. Basically, the amount of reduction in the random errors is a function of the number of observations that go into a particular calculation. The number of observations is dependent on the grid spacing and the initial

survey parameters (i.e., aircraft altitude, aircraft speed and
scan angle). The results of the optimal gridding exercises approach
the theoretical bounds predicted by "normal" statistical theory,
but never attain the predicted minimum values. This is because the
processing routine allows for varying bottom slopes and horizontal
positioning errors to be incorporated into the solution.

The quality of the final (processed) depth information is
dependent on the resultant random error and the residual bias.
It should be pointed out that while taking advantage of data re-
dundancy can help reduce random errors, data redundancy does not
affect the magnitudes of the residual biases. The question thus
arises as to proper technique for combining the resultant random
errors and the residual biases to determine the accuracy of the
final product. According to statistical theory, the final accuracy
can be determined by shifting the mean of the Gausian distribution
by an amount equal to the magnitude of the residual bias and com-
puting the error bounds for given confidence intervals (Guenther,
1980, and Ott, 1977). This calculation can be made using the
"cumulative normal distribution function," $\phi(z) = 1/\sqrt{2\pi} \int_{-\infty}^{z} e^{-t^2/2} dt$
(Hald, 1952). These computations were made for several confidence
intervals using a total allowable error of 28 cm, which is the
amount of error allowed by the HALS specifications. The calculations
showed that for a residual bias of 10.7 cm and a resultant random
error of 5.6 cm, the final product error would be less than 28 cm
better than 99.73% (3σ) of the time.

REFERENCES

1. Bourquin, L. B., and van Norden, M. F., (1980). "The Hydrographic Airborne Laser Sounder : "A planning and Operational Scenario (II)." NAVOCEANO Report, NSTL Station, MS.

2. Byrnes, H. J., (1979). "Operating Scenario for a Hydrographic Airborne Laser Sounder (HALS)." NORDA Technical Note 34, NSTL Station, MS, 30 p.

3. Byrnes, H. J., and Fagin, S. L. (1978). "Optimal Filtering and Analysis of Scanning Laser Data." NORDA Technical Note 24, NSTL Station, MS, 20 p.

4. Davis, T. M., (1974). Theory and Practice of Geophysical Survey Design. NAVOCEANO Reference Publication 13, Washington, DC, 135 p.

5. Fagin, S. L. Associates (1977). "Model for Optimal Laser Surveying." Prepared for NAVOCEANO, Contract No. N68463-76-C 007.

6. Guenther, G. C. (1980). Personal conversations concerning appropriate techniques for statistically combining random errors and biases.

7. Guenther, G. C. and R. W. L. Thomas (1980). "The Effect of Multiple Scattering in Water on Airborne Lidar Bathymeter Accuracy." Results of modeling presented at HALS System Design Review, (Unpublished).

8. Miller, M. G. (1980). "HALS System Timing Errors and Variable Biases." AVCO Everett Research Laboratory, Inc. Report, Everett, MA

9. Ott, L. (1977). An Introduction to Statistical Methods and Data Analysis. Duxbury Press, Belmont, CA   730 p.

10. Hald, A. (1952). Statistical Tables and Formulas. John Wiley and Sons, Inc., New York, NY, 97 p.
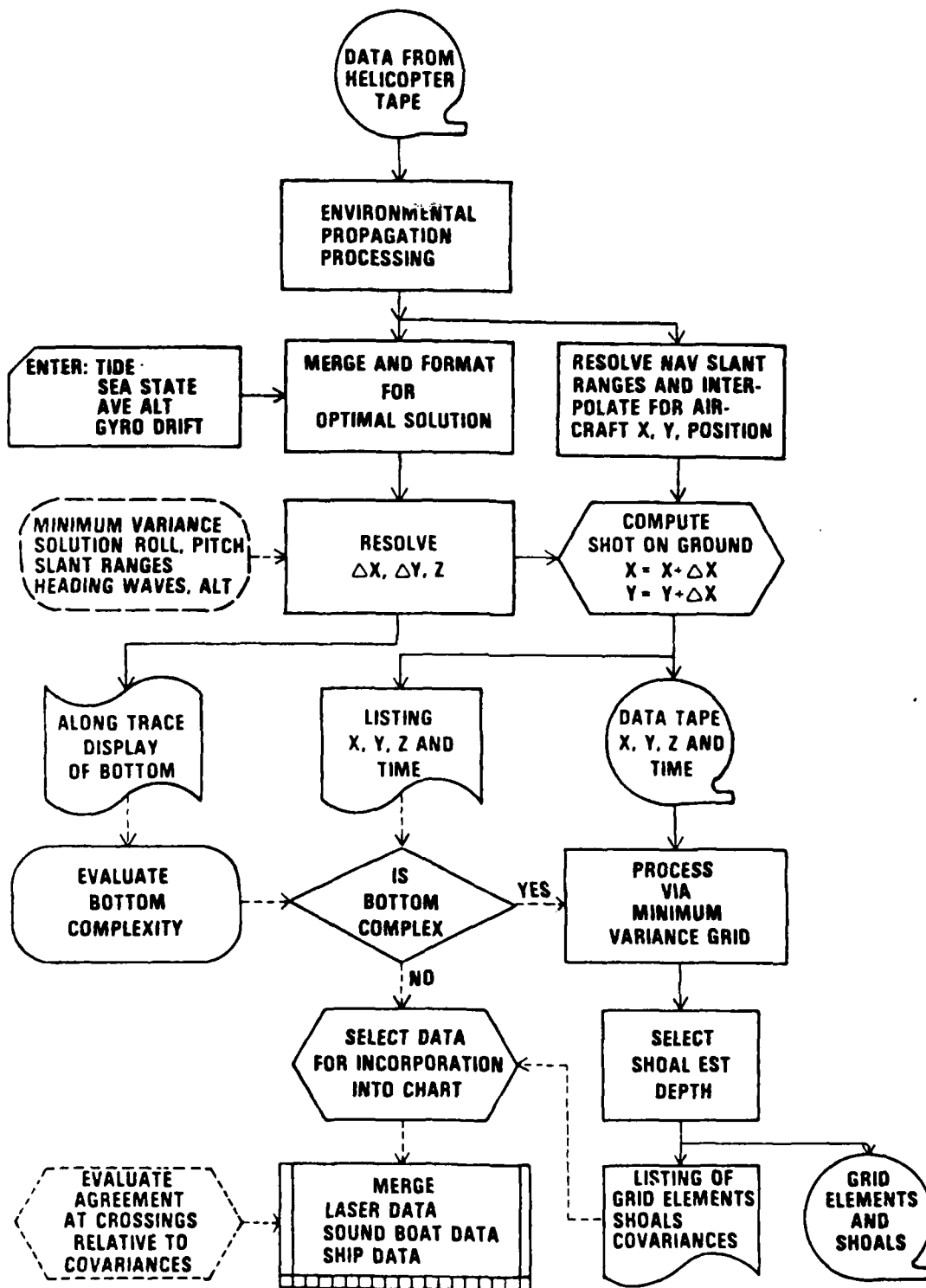
HALS DATA REDUCTION

```
                    ┌─────────────┐
                    │ DATA FROM   │
                    │ HELICOPTER  │
                    │ TAPE        │
                    └─────────────┘
                           │
                           ▼
                  ┌──────────────────┐
                  │  ENVIRONMENTAL   │
                  │  PROPAGATION     │
                  │  PROCESSING      │
                  └──────────────────┘
                           │
              ┌────────────┴────────────┐
              ▼                         ▼
  ENTER: TIDE        ┌──────────────┐  ┌──────────────────┐
     SEA STATE       │ MERGE AND    │  │ RESOLVE NAV SLANT│
     AVE ALT ────────▶ FORMAT       │  │ RANGES AND INTER-│
     GYRO DRIFT      │ FOR          │  │ POLATE FOR AIR-  │
                     │ OPTIMAL      │  │ CRAFT X, Y,      │
                     │ SOLUTION     │  │ POSITION         │
                     └──────────────┘  └──────────────────┘
                           │                    │
  MINIMUM VARIANCE         ▼                    ▼
  SOLUTION ROLL, PITCH ┌─────────┐       ┌──────────────┐
  SLANT RANGES ────────▶ RESOLVE │       │ COMPUTE      │
  HEADING WAVES, ALT   │ ΔX,ΔY,Z │──────▶│ SHOT ON      │
                       └─────────┘       │ GROUND       │
                           │             │ X = X+ΔX     │
                           │             │ Y = Y+ΔX     │
                           │             └──────────────┘
```

ENTER: TIDE
   SEA STATE
   AVE ALT
   GYRO DRIFT

MINIMUM VARIANCE
SOLUTION ROLL, PITCH
SLANT RANGES
HEADING WAVES, ALT

| ALONG TRACE DISPLAY OF BOTTOM | LISTING X, Y, Z AND TIME | DATA TAPE X, Y, Z AND TIME |

EVALUATE BOTTOM COMPLEXITY

IS BOTTOM COMPLEX — YES → PROCESS VIA MINIMUM VARIANCE GRID

NO

SELECT DATA FOR INCORPORATION INTO CHART

SELECT SHOAL EST DEPTH

EVALUATE AGREEMENT AT CROSSINGS RELATIVE TO COVARIANCES

MERGE LASER DATA SOUND BOAT DATA SHIP DATA

LISTING OF GRID ELEMENTS SHOALS COVARIANCES

GRID ELEMENTS AND SHOALS

Figure 1

TABLE 1

HALS ERROR BUDGET

(TRUE VERTICAL DEPTH)

$$D_{MAX} = 20 \text{ M} \quad \text{SCAN ANGLE} = 25^\circ$$

ERROR SOURCE	UNCORRECTED BIAS	CORRECTED BIAS	RANDOM
PROCESSING BIAS			
● SURFACE	($\pm$ 8 CM)	$\pm$ 4 CM	
● BOTTOM	($\pm$ 16 CM)	$\pm$ 4 CM	
TEMPERATURE		$\pm$ 3 CM	
PULSE STRETCHING			
● SURFACE			3 CM
● BOTTOM	($\pm$ 60 CM)		
– ENVIR. PROP.		$\pm$ 7 CM	
– MODEL FIT		$\pm$ 5 CM	
RANDOM NOISE			
● SURFACE			2 CM
● BOTTOM			14 CM
BEAM STEERING			15 CM
TIMING			
● CFD SURFACE			1 CM
● CFD BOTTOM			1 CM
● TIME INTERVAL METER			10 CM
WAVE CORRECTION			18 CM
TOTAL RAW ERROR (RSS)	$\pm$ 62.7 CM		29.3 CM
TOTAL AFTER PROCESSING	$\pm$ 10.7 CM		5.6 CM
NET RESULT			16.3 CM

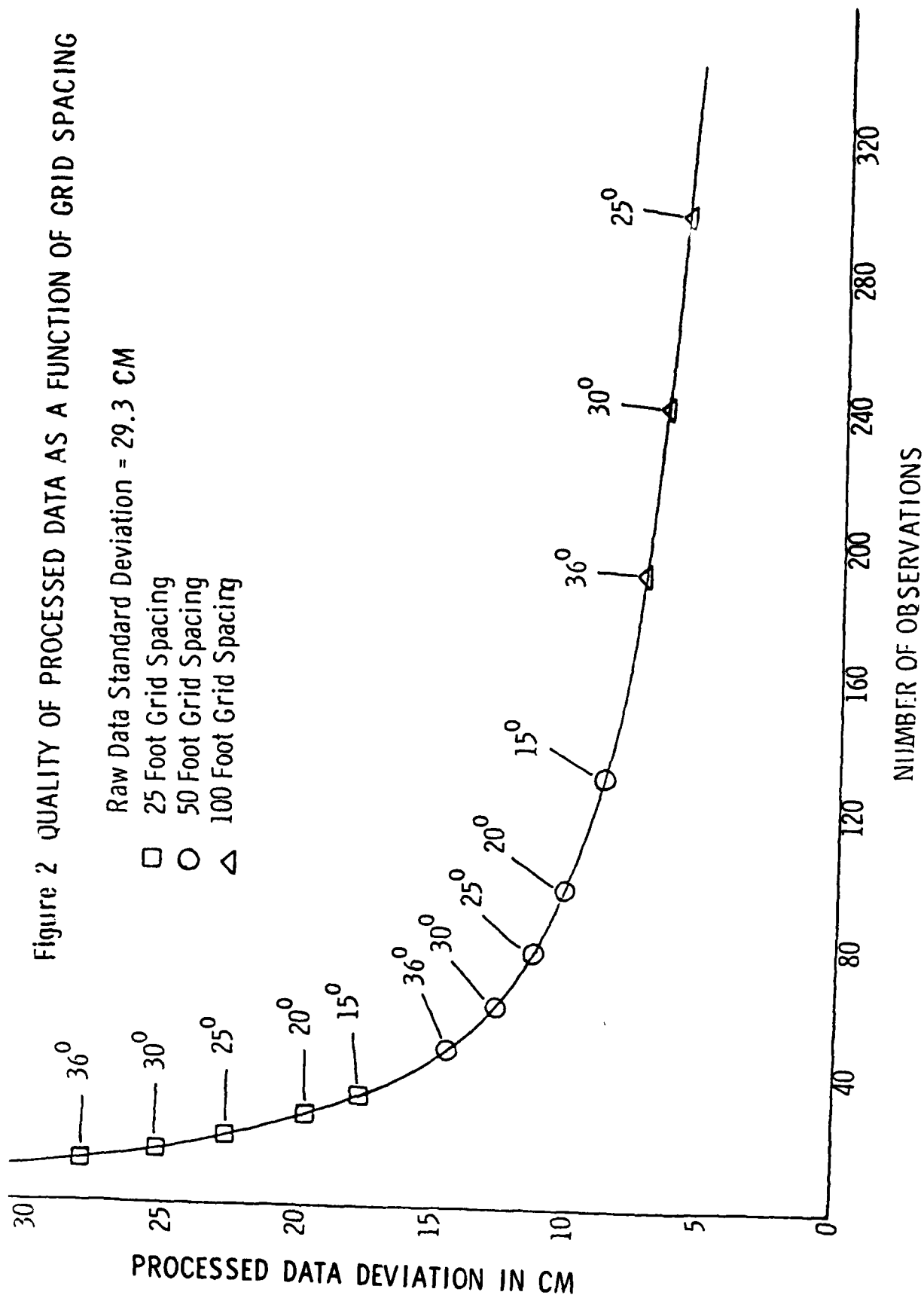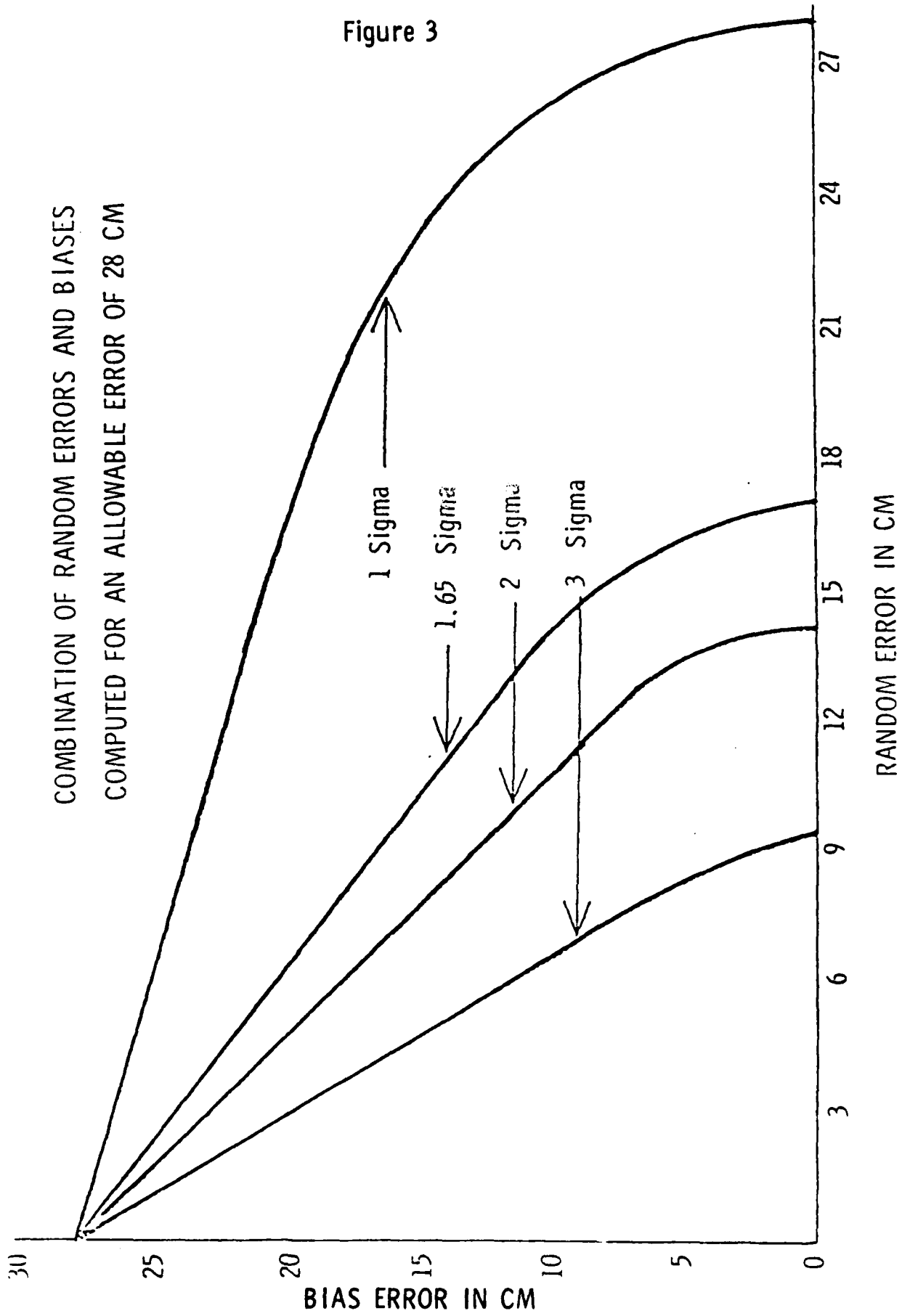Figure 2   QUALITY OF PROCESSED DATA AS A FUNCTION OF GRID SPACING

Figure 3

COMBINATION OF RANDOM ERRORS AND BIASES
COMPUTED FOR AN ALLOWABLE ERROR OF 28 CM

PAPER 27

REMOVAL OF AIRCRAFT VERTICAL MOTION FROM AIRBORNE LASER DATA

William B. Krabill
National Aeronautics and Space Administration
Wallops Flight Center
Wallops Island, Virginia 23337
U.S.A.

and

Robert N. Swift
EG&G/Washington Analytical Services, Inc.
Pokomoke City, Maryland 21851
U.S.A.

SUMMARY

The Wallops' Airborne Oceanographic Lidar (AOL) has been augmented with
an inexpensive servo accelerometer (Columbia Research Labs Model #SA100)
for the purpose of removing contaminating vertical motion from the laser
range data. Originally purchased for application to topographic mapping
projects, the data from the accelerometer has more recently been applied
to ocean wave spectra determination. Other applications include the
development of wave correction data for airborne laser hydrography.

The accelerometer unit is mounted vertically in close proximity to the
laser system. The data is sampled by the AOL computer at the same
repetition rate as the AOL (nominally 200 or 400 Hz for these applications),
formatted into the standard output buffer, and recorded on the system mag
tape unit.

The sensitivity of the accelerometer is such that virtually all high fre-
quency vertical motions of the WFC P-3 aircraft are measured (based on
power spectral density estimates of the accelerometer data).

Thus, with subsequent post-mission data processing, the accelerometer
measurements are doubly integrated into high precision relative vertical
position changes. Unfortunately, the instrument is also subject to drift
and bias errors which, when doubly integrated, produce gross low frequency
errors in the data. For data collection intervals of 3-5 minutes, this
error can be modeled with a quadratic as a function of time. Thus, by
knowing that the ensemble of the laser ranges were made to a flat surface,
the coefficients of a quadratic error function may be solved for, and,
with a subsequent pass through the data, applied to the integrated data.
Thus a vertical reference trajectory for other applications has been
established.

For the topographic mapping application, it was observed that only three
points of known mean sea level (MSL) elevation were required to solve for
the three coefficients. In this mode we typically will identify, in a
plot of range data, points which cross a road or the crest of a hill.
These areas, easily accessable by a ground crew, will be surveyed for
MSL. Subsequent data processing will utilize this data and form the
same type of reference trajectory as above for the entire pass of ground
tracking. Comparison of this technique with standard photogrammetry over
open ground compares to 12-27 cm.

PAPER 28

THE HYDROGRAPHIC AIRBORNE LASER SOUNDER:
A PLANNING AND OPERATIONAL SCENARIO (II)

Larry B. Bourquin
Maxim F. van Norden
U.S. Naval Oceanographic Office
Bay St. Louis, Mississippi 39522

ABSTRACT

The Hydrographic Airborne Laser Sounder (HALS) shows great promise for
solving the U.S. Navy's requirement for rapid hydrographic data collec-
tion for shallow waters. HALS is under development by the U.S. Navy
with funds provided by the Defense Mapping Agency (DMA) and is being
manufactured by AVCO Everett Research Laboratory, Inc. When completed,
HALS will be operated from a U.S. Navy HH-2D helicopter (or equivalent)
attached to a CHAUVENET class survey ship.

The objective of this paper is to describe the planning and operating
scenario being developed for HALS. Emphasis is placed on the inter-
relationship of planning and the effects of environmental parameters
(such as water transparency, sea state, fog, and sun zenith angle) and
operational constraints (such as depth penetration, survey scale,
coverage rate, data density, eye safety, and signal-to-noise ratio) on
HALS operations.

INTRODUCTION

A new method for hydrographic surveying, airborne laser bathymetry,
shows great promise in solving the U.S. Navy's need for rapid shallow
water hydrographic data acquisition. The Hydrographic Airborne Laser
Sounder (HALS) is under development by the Naval Oceanographic Research
and Development Agency (NORDA) with funds provided by the Defense Map-
ping Agency (DMA), and is being manufactured by AVCO Everett Research
Laboratory, Inc. HALS will be mounted on a U.S. Navy HH-2D helicopter
(Figure 1), normally attached to a Naval Oceanographic Office
(NAVOCEANO) coastal hydrographic survey ship.

The purpose of this paper is to describe the planning and operating
scenario being developed for most efficient utilization of this hydro-
graphic survey system considering its operational and environmental
constraints. This description of anticipated HALS operations emphasizes
planning as the key to efficient utilization of HALS both prior to its
deployment to an area and prior to each mission. Since HALS is still
under development, this planning and operational scenario will be sub-
ject to future changes.

THE HALS SYSTEM

Principles of Laser Bathymetry
The technique of using a pulsed scanning laser to remotely measure
water depths can be explained with the aid of Figure 2. A short pulse
of light is emitted from an airborne laser. The pulse of energy propa-
gates through the atmosphere at the velocity of light and impinges upon
the surface of the water. Approximately 2% of this energy is specu-
larly reflected from the air/water interface and detected by the air-
craft receiver. Half of the time difference between the initial laser

pulse and this surface reflection yields the aircraft slant altitude.
The remaining 98% of the laser energy is transmitted into the water,
wherein its velocity is decreased by about 25%. (The transmission
across the air/water interface is dependent on the angle of incidence,
polarization, and on sea state conditions). In addition, the laser
pulse is exponentially attenuated by absorption and scattering within
the water column. If the pulse is of sufficient intensity, it will be
reflected from the water/sediment interface and detected at the
receiver. The time difference between the surface and bottom-sediment
reflections is used to determine the slant water depth. These measure-
ments are complicated by the presence of the water and air backscatter
energy which causes a continuous noise of varying intensity to be detec-
ted by the receiver from the time the pulse leaves the transmitter
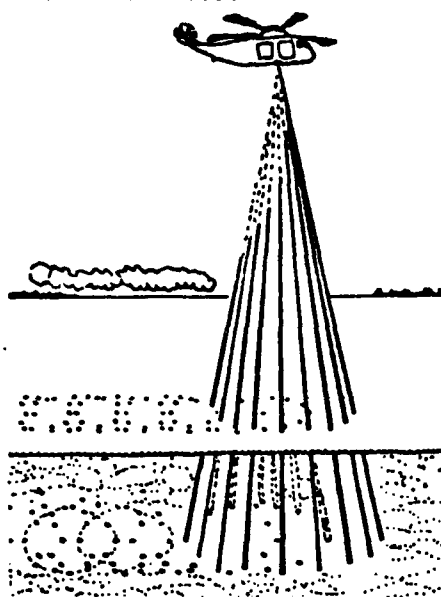until the bottom reflection arrives.

Figure 1. Artist's conception of HALS.

System Description
The HALS system will consist of a transceiver assembly and an electron-
ics system. HALS system specifications are listed in the Appendix.

   Transceiver Assembly. The transceiver (Figure 3) will contain a
laser, output optics, a scanner, receiving optics and detector, atti-
tude measurement unit, and supporting structure.

   The laser will be a high repetition rate frequency doubled Neodymium
YAG laser. This type of laser operates at a wavelength of 532 nm which
is within the transmission window of Jerlov's coastal water types 1-7
(510-580nm).

   The optical system will contain a beam expander to vary the output
divergence of the laser and thus the size of the illuminated spot on
the water surface; folding optics to direct the laser beam to a scan-
ner and provide the capability for laser/receiver alignment; a scanner,
adjustable to a maximum scan angle of 36°; and a receiver with an
adjustable field stop, background rejection filter, and a gateable
detector (a photomultiplier tube).

   Attitude information will be provided by a vertical gyroscope. Roll
and pitch information will be necessary to determine true altitude,

horizontal placement of the laser spot, and water depth at the instant
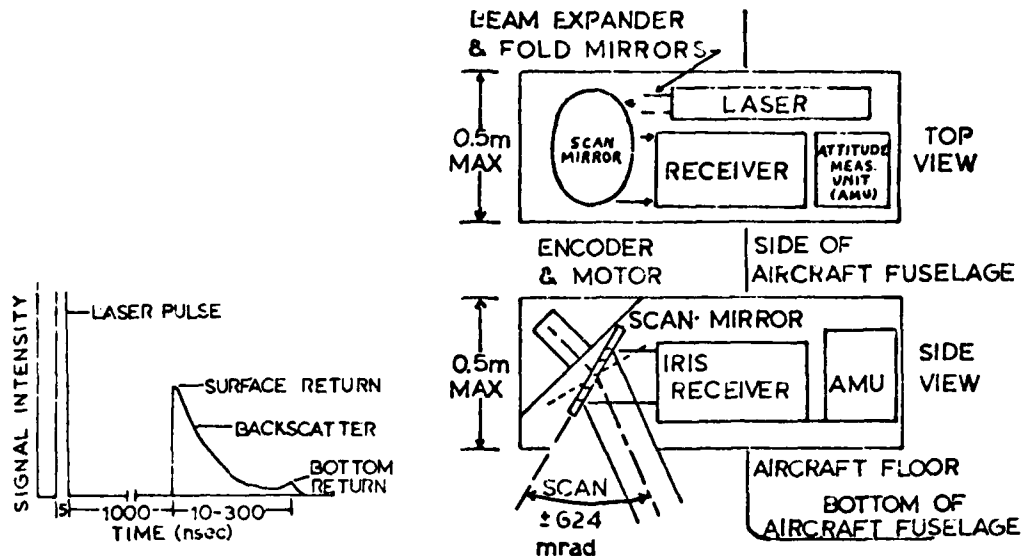a sounding is made.

Figure 2. Laser pulse and
return signals.

Figure 3. Transceiver assembly
schematic. (AVCO Everett, 1979)

Electronics System. The electronics system (Figure 4) will consist
of system controls, data acquisition and processing electronics, a
digital processor, recording and display elements, and an aircraft
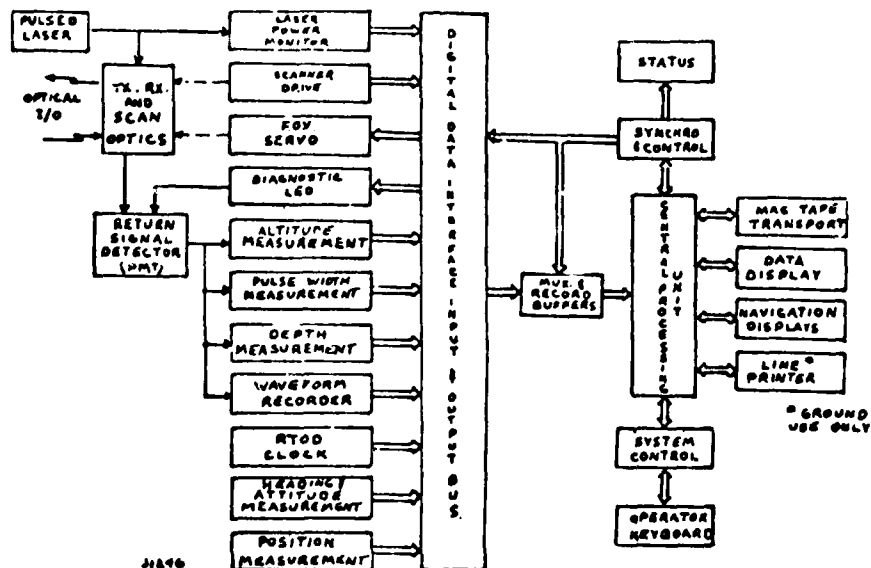positioning system.

Figure 4. Top level electronics system block
diagram. (AVCO Everett, 1979)

Data acquisition and processing will be controlled by a ROLM 1664
computer. Information will be recorded on two MILTOPE CR600 cartridge
recorders. Two recorders will be required to meet the data capacity

and ease of tape change specifications for a two hour flight. Instruc-
tions will be entered via a keyboard or magnetic cartridge. Separate
displays for the operator and pilot will monitor and guide survey
operations.

Horizontal positioning will be obtained from CUBIC ARGO DM-54 or DEL
NORTE Flying Flagman systems (or equivalents). Heading information
will be provided by a free directional gyroscope with a magnetic slave
mode as an option. The necessity for accurate heading becomes critical
as swath width and survey scale increases in order to achieve accurate
horizontal positions for the soundings.

PLANNING A HALS SURVEY

The planning stage will be the most critical stage of a HALS survey.
This planning may be divided into two segments. First, in Pre-deploy-
ment Planning, the hydrographer will decide where and when HALS should
be deployed. Charting requirements are the primary reason for deploy-
ing any hydrographic survey system but for a. HALS deployment, histori-
cal water transparency, bottom topography, and sea state and fog
climates must also be considered. Furthermore, since HALS will initi-
ally be deployed to a survey ship, ship availability must be taken into
account. Second, in Pre-mission Planning, the hydrographer must con-
sider the environmental parameters (water transparency, sea state,
visibility, and sun zenith angle) for "go" or "no go" and the operating
constraints (depth penetration, data density, coverage rate, survey
scale, eye safety, and signal-to-noise ratio) to determine mission
parameters (day/night mission, survey altitude and speed, scan angle,
scanner rotation rate, laser beam divergence, and receiver field-of-
view). These environmental and operational constraints must be consid-
ered in both planning segments for an effective and efficient HALS
survey. Further refinements to this planning should be done after com-
pletion of the HALS cross-check lines. The HALS cross-check lines, as
well as principal lines, should provide feedback on the limits of the
HALS operating area and the adequacy of the planned operating
procedures.

Pre-deployment Planning
The decision to deploy HALS must consider water transparency, the
depth contours, and the sea state and fog climates of those areas.

Water Transparency and Depth. Water transparency and depth contours
will be required parameters for predicting the effectiveness of HALS in
any given area. Investigators have shown that the attenuation of the
laser pulse within the water column may best be approximated by the
irradiance attenuation coefficient, $K(\lambda)$, for downwelling light. The
irradiance attenuation coefficient, $K(\lambda)$, is an apparent, spectrally
dependent optical property that measures the extent to which diffuse
downwelling daylight diminishes exponentially with depth in water.

$$H_z = H_o e{-}K(\lambda)Z \quad \text{or} \quad K(\lambda) = Z^{-1}\ln H_z/H_o$$

where: H_o = solar irradiance at sea surface
        H_z = downwelling irradiance at depth Z
        Z = depth or measurement
        $K(\lambda)$ = irradiance attenuation coefficient
               (λ = 532nm for Nd:YAG lasers).

The performance of laser bathymetry systems may be specified using irradiance attenuation lengths, L, which are the reciprocals of irradiance attenuation coefficients, i.e., $L = 1/K$, the distance in which the irradiance decreases by a factor $1/e$. If d is the depth to the bottom, then d/L or Kd is the number of irradiance attenuation lengths to the bottom depth. Table I lists the maximum predicted Kd values at various scan angles (σ) and day or night conditions for HALS. Because of problems associated with detecting signal returns from large off-nadir scan angles, it appears at this time that the maximum scan will be limited to 20°. Figure 5 shows the predicted depth penetration (d) as a function of Kd and K.

DAY		NIGHT	
SCAN ANGLE	Kd	SCAN ANGLE	KD
36°	3.2	36°	4.2
30°	3.3	30°	4.3
20°	3.7	20°	4.7
10°	4.1	10°	5.2
0°	4.6	0°	5.9

Table 1. Maximum predicted HALS Kd values at various scan angles for an operating altitude of 150 meters. (AVCO Everett, 1979)

Figure 5. Predicted depth penetration at various Kd and K.

Unfortunately irradiance attenuation data is extremely sparse for most of the world. Therefore, K data will have to be inferred from other optical measurements such as Secchi depths and beam attenuation data, and from satellite sensors such as the Coastal Zone Color Scanner on Nimbus 7.

Furthermore, optical properties of coastal water are variable temporally and spatially. The best approach for determining HALS survey areas will be to draw seasonal Kd contours for any area of interest (van Norden and Litts, 1979). Optical seasons could be determined by correlating oceanographic and meteorological conditions with historical K and derived K data (derived from Secchi depth, beam attenuation, and Nimbus 7 data). These Kd contours will serve as a guide to average maximum laser depth penetration over an optical season and therefore, will influence when or where HALS should be deployed. Figure 6 is an example of a coastal area with seasonal Kd contours. In addition, Kd contours will assist in Pre-mission Planning by indicating scan angle setting, operating altitude, and the necessity for night missions.

Sea State and Visibility. The HALS survey season should coincide with the time of year when the prevailing winds are expected to be at Beaufort Force 1-3 and visibility is good. Sea state can effect the performance of HALS in two ways. First, below Beaufort Force 1 (< 2 knots) there is an absence of capillary waves which are necessary for the water surface to reflect energy from off-nadir scanner angles back
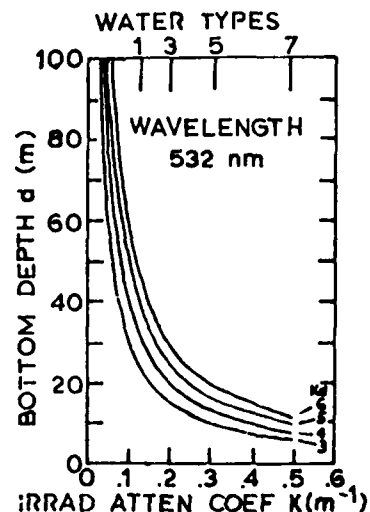
to the receiver. Second, above Beaufort Force 3, higher winds generate
waves with sufficient energy and depth to resuspend bottom sediments
and decrease water clarity to unacceptable levels. Also with the
resulting increase in wave slope, beam spreading through the air/sea
interface becomes significantly large. Reduced visibility, rain and
fog, will decrease the HALS depth penetration performance due to an
increase in atmospheric attenuation and backscatter. A fog or haze
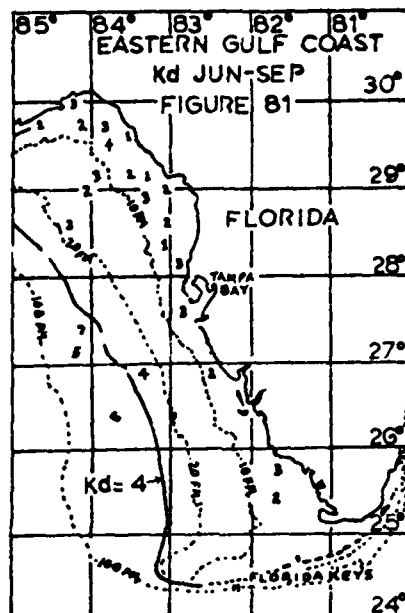layer near the water surface could also cause altitude and depth bias
errors.

Figure 6. Historical Kd = 4 contour for June -
September along coast of Florida. (van Norden &
Litts, 1979)

Pre-mission Planning

The objective of Pre-mission Planning will be to first, decide whether
to "go" or "not go" with a HALS mission depending on the operating
environment and second, if the decision is to go with a HALS mission,
to decide upon the most efficient operating parameters.

   The Operating Environment. The environmental parameters critical
to HALS operations will be sea state, visibility, water transparency,
and sun zenith angle. Sea state must be between Beaufort Force 1-3
and visibility must be better than 5 Km. The effects of water trans-
parency were discussed previously. However, the seasonal Kd contours,
produced in Pre-deployment Planning, will be just a guide to depth
penetration because significant variation in K from the seasonal mean
may occur. This variation could result from unusual storm activity,
strong tidal currents, and plankton blooms.

   The solar zenith angle will be important because full performance
can only be expected at solar zenith angles where direct specular
reflection off the ocean surface does not occur. Specular reflection
that enters the receiver will result in the total loss of data due to
the saturation of the detector and its electronics. The probable maxi-
mum off-vertical angle the receiver can assume is 25° for a 20° scan

angle with a maximum allowed roll angle of 5°. Thus, if the ocean sur-
face is approximated as a flat plane, the receiver will intercept a
solar specular reflection for any solar zenith angle of 25° or less.
Specular reflections at larger solar zenith angles can also occur if
the portion of the ocean surface viewed by the receiver is tilted sig-
nificantly by wave action. For these reasons night operations will be
optimum, but if daylight flights are required (flight restrictions on
night operations), then the two hours after sunrise and the two hours
before sunset will be the best times for HALS surveys.

Operating Parameters. The operating constraints that the hydrogra-
pher must consider are depth penetration, coverage rate, survey scale,
data density, eye safety, and signal-to-noise ratio. These constraints
are a function of operating parameters such as day/night mission, scan
angle, survey altitude and speed, scanner rotation rate, beam diver-
gence, and field-of-view (FOV).

Depth penetration, coverage rate, and survey scale are interrelated
because of their dependence on common operational parameters. Depth
penetration is shown as a function of K, scan angle, altitude, and day/
night mission in Figures 7 and 8 (an optimum FOV was assumed and beam
divergence was ignored). A smaller scan angle, lower operating alti-
tude, or a night mission increase depth penetration. (The increase in
nighttime depth penetration is due to a low level of background noise).
Figure 9 shows that a smaller scan angle and lower altitude will
decrease swath width. Night missions tend to be more hazardous to per-
sonnel and equipment. Therefore, it will be important to select the
largest swath width that still achieves the required depth penetration
in the daytime.

Coverage rate is a function of swath width and speed as shown by

$$C = 2HS \tan \sigma$$

where
C = coverage rate (m²/s)
H = altitude (m)
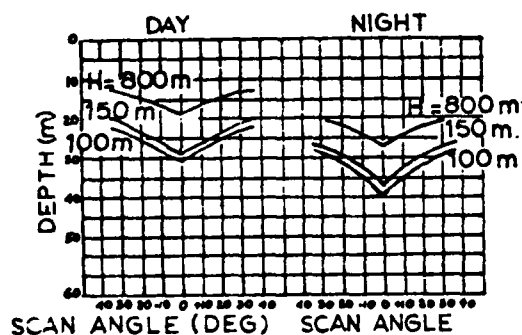S = ground speed (m/s)
σ = scan angle (deg)

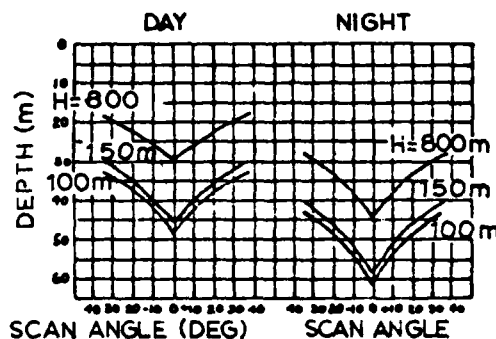Figure 7. K = 0.16 m^{-1} Figure 8. K = 0.10 m^{-1}

HALS system operational depth at various scan
angles and altitudes for day or night missions.
(AVCO Everett, 1979)

Besides depth penetration, the determination of scan angle setting
and operating altitude must also consider the survey scale. The posi-
tions of the soundings relative to the position of the helicopter
decrease in accuracy as a function of swath width due to heading error.

$$E_h = W \sin \frac{\theta}{2}$$

Where E_h = position error due to heading error (m)
        W = swath width (m)
        θ = heading error (rad)

For example, a HALS survey at 1:10,000 scale would require a reduced swath width (usually) by decreasing the scan angle to prevent the total horizontal position error from exceeding the 9.1m allowed at that scale.
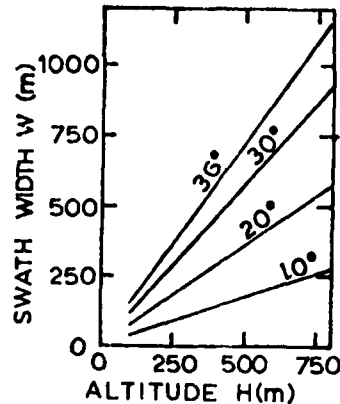

Figure 9. Swath width as a function
of altitude and scan angle.

Data Density. The operating constraints resulting from a specified (from survey project specifications) minimum density of soundings will affect the determination of operating altitude and ground speed, scan angle, scanner rotation rate, and laser pulse rate. Table II lists these parameters and their operating limits.

PARAMETERS	OPERATING LIMITS
Altitude (H)	100-800 meters
Speed (S)	0-60 meters/second
Scan Angle (σ)	0°, 10°, 20°, 30°, 36°
Scan Rotation Rate (f)	0-4 hertz
Laser Pulse Rate (R)	400 hertz (max.)

Table 2. Operating parameters which affect data
density.

A rotating mirror scanner will scan an oval scan pattern as shown in Figure 10. Adding aircraft motion leads to the interlaced pattern shown in Figure 11. Figure 11 shows that the greatest data density occurs at the intersections of succeeding scans, while the minimum density occurs along the flight center line. Survey data density should be designed for soundings along this center line of flight to satisfy the survey specifications.

The scanner rotation rate must be set to provide interlace and relatively equal spot spacing in the lateral and flight directions to achieve optimum efficiency. In the lateral direction, the spacing is approximated by $\pi wf/R$, and in the direction of flight, the spacing is

S/2f) for interlacing. However, interlacing is achieved only if
f = PS/W where P must be an integer. One method to plan for the
required data density is as follows:

(1) After reviewing the Kd contours, choose the maximum swath
width (W) that will achieve the required depth penetration. Normally,
the operating altitude will be 150 m; thus, the desired swath width
which can operate within the constraints of a particular Kd will
usually be achieved by varying the scan angle or by opting for a night
mission.

(2) With the required data density expressed as distance between
soundings (D), and swath width (W) known, Figure 12 can be used to
select a scanner rotation rate (f).

(3) Choose an aircraft speed that satisfies the relationship:

$$S \leq 2fD \quad \text{where} \quad 0 \leq S \leq 60 \text{ (m/s)}$$

(4) Solve the equation $P_1 = Wf_1/S$ where P_1 must equal an integer to
achieve interlacing. If P_1 is not an integer, truncate P_1 to integer
P_2 and find the required scanner rotation rate (f) by solving
$f_2 = P_2 S/W$. (Perfect interlacing will not occur due to varying ground
speed when side, tail or headwinds are present).

Following the above steps will allow any data density to be achieved
for HALS by varying these operational parameters.

AIRCRAFT   DIRECTION
ALTITUDE: 150 m   OF FLIGHT
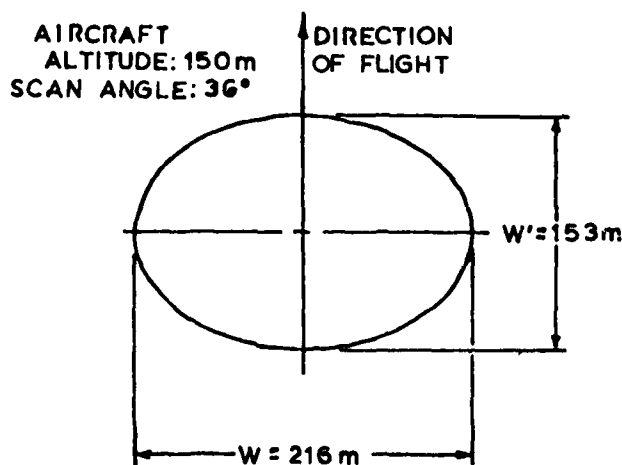SCAN ANGLE: 36°

W' = 153 m

W = 216 m

Figure 10. Elliptical scan pattern
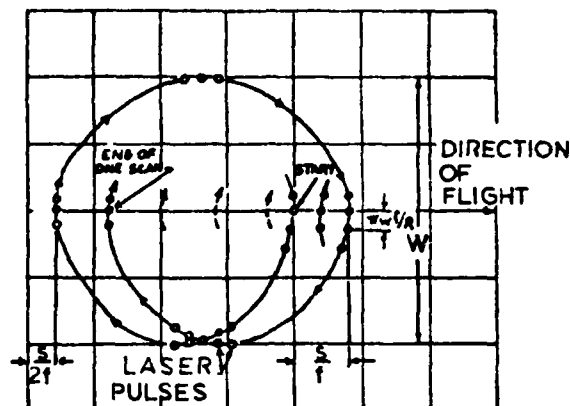without aircraft motion.
AVCO Everett, 1979)

Figure 11. Scan Pattern interlace with
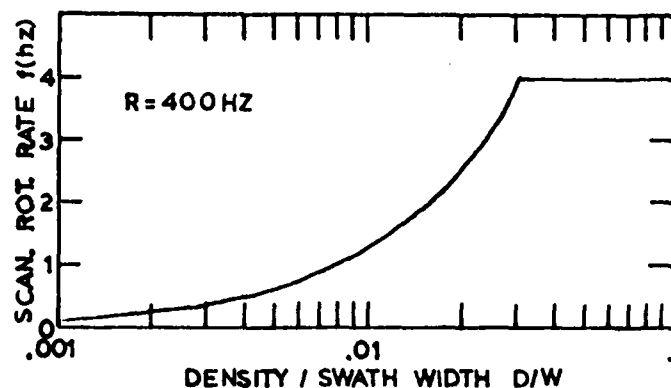aircraft motion. (AVCO Everett, 1979)

Figure 12. Scanner rotation rate as a
function of data density (expressed as
distance between soundings) and swath
width.

Eye Safety. A very important consideration related to laser beam
divergence will be the eye safety of observers on the water/land sur-
face. The divergence of the laser output beam will be variable (1 to
50 mrad) to optimize its interaction with the water surface under con-
ditions of varying sea states. For low sea states with little capil-
lary wave action larger divergence is necessary for the receiver to
register sea surface returns but with greater divergence a decrease in
depth penetration results. However, the computer will limit the mini-
mum beam divergence as a function of altitude to comply with eye
safety standards. The maximum allowable spot size in accordance with
American National Standard for the Safe Use of Lasers, ANSI Z136 is
0.65m in diameter for a transmitter power of 400 KW and negligible
atmospheric attenuation. The following equation gives the minimum
allowable beam divergence:

$$\Delta \theta = 2 \text{ Arc Tan } (0.325/H)$$

where $\Delta \theta$ = allowable beam divergence (rad)

   H = aircraft altitude (m)

At an altitude of 150 meters the transmitted beam must be larger than 4.3 mrad.

Signal-to-Noise Ratio (S/N). An optimum receiver signal-to-noise ratio may be achieved for varying altitudes, background and water conditions by adjusting field-of-view (FOV). An optimum S/N occurs because both the bottom return signal and background noise will increase with increasing FOV. The former occurs because as the FOV is increased, more of the energy reflected from the bottom is collected. However, a point will be reached where the increase in signal is smaller than the increase in noise. The determination of the optimum S/N will be a computer function which will adjust FOV by automatically operating the iris drive system. This S/N algorithm will be based on pre-programmed parameters, some of which will be determined from experimental test data.

Survey Project Field Plan. The survey project field plan will be the integration of the project specifications, the planned HALS operating parameters, and information obtained from HALS cross-check lines. The NAVOCEANO Project Specifications will specify the survey parameters i.e., survey scale, spheroid, geodetic and vertical datum, projection, and grid. Also the Presurvey Review Section of the Project Specifications will list specific items for detailed investigation i.e., shoals, hazards, unverified or questionable charted data. Based upon the planning as previously described, a survey area will be allocated to HALS. This area, based upon shoreline configuration and Kd contours, will be outlined in a polygon and described in UTM coordinates. This polygon will then be further divided into smaller polygons each with constant mission operating parameters determined by the methods of the previous sections. Further refinements will be made to the survey plan upon completion of the HALS cross-check lines. The cross-check lines will be executed prior to the principal survey lines and perpendicular to the depth contours. As such, these lines will delineate the limits of the HALS depth penetration capability. Later the cross-check line soundings will be used as a check on the principle survey line soundings. In addition, completed principal line missions will provide feedback to Pre-mission Planning of succeeding missions.

HALS OPERATING SCENARIO

HALS will be tied directly to ship operations but will only impose minimum changes on normal ship hydrographic procedures. The helicopter is primarily used for the deployment and resupply of navigational aid stations (NAVAIDS). When these missions are completed, HALS will be installed and utilized depending upon the planning of the previous section and the operating environment. There will be three operational types of HALS missions - cross-check lines, principal survey lines, and saturation surveys. All missions will have the same basic scenario except that cross-check lines will be run perpendicular to the depth contours, principal survey lines will be run nearly parallel to depth contours, to maximize their length, and saturation surveys for shoals and hazardous areas will be run at low speed to increase data density. Each HALS mission will not exceed two hours, and there will be a maximum of two missions in the daytime or three at night (or a combination of both).

Pre-Mission Activities

After the NAVAIDS and tide gages are in place and the helicopter is available, the HALS modules will be removed from their crates, hand carried to the aircraft and bolted to the aircraft frame. Interconnecting component and power cables will be installed and the system turned on for checkout. Computer programs will be fed to the computer and diagnostic procedures will be run. Optical alignment will be checked to determine if alignment is correct. The installation and checkout procedures including realignment when necessary, will require less than six hours.

Prior to each HALS mission the aircraft crew will service and perform checkouts on the helicopter while HALS technicians perform final checkout procedures on the HALS. The HALS operator will go down his check off list and verify that all operational parameters such as altitude and speed are known by the pilot and beam divergence, scanner rotation rate, and scan angle are preset. The operator will enter or verify all survey parameters in the ROLM 1664 computer. Survey parameters may be entered via keyboard or magnetic tape cartridge. Besides such necessary items as NAVAID station positions, lanewidth, archive number, date, allowable offline error, spheroid, UTM zone, etc., a Survey Line Coordinate Table must be entered. The Survey Line Coordinate Table will list start and end point coordinates of each line and the order of execution. Besides manual input, the operator will have an option for the computer to establish this table by entering the UTM coordinates of the points that define the HALS survey area, the desired line spacing, and the line orientation.

After entering the survey parameters, the operator then enters the time and the calibrated ARGO lanes adjusted for the position difference between ship and aircraft antennas (microwave positioning systems such as DEL NORTE Flying Flagman do not suffer from lane ambiguity). Finally, the operator must calibrate the HALS heading gyroscope. At this time an external alignment procedure for calibrating the HALS heading gyroscope using optical equipment and the survey ship's Mark 19 gyros is under investigation. It is possible that an external alignment procedure on the ship will not provide sufficient accuracy to meet large scale accuracy requirements i.e., 1:10,000 scale. Therefore, an optical calibration of heading may have to be performed at geodetic azimuths ashore for such surveys. The alternative method of using a magnetic north seeking gyrocompass was rejected for large to medium scale surveys since information on magnetic anomalies is imprecise for many survey areas.

The HALS Survey

After takeoff, in transit to the survey area, the pilot's computer driven steering indicator will guide the aircraft to the start point of the first survey line. The HALS operator will monitor the aircraft's progress to the start point using his display and inserts cartridge tapes in both recorders.

The steering indicator will guide the pilot to the first survey line's start point and once the aircraft is on line guide the pilot to stay on that line. Only when the aircraft is on line within the allowable offline error and has crossed the start point will the HALS system begin laser operation and data collection. After the helicopter has crossed the end point of the survey line, the HALS system ceases laser operation and data collection and the pilot's steering indicator will guide him to the next line. This process is repeated for as many lines as desired.

The operator will have available a number of options to override the
HALS system. Whenever the operator believes a survey line is too
short or too long he/she may override laser operation and data collec-
tion. He/she will also have the option to survey a line out of
sequence, different from that of the Survey Line Coordinate Table, or
skip a line. Finally, the operator may terminate the mission prior to
completion of all lines in the Survey Line Coordinate Table.

After the aircraft returns to the survey ship, close-out calibrations
will be performed for the ARGO DM-54 and the heading gyroscope. Data
tapes will be processed through a "quick look" program to determine
data reliability and whether additional missions will be required.
Maintenance may be performed for additional missions.

Post Processing
Initial processing and editing using the HALS computer while on the
aircraft will be performed for each separate data tape. A data tape
will be read, deblocked, merged with external inputs, and formated for
an optimal solution on the laser slant ranges. (An explanation of
Optimal Filter theory can be found in Byrnes and Fagin, 1978). The
computer will execute a minimum variance solution, generating x, y
coordinates relative to the aircraft position, and depth information
which has been corrected for surface waves. The relative coordinates
will be added to aircraft position, produced on tape and listed as the
processing progresses. Along-track data will also be generated and dis-
played on a CRT as the processing continues. The display will permit
the operator to evaluate bottom complexity and data integrity. If the
data appears reliable and bottom flat, the operator will merely scan
the listing and will extract data to be merged or plotted on the chart.
If the data integrity appears unstable or the bottom complex, the out-
put tape will be read back as input for a second processing pass. The
second pass will process the x, y, z, information into a minimum vari-
ance grid and select the shoalest depths at densities relative to the
intended chart scale (Byrnes, 1979). The second pass will create an
additional listing and a tape containing grid elements, shoals, and
covariances.

The ship's computer processing will apply tidal corrections and com-
bine HALS processed data tapes within the same "smooth sheet" area.
Data verification programs will evaluate agreement between the sound-
ings from the HALS principal survey lines and the HALS cross-check
lines. Further verification will be done with overlapping survey
ship or soundboat data to detect any error biases. Final editing will
be performed and "smooth sheets" produced on the ship's plotters.

SUMMARY

Scanning laser bathymetry systems such as HALS are a viable alternative
to sonic soundings in shallow water areas. The disadvantages of such
systems due to their greater susceptibility to environmental and opera-
tional constraints are more than compensated for by their rapid data
collection capability and by careful planning for their utilization.
Since most of the operational parameters offset each other in effective-
ness, the operational and environmental constraints must be analyzed to
determine the optimum operating procedure. The importance of careful
planning for HALS cannot be overemphasized. Poor or no planning will
diminish the effectiveness of HALS and waste valuable aircraft time.
After HALS becomes operational, field experience and charting results
will provide feedback to the standard planning and operating procedures
to become the ultimate factor affecting the utilization of HALS.

APPENDIX - HALS SPECIFICATIONS

Data Collection
Depth Limits = KD = 3.2, 50m Maximum, 1/2 m Minimum
Accuracy = $\pm$ .28 m for depths $\leq$ 20m, $\pm$ 1m for depths > 20 m
Area Coverage= 8000 m^2/s (optimal)
Data Density = average sounding density of at least one per 20m^2
Positioning = CUBIC ARGO DM-54 (or equivalent) or a microwave
                positioning system
Scan Angles = 0 to $\pm$ 624 mrad (0° to $\pm$ 36°)
Scan Angle Accuracy = 20 mrad or better
Roll & Pitch Accuracy = $\pm$ 20 mrad ($\pm$ 1.15°)
Heading Accuracy = $\pm$ 40 mrad ($\pm$ 2.29°)
Altitude Range = 100 to 800 m (328 to 2,625 ft)
Altitude Accuracy = $\pm$ .1m or 5% along slant range
Safety = Eye safe at 150 m (ANSI Z136)
Mission Time = 2 Hours
Visibility > 5 Km (2-7n.mi.)
Sea State = Beaufort Scale 1-3 (not breaking)
Sun Angle = 46° sun azimuth angle or greater

Data Processing
Inputs = Soundings, altitude, roll, pitch, heading @ 400 Hz; Position-
         ing at 1-2 Hz; Manual Inputs as required.
Computation = Slant ranges from aircraft to water, Slant range water
              depths, S/N of bottom return pulse, Positional data for
              pilot and operator.
Recording = 2 hours of data (system), 30 min. of data (each tape),
            ability to change tapes within 5 min., 9 track odd parity
            800BPI, Read after write capability.

Physical Characteristics
Size = < 2m^3
Weight = < 400 Kz
Total Power Requirement = < 5000W
Salt Spray = Not damaged by salt spray or fog
Temperature = 02° to 54°C (28.4 to 129°F)
Humidity = Operate at relative humidities of 5 to 95%
Shock & Vibration = MIL-STD-810C
Installation = 6 hours (2 men)
Ease of Operation = One operator
Operational Life = 8 years
Reliability = 100 hours MTBF
Maintainability = 4 hours MTTR
Workmanship = MIL-STD-454E
Transport Cases = MIL-C-4150G

REFERENCES

AVCO Everett Research Laboratory, Inc., Proposal for Hydrographic Airborne Laser Sounder, Part I-Technical. Everett, MA: AVCO Corp., 1979.

Byrnes, H. J. and Fagin, Samuel L. Optimal Filtering and Analysis of Scanning Laser Data. NORDA Technical Note 24. NSTL Station, MS: Naval Ocean Research and Development Activity, 1978.

Byrnes, H. J. Operating Scenario for a Hydrographic Airborne Laser Sounder (HALS). NORDA Technical Note 34. NSTL Station, MS: Naval Ocean Research and Development Activity, 1979.

Jerlov, H. G. Marine Optics. Elsevier Oceanography Series, No. 14. New York: Elsevier Scientific Publishing Co., 1976.

Naval Ocean Research and Development Activity. "Hydrographic Airborne Laser Sounder (HALS), Purchase Description.". NSTL Station, MS: Naval Ocean Research and Development Activity, 30 March 1979.

van Norden, Maxim F. and Litts, Steven E. "The Transparency of Selected U.S. Coastal Waters With Applications to Laser Bathymetry." Masters Thesis. Monterey, CA: Naval Post-graduate School, September 1979.

van Norden, Maxim F. "The Hydrographic Airborne Laser Sounder: A Planning and Operational Scenario." Presented at the 19th Annual Canadian Hydrographic Conference, March 1980.

NAVAL AIR DEVELOPMENT CENTER
WARMINSTER, PENNSLYVANIA 18974

AN EXPERIMENTAL LASER RADAR RECEIVER
FOR AIRBORNE OCEAN BOTTOM PROFILIMETRY

8 AUG 1980

V. M. CONTARINO

Introduction

The Naval Air Development Center (NAVAIRDEVCEN) has been designing, fabricating and testing experimental air to underwater laser radar systems for more than 15 years. Recently the Defense Mapping Agency (DMA) established a requirement for an airborne laser radar bottom mapping system for rapid water depth measurements in shallow coastal waters. DMA authorized the NAVAIRDEVCEN to investigate the design of a suitable optical receiver for a Hydrographic Airborne Laser system (HALS). Subsequently, a suitable receiver was designed, fabricated and laboratory tested at NAVAIRDEVCEN. This paper describes the design and testing of the resultant experimental receiver.

Background

The return signal intercepted by the receiver in an air to underwater laser radar system has a complex dependence on both system configuration and environmental parameters [1]. A general overview of the relative return signal amplitudes and expected variations are plotted as a function of time in figure 1. This type of signal pattern is typical for a laser system with narrow optical unpolarized linear receiver optics and detector operating near a wavelength of 530 nm (blue-green in color). Each numbered signal amplitude in figure 1 is qualitatively explained as follows;

1. If the system has a common input-output path the receiver will detect a reflection or multiple reflections as the laser pulse is transmitted via a window, lens or mirror. The peak power of the laser pulse can be large enough that even small reflections produce a substantial signal amplitude.

2. If the receiver field of view intercepts the exiting laser pulse close to the aircraft substantial atmospheric backscatter signal will be received. The atmospheric backscatter changes with weather conditions. A large atmospheric backscatter signal can be received from a light fog or haze even when the fog or haze is near the water surface.

3. The air/water interface return is a complex quantity and is difficult to define. It consists of a varying specular signal dependent upon angle of incidence, laser beam characteristics, and water surface conditions. These dependences can cause the interface return to vary by several orders of magnitude [3].

4. The signal backscatter due to seawater builds up in a timeframe consistent with laser pulse rise time. This event is coincident with the occurrence of the air/water interface signal. The seawater backscatter decays in an approximately exponential fashion with a time constant determined by the seawater attenuation coefficient.

5. Superimposed on the backscatter curve may be large random signal returns from targets illuminated by the laser beam. Experience has shown that schools of fish, shrimp, or large fish give substantial returns. Seaweed and detritus layers can also be expected to appear as targets.
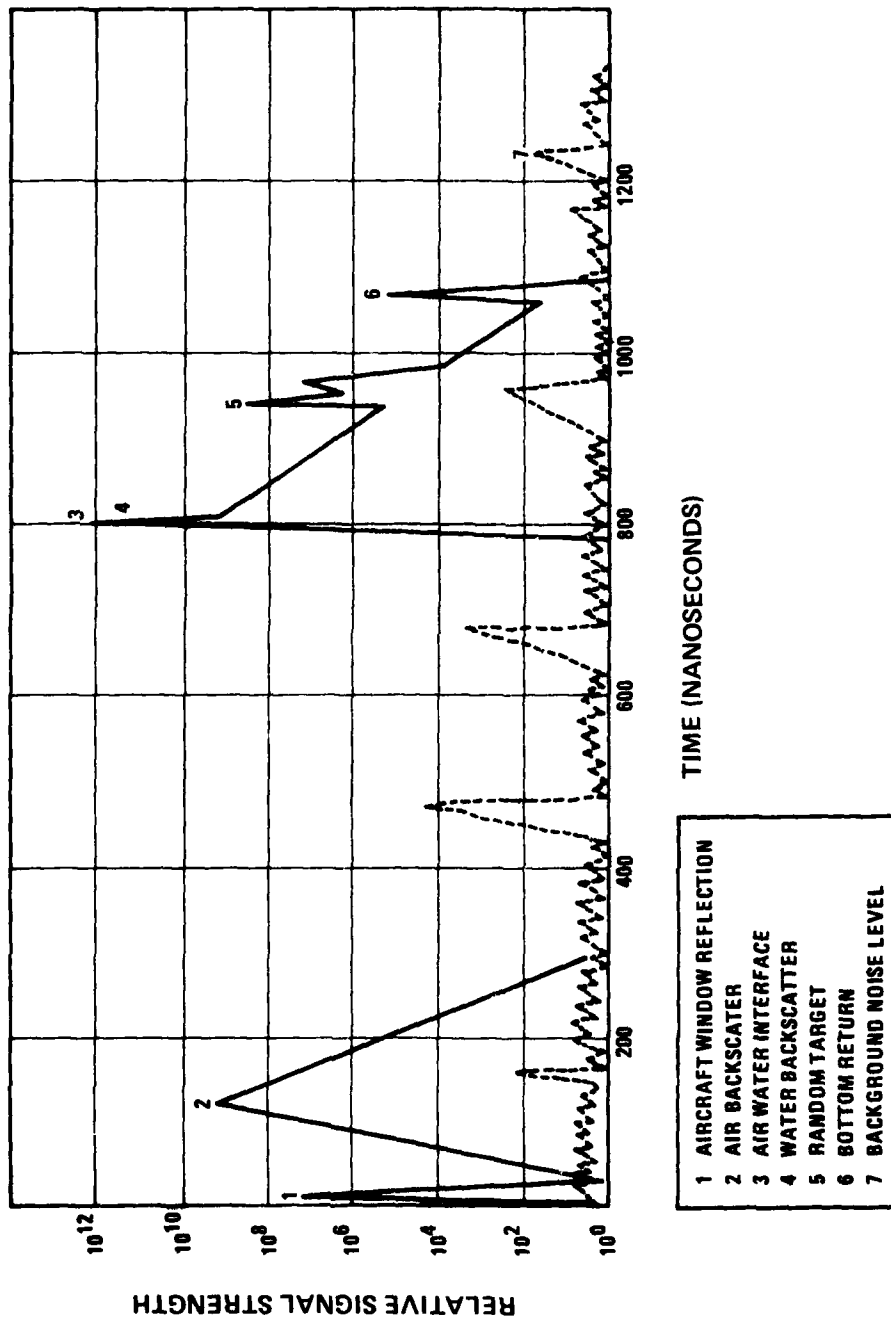
Figure 1. Typical Backscatter Signal Return

6. The target return representing the bottom will occur with relative
consistency, but it will vary in amplitude with changes in many of the
preceding signal components, bottom reflectivity, and depth.

7. Included in figure 1 is background noise. The primary source for
this noise is the sun. This noise source can produce considerable target
like noise depending on the sun angle, seawater conditions, and system
bandwidth.

Considerable effort has been expended in the development of a mathe-
matical model for the backscatter signal return. The Stanford Research
Institute developed a mathmatical model of the signal return as a function[1]
of environmental, system and geometrical parameters for the NAVAIRDEVCEN.
Using the signal return equation as a basis, one can approximate the parti-
cular parameters that are known to obtain those which are unknown. If the
atmosphere and seawater are homogeneous and the targets can be well defined,
the task is not formidable. References (1) and (2) contain examples of
fitting data to the signal return equation. In the event of statistically
random targets and nonhomogenous atmospheric and seawater backscatter, quan-
titative representation is difficult to interpret. Considerable detail of
the signal return equation can be found in reference (1). A simplified
version of this equation was used for the receiver design. Of particular
interest are the relative values of signal amplitude that are obtained from
the signal equation in bottom mapping situations. Experimental values have
verified that signal dynamic ranges of 50 dB occurring in times of 100 nano-
seconds or less can be anticipated. [1,2,3]

Receiver Design Techniques

The large dynamic range of the signal to be received by the radar
system must be compressed or processed into a smaller range for recording
purposes. Most receivers are implemented using a PMT (photomultiplier tube)
with a large photocathode and high current capability. These devices are
well known for their ruggedness, low noise, high gain, large dynamic range
and good gain bandwidth products.

Although the PMT is the best detector choice, it has inadequacies from
a system point of view. Most PMT's have large dynamic ranges, some approach-
ing 60 dB. These ranges are misleading for a pulsed system design because
only 20 or 30 dB is usable in timeframes of less than 400-500 nanoseconds.
After-pulse emissions can occur within the multiplier[4] with magnitudes 20 dB
down from the applied signal power. Each PMT has a signature of these
after-pulse emission effects (figure 2). Another shortcoming of the PMT is
the relatively poor quantum efficiencies available for the photocathodes of
the large surface tubes in the blue-green region. The modified S-20 multi-
alkali type photocathode found on most blue-green tubes has aquantum effi-
cieny of approximately 12%. Other photocathodes such as the GaAsP have
been developed with efficiencies as high as 30% but they are not available
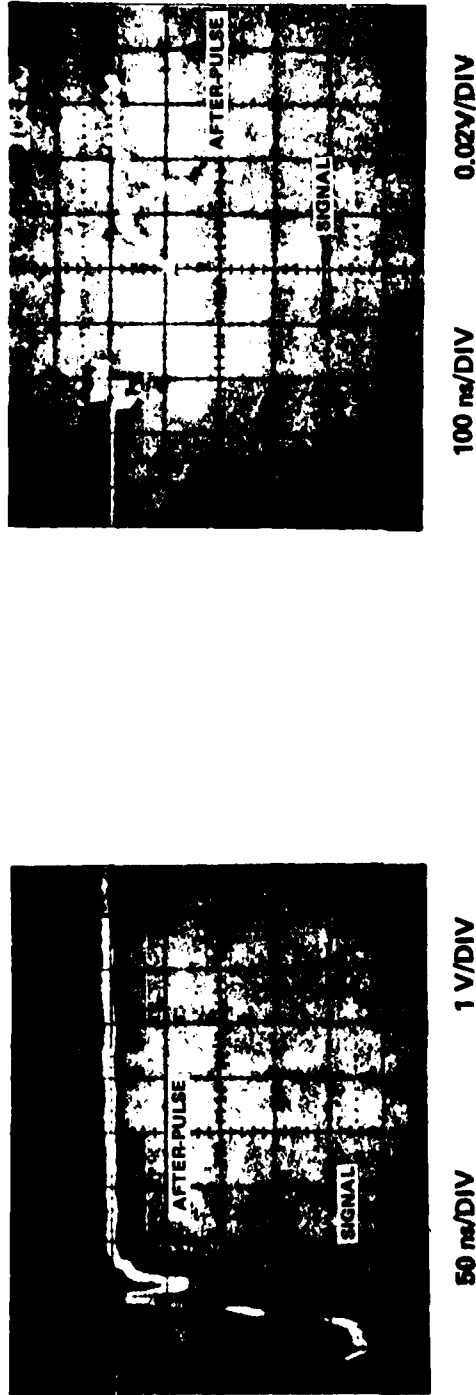on large suface tubes.

Figure 2. Spurious After-pulse Signals from ITT 4084

Several techniques for expanding the effective system dynamic range
have been demonstrated or proposed. Combinations of these techniques can
yield sufficient performance for a particular laser radar system but usually
a major performance trade off occurs. Some of these techniques are summarized
below:

Overload Statistical Correction

The assumption can be made that the receiver and the associated
electronics will be partially overloaded during the data acquisition time.
This means the response of the system will be nonlinear and difficult to
define. The overload response of the system could be carefully tabulated
and the data statistically corrected. Implementation of this technique is
usually not practical in most systems and is only acceptable in special
cases.

Geometrical Signal Compression

These designs are geometrical approaches that are very effective in
reducing the signal dynamic range as seen by the optical receiver. Many
system configurations have been developed for specific needs. Most of
these systems simply increase the intersection of the field of view of the
receiver with the transmitted pulse as the amplitude of the pulse decreases
with propagation time or utilize a spatial filter. Examples are presented
in figure 3.

The major disadvantage of this technique is the difficulty in adapting
a design to the varying signal conditions that may be found in a bottom
mapping system. A reduction in signal collection efficiency usually results
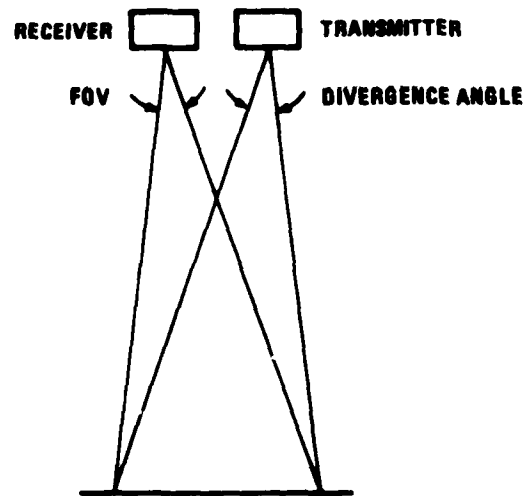which adversely affects the system signal to noise ratio for low level
signals.

Electronic Compression

Amplifiers after the PMT can be useful for compressing the dynamic
range of the signal into a range suitable for recording equipment. The
logarithmic amplifier has long been used for this purpose. A logarithmic
response from an amplifier is difficult to obtain for frequencies exceeding
100 megahertz with the current state of the art. In a bottom mapping
system, a bandwidth of greater than 200 megahertz is desirable. A program-
mable gain change with time for an amplifier (sensitivity time control) is
easier to implement than the logarithmic response, but both techniques
yield a system that is difficult to calibrate. Another technique for
controlling the amplitude of a PMT output makes use of the fact that the
photomultiplier anode is a low impedance current source. By using a
variable load and voltage follower, many programmable responses are possi-
ble. All of these electronic compression techniques fail to improve t:
detrimental effects of the after-pulse emission noise in the PMT,

Dynode Gating

Electrically gating a dynode is an alternate means of gain control for
a PMT. Some reduction in bandwidth occurs due to increased transit time
for the electrons to accelerate to the gated dynode. In addition, high

1. CONTROLLED INTERSECTION OF TRANSMITTER DIVERGENCE WITH RECEIVER
   FIELD OF VIEW

RECEIVER [   ]   [   ]   TRANSMITTER

FOV   DIVERGENCE ANGLE

2. SPATIAL FILTER

FOCAL
PLANE

RECEIVER

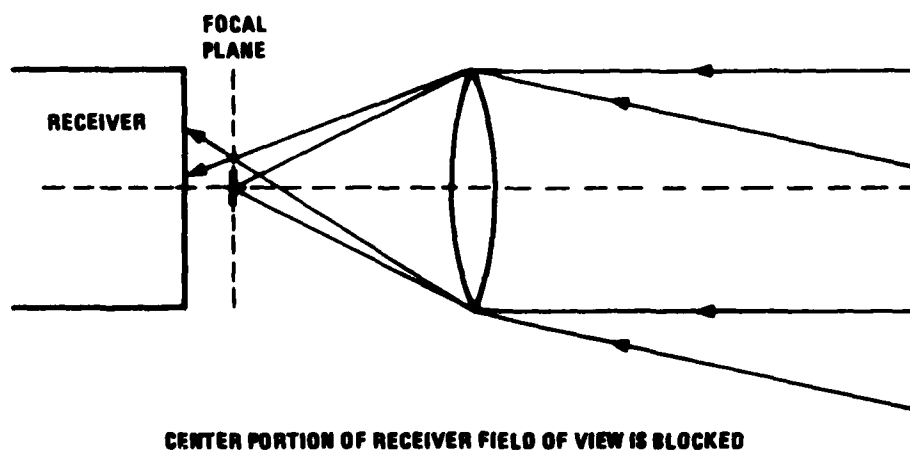CENTER PORTION OF RECEIVER FIELD OF VIEW IS BLOCKED

Figure 3.   Geometrical Signal Compression Techniques

speed gating is difficult due to high potential differences between dynodes.
More significantly, the noise problem associated with after-pulse emissive
effects which occur at the first dynode cannot be reduced by gating later
stage dynodes.

Polarization

Recent data reduction has indicated that the use of cross polarization
can significantly reduce the dynamic range of the return signal. If the
transmitted laser pulse is linearly polarized, a cross-polarized receiver
would see only the depolarized portion of the backscatter. The depolarization
of the pulse increases with pulse propagation time. The major disadvantage
is that a rather large proportion of signal power remains polarized in the
transmitted direction and, therefore, is not received.

Grid Gating

Special PMTs are manufactured with a screen grid between the photocat-
hode and the first dynode. The gating of this grid results in effective
gain control. The after-pulse emissive effects are also reduced propor-
tionately because the first dynode surface is no longer receiving as many
electrons. This grid is in close proximity to the photocathode, so that a
relatively small potential is required for signal gating compared to the
inter-dynode voltages. This lower potential facilitates high speed gating.
The major disadvantage to grid gating is that the gating is equivalent to
varying the quantum efficiency of the photocathode. Since this efficiency
is already low, the statistical noise for signals partially gated off
increases significantly.

Experimental Receiver

The experimental receiver developed at NAVAIRDEVCEN to satisfy bottom
mapping requirements was designed utilizing the grid gating technique.
Implementation of grid gating resulted in a high degree of both after pulse
suppression and dynamic range compression. This technique can be used in
conjunction with most system designs since it is adaptable to many system
configurations. Considerable real time adaptation of the receiver response
is practical to allow for a widely variable operational environment.

The developed grid gated bottom mapping receiver is represented in
block form in figure 4. The constraints imposed on a bottom mapping system
design by the use of this receiver are minimal.

Each of the blocks in figure 4 consist of an electronic subpackage.
These blocks are numbered and they will be referenced by these numbers and
their descriptive titles as they are presented.

The PMT subassembly (block 1 of figure 4) is the heart of the receiver.
All of the receiver circuitry has been designed to support the grid gated
PMT contained in this subassembly. An expanded diagram of this assembly is
shown in figure 5. The PMT (ITT 4084) has six stages and is grid gatable.
The photocathode is a specially processed S20 multi-alkali type formulated
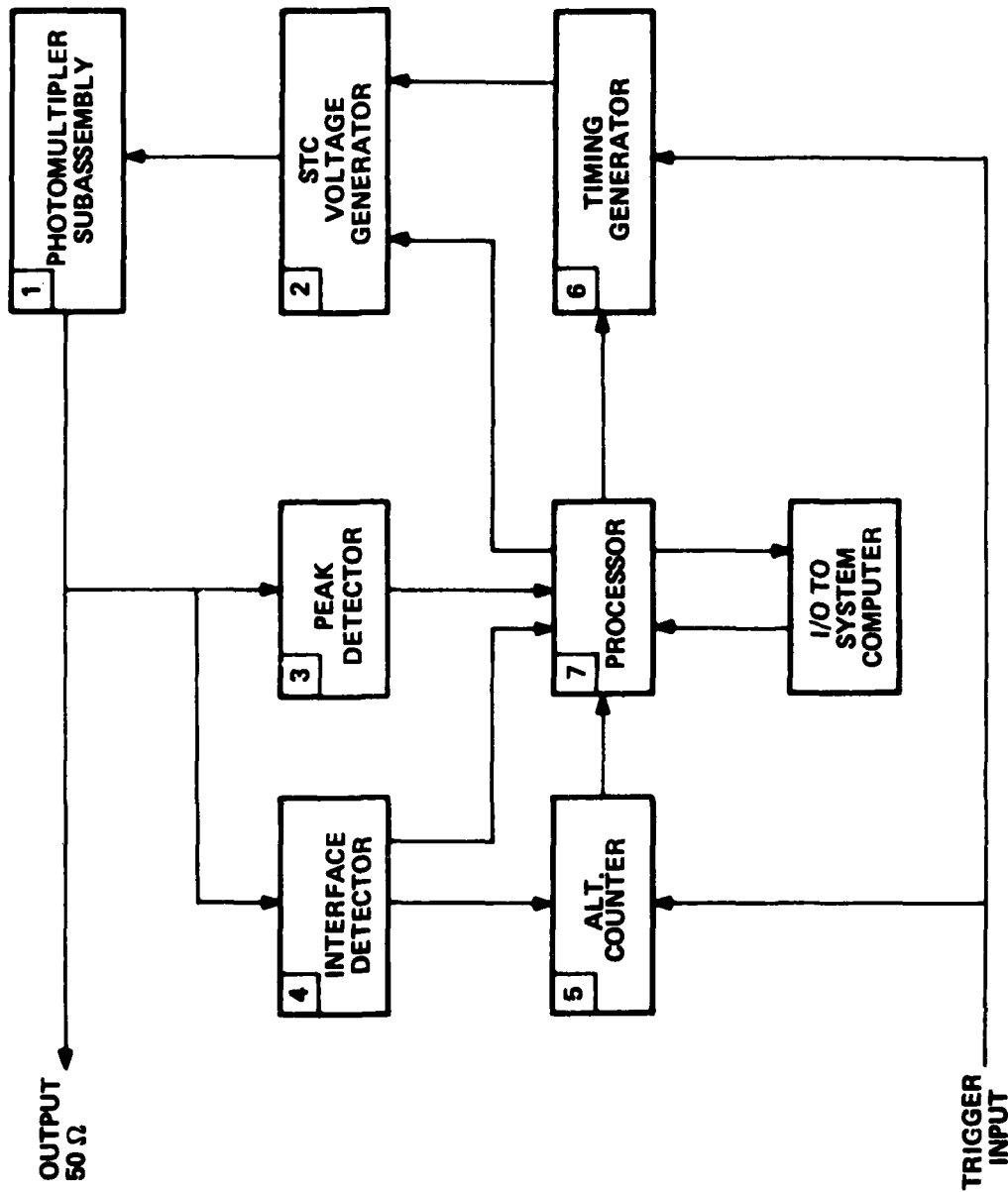for maximum sensitivity at 510 nm.

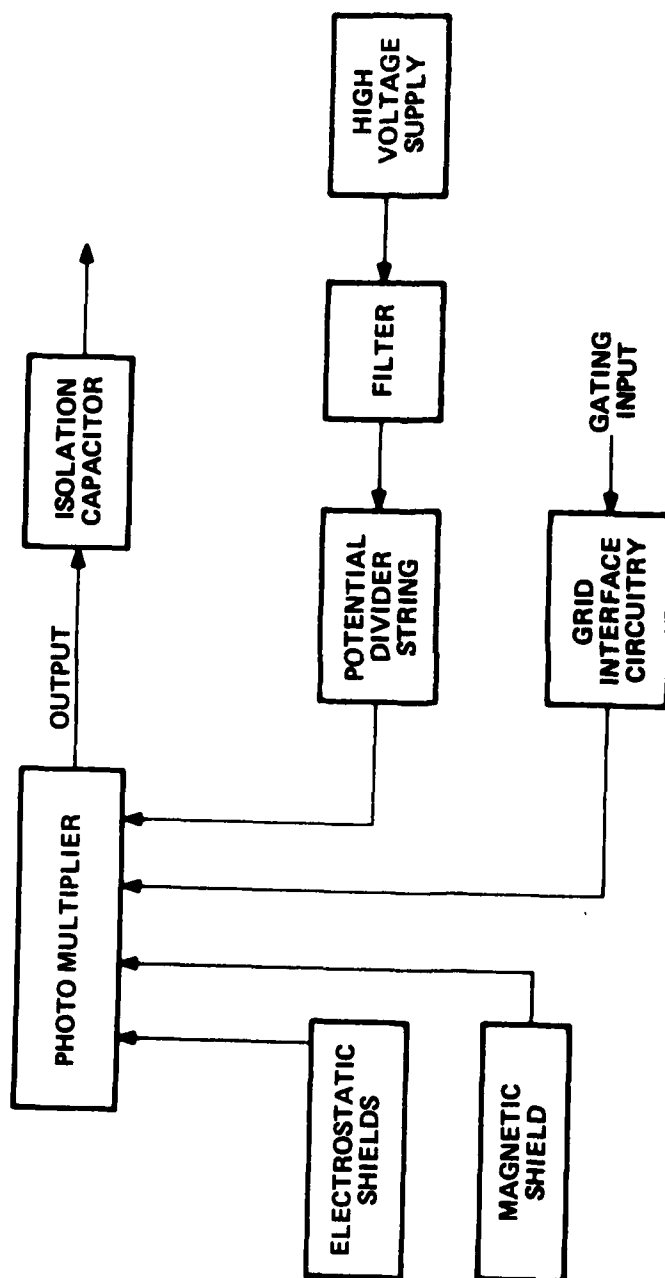Figure 4. Bottom Mapping Receiver Block Diagram

Figure 5.   Photomultiplier Subassembly

Care was exercised in the mechanical design of the PMT housing. The
housing must protect the tube from the vibrational environment of a heli-
copter without compromising the required high frequency electronic inter-
face connections necessary for operation in a bottom mapping mode. The
front of the PMT is mounted with two sets of silver plated circular spring
fingered rings. These rings provide low inductance electrical connections
to the photocathode and grid, while allowing little mechanical stress to be
exerted on the fragile glass to metal seals. Covering the glass envelope
of the PMT is a copper electrostatic shield which is held near the photo-
cathode electrical potential to prevent charge build-up on the glass and
subsequent internal discharging. Without the shield, considerable randomly
distributed discharge noise can occur on the output of the PMT. The entire
mechanical assembly is then enclosed coaxially within a mu-metal magnetic
shield. This shield is desirable because the multiplier electron beams are
quite sensitive to defocusing by magnetic fields.

The potential divider string consists of a resistive divider and
associated capacitors to supply the proper voltages to the dynodes and
focusing electrodes of the photomultiplier. Each dynode is capacitively
bypassed to a brass ring because of the high peak currents and high fre-
quency response required from the photomultiplier. The RC time constant
for each dynode bypass capacitor and associated resistor network was
calculated to prevent signal droop during high current pulses, and to limit
current in the dynodes in the advent of excessive average signal input to
the photomultiplier. The high voltage for the divider is provided by a
regulated power supply. Further filtering of the high voltage output is
done to reduce ripple to less than 1 part in $10.^4$ Also shown in figure 5
is an isolation capacitor on the output of the photomultiplier tube. For
this receiver the positive high voltage is grounded resulting in a negative
going output signal. Although the 4084 PMT has a 50 Ω coaxial output
connector, the outer conductor has a -200 to -500 volt potential from
ground. A coaxial isolation capacitor is incorporated to couple this
connector to standard 50 ohm coax with a grounded shield. A high resis-
tance couples the ground side of the isolator to ground. This prevents
leakage voltage from building up with a disconnected output and subsequent
damage to other equipment when it is reconnected.

The last part of the PMT housing shown in figure 5 is the grid and
photocathode connecting interface. The grid and photocathode reside at
a negative supply potential, normally 2 to 5 kilovolts below ground. A
negative potential of 3 volts or greater between the photocathode and grid
is a fully off or reversed biased condition. A fully on or forward biased
condition exists with a positive potential of 0 5 volts or more. Figure 6
shows the grid gating characteristics. A 3 volt mercury cell is used to
bias the PMT grid to the full off condition. A pulse is then applied via
isolation capacitors to forward bias the PMT. A full off to full on switch
can be made in less than five nanoseconds using a suitable pulse input.
With this gating circuitry the photomultiplier can only be on for a short
time, which protects the tube from a constant overload such as normal
ambient lighting. Included also in this circuit is a neon bulb across the
grid and photocathode. A large potential (> 40 V) may occur across the

grid and photocathode during the initial application of high voltage. The
neon bulb has proven very effective in preventing photocathode damage from
internal grid-cathode arcing. The bulb will visibly flash with most gating
circuitry when power is applied to the receiver. Without some type of
protection the resultant internal arc could damage the photocathode sur-
face.

The STC (Sensitivity Time Control) voltage generator (block No. 2 in
figure 4) contains the pulse shaping generator and pulse driving amplifier
that forward bias the grid on the photomultiplier during signal aquisition.
The precise shape of this pulse is programmed by two analog input voltages.
The shape of the pulse determines the time-gain relationship of the photo-
multiplier as shown in the grid gating curve (figure 6).

By normalizing the received signal output with respect to the laser
pulse backscatter, considerable output dynamic range reduction and target
signal enhancement (including the bottom target return) resulted. The
mathematical model of the pulse shape necessary to normalize was developed
and verified in previous work.[5]

The peak detector is shown in figure 4 as block No. 3. The circuit is
a high speed peak detector capable of capturing 10 ns pulses. This peak
detector is used to hold an analog representation of the maximum output of
the photomultiplier on a shot to shot basis. The detector was designed
with a high impedance input so that it could be connected directly to a
special coax coupling on the PMT output without adversely affecting the
300 MHz receiver bandwidth.

The interface detector shown in figure 4 as block No. 4 is a level
detector with a pulse output. As soon as the PMT output reaches a programmed
output level a pulse is generated. The assumption is that this pulse will
represent the timing of the return from the air-water interface of the
transmitted laser pulse. The interface detector shares the high impedance
connection to the PMT output made by the peak detector.

The altitude counter shown in block No. 5 of figure 4 is a commercial
1 ns resolution counter. It is started by the system laser pulse output
trigger and is stopped by the interface detector output. The count stored
represents the time to the air/water interface, which is equivalent to the
aircraft altitude.

The timing generator, block 6 of figure 4, is also a commercial unit.
It is a dual output delay generator, programmable in increments of 1 ns.
It is used to trigger the STC voltage generator after the system laser
pulse output trigger.

The processor, block No. 7 of figure 4, is used as the control logic
for the entire receiver. It consists of a single board computer with
digital I/O ports and an 8 bit analog I/O interface. The precise program-
ming of the processor is dependent upon the specific bottom mapping system,
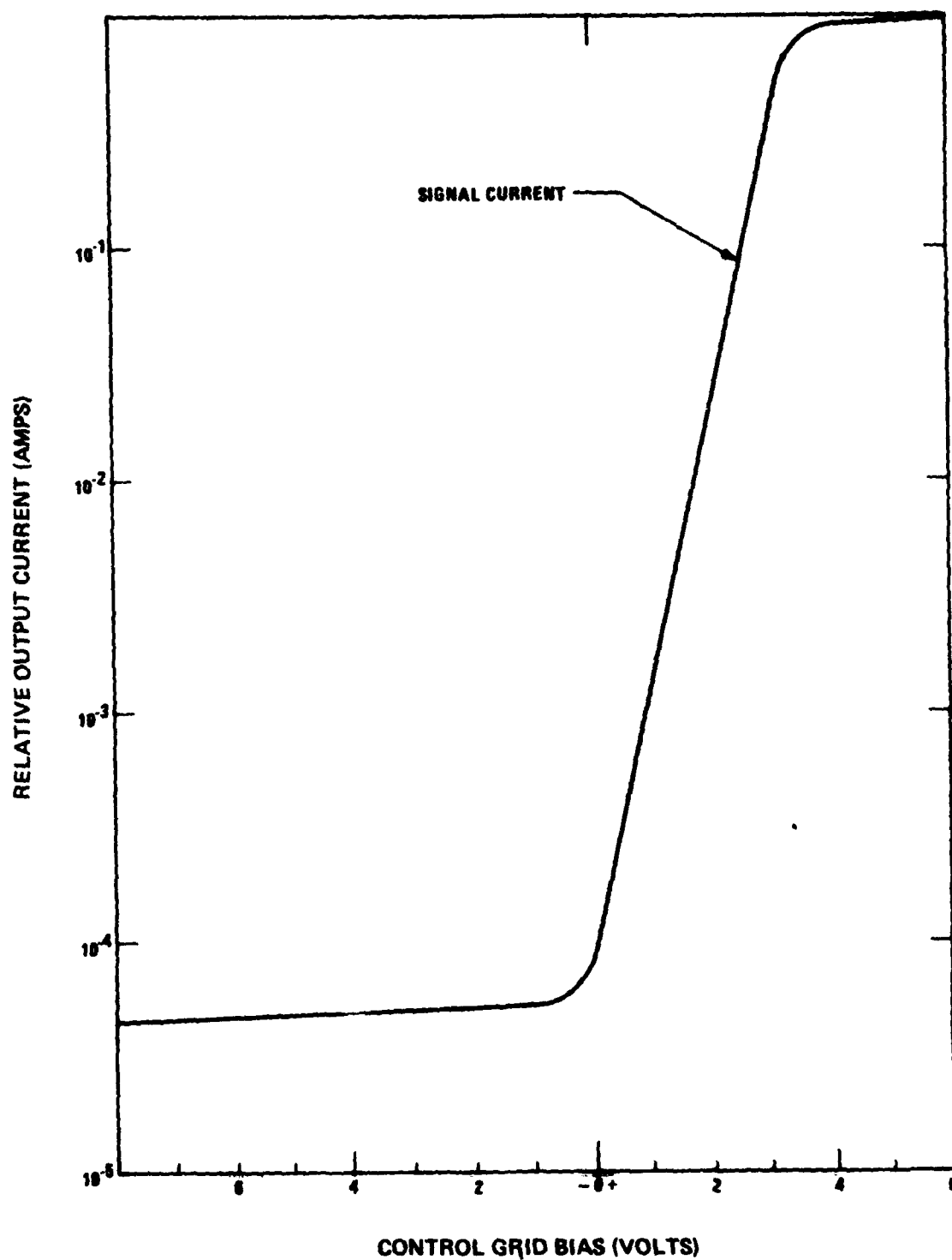so the program resides in an easily changed programmable read only memory.

Figure 6.   Grid Gating Curve

The receiver system operation is completely controlled by the processor. This allows considerable versatility in the number of operating modes available to the user. A typical operational flowchart for the receiver in slave mode with operator and system computer feedback is shown in figure 7. Almost limitless variations in programming can be achieved. At 400 Hertz, the processor can execute approximately 500 machine language instructions, which is sufficient for most applications. Operation of the receiver at 4000 hertz is reasonable but some versatility is sacrificed.

The completed packaged receiver is shown in figure 8, with the ITT 4084 PMT and isolation capacitor in the foreground. Included in the package is the housing, ii.:erface detector, peak detector, and STC voltage generator. The processor, altitude counter and timing generator are rack-mounted. Figure 9 is an internal view of the receiver.

The only external signal required for operation is a system timing trigger, which is normally derived from the transmitted laser pulse. The processor can derive any other received signal information needed for the receiver operation. A single real time signal output is provided to the system recording equipment. In most system designs the interface to the processor would be used for transferring the control functions of the system computer.

Experimental Results

The completed bottom mapping receiver was laboratory tested at NAVAIR-DEVCEN. Some examples of receiver responses to inputs simulating optical signal returns are presented here to demonstrate the receiver capabilities. Combinations of three types of signal inputs were used; A constant input level, a short pulse input, and an exponential decaying pulse. The receiver processor was programmed in BASIC and control was transferred to a CRT computer terminal. This allowed different gating waveforms to be inputed quickly and efficiently under operator control. With the 8-bit digital to analog interface used, 2^8 pedestal settings and 2^8 ramp settings were possible. Photographs were taken from a dual channel 325 MHz Tektronix 485 oscilloscope. The upper trace in each case is the waveform input to the PMT gate. The bottom trace is the photomultiplier output into 50 ohms.

The first three photographs in figure 10 demonstrate the use of dynamic range compression with this receiver. In the upper trace of figure 10a a flat gate is shown as the input to the PMT. This flat gate represents a constant gain. The lower trace shows the PMT output. The corresponding optical input was a short pulse followed by a smaller exponential decaying input 500 ns later. Figure 10b shows the result of simply decreasing the gate pedestal voltage a small amount without changing the optical input. The output trace shows considerably reduced output levels. Note the change of the vertical deflection scale on the lower output trace. A 10^2 gain reduction has been realized. Gain reduction of 10^5 has been measured with other equipment when the gate voltage is reduced further. In the third photograph of the series (figure 10c) the same gate pedestal as in figure 10b was used, but a ramp was added during the exponential decay signal time. This ramp increased the gain logarithmically
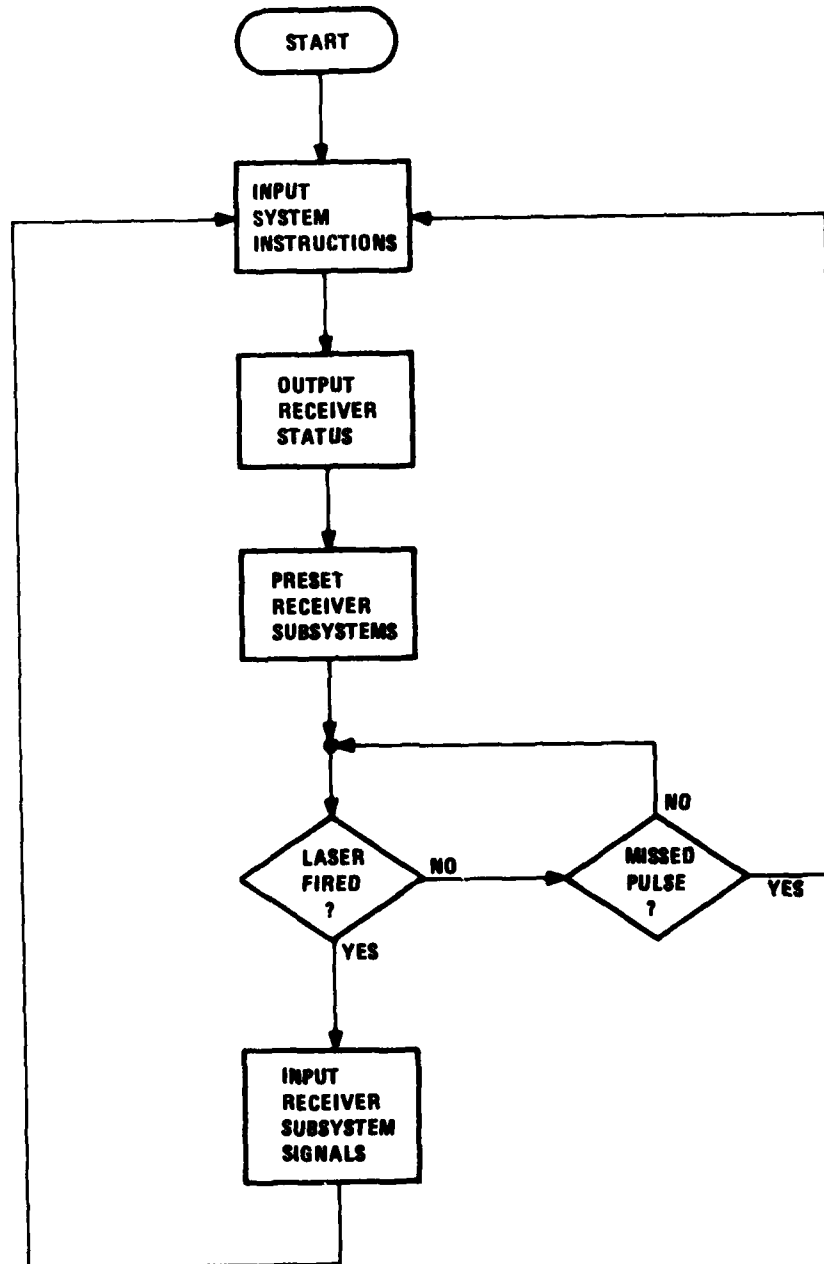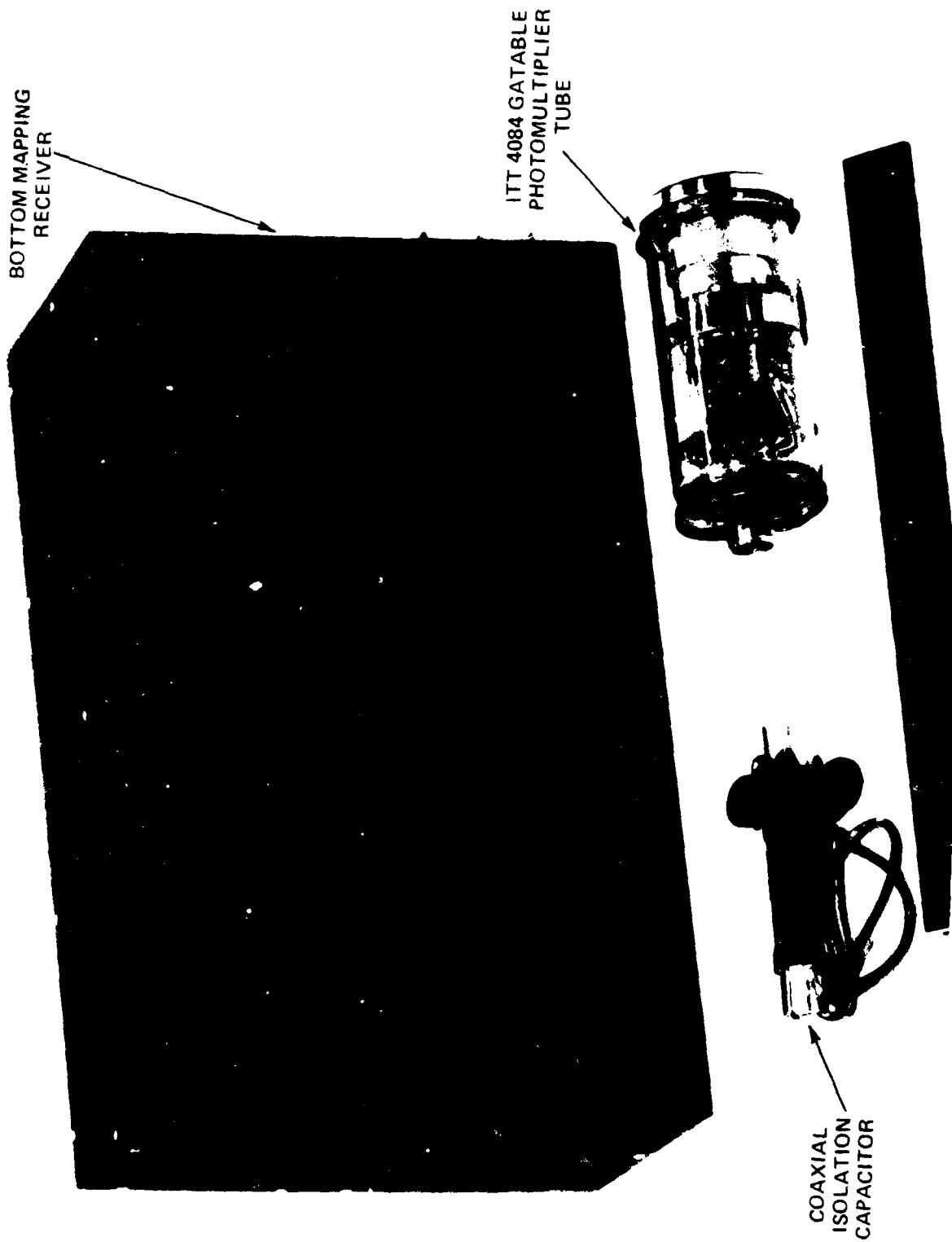
Figure 7. Typical Operational Flowchart

BOTTOM MAPPING
RECEIVER

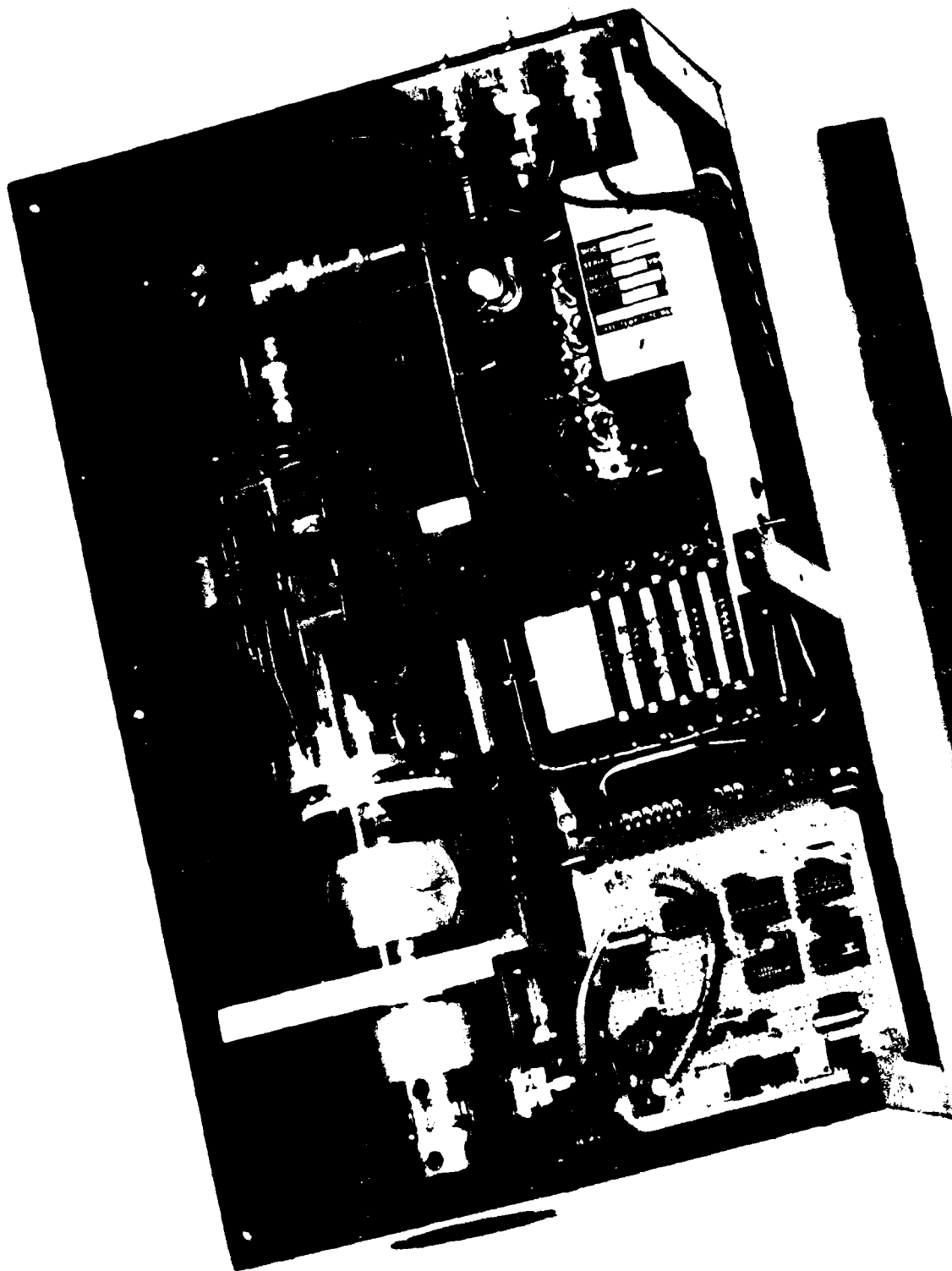ITT 4084 GATABLE
PHOTOMULTIPLIER
TUBE

COAXIAL
ISOLATION
CAPACITOR

Figure 8. Bottom Mapping Receiver

Figure 9. Internal View of Bottom Mapping Receiver

TOP – 2V/DIV
BOTTOM – 0.01V/DIV

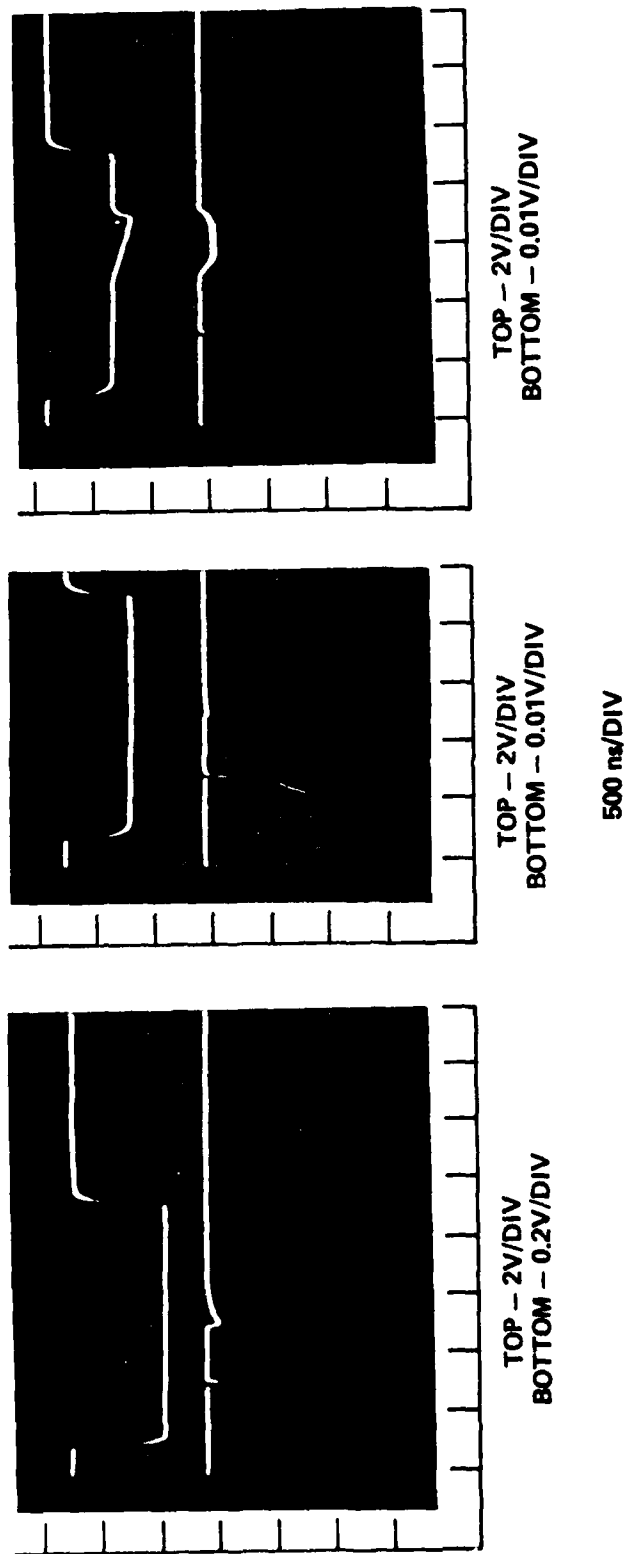TOP – 2V/DIV
BOTTOM – 0.01V/DIV

500 ns/DIV

TOP – 2V/DIV
BOTTOM – 0.2V/DIV

Figure 10.   Simulated Interface and Backscatter

during the exponentially decaying signal, and resulted in a relatively flat
signal output. In a bottom mapping system the short optical pulse would be
similar to an interface return signal. The exponential decay signal,
although displaced in time, is similar to the seawater backscatter. In
this instance the interface signal was compressed and the backscatter was
normalized.

In the next series of photographs in figure 11, the optical input was
an exponentially decaying pulse with a low level short pulse superimposed
near the end. This signal condition approximates a seawater backscatter
return with a target or bottom return included. Figure 11a shows the
output level that results with a fixed pedestal gate. The second photo-
graph of the series (figure 11b) shows the same input partially compressed
and the last half of the exponential normalized. The third photograph
(figure 11c) is compressed a little more than in 11b and the ramp has been
readjusted to provide better normalization to the simulated backscatter
signal. Note the relative enhancement of the small superimposed pulse that
occurs between 11a and 11c.

For some applications a modification of the pedestal-ramp driving
circuitry might be useful. As an example, consider the dual pedestal
approach in figures 12a and 12b. In 12a the PMT output signal is repre-
sent'd on the lower trace with a constant gate pedestal shown in the upper
trac . By superimposing another pedestal on the gate, as shown in figure
12b, the small exponential signal was amplified without affecting the
initial pulse. This multiple pedestal approach is useful because it
allows multiple gain changes in short times, but keeps a linear response
for the photomultiplier output at each gain.

There are some disadvantages encountered in a grid gated receiver
design. Figure 13a shows a constant gain gate input and the PMT output for
a low level constant optical input. Note the rippled output on the lower
trace, and the relatively noisy output indicated by the width of that trace
during signal acquisition. Figure 13b shows data taken under the same
signal and gate conditions, but the top trace representing the gate input
has been expanded vertically by a factor of 2×10^2 to show a small ripple.
The source of the output ripple was actually caused by the ripple on the
gate pedestal. This situation was corrected in the receiver gate generator,
but demonstrates the care necessary in preparing the gating waveform. The
width of the trace in the outputs of both 13a and 13b demonstrates another
inherent problem. This is shot noise, statistical in nature and it is a
direct result of reduced quantum efficiency. The grid gating reduces the
number of electrons reaching the first dynode when in other than maximum
gain situations, causing the effective efficiency of the photocathode to
decrease. This effect is made more obvious by figures 14a and 14b. The
same low level input signals are shown with different gains caused by
different input pedestal levels. Note the relative noise on the output
traces for the two different gain settings. Lowering the gain results in a
decreased signal to noise ratio. Because reduced gain would normally be
used only for large signals, system performance should not be degraded by
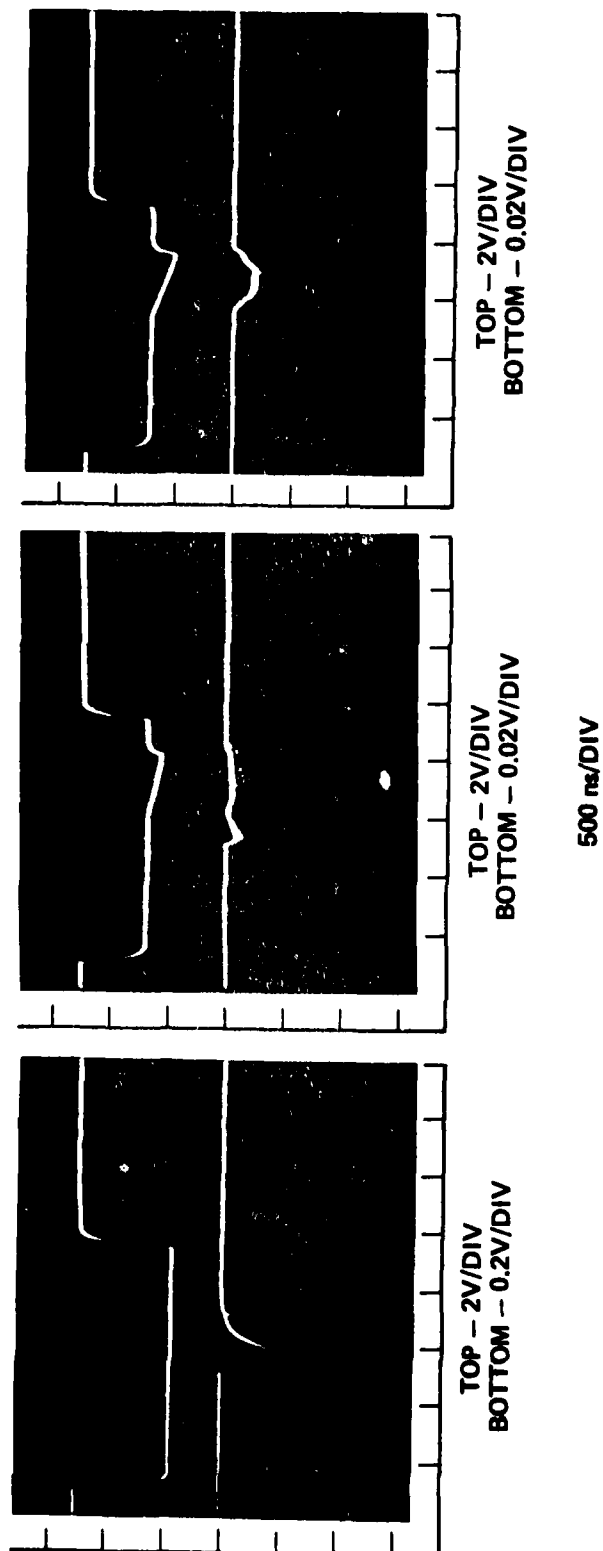this decrease in effective quantum efficiency.

TOP – 2V/DIV
BOTTOM – 0.02V/DIV

TOP – 2V/DIV
BOTTOM – 0.02V/DIV

TOP – 2V/DIV
BOTTOM – 0.2V/DIV

500 ns/DIV

Figure 11.   Simulated Backscatter and Bottom Signals

TOP – 2V/DIV
BOTTOM – 0.02V/DIV

TOP – 2V/DIV
BOTTOM – 0.02V/DIV

500 ns/DIV
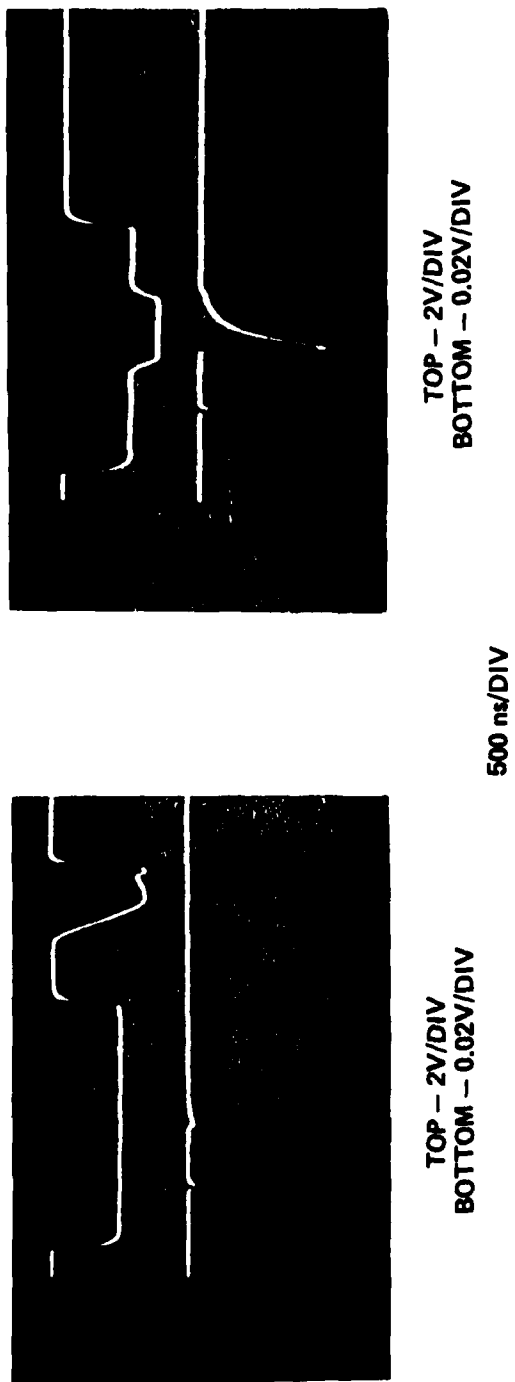
Figure 12.   Dual Gain Demonstration

TOP – .01V/DIV
BOTTOM – 0.02V/DIV

500 ns/DIV

TOP – 2V/DIV
BOTTOM – 0.02V/DIV
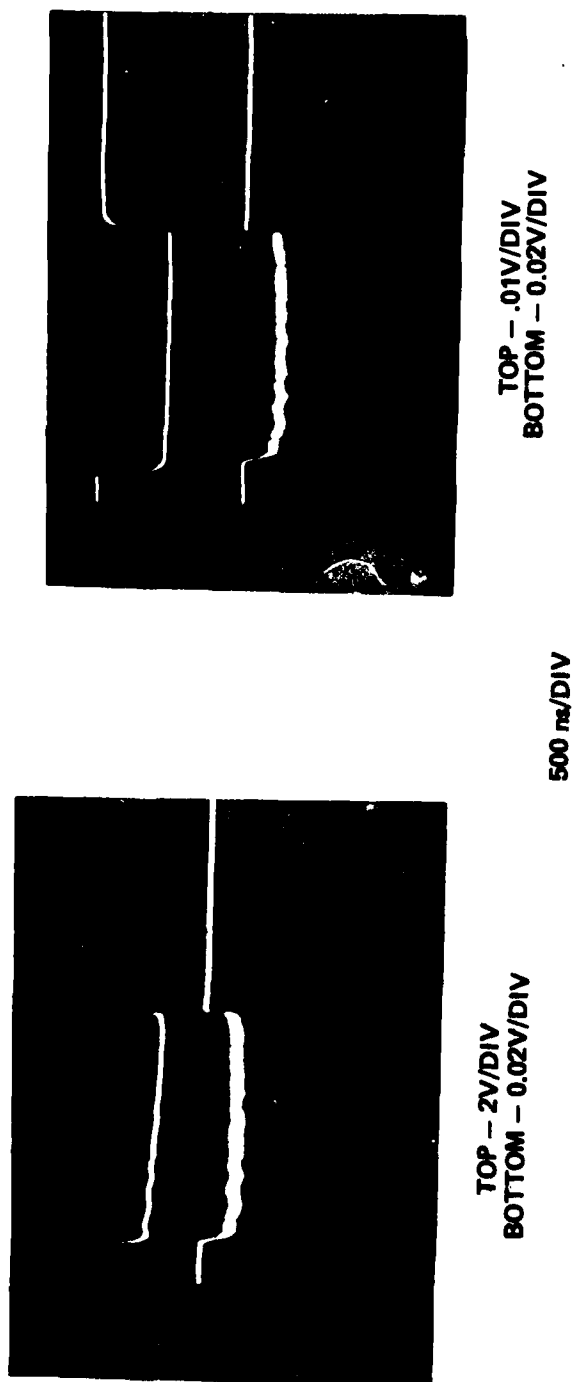
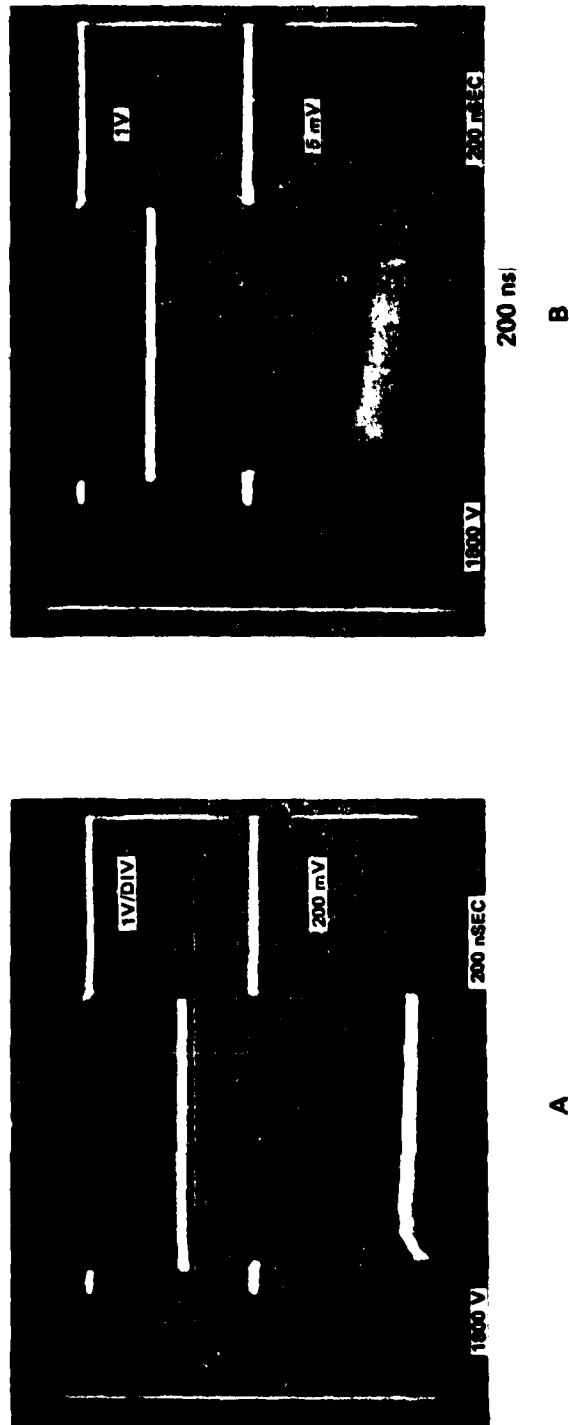Figure 13.   Signal Modulation Caused by Gate Ripple

Figure 14. Quantum Noise Effects

Another characteristic of this PMT is an output spike that occurs if the grid is gated on in less than 20 ns with illumination on the photocathode. The spike is more pronounced with low level input signals and high gains. Figures 15a and 15b show the spike at two different input light levels. This effect can be minimized by gating the photomultiplier in 25 nanoseconds or more. This spike is probably the result of space charge buildup between the photocathode and grid during the off gate time.

Conclusions

The grid gated PMT receiver described in this report has demonstrated significant improvements and advantages over existing designs and techniques. Wide dynamic range signals can be received and compressed without the problem of after pulse noise spikes. Proper circuit design eliminates problems of turn on spike and increased quantum noise. High performance coupled with ease of implementation makes this receiver design an attractive candidate for bottom profilometry applications.
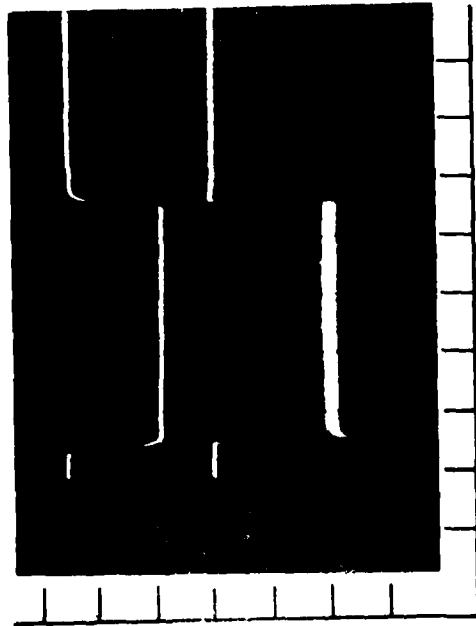
TOP – 2V/DIV
BOTTOM – 0.02V/DIV
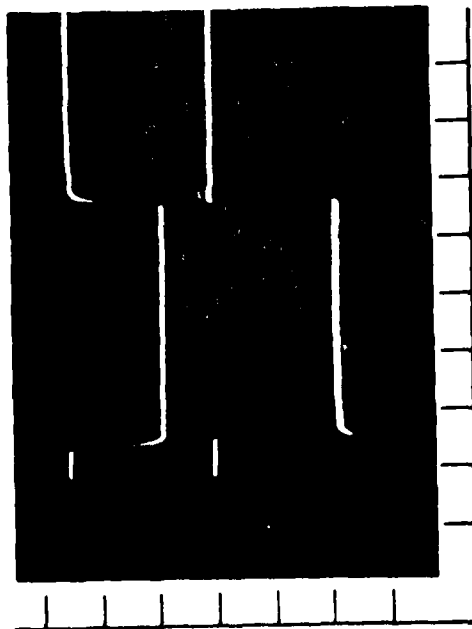
TOP – 2V/DIV
BOTTOM – 0.2V/DIV

500 ns/DIV

Figure 15. PMT Turn on Transient

References

1. Witt, A. K., Shannon, J. G., Rankin, M, B., Fuchs, L. A., "Air/Underwater
    Laser Radar Test Results, Analysis, and Performance Predictions," Naval
    Air Development Report No. NADC76005-20

2. Krumboltz, H., "Experimental Investigation of System Attenuation Coeffi-
    cients for HALS," Naval Air Development Report No. NADC80035-30 Aug 79.

3. Petri, K. J., "Laser Radar Reflectance of Chesapeake Bay Waters as a
    Function of Wind Speed," The Institute of Electrical and Electronics
    Engineers, Inc, Annals No. 704GE006, Vol. GE-15, WO 2, Apr 1977

4. Eberhardt, E. H., Barr, F. H., Henkel, P. R., Final Report - "Research
    in the Development of an Improved Multiplier Phototube," Contract NASW-1576,
    International Telephone and Telegraph corporation, Industrial Laboratories
    Division, Fort Wayne, IN

5. Krumboltz, H., Contarino, V. M., "An Optical Radar Receiver Using
    Programmed Sensitivity Time Control," Proceedings of the Society of
    Photo-Optical Instrumentation Engineers, Vol 160, Ocean Optics V,
    Aug 1978

6. Ross, M., "Laser Receivers - Devices, Techniques, Systems," John Wiley
    and Sons, Copyright 1966, New York, NY

PAPER 30

A LIGHT AIRCRAFT LASER MAPPING/HYDROGRAPHY SYSTEM

F. Cook, G. Dryden, H. Kent, C. McDonough and J. Nunes

Reported by M.G. Miller

Avcc verett Research Laboratory, Inc.
2385 Revere Beach Parkway
Everett, Massachusetts USA   02149

An all digital, airborne pulsed laser mapping system
has recently been developed. This system, obtaining posi-
tion and profile data through both tree canopy and water
is currently being employed as a test and demonstration
model. Ground truth flights were begun in July 1979 when
the system was initially installed in a Cessna 206. While
this system was not fully optimized for weight and size,
it was designed to be installed in photographic, light air-
craft. The 1.1 kW peak electrical power requirement can
be satisfied with, for example, Cessna 310 power or with
system batteries.

The laser used is a commercially available Nd:YAG
operating at 10 Hz. Terrain mapping uses the 1.06μm out-
put whereas hydrographic data is obtained with the 0.532μm
doubled output. The receiver includes a 20 cm aperture
which is non-scanning, optical bandpass filter and two
interchangeable detectors: an avalanche photodiode at
1.06μm and a photomultiplier at 0.532μm. To provide ade-
quate dynamic range, a high bandwidth log amplifier is
used to compress approximately 4 orders of signal magni-
tude to a range consistent with a 6 bit analog to digital
waveform analyzer which has a minimum resolution of two
nanoseconds. The complete digitized return waveform is
stored on magnetic tape for off-line post-processing. The
entire system is under the control of a small computer and
requires only a single operator.

The aircraft is positioned in three axes by use of
three microwave distance measurement transponders located
at known ground sites. This system measures range with
1 m accuracy. Data from a differential barometric altim-
eter is also used in determining height above mean sea
level. Two-axis gyro data locates the laser spot on the
ground or water surface. Position is determined and re-
corded every two seconds. A 35 mm framing boresight cam-
era is also included in the package to aid scene and ground
truth correlation. With the aircraft flying at 915 m
altitude and 216 km/hr, survey measurements are made every
6 m along the flight path with a typical laser spot diameter
of 3 m.

The raw, digitized returns are processed off-line
with a variety of algorithms depending on details of the
application and data needs. Most are based on derivative
type processing coupled with first and last pulse discrim-
ination. Model pulse subtraction, matched filtering and
multipulse processing have also been considered. Algorithm
development and improvements represent an area of continuing
activity.

The system data collection endurance is limited by the
cartridge tape recorder. Upgrades of recording capability
are planned for future implementation. Other planned up-
grades are pilot route display allowing parallel survey paths
of 100 m separation, aircraft attitude measurements along
three axis and extended vertical position capability allowing
wider spacing of the remote ground stations.

Initial hydrographic flight tests were carried out
over Nahant Bay, Massachusetts. This area afforded:geodetic
control; distinctive terrain and hydrographic features; a
60 m wide ship channel with depths from 7 m to 10 m; and,
recent detailed hydrographic sounding data obtained by the
U.S. Corps of Engineers in July 1979 with depth accuracies
cited to 3 cm. Because of the prior existence of convenient
geodetic control points, the ground control spacings of
2.5 km, 3.5 km and 4.5 km were smaller than necessary. Pro-
file runs were typically 2-3 km in length with altitudes of
610 m and 915 m.

The results of one run in this location are shown in
the accompanying figure. Data are plotted as points (single
return) of lines (two returns, i.e., tree and ground or
water surface and bottom). Good correlation with ground
truth can be noted in both the ship channel and shallow
areas. The algorithm used in the reduction required depths
in excess of approximately 1.5 m. Mean low tide channel
depths along track measured nominally 5.9 m with a 1.7 m
tide at the time of the measurements. The water surface
structure of less than 1 m probably includes both system
resolution and wave effects. The only significant differ-
ence between ground truth and laser data appears at the
right side of the channel. Maximum differences are 1.5 m.
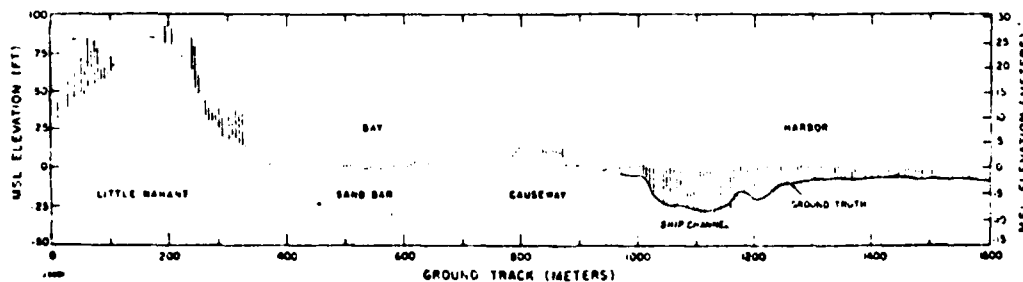
Laser Derived Terrain and Water Depth Profile Data taken
along the Laser Ground Track shown. U.S. Corps of
Engineers hydrographic survey data adjusted for tide is
overlaid in the harbor area.

NAVAL AIR DEVELOPMENT CENTER
WARMINSTER, PENNSLYVANIA   18974

EXPERIMENTAL INVESTIGATION OF SYSTEM ATTENUATION
COEFFICIENT FOR HALS

1 Oct 1980

H. Krumboltz

INTRODUCTION

The Defense Mapping Agency (DMA) has established a requirement for an airborne laser radar bottom mapping system for rapid water depth measurements in shallow coastal waters. This system is called the Hydrographic Airborne Laser Sounder (HALS). In order to determine the depth limitations of such a system in specific areas, it is necessary to know how the system attenuation coefficient (SAC) is related to system and oceanographic parameters. The NAVAIRDEVCEN has been testing an Optical Ranging and Detection/Optical Ranging IFF Communication (ORAD/ORIC) system designed for antisubmarine warfare (ASW) purposes for several years. This system was installed in an SH-3 helicopter and was used in a series of flight tests to determine SAC's for ASW purposes. Since the ORAD/ORIC and HALS systems are similar in concept, the NAVAIRDEVCEN proposed that the SAC applicable to bottom mapping be investigated with the ORAD/ORIC system.

Tests were conducted at Key West during May 1979 in conjunction with ORAD/ORIC ASW tests. The results of the DMA test are described in this paper.

BACKGROUND

The two optical oceanographic measurements that are now made to predict laser radar depth capabilities are beam transmission and diffuse attenuation. Beam transmission is measured with a transmissometer (α meter) that registers the attenuation of a collimated beam of light over a one-meter path at a specific wavelength. This instrument is designed to accept only unscattered light in the beam so that any light scattered out of the beam is lost, resulting in increased attenuation. The transmission measured in clear ocean water can be as great as 95 percent per meter ($\alpha = 0.051$).

Diffuse attenuation is measured with an underwater irradiance meter with the appropriate wavelength filter and the sun or sky as the source of illumination. This instrument accepts unscattered and scattered light, with a result that can indicate less attenuation than the transmissometer measurement. The measurement produced by each instrument is unique and valuable in assessing the optical properties of the ocean but discretion must be used in the application of these measurements to laser radar performance. In coastal waters with a large number of scatterers per unit volume, the beam transmissometer will indicate a greater attenuation than the underwater irradiance meter.

When an airborne laser radar is used to measure water depth, the signal returned from the bottom contains both scattered and unscattered light. If the field of view (FOV) is narrow, little scattered light can be accepted. If the FOV is increased, more scattered light can be accepted. The narrow FOV condition is similar to the transmissometer measurement. The wide FOV condition is similar to the diffuse attenuation measurement. The ASW tests conducted by the NAVAIRDEVCEN in 1974 showed that the SAC approached the oceanographic "K" measured with the underwater irradiance

meter as the FOV was increased. Figure 1 shows the data from this test.
The FOV for the HALS system is related to required depth accuracy. The
output of the HALS system is the depth measurement rather than the target
detection, as with the ORAD/ORIC system.

TEST PROCEDURE

     In order to obtain the necessary data, two ranges were established in
the waters near Key West, Florida. Figure 2 shows the location of these
ranges. The first range consisted of four buoys anchored at various bottom
depths along a north-south line approximately 7.5 miles from the Key West
International TACAN at 165°. The second range consisted of two buoys
anchored at different bottom depths northwest of the first range. This
second range was used to obtain data from an area with a different type of
water.

     Bottom samples were obtained by divers at all buoys so that optical
reflectivity could be measured. The reflectivity of the samples was measured
at Key West by Naval Oceanographic Research and Development Activity (NORDA)
personnel using their reflectometer. Subsequently, the reflectivity was
measured at the NAVAIRDEVCEN using a narrow band reflectometer. Optical
measurements of the water were taken during the tests with a beam trans-
missometer and a diffuse irradiance meter.

     Airborne data were obtained by making a series of passes over each
buoy at specific altitudes using various configurations of the ORAD/ORIC
system. The signal amplitude was recorded in the aircraft in a manner that
would permit the determination of the SAC for each pass. Altitude require-
ments coupled with wind conditions prevented hover at each buoy.

EQUIPMENT DESCRIPTION ORAD/ORIC AIRBORNE SYSTEM

     The ORAD/ORIC equipment in the SH-3 used in these tests is shown in
the block diagram of Figure 3. Descriptions of the individual blocks are
as follows.

Mirror Scanner

     A gyro stabilized mirror is used to position both transmitted laser
beam and receiver FOV in a coaxial arrangement. During the DMA target
tests, the mirror system was used only in the vertical position. Stabi-
lization range is nominally +45° roll and +15° pitch.

Laser

     The laser is a Q-switched Nd:YAG with simmered flash lamp pumping.
The IR output of the laser is frequency doubled to a wavelength of 532 nm.
At 15 pulses per second, the green output is nominally 100 kW with a pulse
width of 15 nsec. An integral power monitor provides an output voltage for
panel meters and recording. A quarter-wave plate in the output beam changes
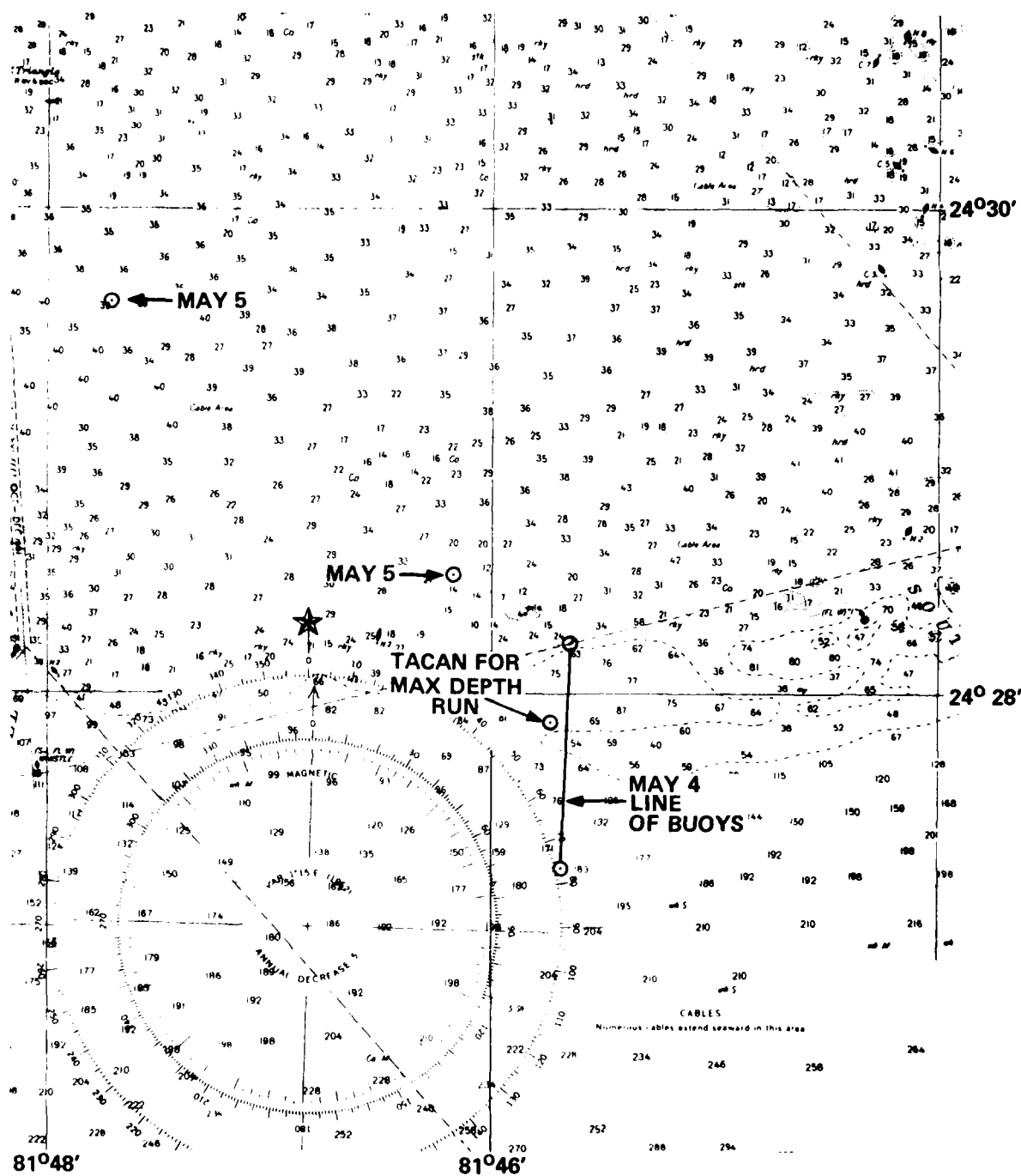the polarization from linear to circular.
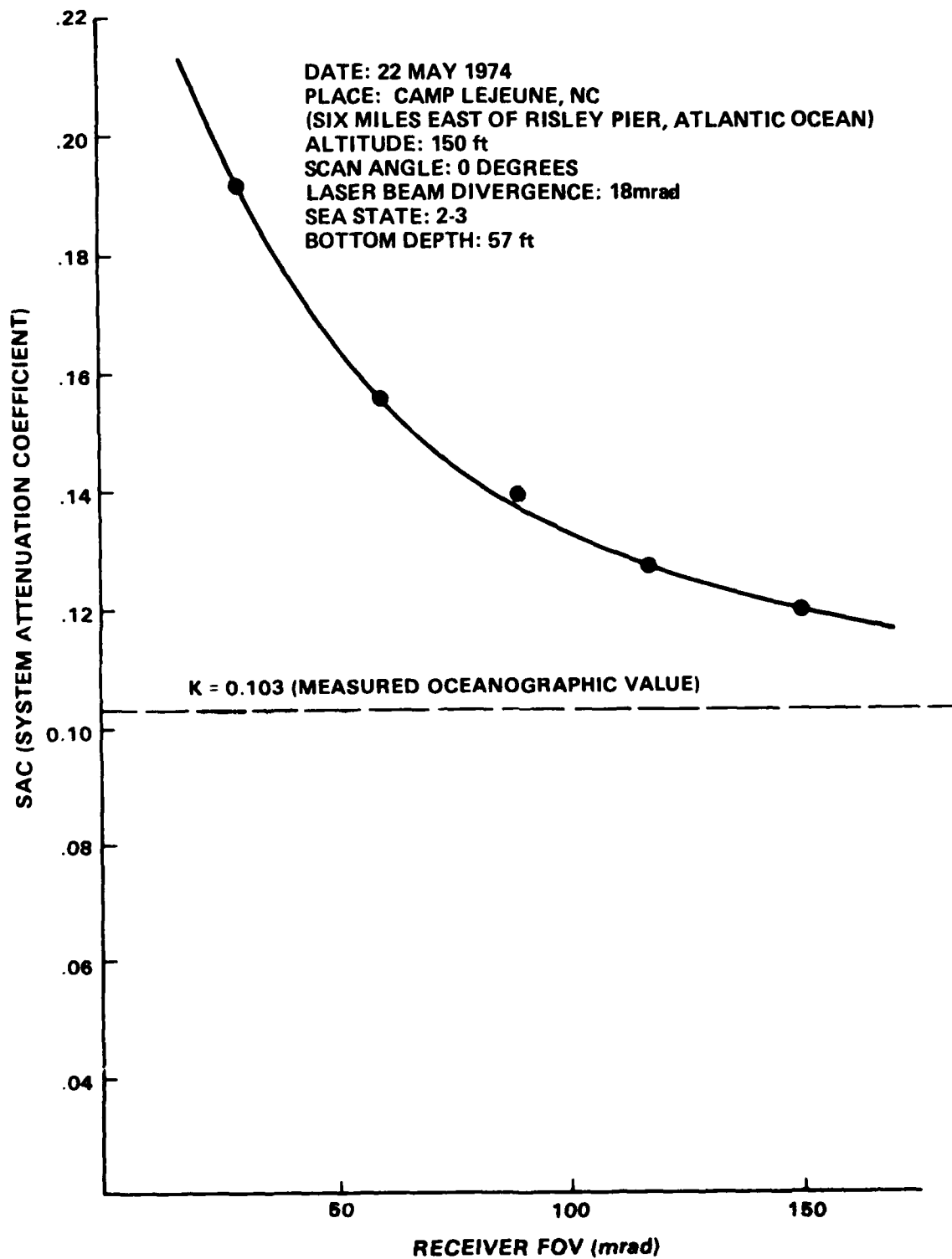
Figure 2.   Range Locations

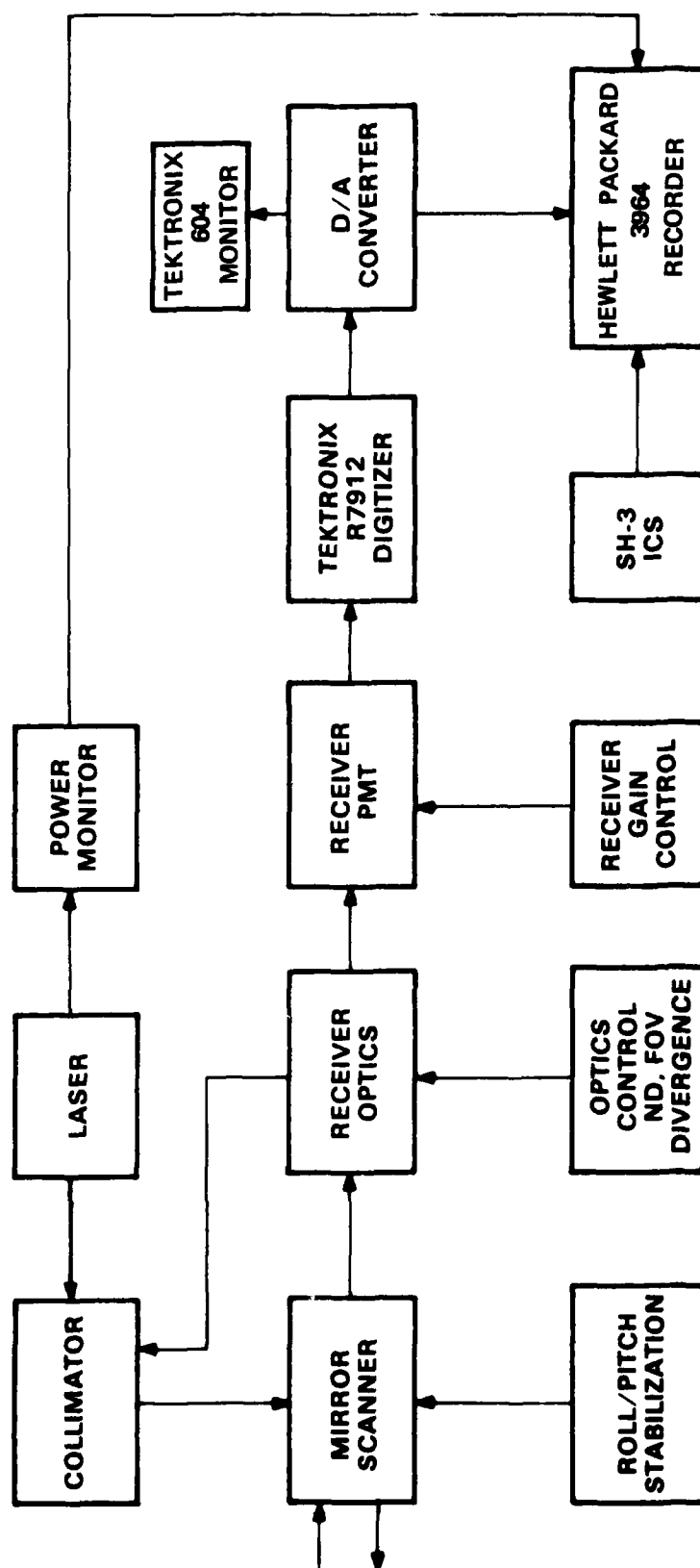Figure 1. SAC as a Function of Receiver FOV for ORAD, 1974.

Figure 3. ORAD/ORICS Installed in SH3.

Optics and Optics Control

The laser output is routed through a variable collimator to provide
the desired beam divergence. The 8-inch diameter collecting optics of the
receiver are located behind a mosaic interference filter centered at 532 nm
with a bandwidth of 2.5 nm. An iris located at the focal point permits the
control of the FOV. A filter wheel with calibrated ND filters is used to
control the signal reaching the PMT. All of these functions are controlled
remotely with the optics control unit.

Receiver Photomultiplier and Gain Control

The receiver PMT is a grid gated F4048 with an S20 surface made by
International Telephone and Telegraph Company. Two gates were applied to
the grid during the DMA tests. An adjustable amplitude gate was used to
set the gain for the interface signal. A second gate, adjustable in time
only, was used to provide a calibrated sensitivity for measurement of
bottom signals.

Tektronix R7912 and D/A Converter

The R7912 is a scan converter type of transient digitizer that reduces
the bandwidth of the signals from the PMT so that they may be conveniently
displayed and recorded. The modified R7912 provides a synchronous digitial
signal that is converted to an analog signal for display and recording.

Recorder and ICS (Intercommunications System)

A Hewlett-Packard 3964 analog magnetic tape recorder is used at 15 in/sec
to record the signal return, laser power, and ICS audio. The ICS audio
contains comments from ORAD/ORIC operators and the flight crew.

OCEANOGRAPHIC INSTRUMENTATION

Transmissometer

A standard Martek XMS transmissometer with a filter centered at 493 nm
was used with a Hewlett-Packard 136 X-Y-Y recorder. The transmissometer
system included a temperature probe and depth sensor so that profiles of
transmission and temperature were obtained on the X-Y-Y recorder.

Irradiance Meter

A irradiance meter designed and constructed by Scripps Institute of
Oceanography (SIO) for the NAVAIRDEVCEN was used with a Hewlett-Packard
7004 X-Y recorder. A filter in the underwater sensor was centered at
531.7 nm. The slope of the plot of underwater irradiance as a function
of depth was used to obtain the oceanographic extinction coefficient "K".

All oceanographic instruments and buoys were deployed from the Key
West Field Station's 135-foot LCU.

SYSTEM CALIBRATION

In order to obtain precise amplitude measurements of bottom signals, it was necessary to calibrate the entire ORAD/ORIC system before each flight. This calibration consisted of making a power measurement independent of the laser power monitor and measuring the power received from a calibrated target at a known distance. For these measurements, a front surface mirror was placed at a 45° angle beneath the aircraft. During these calibration measurements, FOV, divergence, and boresight were checked.

The constants used in the calibration equation are as follows:

Target reflectivity (diffuse) = 90 percent

Mirror reflectivity (specular) = 89 percent

ND calibration

$$ND\ 0 = 0.008$$

$$0.3 = 0.176$$

$$1.0 = 0.881$$

$$2.0 = 1.90$$

$$4.0 = 4.04$$

Receiver sensitivity = $2.92\ (10)^3$ A/W
(includes loss in emitter followers into a 50-ohm load)

Effective receiver aperture = 7.04 inches

The equation used for ground calibration was:

$$F_c = \frac{V}{P_T R_T R_m^2 \left(\frac{3.52}{12\ D}\right)^2 A_{ND}\ S(50)}$$

where:

F_c – system calibration factor

V – PMT output (volts)

P_T – peak power transmitted through window (watts)

R_T – reflectivity of target

R_m – reflectivity of mirror

D – distance to target (feet)

A_{ND}- attenuation of selected ND filter

S - sensitivity of PMT (amperes/watts)

The following calibration factors were measured during the test period:

   3 May _____ 8.74 percent

   4 May 2100 hours   4.9 percent

   5 May 1155 hours   5.2 percent

   5 May 2030 hours   5.1 percent

DATA OBTAINED DURING TESTS

Oceanographic Data

Frequent measurements of beam transmission (α) and relative irradiance (K) were made during the tests. Bottom samples were obtained by divers at each buoy location. These samples were measured by NORDA personnel at Key West and subsequently by NAVAIRDEVCEN personnel. The reflectivity of the bottom samples is listed in table I.

TABLE I

REFLECTIVITY OF BOTTOM SAMPLES

REFLECTIVITY (%)

Date	Buoy No.	NORDA GREEN	NORDA BLUE	NAVAIRDEVCEN (550 nm)
4 May	1	37.4	26.0	35
	2	39.2	30.6	42
	3	41.3	32.2	49
	4	40.6	31.0	52
5 May	1	–	–	44
	2	–	–	52

Laser Radar Measurements

The signal return from the bottom was recorded on magnetic tape in the aircraft. The amplitude of this return signal was measured in the laboratory for each pass over each buoy. Generally, there were three passes for each buoy. The three values of signal return were averaged and used to compute the SAC. In all cases, the laser beam divergence was 20 mrad and the scan angle was zero.

The following equation, derived from the general range equation, was used to compute the SAC values:

$$SAC = \frac{1.64 \; \ln \left| \dfrac{VT_R \, (D + H)^2 \, (8.29) \, (10)^{-5}}{T_x \, F_c \, R_B \, P_T} \right|}{D}$$

where:

SAC — effective system attenuation coefficient

V — signal voltage (volts)

T_R — received pulse width (25 nsec)

T_X — transmitted pulse width (15 nsec)

D — water depth (feet)

H — aircraft altitude (feet)

F_c — system calibration factor (loss)

R_B — reflectivity of ocean bottom

P_T — power transmitted (watts)

The computed values of SAC are listed in table II. A sample plot is shown in figure 4 along with the measured values of α and K.

Maximum Depth Measurement

At the request of DMA, a maximum depth run was made on 5 May. The purpose of this run was to demonstrate the αD and KD capability of the ORAD/ORIC system under existing conditions of ambient light, water clarity, and bottom reflectivity. Since it is very difficult to obtain water clarity and bottom reflectivity measurements at the location of minimum detectable signal, the measurements made at the closest buoy, buoy No. 4, on 4 May were used to compute αD and KD. Table III lists the pertinent data for this run and figure 5 shows the signal received near the maximum depth location. The αD was 14.8 and KD was 3.7 at this point.

TABLE II. COMPUTED VALUES OF SAC FOR ALL TEST CONDITIONS[a]

	BUOY NO.	DEPTH	HEIGHT	α	K	FOV/SAC						
						20	30	40	50	60	70	80
4 May	1	32.8	500	0.462	0.123	0.204	0.176	0.161	0.149	0.142	—	0.134
	2	75.5	500	0.510	0.140	—	—	—	0.173	0.160	0.149	0.143
	3	78.7	500	0.417	0.118	0.203	0.191	0.179	0.168	0.177	0.159	0.149
	4	88.6	500	0.478	0.098	0.191	0.178	—	0.169	—	0.162	0.157
	1	32.8	1500	0.462	0.123	0.186	0.171	—	—	—	—	—
	2	75.5	1500	0.510	0.140	0.175	—	—	—	—	—	0.151
	3	78.7	1500	0.417	0.118	0.172	0.161	—	—	—	—	—
5 May	1	19.7	500	0.357	0.108	0.198	0.148	0.137	0.138	0.132	0.139	0.132
	2	34.4	500	1.12	0.190	0.289	0.266	0.244	0.228	0.215	0.217	0.194
	1	19.7	1500	0.357	0.108	0.162	0.139	0.135	—	—	—	—
	2	34.4	1500	1.12	0.190	0.229	0.203	—	—	—	—	—

[a]Field of view (FOV) is given in indicated mrad*, depth and height in feet.
*Correction necessary for true FOV
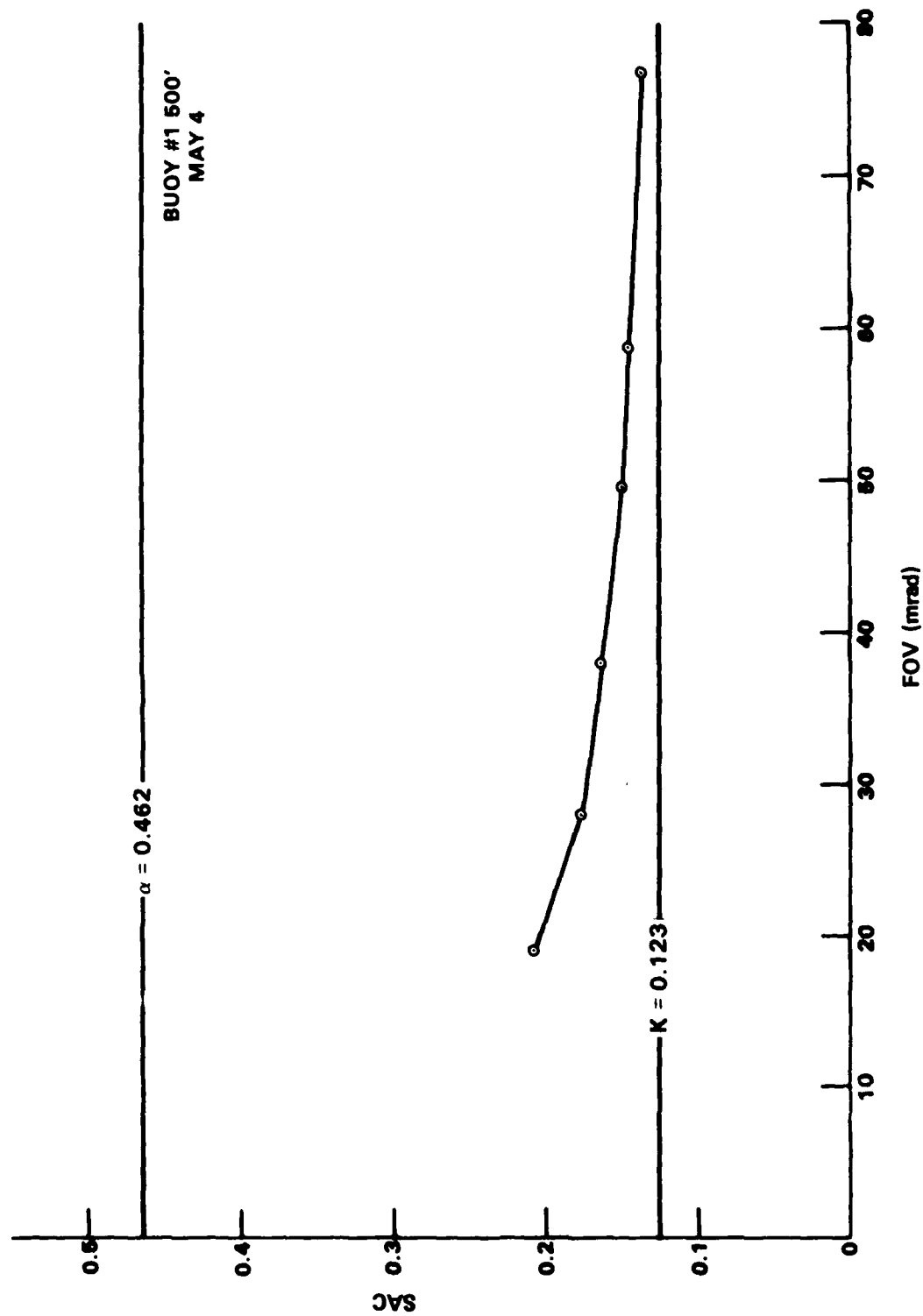
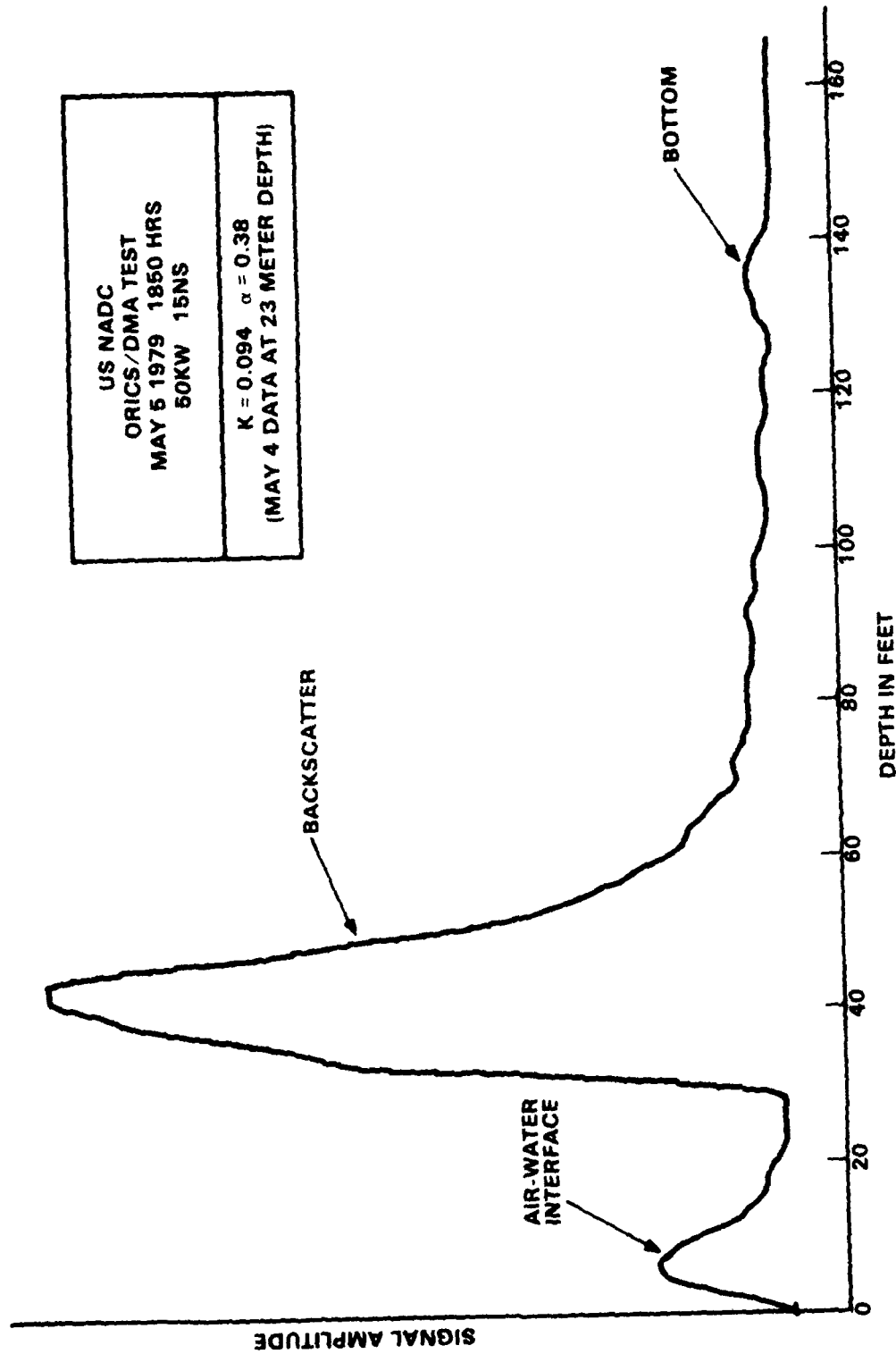Figure 4   SAC as a Function of FOV; 4 May, Buoy #1, 500-ft Altitude.

US NADC
ORICS/DMA TEST
MAY 5 1979   1850 HRS
50KW   15NS

K = 0.094   α = 0.38
(MAY 4 DATA AT 23 METER DEPTH)

BACKSCATTER

BOTTOM

AIR-WATER
INTERFACE

SIGNAL AMPLITUDE

DEPTH IN FEET

Figure 5   Bottom Signal at Maximum Depth

TABLE III

MAXIMUM DEPTH RUN DATA

Date:	5 May, 1850 hours
Altitude:	500 ft
Sea state:	1
Laser divergence:	20 mrad
Field of view:	50 mrad
Laser power:	50 kW
Maximum depth:	125 ft
Water quality:	$\alpha = 0.388$ K = 0.098

CONCLUSIONS

These tests performed for DMA were intended to help establish a reliable method of predicting depth performance of the HALS system. The results of these tests clearly show that the diffuse attenuation coefficient K is more useful in performance prediction than the beam attenuation coefficient.

PAPER 32

DETERMINING THE GEOGRAPHIC COORDINATES OF
LASER-MEASURED DEPTHS

LT(jg) Timothy Rulon
NOAA/NOS
EDL/C61
Rockville, MD 20852

The National Ocean Survey's (NOS) goal is to determine the
horizontal position of each laser-measured depth to an accuracy
of 4.56m (1 sigma) relative to shore control. The system uses
an aircraft-mounted, pulsed laser beam that is scanned at 20^0
off-nadir to collect a swath of discrete soundings along each
flight line. The NOS system will take 600 soundings per second
over a 222m wide swath yielding an average distribution of 1 per
$25m^2$. The system will operate from a light twin-engine aircraft
flying at an altitude of 1000 feet and a velocity of 150 kt.
This paper will examine several technologies suitable for accurately
measuring the positioning parameters.

An error analysis conducted to determine the horizontal error
as a function of the six required parameters (X, Y, Z, ρ, θ, ϕ) is
used to establish the requirement for an onboard inertial system to
determine the heading of the aircraft. Examining the state-of-the
art for both gimbled and strapdown inertial systems, the roll/pitch
and heading accuracy has been determined to be on the order of $.2^0$
(1 sigma). Combined with errors attributable to the laser system,
a proposed error budget has been developed as a means of determining
the horizontal accuracy required for the aircraft.

Proposed Positioning Subsystem Error Budget

Parameter	Accuracy(1 sigma)
Horizontal position (X, Y)	3.9m
Vertical (Z)	1 m
Off-nadir error (pitch and roll)	0.25^0
Heading error (laser pointing plus aircraft heading)	0.5^0

Two candidate horizontal positioning systems capable of
achieving this degree of accuracy, 3.9m (1 sigma), have been identified.
These are a ground-based precision microwave ranging system and a
differential Global Positioning System Satellite receiver. Error analyses
conducted for each of the two systems conclude that this accuracy is
achievable, though by only a slight margin. Results of tests performed
elsewhere for two prototype systems demonstrated similar results,

achieving 3.96m for a microwave system and 3.65m for a
differential GPS satellite receiver.

The microwave alternative was found to have several
disadvantages which impact NOS operational requirements. The
system's limited range (43nm) combined with the Geometric
Dilution of Precision (GDOP) restrict the size of the survey-
able area to such a degree that it may reduce the efficiency
of a survey. Each survey area will also require multiple
shore control stations which must be located at remote points
where Third Order geodetic control has also been established.
Multipath is a potentially large error source in an over-water
environment, requiring special hardware and/or software techniques
such as dual frequency measurements and Kalman filtering to
achieve the required accuracy.

Although offering several advantages, a recent decision by
the GPS Joint Program Office to reduce the number of satellites
from 24 to 18 could limit the availability of GPS for laser
hydrography positioning. While a final constellation has not
yet been determined, the resulting increase in GDOP may restrict
the operation of the system to survey "windows" during which time
GDOP falls within acceptable bounds. The launching of these
operational satellites is not expected to begin until 1983, and the
full 18 will not be in operation until 1987. Commercial receivers
are also not yet readily available, posing both a development and
cost risk.

The proposed error budget has assumed a vertical accuracy of
1m (1 sigma) between the aircraft and the water surface. This
accuracy has been found to be achievable in studies by both the
Navy and Avco Everett using the slant range data from a similar
laser system known as HALS. In order to achieve a stand-alone
capability for the positioning subsystem, however, NOS is now
investigating the possibility of a separate altimeter.

DISTRIBUTION

Copy No.

EXTERNAL

In United States of America

Counsellor, Defence Science, Washington	No copy
Defence Research and Development Attache, Washington	1 - 2
Mr M.T. Cooper, Naval Coastal Systems Center	3
Mr D.B. Enabnit, NOAA/National Ocean Survey	4
Mr G. Ferguson, Naval Air Development Center	5
Mr G.C. Guenther, NOAA/National Ocean Survey	6
Mr M. Houck, Naval Ocean Research & Development Activity	7
Dr M.J. Miller, AVCO Everett Research Laboratories	8
CDR V.K. Nield, Defense Mapping Agency	9 - 29
Mr R.N. Swift, EG&G Washington Analytical Services	30
Dr R.W. Thomas, EG&G Inc. Bedford, Massachusetts	31
Dr M.B. White, Office of Naval Research	32

In Canada

Mr A.J. Dow, Canadian Hydrographic Service	33
Dr R. O'Neil, Canada Centre for Remote Sensing	34 - 39

In United Kingdom

Defence Scientific and Technical Representative, London	No copy
CMDR D.C. Webb, Hydrographic Department	40

In France

Mr P. Souquiere, Hydrographic & Oceanographic Service	41

In Australia

Chief Defence Scientist	42
RAN Hydrographer	43 - 44
Deputy Chief Defence Scientist	45
Controller, Projects and Analytical Studies	46
Superintendent, Science and Technology Programmes	47

Copy No.

Naval Scientific Adviser	48
Director of Naval Meteorology and Oceanographic Services	49
Director, Division of National Mapping, Department of National Resources	50
Director, Joint Intelligence Organisation (DDSTI)	51
Defence Information Services Branch (for microfilming)	52

Defence Information Services Branch for:

United Kingdom, Ministry of Defence, Defence Research Information Centre (DRIC)	53
United States, Defense Technical Information Center	54 - 65
Canada, Department of National Defence, Defence Science Information Service	66
New Zealand, Ministry of Defence	67
Australian National Library	68
Defence Library, Campbell Park	69
Library, Aeronautical Research Laboratories	70
Library, Materials Research Laboratories	71
Mr P. Reich, BDRSS	72
Mr K. Burrows, Hydrographic Service, RAN	73
CAPT M. Calder, Hydrographic Service, RAN	74
Mr J.H. Cohen, DSTO Canberra	75
COL P.R. Eddy, Army Survey Canberra	76
Mr J. Garlick, DSTO Canberra	77
CMDR P.R. Hart, Navy Office Canberra	78
Mr B.A. Murphy, Division of National Mapping	79
Mr J.E. Patterson, DIMP Canberra	80
Mr D. Pender, DSTO Canberra	81
LCDR M.W. Varley, Staff Office, Hydrography	82
LEUT M.F. Gale, Hydrographic Service, RAN	83
GPCAPT R. Green, RAAF: Aircraft Research and Development Unit	84
Dr G. Morgan, RAAF: Aircraft Research and Development Unit	85

	Copy No.
Mr L. Spaans, Surveillance Systems Group	152
DRCS Library	153 - 154
Spares	155 - 162